Summer 2017

Characterization and performance of eco and crack-free high-performance concrete for sustainable infrastructure

Iman Mehdipour

Department: Civil, Architectural and Environmental Engineering

CHARACTERIZATION AND PERFORMANCE OF ECO AND CRACK-FREE HIGH-PERFORMANCE CONCRETE FOR SUSTAINABLE INFRASTRUCTURE

by

IMAN MEHDIPOUR

A DISSERTATION

Presented to the Faculty of the Graduate School of the

MISSOURI UNIVERSITY OF SCIENCE AND TECHNOLOGY

In Partial Fulfillment of the Requirements for the Degree

DOCTOR OF PHILOSOPHY

in

CIVIL ENGINEERING

2017

Approved by

Dr. Kamal H. Khayat, Advisor
Dr. Reza Zoughi
Dr. Lesley H. Sneed
Dr. Dimitri Feys
Dr. Aditya Kumar

ABSTRACT

The main objective of this study is to develop, characterize, and validate the performance of a new class of environmentally friendly, economical, and crack-free high-performance concrete referred to as Eco and crack-free HPC that is proportioned with high content of recycle materials. Two classes of Eco-HPC are designed for: (I) pavement (Eco-Pave-Crete); and (II) bridge infrastructure (Eco-Bridge-Crete). Eco-HPC mixtures were designed to have relatively low binder content up to 350 kg/m^3 and develop high resistance to shrinkage and superior durability. A stepwise mixture design methodology was proposed to: (i) optimize binder system and aggregate skeleton to optimize packing density and flow characteristics; (ii) evaluate synergy between shrinkage mitigating materials, fibers, and moist curing duration to reduce shrinkage and enhance cracking resistance; and (iii) validate performance of Eco HPCs. The composition-reaction-property correlations were developed to link the hydration kinetics of various binder systems to material performance in fresh state (rheological properties) and hardened state (strength gain and shrinkage cracking tendency). Results indicate that it is possible to design Eco-HPC with drying shrinkage lower than 300 μstrain after 250 days and no restrained shrinkage cracking even after 55 days. Reinforced concrete beams made with Eco-Bridge-Crete containing up to 60% replacement of cement with supplementary cementitious materials and recycled steel fibers developed significantly higher flexural toughness compared to the reference concrete used for bridge applications. In parallel, autogenous crack healing capability of concrete equivalent mortar mixtures was monitored using microwave reflectometry nondestructive testing technique. Research is in progress towards analyzing life cycle assessment of Eco-HPCs under field condition.

ACKNOWLEDGMENTS

I would like to foremost, extend my sincere appreciation and gratitude to my mentor and graduate advisor, Professor Kamal H. Khayat for years of guidance, advice, support, encouragement, and friendship. I would like to express my gratitude to Professor Reza Zoughi, who provided me with the opportunity to work at Applied Microwave Nondestructive Testing Laboratory (*amntl*) and perform multidisciplinary research studies pertaining to the scope of my dissertation. I would like to sincerely thank Dr. Aditya Kumar for his constructive comments and valuable discussions on my research. I would like to thank my advisory committee members Dr. Reza Zoughi, Dr. Lesley H. Sneed, Dr. Dimitri Feys, and Dr. Aditya Kumar for their constructive comments and performing a review of my dissertation. I would like to offer my special thanks to Dr. Nicolas Ali Libre for his constructive advice and tremendous mentoring. I would also like to express my gratitude to Professor Jason Weiss and Dr. Shant Kenderian for their tremendous mentoring as parts of benefits received from of my awards.

I would like to gratefully acknowledge the many individuals and organizations that made this research project possible. I would like to acknowledge the financial support provided by Missouri Department of Transportation (MoDOT) as well as the RE-CAST (REsearch on Concrete Applications for Sustainable Transportation) Tier-1 University Transportation Center (UTC) at Missouri University of Science and Technology (Missouri S&T). Special thanks are due to Mr. Bill Stone, Mr. Brett Trautman, and Mr. David Ahlvers for their supports and insightful comments. The cooperation and support from Abigayle Sherman and Gayle Spitzmiller of the Center for Infrastructure Engineering Studies (CIES) is greatly acknowledged, in particular the assistance of Dr. Soo-Duck Hwang, Jason Cox, Zehdi Assioun, Brian Smith, John Bullock, and Gary Abbott.

In closing, from all of my heart, I would like to express my sincere appreciation and gratitude to my lovely wife, Maryam, who has enlightened my life with her love. I would like to extent my deepest appreciation to my parents, sister, and brother for their love, encouragement, and support.

TABLE OF CONTENTS

LIST OF ILLUSTRATIONS

Page

LIST OF TABLES

Page

1. INTRODUCTION

1.1. PROBLEM STATEMENT

As global demand for the use of concrete in construction applications increases progressively, the concrete industry faces the crucial challenge of finding strategies to reduce the CO_2 emissions and embodied energy associated with ordinary Portland cement (OPC) production (Hendriks et al. 1998; Worrell et al. 2001). Portland cement production results in approximately 0.87 ton of carbon dioxide for every ton of cement produced; this accounts for 5%-7% of global CO_2 emissions (Damtoft et al. 2008). The growing demands for new infrastructure, and the need for modernizing existing infrastructure and the associated cement-use has brought into question the viability and sustainability of cement-based materials for the coming decades. This is significant as legislation and climate policy are expected to substantially impact the construction sector as national governments try to meet climate change agreements. In the United States (U.S.), over 150 million tons of cement per year are used. It is estimated that 2 yd^3 of concrete per person is placed each year to support the U.S. infrastructure. Most of our concrete infrastructure is older than 20 years, and the national grand challenge of maintenance and repair is well-known. Approximately 68.5% of all the U.S. bridges are older than 25 years old and 30.8% are over 50 years old. In the area of bridges alone, according to the U.S. National Bridge Inventory (2013), there are over 605,000 bridges of which 11.7% are functionally obsolete and 14.7% are structurally deficient (ASCE 2013; Kirk and Mallett 2013).

Concrete bridge decks usually require the use of HPC due to its low permeability, high abrasion resistance, superior durability, thus extending service life. To meet such requirements, HPC implemented for bridge decks is usually characterized with relatively low water-to-cementitious material ratio (w/cm) [typically less than 0.40] and high binder content. Such features in the mixture design of HPC can inherently elevates the risk of early-age shrinkage cracking (Bentz and Jensen 2004; Holt 2001). Autogenous shrinkage is one of major causes of cracking of HPC. Cracking will occur if the strain from autogenous shrinkage exceeds the tensile strength of the concrete, especially at early-age when concrete has a low tensile strength. The shrinkage cracking in bridge decks

increases the risk of freeze-thaw damage, corrosion of reinforcing steel, and ingress of various deleterious substances. This can lead to premature deterioration and potential structural deficiencies of concrete infrastructure, thus shortening design life of structure. In 2003, a nationwide state DOTs survey conducted by the Michigan DOT (Aktan et al. 2003) on early-age bridge deck cracking issues indicated that 78% of the 31 responding states identified transverse cracking due to the drying shrinkage. Cracking, especially at early age, in HPC can result in a significant decrease in durability and service life of the concrete structures.

Therefore, in order to address the growing technical and environmental requirements for the construction of concrete transportation infrastructures, the aim of this dissertation is to develop and validate the performance of a new class of environmentally friendly and crack-free HPC which is referred to here as Eco- and crack-free HPC. Two types of Eco-HPC are of interest: (i) HPC for pavement construction (Eco-Pave-Crete); and (ii) HPC for bridge desk and transportation infrastructure construction (Eco-Bridge-Crete). Eco-Bridge-Crete can be used in cast-in-place girders, cast-in-place piers and piles, and other bridge elements. Both Eco-HPC types will be designed to ensure high resistance to shrinkage-induced cracking. The rheological properties of these advanced materials are designed to facilitate construction operations and reduce labor and cost. To reduce/limit the clinker factor of cement, a number of strategies have been practiced including: (i) optimization of aggregate proportions to enhance packing density of the granular skeleton and reduce the binder content required to fill the voids; and (ii) utilization of high volume of supplementary cementitious materials (SCMs) as a partial OPC replacement. The combined use of the aforementioned strategies has attracted substantial interest over recent years, which leads to the design and development of ecologically friendly concrete (Eco-concrete).

Table 1-1 summarizes the performance-based specifications that are considered in this research for the design of Eco and crack-free HPC mixtures targeted for various transportation infrastructure applications.

Table 1-1 Performance-based specifications for Eco-HPC mixtures.

Eco-Pave-Crete (with different workability levels)	
Binder content	320 kg/m^3
Slump (without fibers)	50 ± 25 mm
Slump (with fibers)	100 ± 25 mm
Compressive strength at 56 days	≥ 35MPa
Drying shrinkage after 120 days (7-d moist curing)	≤ 300 μstrain
Restrained shrinkage cracking potential	Low (time-to-cracking > 28days according to ASTM C1581)
Durability (frost and abrasion resistance)	High (durability factor higher than 70% after 300 freeze-thaw cycles according to ASTM C666)
Eco-Bridge-Crete (with different workability levels)	
Binder content	350 kg/m^3
Slump (without fibers)	100 ± 25 mm
Slump (with fibers)	200 ± 25 mm
Compressive strength at 56 days	40 to 50 MPa
Drying shrinkage after 120 days (7-d moist curing)	≤ 300 μstrain
Restrained shrinkage cracking potential	Low (time-to-cracking > 28days according to ASTM C1581)
Durability (frost, corrosion, and abrasion resistance)	High (durability factor higher than 70% after 300 freeze-thaw cycles according to ASTM C666)

1.2. RESEARCH OBJECTIVES

The primary objective of this dissertation is to provide new insights into possibilities of extended supplementary cementitious martial (SCM) replacements and reduced cement content, as well as enhanced early-age cracking resistance in high-performance concrete targeted for various transportation infrastructures. An extensive investigation involving laboratory material performance evaluation and large-scale testing was carried out to analyze the interaction between concrete material constituents to develop the mixture design methodology and validate the material performance under reinforced large-scale elements. The specific objectives of this dissertation are described as follows:

- Elucidate the role of SCMs in designing more environmentally friendly binder systems to reduce environmental impacts, while maintaining equivalent performance to that of the plain OPC system.

- Establish composition-reaction-property correlations to link the characteristics of the precursor materials to the development of fresh and hardened properties which can be utilized to proportion more environmentally friendly binders with a reduced cement content.
- Optimize granular skeleton and characteristics based on packing density approach to achieve dense particle packing and reduce paste volume required to fill the voids.
- Explore the synergistic effects between various shrinkage mitigating materials, including shrinkage reducing admixture (SRA), expansive agent (EX), lightweight sand (LWS) for internal curing, and fibers to reduce shrinkage and enhance shrinkage cracking resistance of cementing systems.
- Develop Eco and crack-free HPC made with relatively low binder content, high shrinkage cracking resistance, and various workability levels targeted for transportation infrastructure applications.
- Validate the performance (i.e., shrinkage deformation and structural performance) of Eco and crack-free HPC under reinforced large-scale elements.
- Develop novel and reliable nondestructive testing (NDT) technique to evaluate the distribution of fibers in concrete and link the results to the material performance in the hardened state.
- Evaluate and monitor the crack-healing capability of optimized binders to deliver crack-free properties in cracked cementing system.

1.3. OUTLINE OF THE DISSERTATION

This dissertation consists of 10 sections and two appendices, which are described in detail below:

Section 2 reviews the current state-of-the-art on the relevant topics such as recent advances in the role of SCMs in sustainable concrete, particle packing characteristics of granular materials, shrinkage mitigating materials to reduce shrinkage and enhance shrinkage cracking resistance. The state-of-the-art review has been submitted to *"Construction and Building Materials"*.

Section 3 elucidates the impact of SCMs to develop and formulate sustainable binder systems for various infrastructure construction applications. Focus is placed to evaluate the effect of various binary and ternary SCMs on packing density of the binder, optimum water demand needed to achieve maximum wet density, and compressive strength development of the cement paste. The coupled effect of dispersion state of binder and SCM replacement on packing density and compressive strength of paste suspensions are examined. Further the effect of particle-size distribution and specific surface area of different binary and ternary binder systems on the flow characteristics, packing density of binder and compressive strength development of cement paste are examined. The grading models such as the modified Andreasen and Andersen (A&A), Rosin–Rammler (R–R), and power law models are implemented to identify the ideal particle-size distribution of binder system needed to achieve high packing density, while maintaining relatively low water demand. The results derived from this section have been published in two journal articles in *"ACI Materials Journal"* and *"Cement and Concrete Composites"*.

Section 4 explores fundamental composition-reaction-property correlations in blended binders prepared with PLC, OPC, and SCMs. Focus is given to link the characteristics of the precursor materials to the resultant reactivity, and the development of properties in fresh state (i.e., rheological properties and structural recovery) as well as hardened state (i.e., compressive strength). Outcomes of this work provide novel and reliable means to link the characteristics of the precursor materials to the development of fresh and hardened properties which can be utilized to proportion more environmentally friendly binders with a reduced cement content. The results obtained from this section have been published in one journal articles in *"Materials & Design"*.

Section 5 investigates the physico-mechanical characteristics of cementitious suspensions over transition from dense concentrated to flow onset. This study employs a set of experimental assessments coupled with microstructural simulations to elucidate the effects of w/cm, that characterizes water film thickness covering solid particles, and SCMs on particle packing, rheology, and strength development of cement suspensions at two different states: (i) optimum water demand (OWD) to achieve maximum solid concentration (i.e., concentrated state); and (ii) minimum water demand (MWD) to

initiate flow (i.e., flow onset state). The results will be submitted to the journal *"Cement and Concrete Composites"*.

Section 6 aims at evaluating the effect of solid characteristics on packing density of granular skeleton. This section deals with experimentally optimizing the volumetric proportions of aggregates to achieve the maximum possible packing density. In order to determine the optimum proportioning of aggregate blend, the statistical mixture design (SMD) method is utilized.

Section 7 explores the synergistic interaction between shrinkage mitigating materials, in particular the coupled effect of shrinkage reducing admixture, moist curing, or lightweight sand on autogenous and drying shrinkage as well as compressive strength evolution of expansive agents is evaluated. The results obtained from this section have been submitted to *"Cement and Concrete Composites"* and *"Materials and Structures"*.

Section 8 uses the knowledge and results obtained from pervious sections to design and develop Eco and crack-free HPC mixtures designated for various transportation infrastructure applications. The first part of this section examines the role of SCMs' compositions on compaction behavior, shrinkage, and restrained shrinkage cracking. A focus is placed to link the hydration kinetics of binder systems to shrinkage cracking resistance and tensile creep behavior of Eco-concrete. The second phase aimed at validating the performance of Eco and crack-free HPC mixtures targeted for different construction applications. A number of parameters affecting concrete characteristics are investigated, including binder type and content, fiber type, and use of shrinkage mitigating materials. The results have been submitted to *"Journal of Materials in Civil Engineering"*.

Section 9 discusses the validation of performance of optimized Eco-HPCs in large-scale elements. Emphasis is placed to evaluate the shrinkage deformation of slab sections and flexural performance of reinforced concrete beams made with optimized Eco-Bridge-Crete. The demonstration projects provide insights into the applicability of the developed Eco and crack-free mixtures for practical purposes.

Section 10 finally summarizes the outcomes and findings of the present dissertation, and proposes the perspectives for future studies.

Appendix A studies nondestructively the distribution of steel fibers in cementitious suspensions using two different approaches: (i) near-field microwave reflectometry and (ii) active microwave thermography. The results of such NDT techniques are supported digital image analysis and material performance in the hardened state. The results have been published in two journal articles *"Journal of Materials in Civil Engineering"* and *"Materials and Structures"*.

Appendix B evaluates the crack healing capability of optimized binders to deliver crack-free properties. Microwave near-field reflectometry technique is applied to monitor the crack healing evolution of such advanced binder systems. An independent set of experimental assessments, including water capillary absorption, crack healing quantification, as well as X-ray diffraction and scanning electron microscopy are used to corroborate the results derived from microwave measurements. The results have been submitted to the journal *"Cement and Concrete Composites"*.

The outline of this dissertation focusing on design and development of Eco and crack-free HPC is presented in Figure 1-1.

1.4. LIST OF PUBLICATIONS/SUBMISSIONS AND AWARDS

Peer-reviewed Journal Articles

[1] I. Mehdipour, A. Kumar, K.H. Khayat, "Rheology, Hydration, and Strength Evolution of Interground Limestone Cement Containing PCE Dispersant and High Volume Supplementary Cementitious Materials", Materials & Design, 127 (2017) 54–66.

[2] I. Mehdipour, K.H. Khayat, "Effect of Particle-Size Distribution and Specific Surface Area of Different Binder Systems on Packing Density and Flow Characteristics of Cement Paste", Cement and Concrete Composites, 78 (2017) 120–131.

[3] I. Mehdipour, M. Horst, R. Zoughi, K.H. Khayat, "Use of Near-Field Microwave Reflectometry to Evaluate Steel Fiber Distribution in Cement-Based Mortars", Journal of Materials in Civil Engineering, 1–12.

[4] I. Mehdipour, K.H. Khayat, "Effect of SCM Content and Binder Dispersion on Packing Density and Compressive Strength of Sustainable Cement Paste", ACI Materials Journal, 113 (3) (2016) 361–372.

[5] A. Foudazi, I. Mehdipour, K.M. Donnell, K.H. Khayat, "Evaluation of Steel Fiber Distribution in Cement-Based Mortars Using Active Microwave Thermography", Materials and Structures, 49 (12) (2016) 5051–5065.

[6] I. Mehdipour, K.H. Khayat, "Enhancing the Performance of Calcium Sulfoaluminate Blended Cements with Shrinkage Reducing Admixture or Lightweight Sand" (Revision submitted to Cement and Concrete Composites).

[7] I. Mehdipour, K.H. Khayat, "Synergistic Effect of Moist Curing and Shrinkage Reducing Admixture on Expansion and Strength Evolution of Calcium Sulfoaluminate Blended Cement" (Under review in Materials and Structures).

[8] I. Mehdipour, R. Zoughi, K.H. Khayat, "Feasibility of using Near-Field Microwave Reflectometry for Monitoring Autogenous Crack Healing in Cementitious Materials" (Under review in Cement and Concrete Composites).

[9] I. Mehdipour, K.H. Khayat, "Elucidating the Role of Supplementary Cementitious Materials on Shrinkage and Restrained Shrinkage Cracking of Flowable Eco-Concrete" (Under review in Journal of Materials in Civil Engineering).

[10] I. Mehdipour, K.H. Khayat, "Understanding the Role of Particle Packing Characteristics in Rheo-Physical Properties of Cementitious Suspensions: A Literature Review" (Under review in Construction and Building Materials).

[11] I. Mehdipour, K.H. Khayat, "Physico-mechanical Characteristics of Cement Paste over Transition from Concentrated to Flow State: The Role of Supplementary Cementitious Materials" (To be submitted to Cement and Concrete composite).

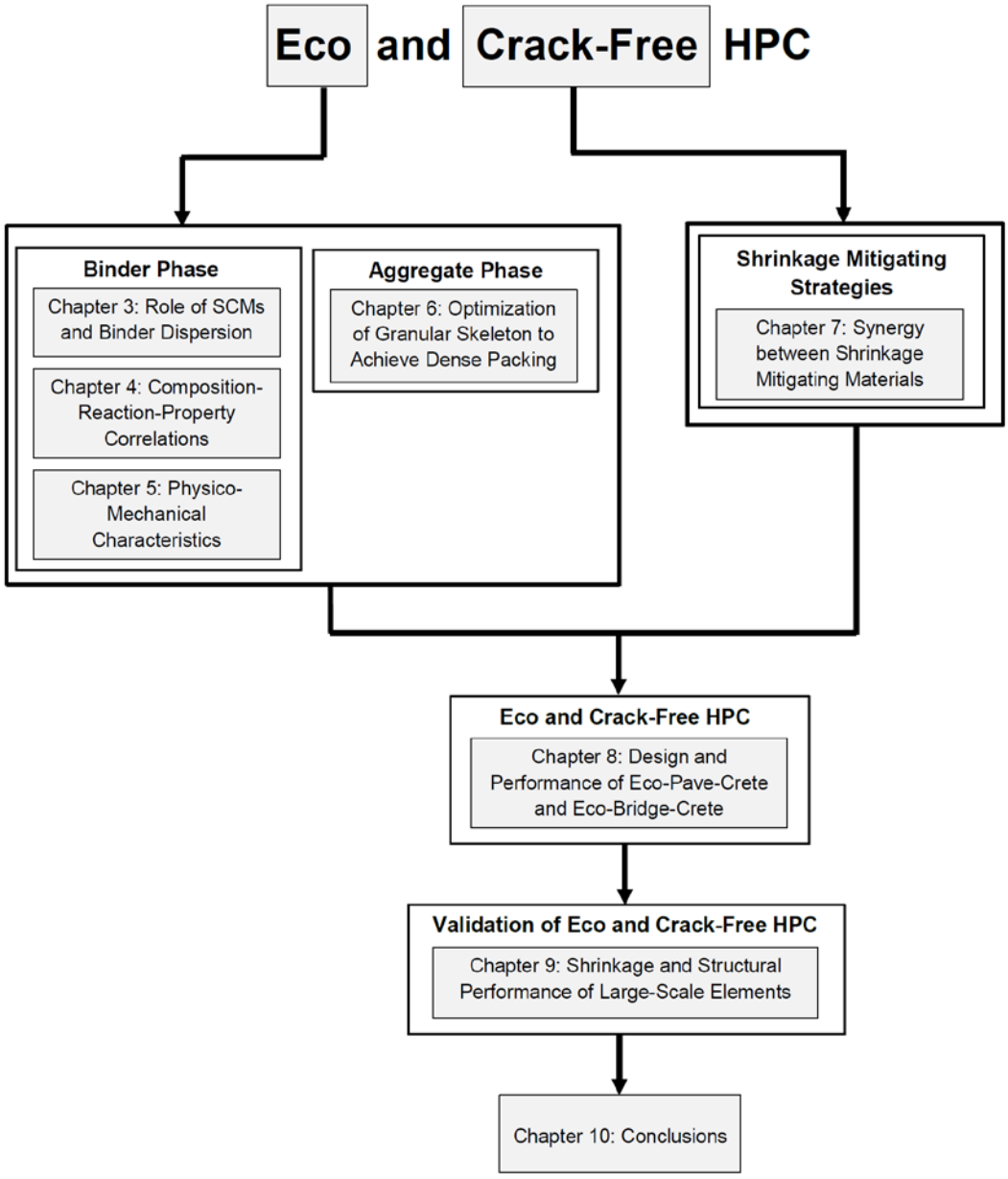

Figure 1-1 Outline of the dissertation.

Refereed Conference Proceedings

[1] I. Mehdipour, N.A. Libre, K.H. Khayat, "Development of Eco-Friendly Superworkable Concrete Using Particle Packing Mix Design Methodology" Presented at American Concrete Institute (ACI) convention, Open Topic Session, Milwaukee, WI, April 17-21, 2016.

[2] I. Mehdipour, R. Zoughi, K. Khayat, “Monitoring of Self-Healing Capability in Cement-Based Mortar Using Near-Field Microwave Reflectometry—Preliminary Results,” Presented at the 25th American Society for Nondestructive Testing (ASNT) Spring Research Symposium, New Orleans, LA, April 11-14, 2016.

[3] I. Mehdipour, K.H. Khayat, “Shrinkage Mitigating Strategies for Low Shrinkage Self-Consolidating Concrete”, 6th North American Conference on Design and Use of Self-Consolidating Concrete, Washington, DC, May 15-18, 2016.

[4] K.H. Khayat, I. Mehdipour, “Optimization of Binder Compositions to Design Ecological Concrete: Wet Packing Density Approach”, ECO-CRETE, International Symposium on Sustainability, Iceland, August 13-15, 2014.

[5] I. Mehdipour, M. Horst, B. Conley, R. Zoughi, K.H. Khayat, “Determination of Steel Fiber Distribution in Cement-Based Materials Using Near-Field Microwave Method”, Presented at the 24th ASNT Research Symposium, California, USA, March 2015, pp. 164-165.

[6] A. Foudazi, I. Mehdipour, K.M. Donnell, K.H. Khayat, “Detection of Steel Fibers in Cement-Based Materials by Active Microwave Thermography”,14th International Symposium on Nondestructive Characterization of Materials, Marina del Rey California, June 22-26, 2015, pp. 22-26.

Technical Reports

[1] K.H. Khayat, I. Mehdipour, Economical and Crack-Free High Performance Concrete for Pavement and Transportation Infrastructure Constructions, Missouri Department of Transportation (MoDOT) and RE-CAST (REsearch on Concrete Applications for Sustainable Transportation) Tier-1 University Transportation Center (UTC), (No. TR2015-03), 2017.

[2] K.H. Khayat, I. Mehdipour, Design and Performance of Crack-Free Environmentally Friendly Concrete “Crack-Free Eco-Crete”, National University Transportation Center, (No. NUTC R322), 2014.

Awards and Honors

2017 ASNT Student Travel Grant for 26th ASNT Research Symposium

2016 ACI Charles Pankow Fellowship, American Concrete Institute

2016 ASNT Student Travel Grant for 25th ASNT Research Symposium

2015 Honorary DJ Belarbi Graduate Scholarship Award, American Concrete Institute Missouri Chapter

2015 ASNT Student Travel Grant for 24th ASNT Research Symposium

2. LITERATURE REVIEW

2.1. INTRODUCTION

The mixture design of high-performance concrete (HPC) is typically characterized by relatively high binder content and use of SCMs and/or fillers and low water-to-cementitious materials ratio (w/cm). High binder content is necessary to ensure high strength and durability. In case of highly flowable HPC, such as self-consolidating concrete (SCC), a high paste volume is also required to increase flowability, which typically ranges between 400 to 550 kg/m^3.

As global demand for concrete increases incessantly, the concrete industry faces the crucial challenge of finding ways to reduce the carbon footprint and embodied energy associated with OPC production (Worrell et al. 2001). In response to this challenge, the use of low-clinker factor cements has been thought as a means to a reduced CO_2 footprint material. One way of achieving this is through the use of SCMs or fillers, such as fly ash, blast furnace slag, silica fume, metakaolin, and limestone. The practical interest of incorporating SCMs is stemming efforts to reduce the clinker factor of OPC. This led to a reduction in clinker in cement from 85% in 2003 to 77% in 2010, and it is projected to further decrease to 71% in the future (Schneider et al. 2011).

Figure 2-1demonstartes how the proportioning of OPC changed over time to use cements combined with other by-product materials. For example, Holcim company achieved in 2010 an average specific CO_2 emission per ton of cement which was 20% lower compared to 1990 (Schneider et al. 2011). SCMs have been widely incorporated to reduce cement fractions while maintaining or sometimes even improving rheology, mechanical properties, and durability of binders (Bouzoubaa and Lachemi 2001; Lothenbach et al. 2011; Mehdipour et al. 2013, 2016; Nehdi et al. 2004; Toutanji et al. 2004). Such improvements in properties despite reduced cement contents are due to physico-chemical interactions between SCMs and the OPC-paste components.

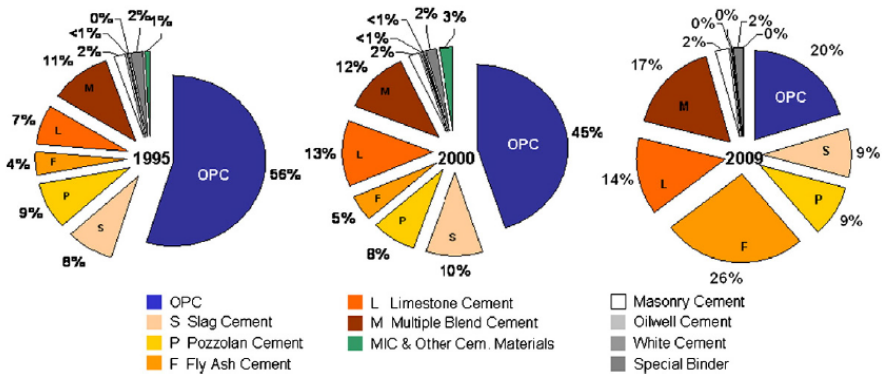

Figure 2-1 Timeline of cement types produced by Holcim adapted from Schneider et al., 2011.

An essential step in designing Eco-HPC is to enhance the packing density of the granular skeleton. For a given paste volume, an increase in aggregate packing density can improve workability due to the increase in excess paste film thickness surrounding the aggregate particles. The use of grading models and theoretical packing density models are effective tools to reduce a number of experimentally packing measurements, especially in the case of selection of two or three aggregate blends from a pool of different aggregates to reach a maximum packing density. The particle-size distribution (PSD) of aggregate significantly affects the packing density of the aggregate skeleton. In addition to the packing density, the PSD can affect the specific surface area (SSA) of the granular skeleton that needs to be coated with paste volume. A higher SSA of the granular skeleton can result in a reduction in paste film thickness surrounding the solid particles, thus leading to a lower workability or higher water/admixture demand for a given consistency (Li and Kwan 2013).

The use of relatively high binder content and low w/cm in HPC can inherently elevate the risk of early-age shrinkage cracking (Bentz and Jensen 2004; Holt 2001). Autogenous shrinkage is one of major causes of cracking of HPC. Cracking will occur if the strain from autogenous shrinkage exceeds the tensile strength of the concrete, especially at early-age when concrete has a low tensile strength. The shrinkage cracking in bridge decks increases the risk of freeze-thaw damage, corrosion of reinforcing steel, and ingress of various deleterious substances. This can lead to premature deterioration and potential structural deficiencies of concrete infrastructure, thus shortening design life

of structure. The cracking potential of concrete depends on the mechanical properties and visco-elastic properties of the mixture. These characteristics are related to the mixture design and constitutive materials. A number of parameters can influence the shrinkage cracking potential of concrete, including mix design, binder type and content, fiber type and volume, and the use of shrinkage reducing materials.

Based on the aforementioned parameters, which can significantly affect the mixture design and selection of material constituents of crack-free Eco-Crete, the literature review undertaken in this investigation consisted of:

- Reviewing the impact of SCMs on packing density, workability, rheology, shrinkage, and mechanical properties, as well as durability.
- Reviewing the effect of aggregate characteristics, including shape, texture, and particle size distribution on packing density, rheology, stability, and mechanical and transport properties.
- Addressing factors and shrinkage mitigating materials influencing autogenous, drying, and restrained shrinkage, as well as shrinkage cracking tendency of cement-based materials.

2.2. SUPPLEMENTARY CEMENTITIOUS MATERIALS

Cement production is currently facing two main challenges: reduction of the environmental impact of cement and increasing its availability. Clinker substitution is a promising strategy to solve both issues. A part of the clinker is replaced by alternative materials, called Supplementary Cementitious Materials (SCMs). SCMs, such as fly ash (FA), blast furnace slag (SL), silica fume (SF), and natural pozzolans, are commonly used as a replacement for a portion of Portland cement in concrete. Energy consumption and embodied CO_2 of concrete can be reduced when cement is replaced by secondary materials, such as co-products from other industries. This strategy can indeed be used to reduce the carbon footprint of the construction materials as well as the life cycle cost for the structure. Depending on their physical properties (particle gradation and shape) or chemical composition, SCMs will have either hydraulic activity and/or a pozzolanic activity. SCMs, such as coal fly ash, blast-furnace slag, and silica fume, are typically composed of calcium oxide (CaO), silicon dioxide (SiO_2), and aluminum oxide (Al_2O_3)

(Juenger and Siddique 2015; Lothenbach et al. 2011), and therefore, represent compositions that are similar to that of OPC. Selected studies have demonstrated excellent properties of concrete designed with relatively high levels (i.e., 10%–70%) of OPC replacement by SCMs (Bouzoubaa and Lachemi 2001; Lothenbach et al. 2011; Mehdipour et al. 2013, 2016; Nehdi et al. 2004; Toutanji et al. 2004). Such improvements in properties despite reduced cement contents are due to chemical reactions between SCMs and the OPC-paste components. More specifically, in systems (i.e., pastes or concrete) prepared with OPC replaced partially by SCM, the silica and alumina present in the latter undergo chemical reactions with aqueous species and phases present in the paste. SiO_2 reacts with calcium hydroxide (i.e., CH: a hydration product present in the paste) to form space-filling pozzolanic calcium-silicate-hydrate (C-S-H) gel - the glue in concrete which binds solid phases together. In addition, Al2O3 reacts with aqueous calcium and silicate species to form crystalline calcium-aluminate (i.e., hydrogarnet: C3AH6) and calcium aluminosilicate (i.e., stratlingite: C2ASH8) hydrates. The formation of pozzolanic C-S-H results in significant microstructural improvements, including: (i) improved solid-to-solid phase connectivity, (ii) reduced porosity, (iii) reduced pore-to-pore connectivity, and, therefore, (iv) higher strength and (v) lower permeability (Antoni et al. 2012; Juenger and Siddique 2015; Lothenbach et al. 2011).

2.2.1. Effect of SCMs on Fresh Properties. This is discussed below.

2.2.1.1 Workability and rheological properties. The effectiveness of incorporating SCMs to enhance workability and rheology is affected by the type and content of the SCM. The FA, SL, and SF are mostly used as a SCM in concrete. Given the spherical shape and smooth surface characteristics of FA, the partial replacement of cement with FA can reduce the friction between particles, thus enhancing the rheology and flow characteristics. For a given cementitious material content, partial substitution of cement with FA, by mass, results in an increase in the paste volume due to the lower specific gravity of FA compared to Portland cement. The higher paste volume provides greater lubricant volume to the concrete, thus enhancing flow characteristics of concrete. Lee et al. (2003) reported that the fluidity of a cement paste made with 20% Class F FA (FFA) can increase by about 50% as the spread between the minimum and maximum size of particles becomes greater. Kwan and Chen (2013) reported that for a given w/cm, the

flow-spread and flow rate of grout mixtures increase as the FA content increases up to 40%. Shi et al. (2002) pointed out that the addition of SF could have a beneficial or adverse effect on the rheology of concrete, depending on the replacement level of the SF. They found the use of 6% SF leads to a considerable reduction in plastic viscosity (40%) and yield stress (80%) of mortar mixtures. However, the substitution of cement with 12% SF resulted in a 30% and 20% increase in yield stress and plastic viscosity, respectively, compared to the control mortar made with 100% cement.

Hwang and Khayat (2006) found that regardless of the type of high-range water reducer (HRWR), concrete equivalent mortars (CEM) made with ternary blends of 25% SL and 5% SF is shown to require lower minimum water demand compared to the control mixture made with 100% ordinary Portland cement (OPC). The investigated mixtures had w/cm varying between 0.35 and 0.42 and binder content of 475 kg/m^3. This can be due to greater packing density and less water adsorption of such blended cement compared to Portland cement. Khayat et al. (2008) investigated the effect of various types of SCMs on plastic viscosity and yield stress for grout mixtures made with w/cm of 0.40. Their results showed that the partial replacement of cement by FA, SF or SL increased the plastic viscosity, regardless of the dosage of HRWR. In the case of ternary systems, the combination of 20% FA with 40% SL resulted in the highest increase in viscosity (90%) among the tested mixtures. Assaad and Khayat (2004) evaluated the effect of binder type and binder content on degree of thixotropy of self-consolidating concrete (SCC). The investigated mixtures had 650 ± 15 mm slump flow values, a w/cm of 0.46, and a binder content ranging between 400 and 550 kg/m^3. The tested binder types included Type I and Type III cements along with three blended cements. The investigated blended binders included: a binary cement containing 8% SF and 92% Type I cement; a ternary cement made with 6% SF, 22% Class F FA, and 72% Type I cement; and a quaternary cement containing 6% SF, 28% FA, 16% SL, and 50% Type I cement. For a given binder content, the degree of thixotropy is shown to be significantly affected by the type of binder; mixtures made with Type III cement exhibit a greater degree of thixotropy compared to those prepared with binary or ternary cement. On the other hand, SCC made with a quaternary cement containing 50% SCM or those with Type I cement without any SCM exhibit a lower degree of thixotropy. For a given binder type, the degree of

thixotropy is shown to increase with a decrease in the binder content. This is attributed to the relative increase in the coarse aggregate volume which can result in a higher level of internal friction between particles.

El-Chabib and Syed (2012) conducted an extensive experimental study to develop a high-performance SCC containing high volume of SCMs. In total, 20 SCC mixtures were prepared with 0.37 w/cm and a binder content of 450 kg/m^3. Mixtures were designed to have up to 70% of Portland cement replaced by cementitious materials such as Class C and Class F FA (30% to 70%), SL (30% to 70%), and SF (5% to 15%). The fresh characteristics, such as flowability, deformability, filling capacity, air content, and segregation resistance of SCC mixtures were evaluated. Mixtures containing 70% of FA and SL (70%) yielded 25% lower HRWR required for a given slump flow compared to the control mixture with 100% cement. Increasing the content of SF from 5% to 10% and 15% resulted in an increase in the dosage of HRWR from 1.31 to 1.37 l/m^3 and 1.43 l/m^3, respectively. Given relatively high surface area of the SF, the mixture containing SF particles exhibited lower bleeding and aggregate segregation compared to other types of SCMs. Ahari et al. (2015) evaluated the rheological properties of SCC containing various amounts of SF (4%, 8%, and 12%), FA (18% and 36%), Metakaolin (MK) at 4%, 8%, 18%, and 36%, and SL (18%) as a partial replacement of cement with various w/cm ranging between 0.44 and 0.56. These SCMs were used in binary, ternary, and quaternary cementitious blends to investigate the variations of some properties, such as HRWR demand and rheological properties. For all w/cm, mixtures containing SF and MK had higher HRWR demand for a given slump flow compared to the other SCMs. Plastic viscosity of the mixtures containing FA and MK was higher than that of the control mixtures, regardless of the w/cm. The highest increase (90%) in plastic viscosity was observed in mixture containing 36% MK and w/cm of 0.50. Among the investigated SCMs, the incorporation of SF has a more significant influence on the viscosity compared to the MK at the same level of cement replacement.

Portland limestone cement (PLC) has recently been approved as a part of the ASTM C595 specifications. These cements are designed to enable more sustainable concrete production by replacing up to 15% of the clinker with interground limestone particles. The use of PLC enables a reduction in CO_2 embodied in the built infrastructure

and extends the life of limestone quarries (Tennis et al., 2011). Based on the information provided in the literature, it appears that there are conflicting results on the role of PLC on workability (Tennis et al., 2011). In general, the degree of fineness of the limestone is the main factor affecting the workability of concrete. The results of literature review undertaken by Tennis et al. (2011) and Barrett et al. (2013) suggest that the use of limestone may alter the water demand, resulting in a slight increase or decrease when PLC is compared to conventional cement. Tsivilis et al. (1999, 2000) investigated the water demand of mortar and concrete containing various replacement levels of cement with limestone (0, 10%, 15%, and 20% limestone). They observed that the use of limestone cement increased the water demand necessary for a given slump value, especially in the case of higher limestone replacement. Ghezal and Khayat (2002) employed response surface method to optimize the mix design of SCC containing limestone filler. The investigated mixtures had various water-to-powder ratios (w/p) of 0.38 to 0.72, cement contents of 250 to 400 kg/m^3, limestone filler additions of 0 to 120 kg/m^3, and HRWR dosages of 0.12% to 0.75% by powder mass. The replacement of 100 kg/m³ of cement with finely ground limestone filler is shown to improve deformability and stability. The increase in limestone filler content was found to reduce the HRWR demand to secure a given deformability, thus leading to producing cost effective SCC. Mixtures containing approximately 300 kg/m^3 of Type I cement and 100 kg/m^3 of limestone filler with Blaine fineness of 565 m^2/kg were found to secure good overall performance. Based on the derived statistical models, concrete made with fine limestone filler as a cement replacement can exhibit up to 10% lower 28-day strength compared with similar concrete without filler.

In general, it has been reported that the influence of limestone on setting time is strongly related to the fineness of the limestone. As the limestone was ground finer, the setting time decreased (Hooton et al. 2007). Mounanga et al. (2010) reported that limestone filler could be used to reduce the setting time for concrete systems containing FA and SL. The partial substitution of cement by limestone can provide a synergistic effect on the rate of hydration and setting time of concrete made with relatively high SCM replacement. Ezziane et al. (2010) also reported that limestone additions to Portland

cement in mortars provided nucleation sites which accelerated hydration according to the Vicat testing results.

2.2.1.2 Packing density of binder system. Optimization of PSD in cement–SCM–filler systems is an approach that is used to design environmentally friendly concrete to optimize the granular skeleton of the powder phase and enhance the rheological properties. Given the higher specific surface area of binder materials compared to other material constituents of concrete, they have substantial influence on water and HRWR demands. The optimization of packing characteristics of binders can reduce the water demand, thus resulting in a reduction in binder content required for a given performance of concrete. For example, Bentz et al. (2012) measured rheological properties of cement–fly ash paste mixtures with different PSD of the FA. They found that yield stress of cement paste is related to particle density of cement and plastic viscosity is related to particle surface area and packing density of the binder. Vance et al. (2013) reported that the rheological properties of paste mixtures containing various types and replacement levels of SCMs, such as limestone filler, MK, and FA depends on total particle specific surface area.

Lange et al. (1997) reported that improving the packing density of the cementitious materials by partially replacing cement with fine SL can significantly reduce the water demand and enhance the overall performance of concrete. Kwan and Wong (2008) concluded that there exists an optimum content of the SF replacement, beyond which the packing density of the binders decreases. The partial replacement of cement with 45% SF exhibited the packing density of 0.67 compared to 0.72 for similar binder containing 30% SF. Zhang et al. (2011 and 2012) reported that a ternary combination of 35% SL and 40% FFA is shown to have 10% higher packing density compared to the control mixture made with 100% cement, thus leading to higher flow characteristics. Kwan and Wong (2008) reported that the ternary blends of cement with FA and SF can significantly enhance the wet packing density of cement paste mixtures. The variation of the packing density with the mix proportions of the ternary cementitious materials is illustrated in Figure 2-2 (Kwan and Wong, 2008). Their results showed that, the ternary blends of 25% cement, 45% FA, and 30% SF exhibited the highest packing density of 0.75 among all investigated binary and ternary systems. The improvement in

packing density of the binder can be attributed to the spherical shape effect of the FA and filling and shape effects of SF which can result in a decrease in the friction between particles and filling the voids between cement grains. Similarly, Amini et al. (2016) pointed out that the partial substitution of cement by FA or MK significantly improved the packing density of the binder system. Knop et al. (2014) investigated the influence of PSD and substitution of limestone powder as partial replacement for Portland cement on packing density and water demand for normal consistency of limestone cement. For a given replacement level of limestone, blended limestone cement with finer particles (3 μm) is shown to require higher water demand to achieve normal consistency compared to the larger particles (53 μm). Depending on the PSD of limestone powder from 3 μm to 53 μm, the increase in the replacement level of limestone from 0 to 20% resulted in 1% to 7% higher packing density compared to the mixture made with 100% OPC (Knop et al., 2014).

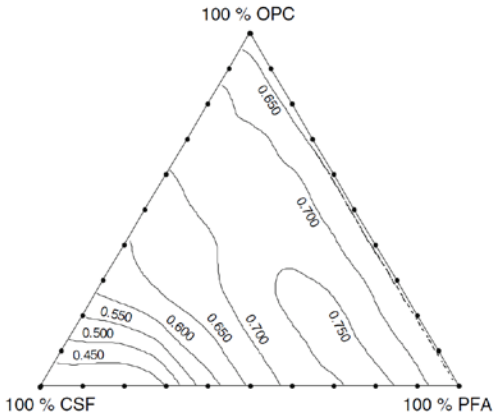

Figure 2-2 Effect of SCM substitutions on packing density of ternary binders (Kwan and Wong, 2008).

2.2.2. Effect of SCMs on Hardened Properties. This is discussed below.

2.2.2.1 Mechanical properties. In general, SCMs can contribute to long-term strength of concrete due to the pozzolanic reaction. Mixtures made with Class F FA exhibit slower strength development than similar mixtures prepared with only Portland cement. The 28-day mechanical properties may be lower for concrete containing FA, particularly Class F FA, however, pozzolanic reaction of FA continues over time, and the

long-term strength of FA concrete can be the same as those of similar concrete mixtures made with 100% Portland cement (Lawler et al., 2007). Depending on the mixture proportions, chemical composition, and Blain fineness, some FAs may require up to 90 days to exceed a 28-day strength of control mixture containing 100% OPC. Jaturapitakkul et al. (2004) compared the compressive strength of concrete made with coarse FA particles (90-100 μm) with those of concrete made with fine FA (3.8 μm). Concrete mixtures prepared with 15% to 50% fine FA can achieve 10% to 30% higher compressive strength compared to concrete mixture containing coarse FA at the same replacement level. Concrete proportioned with Class C FA generally develops higher early-age strength than concrete with Class F FA (Kosmatka and Panarese, 2002, Uysal and Akyuncu, 2012). However, at later ages (beyond 28 days), concrete made with Class C FA may exhibit lower strength development compared to concrete containing Class F FA. El-Chabib and Syed (2012) reported that the partial replacement of cement by 60% Class C FA or by up to 70% of SL developed a 28-day compressive strength slightly lower than or comparable to the control SCC made with 100% OPC. Such mixtures exhibited a 1-day compressive strength of 5 MPa and 9.5 MPa, respectively, compared to 26 MPa for the control mixture.

Ternary cementitious blends of SF or SL with FA can be used to enhance the rate of strength development at early-age. Khayat et al. (2008) reported that the combination of 3% SF with either 10% or 20% FA resulted in 5% to 30% higher 28-day strength compared to the reference grout made with 100% cement and w/cm of 0.40. Hwang and Khayat (2009) pointed out that for SCC mixtures made w/cm of 0.35 and 0.42, the use of 25% SL and 5% SF resulted in 15% to 22% higher compressive strength at 28 days compared to those prepared with 25% Class F FA and 5% SF. This can be due to the relatively high reactivity of the SL compared to the FA. The modulus of elasticity results of such mixtures made with various binder combinations had similar trends as those of compressive strength results for both of w/cm of 0.35 and 0.42. Kuder et al. (2012) investigated the binary and ternary blends of Class C FA and SL on compressive strength of SCC made with a binder content of 410 kg/m^3. Ternary mixtures with 60% SCMs replacement, containing the combination of 25% FA and 75% SL or 50% FA and 50% SL exhibited higher compressive strength than both FA and SL binary mixtures and

developed similar strength to that of the control mixture made with 100% OPC. This is due to the synergetic effect of the combination of SL and FA in the ternary binder, which enhances engineering advantages over a simple binary system and produces more sustainable concrete mixtures.

The strength of concrete produced with PLC is significantly affected by several factors, including the quality and quantity of the limestone, the clinker and other cement ingredients, and the PSD of the blended cement (Tennis et al., 2011). Limestone contents up to 15% may increase early-age strength as a combined result of improving particle packing (Sprung and Siebel 1991), increasing the rate of cement hydration (Vuk et al. 2001; Bonavetti et al. 2003), and production of calcium carboaluminate (Voglis et al. 2005). Barrett et al. (2013) investigated the mechanical properties of concrete mixtures made with PLC and a w/cm varying between 0.38 and 0.46. In general, the PLC mixtures exhibited higher compressive strength at early age that diminished with time, thus resulting in similar 28-day compressive strength as that of the control mixture made with OPC. The flexural strength of the PLCs at 7 days of age was similar to the OPCs at all evaluated w/cm. The replacement of PLC with 20% FA resulted in 10% higher compressive strength at early-age compared to the similar mixture made with OPC and FA. This suggests that the relative high rate of hydration of PLC is able to overcome the slow early-age reaction of mixtures containing FA, thus leading to higher compressive strength at early ages (Barrett et al., 2013).

2.2.2.2 Durability and transport properties. The use of proper type and content of SCMs can fill the voids among cement particles and enhance the density of the microstructure, thus leading to better durability. In general, SCMs can react with calcium hydroxide to form hydration products which can reduce the connectivity of the capillary pores in the concrete, thus leading to refinement of pore structure and enhancement in transport properties. El-Chabib and Syed (2012) reported that SCC mixtures made with binary or ternary blends of SL and/or SF exhibited rapid chloride-ion permeability (RCP) values of 250 to 2100 Coulomb compared to 3700 Coulomb for the control mixture at 56 days. SCC containing 60% Class F FA also showed RCP value of 1510 Coulomb at 56 days. The greatest resistance to chloride ion penetration was observed for ternary blends of 30% Class F FA, 30% SL, and 10% SF with RCP value of 200 Coulomb at 56 days.

Şahmaran et al. (2009) reported that regardless of FA type, SCC mixtures containing FA exhibited lower chloride-ion migration compared to similar mixtures made with 100% cement. Their results also indicated that sorptivity of the concretes containing Class C and Class F FAs decreased with the increase in FA content. Hwang and Khayat (2009) pointed out that for SCC mixtures made with a binder content of 475 kg/m^3 and a w/cm of 0.35 and 0.42, the use of the quaternary blend of FA, SL, and SF resulted in substantial reduction in capillary porosity and critical pore diameter. This can be due to the greater synergistic effect of using three SCMs.

Yurdakul et al. (2013) investigated the influence of SCMs on electrical resistivity of concrete mixtures made with a binder content of 356 kg/m^3 and w/cm of 0.40 and 0.45. For a given w/cm, the increase in the replacement level of Class F FA in binary mixtures can lead to higher electrical resistivity, whereas binary mixtures with Class C FA exhibited similar results to control mixtures. They reported that binary mixtures with slag cement exhibited the greatest resistivity among all of the evaluated mixtures. Uysal et al. (2012) found that SCC mixtures with a w/cm of 0.33 and containing 35% FA or 60% SL are shown to have RCP values of 150 and 120 Coulomb compared to the 1250 Coulomb for the control mixture with 100% OPC. This reduction in chloride ion penetration can be due to the denser microstructure and higher amount of alumina (Al_2O_3) in mixtures containing SL and FA. As the alumina content increases the total charge decreases, which can lead to higher resistance to chloride ion penetration. Uysal and Akyuncu (2012) investigated the effect of Class C and F FAs at replacement levels of 10% and 17% on transport properties and frost durability of concrete mixtures made with various binder contents, varying between 260 and 400 kg/m^3. In general, given higher pozzolanic reaction of Class F FA, mixtures made with Class F FA exhibited higher resistance to chloride ion penetration and lower sorptivity compared to the similar mixture made with Class C FA at 91 days. The rate of weight loss of concrete after freezing and thawing increased when increasing the replacement level of Class C and Class F FAs. Hwang and Khayat (2009) reported that for SCC prepared with w/cm of 0.35 and 0.42 and a binder content of 475 kg/m^3, the use of 25% SL and 5% SF led to 8% higher frost durability compared to those prepared with the 25% Class F FA and 5% SF. Barrett et al. (2013) studied the transport properties of concrete mixtures made with PLC

and a w/cm varying between 0.38 and 0.46. The results from the migration cell testing showed that the chloride diffusion coefficients in mixtures containing PLC may range from 0 to 30% higher than the OPC. In the case of using FA, both OPC and PLC mixtures exhibited up to 90% lower chloride diffusion coefficients than those of the same systems without FA. The bulk resistivity of PLC mixtures were shown to range within ± 25% of their OPC references mixtures. This variation may be related to changes in pore solution conductivity due to the presence of limestone in these systems, however more research is required to determine these effects. Concrete produced with PLC up to 15% replacement can produce concrete with similar resistance to the penetration of fluids. However, an increase in chloride ion penetration can occur in PLC concrete mixtures when proportioning at the same w/cm as OPC mixture (Tennis et al., 2011).

2.2.2.3 Shrinkage and cracking resistance. The shrinkage of the concrete depends on several parameters, including the binder volume, water content, cement type and content, pore size distribution, and aggregate type and content. In general, the binder type has significant influence on shrinkage and cracking potential of concrete. Sounthararajan and Sivakumar (2013) reported that concrete made with binary blend of cement and FA had higher resistance to drying shrinkage. For a given workability, a mixture containing FA has lower water demand, which can contribute to lower drying shrinkage of concrete (Tangtermsirikul, 1995). Lee et al. (2006) reported that for the given w/cm, autogenous shrinkage of concrete made with SL increases with an increase in the replacement level of SL from 0 to 50%. On the other hand, partial substitution of cement by SL can result in lower drying shrinkage (the term “drying shrinkage” refers to “total shrinkage” which includes shrinkage induced by both autogenous and drying shrinkages) due to the denser microstructure and lower capillary porosity (Li and Yao, 2001). Li et al. (2010) investigated the autogenous shrinkage and the pore structure of the cement paste with ternary blends of FA and SF, or FA and SL. Their results indicated that the use of FA can reduce autogenous shrinkage, but using SF can increase autogenous shrinkage, which can be due to the higher surface tension in capillary pores. El-Chabib and Syed (2012) reported that replacing up to 70% of cement by SL decreased the free drying shrinkage of concrete by more than 45% compared to that of the control mixture. They found that the use of Class F FA is more effective than Class C FA in reducing

drying shrinkage at the same replacement level. For example, SCC made with 60% Class F FA resulted in 20% lower free drying shrinkage compared to the similar mixture containing 60% Class C FA. This can be due to the relatively high pozzolanic reaction of Class F FA which can produce denser microstructure and reduce water evaporation. Güneyisi et al. (2010) studied the drying shrinkage of SCC incorporating various binary and ternary SCMs, including FA, SL, MK, and SF at a w/cm of 0.32 and 0.44. In the case of a binary system, the replacement of cement with FA, SL or MK is shown to significantly reduce the free drying shrinkage of SCC at w/cm of 0.32. For example, the drying shrinkage of the concrete mixtures with 5% and 15% MK were 22% and 26% lower than that of the control concrete, respectively. The partial replacement of cement with either 60% FA or 60% SL resulted in 26% and 15% reduction in drying shrinkage, respectively. However, the binary use of SF from 10% to 15% increased the total shrinkage compared to the control mixture made with 100% OPC. The negative effect of SF on the shrinkage of SCCs was relatively eliminated with the ternary use of SCMs. The lowest shrinkage of 300 μstrain was observed for the mixture proportioned with 45% FA and 15% MK compared to the 480 μstrain for the control mixture.

The effect of SCMs on cracking resistance of concrete under restrained shrinkage is not well documented. A delay in the early-age hydration and rate of strength development of the concrete may lower cracking potential due to the increase in the early-age creep and higher stress relaxation. Replacement of cement with Class F FA is typically more effective in delaying the strength gain compared to Class C FA or SL replacement. Hwang and Khayat (2010) evaluated the cracking potential of SCC made with two w/cm values of 0.35 and 0.42, and three blended binder types, including FA, SL, and SF. The type of binder is shown to have considerable influence on shrinkage cracking potential. For a given w/cm, SCC made with the B1 binder (70% OPC + 25% Class F FA + 5% SF) exhibited 130% to 380% greater resistance to restrained shrinkage cracking than similar SCC made with the B2 (70% OPC + 25% SL + 5% SF) or B3 (quaternary blended cement containing Class F FA, SL, and SF) binders. Ray et al. (2012) investigated the effect of three different SCM combinations (B1: 30% SL + 5% SF, B2: 20% FA + 5% SF, and B3: 10% MK) and three different w/cm (0.4, 0.35, and 0.3) on shrinkage cracking potential of HPC targeted for bridge deck. The mixture made

with 10% MK exhibited 10% lower drying shrinkage after 90 days of drying compared to mixtures made with other SCM combinations. In the case of w/cm of 0.40, the mixture with binder type of B1 developed elapsed time to cracking of 22 days compared to 20 days for mixtures made with B2 or B3 binder type. Li et al. (1999) indicated that the use of SF as a partial replacement of cement not only increases the cracking tendency, but also increases the crack width in the restrained shrinkage ring test. Bucher et al. (2008) investigated the autogenous, free drying, and restrained shrinkages of mortars made with three cements containing 0%, 5%, and 10% limestone. The autogenous shrinkage during the first 3 days was highest for mortars without limestone (215 μstrain) and the lowest for mortars with 10% limestone (185 μstrain). The amount of drying shrinkage also decreased with increasing limestone content. Restrained mortar samples produced with cement without limestone exhibited elapsed time to cracking of 87 hours. The presence of limestone increased the time to cracking slightly, but all samples cracked after 96 hours. Based on the obtained results, mortars made with PLC exhibited slightly lower shrinkage and a lower tendency to shrinkage cracking compared with similar mortars produced with OPC.

2.3. AGGREGATE SKELETON

Aggregates typically represent 60%–75% of the volumetric proportion of concrete mixtures. The particle-size distribution (PSD) of aggregates can considerably influence the packing density of the granular skeleton, which in turn, determines the volume of voids to be filled with binder content. As in the case of aggregate, the optimization of PSD and particle packing in cement–SCM–filler systems is effectively employed to design more advanced sustainable concrete mixtures with better rheological properties and workability characteristics. In practice, narrowing or broadening the PSD can be an effective way to control the rheology of a suspension.

The size of the granular particles determines the extent of inter-particle forces, and hence the tendency of particles to be agglomerated or flocculated. Figure 2-3 (taken from (Genovese 2012)) shows the schematic representation of possible arrangements of solid particles in suspension as a function of particle size and dispersion state. The solid particles incorporated in cementitious suspensions can be classified as: (i) non-colloidal

particles such as aggregate particles shown in Figure 2-3(a) that only involve mechanical interactions; and (ii) colloidal particles, such as cementitious materials where particle surface forces (e.g., van der Waals attractive forces) predominate over the gravitational-shear forces, thus particles tend to be agglomerated or flocculated (Genovese 2012). In spite of numerous studies focusing on aggregate optimization, limited information exists regarding the effect of binder composition and its dispersion state on packing density of granular skeleton. The terms dispersion and suspension are generally used to describe a two-phase system where solid particles are dispersed in a suspending fluid medium. The dispersed solid phase suggests that particles are distributed apart from each other (Figure 2-3(a) and (b)) due to the action of either gravitational-shear forces, or repulsive inter-particle forces resulting from incorporating dispersants (i.e., chemical admixtures). However, when attractive forces predominate over repulsive forces, colloidal particles tend to be aggregated, rather than dispersed (Figure 2-3(c)).

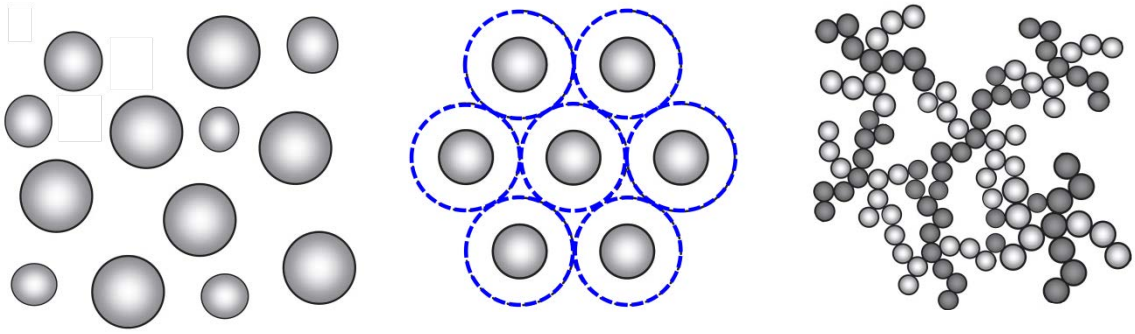

(a) (b) (c)

Figure 2-3 Schematic representation of (a) non-colloidal spheres, (b) dispersed colloidal particles (dashed lines represent repulsive potential; repulsive forces keep particles separated), and (c) aggregated colloidal particles (adapted from Ref. (Genovese 2012)).

2.3.1. Theoretical Particle Packing Models. A number of theoretical particle packing models have been developed to predict the packing density of granular materials. In packing models, various structural effects take into account describing how particles of different size classes are packed.

These structural effects include: (i) the filling effect of the fine particles (filling into the voids of the coarse particles); (ii) the occupying effect of the coarse particles (occupying solid volumes in place of porous bulk volumes of the fine particles); (iii) the

loosening effect of the fine particles (loosening the packing of the coarse particles when pushing themselves into the voids of the coarse particles); and (iv) the wall effect of the coarse particles (disrupting the packing of the fine particles at the wall-like boundaries of the coarse particles) (Alexander and Mindess 2010; De Larrard 1999). The packing model introduced by Powers (Powers 1969) only considers the loosening effect; the packing models developed by Aïm and Goff (Aim and Le Goff 1968) and Toufar et al. (Toufar et al. 1977) account for wall effect; whereas the more advanced packing models developed by Yu et al. (Yu et al. 1996), Goltermann et al. (Goltermann et al. 1997), Stovall et al. (Stovall et al. 1986), De Larrard (De Larrard 1999), and Dewar (Dewar 2002) take into account both the loosening and wall effects.

The loosening effect occurs when the coarse particles are dominant and the fine particles are not sufficiently small to fit into the voids among coarse particles without disturbing the skeleton of the coarse particles, as illustrated in Figure 2-4(a). The squeezing of the fine particles into the voids between coarse particles tends to loosen the frame of the coarse particles, and thus lowering the packing density of granular skeleton (De Larrard 1999). In contrast, the wall effect occurs when fine particles are dominant and the regular packing of the fine particles is interrupted by the wall boundaries provided by coarse particles (and/or container). This results in the formation of additional voids in the vicinity of the surfaces of coarse particles (and/or container), as shown in Figure 2-4(b) (De Larrard 1999). The degree of loosening and wall effects, therefore, depends on the particle size ratio (i.e., ratio of fine to coarse particle size), where a larger spread in particle sizes (i.e., smaller size ratio) between fine and coarse particles features lower loosening and wall effects. These two parameters are expressed as particle interaction functions and are obtained by regression analysis of the packing density experimental results of different blends with varying size ratio. Considering these two parameters to model particle interactions, such models can be collectively classified as a 2-parameter model. Later, De Larrard (De Larrard 1999) introduced the compaction index concept in the 2-parameter packing model called “compressible packing model” (CPM). The term “compaction index” considers the difference between actual and virtual packing densities and characterizes, therefore, the placement procedure and applied compaction effort. In an effort to enhance the accuracy of packing models, Kwan et al.

(Kwan et al. 2013) identified a new particle interaction so-called wedging effect. Similar to the loosening and wall effects, the wedging effect can reduce the packing density. The wedging effect occurs when the fine particles are slightly less than or slightly more than enough to fill the voids between the coarse particles, as indicated in Figure 2-4(c). This effect is more dominant for angular particles compared to the spherical particles (Kwan et al. 2015). More recently, Roquier (Roquier 2016) introduced a new version of CPM so-called the 4-parameter CPM to predict the packing density of bidisperse spherical particle. This model incorporates the loosening effect, the wall effect, the compaction index, and the critical cavity size ratio. The critical cavity size ratio indicates whether a fine particle can fit inside a small cavity without disturbing the frame of larger particles.

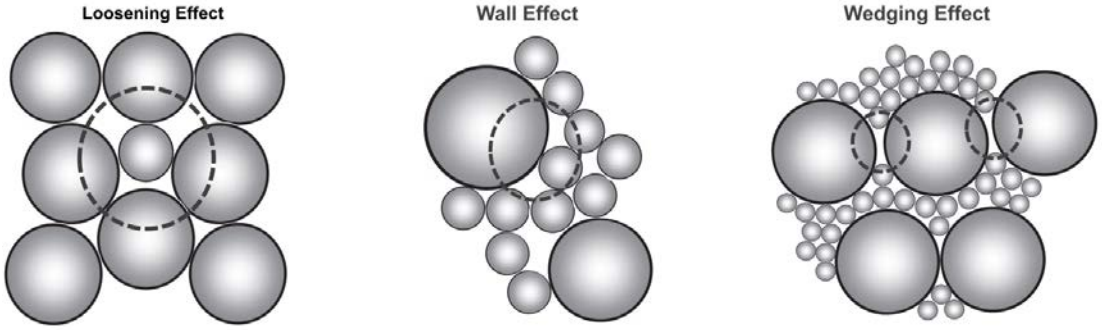

(a) (b) (c)

Figure 2-4 Schematic representation of particle interactions: (a) loosening effect, (b) wall effect, and (c) wedging effect (adapted from Ref. (Wong et al. 2013)).

For further comparison, the particle interaction functions utilized in the aforementioned particle packing models are summarized below, and their variations with respect to the particle size ratio are compared in Figure 2-5.

The interaction functions derived by Yu et al. (Yu et al. 1996) for the 2-parameter packing model:

$$a = 1-(1-s)^{3.3} - 2.8s(1-s)^{2.7} \quad 2\text{-}1$$

$$b = 1-(1-s)^{2} - 0.4s(1-s)^{3.7} \quad 2\text{-}2$$

The interaction functions derived by De Larrard (De Larrard 1999) for the CPM:

$$a = \sqrt{1-(1-s)^{1.02}} \quad 2\text{-}3$$

$$b = 1-\left(1-s\right)^{1.5} \quad 2\text{-}4$$

The interaction functions derived by Kwan et al. (Kwan et al. 2013) for the 3-parameter packing model:

$$a = 1-\left(1-s\right)^{3.3} - 2.6s(1-s)^{3.6} \quad 2\text{-}5$$

$$b = 1-\left(1-s\right)^{1.9} - 2s(1-s)^{6} \quad 2\text{-}6$$

$$c = 0.322\tanh(11.9s) \quad 2\text{-}7$$

where *a*, *b*, and *c* refer to the loosening, wall, and wedging effects, respectively. The parameter s is the particle size ratio. As shown in Figure 2-5, the trends of interaction functions derived from different models are not consistent. For size ratio up to 0.45, the loosening effect derived from CPM model is significantly larger than those obtained by other models, while for larger size ratio this trend is reversed. Similar wall effect trends are observed between packing models. From Figure 2-5(c), it can be observed that the wedging effect progressively increases for particle size ratio up to 0.2, thereafter it becomes constant with further increase in particle size ratio.

2.3.1.1 Limitations of particle packing models. In the majority of the particle packing models, particles are idealized as mono-sized spherical particles. Such assumption limits the application of models for more realistic aggregate cases utilized in concrete. To characterize the size of a non-spherical (i.e., angular) particles, Yu and Standish (Yu and Standish 1993) and Yu et al. (Yu et al. 1993) introduced the concept of equivalent packing diameter and employed this approach to extend the 2-parameter model for non-spherical particles. For multi-component aggregate blends, Goltermann et al. (Goltermann et al. 1997) developed the concept of eigenpacking degree and characteristic diameter of aggregate to overcome the limitations of: (i) perfectly spherical; and (ii) mono-sized particles. In the case of multi-component aggregate blend with polydisperse fractions, a characteristic diameter corresponding to the diameter with 36.8% retained in the fraction can be used. For the ternary blends, they suggested

blending two fractions with the highest particle size ratio and then combining this blended fraction with the third fraction (Goltermann et al. 1997).

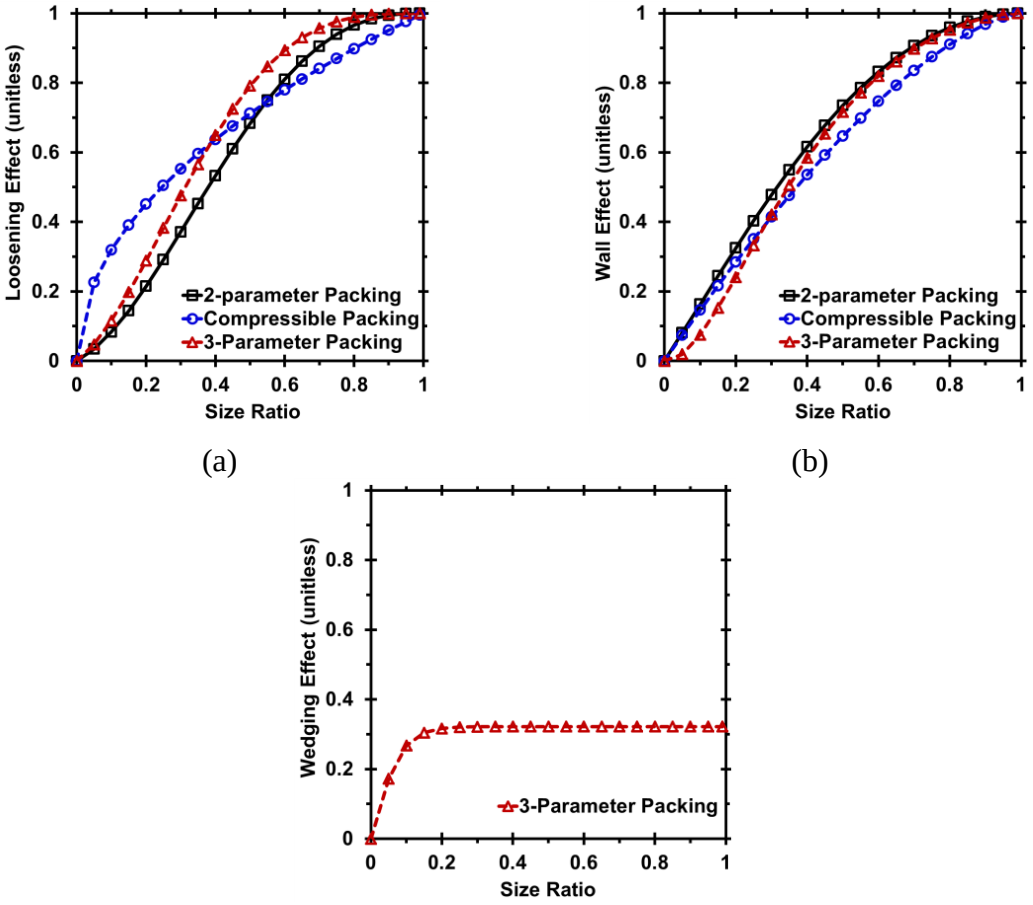

Figure 2-5 Variations of particle interaction functions with particle size ratio for: (a) loosening effect, (b) wall effect, and (c) wedging effect.

Although limited in numbers, several studies have evaluated the accuracy of the theoretical packing density models with experimental data determined for various aggregate types and blends, and noted that the accuracy of the prediction packing density models is strongly sensitive to the particle size ratio. As the size ratio increases the particle interaction effects become more significant (De Larrard 1999). For instance, Jones et al. (Jones et al. 2002) compared the prediction results of four different particle packing models, including modified Toufar, Dewar, and De Larrard's linear packing model (LPM) and CPM to estimate the void content of various aggregate blends. They

noted that the investigated models can estimate the packing density with relatively high accuracy for size ratio around 0.40. Chan and Kwan (Chan and Kwan 2014) evaluated the prediction accuracy of the 2-parameter model (i.e., wall and loosening effects), the CPM (i.e., wall and loosening effects as well as compaction index), and the 3-parameter model (i.e., wall, loosening, and wedging effects). In this study, the experimental data were collected from the published literature for various binary aggregate blends of monodisperse spherical aggregate particles with size ratio ranging from 0.02 to 0.74. The authors found that when the size ratio is smaller than 0.65, the 2-parameter and CPM models tend to either overestimate or underestimate the experimentally measured packing density values. Compared to the 2-parameter and compressible packing models, the predictions derived from the 3-parameter model were noted to be in good agreement with experimental data.

2.3.1.2 Particle packing of colloidal particles. The behavior of colloidal particles differs significantly from non-colloidal particles due to their relatively high surface area-to-mass ratio (Yu et al. 2003). For smaller particles, the SSA becomes relatively larger, generating surface forces such as van der Waals forces and electrostatic forces, which are more dominant than the gravitational-shear forces. Such inter-particle surface forces can increase the tendency of small particles to be agglomerated and form interconnected flocs. The formation of agglomerates significantly drops the packing density of colloidal particles. To mitigate this effect, the dispersants (i.e., chemical admixtures) are typically incorporated. The addition of dispersing admixtures such as polycarboxylate ether (PCE) can change the electrostatic charges and/or induce steric hindrance and mitigate particle agglomeration, resulting in an enhancement of solid concentration in the system (Collepardi 1998; Flatt and Houst 2001).

To determine packing density of binders, Wong and Kwan (Wong and Kwan 2008b) developed the wet packing density approach to measure the solid concentration of binder under wet condition when sufficient water is present in the system. This method involves preparing the paste suspension at various water-to-binder ratios (w/b) and measuring the wet densities of suspension. The maximum solid concentration of binder system corresponds to the w/b at which maximum wet density has achieved (Wong and Kwan 2008b). The maximum solid concentration occurs when the solid particles have

achieved their maximum packing density. Although this approach has been successfully employed to examine the effect of various cementitious materials on packing density of binder, the main difficulty of this approach lies in the estimation of the moment when the maximum wet density occurs at different dosage rates of dispersing admixtures (Lecomte et al. 2009; Mehdipour and Khayat 2016a). Lecomte et al. (Lecomte et al. 2009) used the w/b corresponding to the normal consistency of paste to determine the packing density of binder and found good agreement between measurements and predicted packing densities using CPM with a compaction index of 4.8. This value is different from compaction index of 6.7 that was suggested by the De Larrard (De Larrard 1999) for the wet packing condition. Knop and Peled (Knop and Peled 2016) applied the CPM to predict the packing density of blended cement containing limestone with different median particle sizes varying between 3 and 70 μm. No dispersing admixture was incorporated in paste mixtures and the compaction index was fixed at 4.8, that was similar to the value used by Lecomte et al. (Lecomte et al. 2009). The authors noted that the prediction results fit well with experimental measurements for blended limestone cement with median particle size larger than 23 μm. However, for particle sizes smaller than 23 μm, the predictions were not consistent with those determined from experimental measurements. This is likely due to the formation of particle agglomeration as the particle size decreases. In another study, Der Putten et al. (Van Der Putten et al. 2017) applied the CPM with compaction index of 7 to predict the optimal combination of powders and aggregate fractions for ultra-high performance concrete. The authors concluded that the predictions results derived from CPM is significantly sensitive to the PSD of powders. Two different techniques were applied to determine the PSD of powder materials including a laser light scattering method and a dynamic light scattering method, and the latter was found to deliver more accurate results. Fennis et al. (Fennis et al. 2013a) extended the compressible model called compaction-interaction packing model to predict the packing density of particles smaller than 125 μm. In this model, the agglomeration of small particles due to the particle surface forces is considered by increasing loosening effect for particles smaller than the transition diameter. The transition diameter corresponds to the particle diameter below which the inter-particle surface forces develop considerably, thus inducing a reduction in packing density.

Recently, Mehdipour and Khayat and Mehdipour et al. (Mehdipour et al. 2017b; Mehdipour and Khayat 2016a) have extended the application of wet packing density approach for determining the optimum dosage of dispersing admixture required to achieve the maximum solid concentration for a given binder system. As shown in Figure 2-6, the effectiveness of incorporating SCMs to enhance packing density of binder is significantly sensitive to the dispersion of binder (Mehdipour and Khayat 2016a). For a given binder composition, there exists an optimum dispersant dosage to enhance packing density, beyond which further addition of admixture may not change the packing density appreciably. In another study, Mehdipour et al. (Mehdipour et al. 2017b) have demonstrated that the effect of dispersion state is more dominant for binder system with higher total specific surface area (SSA). This implies that in order to elicit the full benefit of the higher SSA for particle packing improvement and other relevant properties in blended system, it is crucial to incorporate dispersing admixtures at the optimum dosage. Therefore, the packing density of colloidal particles is significantly related to the degree of dispersion of particles.

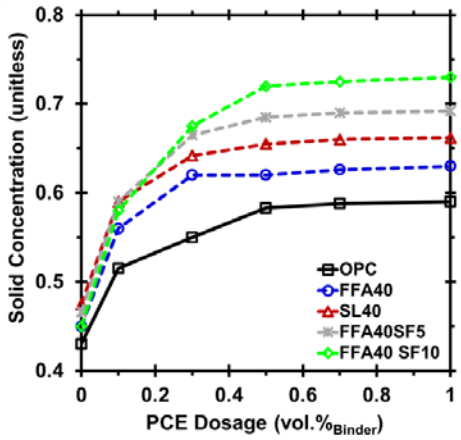

Figure 2-6 Variations in solid concentration in relation to PCE dosage rates for various binders. Here, FFA: Class F fly ash, SL: blast-furnace slag, and SF: silica fume (adapted from Ref. (Mehdipour and Khayat 2016a)).

2.3.2. Characterization of Particle Morphology. The aggregate morphology is a crucial parameter which influences significantly the workability, stability, and rheological properties in the fresh state and mechanical properties in the hardened state of cementitious suspensions (Mehta 1986; Monteiro 2006; Neville and Brooks 1987). The

particle morphology is generally expressed in terms of elongation ratio (i.e., aspect ratio), roundness, sphericity, and surface roughness. Compared to the roundness which describes the degree of sharpness of particle edges/corners, the term “sphericity” is used to characterize the overall form of the granular particle, irrespective of the sharpness of the edges (Alshibli et al. 2014). The latter parameter is a measure of the degree of conformity of particle shape to that of sphere circumscribing the particle.

The term “roundness” was firstly introduced by Wadell (Wadell 1933) and is defined as the ratio of average diameters of curvature in corners to the diameter of inscribing circle. Unlike sphericity, the quantification of roundness is complicated and highly dependent on determination of particle corners (Sun et al. 2014; Zheng and Hryciw 2015). Zheng and Hryciw (Zheng and Hryciw 2015) recommended that the particle corner can be properly identified by fitting the appropriate circle that minimizes the sum of squares of distances from the circle to particle outline pixels. Digital image analysis and computed tomography techniques have been successfully employed to quantitatively characterize the aggregate particle morphology based on two-dimensional (2D) (Al-Rousan et al. 2007; Bessa et al. 2012; Cox and Budhu 2008; Kwan et al. 1999; Shen et al. 2016; Wang et al. 2005; Zheng and Hryciw 2016) or three-dimensional (3D) images (Alshibli et al. 2014; Cepuritis et al. 2017; Fonseca et al. 2012; Garboczi and Bullard 2013; Garbout et al. 2013; Komba et al. 2013; Suh et al. 2017). The schematic illustration of particle morphology characterization using 2D digital image analysis is shown in Figure 2-7. Roundness is computed by determining the maximum possible inscribed circle and fitting the possible circles to the edges/corners of particle, as indicated in Figure 2-7(a) and (b). In order to determine the sphericity of particle, the circumscribing circle diameter should be found, as shown in Figure 2-7(c). The morphology of the aggregate particle can then be quantified as follows (Shen et al. 2016; Suh et al. 2017; Zheng and Hryciw 2016):

$$Elongation\ ratio = \frac{L}{W} = \frac{D_{\max}}{D_{\min}} \geq 1 \qquad 2\text{-}8$$

$$Roundness = \frac{\frac{1}{x}\sum_{i=1}^{x} D_i}{D_{inc}} \leq 1 \qquad 2\text{-}9$$

$$Sphericity = \frac{area\ of\ particle \overset{elliptical\ shape}{\approx} \pi LW/4}{area\ of\ circumscribed\ circle = \pi D_{cc}^2/4} \le 1 \qquad 2\text{-}10$$

$$Surface\ roughness = \frac{1}{mn}\sum_{i=1}^{m}\sum_{j=1}^{n}\left|Z_{ij}\right| \qquad 2\text{-}11$$

where L (or D_{max}) and W (or D_{min}) refer to the length and width of the particle, respectively. In Eq. (2), x is the number of fitted corner circles, D_i is the diameter of the corner circles, and D_{inc} refers to the diameter of the largest possible inscribed circle (see Figure 2-7(a)). In Eq. (3), D_{cc} refers to the circumscribing circle diameter (see Figure 2-7 (c)). In Eq. (4), m and n are number of pixels in the X- and Y-directions, and Z_{ij} represents surface height at a specific pixel relative to the reference mean plane.

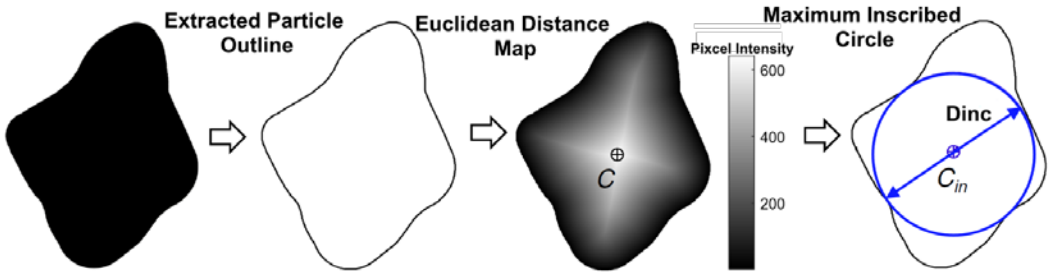

(a)

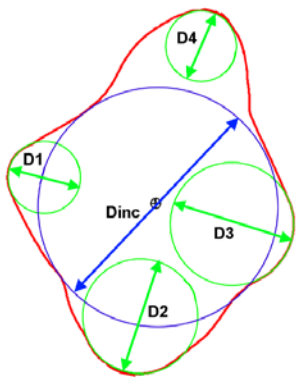

(b)

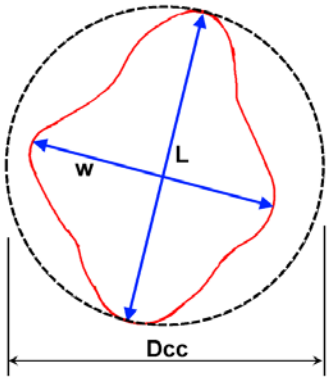

(c)

Figure 2-7 Schematic representation of particle shape analysis: (a) determination of the largest possible inscribed circle, (b) fitting circles to the rounded corners/edges of particle to compute roundness, and (c) determination of the circumscribing circle to compute sphericity of particle (adapted from Ref. (Zheng and Hryciw 2016)).

The increase in aggregate volume fraction and sand-to-total aggregate ratio generally increases the water content required to reach a given workability. The use of higher fine aggregate proportion increases the surface area which necessitates a higher paste volume needed to coat the particles. Rounded aggregate typically has a lower degree of interlocking of particles than angular particles, thus enhancing the workability of concrete. In general, angular aggregate with rough surface texture has higher surface area, which can develop stronger interfacial transition zone between aggregate and paste, thus leading to greater mechanical properties. Westerholm et al. (2008) studied the effect of grading and particle shape of sand on rheology of mortars prepared with 0.57 w/c and a cement content of 635 kg/m^3. A total of 14 fine aggregates (0–2 mm) were used in this research, including 13 crushed sands and a natural sand. The results showed that the rheological properties and water demand of mortars depend significantly on the properties of the fine aggregate. Depending on the shape of fine aggregate, mortars made with crushed sands were shown to have 33% to 133% higher plastic viscosity compared to the mortar prepared with natural sand. Mortar containing elongated sand particles exhibited three times more viscosity than mortar made with spherical sand particles.

Hu and Wang (2011) evaluated the effect of the volume of coarse aggregate on concrete rheology made with w/cm of 0.45. Seven coarse aggregate gradations (four single sizes at 19 mm, 12.5 mm, 9.5 mm, and 4.75 mm and three gradations at G1, G2 and G3) were investigated. Results showed that for a given mortar content, the increase in coarse aggregate volume content from 35% to 41% resulted in 50% to 100% higher yield stress and 40% to 60% higher viscosity. Compared to the single-sized aggregate, continuous graded aggregate can exhibit higher packing density, thus leading to a lower yield stress and plastic viscosity. Aïssoun et al. (2015) investigated the influence of physical characteristics of fine and coarse aggregates, such as fine particle content, shape, texture, and the quantity of elongated particles on the workability and rheological properties of superworkable concrete mixtures made with 0.41 w/cm and a binder content of 400 kg/m^3. The results showed that an increase in the fine content (with diameter smaller than 315 μm) from 8% to 18% resulted in an increase in plastic viscosity from 15 to 40 Pa.s and reduction in surface settlement from 0.47% to 0.14%. For a given w/cm, the increase in the quantity of fine particles increase the cohesion of the paste, thus

leading to an enhancement in static stability. A summary of current literature concerning the optimization of aggregate skeleton is provided in Table 2-1.

Table 2-1 Summary of investigations on aggregate skeleton optimization.

Reference	Methodology	Concluding remarks
Shilstone (1990)	Coarseness factor chart	water demand ↓ workability ↑ compressive strength ↑
Holland (1990)	Percent retained chart (8-18 distribution)	water demand ↓ cement demand ↓ shrinkage ↓ workability ↑ compressive strength ↑
Goltermann et al. (1997)	Packing model (modified Toufar)	Model effectively optimizes packing of binary and ternary aggregate blends
Koehler (2007)	0.45 power curve	packing density ↑ cement demand ↓
Brouwers and Radix (2005); Hüsken and Brouwers (2008); Yu et al. (2013); Wang et al. (2014)	Modified A&A model	water demand ↓ cement demand ↓ shrinkage ↓
Khayat et al. (2000); Mueller et al. (2014)	Particle packing mix design for designing Eco-SCC	HRWR ↓ cement demand ↓ filling capacity ↑
Aïssoun, Hwang, and Khayat (2015)	Physical characteristics of aggregate on properties of super workable concrete	volume of granulates ↑ → water demand ↑ packing density ↑ → stability ↑ fine content ↑ → viscosity ↑ fine content ↑ → stability ↑ rounded aggregate ↑ → packing density ↑ rounded aggregate ↑ → stability ↓ flat and elongated particle ↑ → yield stress ↑

2.3.3. The Role of Particle Packing in Designing Sustainable Concrete.

Proportioning of granular materials for the use in concrete is influenced by morphological characteristics of particles such as shape, angularity, surface texture, and PSD. The aforementioned parameters are collectively reflected in the context of packing density (i.e., ratio of solid volume to bulk volume of solid particles). Packing density of granular materials is an indicator of the voids content of solid skeleton. Aggregate with higher

packing density results in lower void content, which in turn can minimize the lubricant volume required to fill the voids. The combined use of packing density and grading models enhances the optimization procedure and can be applied as a reliable tool for comparison of various aggregate blends and mixture proportioning. For instance, Moini et al., (Moini et al. 2015) noted that multiple criteria should be adopted to select the optimum aggregate proportions for designing sustainable low cement concrete. The authors applied grading models such as power curve and coarseness factor chart in conjunction with experimental and simulated particle packing techniques to select the optimal aggregate proportioning. The coarseness factor chart can be used for elaborating the level of workability and coarseness of a given blended aggregate and cementitious content (Shilstone and others 1990).

The particle packing characteristics have a significant influence on flowability, rheology, porosity, permeability, and mechanical properties of suspensions (Liu 2000; Santomaso et al. 2003; Wu et al. 2005). For instance, Esmaeilkhanian et al. (Esmaeilkhanian et al. 2017b) put forward a mixture design methodology based on the optimization of the volumetric proportions of sand and coarse aggregate according to an ideal particle grading curve for developing SCC with a lower binder content of 315 kg/m^3 (Eco-SCC). Mueller et al. (Mueller et al. 2014) pointed out that an improved particle packing of granular materials can minimize the lubricant volume and enhance the stability of the SCC made with a relatively low binder content of 315 kg/m^3. Yu et al. (Yu et al. 2014) reported that the optimization of solid skeleton by using the modified Andreasen & Andersen (A&A) grading model enables the production of ultra-high performance concrete with a relatively low binder content of 650 kg/m^3 to achieve 28-day compressive and flexural strengths of 150 and 30 MPa, respectively. Recently, Esmaeilkhanian et al. (Esmaeilkhanian et al. 2017b) developed new mixture design method to develop low-powder SCC based on the optimization of volume fraction of aggregate skeleton. Due to the low paste volume of Eco-SCC, it is more difficult to achieve the required flowability. In addition, Eco-SCC is more susceptible to blocking. Therefore, the packing density of the granular skeleton should be high to reduce the lubricant volume, while the total coarse aggregate volume should remain relatively low to reduce risk of blockage. Such design method ensures highly dense and continuous PSD

of aggregate skeleton for which the volume of each size-class is equal or higher than the adjacent coarser class. This results in an increased particle lattice effect which contributes to a perfect segregation resistance (Esmaeilkhanian et al. 2017b).

Apart from aggregate, the optimization of PSD in cement–SCM–filler systems can be utilized to enhance the packing density of solid skeleton and extend the level of OPC replacement as well as minimize the negative impact of reduced early-age properties (Juenger and Siddique 2015). For example, Hooton and Bickley (Hooton and Bickley 2014) reported that the optimization of PSD of SCM-filler system along with aggregate grading enables the reduction of the OPC content for a typical bridge deck concrete mixture from 12% to 3% (by volume). Zhang et al. (Zhang et al. 2011) studied the effect of PSD of OPC on various properties of blended cement pastes and indicated that cement particles coarser than 24 μm have lower water demand, lower heat of hydration, as well as relatively low contribution to strength development. On the other hand, cement particles finer than 8 μm, can lead to a rapid hydration rate due to the relatively high SSA. In spite of having a large amount of hydration products for cement paste made with 8 μm cement particles, a porous microstructure can be formed at early age due to relatively high water demand and low packing density. In another study, Zhang et al. (Zhang et al. 2012) used a gap-graded powder, consisting of fillers, SCMs, and OPC to derive a balance between sustainability and performance at early and later ages. The authors pointed out that the most efficient combination of OPC-SCM-filler system to achieve optimum early and later age properties and environmental impact is to incorporate OPC in the 8–24 μm fraction, with fine-reactive SCMs and fillers occupying the finer fractions and coarse-less reactive SCMs for the coarser fractions.

Several theoretical and empirical grading models have been developed to evaluate the PSD of granular skeleton, such as the Fuller and Thompson model (power law), modified A&A model, and Rosin–Rammler (R–R) model. The modified A&A model proposed by Funk and Dinger (Funk and Dinger 2013) has been widely employed to optimize the granular skeleton for different concrete types, including sustainable concrete (Hüsken 2010), SCC (Brouwers and Radix 2005; Khayat et al. 2014; Mueller et al. 2014), roller compacted concrete (Hüsken and Brouwers 2008; Khayat and Libre 2014), and lightweight aggregate concrete (Yu et al. 2014). A summary of investigations carried out

to optimize the granular skeleton using the modified A&A model is presented in Table 2-2.

Table 2-2 Summary of investigations undertaken on granular optimization using modified A&A grading model.

Ref.	Concrete type	Cementitious materials (kg/m^3)	w/b	Optimized granular materials	A&A distribution modulus
Brouwers and Radix (Brouwers and Radix 2005)	SCC	315	0.55	Aggregate and powder	0.25
Hüsken and Brouwers (Hüsken and Brouwers 2008)	Earth-moist concrete	250	0.49	Aggregate and powder	0.35
Yu et al. (Yu et al. 2013)	Lightweight aggregate concrete	423	0.54	Aggregate and powder	0.25
Yu et al. (Yu et al. 2015)	Eco-friendly ultra-high performance concrete	840	0.20	Aggregate and powder	0.23
Mueller et al. (Mueller et al. 2014)	SCC	317	0.6	Aggregate and powder	0.27
Yu et al. (Yu et al. 2014)	Ultra-high performance fiber reinforced concrete	650	0.33	Aggregate and powder	0.23
Wang et al. (Wang et al. 2014)	SCC	380–450	0.4	Aggregate and powder	0.23–0.29
Khayat and Mehdipour (Khayat et al. 2014)	SCC	315	0.45	Aggregate	0.29
Khayat and Libre (Khayat and Libre 2014)	Roller compacted concrete	300	0.39	Aggregate	0.35

The distribution modulus of the A&A model varies the proportioning between fine and coarse particles in concrete. For example, flowable concrete typically necessitates applying a lower A&A distribution modulus, thus incorporating more fine particles to secure the required deformability and stability. Hunger (Hunger 2010) recommended using distribution moduli in a range between 0.21 and 0.25 for SCC mixtures because higher distribution modulus values can increase the risk of segregation

and blocking. However, lower distribution modulus values deliver fine-rich granular blends which suffer from high cohesion. Hüsken and Brouwers (Hüsken and Brouwers 2012) applied two different A&A distribution moduli of 0.25 (high fine content) and 0.40 (low fine content) for the composed granular mixtures to evaluate the compaction behavior and green strength of zero-slump concrete. Lower distribution modulus resulted in concrete with higher finer content and improved compaction behavior, contributing to reduced void fraction and enhanced green strength.

As in the case of aggregate, the grading models can be applied to optimize the PSD of the binders to enhance packing density and reduce water demand. For instance, Mehdipour and Khayat (Mehdipour and Khayat 2017) employed the modified A&A, Rosine–Rammler (R–R), and power law grading models to optimize the PSD of different binary and ternary binder systems containing fly ash, slag, and silica fume to achieve maximum packing density, while securing relatively low water demand and appropriate compressive strength. The authors pointed out that binder systems with a A&A distribution modulus between 0.21 and 0.235 exhibited 18%–40% lower minimum water demand to initiate flow and 15%–25% higher packing density compared to the plain OPC system. Good correlations were established between the A&A distribution modulus, total SSA, R–R spread factor, and power law distribution exponent. The proposed ideal PSD of binder system with distribution modulus values between 0.21 and 0.235 corresponds to R–R spread factor of 0.87–0.95, power law distribution modulus of 0.39–0.43, and SSA value of 1100–1700 m^2/kg (Mehdipour and Khayat 2017). Such SSA values can be achieved when fine cementitious materials such as silica fume is present in the binder composition.

Brouwers and Radix (Brouwers and Radix 2005) and later Hüsken and Brouwers (Hüsken and Brouwers 2008) proposed a new mixture design method using the modified A&A grading model to adjust the entire PSD of all solids (i.e., cementitious materials-fillers-aggregates) to achieve a target grading. In this method, the modified A&A grading model (Eq. (12)) acts as a target function for the optimization of the composed mixture of granular materials. The proportion of each individual material in the mixture is adjusted until an optimum fit between the composed mixture and the target grading curve is achieved using the least squares method, as presented in Eq. (13). When deviation

between the target grading curve and the composed mixture, expressed by the sum of the squares of the residuals (RSS) at defined particle sizes, is minimized, the obtained composition corresponds to the optimum mixture. This mixture design methodology resulted in improved compressive strength due to the denser granular skeleton and higher solid-to-solid connectivity (Hüsken and Brouwers 2008).

$$P_{tar}(D_i) = \frac{D_i^q - D_{\min}^q}{D_{\max}^q - D_{\min}^q} \quad \forall \; D_i \in \left[D_{\min}, D_{\max} \right] \tag{2-12}$$

$$RSS = \sum_{i=1}^{n} e_i^2 = \sum_{i=1}^{n} \left[P_{\mathrm{mix}}(D_i) - P_{tar}(D_i) \right]^2 \rightarrow \min \tag{2-13}$$

where D_{min} and D_{max} are the minimum and maximum particle sizes, respectively. The parameter q refers to the A&A distribution modulus. The $P_{tar}(D_i)$ and $P_{mix}(D_i)$ represent the cumulative fraction of the particle size smaller than D_i for the target grading curve and the composed mixture, respectively. j is the number of fractions for a given grading curve. The applicability of the mixture design method proposed by Brouwers and Radix (Brouwers and Radix 2005) has been evaluated for various concrete types, such as lightweight aggregate concrete (Yu et al. 2013), fiber-reinforced concrete (Yu et al. 2013, 2014), SCC (Brouwers and Radix 2005; Wang et al. 2014), earth-moist concrete (Hüsken and Brouwers 2008), and zero-slump concrete (Hüsken and Brouwers 2012). For instance, Wang et al. (Wang et al. 2014) developed SCC mixtures having up to 20% lower binder content compared to the control SCC, while securing satisfactory fresh and hardened characteristics.

2.3.4. Implication of Optimum Packing Density Concept. Apart from particle packing, the total SSA of solid particles is an important factor affecting flowability and rheological properties of cementitious suspensions. It is important to note that in spite of improving particle packing, the SSA of the entire solid system increases with addition of fine aggregate particles. The increase in the SSA can result in a reduction in the thickness of suspending fluid covering aggregate particles, which dictates the rheological properties of suspension. Therefore, two competing effects simultaneously occur with incorporating fine particles. First, the addition of fine particles acts to enhance the particle packing of granular skeleton, so the amount of excess suspending fluid increases due to the lower void content. While, this effect can be offset by the second action, i.e., the increase in

total SSA of solids, which decreases the thickness of suspending fluid covering solid particles for a given paste volume. The thickness of suspending fluid, and consequently the rheological properties would decrease or increase depending on whichever effect is dominant (Vance et al. 2013b).

In the context of suspending fluid thickness, which account for the combined effects of packing density, mixture design water content, and SSA of all solid inclusions, the maximum packing density is not necessarily equivalent to the optimal packing density to achieve both the reduced paste volume and enhanced workability and rheological properties. This implies that a balance should be derived between optimum packing density and suspending fluid thickness. For instance, Jones et al., (Jones et al. 2002) noted that the use of aggregate blend with the lowest void content (i.e., the highest packing density) resulted in a harsh concrete. To reduce the degree of harshness and improve workability of concrete, the Day's approach (Day 1999) using a mixture suitability factor was adopted, which reduces the ratio of coarse to fine aggregate content. Nanthagopalan and Santhanam (Nanthagopalan and Santhanam 2012) studied the effect of 10 different aggregate proportions having an equivalent packing density on flowability of SCC mixtures. In spite of having similar aggregate packing density, the flowability and stability of SCC mixtures was found to be significantly affected by the proportioning of aggregate blends. For instance, for a constant packing density value of 0.68, the slump flow was found to vary from 445 to 720 mm depending on the aggregate proportions. Such spread in slump flow is attributed to the increased SSA of solids due to the addition of fine particles. Further, SCC mixtures with higher volume fraction of coarse aggregate exhibited aggregate segregation and blocking (Nanthagopalan and Santhanam 2012). Fennis et al. (Fennis et al. 2013b) noted that concrete mixture with the greatest packing density exhibits relatively high resistance to shear deformation. As a consequence, a larger content of excess water is required to impart fluidity to the mixture. This is attributed to the higher friction and interlocking between particles. This is schematically illustrated in Figure 2-8, which shows that for the same volume fraction of solid particles, the flowable mixture occupies higher volume compared to the stable particle structure (i.e., when water is only used to fill the voids). The excess water present in the flowable mixture increases the inter-particle spacing and reduces particle interlocking effect. This

implies that for a given volume, flowable mixture may have less solid content due to the increased spacing induced by excess water between solid particles (Fennis et al. 2013b).

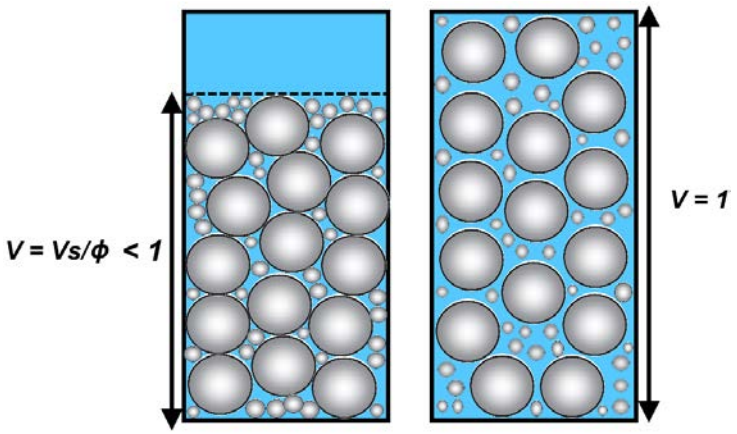

Figure 2-8 Schematic representation of the volume occupied by stable particle structure (left) and workable mixture (right) (adapted from Ref. (Fennis et al. 2013b)). Here: V, V_s, and ϕ are volume, solid volume fraction, and packing density of mixture, respectively.

The effect of packing density of particle interlock was studied by Fung and Kwan (Fung and Kwan 2014) by evaluating the flow rate of various aggregate blends when discharging from V-funnel. They found that the optimum fine content for flow rate is higher than the optimum fine content required to achieve maximum packing density. This is because at the state of maximum packing density, the coarse particles are tightly packed against each other, hence introducing relatively large interlocking action and friction between coarse particles. The difference between the state of maximum packing density and the state of maximum flow rate is schematically depicted in Figure 2-9. At the state of maximum flow rate, the fine content is more than enough to fill the voids between coarse particles so that excess fine particles acts to provide ball-bearing effect (i.e., lubricant) which can facilitate the movement of coarse particles and alleviate the interlocking effect of coarse particles. This has an important implication for the design of flowable concrete to secure adequate resistance of suspension to deformation with optimized particle interlocking effect. Esmaeilkhanian et al. (Esmaeilkhanian et al. 2017b) pointed out that the combined criteria of optimum packing density and maximum limit of coarse aggregate volume fraction should be adopted to properly proportion aggregate skeleton for the design of low-powder SCC mixture. Therefore, in addition to

the packing density criterion, desired proportioning of aggregate combination (e.g., upper limit for coarse aggregate volume fraction) should be applied to properly design concrete with relatively low cementitious materials and appropriate performance (especially fresh characteristics).

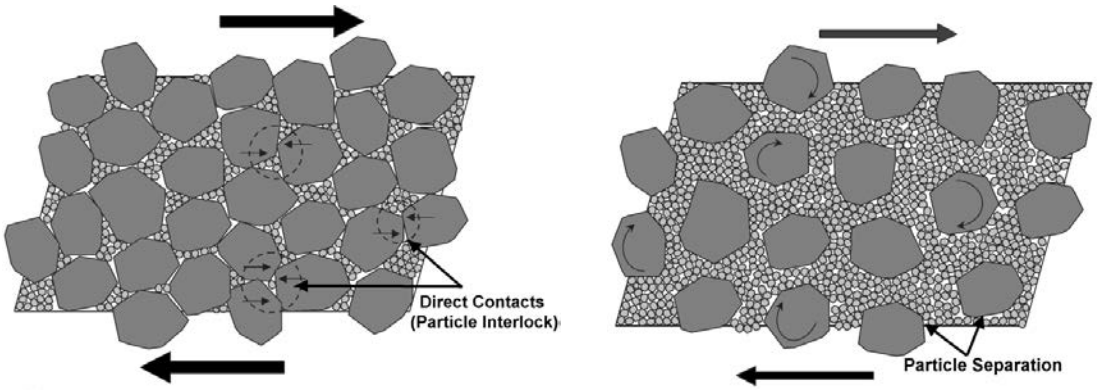

(a) (b)

Figure 2-9 Schematic illustration of aggregate structures for: (a) the state of maximum packing density and (b) the state of maximum flow rate (adapted from Ref. (Fung and Kwan 2014)).

2.3.5. Effect of Particle Characteristics on Rheo-Physical Properties. To predict the rheological properties of suspensions as a function of particle loading, or to determine the maximum possible solid fraction, several equations have been proposed, starting from Einstein's equation (Asaga and Roy 1980) to the Krieger–Dougherty (K–D) equation (Krieger and Dougherty 1959), and other parametric/empirical models (Chong et al. 1971; Liu 2000). Based on the general form of the aforementioned relations, i.e., $\tau_{con} \approx \tau_{cp}\ f(\phi/\phi_m)$, where τ_{con} *and* τ_{cp} are yield stress of concrete and cement paste, respectively, the effect of mono-sized spherical particles on the flow behavior of a suspension is strongly dominated by their normalized solid concentration or relative solid packing fraction (ϕ/ϕ_m, i.e., ratio of solid volume fraction to maximum packing volume fraction). Maximum packing volume fraction of granular skeleton is primarily related to the PSD, shape, and surface texture of particles (Krieger and Dougherty 1959).

When solid inclusions such as sand and gravel particles are suspended in the suspending fluid (i.e., cement paste), the type of particle/particle or fluid/particle interactions may vary with respect to the particle volume fraction present in the system.

At low volume fractions, these interactions can be hydrodynamic. However, at higher volume fraction of granular skeleton, direct contact can occur between aggregate particles, which can lead to transition of particle interactions from hydrodynamic to frictional regime and induce considerable amount of solid contacts throughout the suspension (Yammine et al. 2008). Several studies have experimentally and theoretically evaluated the influence of aggregate particles (i.e., non-colloidal particles) on the rheological behavior of suspensions (De Larrard 1999; De Larrard and Sedran 2002; Geiker et al. 2002; Toutou and Roussel 2006). For instance, Toutou and Roussel (Toutou and Roussel 2006) conducted a multi-scale study on the rheological behavior of mortar (considered as suspension of sand in a cement paste) and concrete (considered as suspension of gravel in a mortar). The yield stress of the mortar was noted to increase with volume fraction of sand inclusions. However, at low volume fraction yield stresses of mortars were found to be lower than the yield stress of cement paste, as shown in Figure 2-10. They attributed this feature to the flocs break down (i.e., de-flocculation) in cement paste due to the presence of the sand inclusions during mixing of the suspension, which is in agreement with observations by Williams et al. (Williams et al. 1999). For a given volume fraction of solid inclusions, the presence of gravel particles in mortar suspension results in a much higher increase in yield stress than adding sand inclusions in cement paste medium, as indicated in Figure 2-10.

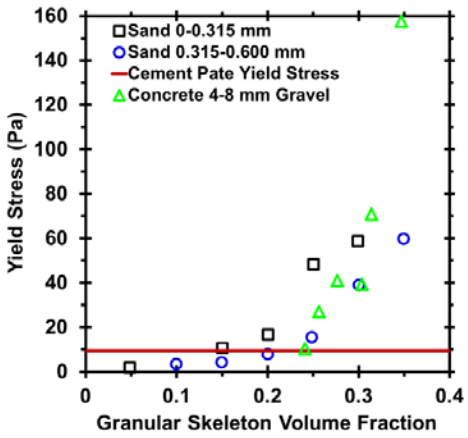

Figure 2-10 Variations in yield stress of suspension as a function of granular skeleton volume fraction (adapted from Ref. (Toutou and Roussel 2006)).

Yammine et al. (Yammine et al. 2008) found that there exists a strong transition in the rheological behavior of concrete between a regime dominated by the friction between aggregate particles and a regime dominated by the hydrodynamic interactions. Figure 2-11 presents the variations in yield stress of concrete in relation to the aggregate volume fraction (Yammine et al. 2008). Three distinct zones can be identified as a function of volume fraction of granular skeleton. For $\phi \geq 70\%$, the yield stress of the concrete is of the order of a couple thousands Pa representing traditional concrete (slump consistency lower than 150 mm). On the other hand, for $\phi \leq 60\%$, the yield stress of the concrete is less than 100 Pa which is typically adopted for SCC. For $60\% \leq \phi \leq 70\%$, there is a strong transition with a variation of almost two orders of magnitude of the yield stress of the concrete. This implies that there exists a critical transition volume fraction (ϕ_c) of granular skeleton so-called percolation volume fraction beyond which direct frictional contacts between particles begin to dominate the rheological behavior of suspension. The highly dissipative nature induced by direct frictional contacts results in a noticeable increase in rheological properties of the concrete. This behavior can be explained by general relations similar to the K–D equation, which links the rheological properties of suspension to the ϕ/ϕ_m. The rheological properties of suspension elevates with increasing ϕ/ϕ_m. In the view of mixture design, this feature has an important implication for the concrete technologists to ensure that the contribution of the granular skeleton to the consistency/rheological properties of the concrete is minimal. It is important to note that in the hydrodynamic regime at which the volume fraction of solid inclusion is less than transition value, the rheological properties of concrete is primarily governed by the rheological properties of suspending fluid (i.e., cement paste). Therefore, in order to design SCC, the aggregate volume fraction should be kept below the transition value as well as the rheological properties of cement paste should be properly adjusted to secure adequate stability of aggregate particles (Roussel 2006). Similar principles have been applied for the design of fiber-reinforced SCC to secure optimal hardened properties, while maintaining proper flow characteristics (Emdadi et al. 2015; Martinie et al. 2010; Mehdipour and Libre 2017). The addition of fibers beyond a critical threshold value results in a significant reduction in rheological properties due to the increased interaction and energy dissipation induced by fiber inclusions.

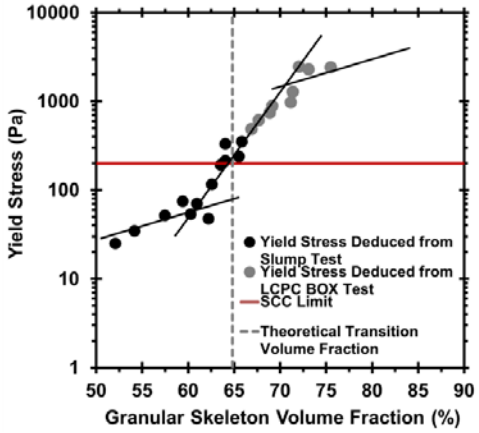

Figure 2-11 Variation in yield stress of concrete as a function of aggregate volume faction (adapted from Ref. (Yammine et al. 2008)).

In another study, Mahaut et al. (Mahaut et al. 2008b) examined the thixotropic behavior of suspensions containing non-colloidal solid particles and developed a theoretical model to predict the yield stress of suspension from that of the cement paste. In this study, mono-sized spherical glass beads with 2 mm diameter were suspended in the cement paste. They noted that if the mechanical impact of the presence of inclusions is to increase the yield stress by a factor $g(\phi)$, then their impact on the structural build-up of the paste is to increase it also by a factor $g(\phi)$. Therefore, it is sufficient to measure the cement paste yield stress evolution (i.e. A_{thix}) in time and the thixotropic in suspension containing coarse inclusions increases with the rate of $A_{thix}g(\phi)$. This conclusion is valid for isotropic suspension of rigid spherical non-colloidal particles in yield stress fluids with no physico-chemical interactions between the particles and paste (Mahaut et al. 2008a).

The effect of various sand morphological characteristics on the rheological properties of the modeled yield stress fluid was studied by Hafid et al. (Hafid et al. 2016) and found good correlations between variations in rheological properties and sand particle morphology. Figure 2-12 demonstrates the relative yield stress of the suspension as a function of volume fraction of sand inclusion. As expected, yield stress of suspension increases with increasing the volume fraction of sand inclusions. The rate of increase in yield stress depends on particle morphology, where irregular particles with higher aspect ratios tend to sharply increase the yield stress of suspension. As can be noticed from

Figure 2-12, depending on the particle morphology, there exists a critical volume fraction of solid inclusion, thereafter yield stress of suspension is strongly dictated by the volume fraction of particles due to the increased frictional interactions and direct contacts between particles. It is important to note that the change in particle morphology from rounded to irregular shape results in lower critical volume fraction of solids. Westerholm et al. (Westerholm et al. 2008) also evaluated the physical characteristics of crushed sand on the rheological properties of mortar. Their results showed that the fine content present in the crushed sand has a strong effect on the water demand and rheology of mortar. The change in sand particle shape from a cubic to elongated shape led to three-fold higher plastic viscosity. The dominant effect of grading, particle shape, and surface texture of crushed sand on rheological properties is strongly dependent on the paste volume, i.e., the thickness of suspending fluid covering sand particles. The negative impact of poor grading, rough surface texture, and irregularity of crushed sand on rheology becomes less dominant with increasing the suspending fluid thickness surrounding particles. This is due to the increased inter-particle spacing and reduced particle interlocking effect.

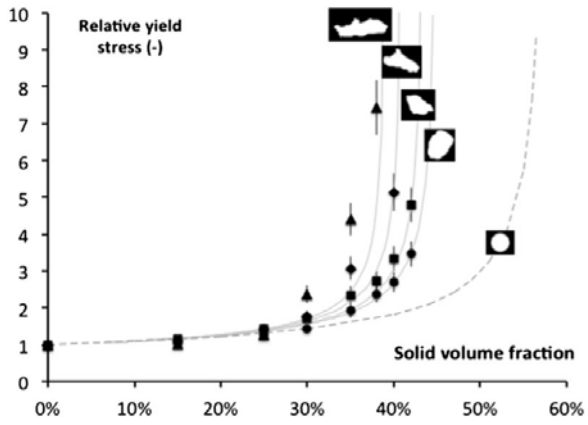

Figure 2-12 Variations in relative yield stress as a function of solid volume fraction (adapted from Ref. (Hafid et al. 2016)). Relative yield stress is the ratio between the yield stress of the mixture and the yield stress of the suspending fluid.

One of the primary parameters influencing the stability of a granular skeleton in a yield stress fluid is PSD of granular materials (Esmaeilkhanian et al. 2017a; Mueller 2012; Wallevik et al. 2009). This effect partially originates from the particle lattice effect (PLE) where for a given fluid the sedimentation behavior of one particle or a group of

particles is modified in the presence of other particles. Inter-particle interactions and modifications in the activated shear area (or flow patterns) around the particles inside the suspending fluid are the two principal phenomena contributing to the PLE (Bethmont 2005; Ramge et al. 2010). The PLE concept becomes more important for the design of highly flowable concrete wherein aggregate particles tend to segregate due to the highly fluid nature of suspending medium (Khayat 1999). The optimization of particle packing of granular skeleton can improve the lattice effect, and consequently enhance the stability characteristics of concrete. For instance, Esmaeilkhanian et al. (Esmaeilkhanian et al. 2017a) applied the PLE concept to evaluate the stability of several groups of bidisperse and polydisperse spherical glass beads (3–19 mm in diameter) suspended in limestone filler paste mediums that were designed with variable rheological properties. The main contribution of PLE to the enhancement of the stability of the system can be attributed to the stabilization of individual fine classes as the volume fractions of such classes are increased. In the context of PLE, an appropriate PSD constitutes of a continuous granular skeleton in which the volume fraction of each class increases with the decrease in the size in order to improve the PLE (Esmaeilkhanian et al. 2017a). When such PSD is employed in a flowable concrete, the fluidity of the mixture can be significantly increased without jeopardizing the stability of the mixture. Therefore, the detrimental effect of the reduction in suspending medium yield stress (e.g., due to the increased water content) on the segregation of a suspension can be masked by using a PSD with an adequate PLE.

To develop a more representative index controlling the stability of mixture, Esmaeilkhanian et al. (Esmaeilkhanian et al. 2017a) applied the concept of PLE in the relation $\delta \approx \tau/\Delta\rho g$ proposed by Roussel (Roussel 2006) for final arrangement of particles in the segregated zone. The correlation between developed index and static stability of suspension in Figure 2-13 shows that the proposed index appears a promising parameter to be employed for the evaluation of stability of SCC mixtures. This index represents the combined effects of PSD, particle volume fraction, particle density, as well as the yield stress and density of suspending fluid medium.

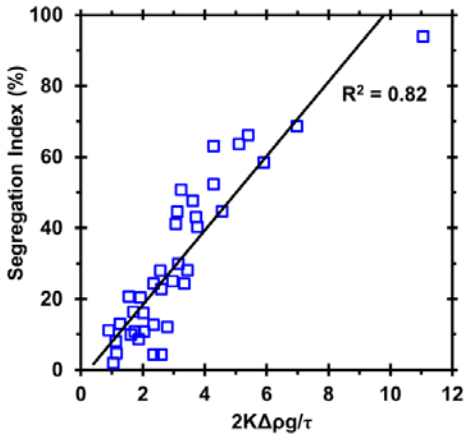

Figure 2-13 Correlation between index controlling static stability of particles and segregation index of SCC mixtures. Here: the term *2K* is the average distance between the particles, τ is the suspending medium yield stress, $\Delta\rho$ is the difference between the densities of particles and the suspending fluid, and g is the gravitational acceleration. Segregation index was identified by the column segregation test (adapted from Ref. (Esmaeilkhanian et al. 2017a)).

Aïssoun et al. (Aïssoun et al. 2016) established a good relationship between quantify of fine particles smaller than 315 μm and stability of flowable concrete, as identified by the surface settlement test. This is due to the increase in the total SSA (and packing density) of granular skeleton which can enhance the cohesion (i.e., increased plastic viscosity) and drag force exerted from suspending fluid on the aggregate particles. For equivalent values of packing density and maximum size of coarse aggregate, concrete made with natural rounded aggregates exhibited higher surface settlement compared to the concrete with crushed coarse aggregate. The smooth surface texture and rounded shape aggregate reduce the cohesion between cement paste and coarse aggregate particles, thus hindering retention of the aggregate in the suspending medium. In another study, Esmaeilkhanian et al. (Esmaeilkhanian et al. 2014) investigated the influence of PSD and maximum size of coarse aggregate on dynamic stability determined from tilting box of SCC mixtures. SCC with well-graded coarse aggregate exhibited 50% decrease in dynamic segregation compared to a similar mixture with uniform grading (narrow range of aggregate size distribution). A wider spread in grading increases both the specific surface area-to-volume ratio and the lattice effect of aggregate, thus enhancing segregation resistance. In addition, for a given paste volume, increasing the maximum

size of coarse aggregate significantly increases the dynamic segregation due to the decreased aggregate specific surface area-to-mass ratio, which is directly proportional to the extent of drag force exerted from mortar to retain aggregates in the suspending medium.

2.4. SHRINKAGE AND CRACKING POTENTIAL OF CEMENTING SYSTEMS

The shrinkage cracking potential of concrete is influenced by the rate of development of mechanical properties and visco-elastic properties of the material. These properties vary with mixture proportioning and raw material characteristics, including binder type and content, aggregate content and type, fiber type and volume, and chemical admixtures. This section reviews the effect of material constituents and mixture proportions on the shrinkage and cracking potential of concrete.

2.4.1. Factors Affecting Shrinkage and Cracking. This is discussed below.

2.4.1.1 Effect of cement type and w/cm content. The type of cement has a considerable effect on the shrinkage cracking potential of concrete. In general, Type II cement reduces cracking potential due to the lower thermal gradient during the early-stage of hydration. Type III cement, on the other hand, may considerably increase cracking potential due to the rapid setting and higher heat of hydration. Higher early-age stiffness results in lower stress relaxation, thus leading to a higher risk of shrinkage cracking (Mehta and Monteiro, 2006). In the evaluation of 32 concrete bridge decks, Schmitt and Darwin (1999) found that concrete bridge decks containing a paste volume more than 27% exhibited relatively high potential of shrinkage cracking. The evaluated concrete bridge decks had a w/cm ranging between 0.36 to 0.44 and cement content varying from 350 to 390 kg/m^3. Yuan et al. (2011) investigated the effect of paste volume on restrained shrinkage using shrinkage ring test. In the case of 0.45 w/c, the mixture made with 28% paste volume exhibited 9 days longer elapsed time to shrinkage cracking compared to the similar mixture prepared with 33% paste volume. Brown et al. (2001) show that concrete made with low w/cm tends to exhibit an increase in early-age shrinkage cracking. This is mainly due to the higher heat of hydration, autogenous shrinkage, and stiffness which result in higher magnitudes of stress development and lower stress relaxation.

Bentz et al. (2008) investigated the influence of cement fineness on early-age properties of cement-based materials. The finer cement had a mean particle diameter of 12 μm compared to 17 μm for coarser cement. In the case of w/c of 0.35 and fine cement, a peak residual stress of 2.45 MPa developed in the ring specimen at 87 h, and a visible crack appeared. On the other hand, for the mixture made with coarse cement, a peak tensile stress of 1.4 MPa developed at a specimen age of 165 h, and no cracking was observed in the coarse cement system during the restrained shrinkage ring test (ASTM C1581). This can be due to lower early-age compressive strength and autogenous shrinkage of mixture made with coarse cement compared to the similar mixture prepared with fine cement. Hwang and Khayat (2010) evaluated the effect of various mix design approaches and binder types on restrained shrinkage cracking potential of SCC used in the repair applications. The first approach incorporated a low w/cm of 0.35, while the second one employed a viscosity-enhancing admixture (VEA) in SCC made with higher w/cm of 0.42. The mixture proportioning of SCC is shown to have significant influence on shrinkage cracking potential. Mixtures made with 0.42 w/cm exhibited approximately 25% to 35% longer time to cracking compared to similar SCC prepared with 0.35 w/cm. The former concrete had lower elastic modulus at 3 days which led to higher tensile creep coefficient, thus resulting in a greater stress relaxation. The SCC made with 0.42 w/cm exhibited slightly higher drying shrinkage after 56 days of drying (595 μstrain) compared to 565 μstrain for similar concrete prepared with 0.35 w/cm. In general, the tested SCC mixtures had higher cracking potential than the reference high-performance and conventional concretes. This may be due to the higher paste volume and lower aggregate content of SCC that resulted in greater drying shrinkage.

2.4.1.2 Effect of internal curing. Shrinkage mitigation through internal curing has recently gained more attention. To implement this technique, several methods have been proposed, including the use of pre-saturated lightweight aggregate (LWA) and super-absorbent polymers. Pre-saturated LWA provides a source of additional water to maintain saturation of the capillary pores in the cementitious paste and avoid self-desiccation. Self-desiccation refers to the reduction in internal relative humidity of concrete stored in a sealed condition, that is, with no transfer of moisture into or out of the concrete. The process of self-desiccation is caused by the chemical shrinkage. As the

cement hydrates, this extra water will be drawn from the relatively large pores in the LWA into the much smaller ones in the cement paste. There are many benefits associated with internal curing that include increased cement hydration, higher strength, less autogenous shrinkage and cracking, reduced permeability and higher durability (Bentz et al., 2005). The efficiency of the LWA varies with the pore structure of aggregate. Generally, larger LWA has a larger pore structure, which results in more efficient internal curing (Hammer et al., 2004). However, it should be noted that well distributed LWA provides efficient internal curing. This is similar case that properly dispersed air voids improve durability. Several studies proved that smaller LWA are better distributed than larger LWA (Bentz and Snyder, 1999, Bentz et al., 2005).

Henkensiefken et al. (2009) investigated the influence of replacement rates of saturated LWA on the performance of self-curing concrete. The inclusion of a sufficient volume of pre-wetted LWA can significantly reduce free drying shrinkage and delay the elapsed time to cracking. In the case of 0.30 w/c and cement content of 700 kg/m^3, mortar mixture containing low volume of LWA of 7.3% by volume exhibited similar free drying shrinkage and cracking behavior to the control mixture without any LWA. This may be due to the fact that in the case of low replacement rate, the LWA particles are dispersed too far from each other to effectively supply internal curing water to the paste. Şahmaran et al. (2009) studied the effect of replacement rate of saturated lightweight sand (LWS) as an internal curing agent on the shrinkage and mechanical behavior of engineered cementitious composites. The addition of saturated LWS was found to be very beneficial in controlling the development of autogenous shrinkage for mixtures made with w/cm of 0.27. A 67% reduction in autogenous shrinkage at 28 days compared to the control mixture can be attained with 20% substitution of normal sand by saturated LWS. In addition, the use of 20% LWS delivered 37% reduction in drying shrinkage after 90 days of drying compared to control specimens. De la Varga et al. (2012) investigated the application of internal curing for mixtures containing low w/cm of 0.30 and high volumes of Class C FA (up to 60%) which are more susceptible to high shrinkage and cracking. They reported that the slower hydration reaction in the high volume FA mixtures results in less initial autogenous shrinkage deformations at early ages. However, due to the pozzolanic reaction and refining the porosity, the rate of autogenous shrinkage increases

in the FA mixtures at later ages. This behavior can lead to higher risk of shrinkage cracking potential at later ages. Their results showed that the use of 15% LWA by volume can be a beneficial method to provide internal curing and reduce tensile stress development caused by restrained shrinkage. Hwang et al. (2013) conducted a factorial design approach to investigate the effect of initial moist curing duration (0 to 6 days) on HPC made with a cement content of 470 kg/m^3 (790 lb/yd^3) and different w/cm (0.30 to 0.40) and replacement rates of LWS (0 to 30% by volume). Concrete made with 30% LWS replacement with no moist-curing exhibited up to 45% lower shrinkage at 9 days compared to similar concrete without any LWS. Combined use of 30 % LWS and 7 days of moist curing can lead to greater decrease in total shrinkage compared to the incorporation of 30% LWS without moist curing or 7 days of moist curing without any LWS.

2.4.1.3 Effect of shrinkage reducing admixture. Shrinkage reducing admixtures (SRA) are used to reduce the rate and magnitude of both autogenous and drying shrinkage of concrete. Several studies have shown that the use of SRA in concrete reduced the shrinkage and cracking potential (Weiss and shah, 2002, Radlinska et al., 2008, Rajabipour et al., 2008). Weiss et al. (1998) showed that the use of SRA significantly reduced drying shrinkage and increased the elapsed time to cracking by reducing the rate and magnitude of the shrinkage. Shah et al. (1992) evaluated the effect of three different SRAs on the restrained shrinkage using the ring-type test. Restrained shrinkage was shown to decrease with the increase in SRA dosage, thus resulting in a delay in shrinkage cracking. The incorporation of SRA also resulted in a reduction in restrained shrinkage crack width. Hwang and Khayat (2008) carried out an experimental program to investigate the influence of SRA on shrinkage cracking of SCC designated for repair applications. Two mixtures were proportioned with moderate and high dosage rates of SRA (4 and 8 l/m^3) and a w/cm of 0.42 to evaluate the effect of SRA addition on shrinkage cracking potential. The incorporation of SRA led to a substantial enhancement in the resistance to restrained shrinkage cracking. Mixtures made with moderate and high dosage rates of SRA developed longer elapsed time to cracking of 13 and 21 days, respectively, compared to 8.8 days for similar SCC made without any SRA. Depending on the dosage of SRA, mixtures containing SRA exhibited 25% to 37% lower drying

shrinkage compared with the control mixture without SRA. Lura et al. (2007) investigated the effect of SRA on the plastic shrinkage cracking of mortars in accordance with ASTM C1579 test. They found that mortars containing SRA exhibited fewer and narrower plastic shrinkage cracks compared to those made without any SRA. The lower surface tension of the capillary pores in the mortars containing SRA results in less evaporation, settlement, and capillary tension.

2.4.1.4 Effect of expansive cement. Expansive cements (EX) can lead to the early-age expansion which later counteracts the tensile stresses developed by drying shrinkage. Type K EX contains Portland cement and calcium sulfoaluminate (CSA-based system) cement, in which the expansion is achieved through formation of ettringite crystals. CSA-based cement also provides a sustainable alternative to Portland cement by reducing CO_2 emission during manufacturing. Type G EX (CaO-based system) is another type of EX in which the formation of calcium hydroxide ($Ca(OH)_2$) crystals results in an expansion. The third type of EX is magnesium oxide-based EX (MgO-based system) in which the hydration of MgO leads to the formation of magnesium hydroxide ($Mg(OH)_2$). $Mg(OH)_2$ has a larger volume than its constituents (MgO) which results in an expansion in concrete (Du, 2005). The efficiency of MgO on the concrete expansion depends on dosage rate and concrete temperature. The increase in concrete temperature can lead to higher and faster hydration of MgO, thus resulting in greater expansion in concrete (Du, 2005).

Chen et al. (2012) evaluated the effect of w/c for cement paste containing calcium sulfoaluminate cement. In the case of w/c of 0.30, there is less space for the formation of hydration products, including ettringite compared to similar mixture made with 0.45 w/c. The expansive pressure from ettringite growth increases when space is restricted, thus leading to a higher expansion. Also, since there is less water available for hydration reactions, fewer hydration products can form prior to self-desiccation, which could lead to expansion later when external water is supplied. Chaunsali and Mondal (2014) evaluated the expansion characteristics of calcium sulfoaluminate cement in the presence of SCMs. The effect of incorporation of Class C FA (15%, by mass), Class F FA (15%, by mass), and SF (5%, by mass) on expansion of cement paste mixtures made with 15% CSA-based EX and different w/cm of 0.34 and 0.44 were investigated. Regardless of the

w/cm, the incorporation of 15% Class F FA replacement led to higher expansion of cement paste compared to the control mixture without any SCMs. This can be due to the lower resistance of material to expansion due to the presence of Class F FA, given the lower compressive strength of such a mixture. On the other hand, the use of Class C FA or SF in CSA-based cement paste is shown to decrease the expansion value compared with the control mixture made with 85% cement and 15% CSA-based EX. The addition of SF resulted in incomplete hydration of CSA-based EX at both w/cm due to self-desiccation which led to lower expansion of CSA-based cement.

2.4.1.5 Effect of fibers. In general, the incorporation of fiber can enhance the resistance of concrete to restrained shrinkage cracking. This is attributed to the higher tensile strength and tensile creep coefficient of concrete containing fibers. Grzybowski and Shah (1990) evaluated the efficiency of different types and volumes of fibers on the reduction in the shrinkage cracking potential of concrete using ring-type specimens. Concrete mixtures were proportioned with steel fibers measuring 25 mm in length and 0.4 mm in diameter as well as 19 mm fibrillated polypropylene fibers. The dosage rates of the steel fibers were 0.25%, 0.5%, 1%, and 1.5%, by volume. These values were 0.1%, 0.25%, 0.5%, and 1% for the polypropylene fiber. Test results revealed that a steel fiber content of 0.25% can substantially reduce the crack width resulting from restrained shrinkage. For a given fiber dosage, the steel fiber was more effective in reducing cracking than polypropylene fiber. Voigt et al. (2004) investigated the effect of different fiber types and geometries on shrinkage and early-age cracking potential. Their results indicated that, for a given fiber type, an increase in the number of fibers increases their effectiveness to reduce shrinkage cracking potential. The steel fiber with flat end and 30 mm length was the best-performing reinforcement in prolonging the age of the first crack and reducing the maximum crack width. Regardless of the fiber type, the incorporation of fiber (even at low fiber volume of 0.25) led to more than 50% reduction in crack width compared to the plain concrete without any fiber. They concluded that the correlation of the maximum crack width to the mortar thickness provides the best measure to characterize the shrinkage cracking behavior of the fiber-reinforced composites. For mortar thickness more than 0.522 mm, the increase in mortar thickness led to higher crack width of restrained shrinkage using the ring test. Hwang and Khayat (2008)

compared the restrained shrinkage results of SCC mixtures made with various synthetic fiber volumes. Two types of polypropylene synthetic fibers were used: a monofilament fiber with a circular cross section measuring 50 mm in length and 0.67 mm in diameter (SyF1) and straight fiber with a rectangular cross section measuring 40 mm (1.6 in.) in length (SyF2). The increase in synthetic fiber volume from 0 to 0.5% resulted in a 40% increase in elapsed time before cracking. This is due to the increase in the tensile creep coefficient resulting from the use of synthetic fibers. The type of synthetic fiber is shown to have a considerable influence on the restrained shrinkage cracking potential. SCC made with 0.25% SyF2 fiber exhibited a longer time to cracking of 8 days compared to 5 days for the same SCC with 0.25% SyF1 fiber.

2.4.1.6 Effect of combination of shrinkage mitigating materials. In general, the combined use of shrinkage reducing and compensating materials can be more effective in reducing shrinkage and cracking tendency. Hwang and Khayat (2008) studied the effect of combined use of fiber and SRA on shrinkage cracking of high-performance SCC designated for repair applications. A ring-type test (ASTM C1581) was used to evaluate the potential for restrained shrinkage cracking and tensile creep behavior of the concrete. The elapsed time before cracking of SCC made with combined use of 0.5% synthetic fiber and 8 l/m^3 SRA was approximately four times longer than that of the similar fiber-reinforced SCC prepared without SRA. This is mainly due to the synergistic effect of fiber and SRA that can increase the tensile creep coefficient and reduce the risk of cracking. Passuello et al. (2009) evaluated the effect of combined use of PVA fiber and SRA on shrinkage and cracking potential of concrete mixtures made with a 0.50 w/c and a cement content of 400 kg/m^3. The risk of cracking was evaluated in accordance with the standard ASTM C1581, however, some geometry modifications were made. In their study, the thickness of the concrete ring was increased from 38 mm suggested by the ASTM C1581 to 50 mm to provide better situation for casting and vibration for the fiber reinforced concrete made with macro fibers. The incorporation of 4 kg/m^3 SRA delays the time to cracking and reduces the crack width by 40% compared to the control mixture. The addition of fibers on the other hand, does not greatly increase elapsed time before cracking, but it can reduce the crack width by about 70% with the use of 0.5% fiber volume. The addition of SRA to the fiber-reinforced concrete produced a better

cracking behavior, even at a lower fiber volume of 0.25%. Kassimi and Khayat (2013) investigated the effect of combination of fiber, SRA, and EX on shrinkage cracking of SCC mixtures made with a w/cm of 0.42 designated for repair applications. Fiber used in this investigation included multifilament synthetic fibers and hooked-end steel fibers with lengths of 50 and 30 mm and aspect ratios of 74 and 55, respectively. The SRA and EA concentrations were set to 2% and 6%, by mass of cementituous materials. The highest resistance to restrained shrinkage cracking was observed for SCC made with 0.8% steel fiber and EX with an elapsed time to cracking of 36 days and a crack width of 85 μm. Soliman and Nehdi (2014) evaluated the effect of SRA and wollastonite microfibers on the early-age shrinkage behavior and cracking potential of ultra HPC. Wollastonite microfibers were added at rates of 0, 4%, and 12%, by volume and SRA was used at 1% and 2%, by cement weight. The combined use of wollastonite microfibers and SRA in such concretes prolonged the time to cracking through the synergistic effect of reducing shrinkage strains and bridging micro cracks. For instance, the incorporation of 1% SRA and 4% wollastonite microfiber resulted in 84%, 33%, and 43% longer elapsed time before cracking compared to the control mixture (without fiber and SRA), mixture made with 1% SRA, and mixture incorporating 4% wollastonite microfiber, respectively. They found that the use of wollastonite microfibers can promote pore discontinuity, thus leading to lower mass loss and less drying shrinkage. Meddah et al. (2011) evaluated the induced stress development during autogenous shrinkage of HPC mixtures prepared with combined use of CaO-based EX and SRA. Concrete mixtures were proportioned with 6 kg/m^3 SRA and different replacement rates of 15, 20, and 25 kg/m^3 of EX. Self-induced stress measurements were performed using a reinforcing bar embedded at the center of specimens measuring 100 × 100 × 1400 mm to provide partial restraint to the concrete specimen. The authors reported a substantial reduction of up to 50% of autogenous shrinkage and the induced self-tensile stress for concrete made with a combination of SRA and EX and w/cm of 0.15. Meddah and Sato (2010) investigated the effect of different shrinkage reducing materials, including a binary system of SRA and EX and ternary system of internal curing provided by the porous ceramic coarse aggregate, SRA, and EX on autogenous shrinkage and internal self-stress of HPC mixtures made with 0.15 w/c. Their results indicated that the ternary shrinkage reducing system containing 6 kg/m^3

SRA, 15 kg/m^3 CaO-based EX, and 20% of the porous aggregate significantly mitigated both autogenous shrinkage and induced tensile stress compared to the binary curing system of SRA and EX.

2.4.2. Research on Low Cracking Concrete Bridge Deck Shrinkage by DOTs. Texas Department of Transportation (TxDOT) evaluated the effectiveness of using alternative materials to control shrinkage cracking in concrete bridge deck (Folliard et al., 2003). The authors found that crack-free or highly crack-resistant concrete with a relatively low drying shrinkage and early-age modulus of elasticity, and high early-age tensile strength should exhibit no cracking when tested in the shrinkage ring test. The incorporation of shrinkage reducing materials, such as using high volume FA replacement, SRA, Type K EX (calcium sulfoaluminate based), and polypropylene fiber are shown to provide higher resistance to early-age shrinkage cracking.

Kansas DOT (KDOT) studied the effect of various factors on the drying shrinkage behavior of concrete mixtures (Deshpande et al., 2007). The results showed that drying shrinkage of concrete increases with a reduction in aggregate content and curing period. Darwin et al. (2010) proposed a new class of HPC with low shrinkage cracking designated for bridge construction. Some of the mix design specifications of such HPC include: optimization of aggregate gradation using coarseness factor and percent retained chart, moderate w/cm (0.43-0.45), air volume of 8% ± 1.5%, low slump of 40 to 90 mm, and low cementitious materials content (less than 320 kg/m^3).

New Jersey DOT (NJDOT) performed a research project to investigate the shrinkage cracking potential of the HPC mixtures for bridge decks in New Jersey State (Nassif et al., 2007). An extensive experimental program was conducted, including compressive strength, splitting tensile strength, modulus of elasticity, free drying shrinkage, and restrained shrinkage. The content of cementitious materials, content of coarse aggregate, and coarse-to-fine aggregate volume ratio are shown to have a significant effect on both drying and restrained shrinkages. They reported that the use of high content of coarse aggregate (more than 1110 kg/m^3) with high coarse-to-fine aggregate volume ratio (more than 1.5) and limitation of cementitious material to 415 kg/m^3 can significantly reduce the risk of shrinkage cracking. The lower drying shrinkage

of 450 μstrain at 56 days was recommended to ensure the high cracking resistance for bridge decks made with HPC.

New York DOT (NYDOT) investigated the effectiveness of ternary cement blends containing SF and Class F FA on shrinkage cracking reduction of HPC (Subramaniam and Agrawal, 2009). The combined use of FA and SF is shown to reduce the shrinkage cracking potential under restrained condition. This can be attributed to the lower magnitude of elastic modulus with a slower rate of strength development, which can lead to a relatively high stress relaxation compared to the control mixture made with 100% cement.

Colorado DOT (CDOT) focused on changes in material specifications and construction practices to reduce the concrete bridge deck cracking (Shing and Abu-Hejleh, 1999). The use of Type II cement and Class F FA was suggested to reduce heat of hydration and early-age strength development. A maximum 6% SF by mass of the binder and well-graded aggregate blends were recommended to reduce shrinkage cracking of concrete bridge decks.

Ohio DOT (ODOT) investigated the bridge deck cracking issues through an in-state field survey (Crowl and Sutak, 2002), laboratory testing (Delatte et al., 2007), and a full-scale bridge deck study (Delatte and Crowl, 2012). The field survey included a total of 116 HPC bridge decks constructed between 1994 and 2001. The results of the survey showed that concrete bridge decks made with coarse aggregate with a relatively high absorption capacity (more than 1%) exhibited minimal or no cracking. Laboratory testing results indicated that the internal curing provided by fine lightweight aggregate reduced the shrinkage behavior of HPC mixtures, especially in the case of using high absorptive coarse aggregate (more than 1%).

Pennsylvania DOT (PennDOT) performed a comprehensive experimental investigation on the material properties of concrete mixtures typically used for PennDOT bridge deck projects to evaluate the early-age and long-term performance and the risk of cracking of concrete mixtures (Rajabipour et al., 2012). The risk of plastic shrinkage cracking should be eliminated by implementing water curing with adequate duration (minimum of 7 days) to minimize water evaporation from the surface of fresh concrete during construction and reduce the restrained shrinkage cracking. Based on the review of

literature, a summary of research recommendations provided by different DOTs for low shrinkage concrete bridge decks is presented in Table 2-3.

Based on the review of current literature and considering the goals defined in the dissertation, the research objectives are outlined in Figure 1-1.

Table 2-3 Summary of recommendations provided by DOTs for low cracking concrete bridge decks.

DOT	Reference	Recommendations
TxDOT	Folliard et al. (2003)	High tensile strength and low elastic modulus using fibers and SRA Type K expansive agent with high volume fly ash
KDOT	Deshpande et al. (2007) Darwin et al. (2010)	Optimized aggregate gradation Binder content ≤ 320 kg/m^3 Moderate w/cm (0.43-0.45) Lightweight sand of 20-25%, by volume
NJDOT	Nassif et al. (2007)	Coarse-to-fine aggregate volume ratio of 1.5 Cementitious material ≤ 415 kg/m^3 lower drying shrinkage of 450 μstrain at 56 days
NYDOT	Subramaniam and Agrawal (2009)	Ternary blends of Class F FA and SF
CDOT	Shing and Abu-Hejleh (1999)	Type II cement and Class F FA Well-graded aggregate blends Silica fume ≤ 6%, by mass
ODOT	Delatte and Crowl (2012)	Lightweight aggregate and high absorptive coarse aggregate (more than 1%) for internal curing
PennDOT	Rajabipour et al. (2012)	Water curing with sufficient duration (minimum of 7 days)

Based on the aforementioned literature, the specific objectives that this dissertation aims to elucidate are as follows:

- Elucidating the role of SCMs in designing more environmentally friendly binder systems to reduce environmental impacts, while maintaining equivalent performance to that of the plain OPC system.
- Establishing composition-reaction-property correlations to link the characteristics of the precursor materials to the development of fresh and hardened properties which can be utilized to proportion more environmentally friendly binders with a reduced cement content.

- Optimizeing granular skeleton and characteristics based on packing density approach to achieve dense particle packing and reduce paste volume required to fill the voids.
- Exploring the synergistic effects between various shrinkage mitigating materials, including shrinkage reducing admixture (SRA), expansive agent (EX), lightweight sand (LWS) for internal curing, and fibers to reduce shrinkage and enhance shrinkage cracking resistance of cementing systems.
- Developing Eco and crack-free HPC made with relatively low binder content, high shrinkage cracking resistance, and various workability levels targeted for transportation infrastructure applications.
- Validating the performance (i.e., shrinkage deformation and structural performance) of Eco and crack-free HPC under reinforced large-scale elements.

3. DESIGN AND FORMULATION OF SUSTAINABLE BINDER SYSTEMS: THE ROLE OF SUPPLEMENTARY CEMENTITIOUS MATERIALS

Proper substitution of cement by SCMs with adequate degree of dispersion can secure greater packing density of solid particles, reduce water and admixture demands, and improve fluidity of cement-based materials. Therefore, the primary objective of this section is to elucidate the role of SCMs to develop sustainable concrete for various infrastructure construction applications. This section is comprised of three phases as follows:

- Phase I focuses on evaluating the effect of various binary and ternary SCMs on packing density of the binder, optimum water demand (OWD) needed to achieve maximum wet density, and compressive strength development of the cement paste. The coupled effect of dispersion state of binder and SCM replacement on packing density and compressive strength of paste suspensions were examined. Correlation between packing density of the binders and overall performance of the investigated cement paste was established which can effectively be used to design sustainable cement-based materials.
- Phase II explores the effect of PSD and SSA of different binary and ternary binder systems on the minimum water demand (MWD) needed to initiate flow, the relative water demand (RWD) required to increase fluidity, packing density of binder, and compressive strength development of cement paste. The modified A&A, R–R, and power law grading models were employed to determine the ideal PSD of binder system needed to achieve maximum packing density, while maintaining relatively low water demand. Correlations between A&A distribution modulus, SSA, RR spread factor, and power law distribution exponent were established.
- Phase III, the results derived from previous phases are used to select optimum binder systems for various construction applications. Further key engineering properties of such binder systems are evaluated to select the optimum binder system to develop Eco and crack-free HPC designated for pavement and bridge applications.

3.1. EXPERIMENTAL PROGRAM

3.1.1. Materials and Mixture Proportions. A Type I/II ordinary Portland cement (OPC) was employed for all mixtures. Class C and Class F FAs, SL, and SF were used in the binary and ternary systems. Figure 3-1 shows the particle-size distribution (PSD) of the cementitious materials in use. The physical and chemical characteristics of the cementitious materials are summarized in Table 3-1. Based on the PSD of the binder and assuming spherical shape of the particles, the SSA per unit mass of binder can be estimated as follows:

$$SSA = \sum_{i=1}^{j} N_i \times \pi D_i^2 \qquad 3\text{-}1$$

$$N_i(number\ of\ \ particles) = \frac{V_i}{\pi D_i^3 / 6} \qquad 3\text{-}2$$

where D_i is the average particle diameter between two successive particle sizes (μm) and j is the number of fractions for a given grading curve. *Vi* refers to the volume passing between two successive particle sizes. A polycarboxylate-based HRWR with a solid content of 23% and a density of 1.05 was employed. The water present in the HRWR was considered as a part of mixing water in mixture proportioning.

Table 3-1 Chemical and physical characteristics of cementitious materials.

Properties	OPC	FFA	CFA	SL	SF
SiO_2, %	19.8	49.4	36.1	36.8	91.5
Al_2O_3, %	4.5	20.2	23.7	9.2	0.4
Fe_2O_3, %	3.2	15.0	4.9	0.76	0.5
CaO, %	64.2	6.8	27.9	37.1	–
MgO, %	2.7	1.1	4.9	9.5	–
SO_3	3.4	2.12	2.5	0.06	–
Na_2O eq., %	–	–	–	0.34	–
Blaine surface area, m^2/kg	380	425	490	565	–
B.E.T., m^2/kg	–	–	–	–	16500
Specific gravity	3.14	2.45	2.71	2.86	2.3
Loss of ignition, %	1.5	0.95	0.5	0	2
D50 (μm)	16	12	11.5	8.5	0.4
D10 (μm)	2	2	2	1.6	0.11

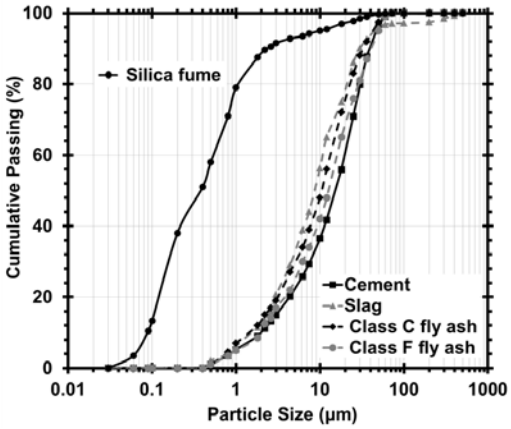

Figure 3-1 PSD of cementitious materials.

In total, 38 binder combinations were evaluated using different types and replacement levels of binary and ternary SCMs, as indicated in Table 3-2. As the cementitious materials have different solid densities, the cement paste mixtures were designed using volume replacement to maintain constant volume of solid particles. The mixing sequence consisted of adding water and HRWR followed by gradually introducing the binder materials over 3 minutes, while mixing was turned on. The cement paste was mixed for 60 sec at a constant rotation speed of 140 rpm. After a rest period of 30 sec, the mixing continued for 60 sec at high rotation speed of 285 rpm.

3.1.2. Test Methods and Interpretation. The mini-slump flow cone test was used to evaluate the flow characteristics of the cement paste, including the determination of the MWD necessary to initiate flow and the RWD needed to increase fluidity. The packing density of cementitious materials was measured based on the "wet packing approach" proposed by Wong and Kwan (2008). The test procedure for cement paste made with 100% OPC and 0.12% HRWR is shown in Figure 3-2. The method involves the preparation of mixtures with various water-to-cementitious material ratio, by volume V_w / V_{cm} and measuring the wet density of the cement paste. The wet density is determined using a cylindrical mold of 400 mL in volume, filled with paste and consolidated using a vibration table for 30 seconds before measuring the wet density. This can enable any large air bubbles entrapped during mixing to rise to the surface. The air content of the paste mixture was determined using gravimetric method in accordance with ASTM C138. The air content of the paste mixtures varied between 2.2% and 3.4%.

Table 3-2 Mixture proportions and test results of evaluated cement pastes.

Binder type	Mixture code	Cementitious materials (% by volume)					OWD*	Packing density**
		OPC	FFA	CFA	SL	SF		
Control	C	100	0	0	0	0	0.63	0.58
Binary systems	FFA30	70	30	0	0	0	0.50	0.60
	FFA40	60	40	0	0	0	0.42	0.62
	FFA50	50	50	0	0	0	0.36	0.61
	SL30	70	0	0	30	0	0.50	0.63
	SL40	60	0	0	40	0	0.38	0.66
	SL50	50	0	0	50	0	0.34	0.62
	SF5	95	0	0	0	5	0.48	0.62
	SF10	90	0	0	0	10	0.70	0.69
	SF15	85	0	0	0	15	0.78	0.66
	CFA30	70	0	30	0	0	0.48	0.61
	CFA40	60	0	40	0	0	0.46	0.63
	CFA50	50	0	50	0	0	0.45	0.62
	CFA60	40	0	60	0	0	0.42	0.61
	CFA70	30	0	70	0	0	0.46	0.58
Ternary systems	FFA30SF5	65	30	0	0	5	0.48	0.67
	FFA40SF5	55	40	0	0	5	0.41	0.69
	FFA50SF5	45	50	0	0	5	0.36	0.68
	FFA30SF10	60	30	0	0	10	0.58	0.71
	FFA40SF10	50	40	0	0	10	0.53	0.72
	FFA50SF10	40	50	0	0	10	0.49	0.71
	FFA30SF15	55	30	0	0	15	0.74	0.62
	FFA40SF15	45	40	0	0	15	0.65	0.65
	FFA50SF15	35	50	0	0	15	0.58	0.66
	SL30SF5	65	0	0	30	5	0.45	0.68
	SL40SF5	55	0	0	40	5	0.42	0.71
	SL50SF5	45	0	0	50	5	0.34	0.67
	SL30SF10	60	0	0	30	10	0.53	0.68
	SL40SF10	50	0	0	40	10	0.47	0.73
	SL50SF10	40	0	0	50	10	0.41	0.67
	SL30SF15	55	0	0	30	15	0.68	0.62
	SL40SF15	45	0	0	40	15	0.62	0.66
	SL50SF15	35	0	0	50	15	0.54	0.65
	CFA30SF5	65	0	30	0	5	0.50	0.66
	CFA40SF5	55	0	40	0	5	0.48	0.68
	CFA50SF5	45	0	50	0	5	0.46	0.65
	CFA50SF7.5	42.5	0	50	0	7.5	0.50	0.69
	CFA60SF7.5	32.5	0	60	0	7.5	0.53	0.66

*Peak wet density, 0.12% HRWR dosage, by mass of total binder.

**At 0.12% HRWR dosage, by mass of total binder, and OWD of each binder system.

Note: OPC: ordinary Portland cement; FFA: Class F fly ash; CFA: Class C fly ash; SL: slag; SF: silica fume; OWD: optimum water demand to achieve a maximum density

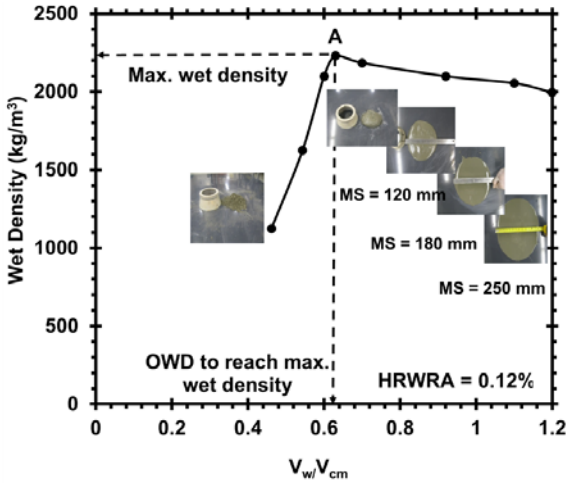

Figure 3-2 Variation in wet density with water addition for paste made with 100% OPC and 0.12% HRWR (MS refers to mini-slump flow).

In this study, the "wet packing density approach" was also employed to evaluate the effect of dispersion state of the binder on packing density of the cement paste. This method involves measuring the packing density of a given cement paste at various HRWR concentrations to determine the dosage of HRWR necessary to achieve the maximum possible packing density in the dispersed system. For a given HRWR dosage, seven mixtures were prepared to determine the maximum wet density and OWD of a given binder. For example, the effect of HRWR dosage on wet density and OWD for paste made with 100% OPC is plotted in Figure 3-3. The use of HRWR is shown to significantly increase the wet density and reduce the OWD from 1.30 for the mixture made without any HRWR to 0.60 for the mixture with 0.23% HRWR.

The measurement of the mass and OWD corresponding to the maximum wet density enables the calculation of packing density of the binder at various HRWR dosages, as shown in Figure 3-4. For each binder, a total of 42 mixtures were prepared at various concentrations of HRWR to obtain the results in Figure 3-4. The addition of HRWR from 0 to 0.12%, by mass of total binder, resulted in considerable improvement in packing density from 0.43 to 0.58. Further incorporation of HRWR from 0.12% to 0.23% did not lead to any significant change in packing density, as indicated in Figure 3-4. The optimum HRWR dosage corresponds to a concentration of HRWR beyond which there is no further improvement in packing density for a given binder in the well-

dispersed system. As shown in Figure 3-4, the optimum HRWR dosage corresponds to 0.12% for binder made with 100% OPC to achieve the maximum possible packing density of 0.58.

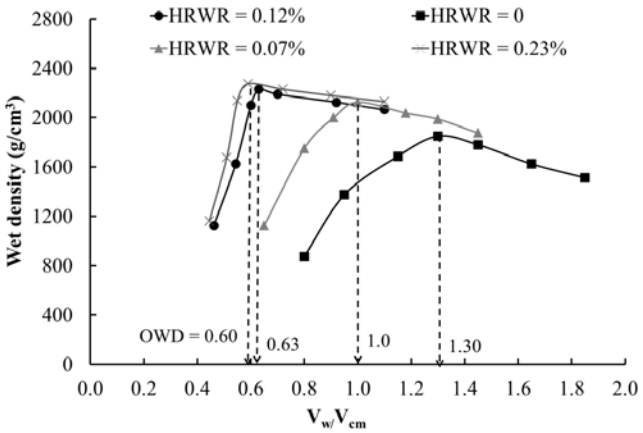

Figure 3-3 Effect of HRWR dosage on wet density for paste made with 100% OPC. Values of OWD correspond to peak wet densities.

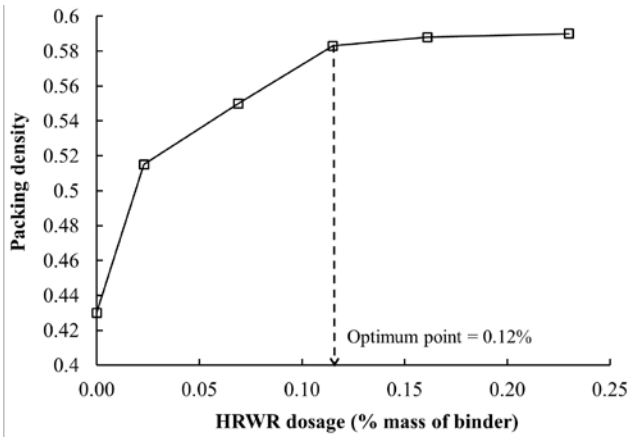

Figure 3-4 Variation in packing density with HRWR addition for paste made with 100% OPC. OWD values correspond to values obtained for each HRWR dosage from Figure 3-3.

The coaxial cylinders rheometer with inner and outer radii of 50 and 62 mm, respectively, was used to determine the rheological properties of mortar, as shown in Figure 3-5. The testing procedure consisted of pre-shearing the sample at the maximum rotational velocity applied during the test for 30 s, followed by a time step decrease of the rotational velocity from 0.5 rps (10 steps) to 0.025 rps. The rheological properties were

obtained by taking the average of the torque and rotational velocity during the last four seconds of each step, ensuring the fact that the torque was in equilibrium. The Reiner–Riwlin transformation was applied to calculate yield stress and plastic viscosity. Special attention was provided during the measurements and analysis to identify and eliminate artefacts, such as thixotropy, segregation, and plug flow. In the case of potential plug flow, the correction was applied by means of an iterative procedure (Feys et al., 2015). In parallel to the rheological properties, the mini-slump flow test was used to evaluate the fluidity retention of the mortar mixtures at 10 and 70 min following the first contact of cementitious materials with water.

Figure 3-5 Coaxial cylinders rheometer.

Drying shrinkage of mortar (ASTM C596) was determined using a digital type extensometer to measure changes in length of prismatic specimens measuring 25 × 25 × 285 mm (1 × 1 × 11.25 in.), as shown in Figure 3-6. After demolding at 24 h, the beam specimens were immersed in water for 6 days, then the samples were transferred to a temperature and humidity controlled room set at 23 ± 1°C and 50% ± 3% RH, and the shrinkage was monitored until the age of 56 days.

The 7-, 28-, and 56-day compressive strengths of cement paste were determined using 50-mm cube specimens. The cubes were demolded after one day and stored in lime-saturated water at 21 ± 2 °C until the age of testing. The results of compressive strength represent the average values of three specimens.

Figure 3-6 Drying shrinkage measurement.

The electrical resistivity measurement was used to classify the concrete according to the corrosion rate. The measurement of electrical resistivity was determined using two different methods; direct two-electrode method (ASTM C1760) and the four-point Wenner probe method (AASHTO TP 95-11), corresponding to bulk electrical conductivity and surface resistivity, respectively (Figure 3-7). The electrical resistivity was measured using cylindrical samples measuring 100 mm in diameter and 200 mm in height and cured in saturated lime water until the age of testing. The electrical resistivity is calculated as follows:

$$\rho = R \times k \tag{3-3}$$

where ρ is the resistivity, and R and k refer to measured resistance and geometry correction factor, respectively. The geometry correction factor for surface resistivity and bulk electrical conductivity can be calculated as:

$$k\,(surface\ resistivity) = \frac{2\pi a}{1.1 - \frac{0.73}{d/a} + \frac{7.82}{(d/a)^2}} \tag{3-4}$$

$$k\,(bulk\ electrical\ conductivity) = \frac{A}{L} \tag{3-5}$$

where d, A, a, and L refer to diameter, cross section area, probe spacing, and length of the specimen, respectively.

Figure 3-7 Bulk electrical conductivity (left) and surface resistivity (right).

3.2. DETERMINATION OF IDEAL PSD FOR BINDER SYSTEM

In order to determine the ideal PSD for binder systems, the effect of PSD of various binary and ternary cementitious binders on the performance of cement paste was evaluated. The modified A&A, RR, and power law grading models were employed to quantitatively describe the PSD of the investigated binder systems. For each binder, the A&A distribution modulus, RR spread factor, and power law distribution exponent were determined. A detailed protocol of determination of the A&A distribution modulus and RR spread factor is described below. A curve fitting algorithm was developed to determine the A&A distribution modulus of blended cements. Where the A&A distribution modulus is adjusted to achieve the best fit with the PSD of blended cement using the least squares method. In this method, the residual spread between the PSD of the blended cement and grading curve given by the modified A&A model is minimized as follows:

$$RSS = \sum_{i=1}^{j} e_i^2 = \sum_{i=1}^{j} \left[P_{\text{modified A\&A}(q_i)}(D_i) - P_{\text{mixture}}(D_i) \right]^2 \rightarrow \min \qquad 3\text{-}6$$

where RSS is sum of the squares of residuals, and j refers to the number of fractions for a given grading curve. The $P_{\text{mixture}}(D_i)$ represents the cumulative fraction of the particle size smaller than D_i for a given blended cement, which is obtained as:

$$P_{\text{mixture}}(D_i) = \sum_{j=1}^{N} k_j P_j(D_i) \quad \forall \quad \sum_{j=1}^{N} k_j = 1 \qquad 3\text{-}7$$

where N and K_j refer to the number of powders and replacement rate of each powder incorporated in a blended cement, respectively. The $P_j(D_i)$ corresponds to the cumulative fraction of the particle size smaller than D_i for each individual powder used in the blended cement.

The $P_{\text{modified A\&A}(q_i)}(D_i)$ used in Eq. (7) refers to the cumulative fraction of the particle size smaller than D_i for the modified A&A model, which is expressed as:

$$P_{\text{modified A\&A}(q_i)}(D_i) = \frac{D_i^{q_i} - D_{\min}^{q_i}}{D_{\max}^{q_i} - D_{\min}^{q_i}} \quad \forall \; D_i \in \left[D_{\min}, D_{\max}\right] \text{ and } q_i \in \left[0.01, 0.5\right] \tag{3-8}$$

where $D_{\min}$ and $D_{\max}$ are the minimum and maximum particle sizes, respectively, which are known for a given PSD of binder system. The factor q represents the A&A distribution modulus that varies from 0.01 to 0.5 to achieve the best fit to the PSD of a given binder.

The R-R distribution model has been widely employed in the cement industry to describe the PSD of cement. The PSD of the blended cements can be evaluated using the spread factor of the RR distribution model expressed as:

$$P(D_i) = 100 - \exp\left[-(\frac{D_i}{D'})^n\right] \tag{3-9}$$

where D' is the size parameter of the distribution, which is a measure of the fineness of a powder. The term n refers to the spread of the PSD, where a higher spread factor results in a narrower PSD (uniform distribution). For a given binder, the spread factor value can be determined by taking logarithms on both sides of Eq. (10) and rewritten, as follows:

$$\ln\ln\left[\frac{1}{100 - P(D_i)}\right] = n\ln(D_i) - n\ln(D_0) \tag{3-10}$$

The relationship between $\ln\ln\left[\frac{1}{100 - P(D_i)}\right]$ and $\ln(D_i)$ will result in a straight line, if the behavior of powder fits the RR model. Therefore, the slope of this linear relationship represents the spread factor value for a given PSD of binder system.

Brouwers (2006) indicated that the multiple discrete packing theory can be transformed to a continuously graded system with a power law distribution, where the

packing fraction of the polydisperse packing is governed by the distribution exponent. The PSD of the blended cement can be expressed using the power law grading model as follows:

$$\ln P(D_i) = \alpha \ln(\frac{D_i}{D_{\max}}) \quad \text{3-11}$$

The factor α represents the power law distribution exponent. The correlation between $\ln P(D_i)$ and follows a straight line, and the slope of this linear relationship corresponds to the α value for a given PSD of binder system. Depending on the binder composition, the fitted A&A distribution modulus, RR spread factor, and power law distribution exponent varied from 0.181–0.286, 0.777–1.089, and 0.363–0.496, respectively.

3.3. RESULTS AND DISCUSSION

3.3.1. Phase I: Effect of SCM Content and Binder Dispersion on Packing Density and Compressive Strength of Sustainable Cement Paste.

3.3.1.1 Effect of HRWR dosage on packing density of binder. Figure 3-8 shows the effect of the HRWR dosage on the packing density of various binary and ternary cementitious systems. Seven binders with different substitution rates of SCMs were prepared with various dosage rates of HRWR to evaluate the effect of dispersion state of the binders on packing density of the cement paste. The investigated binders included a control mixture with 100% OPC, three binary mixtures with different types of SCMs (40% FFA, 40% CFA, and 40% SL), as well as three ternary mixtures containing various combinations of FFA and SF (FFA40SF5, FFA40SF10, and FFA40SF15). The active dosage of HRWR varied from 0 to 0.24%, by mass of binder.

As shown in Figure 3-8, the effect of SCMs on packing density of the binder depends on the dosage rate of HRWR. For example, in the case of without using any HRWR, the partial replacement of cement with 40% FFA had merely 3% higher packing density compared to the control binder made with 100% OPC. This value, however, was 5 times greater when the HRWR dosage of 0.07% was employed. In other words, the use of 40% FFA replacement and incorporating 0.07% HRWR decreased the void ratio by 23% compared to the control binder made with 100% OPC and 0.07% HRWR dosage.

The incorporation of sufficient HRWR changes the degree of dispersion of solid particles in the matrix from a less-dispersed to well-dispersed system, thus resulting in greater packing density of the binder. When incorporated in the well-dispersed system (higher HRWR dosage), the use of binary and ternary systems led to a substantial increase in packing density from 0.63 to 0.73 compared to 0.59 for the reference binder with 100% OPC. The greatest enhancement in packing density with HRWR addition was observed in the ternary system containing 10% SF and 40% FFA. The FFA40SF10 mixture made with 0.12% HRWR exhibited 65% higher packing density compared to the similar mixture without any HRWR. This can be due to the fact that the use of HRWR results in a greater dispersion and a lower degree of agglomeration of the binders, especially in the case of binder containing fine SF particles. In a well-dispersed system, the filling effect of the SF can be effectively mobilized to fill voids among cement grains, thus leading to significant improvement in packing density of the binder system.

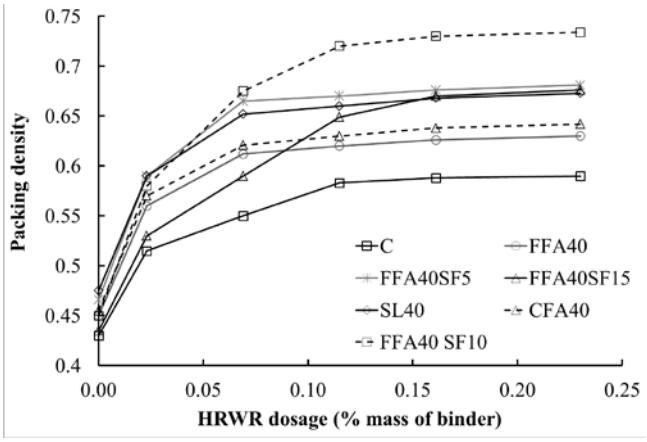

Figure 3-8 Effect of HRWR dosage on packing density of various binders.

For a given binder composition, there exists an optimum HRWR dosage required to enhance packing density, beyond which further addition of HRWR may not lead to any significant changes in packing density. For example, the increase in HRWR dosage from 0 to 0.12% resulted in 35% improvement in packing density of the 100% OPC system. However, further increase in HRWR dosage from 0.12% to 0.24% led only to 1.2% increase in packing density.

The optimum HRWR dosages necessary to achieve maximum packing density of various are compared in Figure 3-9. The optimum HRWR point is shown to vary from 0.07% to 0.16%. The binder made with 100% OPC required 72% higher HRWR content compared to binary systems containing 40% FFA, 40% CFA, or 40% SL. The spherical shape of FA particles can reduce the friction between the cement particles, leading to better flowability and lower admixture demand. The relatively low HRWR demand in the paste made with 40% SL can be possibly due to the morphology of glassy slag particles that can develop relatively low degree of HRWR adsorption.

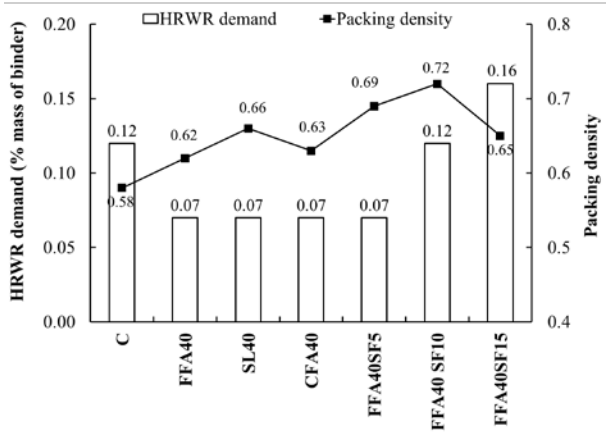

Figure 3-9 Effect of SCM substitutions on HRWR demand to reach maximum packing density.

In the case of ternary systems, the optimum HRWR demand to reach maximum packing density corresponded to 0.07%, 0.12%, and 0.16% for the FFA40SF5, FFA40SF10, and FFA40SF15 mixtures, respectively. The optimum HRWR content increased with increasing the replacement level by SF. This is probably due to the higher specific surface area (SSA) of the SF particles that increases the adsorbed HRWR and necessitates higher HRWR content to disperse the fine SF particles. As shown in Figure 3-9, the effect of SF on the HRWR dosage varied with the replacement level of the SF. For example, the ternary binder with 40% FFA and 5% SF resulted in similar HRWR demand as that of the binary system made with 40% FFA. Given the ball-bearing effect of the FA and SF and filling effect of the SF, the FFA40SF5 mixture exhibited 9% greater packing density compared to the similar mixture made without any SF at the same

HRWR dosage. On the other hand, the ternary system containing 15% SF and 40% FFA required the highest HRWR dosage of 0.16% among the tested binders. Based on the results, at a lower SF substitution (less than 5%, by volume), the small and spherical particles of SF can reduce the friction between particles and fill the voids between solid particles. Consequently, an increase in packing density and reduction in friction can counteract the adverse effect of an increase in surface area of the binder, which can lead to decrease in HRWR demand. On the other hand, the incorporation of a higher replacement rate of SF (higher than 5%, by volume) results in a substantial increase in surface area of the binder, thus increasing the HRWR demand. It is important to note that even with the higher HRWR dosage, mixture made with 15% SF, by volume, exhibited a lower packing density of 0.67 compared to 0.72 for similar ternary mixture made with 10% SF and 0.12% HRWR. Such decrease in packing density can be attributed to the loosening effect of fine particles which can push the larger particles apart. This is the case for binders incorporating fine particles in excess of that needed to fill the voids between larger particles. Therefore, the effect of SF on packing density varies with the replacement level of SF.

Based on the obtained results, a HRWR dosage of 0.12% can correspond to moderate dosage of HRWR demand among the tested mixtures. This value corresponds to the optimum HRWR dosage for binder with 100% OPC to achieve maximum packing density, as indicated in Figure 3-9. In the next section, the HRWR dosage of the 38 investigated cement pastes was fixed at 0.12% to evaluate the effect of binary and ternary SCMs on packing density of the binder.

3.3.2. Effect of SCMs on Packing Density of Binder. Figure 3-10 shows the effect of SCM substitution on packing density of binary systems with fixed HRWR dosage of 0.12%. In general, the partial substitution of cement by FA, SL, or SF significantly improved the packing density of the binder. For example, mixtures made with 40% FA or 40% SL exhibited 7% and 14% higher packing density, respectively, compared to the control binder made with 100% OPC. Given the spherical shape and smooth surface characteristics of FA particles, the partial replacement of cement with FA can lead to lower internal friction between particles and higher ball-bearing effect at the contact point. In addition, the FA and SL have higher mean diameter (D50) and greater

SSA of 490 and 590 m^2/kg, respectively, compared to 410 m^2/kg for the portland cement. This can lead to filling the voids between cement particles and increase the packing density of solid particles.

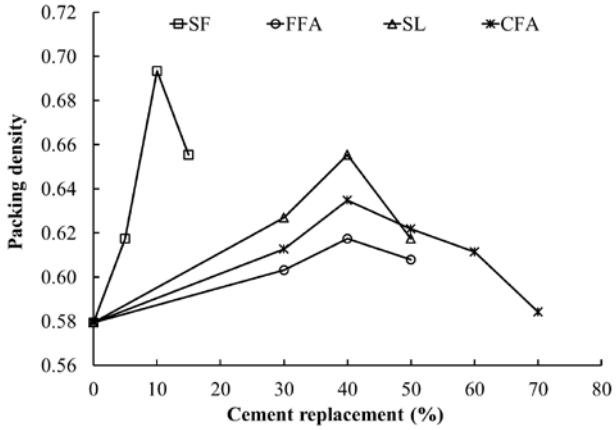

Figure 3-10 Effect of SCM substitutions on packing density of binary systems made with 0.12% HRWR.

Binders containing SF are shown to have substantially higher packing density compared to other binary mixtures. For example, the substitution of cement by 10% SF resulted in 20% increase in packing density compared to binder with 100% OPC. This is due to the both filling effect and spherical shape of the SF particles that enhance the packing density of the binder. The SF employed in this study has a D50 of 0.4 μm, which is approximately 40 times finer than that of the OPC. It is important to note that even at a relatively high SCM substitution (50% by volume), all of the investigated binary systems exhibited greater packing density compared to 0.58 for binder made with 100% OPC. As shown in Figure 3-10, the incorporation of relatively high SCM replacement led to a reduction in the packing density of binder. For instance, the use of 10% SF led to an increase in the packing density from 0.58 to 0.69. Further increase in SF to 15% resulted in lower packing density of 0.66. Similar tendency was observed for other binary systems, such as 50% FFA, 50% CFA, and 50% SL, which exhibited 2% to 6% lower packing density compared to the similar mixtures with 40% SCM replacements. This may be due to the loosening effect of fine particles that cannot perfectly fit in the voids

among larger particles. Consequently, the larger size particles tend to dilate, which can lead to an increase in the void content among the binder particles.

The reduction in packing density observed with mixture containing 15% SF and 0.12% HRWR may be due to the combination of both the loosening effect and lack of dispersion of the SF particles in the binder. As shown in Figure 3-9, the mixture incorporating 15% SF is shown to require a higher HRWR dosage to disperse the SF particles than that with 0.12% HRWR.

The ternary packing diagram (TPD) that was developed for the ternary binders is shown in Figure 3-11. The TPD was developed using the MATLAB program based on the packing density of measured and interpolated data. Given different types and replacement rates of SCMs, the packing density of ternary systems varied from 0.50 to 0.72. In the case of ternary systems containing SF with either FFA or SL, the spread between the minimum and maximum packing densities is 0.22. The greatest enhancement in packing density was observed in ternary systems containing 10% SF with either 40% FFA or 40% SL. The FFA40SF10 mixture is shown to have 16% and 5% higher packing density compared to the FFA40 and SF10 binary systems, respectively.

As in the case of binary system, the incorporation of 15% SF resulted in a reduction in the packing density of ternary binders. For instance, binder made with 15% SF and 40% FFA exhibited 10% lower packing density compared to similar ternary system prepared with 10% SF and 40% FFA. The comparison between Figure 3-9 and Figure 3-11 reveals that the use of 15% SF in the ternary systems resulted in lower packing density of binders containing 10% SF, regardless of the HRWR dosage. In the case of 0.16% HRWR, corresponding to the well-dispersed system, the FFA40SF15 mixture exhibited the packing density of 0.67 compared to 0.65 for similar mixture with 0.12% HRWR, corresponding to the moderate-dispersed system. These values of packing density are less than 0.72 determined for ternary mixture containing 40% FA and 10% SF at HRWR dosage of 0.12%. This indicate that regardless of the dispersion state of binders, the incorporation of 15% SF in binary or ternary systems can result in a lower packing density compared to 10% SF.

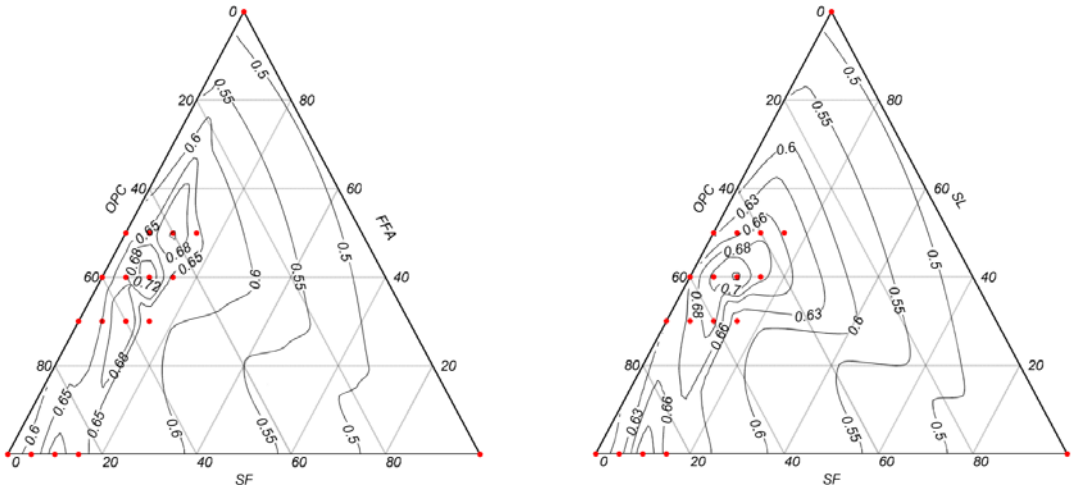

(a) (b)

Figure 3-11 Effect of SCM substitutions on packing density of ternary systems made with 0.12% HRWR for (a) ternary system of OPC, SF, and FFA and (b) ternary system of OPC, SF, and SL.

3.3.1. Effect of SCMs on Optimum Water Demand of Binary and Ternary Binders. Figure 3-12 plots the effect of SCM substitution on OWD at which maximum wet density occurs. Depending on the binder composition, the OWD of tested binders made with 0.12% HRWR ranged from 0.35 to 0.78. The lowest and highest OWD values corresponded to the FFA50 and SF15 mixtures, respectively.

In general, the partial substitution of cement by FA and SL decreased the OWD needed to reach maximum wet density. For example, the partial replacement of cement with 50% SL or 50% FFA resulted in 46% reduction in OWD compared to the control mixture made with 100% OPC. The relatively low OWD in binders made with SL can be due to the morphology of glassy surface texture and relatively low water adsorption potential of the SL. Furthermore, the particle replacement of cement by SL reduces the aluminate phase in the binder, consequently lowering the degree of HRWR adsorption.

Figure 3-13 shows the effect of SF substitution on OWD of ternary systems made with 0.12% HRWR. The effect of SF on the OWD is shown to vary with the replacement level of the SF. For instance, the ternary combination of 5% SF and 50% SL resulted in similar OWD as that of binary mixture containing 50% SL. On the other hand, the ternary system containing 15% SF and 50% SL is shown to increase the OWD by 60% compared to a similar ternary mixture made with 5% SF and 50% SL.

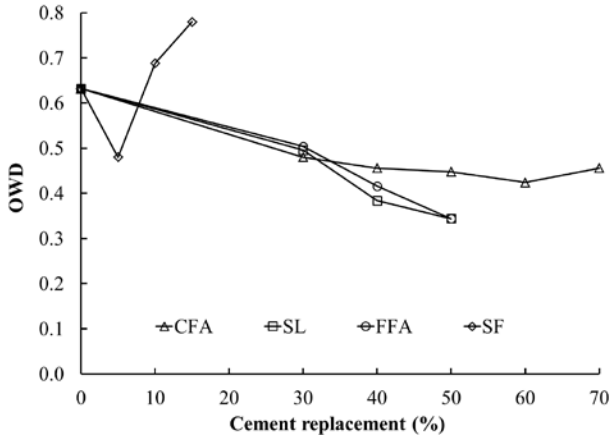

Figure 3-12 Effect of SCM substitutions on OWD of binary systems made with 0.12% HRWR.

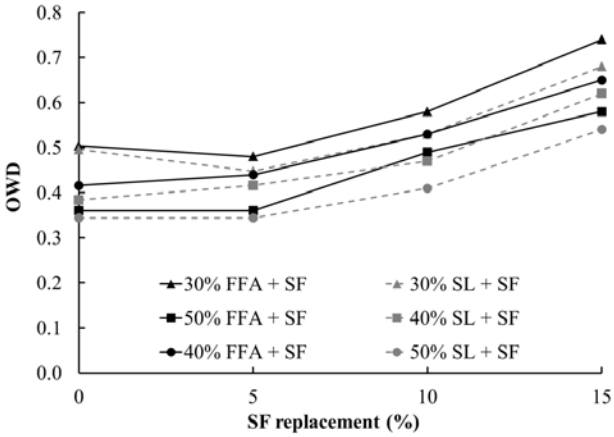

Figure 3-13 Effect of SF substitutions on OWD of ternary systems made with 0.12% HRWR.

Similar tendency was observed for other combinations of ternary systems. This can be due to the fact that the use of SF affects both the packing density and SSA of the binder. At a lower SF substitution, the small and spherical particles of the SF can fill the voids between cement particles, thus leading to a decrease in the OWD without a significant change in SSA of the binder. On the other hand, the incorporation of higher replacement rate of the SF (more than 5%) leads to substantial increase in SSA of solid particles and hence higher water demand.

3.3.2. Effect of SCMs on Compressive Strength of Cement Paste. The compressive strength of each mixture was determined at the OWD. Depending on the binder, the OWD varied between 0.35 and 0.78. The compressive strengths at 7, 28, and 56 days of the evaluated mixtures ranged from 18 to 68 MPa, 29 to 91 MPa, and 43 to 105 MPa, respectively. The coefficient of variation (COV) values of compressive strength results determined at 7, 28, and 56 days were lower than 3%, 2%, and 3%, respectively. The relative 56-day compressive strengths of cement paste with various binary and ternary systems are shown in Figure 3-14. The greatest enhancement in the 56-day compressive strength (+33%) was observed with binary system made with 10% SF. The substitution of cement by 15% SF resulted in 11% reduction in compressive strength compared to the mixture made with 10% SF. This can be due to the fact that the SF10 mixture yielded 5% higher packing density and 12% lower OWD compared to binary mixture with 15% SF. The partial substitution of cement with up to 40% SL resulted in similar 56-day compressive strength as that of the control mixture with 100% cement. In the case of binary systems, lower strength values were obtained with increasing FA substitutions (for both CFA and FFA). The substitution of cement by either 50% FFA or 50% CFA resulted in 33% and 21% reduction in 56-day compressive strength, respectively, compared to the control mixture.

In the case of ternary systems, the use of SF significantly improved the compressive strength of ternary systems, especially for binders made with FFA. The combination of 10% SF with either 50% FFA or 50% SL yielded only 12% and 2% lower 56-day compressive strength, respectively, compared to the reference mixture made with 100% OPC. Regardless of the SF replacement rate, all ternary mixtures made with SL exhibited 11% to 23% higher 56-day strength than those prepared with FFA. This can be in part due to the relatively high reactivity of the SL compared to FA. In addition, binders containing SL have higher packing density and lower OWD compared to the binders prepared with FA. As in the case of binary systems, the ternary mixtures containing 10% SF developed 3% to 8% greater compressive strength than similar mixtures prepared with 15% SF. Ternary systems incorporating 10% SF yielded 10% to 16% higher packing density and 15% to 24% lower OWD compared to ternary binders containing 15% SF.

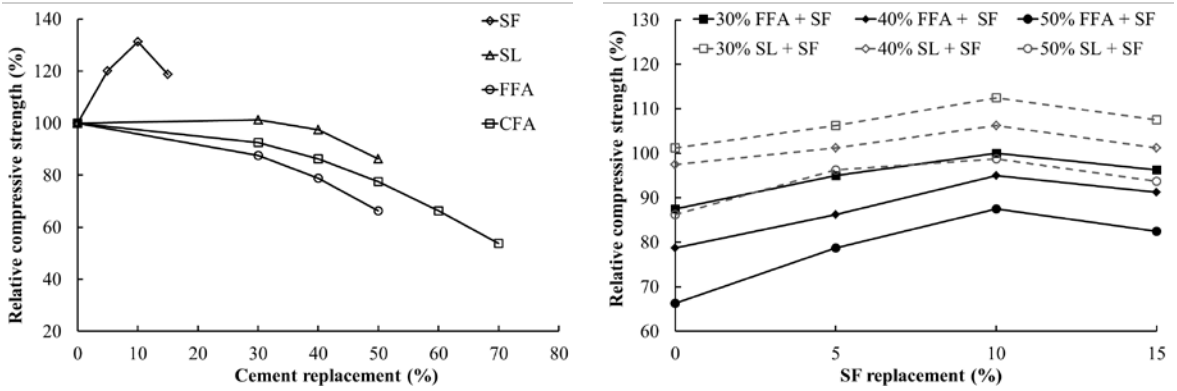

(a) (b)

Figure 3-14 Effect of SCM substitutions on relative 56-day compressive strength of cement pastes made with 0.12% HRWR and V_w/V_{cm} values corresponding to OWD of each binder for (a)binary systems and (b) ternary systems.

3.3.3. Selection of Optimum Binder Composition. Based on the obtained results the evaluated cement pastes were ranked to select the optimum binder composition. Table 3-3 summarizes the normalized responses of the investigated mixtures, which is calculated for each property as follows:

$$Normalized\ response\,(\%) = \frac{R_i - R_{\min}}{R_{\max} - R_{\min}} \times 100 \qquad 3\text{-}12$$

where R_i is the test response of the investigated mixture, for a given property; and R_{max} and R_{min} are the maximum and minimum test response among the investigated mixtures for any particular property. The normalized response varies from 0 to 100%, corresponding to the least and best performing mixtures among the investigated systems. The investigated properties included OWD, compressive strengths at 7 and 56 days, and CO_2 emission. The overall performance of the tested mixtures was calculated as the average of normalized responses, as presented in Table 3-3. The CO_2 emissions associated with the manufacturing of the binder materials used in this study were calculated based on values provided by the Environmental Protection Agency.[22,23] The estimated values do not take into consideration the emissions associated from transportation. Mixtures with higher overall performance are expected to ensure a lower water demand, lower CO_2 emission, and greater compressive strength, and can be adopted for use in sustainable cement-based materials.

Table 3-3 Overall performance of investigated cement pastes.

Mixture code	Packing density*	Normalized response (%)				Normalized overall performance (%)	Zone
		OWD**	Compressive strength		CO_2 emission		
			7-d	56-d			
SL50SF5	0.67	100.0	74	55	73	100	I (>80%) (Packing density > 0.67)
SL50SF10	0.67	84.1	74	58	80	96	
SL40SF10	0.73	70.5	80	68	67	87	
SL40SF5	0.71	81.8	72	61	60	80	
SL30SF5	0.68	75.0	78	68	47	74	II (50% to 80%) (0.62 < Packing density < 0.72)
SL50SF15	0.65	54.5	72	52	87	72	
SL30SF10	0.68	56.8	78	76	54	71	
SL40	0.66	90.9	60	56	53	68	
SL50	0.62	100.0	46	42	66	63	
SF5	0.62	68.2	92	85	7	62	
CFA30SF5	0.66	63.6	76	63	50	62	
CFA50SF7.5	0.69	63.6	58	48	82	62	
CFA40SF5	0.68	68.2	64	55	64	61	
SL40SF15	0.66	36.4	78	61	74	60	
FFA40SF5	0.69	84.1	58	42	64	59	
CFA50SF5	0.65	72.7	54	42	79	58	
FFA40SF10	0.72	56.8	62	53	71	55	
FFA30SF5	0.67	68.2	68	53	50	52	
FFA50SF10	0.71	65.9	42	44	86	50	
FFA50SF5	0.68	95.5	28	32	79	48	III (<50%) (Packing density < 0.66)
FFA30SF10	0.70	45.5	72	60	57	48	
SF10	0.69	18.2	100	100	14	47	
SL30	0.63	63.6	66	61	40	45	
SL30SF15	0.62	22.7	72	69	61	41	
CFA40	0.63	72.7	48	42	57	37	
CFA30	0.61	68.2	58	50	43	36	
FFA40SF15	0.65	29.5	58	48	79	33	
FFA50SF15	0.66	45.5	38	37	93	32	
CFA60SF7.5	0.66	56.8	30	29	96	31	
CFA50	0.62	75.0	32	31	71	29	
FFA40	0.62	81.8	32	32	57	24	
CFA60	0.61	81.8	16	16	86	21	
FFA30	0.6	63.6	48	44	43	20	
FFA30SF15	0.62	9.1	68	55	64	19	
FFA50	0.61	95.5	13	16	71	19	
SF15	0.66	0.0	90	84	21	18	
CFA70	0.58	72.7	0	0	100	1	
C	0.58	34.1	78	60	0	0	

* At 0.12% HRWR dosage, by mass of total binder, and OWD of each binder system.
** Peak wet density, 0.12% HRWR dosage, by mass of total binder.

The relationship between packing density and normalized overall performance of the investigated cement pastes made with 0.12% HRWR dosage is shown in Figure 3-15.

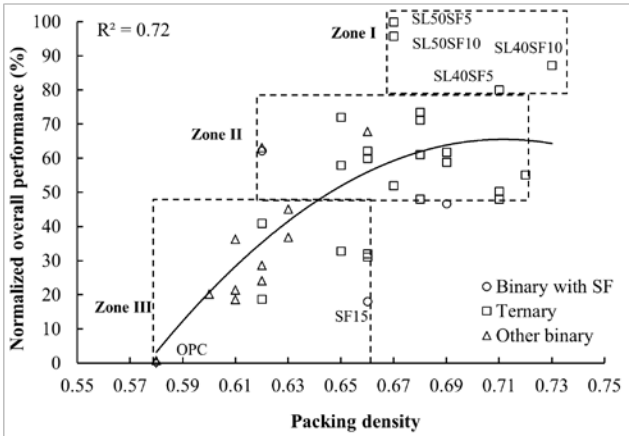

Figure 3-15 Correlation between packing density and normalized overall performance.

The overall performance of the investigated mixtures is classified into three zones. Mixtures in the first zone (overall performance > 80% and packing density greater than 0.67) corresponds to binders with relatively low CO_2 emission and high compressive strength levels at 7 and 56 days. All mixtures in zone I were proportioned with ternary systems of SF (up to 10%) with SL. Mixtures in zone II (overall performance between 50% and 80% and packing density of 0.62 to 0.72) are considered to have a moderate OWD and compressive strength. Majority of mixtures in this region were proportioned with ternary combinations of SF with FFA, CFA, or SL. Mixtures in category III (overall performance < 50% and packing density < 0.66) corresponds to binders with relatively low packing density, high OWD, low compressive strength, and low potential of CO_2 reduction. It is interesting to note that the control mixture with 100% OPC and majority of binary mixtures were classified in the third category. The greatest and lowest overall performance levels were observed for the SL50SF5 and OPC mixtures with packing densities of 0.67 and 0.58, respectively. In general, a binder with higher packing density can lead to higher overall performance, as shown in Figure 3-15. The best overall performance was observed for the ternary combination of SL (40% - 50%) and SF (5% - 10%), by volume of total binder. Such binder compositions can ensure lower water demand (OWD), greater packing density, lower CO_2 emission, and

higher compressive strength, which can be adopted for use in sustainable cement-based materials. It should also be pointed out that the highest normalized overall performance, corresponding to SL50SF5 and SL50SF10, did not reflect the highest packing density (packing density of 0.67). On the other hand, the binary mixture with 15% SF had a packing density of 0.66 and normalized overall performance of 18 due to high OWD and low potential of CO_2 reduction. As mentioned earlier, the effectiveness of incorporating a SCM to enhance packing density depends on the SCM type and content as well as the degree of dispersion of the binder resulting from the use of HRWR Figure 3-16 compares the results of OWD, packing density, and 56-day compressive strength of binders made with different HRWR dosages. The OWD values corresponding to each HRWR dosage and binder system are indicated and vary with the degree of dispersion.

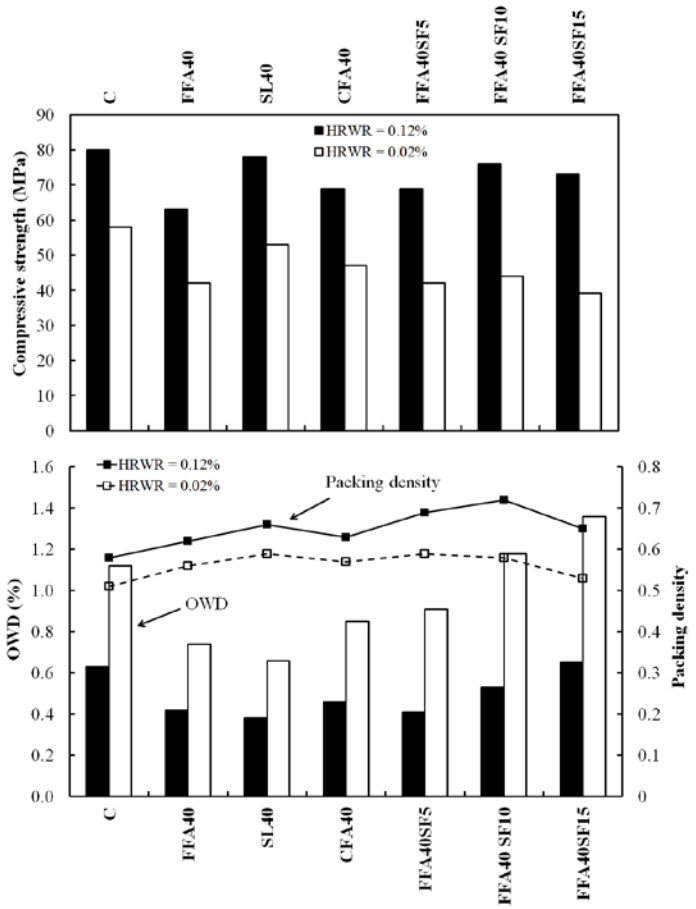

Figure 3-16 Effect of binder dispersion on 56-day compressive strength of cement pastes made with different HRWR dosages.

The degree of dispersion of binders is shown to have significant influence on compressive strength. The incorporation of sufficient HRWR dosage changes the degree of dispersion of solid particles, thus resulting in lower OWD, greater packing density, and higher compressive strength. For example, for the FFA40SF10 mixture, an increase in HRWR dosage from 0.02% to 0.12%, by mass of total binder, resulted in 55% reduction of OWD and 25% increase in packing density. The coupled effect of dispersion of binder system and reduction of water demand (OWD) led to 70% increase in 56-day compressive strength.

3.3.4. Phase II: Effect of Particle-Size Distribution and Specific Surface Area of Different Binder Systems on Packing Density and Flow Characteristics of Cement Paste.

3.3.4.1 Effect of SSA of binder system on cement paste performance. Figure 3-17(a) and (b) show the effect of SSA (calculated from the PSD) of binder systems on flow characteristics of the cement paste. Depending on the binder composition, the SSA values of the evaluated blended cements varied from 425 to 2200 m^2/kg. The lowest and highest SSA values correspond to 100% OPC (425 m^2/kg) and ternary system containing 50% SL and 15% SF (2200 m^2/kg), respectively. In the case of binder systems with $SSA < 1200\ m^2/kg$, the increase in SSA resulted in a reduction in MWD to initiate flow. This tendency was, however, reversed with further increase in surface fineness ($SSA > 1200\ m^2/kg$) of binders. This is due to the fact that, the incorporation of SF affects both the packing density and surface area of a binder at the same time. As indicated in Figure 3-17, the $SSA < 1200\ m^2/kg$ corresponds to binary systems (FA, SL, and 5% SF) or ternary systems containing 5% SF. On the other hand, $SSA > 1200\ m^2/kg$ represents binary and ternary binders incorporating more than 5% SF replacement. At a lower SF substitution (less than 5%, by volume), the small and spherical particles of the SF can reduce the friction between particles and fill the voids between solid particles, thus leading to a decrease on the minimum water demand needed to initiate flow. On the other hand, the use of a higher replacement rate of the SF (higher than 5%, by volume) substantially increases the SSA of the binder, thus reducing the amount of water per surface area of binder grains. Therefore, the effect of SF on water demand varies with the

replacement rate of SF. There exists a threshold content of incorporating SF particles to reduce water demand, beyond which a further addition of fine particles significantly increases the surface fineness of the binder, thus resulting in an increase in the MWD to initiate flow. As indicated in Figure 3-17, the highest MWD required to initiate flow was observed for binary or ternary pastes containing 15% SF replacement.

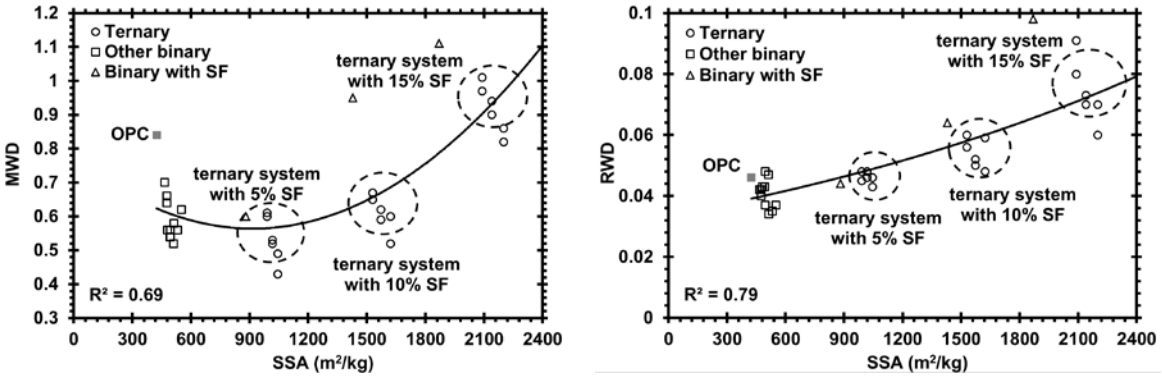

(a) (b)

Figure 3-17 Effect of SSA of blended cements on flow characteristics of binders made with 0.12% HRWRA (a) MWD to initiate flow (b) RWD to increase fluidity.

The increase in SSA of blended cements was shown to increase the RWD, as presented in Figure 3-17(b). For example, the increase in SSA of binder from 425 to 2200 m^2/kg resulted in 80% higher RWD compared to the mixture made with 100% OPC. The linear relationship between SSA and RWD in Figure 3-17(b) can be divided into three regions, as a function of SF replacement. Ternary binders containing 15% SF had the greatest RWD values among the evaluated mixtures. The SF has a mean diameter (D50) of 0.4 μm, which is approximately 40 times lower than that of the OPC. Higher content of fine particles and greater SSA of the SF result in higher RWD to increase fluidity, thus indicating lower sensitivity of binder to water addition.

The variation in packing density with calculated SSA of various binary and ternary binders is shown in Figure 3-18. Given their higher SSA values, blended cements were shown to have higher packing densities compared to the control mixture with 100% OPC. In the case of binder systems with SSA lower than 1600 m^2/kg, the increase in SSA resulted in an improvement in the packing density of the granular skeleton. On the other hand, for $SSA > 1600\ m^2/kg$, this tendency was reversed, and the packing density

decreased with further increase in the SSA of the binder. For example, the increase in SSA from 425 to 1600 m^2/kg led to an improvement in packing density from 0.58 to 0.73, while a further increase in SSA to 2200 m^2/kg reduced the packing density to 0.62.

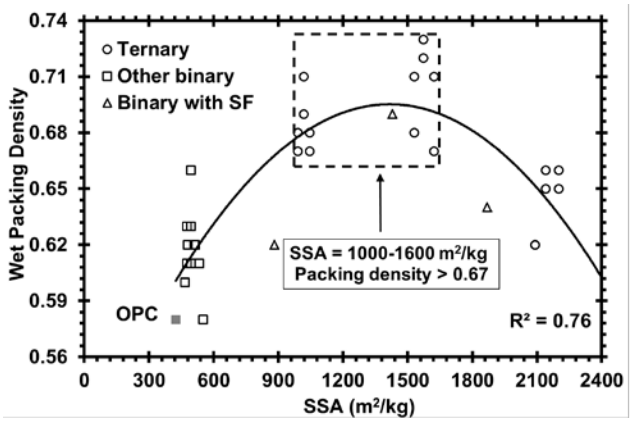

Figure 3-18 Effect of SSA of blended cements on packing density of binders made with 0.12% HRWRA.

The incorporation of high content of SF can lead to an increase in the inter-particles distance due to the loosening effect of fine particles. The use of excessive fine particles can push the larger particles apart, thus resulting in a lower packing density and higher water demand to fill the voids between solid particles. Yu et al. (1997) reported that the inter-particle forces can become relatively large when the particle size decreases, which can lead to a decrease in the packing density. Therefore, as in the case of water demand, there exists a threshold content of SF replacement to enhance the packing density. As indicated in Figure 3-18, binder systems with SSA ranging from 1000 to 1600 m^2/kg can exhibit packing density greater than 0.66 compared to 0.58 for binder with 100% OPC.

3.3.4.2 Effect of PSD of binder system on cement paste performance. The effect of PSD of different binder systems on cement paste performance was evaluated using the distribution modulus of the modified A&A model. Figure 3-19 plots the variation of flow characteristics with the A&A distribution modulus (q) corresponding to the PSD of the investigated binder systems. The relationship between q and MWD to initiate flow of the investigated binders can be classified into two zones, as shown in Figure 3-19(a). In the first zone, binders with q values between 0.21 and 0.28 were shown to have a lower MWD to initiate flow compared to the control mixture made with 100%

cement. On the other hand, for binders in the second region, corresponding to q values lower than 0.21, this trend was reversed, and further reduction in q led to a substantial increase in the MWD to initiate flow. For example, the FFA50SF5 mixture with q value of 0.245 exhibited 27% lower MWD compared to the control mixture with q value of 0.286. On the other hand, the SL30SF15 mixture with q of 0.19 developed 16% higher MWD compared to the mixture with 100% OPC. Such increase in MWD is due to the incorporation of high content of the SF particles which can lead to significant increase in SSA value. Hunger (2010) reported that mixtures with a lower q of 0.21 yielded fines-rich granular blends which can exhibit high cohesiveness due to the high amount of fine particles. The linear relationship between RWD and q in Figure 3-19(b) indicates that binder systems with wider PSD (lower distribution modulus) can develop higher RWD. For example, a decrease in the q value from 0.286 to 0.19 was shown to result in 80% increase in the RWD.

The correlation between q and OWD needed to achieve maximum wet density of the investigated binders is shown in Figure 3-19(c). Similar tendency was observed between q and OWD to reach maximum wet density as those obtained for q and MWD to initiate flow. Regardless of binder composition, all OWD values required to reach maximum wet density were lower than their corresponding MWD needed to initiate flow. Depending on the binder composition, the OWD of binders made with 0.12% HRWRA ranged from 0.34 to 0.78. The lowest and highest OWD values corresponded to the SL50 and SF15 mixtures, respectively. In general, the partial substitution of cement by FA and SL decreased the OWD needed to reach maximum wet density. As in the case of MWD, the effect of SF on the OWD was found to vary with the replacement level of the SF. For instance, the ternary combination of 5% SF and 50% SL resulted in similar OWD as that of binary mixture containing 50% SL. On the other hand, the ternary system containing 15% SF and 50% SL was shown to increase the OWD by 60% compared to a similar ternary mixture made with 5% SF and 50% SL.

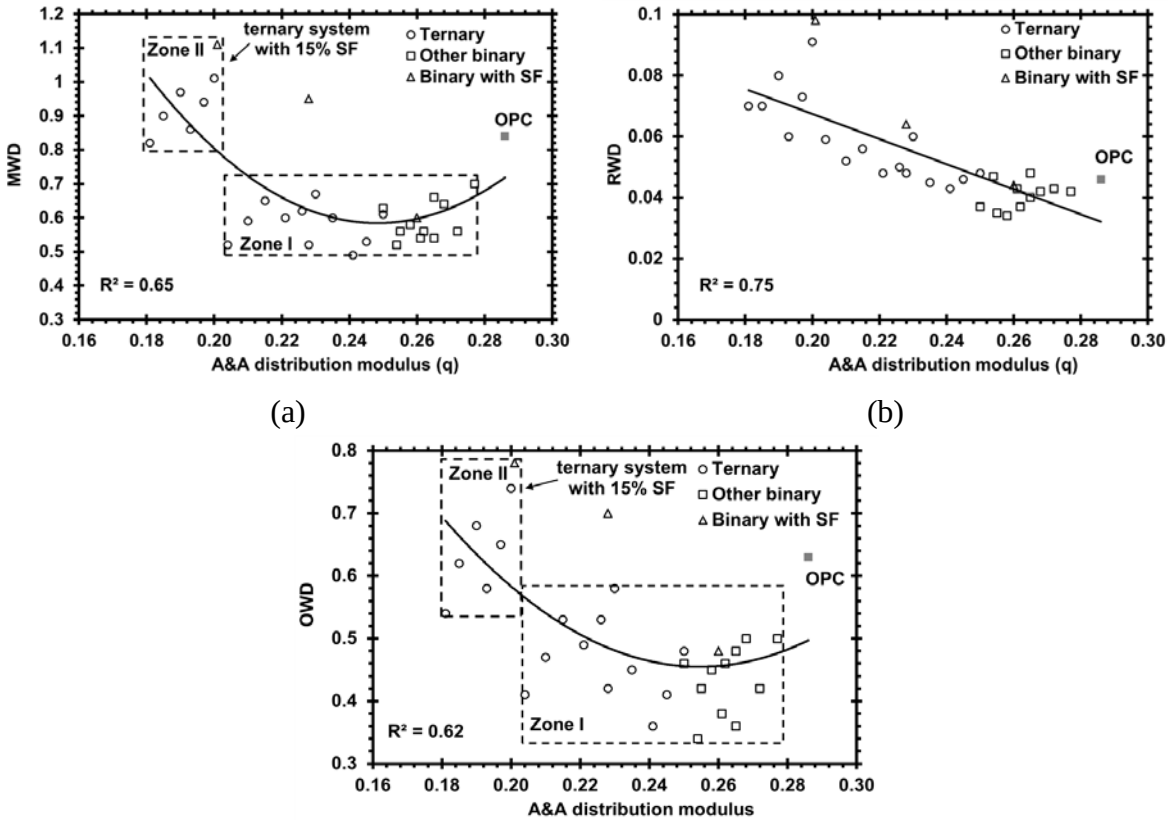

Figure 3-19 Effect of A&A distribution modulus of blended cements on flow characteristics of binders made with 0.12% HRWRA (a) MWD to initiate flow (b) RWD to increase fluidity (c) OWD to achieve maximum wet density.

The relationship between the A&A distribution modulus and packing density of binders is illustrated in Figure 3-20. A parabolic relationship was found between q and packing density of the investigated binders with 0.12% HRWRA. The reference mixture containing 100% cement had the highest q value of 0.286, which resulted in the lowest packing density of 0.58 among the evaluated binary and ternary binders. The highest packing density of 0.73 was observed for the ternary binder with q value of 0.21. This can be due to the fact that binders with lower q values exhibit wider spread of PSD and higher content of fine particles; the fine particles can ideally fill the voids between large particles, thus enhancing the packing density of powder materials. As shown in Figure 3-20, a lower q value did not always result in an increase in packing density of binders. For example, the decrease in the q from 0.28 to 0.21 resulted in 25% higher packing density, while further reduction in q from 0.21 to 0.18 decreased the packing density by

about 12%. The dashed region in Figure 3-20 suggests the existence of an optimum q value between 0.21 and 0.235 to achieve the packing density of the powder phase greater than 0.68.

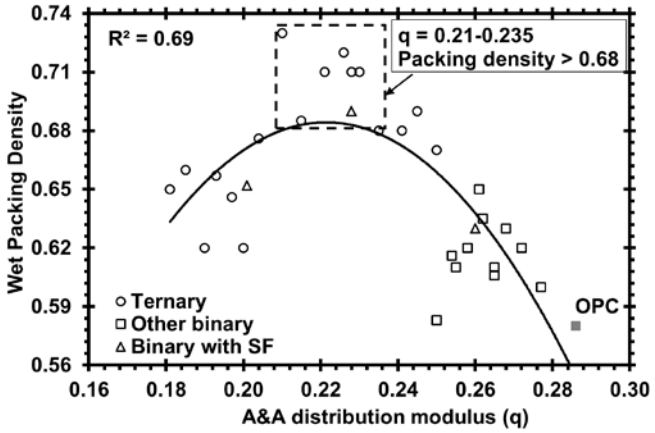

Figure 3-20 Effect of A&A distribution modulus of blended cements on packing density of binders made with 0.12% HRWRA.

3.3.4.3 Ideal PSD of binder system. The effect of A&A distribution modulus (q) on the relative MWD and packing density of the binders is illustrated in Figure 3-21. The relative property is calculated as the percentage of the difference between responses obtained with and without SCMs to that of the control mixture made with 100% OPC. Thus, a positive value of the relative MWD reflects a higher water demand to initiate flow of paste made with a SCM compared to that of the control mixture with 100% OPC. Based on the results, the effect of PSD of different binder systems on flow characteristics and packing density can be classified into four categories.

Binary cements in category I (q of 0.255–0.28) had MWD of 0.52 to 0.86 and packing density ranging from 0.58 to 0.63. Such binary mixtures had similar SSA value as that of Portland cement, but spherical shape and/or smooth surface texture of the SCMs substitution resulted in a lower MWD and a higher packing density compared to the binder with 100% cement. Mixtures classified under category II (q of 0.235–0.255) correspond to the ternary blended cements containing 5% SF, which exhibited MWD of 0.55 to 0.60 and packing density of 0.64 to 0.68. Such improvement in packing density and MWD is due to the incorporation of low content of SF that can provide filling and

shape effects. It is interesting to note that for such ternary binders, the increase in SSA from 450 to 1000 m^2/kg did not lead to an increase in MWD needed to initiate flow. These mixtures had higher RWD compared to the mixtures in the first category (binary systems), thus reflecting higher level of robustness.

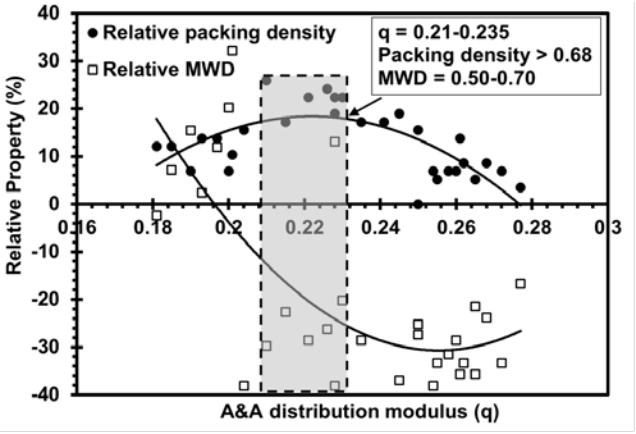

Figure 3-21 Effect of A&A distribution modulus on relative MWD and packing density of binders made with 0.12% HRWRA.

Mixtures in the third category (q of 0.21–0.235) represent the ternary binder systems containing 10% SF. These mixtures exhibited MWD of 0.50–0.70 and packing density of 0.68–0.73. As mentioned previously, the greatest enhancement in packing density was obtained for this category of mixtures. Despite a remarkable increase in packing density, such mixtures yielded higher MWD to initiate flow compared to the ternary mixtures in the second category, given higher substitution rate of SF. Mixtures in the fourth category (q of 0.18–0.21) correspond to binary and ternary binders containing 15% SF, which exhibited lower packing density of 0.62 to 0.67 and higher MWD of 0.80 to 1.11. It is noted that the binary blend of OPC and 10% SF had a q value of 0.228 and packing density of 0.69, which lies in the third category. However, this system had a MWD of 0.95, which belongs to the fourth category. The shaded area in Figure 3-21 indicates mixtures with q value of 0.21 to 0.235, where binders developed 20%–40% lower MWD and 15%–25% higher packing density compared to the plain OPC system. Such q values can correspond to the ideal PSD of blended cement to achieve a densely graded binder system without increase in water demand. Therefore, despite an increase in

the SSA, there exists an optimum replacement rate of SF which can enhance the packing density of solid particles and maintain relatively low water demand.

3.3.4.4 Correlations between SSA, A&A distribution modulus, R-R spread factor, and power law distribution exponent. The correlation between the A&A distribution modulus (q) and calculated SSA of the investigated binder systems is shown in Figure 3-22. In general, binder with lower q value was shown to have greater SSA, given the wider PSD and higher content of fine particles. Based on the results in Figure 3-22, a linear correlation can be established between the SSA and q, as follows:

$$SSA(m^2/kg) = 6045 - 20758 \times q \qquad 3\text{-}13$$

As illustrated in Figure 3-22, q values between 0.21 and 0.235 correspond to SSA of 1100 to 1700 m^2/kg. Such SSA values represent the ternary binder systems containing 5% to 10% SF replacement.

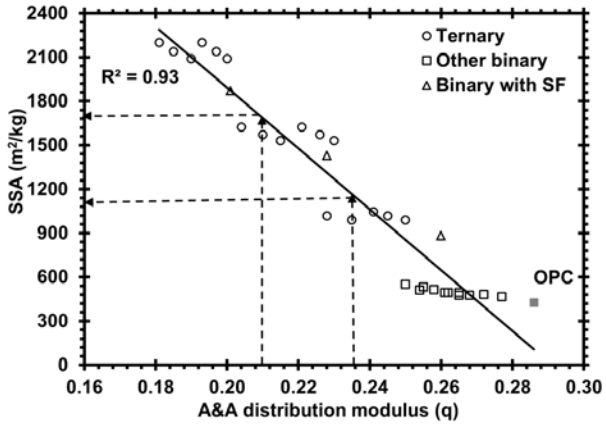

Figure 3-22 Correlations between SSA and A&A distribution modulus for binders made with 0.12% HRWRA.

The relationship between q (determined from modified A&A model), R-R spread factor (determined from R-R model), and distribution exponent (determined from power law model) is plotted in Figure 3-23. In general, the R-R spread factor and power law distribution exponent was found to reduce with decreasing the q values. Based on the derived correlations, the relationship between q, R-R spread factor, and power law distribution exponent (α) can be expressed as follows:

$$RR\,spread\;\;factor = 0.1574 + 3.3541 \times q \quad \text{3-14}$$

$$\alpha = 0.14 + 1.21 \times q \quad \text{3-15}$$

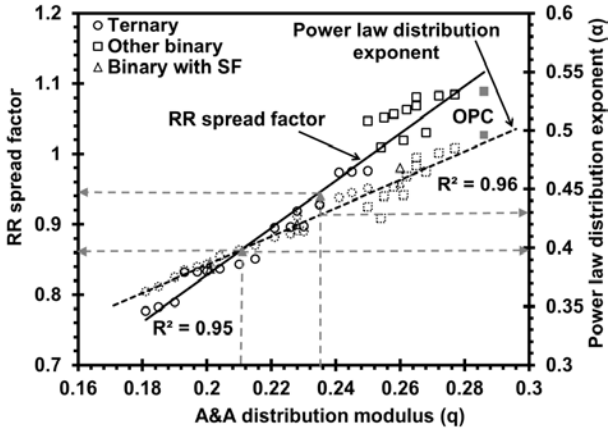

Figure 3-23 Correlation between A&A distribution modulus, RR spread factor, and power law distribution exponent for binders with 0.12% HRWRA.

Depending on the binder composition and its PSD, the fitted A&A distribution modulus, RR spread factor, and α varied from 0.181–0.286, 0.777–1.089, and 0.363–0.496, respectively. As identified in Figure 3-23, the ideal PSD of binder system with q values between 0.21 and 0.235 corresponds to RR spread factor of 0.87 to 0.95 and power law distribution modulus ranging from 0.39 to 0.43. Based on the derived correlations in Figure 3-22 and Figure 3-23, the A&A distribution modulus offers a good indication for SSA, RR spread factor, and power law distribution exponent of blended cement. Therefore, distribution modulus is an important factor which can be effectively employed to adjust the proportioning of powders in a binder composition.

3.3.5. Phase III: Optimization of Binder Composition for Eco-HPC Designated for Various Construction Applications. The results obtained from sections 1-4 were consolidated to optimize the binder composition designated for two different construction applications including: (i) pavement application (Eco-Pave Crete); and (ii) bridge transportation construction (Eco-Bridge-Crete). This phase was conducted on concrete equivalent mortar (CEM) formulated from environmentally friendly Eco-HPC mix design proportioned with different binder contents.

In total, 11 CEM mixtures were made with different types and replacement levels of binary and ternary cementitious materials to further evaluate the key engineering properties such as shrinkage and durability characteristics. The mixture proportions of the evaluated mortar mixtures are presented in Table 3-4. The binder contents of the mortars varied between 320 kg/m^3 and 350 kg/m^3 targeted for Eco-Pave-Crete and Eco-Bridge-Crete, respectively. As presented in Table 3-4, the partial substitution of cement by SCMs varied from 40% to 70%, by total volume of binder content. Given different target slump consistencies aimed for different applications, the HRWR dosage was adjusted to secure the mini-slump flow of 135 ± 10 mm and 190 ± 10 mm for Eco-Pave-Crete and Eco-Bridge-Crete, respectively. The water-to-cementitious material ratio (w/cm) was fixed at 0.4 for all mixtures.

Table 3-4 Mixture proportions of investigated CEM mixtures (volume-basis).

Type	Codification	OPC	SL	CFA	SF	Binder content (kg/m^3)	HRWR (%)
Eco-Pave-Crete	1-OPC	100	0	0	0	320	0.34
	1-FA55	45	0	55	0	320	0.27
	1-SL60	40	60	0	0	320	0.28
	1-SL20FA35	45	20	35	0	320	0.26
	1-SL20FA50	30	20	50	0	320	0.29
Eco-Bridge-Crete	2-OPC	100	0	0	0	350	0.42
	2-FA40	60	0	40	0	350	0.27
	2-SL60	40	60	0	0	350	0.28
	2-FA40SF5	55	0	40	5	350	0.38
	2-SL60SF5	35	60	0	5	350	0.38
	2-SL20FA35	45	20	35	0	350	0.27

Note: CFA: Class C fly ash, SL: slag, and SF: silica fume

3.3.5.1 HRWR demand. The HRWR dosages necessary to achieve target fluidity of the investigated mixtures are compared in Figure 3-24. All mixtures made with SCM replacements exhibited lower HRWR demand compared to the control mixture containing 100% OPC. The lowest HRWR demand was observed for mixtures made with 20% SL combined with 35% FA. For a given fluidity, this mixture necessitated 24% lower HRWR dosage compared to the control mixture. Despite the relatively high surface

area associated with SF replacement, the incorporation of 5% SF in combination with FA and SL resulted in no significant increase in HRWR demand. The spherical shape of FA particles can reduce the inter-particle friction between the cementitious grains, leading to higher flowability and lower admixture demand. The relatively low HRWR demand in the mixture containing SL can be possibly due to the morphology of glassy slag particles that can develop a relatively low degree of HRWR adsorption (Khayat et al., 2008; Mehdipour and Khayat, 2016). Therefore, the proper substitution of cement by SCMs enables the reduction in HRWR concentration required to achieve target fluidity, thus resulting in more cost effective concrete materials.

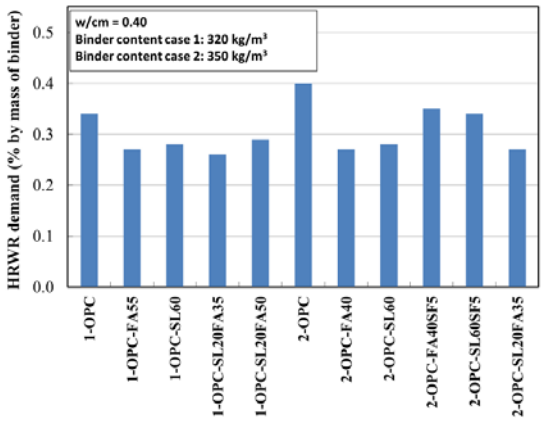

Figure 3-24 Comparison of HRWR demand for CEMs made with various SCM substitutions.

In general, the partial substitution of cement by FA, SL, or FA improved the packing density of mortar mixture. All of the investigated binary and ternary binders exhibited higher packing density compared to the reference mortar mixture. For instance, the mixture made with the combination of 20% SL and 35% FA replacements had a packing density of 0.775 compared to 0.73 for the control mixture. Given the spherical shape and smooth surface characteristics of FA particles, the partial replacement of cement with FA can lead to lower particle inter-locking and higher ball-bearing effect at the contact point. In addition, the FA and SL have higher median diameter (D_{50}) and greater SSA of 490 and 590 m^2/kg, respectively, compared to 410 m^2/kg for the Portland cement. This can lead to filling the voids between cement particles and increase the

packing density of solid particles. The greatest packing density of 0.796 was observed for the ternary binder composition containing 60% SL and 5% SF. The use of 5% SF was shown to significantly enhance the packing density of the binder. This is due to both the filling effect and spherical shape of the SF particles that enhance the packing density of the binder. The SF employed in this study has a D_{50} of 0.4 μm, which is approximately 40 times finer than that of the OPC. An increase in the packing density can generally reduce the water/admixture demand. Therefore, for a given workability, the increase in the packing density of cementitious materials can result in a decrease in the paste volume needed to fill the voids between particles, which is essential for the design of ecological and economical concrete.

3.3.5.2 Time dependent rheological properties. The effect of SCM substitutions on time dependent rheological properties of the investigated binary and ternary binder compositions is presented in Figure 3-25. The retention of rheological properties was evaluated over 60 min following the initial contact of the cementitious material with water. The tested mixtures remained covered in the recipient of the viscometer at rest between the 10- and 60-min test durations. Regardless of the binder composition, all of mixtures exhibited similar yield stress values, which is due to the similar initial fluidity values. Except for binary mixture containing 60% slag replacement, all of the investigated binary and ternary mixtures had relatively lower yield stress and plastic viscosity values at 70 min of age compared to the reference mixture made with 100% OPC.

In general, the high volume replacement of cement by slag was shown to increase the yield stress and plastic viscosity by 20% and 15%, respectively, after 70 min of age compared to the reference mixture. However, the ternary blends of 60% SL and 5% SF exhibited lower yield stress and plastic viscosity. This can be attributed to the lower inter-particle friction and higher packing density of such binder due to the use of SF replacement, thus reflecting lower changes in rheological properties over time. The highest retention of rheological properties (lowest variations in results between 10- and 70-min of age) was observed for binary mixture containing 40% FA. This corresponds to the fact that the proper substitution of cement by SCMs can lead to longer retention of rheological properties and lower fluidity loss with respect to the mixture with 100%

cement. It is important to point out that all mixtures made with 350 kg/m^3 and initial mini-slump flow value of 190 ± 10 mm had lower variation in rheological properties over time compared to the similar mixtures made with 320 kg/m^3 and initial mini-slump flow of 135 ± 10 mm. Lower degree of variation in rheological properties contributes to the ease of handling and casting operations of the mixture.

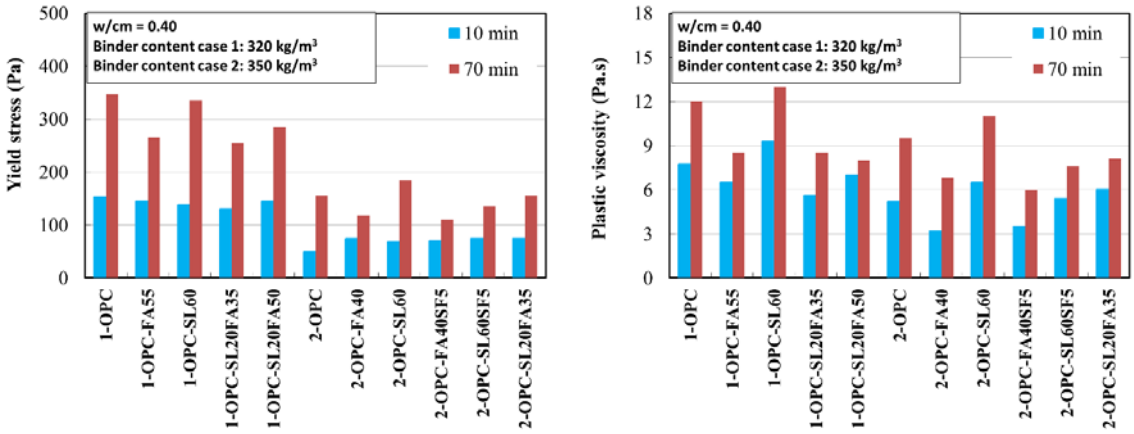

(a) (b)

Figure 3-25 Effect of SCM substitutions on rheological properties of mortars: (a) yield stress and (b) plastic viscosity.

3.3.5.3 Compressive strength development. Figure 3-26 indicates the compressive strength development of the evaluated CEM mixtures made with different binder compositions. The compressive strengths at 3 and 91 days of the evaluated CEM mixtures ranged from 14 to 40 MPa and 40 to 71 MPa, respectively. As expected, the greatest early-age compressive strength of 40 MPa at 3 days was observed for mortar made with 100% OPC followed by 27.5 MPa for ternary binder composition containing 20% SL and 35% FA replacements. On the other hand, regardless of the binder content, all of the evaluated binder compositions exhibited approximately comparable long-term compressive strength to that of the control mixture, with the exception of the mortar made with 20% SL and 50 FA. The SL20FA50 and FA40SF5 mixtures had the lowest and greatest strengths among the evaluated SCM combinations. Given higher reactivity, the incorporation of 5% SF combined with other cementitious materials was shown to be fully effective in developing compressive strength at both early and later ages. For example, the ternary mixture made with 40% FA in combination with 5% SF resulted in

17% and 20% higher compressive strength values at 3 and 91 days, respectively, compared to the similar mixture made with only 40% FA replacement.

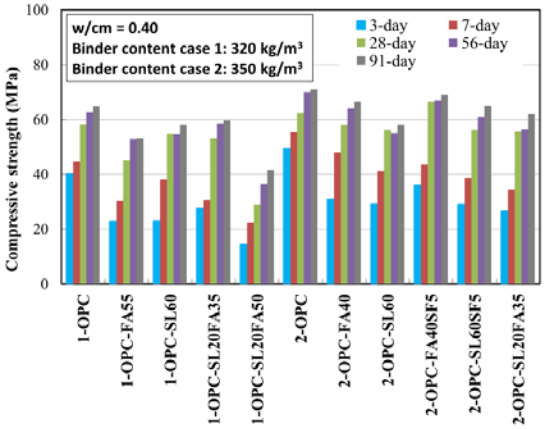

Figure 3-26 Effect of SCM substitutions on compressive strength development of mortars.

3.3.5.4 Electrical resistivity. The effect of binder composition on the electrical resistivity of the mortar mixtures is compared in Figure 3-27 as a function of time. All of the investigated binder compositions exhibited larger bulk resistivity, especially in the case of incorporating SL and SF. The ternary blends of 5% SF and 40% FA had 2.5 times higher electrical resistivity compared to the similar mixture made with 40% FA replacement. The highest electrical resistivity was observed for mixtures made with ternary blends of 60% SL and 5% SF replacements. This mixture exhibited 10 times higher bulk resistivity compared to 8 kΩ.cm for the reference mixture made with 100% OPC. This can be attributed to the higher density of the microstructure and lower capillary porosity of such mixtures, thus resulting in lower permeability and higher resistivity. Regardless of the binder compositions, good agreement was observed between the results of surface resistivity and bulk resistivity. Chini et al. (2003) investigated the correlation between surface resistivity and rapid chloride ion permeability. The experimental program included a wide range of concrete mixtures made with various binder types, binder contents, and w/cm.

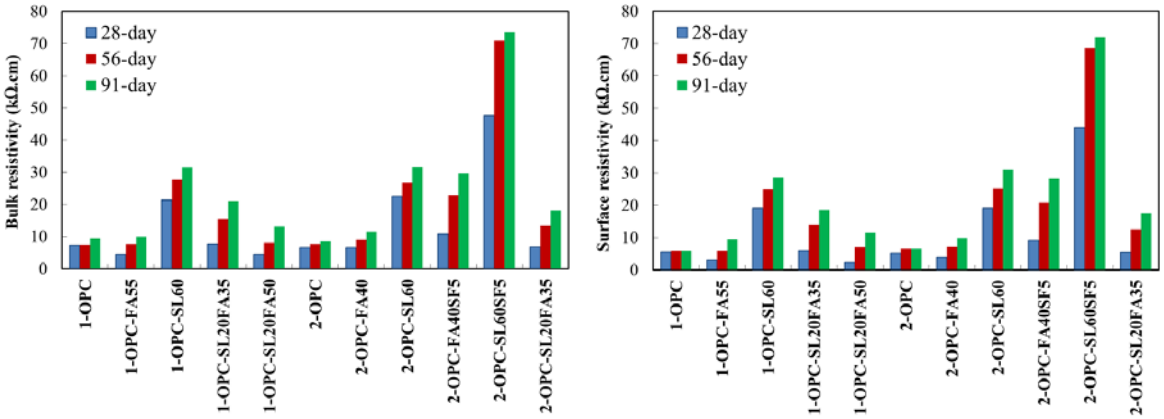

(a) (b)

Figure 3-27 Comparison of electrical resistivity for mortars made with various SCM substitutions: (a) bulk resistivity and (b) surface resistivity.

Table 3-5 presents the relationship between the surface resistivity and the rapid chloride ion permeability which was proposed by proposed by Chini et al. (2003). According to the proposed criteria, mixtures containing either 60% SL, combinations of 40% FA and 5% SF, or 20% SL and 35% FA can be categorized as relatively low chloride ion permeability. Ternary blends of 5% SF combined with 60% SL can be considered as a very low chloride ion permeability. Other tested binder compositions can be classified with moderate chloride ion permeability.

Table 3-5 Correlation between the surface resistivity and chloride ion permeability proposed by Chini et al. (2003).

Chloride ion permeability	RCP test	Surface resistivity
	Coulomb	(kΩ.cm)
High	>4000	<12
Moderate	2000-4000	12-21
Low	1000-2000	21-37
Very low	100-1000	37-254
Negligible	<100	>254

3.3.5.5 Drying shrinkage. The effect of SCM substitution on drying shrinkage of the investigated mortar mixtures is presented in Figure 3-28. Regardless of the binder content, all binary and ternary blends of SCMs resulted in lower drying shrinkage compared to that of the control mixture made with 100% OPC. As expected, the increase

in the binder content resulted in higher drying shrinkage, regardless of the binder compositions. The control mixtures with binder contents of 320 kg/m^3 and 350 kg/m^3 and containing 100% OPC exhibited the highest drying shrinkage values of 840 and 940 µstrain, respectively, after 150 days of drying, among the investigated binder compositions. Mixtures proportioned with SCMs exhibited drying shrinkage values ranging between 520-790 and 695-810 µstrain for binder contents of 320 kg/m^3 and 350 kg/m^3 after 150 days of drying. The mixture made with 320 kg/m^3 containing 20% SL and 50% FA exhibited the lowest drying shrinkage value of 520 µstrain after 150 of drying. In addition, in the case of binder content of 350 kg/m^3, the ternary blends of 40% FA and 5% SF was shown to have the lowest drying shrinkage of 695 µstrain after 150 of drying. Therefore, the incorporation of Class C FA was shown to be quite beneficial in mitigating drying shrinkage. This can be attributed to the slower reactivity at early-age and pozzolanic reactivity at later ages, which can lead to a denser microstructure and reduce the capillary porosity.

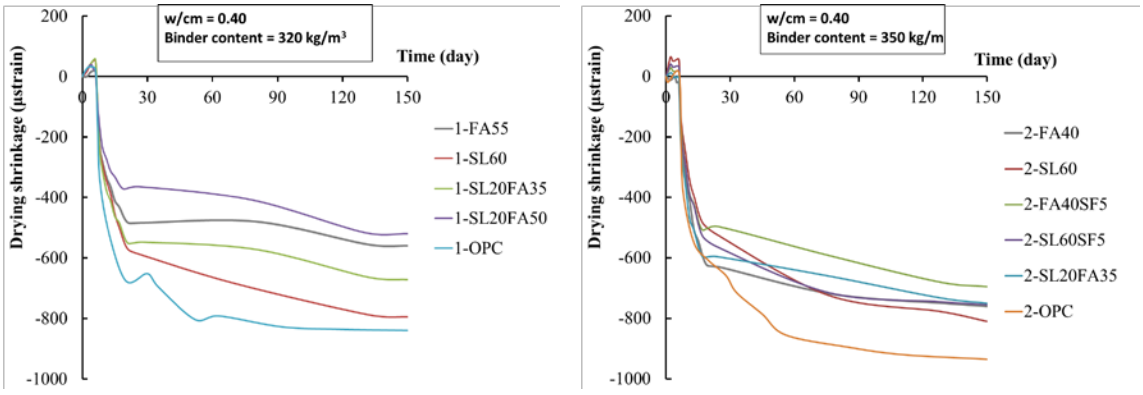

(a) **(b)**

Figure 3-28 Drying shrinkage of mortars made with different SCM substitutions for (a) mortars made with binder content of 320 kg/m^3 and (b) mortars made with binder content of 350 kg/m^3.

3.3.5.6 Selection of optimum binder composition. In order to select the optimum binder compositions for construction applications defined in this investigation, the performance rank analysis was carried out. The selected test properties for the selection of optimum binder composition and the weighted factor assigned to each test

property are presented in Table 3-6 and Table 3-7 for Eco-Pave-Crete and Eco-Bridge-Crete, respectively.

Table 3-6 Selected test properties to optimize binder composition for Eco-Pave-Crete.

Fresh properties (weighted factor)	Hardened properties (weighted factor)
HRWR demand (2) Initial plastic viscosity (1) Variation in plastic viscosity (1) CO_2 emission (2)	Compressive strength at 3 days (1) Compressive strength at 91 days (1) Drying shrinkage at 3 days of moist-curing (1) Drying shrinkage at 120 days of drying (2)

Table 3-7 Selected test properties to optimize binder composition for Eco-Bridge-Crete.

Fresh properties (weighted factor)	Hardened properties (weighted factor)
HRWR demand (2) Initial plastic viscosity (1) Variation in plastic viscosity (1) CO_2 emission (2)	Compressive strength at 3 days (1) Compressive strength at 91 days (1) Drying shrinkage at 3 days of moist-curing (1) Drying shrinkage at 120 days of drying (2) Electrical resistivity at 91 days (2)

Based on the obtained results from fresh and hardened characteristics of the investigated binders, all mixtures were ranked using performance rank analysis. The normalized response of the investigated mixtures for each property is calculated as follows:

$$Normalized\ property\,(\%) = \frac{R_{\max} - R_i}{R_{\max} - R_{\min}} \times 100 \qquad 3\text{-}16$$

where R_i is the test response of the investigated mixture, for a given property; and R_{max} and R_{min} are the maximum and minimum test response among the investigated mixtures for any particular property. The normalized response ranges from 0 to 100%, corresponding to the least and best performing mixtures among the investigated systems. Figure 3-29 indicates the normalized ranking analysis of the investigated binders targeted for Eco-Pave-Crete and Eco-Bridge-Crete. For both types of binder optimization, the lowest performance was obtained for the control mixture made with 100% OPC. The ternary blend of 20% SL and 35% FA was shown to have desirable performance for both the pavement and transportation infrastructure applications. The ternary combination of

60% SL and 5% SF was considered to be the best binder among the investigated mixtures made with binder content of 350 kg/m^3. Therefore, proper substitution of cement by SCMs can ensure greater packing density of solid particles, reduce water/admixture demand, and improve rheological and hardened properties of cement-based materials.

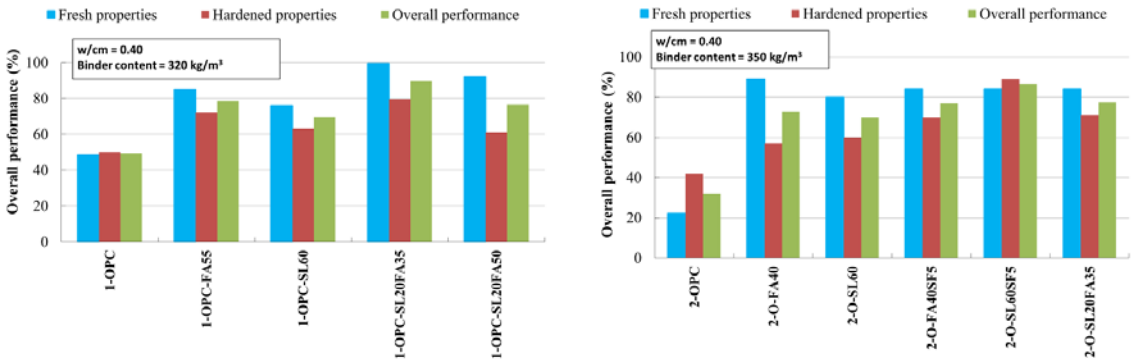

(a) (b)

Figure 3-29 Overall performance of mortars for (a) 320 kg/m^3 binder content and (b) 350 kg/m^3 binder content.

Based on the obtained results from fresh and hardened characteristics of the investigated binary and ternary binders in this phase, the selected optimum binder compositions for the Eco-Pave-Crete and Eco-Bridge-Crete applications are summarized in Table 3-8 that will be incorporated to design the Eco-HPC mixtures. The performance concrete mixtures made with such binders in combination with shrinkage mitigating materials are evaluated in detail later.

Table 3-8 Selected optimal binder compositions.

Concrete type	Cementitious materials content	Codification	Replacement rate of cementitious materials (% by volume)			
			OPC	SL	CFA	SF
Reference		Ref	100	0	0	0
Eco-Pave-Crete	320 kg/m^3	1-FA40	60	0	40	0
		1-SL20FA35	45	20	35	0
Eco-Bridge-Crete	350 kg/m^3	2-SL60SF5	35	60	0	5
		2-SLA20FA35	45	20	35	0

OPC: Ordinary Portland cement, SL: Blast furnace slag, CFA: Class C fly ash, and SF: silica fume

3.4. SUMMARY

Based on the obtained, the following conclusions appear to be warranted:

- The effectiveness of incorporating of high volume of SCM to enhance packing density of binder increases with the HRWR content resulting from greater degree of dispersion of the binder. The addition of HRWR led to lower OWD needed to achieve maximum density and higher packing density.
- The HRWR demand necessary to achieve a maximum packing density varies with the binder composition. For a given composition, there exists an optimum HRWR dosage needed to enhance packing density, beyond which further addition of HRWR would not lead to significant increase in packing density. Depending on the binder composition, the optimum active HRWR dosage is shown can vary from 0.07% to 0.16%, by mass of total binder.
- When incorporated in a well-dispersed system, the use of binary and ternary binders resulted in substantial increase in packing density that varied from 0.63 to 0.73 compared to 0.58 for the 100% OPC reference mixture.
- Given the relatively high SSA value associated with the use of SF, the influence of SF on OWD necessary to achieve maximum wet density varied with the replacement level of SF. Ternary paste with 50% SL and 5% SF resulted in similar OWD as that of binary paste with 50% SL. On the other hand, ternary system containing 50% SL and 15% SF had 60% higher OWD compared to a similar ternary mixture with 50% SL and 5% SF.
- The effect of SF on packing density varies with the replacement level of SF. Ternary mixture with 40% FFA and 10% SF had a packing density of 0.72 compared to 0.69 and 0.67 for the FFA40SF5 and FFA40SF15 mixtures, respectively.
- The incorporation of sufficient HRWR dosage is shown to lead to lower OWD and greater packing density. The coupled effect of these changes results in higher compressive strength.
- The best overall performance was observed for the ternary systems containing 40% or 50% SL and 5% or 10% silica fume, by volume of total binder. Such binder compositions can ensure lower water demand (OWD), greater packing

density, lower CO_2 emission, and higher compressive strength. Such binder systems can be adopted for use in sustainable cement-based materials.

- The SSA of binder system was found to have considerable influence on flow characteristics and packing density of binders. Blended cements with higher SSA values developed greater RWD, thus reflecting higher robustness compared to the control mixture with 100% OPC.
- The packing density of binders varies with the SSA values. The increase in SSA of binders from 425 to 1600 m^2/kg led to an improvement in the packing density from 0.58 to 0.72, while further increase in SSA from 1600 to 2200 m^2/kg reduced the packing density from 0.72 to 0.62.
- The modified A&A model can be used to optimize the PSD of binder system to achieve maximum packing density, while maintaining relatively low water demand. Binder systems with the A&A distribution modulus (q) between 0.21 and 0.235 were shown to have 20% to 40% lower MWD to initiate flow, 8% to 35% lower OWD to reach maximum wet density, and 15% to 25% higher packing density compared to the binder with 100% OPC.
- Given lower OWD and greater packing density, ternary systems containing 10% SF replacement developed higher compressive strength at 7, 28, 56 days compared to the similar ternary systems made with 15% SF substitution.
- Good correlations were established between the A&A distribution modulus, SSA, RR spread factor, and power law distribution exponent. The proposed ideal PSD of binder system with q values between 0.21 and 0.235 corresponded to RR spread factor of 0.87 to 0.95, power law distribution modulus of 0.39 to 0.43, and SSA value of 1100 to 1700 m^2/kg. Such SSA values can be achieved when incorporating SF replacement in the binder composition. It should be pointed out that the PSD and SSA of binders were varied by altering the volumetric composition of the investigated blended cements. Therefore, the ideal PSD determined from grading models is valid for the particular binder compositions employed in this study.

4. LINKING HYDRATION KINETICS TO RHEOLOGICAL PROPERTIES AND STRENGTH EVOLUTION OF BLENDED CEMENTS

In spite of a large body of evidence demonstrating the benefits of using SCMs in combination with limestone to partially replace OPC, a generalized recipe for designing sustainable (i.e., low OPC) concretes using SCMs and limestone has remained a theoretical construct rather than a practical solution. This is primarily because the interactions between OPC, SCM, and limestone, and their influence on the development of fresh and later age properties, especially in the presence of dispersants, have not been understood. The incorporation of dispersants, such as PCE, is expected to alleviate the agglomeration and improve fluidity. Therefore, a more comprehensive understanding of the correlations between the characteristics of the precursor materials (i.e., composition, particle size distribution, and particle dispersion), hydration kinetics and property evolution is required to provide new strategies for optimizing and developing advanced sustainable binders. The subject of this section is to elucidate fundamental composition-reaction-property correlations in blended binders prepared with PLC, OPC, and SCMs. The investigated SCMs include a Class C fly ash (subsequently abbreviated as FA) and a blast-furnace slag (subsequently abbreviated as SL), both of which are used to partially replace PLC at high replacement levels of 55% and 60%, by volume, respectively. Focus is placed to isolate and quantify the synergy between the PLC-SCM and OPC-SCM systems in terms of rheology, hydration kinetics and improvements in properties, and benchmark them against akin blends prepared with OPC and the corresponding SCMs. Evaluations are carried out in mortars provisioned with optimum dosages of PCE to simultaneously improve fluidity and mitigate agglomeration of particles. The kinetics of hydration in the mortars provisioned with PCE is tracked using isothermal conduction calorimetry, and the subsequent evolution of hydration products and properties are probed using a combination of experimental techniques. Focus is given to link the characteristics of the precursor materials to the resultant reactivity, and the development of properties in fresh state (i.e., rheological properties and structural recovery) as well as hardened state (i.e., compressive strength). Outcomes of this work provide novel and reliable means to link the characteristics of the precursor materials to the development of

fresh and hardened properties which can be utilized to proportion more environmentally friendly binders with a reduced cement content.

4.1. MATERIALS AND TEST METHODS

4.1.1. Materials. Commercially available Type I/II OPC conforming to ASTM C150 (Annual Book of ASTM Standards n.d.), and PLC conforming to ASTM C595 (Annual Book of ASTM Standards n.d.) were used in this study. The PLC has a limestone content of 10.5%, by mass (i.e., 12.5% by volume), with the limestone intermixed and ground with the cement clinker during the manufacturing process. Commercially available Class C FA and SL were incorporated as SCMs for partial replacements of the OPC and PLC. The oxide and the Bogue phase compositions (Bogue 1947) of the cementitious materials are summarized in Table 4-1.

The PSDs of cementitious materials used in this study are shown in Figure 4-1(a). The PSDs were determined using a Microtrac S3500 laser diffraction analyzer after the diluted powders were dispersed in isopropanol solvent via untrasonification techniques. The median particle sizes (d_{50}, μm) of OPC, PLC, FA, and SL were determined as 15, 12, 11, and 8.5 μm, respectively. Based on the PSDs of the cementitious systems, and factoring the bulk density of the materials (i.e., 3140, 3110, 2710, and 2860 kg/m^3 for OPC, PLC, FA, and SL, respectively, as measured using a pycnometer), the total specific surface area (SSA) of OPC, PLC, FA, and SL were calculated to be 341, 443, 481, and 535 m^2/kg, respectively. It is clarified here that the calculation of the SSA following this procedure involves the assumption of the spherical geometry of the particulates. However, as shown in the scanning electron microscopy (SEM) images (Figure 4-2) of the powders, this assumption only holds reasonable for FA particles. It is noted that these results were found to be in good agreement with the BET specific surface areas provided by the suppliers of these materials. In addition to the cementitious materials, a continuously graded natural sand (see Figure 4-1(b)) with a maximum size of 5 mm, density of 2500 kg/m3, and water absorption capacity of 0.6% was used.

Table 4-1 Oxide and phase compositions of cementitious materials (% by mass).

Component (%)	OPC	PLC	Class C FA	SL
SiO_2	19.32	16.31	35.64	39.32
Al_2O_3	4.38	3.62	23.76	9.75
Fe_2O_3	3.15	2.81	4.95	0.81
CaO	62.53	58.24	27.72	39.58
MgO	2.63	0.91	4.95	10.16
SO_3	3.31	3.16	2.47	0.06
Na_2O eq.	–	–	–	0.32
LOI	1.46	4.45	0.51	–
$CaCO_3$	3.21	10.50	–	–
C_3S	61.22	55.51	–	–
C_2S	12.35	11.16	–	–
C_3A	6.14	5.46	–	–
C_4AF	9.25	8.19	–	–

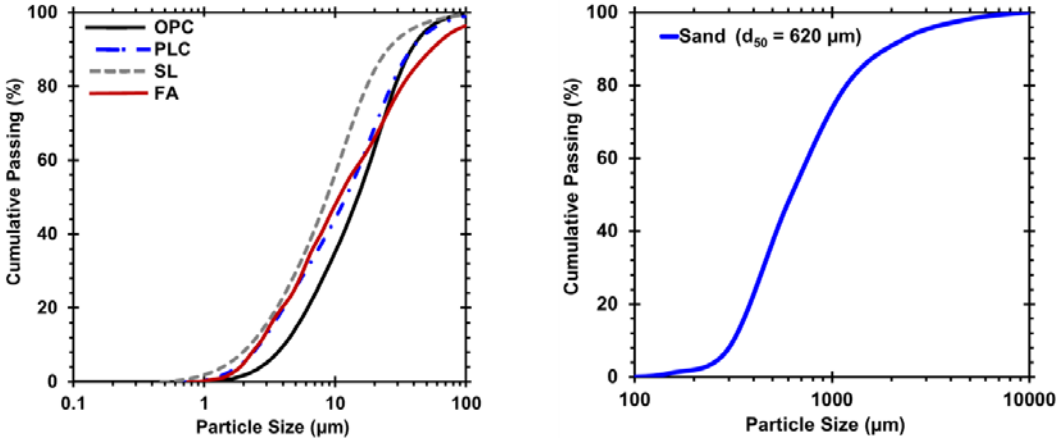

(a) (b)

Figure 4-1 PSD of (a) cementitious materials and (b) sand. Based on 6 replicate measurements, the uncertainty in the median particle diameter (d_{50}) was quantified as ±3%.

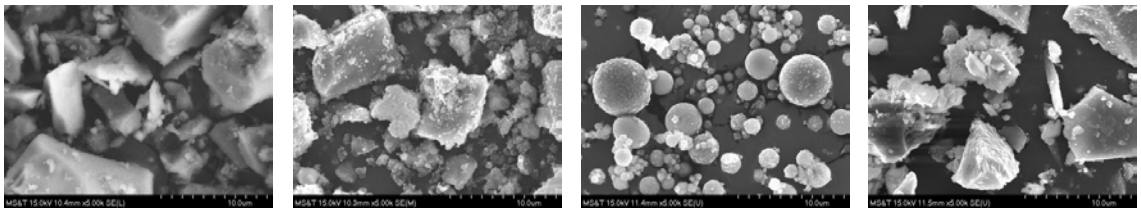

(a) (b) (c) (d)

Figure 4-2 SEM images of the investigated powders: (a) OPC, (b) PLC, (c) FA, and (d) SL. All SEM images were acquired in the secondary electron mode, while operating at an acceleration voltage of 15 kV. The magnification of each image is 5000x.

All experimental evaluations were carried out on concrete equivalent mortars (subsequently abbreviated as mortars) (Erdem et al. 2009). The mortar was formulated from environmentally-friendly high-performance concrete made with a low volume fraction of cementitious materials of 20%. In total, six mortar mixtures were prepared using different types and replacement levels of SCMs for OPC and PLC systems including: (i) plain OPC and PLC mortars (subsequently designated as OPC and PLC); (ii) mortars in which $55\%_{vol}$ of cement was replaced by class C FA (subsequently designated as OPC-FA and PLC-FA); and (iii) mortars in which $60\%_{vol}$ of cement was substituted by SL (subsequently designated as OPC-SL and PLC-SL). All mortar systems were designed by proportioning materials to secure a constant liquid-to-solid ratio. The volumetric water-to-binder ratio $(w/b)_v$ of 1.26 and sand-to-binder ratio $(s/b)_v$ of 2.6 were used for all mixtures.

A commercially-available PCE dispersant with a solid mass content of 23% and a density of 1050 kg/m^3 was used to improve the fluidity of suspension and enhance solid concentration of cementitious particles. The dosages of PCE for all mortars were adjusted to simultaneously achieve both maximum solid concentration and target fluidity in systems, as described further in Section 2.2. It is clarified that all PCE dosages reported in this study represent the total (i.e., solid + liquid) mass of the PCE.

The mixing sequence consisted of homogenizing sand for 60 sec before introducing half of the mixing water. The cementitious materials were then added and mixed for 30 sec followed by the addition of PCE. The mortar was then mixed for another 3 min at a constant velocity of 140 revolutions-per-minute (rpm), followed by a 30 sec mixing at a high velocity of 285 rpm. The mortar was then kept at rest for 2 min for fluidity adjustment before remixing for another 3 min at a velocity of 140 rpm, as outlined in ASTM C305 (Annual Book of ASTM Standards n.d.).

4.1.2. Experimental Procedures. Flow spread: The mini-slump cone test was used to evaluate the flow spread of mortars (Okamura and Ouchi 2003; Yahia and Khayat 1998), as well as to adjust the PCE dosage to achieve a target fluidity of 130 ± 10 mm. A truncated mini-cone with a top diameter of 70 mm, a bottom diameter of 100 mm, and a height of 60 mm was used. The test procedure consists of placing the mini-slump cone at the center of the plate, followed by filling with the fresh mortar sample. Subsequently,

the mini-cone is smoothly lifted and two perpendicular spread diameters (d_1 and d_2, in mm) are recorded once the flow has stopped. The mini-slump flow spread is calculated as the average of the two measured diameters.

Determination of solid concentration in fresh state: In this study, the solid concentrations of the investigated mortar systems at various PCE dosages were measured using wet density approach (Wong and Kwan 2008b) in order to determine the optimum PCE dosage corresponding to the maximum possible solid concentration for a given system. The addition of PCE improves the dispersion of particles, and hence the agglomeration of solid particles is mitigated and solid concentration is enhanced in system. Consequently, these features results in an increase in the particle packing of the system. The test involves measuring the wet density of mixtures at various $(w/b)_v$ and PCE dosages. Towards this, a cylindrical mold of 400 ml in volume is filled with mortar and consolidated using a vibrating table for 30 sec. As indicated in the representative example shown in Figure 4-3, there is an optimum w/b (point A in Figure 4-3(a)) at which maximum solid concentration in system is achieved. The maximum solid concentration occurs when the particles have achieved their maximum packing density. However, beyond the optimum w/b, further addition of water drops the solid concentration (i.e., reduction in wet density) in the system. It is clarified that no signs of segregation, such as bleeding and sedimentation of cementitious grains, for the investigated mixtures were observed throughout the solid concentration test. For the descending part of solid concentration curve, the w/b of the investigated mixtures was increased to the extent that the mixture maintained its homogeneity and stability. The volume of the solid phase in system can be quantified as follows:

$$V_s = \sum_i^n V_{si} = \frac{M_{\max}}{\rho_w (w/b)_V + \sum_i^n \rho_{si} R_{si}} \qquad 4\text{-}1$$

where, V_s (m^3) is the total volume of solid phase in the mold, $\sum_i^n V_{si}$ represents the sum of volumes of all solid phases, and M_{max} (kg) is the mass of sample corresponding to the maximum wet density. ρ_w and ρ_{si} (kg/m^3) are the density of water and solids (cementitious grains and sand particles), respectively. R_{si} (unitless) refers to the

volumetric ratio of solids (i.e., ratio of the volume of cementitious materials to the volume of sand).

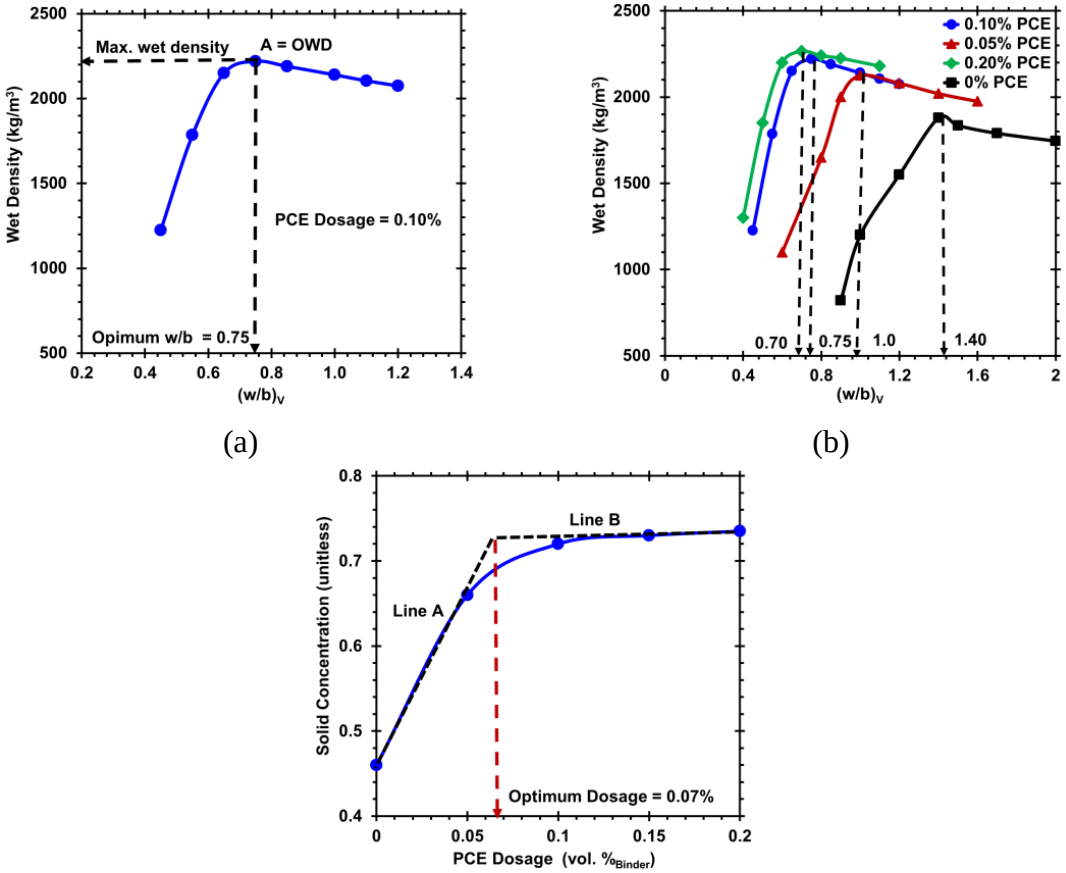

Figure 4-3 Determination of optimum PCE dosage to achieve maximum possible solid concentration in system. (a) Variations in wet density with water addition for the reference OPC mortar provisioned with 0.10% PCE dosage, (b) variations in wet density with water addition for the reference OPC mortar provisioned with various PCE dosages, and (c) variations in solid concentration with respect to PCE dosage for the reference OPC mortar. In all cases, PCE dosage is expressed as vol.% of binder.

In order to determine the optimum PCE dosage required to achieve the maximum possible solid concentration, the procedure described above was replicated at various PCE dosages (see Figure 4-3(b)). As expected, PCE addition improved the wet density markedly due to the mitigation of agglomeration of particles. From Figure 4-3(b), it can be seen that at PCE dosages between 0% and 0.10%, there is a significant enhancement in the wet density. However, further PCE addition (e.g., beyond 0.10%) leads to no

distinct changes in wet density. This is better shown in Figure 4-3(c), which plots the variations in solid concentration of system in proportion to the PCE dosage. In this study, the optimum PCE dosage was estimated from the intersection between two linear segments (i.e., lines A and B in Figure 4-3(c)), which represent linear fits to the two regimes. This intersection corresponds to threshold PCE dosage, beyond which there is less than 5% deviation in solid concentration compared to that obtained for the highest PCE dosage.

Rheological properties: The time-dependent rheological properties of mortars were evaluated over 70 min following initial contact of cementitious materials with water. The rheometer used in this study consists of coaxial cylinders (ConTec Viscometer 6) with inner and outer radii of 50 and 62 mm, respectively. This rheometer, therefore, has a gap of 12 mm between inner and outer cylinders, which is three times larger than the nominal maximum size of sand used in this study. The testing procedure consists of pre-shearing the fresh sample at the maximum rotational velocity of 18 rpm for 60 sec, followed by a step-wise (10 steps of 5 seconds each) decrease of the rotational velocity from 18 rpm to 1.5 rpm. Attention was paid to identify and eliminate artifacts, such as thixotropy (i.e., structural recovery of suspension when maintained at rest), plug flow (i.e., un-sheared part of suspension due to relatively high yield stress), and segregation (i.e., inhomogeneity of suspension due to shear-induced particle migration). The Reiner–Riwlin transformation (Reiner 1949) was applied to calculate fundamental rheological properties, namely dynamic yield stress (i.e., stress required to initiate flow) and plastic viscosity (i.e., internal resistance of suspension to flow once applied stress is more than yield stress) of suspension, as follows:

$$\tau_0 = \frac{G}{4\pi h}\left(\frac{1}{R_i^2}-\frac{1}{R_0^2}\right)\frac{1}{\ln\left(\frac{R_0}{R_i}\right)} \qquad 4\text{-}2$$

$$\mu = \frac{H}{8\pi^2 h}\left(\frac{1}{R_i^2}-\frac{1}{R_0^2}\right) \qquad 4\text{-}3$$

where, τ_0 and μ are dynamic yield stress (Pa) and plastic viscosity (Pa.s), respectively, G (Nm) and H (Nm.s) are intercept and slope of the linear relationship between torque and rotational velocity using the Bingham model (Bingham 1922). h (m) is height of inner

cylinder submerged in the mortar, and R_i (m) and R_o (m) refer to the cylinder's inner and outer radii, respectively. In addition to the rheological properties (i.e., dynamic yield stress and plastic viscosity), the thixotropy (structural recovery) of mortars were evaluated using the static yield stress at rest approach (i.e., stress growth method) at 10 and 70 min after initial contact with water. Towards this, a constant rotational velocity of 1.5 rpm was applied and the resulting torque was measured as a function of time. The torque-time profile typically shows a linear elastic region followed by a yielding moment where torque reaches a maximum value, indicating that the majority of the bonds are broken (Assaad et al. 2003). The presence of such maximum torque response is an indication of thixotropy that can be explained by the concept of structural recovery and breakdown of the bond in the system when maintained at rest (Assaad et al. 2003; Roussel et al. 2012; Saric-Coric et al. 2002).

Hydration kinetics: The rate of hydration heat evolution and extent of heat release for the investigated systems were monitored up to 7 days using isothermal induction calorimetry (Calmetrix I-CAL 8000) programmed to maintain the sample at a constant temperature of 20 ± 0.1 °C. The thermal power and energy measured to maintain the temperature of the samples at 20 °C were used to evaluate the influence of SCM and PLC replacements on hydration kinetics of the binders.

Thermogravimetric and X-ray diffraction analyses: A Netzsch STA 409 PC thermal analyzer was used to identify and measure the quantities of phases present in mortars. The mass loss (TG) and the differential mass loss (DTG) traces at 7 days were used to calculate residual CH content present in the system. The amounts of phases derived from such analyses were consistently normalized by the OPC fraction in the mortar to account for the dilution effect. In addition, for the plain OPC and PLC systems, the non-evaporable water content derived from TGA/DTG traces was used to estimate the degree of hydration of the cement (Stoian et al. 2015).

X-ray diffraction (XRD) analysis was conducted on powdered cementitious mixtures after 7 days of hydration using a Philips X'pert diffractometer in a θ–θ configuration using CuKa (k = 1.54 Å) radiation. Samples were scanned between 5° and 90° (2θ) in continuous mode with an integrated step scan of 0.025° (2θ) using a PiXcel

detector with a time per step of 150 sec. A rotating stage was used to suitably sample the powder during acquisition.

Compressive strength: The 1, 3, 7, 28, 56, and 91 days compressive strengths of mortars were determined using 50 mm cubes as outlined in ASTM C109 (Annual Book of ASTM Standards n.d.). After demolding at 24 h, all mortar samples were stored in lime-saturated solution at 21 ± 2 °C until testing. The results of compressive strength represent the average of three replicate specimens. Among triplicate specimens, the coefficient of variation in the compressive strength for the investigated mixtures was found to be less than 6%.

4.2. THERMODYNAMIC CALCULATIONS

A thermodynamic model developed in a Java environment was used to calculate the composition of the pore solution and the solid phase assemblage as function of the reacted fraction of precursor materials. The model used herein is similar to the Gibbs Energy Minimization Scheme (GEMS (Kulik et al. 2013)), which has previously been used by several researchers to predict phase assemblages in cement-based systems (Lothenbach et al. 2008a; Lothenbach 2013; Lothenbach and Winnefeld 2006). It is, however, clarified that the model uses an ion-activity model and interaction coefficients between ions/complexes based on the database developed by the Lawrence Livermore National Laboratory (LLNL). Based on the review conducted by Vincze et al. (Vincze et al. 2010), the LLNL-based ion-activity model and interaction coefficients are considered to be accurate and better suited for this study due to the ability to treat concentrated (e.g., highly caustic) aqueous electrolytes, as well as the availability of ion-interaction parameters across a wide range of ion types and solution conditions.

The model requires the initial composition of the precursor materials (i.e., oxide composition of the solids, solution composition, and w/b) as input. As the solid phases dissolve (i.e., complete dissociation is assumed) and ions are released into the solution, the calculation of the thermodynamic variables (e.g., ion activities, speciation) are described using laws of mass action and ion-interaction model/parameters based on the LLNL database (Charlton et al. 1997; Karpov et al. 2001; Koukkari and Pajarre 2006, 2011; Parkhurst et al. 1999), which has been shown to compare favorably to

determinations based on the Pitzer ion-interaction approach (Elizalde and Aparicio 1995; Kim and Frederick Jr 1988; Pitzer 1973). To describe chemical transformations (i.e., phase transformation or precipitation), thermodynamic constants (e.g., ΔG: Gibbs energies of formation, K/K_{sp}: equilibrium constants/solubility product) and molar volumes of species and precipitates (e.g., C-S-H, ettringite, monosulfoaluminate, portlandite) are drawn from standard thermodynamic databases (Damidot et al. 2011; Lothenbach et al. 2008a; Lothenbach 2013; Lothenbach and Winnefeld 2006; Puerta-Falla et al. 2015b). A Gibbs energy minimization module is then employed to calculate phase relations using a non-linear Lagrangian algorithm, which follows a convex programming approach to iteratively evaluate the cumulative free energy of several potential solid/liquid phase assemblages, to ultimately yield the most probable (i.e., lowest free energy) one at equilibrium (Koukkari and Pajarre 2006, 2011). The implementation thus reveals, in an orderly fashion, the evolution of the reactant and product phases (i.e., mass and volume) and solution composition (i.e., concentrations of different aqueous species) as outputs. The model, therefore, can be used to describe the roles of various compositional descriptors of precursor materials on the development of the phase assemblage.

4.3. RESULTS AND DISCUSSION

4.3.1. Determination of Optimum PCE Dosages. The optimum PCE dosages for the investigated mortars were determined using a combination of two approaches, i.e., (i) wet density approach: to determine PCE dosage needed to achieve the maximum possible solid concentration, and (ii) flow spread technique: to determine PCE dosage required to secure a target fluidity.

First, the variations in solid concentration of mortars were evaluated at different PCE dosages ranging from 0% to 0.5%, by volume of binder (see Figure 4-4(a)) using the wet density approach. As expected, the incorporation of PCE evokes steric forces and alleviates agglomeration of fine particles, resulting in an enhancement of solid concentration in the system. The improved solid concentration is more dominant for PLC systems, as shown in Figure 4-4(b). This is attributed to the presence of a larger fraction of finer particles in PLC (see Figure 4-1(a)), which necessitates higher PCE dosages. This

implies that the beneficial effect of fine particles to enhance particle packing in PLC system is strongly related to the dosage of PCE. When no PCE is incorporated, the OPC system has slightly larger extent of solid concentration than that of the corresponding PLC system. However, this trend is reversed when PCE is added. Therefore, to elicit the full benefits of the higher SSA for particle packing improvement in blended system, it is vital to incorporate dispersing admixtures, such as PCE, at the optimum dosage (Bentz et al. 2012b; Mehdipour and Khayat 2016a; Wong and Kwan 2008a). These differences in solid concentration between OPC and PLC mortars also carry over to mortars prepared with SCM replacements (i.e., OPC-SCM and PLC-SCM systems). Here, it is noted that in the presence of SCMs (i.e., FA and SL), solid concentration improves for both PLC and OPC mortars, wherein PLC-SCM mortars develop larger solid concentration values compared to their OPC-SCM counterparts due to their higher overall SSA.

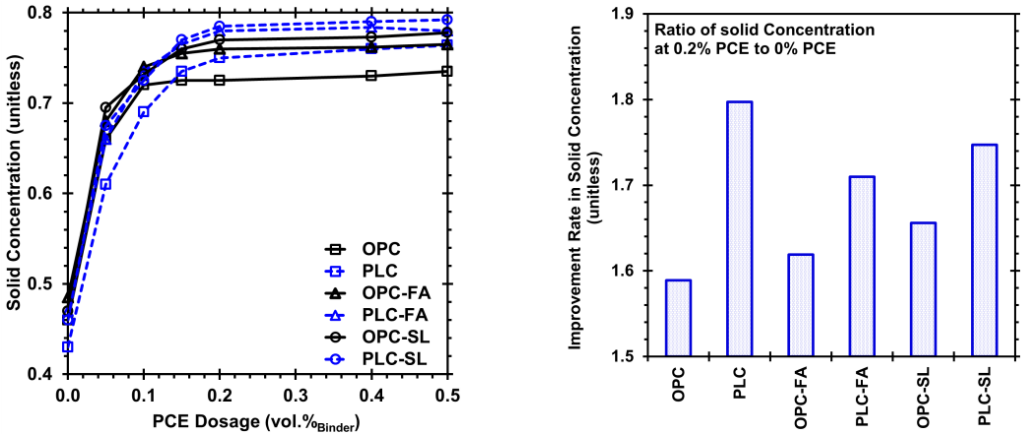

(a) (b)

Figure 4-4 (a) Variations in solid concentration in relation to PCE dosage and (b) improvement rate in solid concentration provisioned with PCE. In (b), the improvement rate for a given system was obtained by dividing the maximum solid concentration of each mixture by its corresponding solid concentration at 0% PCE.

To study the effects of PCE and PSD of blended cements on particle packing, the overall SSA of the binders was plotted against the maximum solid concentration achieved for the cases of without and with PCE additions (Figure 4-5(a)). While no clear trend is observed between SSA and solid concentration in the absence of PCE, a broadly linear correlation can be established in the systems provisioned with PCE.

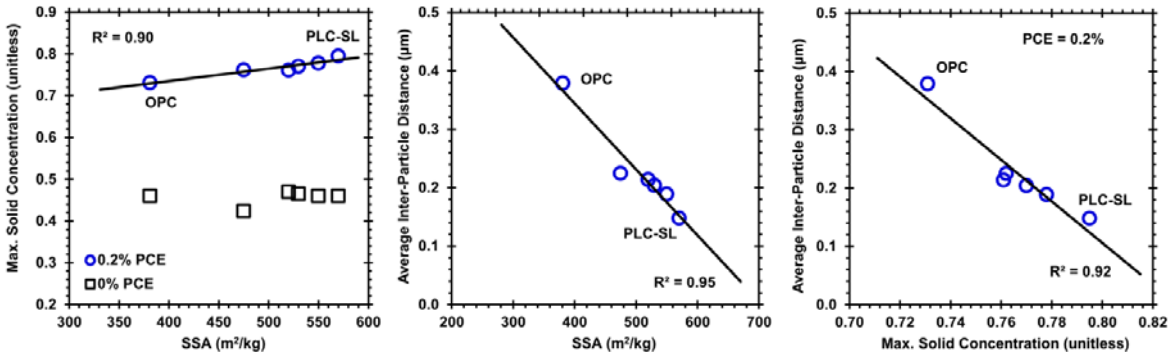

(a) (b) (c)

Figure 4-5 Correlations between: (a) overall SSA of binders and maximum solid concentration at two different PCE dosages, (b) SSA and average inter-particle distance, and (c) maximum solid concentration and average inter-particle distance. The overall SSA of the binders was calculated in an additive manner, by using the SSA of the individual components and their vol. % in the binder.

To better understand this correlation, a microstructural stochastic packing algorithm with periodic boundary conditions was implemented to evaluate the inter-particle spacing between cementitious particles (Kumar et al. 2013b). The algorithm uses the measured PSDs and volumetric fractions of the paste component of the mortar (i.e., OPC/PLC, SCM, and water) as inputs, to generate a three-dimensional (3D) microstructure indicative of the system immediately after mixing with water. As shown in Figure 4-6 representative 2D slices extracted from 3D-REV (representative elementary volume), the binders are represented as spherical particles packed in a 3D-REV of 100 × 100 × 100 μm^3. Once the sought packing is achieved, the average spacing between solid surfaces is calculated using algorithms described in (Kumar et al. 2013b). It is noted that the presence of PCE as a separate component was not considered in the microstructural packing simulations. However, in order to ensure the dispersion of particles, as induced by PCE, cementitious particles were packed such that the contact between any two particles is prevented. As can be seen in Figure 4-5(b), the average spacing between the particles decreases with increasing overall SSA of the particles. Since smaller inter-particle spacing is an indication of improved particle packing, a corresponding enhancement in the solid concentration is also noted (Figure 4-5(c)). This correlation between simulations and experimental measurements thus proves that in the good

dispersive systems (i.e., PCE containing systems), binders with higher SSA of particles results in smaller inter-particle spacing, and thus enhanced particle concentration.

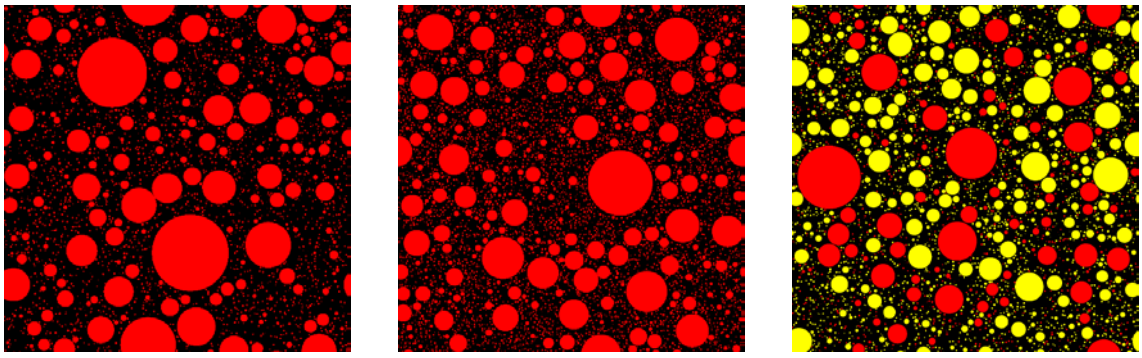

(a) (b) (c)

Figure 4-6 Virtual microstructure of paste components of: (a) OPC, (b) PLC, and (c) 40% OPC – 60% SL systems in fresh state. The 2D slice images represent the distribution of clinker (red) and slag (yellow) particles at the center (z = 0 of the x-y plane) of the representative 3D-REV of 100 × 100 × 100 μm^3.

Next, the results of optimum PCE dosages derived from the wet density and the flow spread (i.e., mini-slump cone test) approaches for the investigated mortars are compared in Figure 4-7(a). Based on the results obtained from the wet density approach, a PCE dosage of 0.20% would correspond to the optimum dosage of PCE among mortars to achieve maximum possible solid concentration. However, all mortars were found to require higher PCE dosages to achieve a target flow spread of 130 mm compared to those obtained from the wet density approach. To understand this discrepancy, it is important to contrast the role of PCE in the two methods. Specifically, in the mini-slump flow test, PCE (when provisioned at adequate dosages) acts to initially counteract the inter-particle attractive forces (e.g., van der Waals) and reduce inter-particle friction by maintaining a finite spacing between particles. This facilitates the movement of particles (i.e., lowering resistance of suspension to flow onset). However, in the case of the wet density approach, because the flow of the suspension is not required, a smaller dosage of PCE is needed, since its role is limited to mitigate agglomeration and enhance solid concentration in system.

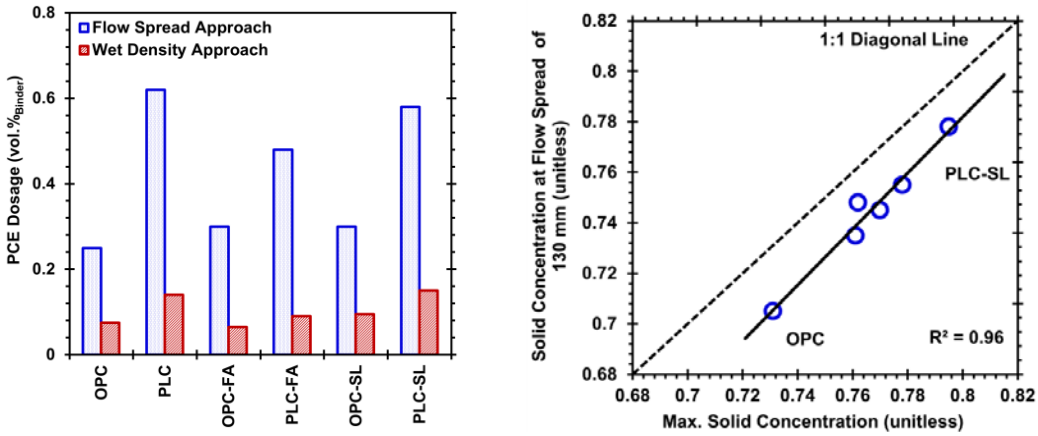

(a) (b)

Figure 4-7 (a) Comparison of PCE dosages needed to achieve a flow spread of 130 mm and those required to reach maximum possible solid concentration and (b) comparison of solid concentrations of binders at flow spread and maximum possible solid concentration state.

The correlation between solid concentrations of binders at the flow spread, as determined from the mini-slump flow test, and at the maximum possible solid concentration state, as determined from the wet density approach, is shown in Figure 4-7(b). As can be seen, the results of solid concentration identified by these two test methods are well-correlated (i.e., broadly linear relationship), although the solid concentrations at flow spread of 130 mm are consistently lower than those determined using the wet density approach. This is on account of higher w/b of pastes prepared for flow spread test compared to the corresponding mixtures at maximum possible solid concentration state. It is important to note that at maximum solid concentration, the amount of water is not sufficient to provide fluidity in mixture. Based on these results, in the subsequent sections, for each mortar system, the PCE dosage has been fixed at the values obtained from the mini-slump flow test, so as to secure both target fluidity as well as enhanced particle concentration.

4.3.2. Time-Dependent Rheological Properties. Figure 4-8 compares the time-dependent rheological properties of the evaluated mortars provisioned with their optimum PCE dosages that were determined in section 3.1. The changes in rheological properties were evaluated over 70 min following the initial contact of cement with water. Regardless of the binder composition, all mortars exhibited similar initial dynamic yield

stress at 10 min. This is expected because all mortars were prepared at the same $(w/b)_v$ of 1.26, and provisioned with the optimum PCE dosage to achieve equivalent initial fluidity (i.e., 130 mm). In spite of having the same initial yield stress at the age of 10 min, PLC systems develop higher plastic viscosity and static yield stress at rest (Figure 4-8) compared to their OPC counterparts. This difference between rheological properties of PLC and OPC mortars further manifests at later ages (i.e., at 70 min). This is attributed to the coupled effect of higher SSA and lower inter-particle spacing among cementitious particles in PLC mortars as compared to OPC mortars (see Figure 4-5). The latter point (i.e., inter-particle spacing) is particularly important as it is an indication of higher resistance of suspension to the applied shear force, which in turn, leads to greater thixotropic structural build-up over elapsed time (Khayat and Assaad 2006; Vance et al. 2013b, 2015).

More specifically, when a mixture is maintained at rest, individual cementitious particles begin to flocculate (i.e., on account of inter-particle forces) causing progressive changes in the microstructure (Assaad et al. 2003; Roussel et al. 2012; Saric-Coric et al. 2002). The higher the SSA of the material, or the longer the material is maintained at rest, this thixotropic structural build-up becomes more dominant. The difference between dynamic yield stress and static yield stress at rest for the investigated mixtures is shown in Figure 4-8(c). Expectedly, the static yield stress required to break down the structure in system is larger than dynamic yield stress recorded to initiate flow in the mixture (Assaad et al. 2003). This contrast is more evident for PLC systems. At both ages of 10 and 70 min, all of the measured rheological parameters (i.e., dynamic yield stress, plastic viscosity, and structural build-up at rest) were found to be the highest for the binary blend of PLC and SL. This is attributed to the higher overall SSA, as well as a relatively more angular geometry of the particles (slag in particular; see Figure 4-2) in the binder. More specifically: (i) higher SSA leads to enhanced particle packing and reduced water film thickness on the particles' surfaces, and consequently lower inter-particle spacing, and (ii) the angular geometry of the particles enhances the likelihood of inter-particle contacts, thus elevating the inter-particle friction among the particles. A combination of these effects, therefore, explains the higher yield stress and plastic viscosity.

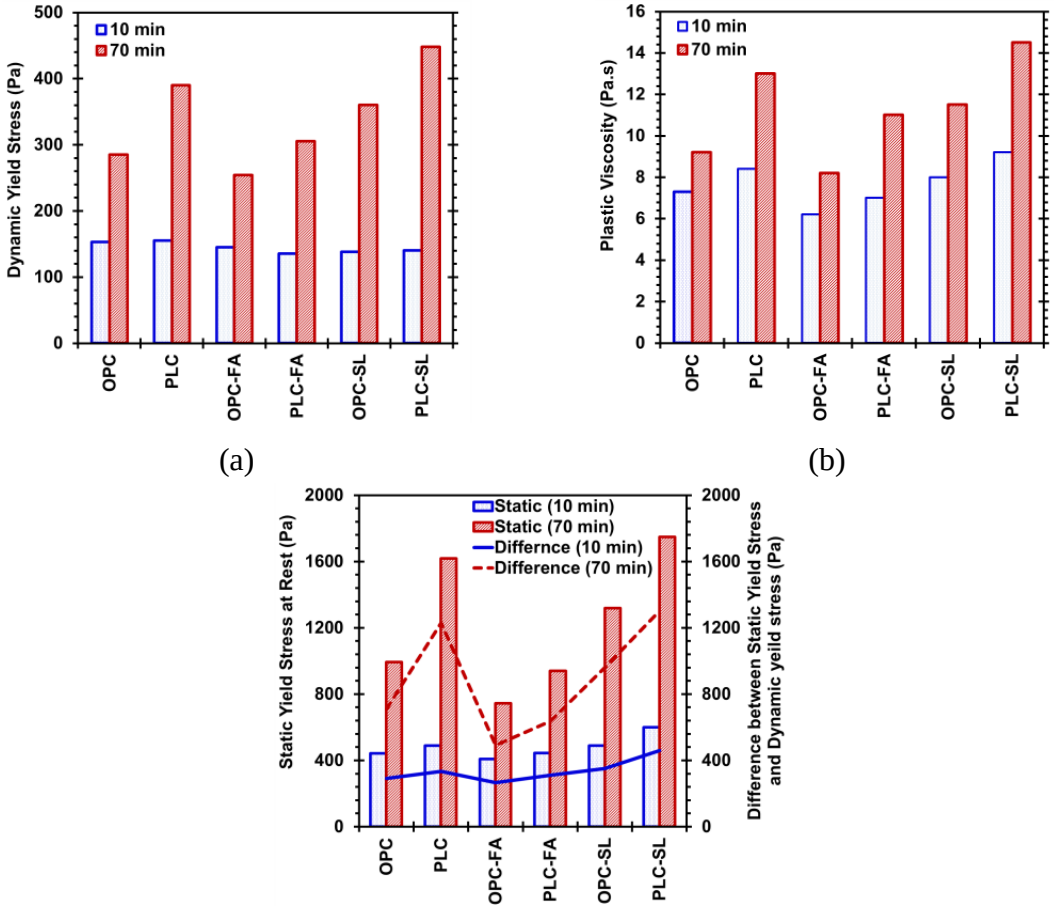

Figure 4-8 Time-dependent rheological properties of OPC-SCM and PLC-SCM systems provisioned with PCE: (a) dynamic yield stress, (b) plastic viscosity, and (c) static yield stress at rest. In (c), the secondary y-axis represents the difference between static yield stress and dynamic yield stress for the investigated mixtures.

To further elaborate on the importance of particle geometry, the evolution of rheological properties in the PLC-FA mortar can be highlighted. The said mortar exhibited lower rheological properties compared to that of the plain PLC or the PLC-SL systems (see Figure 4-8). This is attributed to lower inter-particle friction facilitated by the spherical shape of FA particles (as shown in Figure 4-2), which can act to mitigate the effects of increased SSA. It is also interesting to note that the effect of FA replacement on retention of rheological properties (i.e., lower variation in rheological properties over elapsed time) is more pronounced for PLC as compared to OPC systems. This is an important point as it suggests that the reduced inter-particle friction associated with

spherical geometry of FA particles becomes more significant when incorporated in a binder with higher surface area and inter-particle links.

4.3.3. Hydration Kinetics. Figure 4-9 depicts the heat flow rate and cumulative heat release (normalized by cement fraction in mixture) of the evaluated mortars provisioned with their optimum PCE to achieve both enhanced solid concentration and improved fluidity. Despite higher required PCE dosages in PLC systems to achieve maximum solid concentration compared to the OPC systems, the PLC systems exhibited larger extent of hydration kinetics as indicated by higher magnitude of heat at main hydration peak and faster occurrence of the main hydration peak, as well as higher extent of heat release throughout the hydration process. In the case of PLC, the softer limestone is ground more readily than the harder Portland cement clinker, leading to finer particles of limestone. The finer limestone particles (i.e., higher SSA), in turn, enhance the reactivity (i.e., dissolution rate) of the limestone, and also accelerate hydration of the cement by providing additional surface area for the heterogeneous nucleation of the main hydration product, i.e., C-S-H (Arora et al. 2016; Kumar et al. 2013a; Vuk et al. 2001).

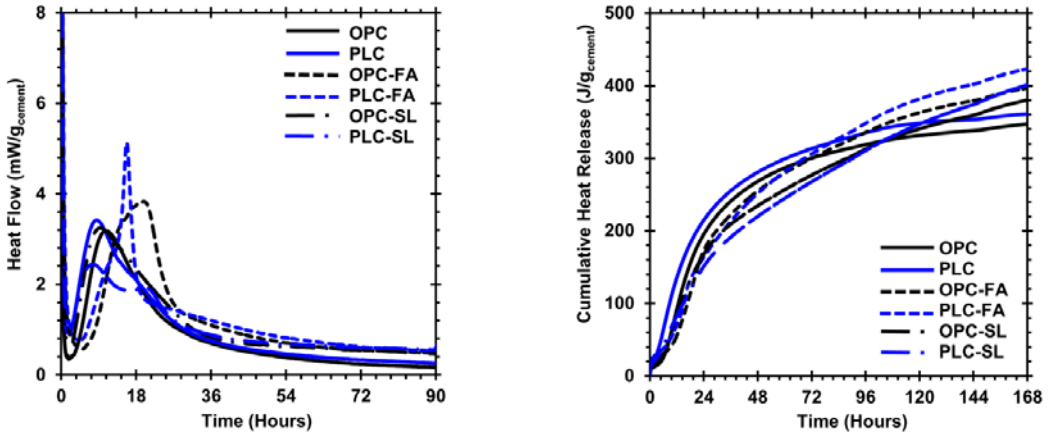

(a) (b)

Figure 4-9 Hydration kinetics of OPC-SCM and PLC-SCM systems provisioned with PCE: (a) heat flow rate and (b) cumulative heat release.

It is important to note that although the presence of PCE can suppress the cement hydration (Artioli et al. 2014; Cheung et al. 2011; Jansen et al. 2012; Valentini et al. 2016; Zhang and Kong 2015; Zhang et al. 2015), this retarding effect can be mitigated through the provision of additional surface area (i.e., higher SSA) in the binder (Meng et

al. 2016). Both FA and SL replacements lead to greater extents of hydration of cement in mortars prepared with SCMs compared to those prepared without SCMs. This is due to a combination of the physical (i.e., filler effect) and chemical effects induced by the SCMs. In the context of the physical effect, the SCMs are also able to act as fillers. Though this filler effect manifests at early ages, i.e., at the time of C-S-H nucleation, the resultant acceleration is carried over to later ages, which reflects higher cumulative heat, as shown in Figure 4-9(b).

To better describe the chemical interactions of FA and SL with the paste components, equilibrium phase assemblages in OPC-SCM and PLC-SCM systems, as calculated from the thermodynamic model (Section 2), are shown in Figure 4-10. Firstly, OPC-SCM systems are described. As can be seen, both FA and SL possess pozzolanic properties (i.e., due to the presence of amorphous SiO2), wherein the H2SiO4- resulting from their dissolution combines with CH to form pozzolanic C-S-H. Based on the thermodynamic simulations, which show complete consumption of CH after 57% and 98% of FA and SL have reacted, respectively (Figure 4-10(a) and (b)), it can be said that FA is a superior pozzolan as compared to SL. However, it is noted that the thermodynamic model does not consider the kinetics of reaction processes, and, therefore, is only able to reveal the equilibrium phase assemblage after the precursor materials have reacted to a given extent without accounting for the time required to react up to that extent. When we consider the kinetics, by incorporating the residual CH contents in the system, as calculated from TGA (shown as dashed lines in Figure 4-10), it is seen that after 7 days of hydration only 10% and 27% of FA and SL, respectively, have reacted. It is hypothesized that the higher extent of SL's reaction is due to its higher SSA, which, in turn, enhances its dissolution rate. As a result, the reduction in CH content due to pozzolanic reaction is higher in OPC mortars containing SL as compared to those prepared with FA (Figure 4-11). This theory is corroborated from: (i) isothermal calorimetry results (Figure 4-9(b)), which show that at later ages (i.e., when pozzolanic reactions are in progress), the cumulative heat release in the OPC-SL system remains higher compared to the OPC-FA system, and (ii) XRD results (Figure 4-12(a)), which show that among OPC, OPC-FA and OPC-SL systems, the intensity of the principle

portlandite peak reduces the most in the OPC-SL system, thus suggesting superior pozzolanic reaction of SL compared to FA.

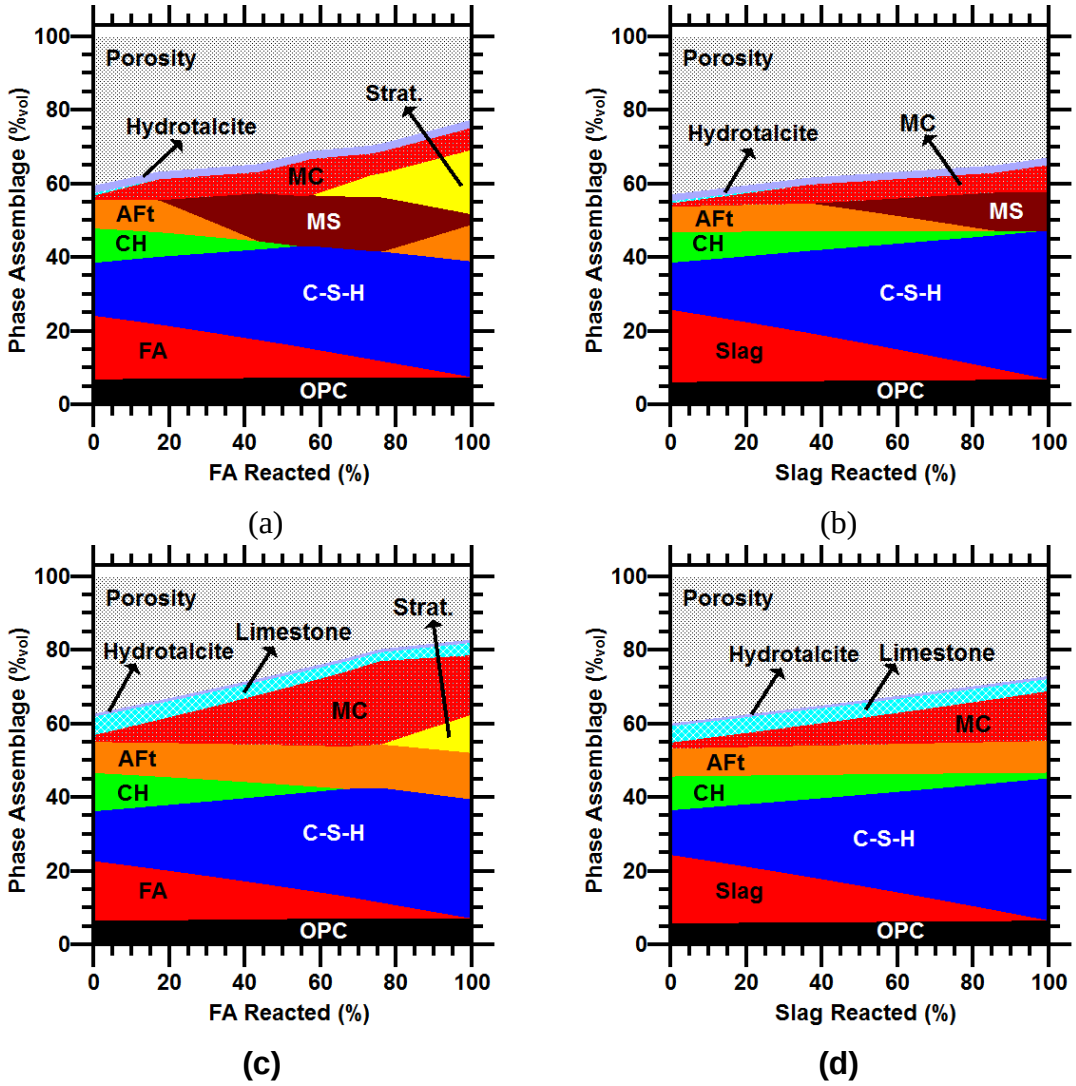

Figure 4-10 Volumetric phase assemblages in pastes prepared with binders composed of: (a) OPC-FA, (b) OPC-SL, (c) PLC-FA, and (d) PLC-SL as functions of the reacted SCM content (%). All calculations are carried out by applying a progressive equilibrium approach, wherein 65% of the cement (i.e., OPC or PLC) is assumed to have reacted (based on TGA determination of cement's degree of hydration in both pure OPC and PLC systems), and the SCM is allowed to react in fractional quantities. The dashed lines represent the extent of SCM reacted at the age of 7 days, based on residual amounts of portlandite, as determined from TGA (Stoian et al. 2015). The dotted space represents capillary porosity. AFt: ettringite, MS: monosulfoaluminate, MC: monocarboaluminate + hemicarboaluminate, and Hydrotalcite: $Mg_4Al_2(OH)_{14}.3H_2O$.

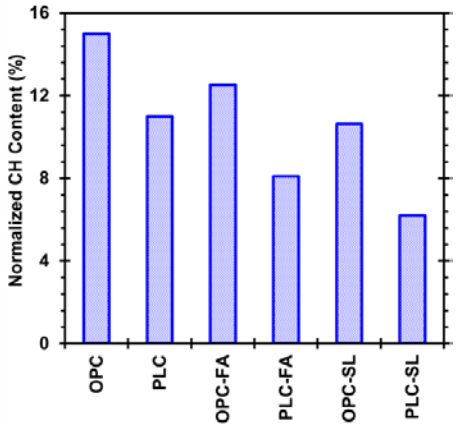

Figure 4-11 Normalized CH contents at 7 days determined from DTG for OPC-SCM and PLC-SCM systems provisioned with PCE. Results were normalized by OPC fraction to account for OPC replacements (i.e., dilution effect).

Between FA and SL, another differentiating factor is the Al_2O_3 content, the effect of which is seen in the balance of ettringite and monosulfoaluminate phases in OPC systems (Figure 4-10). Due to its higher Al_2O_3 content (Table 4-1), FA causes larger alterations in the SO_3/Al_2O_3 of the binder as compared to SL. Due to such alterations, the characteristic “shoulder” aluminate hydration peak in the OPC-FA system occurs later as compared to pure OPC or OPC-SL systems (Figure 4-9(a)). Furthermore, as FA continues to dissolve, it also acts to destabilize ettringite, and enforce its transformation to monosulfoaluminate (Figure 4-10(a)). Destabilization of ettringite, and its subsequent transformation to monosulfoaluminate in the presence of Al2O3-rich SCMs has been reported previously (De Weerdt et al. 2011; Puerta-Falla et al. 2015a). Such destabilization of ettringite is also observed in the OPC-SL system, but this occurs only after over 40% of the SL (as opposed to 17% of FA) has reacted (Figure 4-10(b)). This is attributed to lower Al2O3 content in SL, thus necessitating higher extents to reaction to destabilize ettringite. However, because of the slow dissolution kinetics of both FA and SL, these effects of destabilization of ettringite are expected to affect phase assemblages only at later ages (i.e., > 7 days). Here, it is pointed out that in addition to ettringite and monosulfoaluminate, the formation of carboaluminate hydrates (i.e., hemicarboaluminate, and minor amounts of monocarboaluminate) as secondary AFm phases is also predicted in the thermodynamic simulations. This is on account of the presence of limestone in OPC, albeit in minor quantity (i.e., 3.21 mass %). Since, limestone amounts to a small

fraction of the total OPC content, the formation of carboaluminate hydrates does not occur in large quantities (Figure 4-12(b)) and, therefore, is unable to prevent destabilization of ettringite in blended (i.e., OPC-FA and OPC-SL, as shown in Figure 4-10) systems.

Next, equilibrium phase assemblages in PLC systems are described. As can be seen in Figure 4-10(c) and (d), due the presence of limestone in PLC (i.e., 10.5% by mass), ettringite in stabilized, and carboaluminate hydrates precipitate as the predominant AFm phase instead of monosulfoaluminate (De Weerdt et al. 2011). This explanation is in agreement with XRD results, which confirm the formation of CO_3-AFm phases in pure PLC mortars (Figure 4-12(b)). Because of the higher Al_2O_3 content in FA, at any given extent of SCM's reaction, the total amount of carboaluminate hydrates in the PLC-FA system is higher than the PLC-SL system. Similar to the OPC-FA system, on account of inducing larger alterations in the SO_3/Al_2O_3 of the binder, the time of occurrence, as well as the intensity, of the aluminate hydration peak in PLC-FA system differs significantly from the pure PLC system (Figure 4-9(a)). On the other hand, the SO_3/Al_2O_3 content in the PLC-SL system is not significantly different from the pure PLC system. As such, the early-age (i.e., age < 20h) heat evolution profiles of the PLC-SL system and the pure PLC system are broadly similar, with no significant changes in the aluminate hydration peak. Both FA and SL react pozzolanically with CH in PLC-SCM systems. Here again, due to its higher SSA, the extent of SL's reaction after 7 days is higher compared to that of FA (i.e., 55% and 25% for SL and FA, respectively), as shown in Figure 4-10(c) and (d). This is better shown in Figure 4-11, which shows that at the age of 7 days, the residual CH content in the PLC-SL system is lower compared to the PLC-FA system. XRD patterns (not shown) also confirm lower portlandite contents in the PLC-SL system as compared to the PLC-FA system.

Upon comparisons of the OPC-SCM systems with the PLC-SCM systems, it is interesting to note that the extents of reaction of both SL and FA at the age of 7 days are higher in PLC-SCM systems. While the reasons of this are not fully clear at this point, it is speculated that the enhanced kinetics of SCM's reaction in PLC systems is due to faster hydration kinetics of the PLC itself. As the PLC dissolves faster, at any given time, the concentration of aqueous species (e.g., Ca^{2+}, $H_2SiO_4^{2-}$), as well as the solid hydrates

(e.g., CH), is expected to be larger in the PLC system compared to OPC system. Consequently, the reactions between the SCMs and cementing paste components (i.e., ionic species and hydrates) are expected to occur at a faster rate in PLC systems compared to the OPC systems.

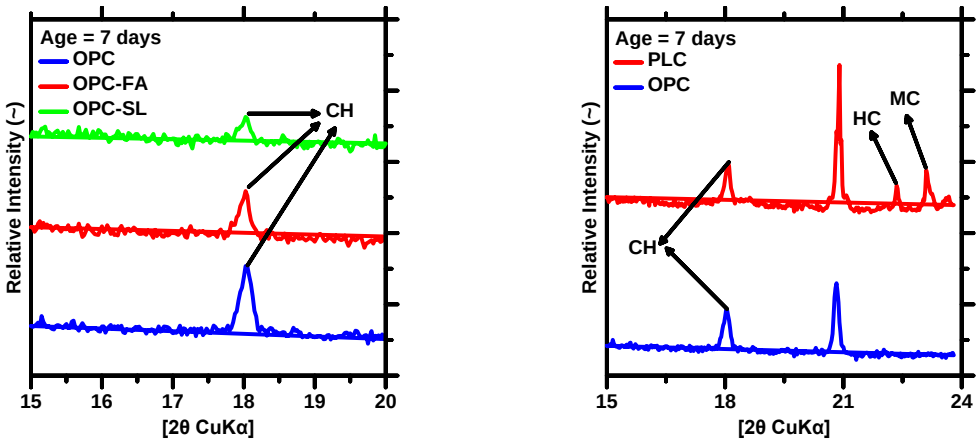

(a) (b)

Figure 4-12 Representative XRD patterns at 7 days for (a) OPC, OPC-SL and OPC-FA systems, and (b) pure OPC and PLC systems. Here, Hc: hemicarboaluminate, Mc: monocarboaluminate, and CH: portlandite.

4.3.4. Compressive Strength Development. Figure 4-13 shows the compressive strength evolution and the improvement in compressive strength between 1 day and subsequent ages (subsequently referred to as rate of strength gain) for the mortars provisioned with PCE. The plain PLC mortar consistently shows slightly lower compressive strength compared to the pure OPC mortar. This reduction in strength is more dominant at early ages, which can be due to both the dilution effect and higher PCE dosage used in this system compared to the pure OPC mixture. At later ages (i.e., > 1 day), however, the plain PLC mortar gains strength more rapidly (see Figure 4-13(b)), which in turn, leads to compressive strength that is commensurable to that of pure OPC mortar. This rapid gain of strength at later ages is expected to occur due to the reaction between limestone and the aluminate phase in cement leading to the formation of space-filling carboaluminate hydrates, which improve solid-to-solid phase connectivity and enhance strength. Expectedly, all mortars prepared with SCMs show lower strengths compared to the pure systems at 1 day due to the dilution of the cement content. Beyond

the age of 1 day, both OPC-SCM and PLC-SCM mortars exhibit higher rate of strength gain (see Figure 4-13(b)), ultimately developing 91-day strengths that are comparable to the pure OPC or PLC mortars. This higher rate of strength gain in mortars containing SCMs is primarily due to the later-age (i.e., age > 1 day) pozzolanic reaction between the SCMs and the CH, resulting in the formation of space-filling pozzolanic C-S-H, which acts to offset the effects of dilution of the cement content. Between the OPC-SCM and PLC-SCM systems, while both feature the formation of pozzolanic C-S-H, the latter consistently show higher later-age strengths, as well as higher rate of strength gain, as compared to the former systems. Higher later-age strength in PLC-SCM systems is hypothesized to be on account of: (i) larger amount of limestone in PLC, which enables the formation of space-filling carboaluminate hydrates in the PLC-SCM system, and (ii) larger amount of pozzolanic C-S-H in PLC-SCM systems, as evidenced by TGA datasets that show smaller amounts of residual portlandite contents in PLC-SCM systems compared to those in OPC-SCM systems.

The highest strength gain is found for the PLC-SL system. When the PLC-SL and the PLC-FA mortars are compared, it is seen that the strengths of the former are consistently higher compared to the latter. In addition to the alumina content in SL (which is lower than that in FA) which facilitates limestone-aluminate synergistic reactions, SL demonstrates both the cementitious (albeit slow) and pozzolanic reactivity (Lothenbach et al. 2011). In addition to chemical features, the faster strength gain in SL compared to the FA is hypothesized to be due to the higher SSA of SL, which ensures faster dissolution, thus enabling relatively larger formation of pozzolanic C-S-H at any given age. This hypothesis is corroborated in Figure 4-10, which shows that after 7 days of reaction, the amount of C-S-H formed in SL systems are consistently higher than in FA systems. Alternately, the residual CH contents shown in Figure 4-11 also prove higher pozzolanic activity of SL over FA. The aforementioned discussion highlights the links between the properties (i.e., physical and chemical) of the precursor materials and the strength gain. Therefore, based on these results, it is concluded that for assessments of properties in binary (or ternary) cementitious systems, it is important to account for both physical and chemical properties of the precursor materials.

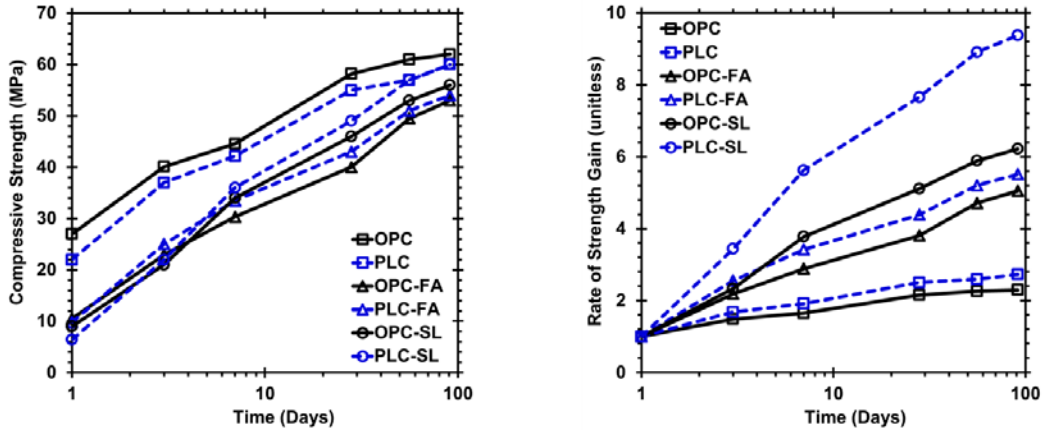

(a) (b)

Figure 4-13 Compressive strength development of OPC-SCM and PLC-SCM systems provisioned with PCE: (a) Compressive strength evolution with specimen age and (b) rate of strength gain with specimen age. In (b), the rate of strength gain of a given system was obtained by dividing the later age strengths of each mixture (i.e., age = 3, 7, 28, 56, and 91 days) by its corresponding 1-day compressive strength.

4.4. LINKING HYDRATION KINETICS TO MATERIAL PERFORMANCE IN FRESH AND HARDENED STATES

To better understand the composition-reaction-property correlations in OPC-SCM-limestone systems provisioned with PCE, an attempt was made to link the hydration kinetics to the rheological properties and structural recovery in the fresh state and compressive strength development in the hardened state. In the first part, the characteristic calorimetric parameters indicative of acceleration or retardation in hydration kinetics, i.e., the time of occurrence of the main hydration peak and the time corresponding to the end of the induction period (i.e., onset of acceleration regime), were extracted from the calorimetry profiles (Figure 4-9) to construct rheology-reactivity plots in Figure 4-14. As can be seen, the rheological properties measured at the age of 70 min (i.e., dynamic yield stress, plastic viscosity and static yield stress at rest) of the investigated mortars are well-correlated with the times at which the induction periods end, and the main hydration peaks occur. In mortars with faster early-age hydration kinetics, both the onset of acceleration regime and the main hydration peak occur earlier compared to those with slower early-age hydration kinetics. As faster hydration kinetics implies formation of larger quantities of hydration products and development of elastic properties at a given amount of time, it is expected that in mortars with higher reactivity,

the transition from a “slurry” state to “plastic” state would occur faster. This is because the nucleation of hydrates, especially C-S-H, turns the soft colloidal interaction among cementitious grains into more rigid interactions. The continuing nucleation of hydrates in such mortars increases the development of rigidity (i.e., elastic properties) of system, thus leading to a larger increase in rheological properties. In contrast, mortars with slower early-age reactivity feature slower formation of hydration products, and thus lower rheological properties.

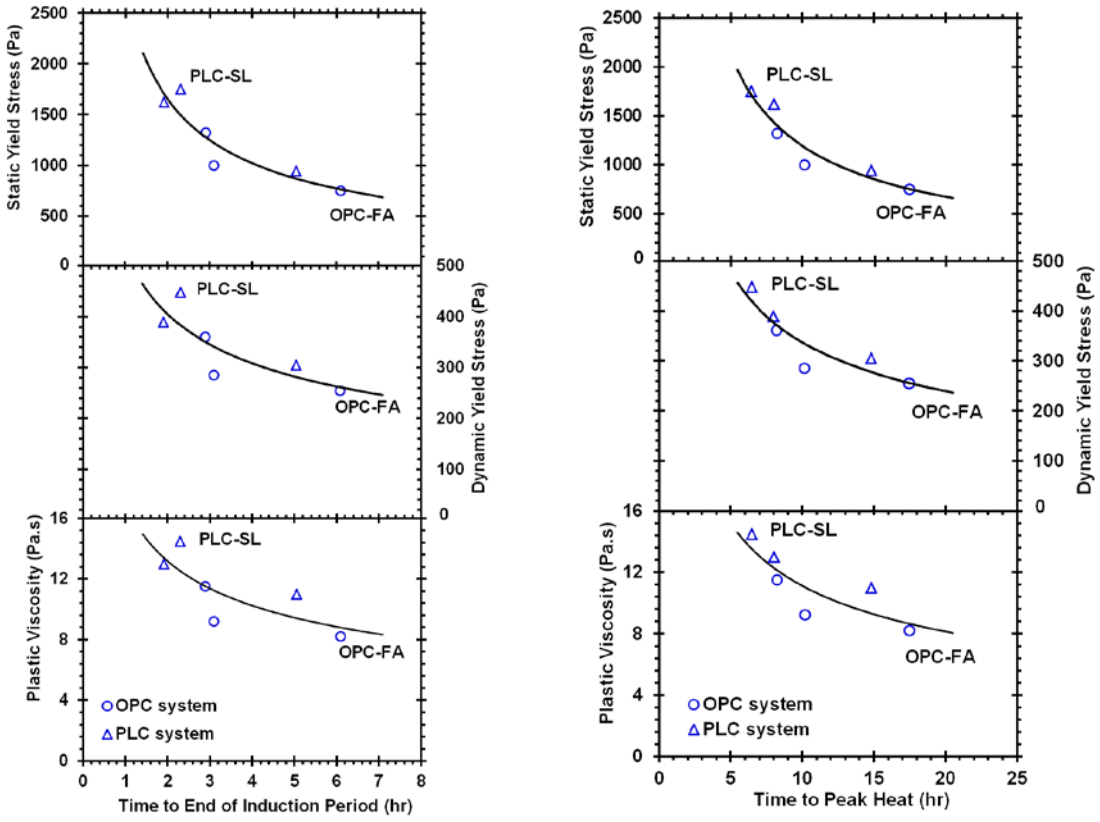

(a) (b)

Figure 4-14 Correlations between rheology and reaction kinetics of OPC-SCM and PLC-SCM systems provisioned with PCE: (a) time corresponding to end of the induction period vs. rheological properties and (b) time of occurrence of the main hydration peak vs. rheological properties.

In the second part, a focus was placed to link hydration kinetics to the development of hardened properties (i.e., compressive strength). Several studies have shown that compressive strength evolution is linearly correlated to the release of heat

through hydration (Bentz et al. 2012a; Kumar et al. 2013b; a; Lothenbach et al. 2008b). To further examine the implication of this correlation for the evaluated OPC-SCM and PLC-SCM systems provisioned with PCE, the strengths at ages of 1, 3, and 7 days were plotted against the cumulative heat release in Figure 4-15. Here, the cumulative heat release was normalized by water content of the mixtures, since the initial water content serves a measure of the initial porosity of system which needs to be filled by the hydration products for the evolution of the microstructure and the development of properties. As can be seen, a generic linear relationship can be established between compressive strength evolution and cumulative heat release encompassing all systems investigated in this study. The majority of data points lies within the ± 20% bound of the linear best fit line, thus validating that the cumulative heat release of binders can be effectively utilized to estimate the compressive strength development of mortars, regardless of the binder composition or the presence/absence of dispersants (e.g., PCE). As identified in Figure 4-15, the established linear trend-line has a non-zero x-intercept, reflecting that a critical degree of hydration of the cement is needed to percolate solid-phase networks, and thus contribute to the gain in strength.

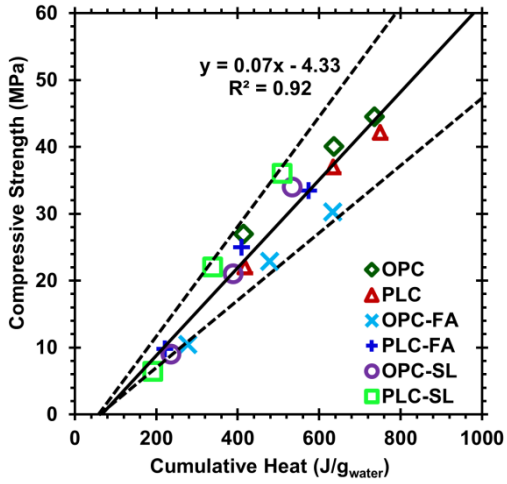

Figure 4-15 Correlation between compressive strength development at 1, 3, and 7 days and cumulative heat release normalized by initial water content for OPC-SCM and PLC-SCM systems provisioned with PCE. The solid line represents linear best fit line with 20% bounds placed on either direction (dashed lines).

These correlations, shown in Figure 4-14 and Figure 4-15, can be used as useful means to estimate the time-dependent material performance of binary blends in both fresh (rheological properties) and hardened state (compressive strength) by simply using the experimentally measured calorimetry profiles as the input. This approach is powerful in that it proposes a reliable means for concrete technologists to perform apriori estimation of key engineering properties of a cementitious system by simply using the experimental measurement of its heat release as the sole input.

4.5. SUMMARY

A series of PLC-SCM and OPC-SCM mortars were evaluated to compare and contrast their performance in terms of their particle packing, time-dependent rheological properties, hydration kinetics, and compressive strength evolution. All binders were provisioned with the presence of PCE to improve fluidity and enhance solid concentration of cementitious particles.

- The benefit of larger SSA in PLC systems to improve solid concentration is strongly related to the presence of PCE. PLC binders with higher SSA of particles necessitated a higher dosage of dispersant to improve fluidity and achieve maximum possible solid concentration.
- Although PLC systems necessitate higher PCE dosages due to its higher SSA as compared the OPC systems, the former systems show faster hydration rate and larger extents of heat release due to the higher solid concentration and greater SSA.
- PLC systems develop larger rheological properties (i.e., dynamic yield stress, plastic viscosity, and static yield stress at rest) compared to their OPC counterparts, especially at later ages. This is attributed to the coupled effect of higher SSA and lower inter-particle spacing in the former systems as compared to the latter mixtures.
- Aluminosilicate SCMs are more effective in terms of improving strength in PLC systems as compared to OPC systems. While SCMs are capable of invoking pozzolanic reactions (leading to formation of pozzolanic C-S-H) in either systems, the superiority of the PLC system is attributed to: (i) the higher SSA of

the PLC, which improves solid concentration and ensures faster hydration kinetics, and (ii) the carbonate-rich chemistry of PLC, which allows PLC to partake in chemical reactions with the SCM leading to the formation of space-filling carboaluminate hydrates. The combined effects of optimized particle size distribution (i.e., higher SSA), optimized particle packing, and optimized chemistry of the PLC-SCM systems lead to equivalent or even higher compressive strength than that of pure OPC or OPC-SCM systems.

- Hydration kinetics is found to correlate well with rheological properties and compressive strength development of OPC and PLC systems containing high volume of SCM replacements that are provisioned with PCE. Such correlations provide a reliable basis for apriori estimation of key engineering properties, both in the fresh and hardened state, and thus enable the optimization of binder formulation to provide more sustainable solution for concrete construction applications.

5. PHYSICO-MECHANICAL CHARACTERISTICS OF CEMENT PASTE OVER TRANSITION FROM CONCENTRATED TO FLOW STATE: THE ROLE OF SUPPLEMENTARY CEMENTITIOUS MATERIALS

Apart from the mechanical properties improvement, the incorporation of SCMs affects considerably the particle-size distribution (PSD) and total specific surface area (SSA) of the powder system present in the suspension. Such features induced by the use of SCMs dictate the flow characteristics and rheological properties of suspension due to the changes in solid concentration (i.e., particle packing) and water film thickness (WFT) covering solid particles. The formation of water film acts as a lubrication layer to increase inter-particle spacing. For a given paste suspension, the amount of filling water is related to the packing density of powder system, while the WFT formed on the surface of solid particles is affected by both packing density and total SSA of the particles. At a given water-to-cementitious material ratio (w/cm), a higher packing density of solid phase reduces the required filling water, thus increasing the amount of excess water available to lubricate the particles. The increase in total SSA of solids due to the use of SCMs can increase the packing density, and thus the amount of excess water will also increase. However, the effect of increased excess water on elevating WFT around particles can be counteracted due to the increase in total surface area of solid particles that need to be coated. A more comprehensive understanding of the correlations between the characteristics of the precursor materials and property evolution is required in concentrated system to provide new strategies for optimizing and developing advanced sustainable binder systems for the use in high-performance concretes provisioned with relatively low w/cm. The subject of this study is to investigate the physico-mechanical characteristics of cement pastes over transition from dense concentrated to flow onset. This study employs a set of experimental assessments coupled with microstructural simulations to elucidate the effects of w/cm, that characterizes WFT covering solid particles, and SCMs on particle packing and strength development of cement pastes at two different states: (i) optimum water demand (OWD) to achieve maximum solid concentration (i.e., concentrated state); and (ii) minimum water demand (MWD) to initiate flow (i.e., flow onset state). The investigated SCMs included a Class F fly ash,

blast-furnace slag, and silica fume as replacements for OPC in binary and ternary systems.

5.1. EXPERIMENTAL APPROACH

5.1.1. Materials and Mixture Proportions. A Type I/II OPC comforting to ASTM C150 (*Annual Book of ASTM Standards* n.d.) with an Bogue phase composition (mass fraction) of 61.2% C_3S, 12.3% C_2S, 6.1% C_3A, and 9.2% C_4AF was used. The investigated SCMs included Class F fly ash (hereinafter referred to as FA), blast-furnace slag (hereinafter referred to as SL), and silica fume (hereinafter referred to as SF) were incorporated as partial replacements for OPC in binary and ternary systems. The oxide compositions of the cementitious materials used in this study are presented in Table 4-1.

The particle-size distributions (PSDs) of the cementitious materials were measured using a Microtrac S3500 laser diffraction analyzer on a dilute suspension of ultrasonificated powder particles in isopropanol suspending liquid. The PSDs and scanning electron microscopy (SEM) images of the cementitious materials are presented in Figure 5-1(a) and (b). The median particle size diameters (d_{50}) were determined to be 15, 13, 8.5, and 0.4 μm for OPC, FA, SL, and SF, respectively. Based on the PSDs of the cementitious systems, and factoring in the density of the materials (3140, 2450, 2860, and 2300 kg/m^3 for OPC, FA, SL, and SF, respectively, as measured using a pycnometer), the total SSA of OPC, FA, SL, and SF were calculated to be 341, 411, 535, and 14500 m^2/kg, respectively. The total SSA results were found to be in good agreement with the Brunauer–Emmett–Teller specific surface areas provided by the materials suppliers.

A total of eight different cement paste systems were prepared using various types and replacement rates of SCMs, including: (i) plain OPC system (subsequently designated as OPC); (ii) two binary systems with 40% replacement of OPC (by volume) with FA or SL (subsequently designated as 40FA and 40SL); and five ternary systems with either 40% FA or 40% SL in combination with SF in an increment of 5%, by volume (subsequently designated as 40FA5SF, 40FA10SF, 40FA15SF, 40SL5SF, and 40SL10SF). These eight cement pastes were proportioned at 8 different volumetric w/cm ratios $(w/cm)_v$ to evaluate the flow characteristics and solid concentration of the investigated systems, as described further in Section 2.2. It is important to note that as the

fresh and hardened characteristics of a suspension are affected by the volume fraction of solids (Chong et al. 1971; Jeffrey and Acrivos 1976), all OPC replacement materials were carried out on the volume-based mixture proportioning in order to maintain a constant solid content.

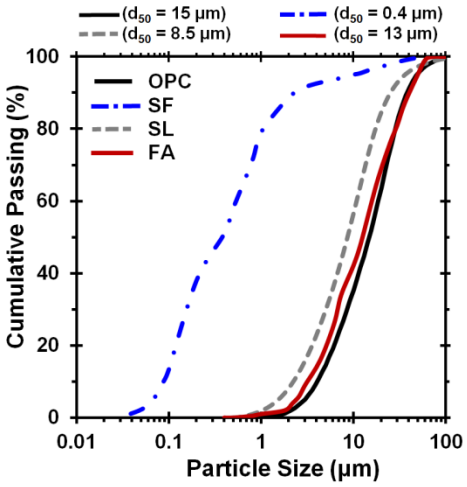

(a)

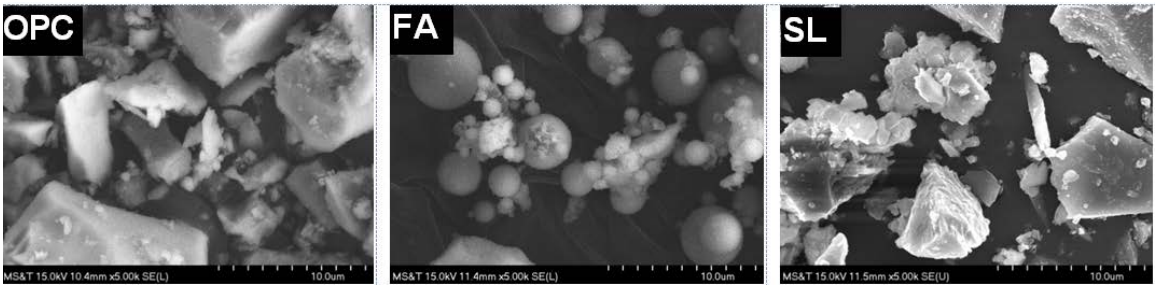

(b)

Figure 5-1 (a) Particle-size distributions and (b) SEM images of the investigated cementitious materials. Based on six replicate measurements, the uncertainty in the median particle size diameter (d_{50}) was quantified as ±3%. All SEM images were acquired in the secondary electron mode, while operating at an acceleration voltage of 15 kV with magnification of 5000x.

A polycarboxylate ether (PCE) dispersant with a solid mass content of 23% and a density of 1050 kg/m^3 was used to enhance dispersion and mitigate agglomeration potential of cementitious particles due to the electrostatic and steric repulsive forces (Cheung et al. 2011; Ferrari et al. 2011; Zhang and Kong 2015; Zingg et al. 2008). The dosage of PCE dispersant was remained constant at 0.50%, by volume of the cementitious materials. This dosage corresponds to the saturation point of the PCE, which

was carried out on the plain OPC paste using the mini-slump flow cone test. Further, this PCE dispersant dosage was found to be sufficient for alleviating agglomeration in binder systems containing SF, using a protocol described in Ref (Mehdipour and Khayat 2016b). It is clarified that this dosage corresponds to the total (i.e., solid + liquid) mass of the PCE; the aforementioned dosage amounts to ~0.12% of the active solid component of the PCE dispersant.

The mixing sequence consisted of adding water and PCE dispersant followed by gradually introducing the binder materials over 3 min. The cement paste was then mixed for 3 min at a constant velocity of 140 revolutions-per-min (rpm), followed by 30 sec mixing at a high velocity of 285 rpm. The cement paste was maintained at rest for 2 min before remixing for additional 3 min at a velocity of 140 rpm, as outlined in ASTM C305 (Annual Book of ASTM Standards n.d.).

5.1.2. Experimental Methods. Flow spread: The mini-slump flow cone test was used to evaluate the flow characteristics of the cement paste, including the determination of minimum water demand (MWD) required to initiate flow and relative water demand (RWD) needed to increase fluidity (Okamura and Ouchi 2003; Yahia and Khayat 1998). The test involves determining the variations in fluidity for a given mixture with changes in $(w/cm)_v$, as schematically illustrated in Figure 5-2. A truncated mini-cone with a top diameter of 70 mm, a bottom diameter of 100 mm, and a height of 60 mm was used. The test procedure consists of placing the mini-slump cone at the center of the plate, followed by filling with the fresh cement paste sample. Subsequently, the mini-cone is smoothly lifted and two perpendicular spread diameters (d_1 and d_2, in cm) are recorded once the flow has stopped. The relative slump flow (Γ_p) is calculated as follows:

$$\Gamma_p = \left(\frac{\frac{d_1 + d_2}{2}}{10} \right)^2 - 1 \qquad 5\text{-}1$$

The intercept of the best linear fit line between $(w/cm)_v$ and Γ_p with the Y-axis identifies the MWD to initiate flow. Furthermore, the slope of this linear relationship represents the RWD to increase fluidity. The RWD reflects the sensitivity of a mixture to variations in water content, wherein higher RWD value corresponds to greater robustness for mixture.

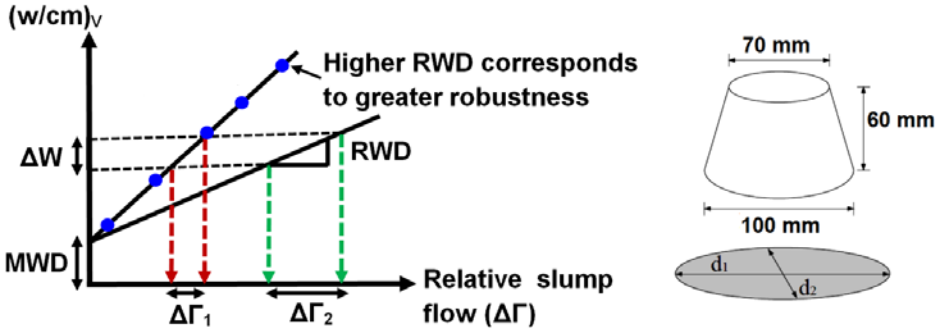

Figure 5-2 Determination of flow characteristics of cement paste using mini-slump flow cone test.

Solid concentration and water film thickness in fresh paste: The solid concentration of the investigated paste systems at various $(w/cm)_v$ was determined using the wet density approach to identify the optimum water demand (OWD) corresponding to the maximum solid concentration for a given system. The test involves determining the solid concentration of mixtures at various $(w/cm)_v$ using a cylindrical mold of 400 ml in volume, which is filled with paste and consolidated using a vibrating table for 30 sec. As indicated in the representative example shown in Figure 5-3(a), there is an optimum w/cm at which maximum solid concentration in system is achieved (i.e., point A in Figure 5-3(a)). The maximum solid concentration occurs when the particles are fully packed, which can be an indication of packing density of system. The further water addition beyond OWD acts as a separation medium and increases the distance between neighboring solid particles, thus reducing the extent of solid concentration in system. Therefore, this test probes the moment at which the amount water is sufficient to fill the voids among solid grains in system. The solid concentration (ϕ, unitless) at a certain $(w/cm)_v$ in cement paste can be quantified as follows:

$$\phi = \frac{V_s}{V} \qquad 5\text{-}2$$

where V_s (cm^3) refers to the total volume of solid phase in the mold, which is calculated as follows:

$$V_s = \sum_i^n V_{si} = \frac{M_{\max}}{\rho_w (w/cm)_V + \sum_i^n \rho_{si} R_{si}} \quad 5\text{-}3$$

where $\sum_i^n V_{si}$ represents the sum of volumes of all solids, and M_{max} (g) is the mass of sample corresponding to the maximum wet density. ρ_w and ρ_{si} (g/cm^3) are the densities of water and solids (cementitious materials), respectively. R_{si} (unitless) refers to the volume fraction of solids (i.e., cementitious materials) present in cement paste. To correlate the rheological properties of the pastes to the water film thickness covering solids in a cement paste, the value of maximum solid concentration for each system was used to calculate the water film thickness (WFT, μm) as follows:

$$WFT = \frac{w_{exc}}{SSA} \quad 5\text{-}4$$

where SSA (m^2/m^3) is the total specific surface area of solids (i.e., cementitious particles) and w_{exc} is the excess water present in system which is obtained as follows:

$$w_{exc} = (w/cm)_V - e_{\min} \quad 5\text{-}5$$

where e_{min} is the minimum void ratio of solids at the maximum solid concentration state (i.e., at OWD, point A in Figure 5-3(a)) which is calculated as follows:

$$e_{\min} = \frac{1-\phi_{OWD}}{\phi_{OWD}} \quad 5\text{-}6$$

where ϕ_{OWD} refers to the maximum solid concentration determined at OWD for a given cement paste.

Compressive strength: The 7, 28, and 56 days compressive strengths of cement pastes were determined in accordance with ASTM C109 (Annual Book of ASTM Standards n.d.). The 50 mm cubes were demolded after 24 h, and subsequently were cured under sealed condition (i.e., sealed bag to minimize evaporation) at temperature of 23 ± 1 °C until testing age. In order to examine the effect of excess water present in system on strength evolution, the compressive strength of all mixtures were evaluated at two different w/cm ratios corresponding to their OWD needed to achieve maximum solid

concentration and MWD required to initiate flow. The results of compressive strength represent the average of three replicate measurements.

5.2. MICROSTRUCTURAL SIMULATION

To better understand the effects of SCM types and replacement levels on particle packing, rheology, and strength development of the investigated systems, a series of virtual microstructure modelling were implemented using continuum integrated model HYMOSTRUC (Koenders 1997; Van Breugel 1991). Within the framework of the HYMOSTRUC model, the rate of hydration and the formation of inter-particle contacts are modeled in a three-dimensional (3D) microstructure as a function of particle size distribution, chemical composition, w/c, and reaction temperature.

First, in order to determine the effect of SCMs on inter-particle spacing, the PSDs of the investigated blended systems and volume fraction of phases (i.e., binder and water) were used as inputs in microstructural modelling to generate a representative 3D microstructure of the cement paste immediately after mixing. For a given blended binder system, the combined PSD of solid phase was discretized to extract the number of particles present in the system in a representative element volume (REV) of 100 × 100 × 100 μm^3. The binder particles are represented as spherical particles and randomly distributed in the 3D-REV, within the constraint that particles cannot be in contact. Once the sought packing is achieved, average distances between particles (center-to-center distance due to the spherically of particles) were calculated in the REVs for different binder systems. It should be noted that the inter-particle spacing is an important parameter that dictates particle pacing characteristics and rheological properties of system.

Next, 3D numerical modelling was carried out to evaluate the connectivity of solid phase due to the cement hydration as a function of w/c. The hydration process and microstructural development in a REV of a 100 × 100 × 100 μm^3 of cement paste was simulated at both OWD (i.e., concentrated state) and MWD (i.e., flow onset) states. As the cement hydration progresses, solid-to-solid connectivity increases and connected networks are formed (Koenders 1997; Van Breugel 1991). To better understand the effect of excess water at flow onset state on solid structure formation and mechanical property

development (i.e., strength) of cement paste, the volume fractions of total solid phase and connected solid phase in the REV were determined as a function of time. The connected solid phase was characterized as a formation of continuous solid phase path from one side of the REV to another side using the procedure described in Refs (Bentz and Garboczi 1991; Sun et al. 2005). The image processing technique was applied to calculate the volume fraction of connected solid phase at different ages as the hydration progresses. The results of connected solid volume are correlated to the compressive strength development.

It is important to note that in the HYMOSTRUC model, only a single hydration product is formed by the growth of new layers of hydrates on the cement grains, as the hydration progresses (Bishnoi and Scrivener 2009). This limitation in the HYMOSTRUC hinders the representation of other hydration products, such as portlandite that tends to form new clusters in the pores, rather than forming on cement grains. Further, the model does not consider the hydration of each individual particle. The model applies statistical approach to reaction rates for the entire microstructure, assuming that the reaction rate of each particle is related to its particle size (Thomas et al. 2011). Such limitations in the HYMOSTRUC model, prevent an accurate estimation/representation of the evolution of the cement microstructure (Bishnoi and Scrivener 2009; Thomas et al. 2011). In parallel with simulation, therefore, simultaneous thermal analysis (thermogravimetric analysis (TGA) and derivative thermal analysis (DTA)) using a Netzsch Simultaneous instrument (Model 429) was carried out on OPC pastes made with different water contents (i.e., concentrated state and flow onset) to determine the non-evaporable water content. The chemically bound water is a measure of degree of hydration of cement, it is determined as the difference between the mass measurements at 950 °C and 105 °C, and corrected for the loss on ignition of the cement powder (based on its mass fraction in the paste) and the calcium carbonate content (650–800 °C).

5.3. RESULTS AND DISCUSSION

5.3.1. Determination of Water Demand. The water demands of the investigated OPC-SCM systems were determined using two different approaches: (i) OWD needed to fill the voids and reach maximum solid concentration (i.e., concentrated state) using wet

density approach and (ii) MWD required to lubricate surface of solid particles and impart fluidity in paste using the mini-slump flow cone test (i.e., flow onset state).

Figure 5-3 shows the representative example for the plain OPC system provisioned with 0.12% PCE dispersant dosage. As indicated in in Figure 5-3(a), there is an optimum w/c at which maximum solid concentration in system is achieved. This w/c corresponds to the optimum water demand required to fill the voids among solid particles and create a dense particle packing, thus manifesting maximum solid concentration in the system. This point probes the moment of transition from “semi-solid state” to “concentrated state” of system at which particles are fully packed. However, water content at OWD is not sufficient to provide fluidity to the cement paste, as indicated in Figure 5-3(b).

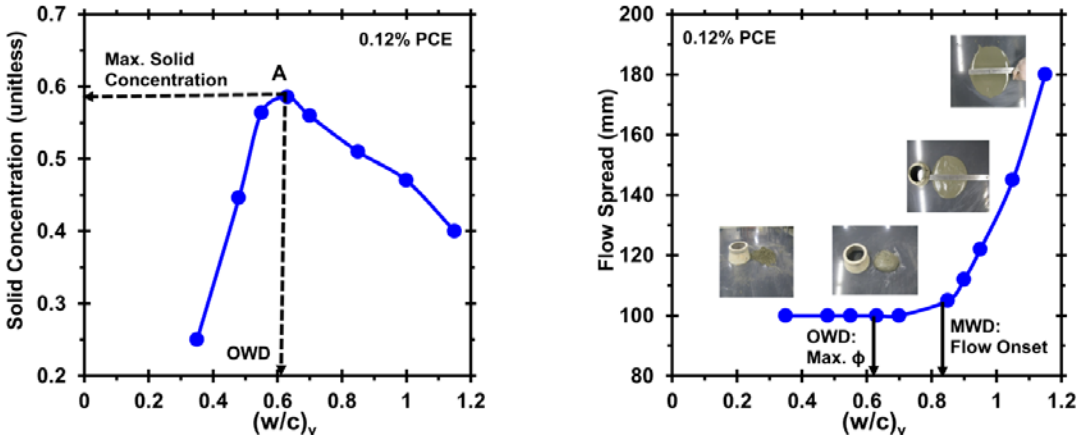

(a) (b)

Figure 5-3 Determination of OWD and MWD corresponding to maximum solid concentration and flow onset, respectively, for the plain OPC system provisioned with 0.12% PCE dosage. (a) Variations in solid concentration with water addition using wet density approach and (b) variations in flow spread with water addition using mini-slump flow cone test.

Upon further water addition beyond point OWD, the solid concentration in cement paste starts to decrease consistently wherein water acts to separate solid particles and reduce inter-particle contacts. As such, the amount of water covering solid particles (i.e., WFT) increases which contributes toward fluidity of cement paste. From Figure 5-3(b), it can be noticed that in spite of forming water film around solid particles, cement paste exhibits no fluidity over water contents between OWD and MWD (e.g., 0.63 and

0.83 for cement paste in this study). This implies that a minimum extent of WFT covering particles is required to facilitate the movement of solid particles at which paste nature changes from “concentrated state” to “flow state” (i.e., flow onset). As can be seen in Figure 5-3(b), the plain OPC system indicated no fluidity up to the w/c = MWD, however, over 35% increase in water content from MWD, the fluidity of cement paste increased significantly by a factor of around 2. This is attributed to the increased inter-particle spacing and reduced friction/contacts among particles, which decreases the resistance of paste to the shear induced by the slump cone test.

To better understand the effect of water content on solid concentration and inter-particle- spacing, representative 2D slices extracted from 3D-REV for the plain OPC system immediately after mixing are shown in Figure 5-4. The OPC system simulated at w/c of OWD has higher solid concentration and lower inter-particle spacing compared to the similar system at MWD. An increase in water content in excess of that needed to fill the voids will act to separate particles and increase the inter-particle spacing, thus resulting in lower particle packing in system.

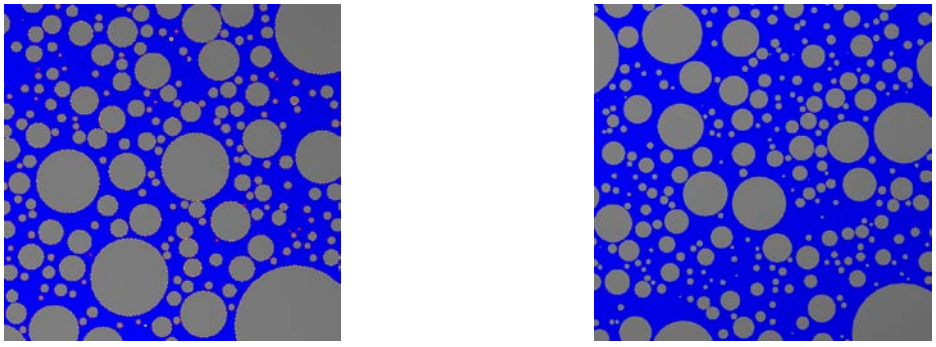

(a) (b)

Figure 5-4 Representative 2D slices extracted from 3D-REV of 100 × 100 × 100 μm^3 using virtual microstructure model for the pure OPC system immediately after mixing with water at two different water contents: (a) $(w/c)_v$ = 0.58 corresponding to its OWD and (b) $(w/c)_v$ = 0.84 corresponding to its MWD.

The solid concentration values for the systems shown in Figure 5-4 were calculated to be 0.572 and 0.495 at OWD and MWD, respectively, using image analysis technique based on six replicate models with uncertainty less than 4%. The simulation results are in good agreement with experimental observation determined from wet density

approach, at which solid concentrations were obtained as 0.583 and 0.512 at OWD and MWD states, respectively. The effect of water addition on inter-particle spacing for the evaluated binder systems is quantitatively discussed later.

5.3.2. Particle Packing and Flow Characteristics of OPC-SCM Systems. Figure 5-5 shows the influence of SCM types and replacement rates on particle packing characteristics of pastes using wet density approach. Except in the case of 15% SF replacement, all of the investigated binders necessitated lower optimum water demand compared to the plain OPC paste.

In view of OWD results, all blended binder systems developed higher solid concentration than that of the plain OPC system. For example, the binary blends of 40% FA or 40% SL were found to have 7% higher solid concentration than that of the pure OPC system. The enhanced solid concentration due to the SCM replacements becomes more dominant for ternary blends of either FA or SL with SF. For instance, the ternary combination of 10% SF with 40% FA resulted in greater solid concentration of around 25% compared to the pure OPC system. This is attributable to both the filling (since they have finer SSA value and broader PSD) and shape features (e.g., spherical shape and smooth surface) of SCMs which can effectively fill the voids among cement grains and produce more efficient arrangement of solid particles. It is noted that in the presence of SF, particle packing improves for both OPC-FA and OPC-SL pastes, wherein OPC-SL systems develop slightly larger solid concentration values compared to their corresponding OPC-FA systems. This is likely due to the higher SSA of SL compared to FA. From Figure 5-5(b), it can be seen that the improvement in solid concentration due to the SF replacement does not carry over to the 15% SF containing mixture. In spite of having the largest SSA for the 40FA15SF system, this mixture was found to have 11% lower solid concentration than that of the similar ternary system prepared with 10% SF replacement. This reduced solid concentration is attributed to the loosening effect and agglomeration formation with increasing inter-particle interactions. The loosening effect associated with the presence of high content of fine particles in paste can push the larger particles apart, and thus hinders the dense arrangement of solid particles (Kwan and Wong 2008; Yu et al. 1997). In addition to the loosening effect, the agglomeration formation of fine particles acts to trap water between flocs which can de-water the paste

and reduce the packing density of cement paste (Roussel et al. 2010). Some studies have demonstrated that in order to elicit the full benefits of the higher SSA in blended system, it is necessary to secure dispersion of the particles in the cement paste, which in turn requires the incorporation of dispersing admixtures, such as PCE, at the optimum dosage rate (Bentz et al. 2012b; Mehdipour et al. 2017b; Mehdipour and Khayat 2016b; Wong and Kwan 2008a). Although the results in this study were reported for a constant PCE dispersant of 0.12% for all binders, the 40FA15SF system was found to have consistently lower solid concentration values across further addition of PCE dispersant dosages compared to the similar ternary mixture containing 10% SF. Similar results were observed by Mehdipour and Khayat (Mehdipour and Khayat 2016b) who noted that there is a threshold content of SF replacement to improve packing density, beyond which further addition of SF does not result in higher solid concentration even with increasing dispersing admixture. This implies that there exists a saturation surface area effect to enhance packing density, beyond which the increased SSA does not necessarily lead to an increment of the particle packing in the cement paste.

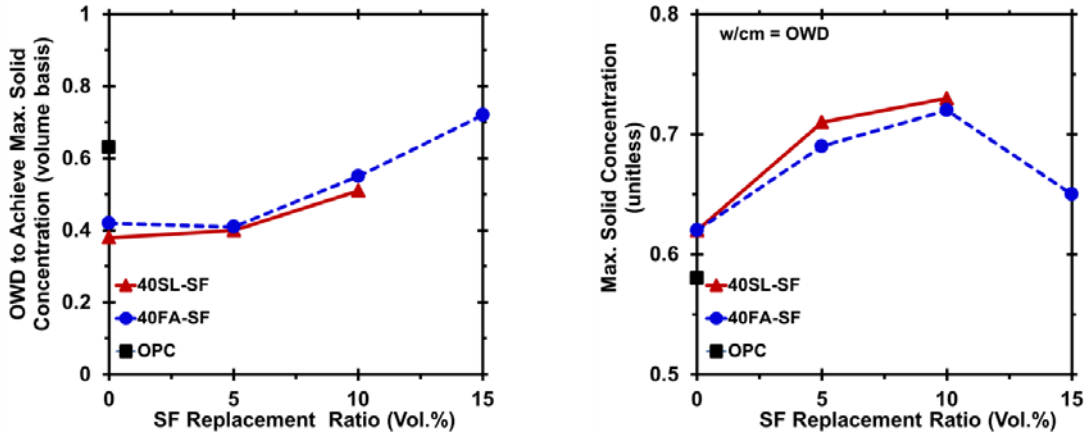

(a) (b)

Figure 5-5 Particle packing characteristics of the investigated OPC-SCM systems using wet density approach: (a) OWD to achieve maximum solid concentration and (b) maximum solid concentration. For all systems, the PCE dosage was remained constant at 0.12%, by volume of binder.

Figure 5-6 presents the flow characteristics (i.e., MWD and RWD) of the investigated paste systems using mini-slump flow cone test. As expected, all binder

systems exhibited higher water demand to initiate flow (i.e., MWD) compared to those needed to fill the voids (i.e., OWD). The larger extents for MWD is primarily because of further separation needed between neighboring particles to reduce inter-particle contacts and interactions, which can facilitate the movement of solid particles. While the values are different, a good linear relationship (R^2 = 0.97) is observed between MWD and OWD for the evaluated OPC-SCM systems, as shown in Figure 5-6(c).

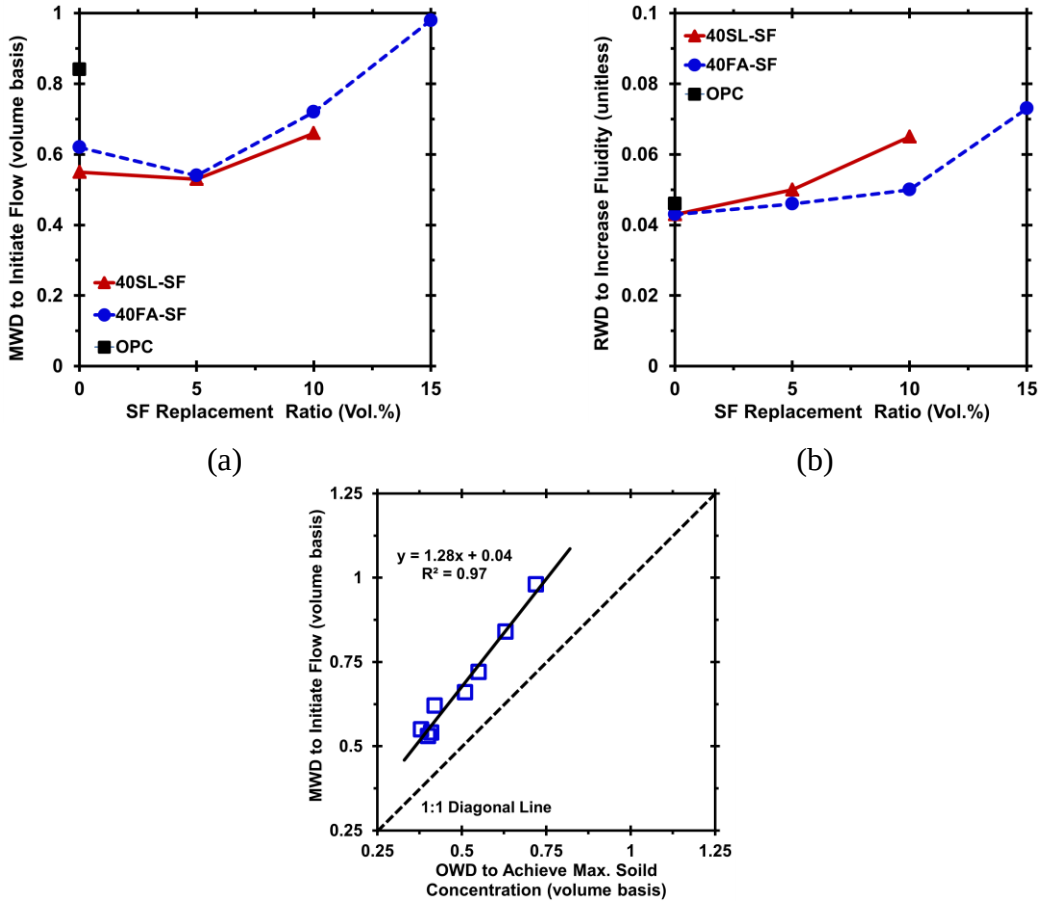

Figure 5-6 Flow characteristics of the investigated OPC-SCM systems using mini-slump flow cone test: (a) MWD to initiate flow and (b) RWD to increase fluidity. (c) Showing correlation between OWD and MWD of the investigated OPC-SCM systems. For all systems, the PCE dosage was remained constant at 0.12%, by volume of binder.

The underlying mechanism of the role of excess water (i.e., free water) in fluidity enhancement can be explained by the electric double layer (EDL) which forms on the surface of solids (e.g., cement grains) upon contact with water. The EDL constitutes: (i)

an inner stern layer of tightly held ions that carries a charge opposite to that on the particle surface and (ii) the more weakly held ions in the diffuse outer layer having the same charge as the particle surface (Hodne and Saasen 2000; Verwey and Overbeek 1955). As water content increases, the thickness of water film around the particles increases and a diffusion layer gradually forms. The diffusion layer cannot pass the hydrostatic pressure and provide fluidity in paste. As water continues to increase, the water molecules can exceed the scope of the gravitational influence of the electric field and become free water. This excess water can further lubricate the particles and act to elevate the separation among solid particles, thus providing fluidity to paste (Zhao et al. 2016).

It is interesting to note that in spite of having larger SSA, the lowest MWD was observed for ternary systems containing 5% SF. This can be explained by the competition of two simultaneous effects, while increasing the SF content increases the total SSA of solid particles, the amount of excess water will also increase (since the packing density of the solid particles is increased). The latter effect can offset the effect of increased SSA of solid particles due to the SF addition. However, opposite trend was observed for ternary system containing 15% SF. On account of its very high SSA and reduced solid concentration, the 40FA15SF paste is found to require the highest water demand. Figure 5-6(b) shows the effect of binary and ternary blended cements on RWD to increase fluidity extracted from mini-slump flow cone test. On account of higher SSA, SF containing systems develop higher RWD compared to the plain OPC system. This feature is more dominant for ternary systems of SL and SF than those observed for ternary blends of FA and SF. This is attributed to the higher overall SSA, as well as a relatively more angular geometry of the SL particles, which can elevate the inter-particle friction, thus lowering the sensitivity of cement paste to water addition.

To further investigate the effect of excess water on material behavior of pastes over transition from “concentrated state” to “flow state”, the particle packing and WFT covering solid particles at MWD were evaluated. Figure 5-7(a) shows relative solid concentration (ϕ_{MWD}/ϕ_{OWD}) of the investigated binder systems. This parameter for a given system was calculated as the ratio of solid concentration at MWD to its corresponding maximum solid concentration as identified at OWD. As expected, all

binder systems exhibit lower solid concentration at MWD compared to that of OWD. Figure 5-7(b) shows a good linear correlation between relative solid concentration and total SSA of solid particles present in system. While the highest reduction in solid concentration was observed for the plain OPC system, the OPC-SCM systems were found to have lower drop over transition from concentrated to flow onset state. The negative impact of excess water available at MWD on solid concentration is less pronounced for ternary systems containing SF. For example, the 40SL10SF exhibited merely 2% reduction in solid concentration at MWD compared to its particle packing at OWD state.

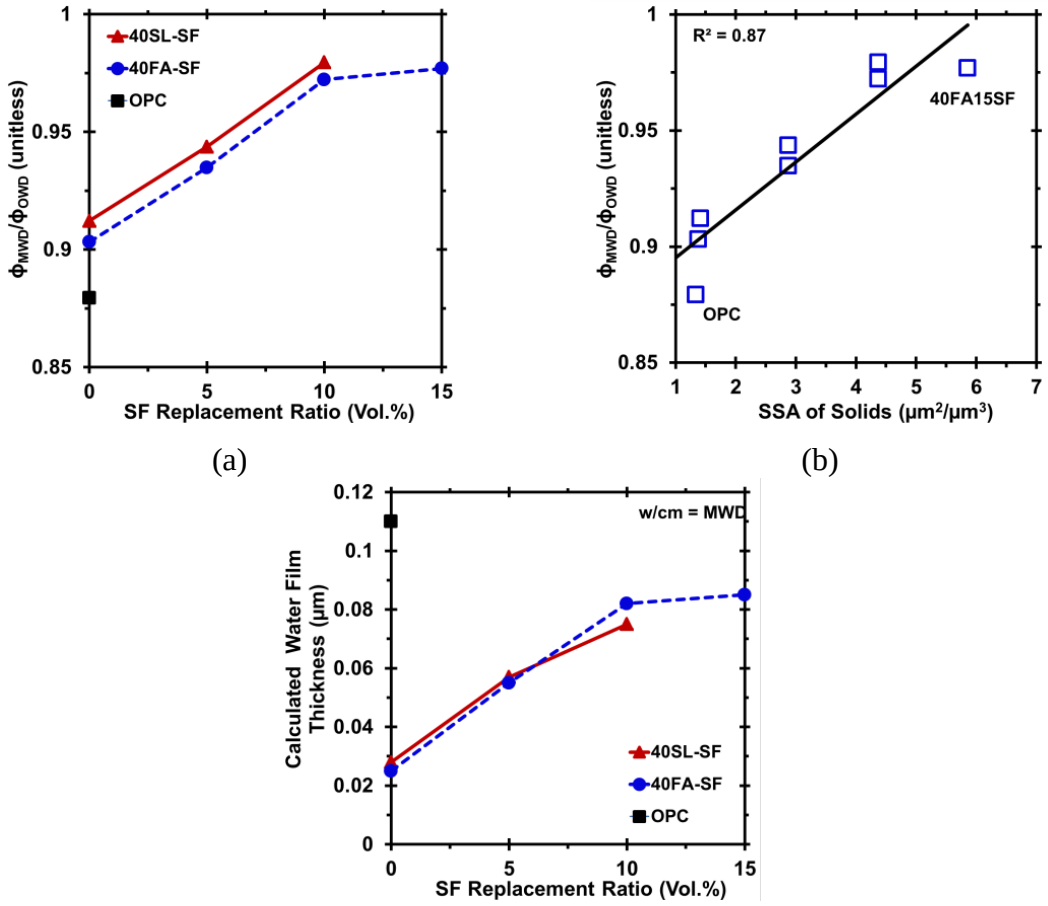

Figure 5-7 Variations in: (a) relative solid concentration in relation to SCM replacements, (b) relative solid concentration in relation to total SSA of solid particles present in system, and (c) WFT covering solid particles calculated at MWD state. In (a) and (b), the relative solid concertation for a given system was obtained by dividing the solid concentration at MWD by its corresponding maximum solid concentration.

This is hypothesized to be due to the reduced WFT needed to initiate flow (i.e., less separation between particles) in OPC-SCM systems as well as ball-bearing effect of SF and/or FA particles. This is corroborated in Figure 5-7(c), which shows the WFT covering solid particles at MWD state for the investigated binder systems. On account of their lower MWD, all OPC-SCM systems were found to have lower WFT around solid particles compared to the plain OPC system. The reduced WFT needed to initiate flow reflects that lower lubrication layer is required for transition from “concentrated state” to “flow state” in OPC-SCM systems. In addition to water demand, the presence of spherical particles in cement paste can reduce inter-particle friction, thus facilitating the movement of particles. This is an important finding as it suggests that the OPC-SCM systems with higher packing density and containing higher spherical geometry of solid particles require lower thickness of water film around solid particles to impart fluidity to paste compared to that of the pure OPC system. The scatter seen in Figure 5-7 for ternary system containing 15% SF is likely due to the effects of agglomeration and inter-particle interactions which can have a significant influence on packing density, free water availability, and inter-particle spacing in this system, thus demonstrating poor relationship.

To further elaborate on the effect of excess water on particle packing of the investigated blended systems, the average inter-particle spacing was calculated using microstructural simulations. As can be seen in Figure 5-8, at both OWD and MWD states, the average spacing between solid particles decreases marginally when OPC is partially replaced by SL or FA, and reduces dramatically when a small content of SF is incorporated in system. The effect of SF incorporation on reducing inter-particle spacing is more significant for up to 10% replacement. Upon further increase in SF content, the inter-particle spacing does not change appreciably. For example, in the ternary systems of FA and SF at OWD state, the increase of SF content from 0% to 5% and 10% resulted in reduction in inter-particle spacing of around 91% and 50%, respectively. However, with further addition of SF from 10% to 15%, the average of spacing between particles was only altered by 7%. On account of its higher SSA, the SL containing systems exhibits smaller inter-particle spacing in both binary and ternary systems as compared to FA containing mixtures. Irrespective of the SCM types and contents, all systems in

concentrated state (i.e., OWD) had smaller inter-particle spacing than corresponding mixtures at flow state (i.e., MWD). Since smaller inter-particle spacing is an indication of improved particle packing, a corresponding enhancement in the solid concentration is also noted. From Figure 5-8, it can be noticed that the effect of increasing inter-particle spacing due to the free water available at MWD state (i.e., flow onset) becomes less dominant with increasing SF content. The correlation between simulations and experimental measurements proves that in the OPC-SCM systems, binders with higher total SSA results in smaller reduction in particle packing during transition from "concentrated state" to "flow state".

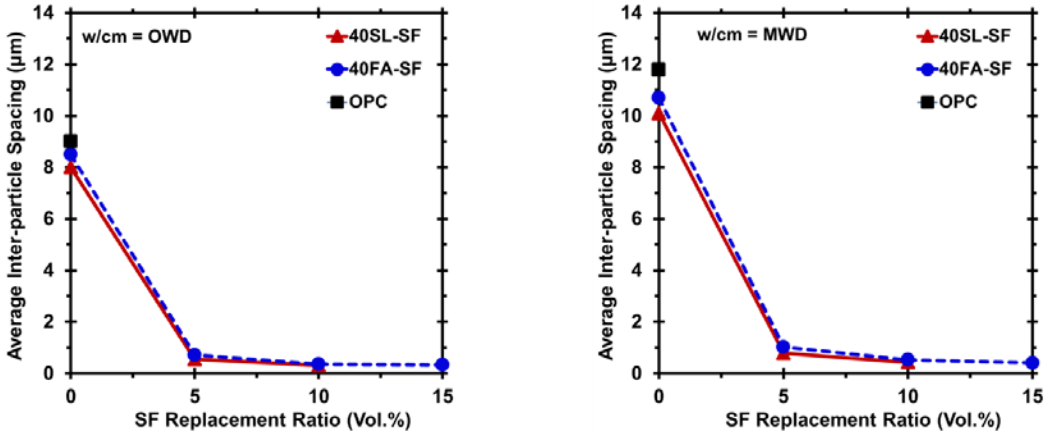

(a) (b)

Figure 5-8 Variations in average inter-particle spacing extracted from microstructural generation for the investigated OPC-SCM systems at two different states: (a) $(w/cm)_v$ = OWD and (b) $(w/cm)_v$ = MWD. Based on six replicate simulations, the uncertainty was quantified to be less than 5%.

5.3.3. Compressive Strength Development of OPC-SCM Systems. Figure 5-9 shows the compressive strength development for the investigated OPC-SCM systems at two different states: OWD and MWD. While the trends of compressive strength evolution are similar between concentrated and flow states, all systems at concentrated state (i.e., OWD) developed higher compressive strength at both early and later ages compared to the corresponding mixtures at flow onset (i.e., MWD). The presence of excess water in cement paste at flow onset increases the distance between solid particles and elevates capillary porosity, thus leading to a lower solid-to-solid connectivity in

system. However, for cement paste at concentrated state, the mixing water is only sufficient to fill the voids (i.e., WFT covering solid particles is close to zero), thus leading to a denser arrangement of solid particles.

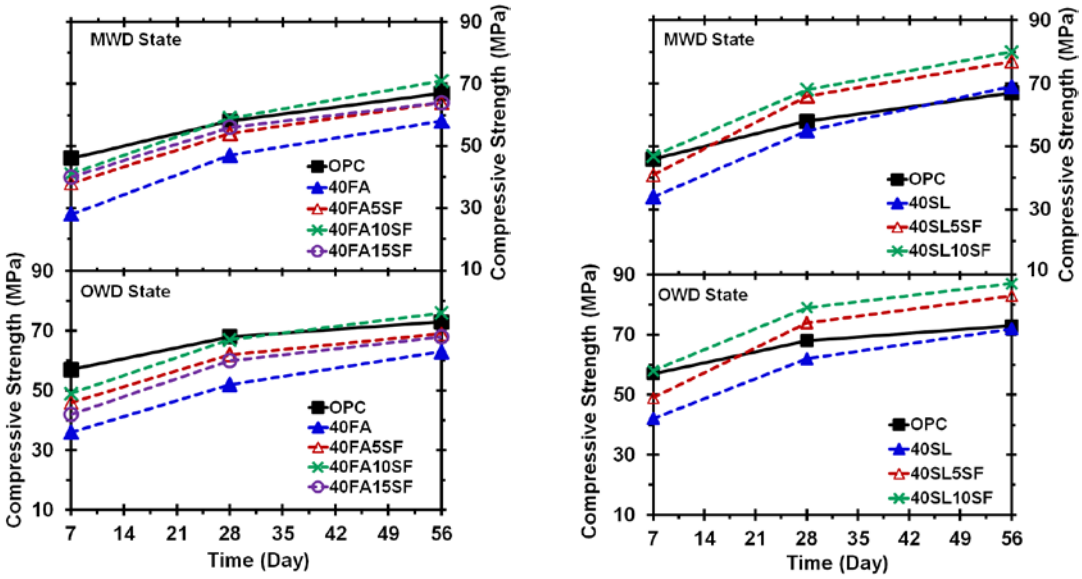

Figure 5-9 Compressive strength development of the OPC-SCM systems at OWD and MWD states: (a) FA blended systems and (b) SL blended systems. For all systems, the PCE dosage was remained constant at 0.12%, by volume of binder.

The effect of free water available at flow onset on reduced compressive strength is less pronounced for SCM containing systems. In addition to the chemical effect, when a SCM with relatively high SSA, such as SF, is incorporated as a partial replacement for OPC, the extent of induced separation between particles by water is reduced (as confirmed by the microstructural simulations), thus leading to smaller reduction in solid concentration than plain OPC system. For example, the plain OPC system at MWD state exhibited 24%, 18%, and 9% lower compressive strengths at 7, 28, and 56 days, respectively, as compared to the OWD state. However, for the 40SL10SF mixture, the extents of strength reduction due to the availability of free water in system were 18%, 12%, and 7% at 7-, 28-, and 56-day, respectively. From Figure 5-9, it can be noted that while all mixtures at MWD state exhibited consistently lower compressive strengths than corresponding mixtures at OWD state, the former mixtures developed larger rate of

strength gain than latter systems. This was identified by the larger slopes of strength-time relationships observed for mixtures at MWD state (i.e., flow onset state). The higher rate of strength gain for systems at flow state is hypothesized to be due to the higher availability of water to complete the hydration of cementitious materials which promotes the formation of pozzolanic C-S-H gel, thus improving solid-to-solid connectivity. It is important to note that while a volumetric w/c of 1.12 (i.e., mass-based w/c of 0.36) is theoretically adequate for complete hydration of OPC (Jensen and Hansen 2001; Powers 1958), the amounts of water present at both OWD and MWD states are theoretically insufficient. This implies that a portion of cementitious materials remains unhydrated which can suppress the rate of strength improvement in system. This effect would be more evident for the cement paste at concentrated state (i.e., OWD) as compared to the flow state (i.e., MWD), especially when external moist curing is not adopted. This hypothesis will be corroborated further using virtual microstructure modelling and TGA data in the next section. Irrespective of the cement paste state (i.e., concentrated or flow state), the ternary systems containing SF developed consistently higher compressive strength than corresponding binary mixture devoid of any SF. The highest compressive strength was found for the ternary system containing 40% SL and 10% SF. This mixture had 20% and 16% higher 56-day strengths at OWD and MWD states, respectively, compared to the plain OPC system. This is attributed to a combination of both physical and chemical effects induced by SCMs. The higher SSA in this system enhanced the solid concentration and decreased the inter-particle spacing, and hence reduced the amount of water required to fill the voids among particles. In addition to the physical effects, the enhanced strength is expected primarily due to pozzolanic reaction between the SCMs and the calcium hydroxide (CH), resulting in the formation of space-filling pozzolanic C-S-H, which acts to offset the effect of dilution of the cement content. Further, the reaction between limestone present in cement and the aluminate phase in SL leads tothe formation of space-filling carboaluminate hydrates, which improves solid-to-solid connectivity and enhance strength (Lothenbach et al. 2008b; Matschei et al. 2007a; b; c; Vance et al. 2013a). These features, therefore, counteract the dilution effect (i.e., OPC replacement), which in turn results in equivalent or even higher compressive strength to that of the plain OPC mixture at both early- and later-age.

When the OPC-SL and the OPC-FA mortars are compared, it is seen that the strengths of the former are consistently higher compared to the latter. This is because SL demonstrates both the cementitious (albeit slow) and pozzolanic reactivity (Lothenbach et al. 2011). In addition to chemical features, the higher SSA of SL ensures faster dissolution, thus enabling relatively larger formation of pozzolanic C-S-H at any given age. The scatter in fresh properties observed for 40FA15SF mixture was also carried to the hardened properties. This mixture exhibited lower compressive strengths at both early- and later-age than that of similar ternary mixture containing 10% SF. This divergence can be due to the lower solid concentration and higher water demand in former system. In addition, the agglomeration formation of SF particles can reduce their exposed surface area, and thus a large portion of its surface is rendered unavailable for pozzolanic C-S-H reaction (Diamond et al. 2004; Mitchell et al. 1998). To account for a dilution (i.e., OPC replacement), the 56-day compressive strength of the investigated systems is shown in Figure 5-10 as a function of clinker factor at both OWD and MWD.

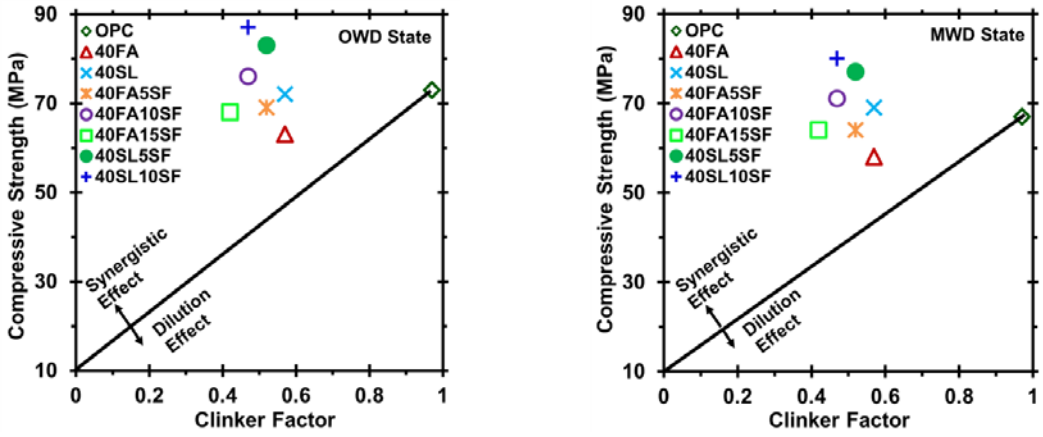

(a) (b)

Figure 5-10 56-day compressive strength as the function of clinker factor for the investigated OPC-SCM systems at: (a) OWD state and (b) MWD state. For all mixtures shown in the figure, PCE dosage = 0.12%. The dilution line traces the extent of compressive strength reduction that would occur as the OPC content is systematically reduced. For the pure OPC paste, CF = 0.968, given the presence of limestone therein.

Clinker factor is defined as the ratio of the volume of OPC to total volume of powder materials present for a given system. This is an important parameter which

characterizes the degree of sustainability of system. As indicated in Figure 5-10, the distribution of data points is similar between OWD and MWD states, signifying the fact that the effect of SCM types and replacement levels on the trend (and not value) of compressive strength is not affected by the state of cement paste. The strength values for all of the investigated systems lie above the dilution line, reflecting OPC-SCM synergistic effects. For an equivalent value of clinker factor, SL containing systems developed higher compressive strength than those observed for FA blended mixtures.

5.3.4. Effect of Excess Water on Microstructural Development. To obtain better understanding of the influence of excess water on degree of hydration and connectivity of solid volume, a series of virtual microstructure simulations were performed on the plain OPC pastes at two different states: OWD and MWD. The simulated degree of hydration and volumetric phase assemblage for the OPC systems at OWD and MWD states are shown in Figure 5-11. The difference in the degree of hydration for these two systems was found to further magnify at later ages. While both OPC systems exhibited initially similar hydration kinetics at early age, OPC system at flow onset (i.e., MWD state), wherein excess water is present, developed higher degree of hydration at later ages. Comparison between simulated phase assemblage in Figure 5-11(b) and (c) shows that while OPC paste at OWD state have lower capillary porosity than that of similar system at MWD state, a larger portion of cement remains unhydrated after 56 of hydration in the former system due to the lack of water for cement hydration. The simulated results are in agreement with previous studies. Several studies have reported that although w/c has little or no effect on early-age hydration kinetics of cement pastes (Masoero et al. 2014; Oey et al. 2013; Thomas 2007), higher w/c cement pastes generally exhibit higher degree of hydration than lower w/c cement pastes at later ages (Bentz 1997, 2006a; Kirby and Biernacki 2012). This is likely due to the availability of more space for the dissolution of reactants and higher nucleation/precipitation of hydration products in system with higher w/c (Bentz 1997, 2006a; Kirby and Biernacki 2012).

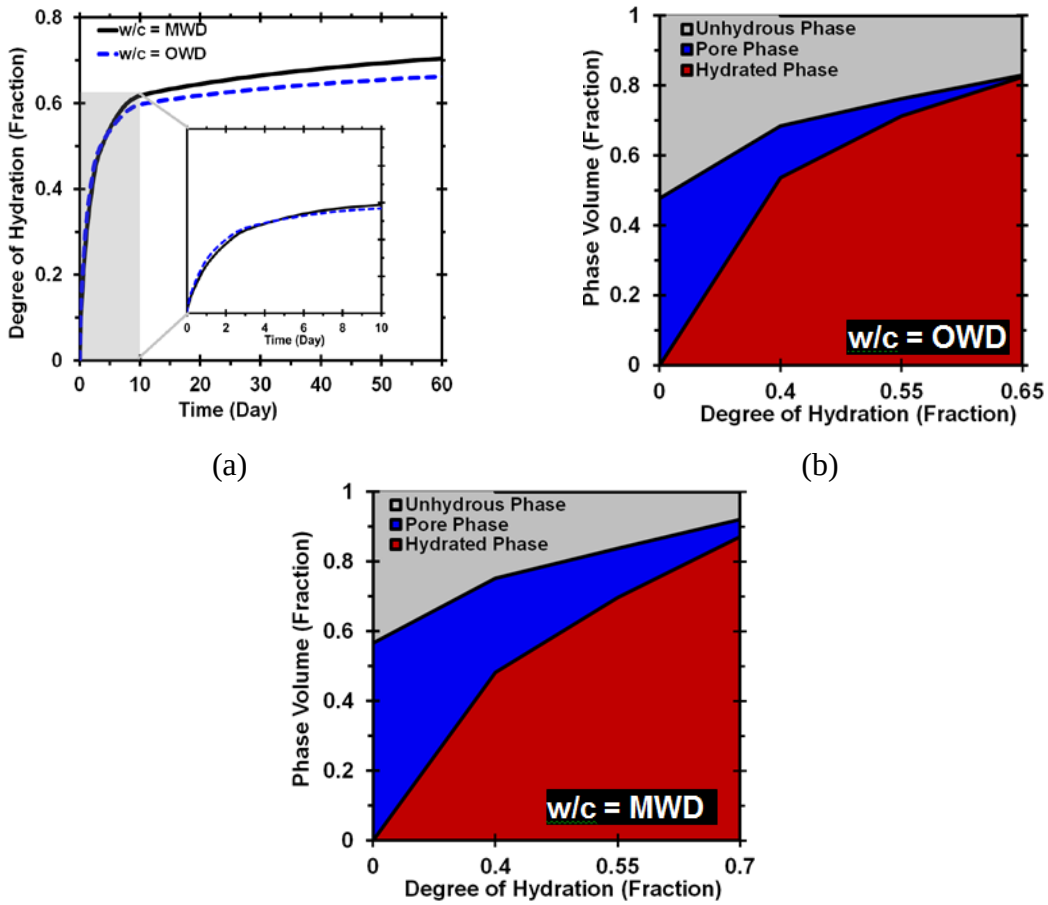

(a) (b)

(c)

Figure 5-11 For the plain OPC system: (a) simulated degree of hydration as a function of time, (b) simulated phase assemblage at concentrated state (i.e., OWD), and (c) simulated phase assemblage at flow onset (i.e., MWD) as a function of degree of hydration occurring during 56 days. All results were extracted from the virtual microstructure simulations. Based on six replicate simulations, the uncertainty was quantified to be less than 5%.

Figure 5-12(a) depicts the relationship between evolution of connectivity of solid phase and compressive strength development for OPC systems at OWD and MWD states. The evolution of connected solid volume was calculated as the ratio of volume fraction of connected solid phase to the volume fraction of total solid phase present in system as a function of time. An example of continuous formation of connected solid network in OPC systems at both OWD and MWD states is shown in Figure 5-12(b). While OPC system at OWD state had consistently higher connected solid volume and compressive

strengths than that of MWD state, the latter system was shown to have larger rate in connected solid volume.

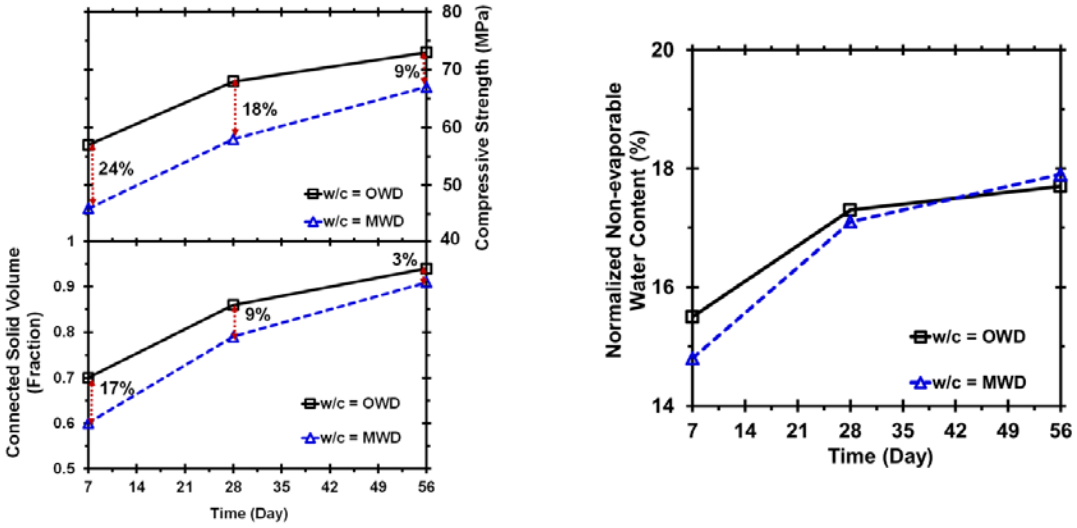

(a) (b)

Figure 5-12 (a) Correlation between compressive strength and connected solid volume (calculated from HYMOSTRUC model) for the plain OPC systems at OWD and MWD states. Based on six replicate simulations, the uncertainty was quantified to be less than 4%. (b) Non-evaporable water contents for the plain OPC systems at OWD and MWD states.

The larger rate of connectivity of solid phase for OPC system at MWD state results in higher rate of strength gain at later ages as compared to the similar system at OWD state. Therefore, the difference in compressive strength results between OWD and MWD states decreases with progressing cement hydration, as indicated in Figure 5-12. The normalized non-evaporable water contents (determined from TGA data) for the plain OPC system at OWD and MWD states are shown in Figure 5-12(b) as a function of time. The non-evaporable water content is typically considered as an indicator of hydration reaction progress in cement. Although, the OPC mixture at OWD exhibited higher early-age non-evaporable water content than that of the corresponding mixture at MWD state, this trend was not propagated at later ages, and two systems had equivalent non-evaporable water contents at later ages. The increase in non-evaporable water content was faster in the OPC system at OWD state, as identified by the larger slope of non-evaporable water content-time results in Figure 5-12(b). This suggests a higher degree of

hydration of cement at later ages for the system at MWD state than that of OWD state. The enhanced hydration kinetics of cement can manifest progressive increase in the compressive strength of system at later ages, as the cement hydration progresses and solid-to-solid connectivity increases. These results are consistent with simulation observations in Figure 5-11 and Figure 5-12(a).

5.4. SUMMARY

A series of experiments coupled with virtual microstructural simulations were carried out to evaluate the combined effects of SCMs and w/cm on physico-mechanical characteristics of cement paste over transition from concentrated state to flow onset. The material properties of the investigated binary and ternary OPC-SCM systems were characterized at two different states: (i) concentrated state as identified at w/cm = OWD and (ii) flow onset state as identified at w/cm = MWD. Based on the obtained results from this study, the following conclusions can be drawn:

- Irrespective of the nature of cement paste, ternary systems of SF and SL or FA have markedly higher particle packing and lower inter-particle spacing compared to the plain OPC system. However, there exists a saturation surface area effect of SF, beyond which the increased SSA does not necessarily lead to enhanced particle packing. This is due to the loosening effect and agglomeration of SF particles, which becomes progressively dominant with increasing SF content.
- Although transition of cement paste from concentrated to flow onset state reduces particle packing and elevates solid-to-solid distances, these effects becomes less pronounced for OPC-SCM systems than pure OPC system. The ternary system of 40% SL and 10% SF exhibited merely 2% reduction in solid concentration compared to 13% for the plain OPC mixture over concentrated-flow onset transition. This is attributed to the smaller thickness of water film (i.e., smaller inter-particle spacing) required to initiate flow for OPC-SCM systems compared to the pure OPC mixture.
- The volume of solid connectivity and mechanical property development are strongly related to the cement paste state due to changes in initial water content. While all OPC-SCM mixtures at MWD state exhibited consistently lower

compressive strength than corresponding systems at OWD state, the former mixtures developed larger rate of strength gain than latter systems. This is on account of the higher degree of hydration at later ages and larger rate of connected solid network formation for mixtures at flow state (i.e., MWD) than that of the concentrated state (i.e., OWD).

6. OPTIMIZATION OF GRANULAR SKELETON TO ACHIEVE DENSE PARTICLE PACKING

Aggregates typically represent 60%–75% of the volumetric proportion of concrete mixtures. The particle-size distribution (PSD) of aggregates can considerably influence the packing density of the granular skeleton, which in turn, determines the volume of voids to be filled with binder content. As in the case of aggregate, the optimization of PSD and particle packing in cement–SCM–filler systems is effectively employed to design more advanced sustainable concrete mixtures with better rheological properties and workability characteristics. In practice, narrowing or broadening the PSD can be an effective way to control the rheology of a suspension. This section aims at optimizing the volumetric proportions of aggregates to achieve the maximum possible packing density. In total, 17 different aggregate types (fine, intermediate, and coarse aggregates) were selected from different aggregate quarries located in Missouri to evaluate the effect of aggregate characteristics on packing density of the granular skeleton. The packing density of aggregate was measured using three different methods, including loose packing (ASTM C29), dense packing using rodding procedure (ASTM C29), and dense packing using gyratory intensive compactor tester (ICT). The selected aggregate combinations were proportioned with various sand-to-total aggregate ratios to optimize the proportioning for a given aggregate combination. In order to determine the optimum proportioning of aggregate blend, the statistical mixture design (SMD) method was utilized.

6.1. OPTIMIZATION OF AGGREGATE SKELETON

6.1.1. Aggregate Characteristics. Figure 6-1 shows the locations of various aggregate quarries visited in this investigation to study the aggregate characteristics. In total, 17 different aggregate samples with different shapes, textures, and PSDs were taken from various aggregate quarries for preliminary evaluation, as listed in Table 6-1.

The physical characteristics of aggregates, including specific gravity and water absorption, were collected from aggregate producers. A photograph of selected aggregates employed for preliminary evaluation is shown in Figure 6-2.

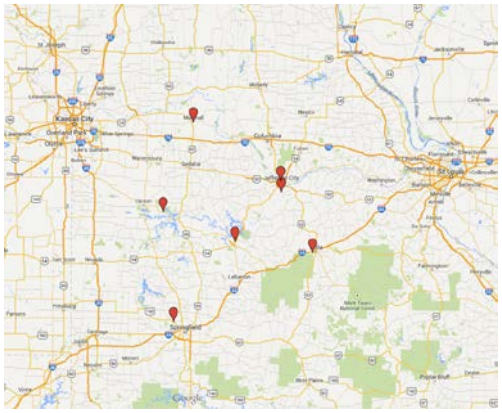

Figure 6-1 Location of aggregate quarries visited in this investigation.

Table 6-1 Selected aggregates from different quarries for preliminary evaluation.

Name	Producer	Quarry	Size	Angularity
River sand	Rolla ready Mix	Jefferson City, Missouri River	Fine	Rounded
3/8" Clean CapitCoInc	Capital Sand Company, Inc.	Wardsville, Osage River	Intermediate*	Crushed
Gravel (5/16") CapitCoInc	Capital Sand Company, Inc.	Jefferson City, Missouri River	Intermediate	Rounded
Gravel (7/16") CapitCoInc	Capital Sand Company, Inc.	Jefferson City, Missouri River	Intermediate	Rounded
Sand (Osage riv.) CapitCoInc	Capital Sand Company, Inc.	Wardsville, Osage River	Fine	Crushed
3/8" Minus CapitCoInc	Capital Sand Company, Inc.	Wardsville, Osage River	Intermediate	Crushed
1/2" Clean CapitCoInc	Capital Sand Company, Inc.	Wardsville, Osage River	Intermediate	Crushed
Sand (Osage riv.) CapitCoInc	Capital Sand Company, Inc.	Wardsville, Osage River	Fine	Rounded
1" Clean CapitCoInc	Capital Sand Company, Inc.	Wardsville, Osage River	Coarse	Rounded
1/2" (Captial Quar)	Capital Quarries	Rolla	Intermediate	Crushed
3/8" (Captial Quar)	Capital Quarries	Rolla	Intermediate	Crushed
1" (Captial Quar)	Capital Quarries	Rolla	Coarse	Crushed
Crushed Dolo (1/2")	Capital Quarries	unknown	Intermediate	Crushed
APAC 1", LinCreek	APAC - Missouri, Inc	Linn Creek Quarry, Gasconade	Coarse	Crushed
APAC MFS, LinCreek	APAC - Missouri, Inc	Linn Creek Quarry, Gasconade	Fine	Crushed
1” Dolo	Riverstone Quarry Inc	Sullivan	Coarse	Crushed
APAC MFS, Tightwad	APAC - Missouri, Inc	Tightwad Quarry, Burlington	Fine	Crushed

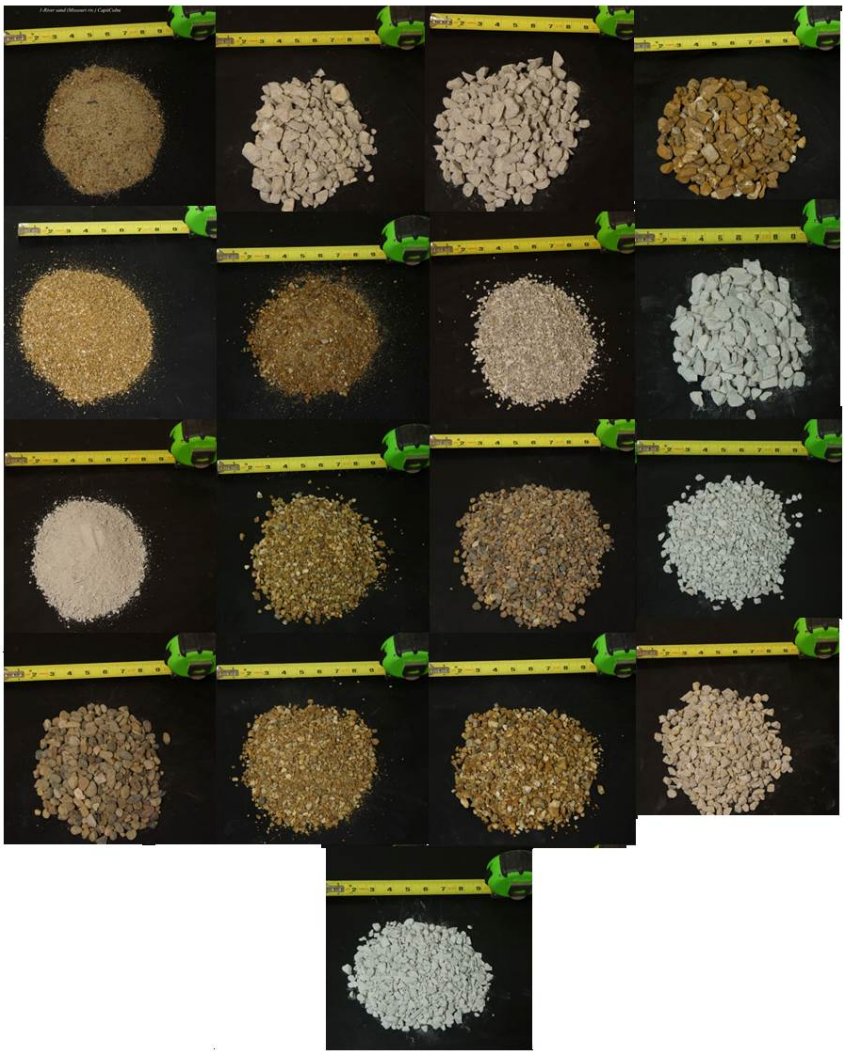

Figure 6-2 Photo of sampled aggregates.

The PSDs of the fine, intermediate, and coarse aggregates are shown in Figure 6-3. The PSDs of sampled aggregates represent a wide range of aggregates located in Missouri. The fineness modulus of fine aggregates varies from 2.56 to 4.2. The maximum nominal size of coarse aggregate was limited to 25 mm, which is typically used for pavement and transportation infrastructure applications.

The influence of physical characteristics of aggregates, including shape, texture, PSD, and fineness modulus on packing density was determined. The packing density of aggregate was measured using three different methods. This included the loose packing (ASTM C29), dense packing using rodding procedure (ASTM C29), and dense packing using intensive compaction tester (ICT), as shown in Figure 6-4.

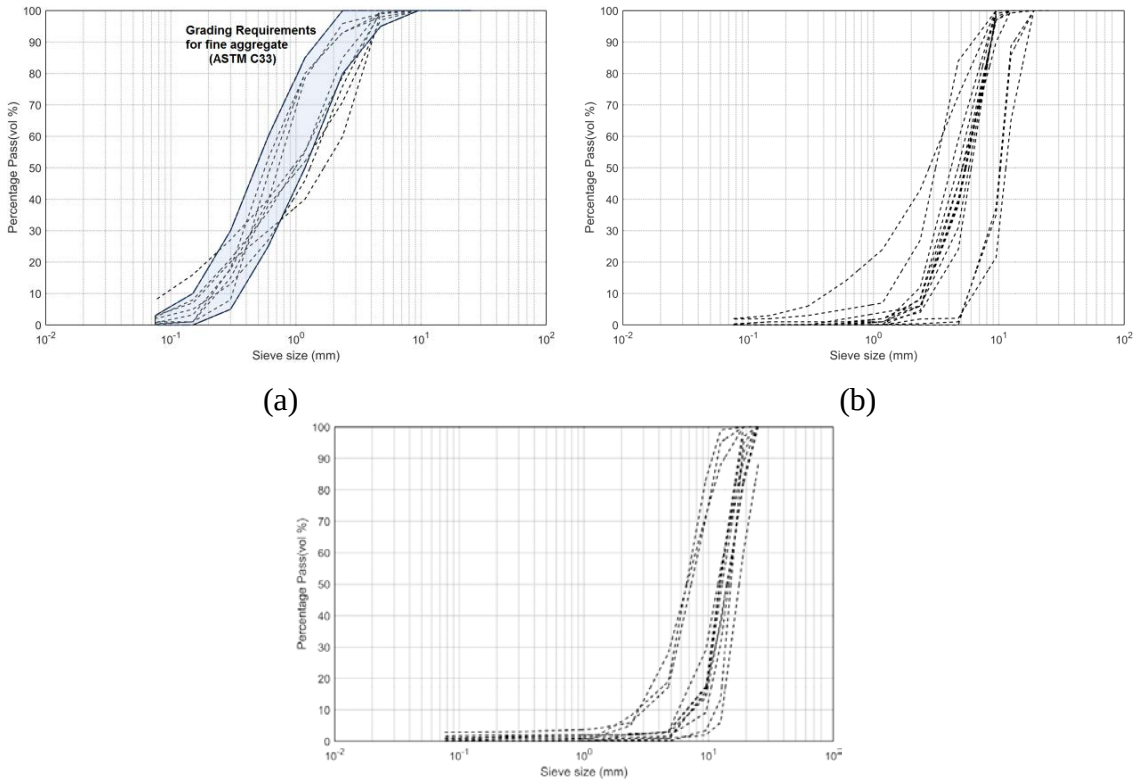

Figure 6-3 PSDs of investigated aggregates: (a) fine aggregates, (b) intermediate aggregates, and (c) coarse aggregates.

ICT is generally used for compaction of granular materials, such as soil, as well as zero slump/stiff concrete such as roller compacted concrete. A constant vertical pressure is applied on a sample placed inside the cylinder mold that rotates at a gyratory angle for a maximum of 512 cycles. Due to the gyratory inclination, a shear body develops during the measurement. Shear movement under vertical pressure allows solid particles to get closer to each other, thus leading to achieving a higher packing density. The packing density of granular materials (ϕ) is calculated as follows:

$$\phi = \frac{\rho_d}{\rho_{d\max}} \tag{6-1}$$

$$\rho_{d\max} = \frac{1}{\frac{P_1}{\rho_1} + \frac{P_2}{\rho_2} + \frac{P_3}{\rho_3} + \ldots} \tag{6-2}$$

where P_1, P_2, and P_3 are mass percentages of the various materials used in the mixture, and ρ_1, ρ_2, and ρ_3 refer to specific gravity values of the different materials. The applied

vertical pressure should be selected below a critical value that would lead to grinding or crushing of the particles. The critical pressure for tested granular material can be determined using the difference between its PSD before and after applying the various pressure values. After preliminary evaluation of various types of aggregates under different pressure values and consolidation cycles, the parameters of ICT were fixed, as presented in Table 6-2. The vertical pressure was adjusted to 2 bar (29 psi) to avoid aggregate crushing or grinding during the IC-testing.

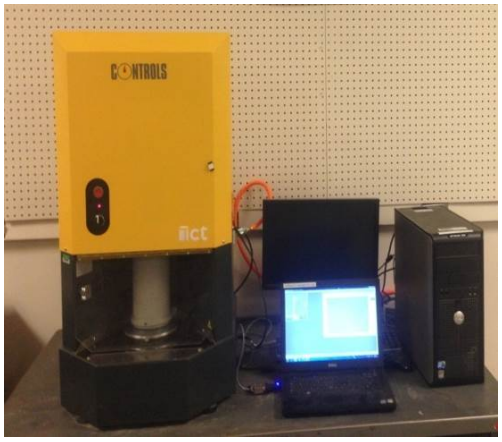

Figure 6-4 Gyratory intensive compaction tester.

Table 6-2 Testing parameters selected for ICT.

Parameter	Unit	Available range	Selected
Vertical pressure	bar	0.5-10	2
Number of cycles		2-512	256
Velocity	rpm	0-60	60
Gyratory angle	mrad	0-50	40

6.1.2. Packing Density of Mono Aggregate. The results of packing densities determined with different methods for the investigated aggregates are presented in Table 6-3.

Table 6-3 Packing densities of investigated aggregates.

	Name	Bulk density (kg/m^3)			Packing density		
		ICT	loose	rodding	ICT	loose	rodding
Fine Aggregate	Sand (Osage riv.) CapitCoInc	1834	1677	1799	0.730	0.668	0.717
	Sand (Osage riv.-Manufactured) CapitCoInc	1616	1454	1549	0.652	0.586	0.624
	River Sand, Missouri River	1816	1729	1793	0.721	0.687	0.712
	APAC MFS, LinCreek	1535	1353	1493	0.594	0.524	0.578
	APAC MFS, Tightwad	1891	1670	1760	0.726	0.641	0.675
Intermediate Aggregate	Gravel (7/16") CapitCoInc	1660	1583	1652	0.641	0.611	0.638
	3/8" Clean CapitCoInc	1485	1354	1471	0.611	0.557	0.605
	Gravel (5/16") CapitCoInc	1698	1604	1695	0.645	0.619	0.654
	1/2" Clean CapitCoInc	1537	1415	1505	0.655	0.582	0.619
	3/8" Minus CapitCoInc	1651	1546	1653	0.674	0.631	0.675
	1/2" (Captial Quar)	1613	1452	1570	0.640	0.590	0.637
	3/8" (Captial Quar)	1518	1362	1473	0.620	0.560	0.600
	Crushed Dolo (1/2")	1642	1502	1622	0.601	0.550	0.594
Coarse Aggregate	1" Clean CapitCoInc, Osage River	1485	1426	1499	0.606	0.582	0.612
	1" (Captial Quar)	1515	1464	1534	0.591	0.569	0.596
	1” Dolo Riverstone Quarry	1500	1419	1531	0.583	0.552	0.596
	APAC 1", LinCreek	1644	1471	1584	0.611	0.547	0.589

Variations in packing density of mono aggregates are shown in Figure 6-5. The packing densities of aggregates were shown to vary with size, shape, surface texture, and angularity of aggregate. The packing densities of the investigated fine, intermediate, and coarse aggregates vary between 0.58-0.73, 0.6-0.73, and 0.57-0.61, respectively.

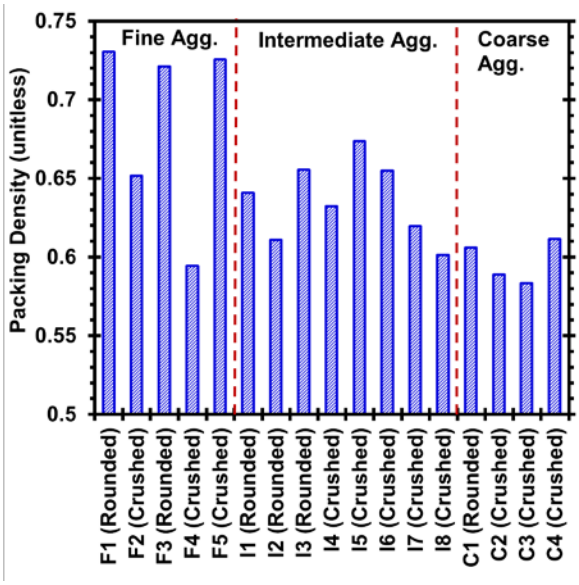

Figure 6-5 Variations in packing density of aggregates using ICT.

6.1.3. Packing Density of Aggregate Combination. This is discussed below.

6.1.3.1 Packing density of binary blends. As presented in Table 6-4, nine different binary mixtures were tested at different fine-to-total aggregate ratios (F/A) to determine the optimum combination of binary aggregate blends. For each set of aggregate blend, 7 to 12 different combinations were examined to determine the packing density as a function of F/A.The variations in packing density for different aggregate types and proportions are shown in Figure 6-6. Regardless of aggregate type, the packing density of blended aggregate increases with the increase in F/A up to a certain threshold value, beyond which the maximum packing density decreases with further increase in fine aggregate replacement. This decrease in packing density can be due to the loosening and wall effects, which can push the large particles away, thus resulting in lower packing density. For instance, for B1 blend proportioned with rounded fine and coarse aggregates, the increase in F/A from 0 to 50% resulted in an increase in the packing density from 0.61 to 0.78, while the use of 80% F/A reduced the packing density to 0.76. Therefore, there exists an optimum F/A corresponding to the maximum achievable packing density, which varies with aggregate types and combinations. Blends made with rough and angular aggregate need more content of fine particles to reach similar packing density as those of mixtures proportioned with smooth and rounded aggregate blends. This can be attributed to the higher internal friction between crushed particles which requires more

fines to reduce the inter-particle friction and achieve maximum packing density. Among the investigated binary blends, the B1, B3, and B5 blends exhibited packing density higher than 0.75.

Table 6-4 Packing density of binary aggregate blends.

Blend	Aggregate 1	Aggregate 2	Φ_2/Φ_1	proportion corresponding to Φ_{max}	Φ_{max}
B1	River Sand, Missouri River	1" Clean CapitCoInc, Osage River	0.84	50% – 50%	0.79
B2	Gravel (5/16") CapitCoInc	1" Clean CapitCoInc, Osage River	0.93	80% – 20%	0.608
B3	River Sand, Missouri River	1" Dolo Riverstone Quarry	0.88	60% – 40%	0.783
B4	3/8" Clean CapitCoInc	1" (Capital Quarry)	0.96	50% – 50%	0.642
B5	Sand (Osage riv.) CapitCoInc	1" (Capital Quarry)	0.81	60% – 40%	0.774
B6	APAC MFS, LinCreek	APAC 3/4", Marshall	0.98	50% – 50%	0.685
B7	Sand (Osage riv.-Manufactured)	Gravel (5/16") CapitCoInc	1.00	50% – 50%	0.709
B8	Sand (Osage riv.-Manufactured)	APAC 3/4", Marshall	0.89	50% – 50%	0.740
B9	Sand (Osage riv.) CapitCoInc	3/8" Minus CapitCoInc	0.92	40% – 60%	0.714

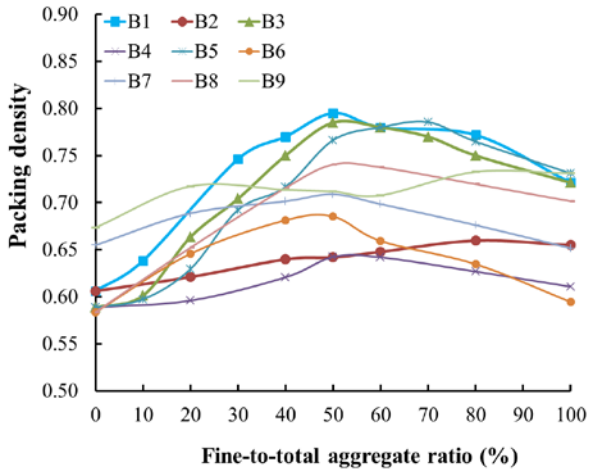

Figure 6-6 Variations in packing density for binary aggregate blends.

6.1.3.2 Packing density of ternary blends. Based on the results of packing density determined for mono and binary aggregates, five ternary combinations of

aggregate were selected. The investigated ternary aggregate blends are presented in Table 6-5. For each ternary combination, 15 to 25 different proportions were made by varying fine-intermediate-coarse aggregate proportions to cover a wide range of experimental domain.

Table 6-5 Packing density of ternary aggregate blends.

Code	Type	Aggregate name	Packing density	Mix proportion (at Φ_{max})	Φ_{max}
TM1	Fine	River Sand, Missouri River	0.721	55%	0.803
	Inter.	3/8" Clean CapitCoInc	0.611	6%	
	Coarse	1" (Capital Quarry)	0.589	39%	
TM2	Fine	River Sand, Missouri River	0.721	40%	0.815
	Inter.	Gravel (5/16") CapitCoInc	0.655	20%	
	Coarse	1" Clean CapitCoInc, Osage	0.606	40%	
TM3	Fine	River Sand, Missouri River	0.721	56%	0.787
	Inter.	1/2" Clean CapitCoInc	0.632	15%	
	Coarse	APAC 3/4", Marshall	0.583	29%	
TM4	Fine	River Sand, Missouri River	0.721	40%	0.808
	Inter.	3/8" Minus CapitCoInc	0.674	25%	
	Coarse	1” Dolo Riverstone Quarry	0.58	35%	
TM5	Fine	APAC MFS, Tightwad	0.674	56%	0.780
	Inter.	1/2" (Capital Quarry)	0.64	0%	
	Coarse	APAC 1", LinCreek	0.611	44%	

Ternary packing diagrams (TPD) for the investigated aggregate blends are shown in Figure 6-7. Given different aggregate blends and proportions, packing density varied from 0.63 to 0.82. The maximum packing density obtained for each ternary aggregate blend and its corresponding proportion are given in Table 6-5. The maximum packing density of rounded and crushed aggregates were 0.815 and 0.809, respectively. In general, smooth and rounded blends exhibited higher packing density compared to the crushed and rough aggregate combinations. In the case of rounded aggregates, the difference between minimum and maximum packing density is 0.21, which should be filled with the paste.

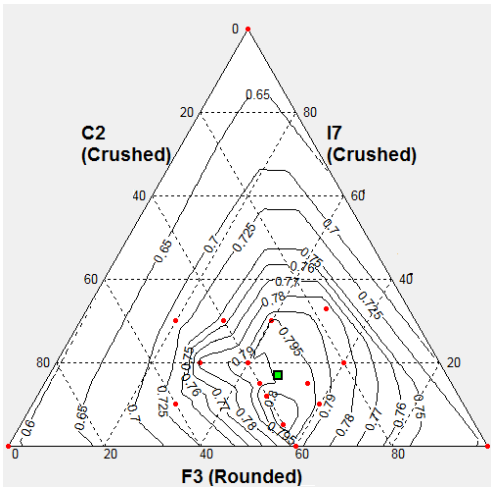

(a)

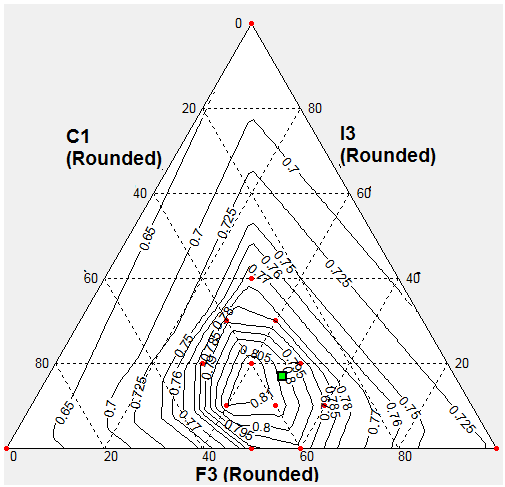

(b)

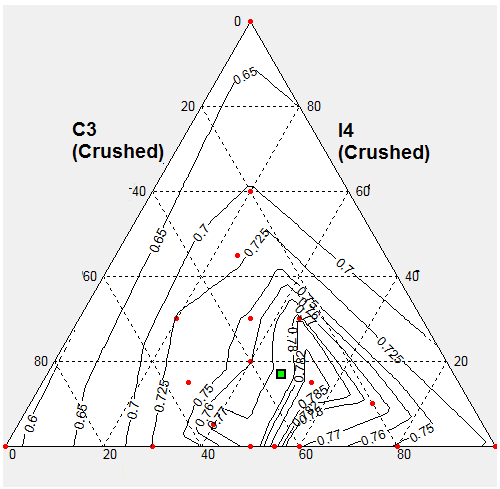

(c)

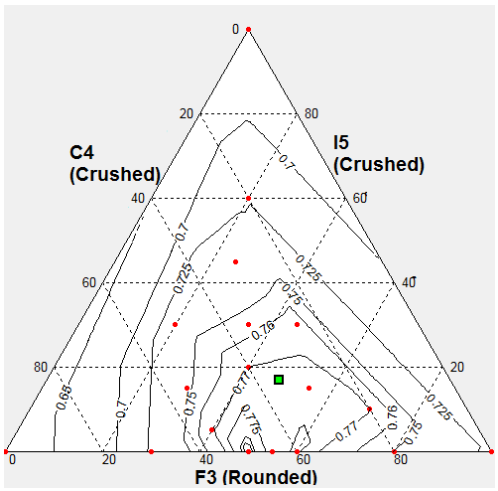

(d)

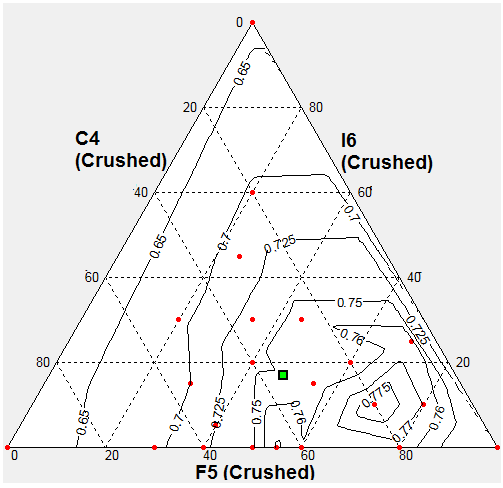

(e)

Figure 6-7 Variations in packing density of ternary aggregate blends measured by ICT for (a) TM1, (b) TM2, (c) TM3, (d) TM4, and (e) TM5.

Therefore, there exists an optimum value of aggregate proportions, corresponding to maximum packing density, which can significantly reduce the void volume between particles, thus lowering the paste volume required to fill the voids between the granular skeleton. This is an essential step and key parameter in the design and mixture proportioning of Eco-Crete. The packing density contours in Figure 6-7 indicates that higher packing density of blended aggregate was obtained with low volume of medium aggregate, regardless of the aggregate types. In other words, coarse and fine aggregates play a more dominant role in the increase of packing density. The highest packing density (more than 0.80) values were obtained for the blends TM2 and TM4.

6.1.4. Optimization of Aggregate Proportions using Statistical Approach. The aim of using statistical mixture design (SMD) technique is to determine the optimum aggregate proportioning to achieve maximum possible packing density as well as derive the statistical model to estimate the packing density of the blended aggregate. SMD method provides an efficient tool for determining the predicted model as well as for optimizing the mixture proportion.

In this method, the main principle is that the sum of all constituents for a given mixture is equal to 1. In general, assuming that the mixture consists of n constituents at which x represents the proportion of the i*th* constituent in the mixture, the sum of the material constituents is expressed as follows:

$$0 \le x_i \le 1 \qquad i = 1, 2, ..., n \qquad \sum_{i=1}^{n} x_i = 1 \qquad \text{6-3}$$

This method can be effectively employed to determine the optimum proportions of blended aggregates to achieve the maximum possible packing density. The results of packing density of blended aggregates are used as input to derive the prediction model for packing density response. The derivation of numerical model enables the determination of optimal aggregate proportion corresponding to the maximum achievable packing density.

This phase was carried out on the TM4 blend that was one of the optimal aggregate combinations among the investigated aggregate blends in the previous section. In order to cover a wide range of experimental domain, the packing density of 20 different aggregate proportions were experimentally measured using ICT. The red points

in Figure 6-8 refer to experimentally measured data points. The significance of variables and their interactions was determined by the analysis of variance (ANOVA) using the least squares fitting technique. Statistical models presented in this study were established by multi-regression analysis, as follows:

$$Y = \beta_0 + \sum_{i=1}^{n} \beta_i X_i + \sum_{i<j}^{n} \sum_{j}^{n} \beta_{ij} X_i X_j \qquad 6\text{-}4$$

where Y is the predicted response, X_i and X_j are the coded values of the modeled variables, β_i is linear coefficient, β_{ij} is the coefficient of the interaction, and n is the number of the modeled parameters. The contour diagram and surface response of the packing density for the ternary aggregate blend are shown in Figure 6-8. Depending on the aggregate proportions, the packing density values varied from 0.60 to 0.80. The packing density of blended aggregate is shown to increase with incorporating fine aggregate to a maximum possible packing density, thereafter the packing density of blended aggregate decreased with further fine particles addition.

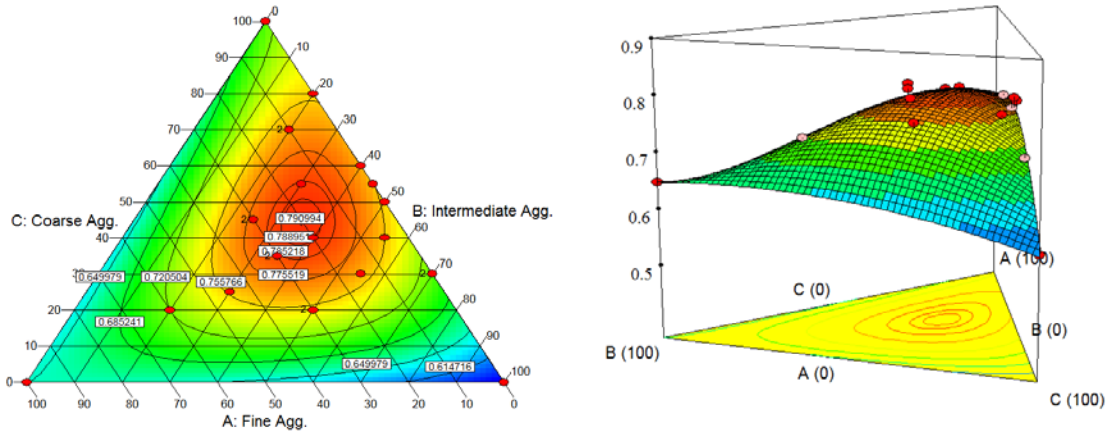

(a) (b)

Figure 6-8 Variations in packing density of ternary aggregate blends using mixture design method: (a) contour diagram and (b) surface response.

Based on the statistical model, the derived statistical model to estimate the packing density is as follows:

$$
\begin{aligned}
&\textit{Packing density} = \\
&+ 0.71 * \textit{Fine Agg}. \\
&+ 0.45 * \textit{Intermediate Agg}. \\
&+ 0.62 * \textit{Coarse Agg}. \\
&- 0.14 * \textit{Fine Agg}. * \textit{Intermediate Agg}. \\
&+ 0.42 * \textit{Fine Agg}. * \textit{Coarse Agg}. \\
&+ 0.12 * \textit{Intermediate Agg}. * \textit{Coarse Agg}.
\end{aligned}
\qquad \text{6-5}
$$

The correlation coefficient (R^2) of the derived model is 0.95. As indicated in Eq. (4-3), the fine aggregate has a higher significant effect on the packing density of the blended aggregated compared to other constituents. A multi-objective optimization technique was carried out to determine the optimum combination of aggregate blends required to achieve maximum packing density. This technique involves satisfying the defined properties without compromising any of the requirements (Montgomery, 2005). For the targeted properties, the desirability functions (d_i) are obtained and these functions are simultaneously optimized to determine the best combination. The overall desirability function (D) proposed by Derringer and Suich (1980) is expressed as follows:

$$D = (d_1^{r_1} \times d_2^{r_2} \times d_3^{r_3} \times \ldots \times d_n^{r_n})^{1/\sum r_i} = (\prod_{i=1}^{n} d_i^{r_i})^{1/\sum r_i} \qquad \text{6-6}$$

where n is the number of individual responses in the optimization, and r_i refers to the relative importance of each individual property. The r_i varies from 1 to 5, reflecting the least to most important, respectively. The d_i ranges between 0 (for a completely undesired response) and 1 (for a fully desired response). The D value close to 1 reflects that the optimal combination of variables is able to secure the target properties. The contour diagram of overall desirability for target property (maximum possible packing density) is shown in Figure 6-9. The highest desirability value of 0.96 was achieved for the aggregate combination of 43% fine aggregate (River Sand, Missouri River), 22% intermediate aggregate (3/8" Minus CapitCoInc), and 35% coarse aggregate (1” Dolo Riverstone Quarry) that resulted in packing density of 0.801.

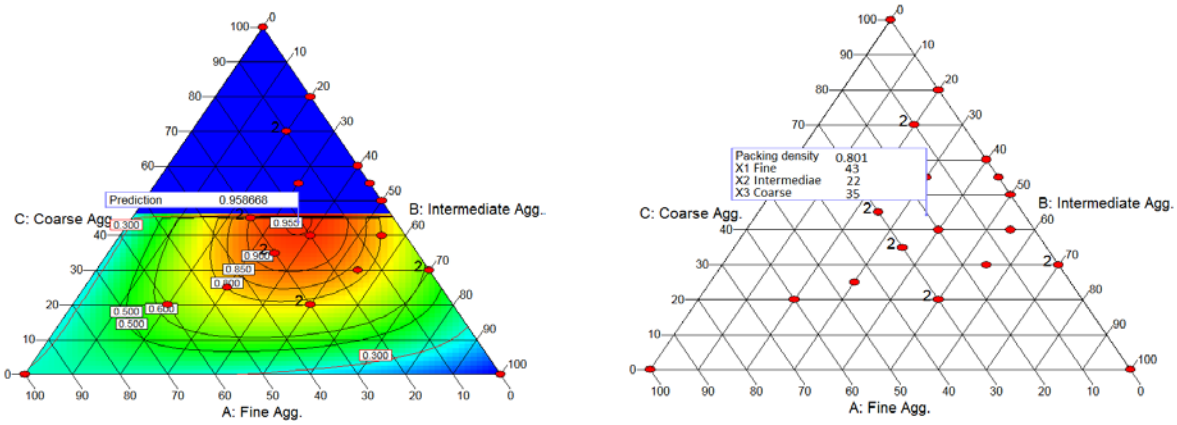

Figure 6-9 Contour diagram of desirability to achieve maximum packing density.

Based on the derived statistical model, the optimum proportioning for the investigated aggregate blend, corresponding to maximum packing density, is presented in Table 6-6. The optimal aggregate proportioning determined from the SMD method is consistent with those determined from experimentally measured packing density.

Table 6-6 Optimum aggregate proportions using SMD method.

Type	Aggregate name	Proportion	Max. packing density
Fine Agg.	River Sand, Missouri River	40%	0.808
Intermediate Agg.	3/8" Minus CapitCoInc	25%	
Coarse Agg.	1” Dolo Riverstone Quarry	35%	

6.1.5. Theoretical Grading Models for PSD Optimization. The distribution modulus (q) of the modified Andreasen & Andersen (A&A) grading model has significant influence on packing density of aggregate. The use of a lower q value results in a mixture with higher content of fine materials that can improve the packing density by reducing the inter-particle friction and reduces the risk of segregation. On the other hand, the PSD of the combined aggregate can influence the mean particle size and specific surface area of the aggregate. For a given lubricant volume, an increase in the specific surface area will result in a smaller paste film thickness around the aggregates, thus leading to a lower workability. Investigations on highly flowable mixtures showed that the A&A grading model with $0.22 < q < 0.30$ provides appropriate PSD for SCC

mixtures. An optimization algorithm was developed to determine q value of A&A grading model representing the PSD of the aggregate blend. This was done to determine the optimum q value corresponding to the maximum packing density experimentally measured from ICT. This optimization was carried out by minimizing the difference between combined gradation of blended aggregate and A&A grading model. Least squares technique was used to minimize the residual between the gradation of the densely packed mixture and the A&A grading model as follows:

$$RSS = \sum_{i=1}^{n} e_i^2 = \sum_{i=1}^{n} (P_{\text{modified A\&A}(q_i)}(d_i) - P_{\text{target mixture}}(d_i))^2 \rightarrow \min \qquad 6\text{-}7$$

$$P_{\text{modified A\&A}(q_i)}(d_i) = \frac{d_i^{q_i} - d_{\min}^{q_i}}{d_{\max}^{q_i} - d_{\min}^{q_i}} \quad \forall\, d_i \in [d_{\min}, d_{\max}] \text{ and } q_i \in [0.01, 0.5] \qquad 6\text{-}8$$

where RSS is sum of the squares of residuals. $P_{\text{modified A\&A}(q_i)}$ is the fraction of the particle size smaller than diameter d for the modified Andreasen with q_i, and $P_{\text{target mixture}}$ refers to the fraction of the particle size smaller than diameter d_i for the gradation of the target mixture, respectively. Based on the obtained results from different types and proportions of aggregate investigated in this study, the combination of river sand, river gravel 5/16", and river gravel 1" with the proportions of 42%, 20%, and 38%, respectively, was selected for the design of the Eco-crete. The PSD of the selected aggregate combination is plotted in Figure 6-10.

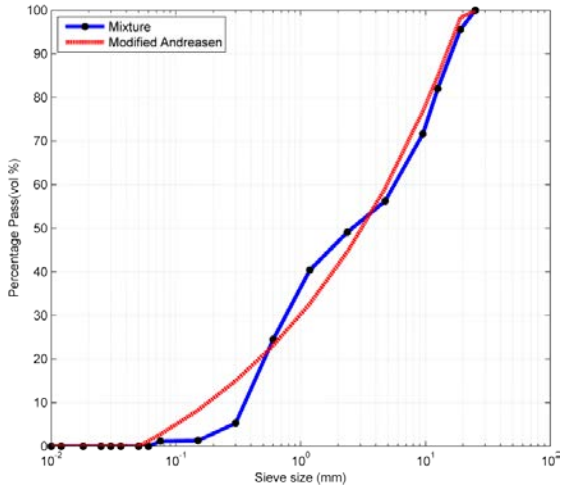

Figure 6-10 PSD of selected aggregate combination in comparison with distribution modulus of 0.275 of A&A grading model.

The selected aggregate blend had a packing density of 0.808 and its PSD is close to the A&A grading model with a q value of 0.275. This value is consistent with previous studies. For instance, Mueller et al. (Mueller et al. 2014) reported that the modified A&A model with distribution modulus of 0.27 can be effectively used for the design of Eco-SCC. Brouwers and Radix (Brouwers and Radix 2005) also pointed out that A&A distribution modulus between 0.25 and 0.29 can yield appropriate PSD to enhance flow characteristics and stability of SCC mixtures.

6.2. SUMMARY

In total, 17 different aggregate samples with different shapes, textures, and PSDs from various aggregate quarries were evaluated to study the effect of aggregate characteristics on packing density of aggregate skeleton.

- The packing densities of aggregates are shown to vary with size, shape, surface texture, and angularity of aggregate. The packing densities of the investigated fine, intermediate, and coarse aggregates varied between 0.58-0.73, 0.6-0.73, and 0.57-0.61, respectively.
- The proportion of blended aggregate has substantial influence on the packing density of concrete. Based on the obtained results, the packing density of various aggregate proportions varied from 0.65 to 0.815 and 0.65 to 0.80 for rounded and crushed aggregates, respectively. The difference between the packing density of poorly-graded aggregate and well-graded aggregate was about 0.15, which significantly affects the required paste volume to fill the voids between solid particles. This can have considerable effect of material cost, CO_2 emission, and shrinkage.
- There exists an optimum sand-to-aggregate ratio (S/A) corresponding to the maximum achievable dry density, which is affected by the type and proportion of blended aggregate.
- A proposed statistical mixture design method was shown to be an effective in optimizing the proportioning of the blended aggregate to achieve the maximum possible packing density as well as to predict the packing density of the blended aggregates.

- The selected aggregate blend for the investigated concrete mixtures had a packing density of 0.81. The PSD of such aggregate was close to the modified Andreasen and Andersen model with a q value of 0.275.

7. SHRINKAGE MITIGATING STRATEGIES FOR LOW SHRINKAGE CONCRETE

Cement-based materials typically exhibit autogenous and drying shrinkage due to self-desiccation and water evaporation. Under restrained conditions, the shrinkage of such materials can result in early-age cracking, which shortens the service life of the concrete structure. A number of shrinkage mitigating materials can be employed to reduce the early-age shrinkage of cement-based materials. The synergy between shrinkage mitigating materials can promote the efficiency of such materials in reducing shrinkage and early-age cracking potential. Depending on the water consumption of expansive agent, the efficiency of such material may not be fully generated to develop its early-age expansion when insufficient water is provided. Limited studies have been carried out to assess the performance of EX in combination with other shrinkage mitigating materials. Therefore, a more comprehensive understanding of the synergy between EX and other shrinkage mitigating materials is required to magnify the beneficial effect of EX in compensating shrinkage, especially in the absence of adequate moist curing. This section aims at evaluating the effect of wet curing and SRA on autogenous and drying shrinkage as well as compressive strength evolution of CSA-based and CaO-based EX systems. The investigated wet curing conditions included the IMCP (i.e., external wet curing) and the internal wet curing content provided through LWS. The hydration reaction, autogenous and drying shrinkage, internal relative humidity (RH), thermogravimetry, and scanning electron microscopy (SEM) were studied to examine the expansion potential of EXs. The investigation was carried out using concrete equivalent mortar (CEM) formulated from environmentally friendly self-consolidating concrete (SCC) mix design proportioned with a low binder content of 315 kg/m^3 and a water-to-binder ratio (w/b) of 0.40.

7.1. EXPERIMENTAL PROGRAM

7.1.1. Materials. A Type I/II OPC was used in this study. In order to evaluate the effect of EX type on shrinkage, two types of EX were used, including CSA-based and CaO-based EX systems. The chemical and physical properties of the OPC and EXs are presented in Table 7-1. The CSA-based EX consists of ye'elimite, belite (C_2S) and

calcium sulfates. The hydration of ye'elimite in presence of calcium sulfate and water forms ettringite and AH_3, which contribute to the expansion and early-age properties development in CSA-based EX (Kasselouri et al., 1995). The hydration reaction in CSA-based EX is expressed as follows:

$$\underset{(610)}{C_4A_3\hat{S}} + \underset{(136)}{2C\hat{S}H_2} + \underset{(18)}{34H} \rightarrow \underset{(1254)}{C_6A\hat{S}_3H_{32}} + \underset{(156)}{2AH_3} \quad 7\text{-}1$$

The expansion caused by CaO-based EX is based on the crystal growth pressure caused by the formation of calcium hydroxide ($Ca(OH)_2$) crystals, as follows:

$$\underset{(56)}{CaO} + \underset{(18)}{H_2O} \rightarrow \underset{(74)}{Ca(OH)_2} \quad 7\text{-}2$$

Each number in parenthesis under the compound formula in Eqs. (1) and (2) refers to its molecular weight.

Table 7-1 Chemical and physical characteristics of OPC and EXs.

Properties	OPC	CSA-based EX	CaO-based EX
SiO_2, %	19.8	7.7	10.6
Al_2O_3, %	4.5	7	5.7
Fe_2O_3, %	3.2	1.2	1.5
CaO, %	64.2	50.1	82.5
MgO, %	2.7	0.1	0.1
SO_3	3.4	26	–
Specific gravity	3.14	3.01	3.12

Continuously graded natural sand with 5 mm nominal maximum size, specific gravity of 2.50, and water absorption of 0.6% was employed. The LWS with 6 mm nominal maximum size and specific gravity of 1.65 was used. The LWS has a 72 h water absorption of 13% and a desorption capacity of 90% at 94% RH in accordance with ASTM C1761. The LWS was pre-saturated to secure a saturated surface-dry (SSD) condition 72 h before batching. A polycarboxylate-based high-range water reducer (HRWR) with a solid content of 23% and a specific density of 1.05 was employed. A commercially available SRA made of propylene glycol ethers was incorporated to mitigate shrinkage. The SRA and EX contents were considered as parts of mixing water and binder materials, respectively, for the mixture proportioning.

7.1.2. Experimental Design and Mixture Proportioning. Factorial design approach was conducted to evaluate the effect of different shrinkage mitigating materials on autogenous and drying shrinkage as well as compressive strength of CEM. The modeled parameters (input factors) included the use of CSA-based and CaO-based EXs, SRA, LWS, and changes in IMCP. All of the investigated CEMs were designed based on the environmentally friendly SCC mixture proportioning with a low binder content of 315 kg/m^3 and a w/b of 0.40. The quantity of LWS was theoretically estimated based on the internal curing water required to eliminate the self-desiccation (Bentz et al., 2005), which is expressed as follows:

$$M_{LWS} = \frac{C_f \times CS \times \alpha_{max}}{S \times W_{LWS}} \quad 7\text{-}3$$

where M_{LWS} and C_f refer to the dry mass of LWS (kg/m^3) and binder content (kg/m^3), respectively. The CS is the chemical shrinkage of the binder (kg of water per kg of binder) and α_{max} is the maximum potential degree of hydration of binder varying from 0 to 1. The S value represents the degree of saturation of the LWS, and W_{LWS} is the mass of internal curing water released by LWS. In this study, the CS and α_{max} values were considered to be 0.07 and 1, respectively (Bentz et al., 2005). The partial replacement of sand by 25% LWS, corresponding to M_{LWS} of 170 kg/m^3, can provide internal curing water of 22 kg/m^3.

The factorial design approach consisted of three portions; the factorial points (2^n), central points, and points used for validation, where n refers to the number of the modeled parameters. In this study, n corresponded to four parameters; SRA, EX, LWS, and IMCP. The statistical design enables the evaluation of the selected parameters at two distinct levels of −1 and +1 (minimum and maximum levels). The actual and coded values of the modeled parameters are presented in Table 7-2. The upper limits of the investigated materials were selected based on the recommended dosages provided by materials suppliers.

All modeled parameters were coded by calculating the difference between the actual values and values corresponding to the central points divided by the difference between the actual values corresponding to the 0 and 1, as follows:

$$
\begin{aligned}
&Coded\ \ CSA-based\ \ EX = (absolute\, EX - 7.5)/7.5 \\
&Coded\ \ CaO-based\ \ EX = (absolute\, EX - 5)/5 \\
&Coded\ SRA = (absolute\, SRA - 1)/1 \\
&Coded\ LWS = (absolute\, LWS - 10)/10 \\
&Coded\ IMCP = (absolute\, IMCP - 3)/3
\end{aligned}
\qquad 7\text{-}4
$$

Table 7-2 Coded and actual values of modeled parameters.

Parameter	Coded factor		
	−1	0	1
CAS-based EX (% by mass)	0	7.5	15
CaO-based EX (% by mass)	0	5	10
SRA (% by mass)	0	1	2
LWS (% by volume)	0	12.5	25
IMCP (day)	0	3	6

In order to separately evaluate the effect of EX type on modeled responses, two different sets of experimental matrixes were designed. Table 7-3 and Table 7-4 present two different experimental matrixes for CSA-based and CaO-based EX systems, respectively. Each experimental design consisted of 16 mixtures (2^4) at two levels for the factorial portion. The central portion of the factorial design was repeated four times to estimate the relative experimental error for the modeled responses. Subsequently, five additional mixtures were designed within the experimental domain of modeled parameters to evaluate the accuracy of the derived statistical models. The significance of variables and their interactions were determined by the analysis of variance (ANOVA) using the least squares fitting technique. In this study, the probability (P-values) less than 0.1 were considered as a significance level. This identifies which variable has a significant influence on the modeled response. Student tests were run to evaluate the significance of the factors and their second-order interactions on a given response.

7.1.3. Mixing Procedure and Test Methods. The mixing sequence consisted of homogenizing the sand and LWS (if used) for 60 sec, before introducing half of the mixing water. The OPC and EX (if used) were then added and mixed for 30 sec followed by the HRWR diluted in the remaining water. After 30 sec of mixing, the SRA (if used) was added, and the mortar was mixed for 3 min. The mortar remained at rest for 2 min

for fluidity adjustment before remixing for 3 additional min. The HRWR dosage was adjusted to secure a mini-slump flow of 220 ± 25 mm for all CEM mixtures.

Table 7-3 Experimental design for mixtures containing CSA-based EX.

Type	Mix description	Coded value				Absolute value			
		SRA	CSA-based EX	LWS	IMCP	SRA (%)	CSA-based EX (%)	LWS (%)	IMCP (day)
Factorial points	C	-1	-1	-1	-1	0	0	0	0
	C-6	-1	-1	-1	1	0	0	0	6
	L	-1	-1	1	-1	0	0	25	0
	L-6	-1	-1	1	1	0	0	25	6
	S	1	-1	-1	-1	2	0	0	0
	S-6	1	-1	-1	1	2	0	0	6
	S-L	1	-1	1	-1	2	0	25	0
	S-L-6	1	-1	1	1	2	0	25	6
	EX1	-1	1	-1	-1	0	15	0	0
	EX1-6	-1	1	-1	1	0	15	0	6
	EX1-L	-1	1	1	-1	0	15	25	0
	EX1-L-6	-1	1	1	1	0	15	25	6
	EX1-S	1	1	-1	-1	2	15	0	0
	EX1-S-6	1	1	-1	1	2	15	0	6
	EX1-S-L	1	1	1	-1	2	15	25	0
	EX1-S-L-6	1	1	1	1	2	15	25	6
Central points	CP1	0	0	0	0	1	7.5	12.5	3
	CP2	0	0	0	0	1	7.5	12.5	3
	CP3	0	0	0	0	1	7.5	12.5	3
	CP4	0	0	0	0	1	7.5	12.5	3
points used to validate models	V1	2/3	- 1/3	1	-1	1.7	5	20	0
	V2	2/3	- 1/3	1	-1	1.7	5	20	6
	V3	- 1/3	1/3	- 1/3	1	0.7	10	6.7	0
	V4	- 1/3	1/3	- 1/3	1	0.7	10	6.7	6
	V5	1	2/3	1	1/3	2	12.5	20	4

Notes: C: control mixture, L: lightweight sand, S: shrinkage reducing admixture, EX1: CSA-based expansive additive
Codification: EX1-S-L-6 = CSA-based EX + shrinkage reducing admixture + lightweight sand + 6 days of IMCP.

Mini-slump cone test: The mini-slump cone test was used to evaluate the flow spread of mortars (Okamura and Ouchi 2003; Yahia and Khayat 1998) and adjust the PCE dispersant dosage to achieve a target fluidity of 220 ± 20 mm. A truncated mini-cone with a top diameter of 70 mm, a bottom diameter of 100 mm, and a height of 60 mm was used. The test procedure consists of placing the mini-slump cone at the center of the plate, followed by filling with the fresh mortar sample. Subsequently, the mini-cone is

smoothly lifted and two perpendicular spread diameters (d_1 and d_2, in mm) are recorded once the flow has stopped. The mini-slump flow spread is calculated as the average of the two measured diameters.

Table 7-4 Experimental design for mixtures containing CaO-based EX.

Type	Mix description	Coded value				Absolute value			
		SRA	CaO-based EX	LWS	IMCP	SRA (%)	CaO-based EX (%)	LWS (%)	IMCP (day)
Factorial points	C	-1	-1	-1	-1	0	0	0	0
	C-6	-1	-1	-1	1	0	0	0	6
	L	-1	-1	1	-1	0	0	25	0
	L-6	-1	-1	1	1	0	0	25	6
	S	1	-1	-1	-1	2	0	0	0
	S-6	1	-1	-1	1	2	0	0	6
	S-L	1	-1	1	-1	2	0	25	0
	S-L-6	1	-1	1	1	2	0	25	6
	EX2	-1	1	-1	-1	0	10	0	0
	EX2-6	-1	1	-1	1	0	10	0	6
	EX2-L	-1	1	1	-1	0	10	25	0
	EX2-L-6	-1	1	1	1	0	10	25	6
	EX2-S	1	1	-1	-1	2	10	0	0
	EX2-S-6	1	1	-1	1	2	10	0	6
	EX2-S-L	1	1	1	-1	2	10	25	0
	EX2-S-L-6	1	1	1	1	2	10	25	6
Central points	CP1	0	0	0	0	1	5	12.5	3
	CP2	0	0	0	0	1	5	12.5	3
	CP3	0	0	0	0	1	5	12.5	3
	CP4	0	0	0	0	1	5	12.5	3
points used to validate models	V1	-1/3	2/3	1	-1	0.7	8.3	25	0
	V2	-1/3	2/3	1	1	0.7	8.3	25	6
	V3	2/3	-1/3	-1/3	-1	1.7	3.3	6.7	0
	V4	2/3	-1/3	-1/3	1	1.7	3.3	6.7	6
	V5	1	1/3	1	1/3	2	6.7	20	4

Notes: EX2: CaO-based expansive additive
Codification: EX2-S-L-6 = CaO-based EX + shrinkage reducing admixture + lightweight sand + 6 days of IMCP.

Hydration heat evolution: The heat flow evolution during hydration of CEM was determined using isothermal calorimetry at a constant temperature of 20 °C for 72 h. The thermal power and energy measured to maintain the temperature at 20 °C were then used to evaluate the influence of different shrinkage mitigating materials on rate of hydration reaction and cumulative heat release.

Shrinkage measurement: Autogenous shrinkage was determined in accordance with ASTM C1698. For each mixture, two corrugated samples were prepared using polyethylene tubes. The initial reading (time zero) for the autogenous shrinkage corresponded to the final setting time determined in compliance with ASTM C403. Drying shrinkage was evaluated using a digital type extensometer in the prismatic specimens measuring 25 × 25 × 285 mm in accordance with ASTM C157. After demolding at 24 h, the initial length of specimens was recorded. In order to evaluate the effect of IMCP on drying shrinkage, the specimens were subjected to initial moist curing of 0 to 6 days before exposure to air drying at 23 ± 1 °C and 50% ± 3% RH. It should be pointed out that the term ‘‘drying shrinkage’’ used in this paper refers to ‘‘total shrinkage’’ which includes shrinkage induced by drying and autogenous shrinkage.

Internal relative humidity measurement: The effect of shrinkage mitigating materials on internal RH of CEM was measured using cast-in sensors under sealed and unsealed conditions. The sequence of measurement procedure is schematically illustrated in Figure 7-1.

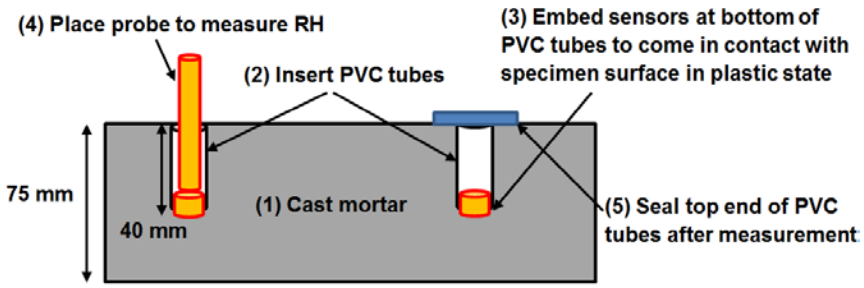

Figure 7-1 Schematic illustration of internal RH measurement in mortars prepared with various shrinkage mitigating materials.

The CEM is cast in prism measuring 75 × 75 × 285 mm, then two hollow PVC tubes with diameters of 20 mm and embedment depth of 40 mm are inserted into the fresh mixture. Steel bars are then placed into the hollow PVC tubes to prevent mortar flow inside the tubes. Following final set, the steel bars are removed, and sensors are embedded at the bottom of PVC tubes in contact with the CEM surface. The internal RH is measured by inserting probe into PVC tube after contact with embedded sensors. After each set of measurement, the top end of the PVC tube is sealed using adhesive foil to

prevent any moisture exchange with the environment. In order to evaluate the effect of sealing condition on internal RH, the specimen was wrapped using two layer of self-adhesive aluminum sheet to prevent any moisture loss due to the drying. All sealed and unsealed specimens were placed in temperature and humidity controlled room at 23 ± 1 °C and 50% ± 3% RH.

Thermo-gravimetric and X-ray diffraction analyses: Thermo-gravimetric analysis (TGA) was carried out to quantitatively estimate the amount of hydration products of samples made with different shrinkage mitigating materials under various IMCPs. After 28 days of age, samples were placed into a vacuum drying chamber to reach a constant mass. Samples were then ground to powder and sieved on a 0.15 mm sieve. A powdered sample of 20 mg was heated from 20 to 1000 °C in a nitrogen gas (to prevent carbonation) flow at a heating rate of 10 °C/min.

X-ray diffraction (XRD) analysis was conducted on powdered cementitious mixtures at 28 days using a Philips X'pert diffractometer in a θ–θ configuration using CuKa (k = 1.54 Å) radiation. Samples were scanned between 5° and 90° (2θ) in continuous mode with an integrated step scan of 0.025° (2θ) using a PiXcel detector with a time per step of 150 sec. A rotating stage was used to suitably sample the powder during acquisition.

Scanning electron microscopy observation: Samples measuring 15 × 15 mm were used for SEM examination. The sample preparation consisted of immersing samples in isopropyl alcohol to stop further hydration along with drying at 60 °C in a vacuum oven until reaching a constant mass. They were ground to achieve a relatively smooth surface, then mounted in epoxy resin and subjected to further grinding and polishing to ensure high smooth surface quality. The polished samples were then coated and examined using a Hetachi S4700-SEM with the back-scattered detector in high vacuum mode. The SEM observations were made based on the analysis carried out on several images per sample.

Compressive strength and ultrasonic pulse velocity (UPV): The 7-, 28-, and 91-day compressive strengths of CEM were determined using 50-mm cube specimens. Specimens were cast in one lift without applying any mechanical consolidation. After demolding at 24 hours, specimens were subjected to different IMCP of 0 to 6 days.

Following the IMCP, all specimens were exposed to air drying at 23°C and 50% RH until the age of testing.

The propagation velocity of longitudinal stress wave through the mortar specimens were determined to evaluate the stiffness of the investigated systems in accordance with ASTM C597 (*Annual Book of ASTM Standards* n.d.). In this test, the 54 kHz transducers were positioned in the middle of each opposing face of prismatic samples measuring 75 × 75 × 285 mm and the transmission time of the ultrasonic waves transmitted through the 285 mm long prismatic specimens was measured with accuracy up to 0.1 μs. The UPV is calculated as the ratio of length traveled by the pulse (i.e., 285 mm) to the measured time. To correlate the results with compressive strength, the transmission times of wave propagation were measured at 7, 28, and 91 days.

7.2. TEST RESULTS AND DERIVED STATISTICAL MODELS

Table 7-5 summarizes the fresh and hardened properties of the investigated CEMs. The HRWR demand of CEMs varied between 1.3 and 2.2 l/m^3 compared to 1.4 l/m^3 for the control mixture. For a given fluidity, mortars containing EX necessitated higher amount of HRWR, especially in the case of CSA-based EX system. For instance, the partial replacement of cement with either 15% CSA-based EX or 10% CaO-based EX led to 50% and 35% higher HRWR demand, respectively, compared to the control mixture. Regardless of EX type, the combination of EX with other shrinkage mitigating materials, such as SRA and LWS, resulted in similar HRWR demand to those prepared with only EX. As presented in Table 7-5, the setting time values of the evaluated CEMs ranged from 320 to 520 min and 425 to 685 min for the initial and final setting times. Based on the results, the effect of tested shrinkage mitigating materials on setting time can be categorized into two groups. The CEMs incorporating LWS or SRA exhibited longer setting times than that of the control mixture. On the other hand, mixtures made with EX replacement resulted in shorter setting times, especially for CSA-based EX. For example, the EX1 mixture containing 15% CSA-based EX had 70 and 95 min shorter initial and final setting values, respectively, compared to the control mixture. This is attributed to the relatively high water consumption occurred for ettringite formation which can increase the rate of reaction, thus shortening setting time (Ioannou et al.,

2014). On the other hand, mortar containing 2% SRA exhibited 110 and 155 min longer initial and final setting times, respectively, compared to the control mixture. This is due to the reduction in alkalinity of pore solution which slows down the cement hydration (Rajabipour et al., 2008). Furthermore, the incorporation of SRA can maintain a higher internal RH within the paste matrix for a longer duration, thus extending the setting time (Lura et al., 2007(a)).

Table 7-5 Fresh and hardened characteristics of CEMs made with different shrinkage mitigating materials and IMCP.

Mix description	HRWR demand (l/m^3)	Setting time (min)		Compressive strength (MPa)			Autogenous shrinkage (μstrain)		Drying shrinkage (μstrain)		
		Initial	Final	7-d	28-d	91-d	3-d	28-d	3-d	28-d	180-d
C-0	1.4	390	510	38	46	53	-230	-285	-385	-666	-765
C-6				48	61	67	-230	-285	40	-565	-687
L-0	1.3	405	555	45	55	63	-65	-61	-200	-518	-591
L-6				49	64	75	-65	-61	87	-419	-575
S-0	1.4	500	665	34	44	47	-50	-150	-207	-487	-589
S-6				40	52	58	-50	-150	-207	-487	-589
S-L-0	1.5	520	685	40	52	59	-39	-26	-98	-379	-417
S-L-6				45	61	67	-39	-26	59	-343	-410
EX1-0	2.1	320	415	30	41	48	153	-25.6	-428	-670	-768
EX1-6				45	65	72	153	-25.6	358	-150	-320
EX1-L-0	2.1	340	445	46	59	68	245	119	-115	-222	-428
EX1-L-6				49	69	74	245	119	435	-125	-294
EX1-S-0	2.1	400	540	35	45	55	203	84	-168	-338	-421
EX1-S-6				44	63	69	203	84	405	192	91
EX1-S-L-0	2.2	425	565	42	54	64	315	198	-37	-190	-358
EX1-S-L-6				45	65	73	315	198	505	129	38
EX2-0	1.9	370	490	41	50	52	1241	1410	-182	59	95
EX2-6				42	65	71	1241	1410	1856	1425	1352
EX2-L-0	1.8	430	535	46	55	58	1618	1700	-112	105	168
EX2-L-6				47	68	72	1618	1700	1287	988	792
EX2-S-0	2.0	460	610	38	47	48	1620	1760	-14	181	240
EX2-S-6				38	66	68	1620	1760	2087	1657	1479
EX2-S-L-0	1.9	450	590	41	51	53	1720	1790	84	70	31
EX2-S-L-6				43	65	66	1720	1790	1510	1210	958

The synergistic effect between EX and other shrinkage mitigating materials on hardened characteristics is discussed in the next section using statistical models derived

from factorial design approach. The derived statistical models of the modeled responses are summarized in Table 7-6 with variables expressed as actual values. The derived mathematical models were arranged in descending order of the factors with the highest effect on the modeled property. The estimate coefficient of each factor refers to the contribution of that factor to the modeled response. A negative value of estimate coefficient indicates that an increase in the modeled parameters results in a reduction in the response. The correlation coefficient (R^2) and adjusted correlation coefficient (R^2_{adj}) of the derived models ranged between 0.89–0.98 and 0.88–0.97, respectively. The degree of experimental error and comparison between predicted and measured properties were evaluated to validate the accuracy of the derived statistical models.

Table 7-6 Derived statistical equations for modeled responses.

Experimental design	Modeled response	Age (day)	Derived equation (actual values)	R^2
First set for mixtures containing CSA-based EX	Compressive strength (MPa)	7	$35.81-1.6\,SRA+1.6\,IMCP+0.45\,LWS$	0.89
		91	$51.2+2.3\,IMCP-2SRA+0.5\,LWS+0.3\,EX1$	0.95
	Autogenous shrinkage (μstrain)	3	$-184.2+40.7\,SRA+21.6\,EX1+4.7\,LWS$	0.97
		28	$-278+61SRA+16.5\,EX1+10.3\,LWS+0.14(LWS\times EX1)$	0.98
	Drying shrinkage (μstrain)	3	$-369+77.2SRA+60\,IMCP+6.9\,LWS+3.5\,(EX1\times IMCP)+2.3\,EX1$	0.95
		28	$-671+94\,SRA+13.2\,IMCP+10.5EX1+6.4\,LWS+3.2\,(EX1\times IMCP)$	0.98
		180	$-765+114SRA+7IMCP+6.45\,EX+6\,LWS+4.1\,(EX1\times SRA)+3.7\,(EX1\times IMCP)$	0.98
Second set for mixtures containing CaO-based EX	Compressive strength (MPa)	7	$35.81-1.6\,SRA+1.6\,IMCP+0.45\,LWS$	0.92
		91	$51.2+2.3\,IMCP-2SRA+0.5\,LWS+0.3\,EX1$	0.93
	Autogenous shrinkage (μstrain)	3	$-184.2+40.7\,SRA+21.6\,EX1+4.7\,LWS$	0.98
		28	$-260+159.4\,EX2+42.5\,SRA+17.8\,(SRA\times EX2)+8.7\,LWS+1.5(EX2\times LWS)$	0.98
	Drying shrinkage (μstrain)	3	$-222+45.3\,IMCP+24.5\,(EX2\times IMCP)+16.5\,EX2$	0.92
		28	$-512+61.6\,EX2+19\,(EX2\times IMCP)+13\,IMCP$	0.94
		180	$-590+72\,EX2+16.2\,(EX2\times IMCP)+6.2\,IMCP$	0.93

7.2.1. Validation of Derived Statistical Models. The degree of experimental error for the modeled responses is presented in Table 7-7 using four replicate central

points for each experimental set. The degree of experimental error was evaluated by calculating the coefficient of variation (COV) and relative error (RE) corresponding to 90% confidence interval (CI) as follows:

$$COV = \frac{\sigma}{\overline{x}} \quad 7\text{-}5$$

$$\mathrm{RE}\,(\%) = 2.353 \times \frac{COV}{\sqrt{\mathrm{n}}} \times 100 \quad 7\text{-}6$$

$$CI = \overline{x} \pm 2.353 \times \frac{\sigma}{\sqrt{\mathrm{n}}} \quad 7\text{-}7$$

where σ is the standard deviation; $\overline{x}$ is the mean value of the observations; and 2.353 refers to the coefficient corresponding to 90% confidence interval for the Student's distribution for a number of observations (n = 4). As presented in Table 7-7, the estimated *RE* corresponding to 90% CI varied from 0.1% to 11% and 0.05% to 7% for CSA-based EX and CaO-based EX systems, respectively.

Table 7-7 Relative error of central points.

Experimental design	Modeled response	$\overline{x}$	σ	COV (%)	RE90 (%)
First set for mixtures containing CSA-based EX	7-day compressive strength	41.4	1.25	0.03	1.50
	91-day compressive strength	64.1	0.85	0.01	1.01
	3-day autogenous shrinkage	61.3	5.11	0.08	6.01
	28-day autogenous shrinkage	-12.5	5.26	0.42	6.20
	3-day drying shrinkage	-12.5	8.66	0.70	10.21
	28-day drying shrinkage	-230.7	9.00	0.04	10.6
	180-day drying shrinkage	-452.7	4.57	0.01	5.40
Second set for mixtures containing CaO-based EX	7-day compressive strength	42.0	1.83	0.04	1.50
	91-day compressive strength	64.5	1.30	0.02	1.10
	3-day autogenous shrinkage	642.5	3.79	0.01	3.11
	28-day autogenous shrinkage	748.0	2.94	0.0	2.42
	3-day drying shrinkage	301.2	8.54	0.03	7.02
	28-day drying shrinkage	50.0	7.07	0.14	5.82
	180-day drying shrinkage	-19.2	6.50	0.34	5.35

Ten additional mixtures were proportioned within the experimental domain of the modeled parameters to validate the accuracy of the derived statistical models. These mixtures were chosen to cover a wide range of mixture proportions within the modeled region. Figure 7-2 compares the predicted-to-measured compressive strength and drying

shrinkage at different ages. The two diagonal dashed lines in Figure 7-2 represent the upper and lower estimated error at 90% CI. Despite the narrow ranges of limits corresponding to 90% CI, the majority of the predicted values lie close to the 1:1 diagonal line, thus demonstrating that the derived statistical models offer satisfactory prediction of the investigated responses within the experimental domain of the modeled parameters. On average, the predicted-to-measured ratios of compressive strength and drying shrinkage values were 0.98 and 0.92, respectively.

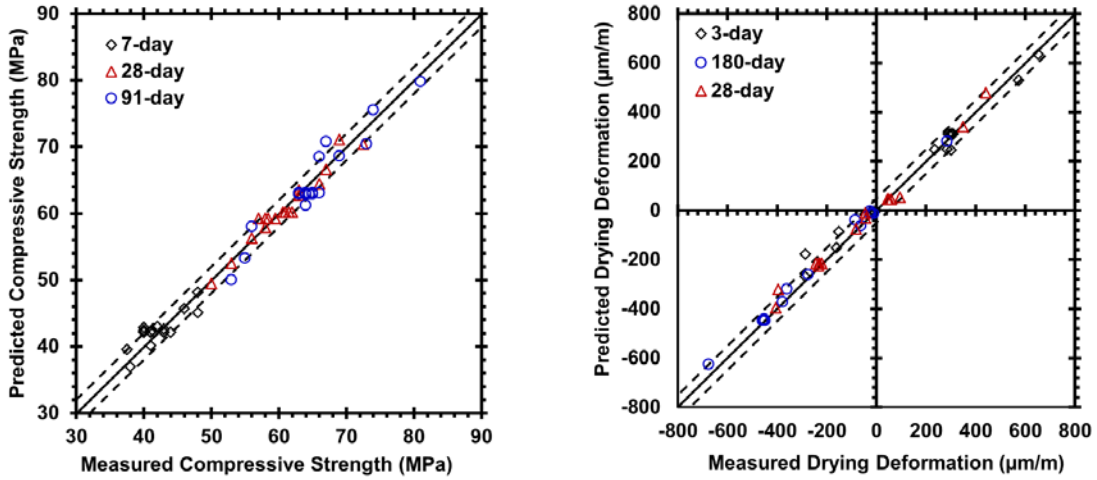

(a) (b)

Figure 7-2 Comparison between predicted and measured responses for (a) compressive strength and (b) drying shrinkage

7.2.2. Exploitation of Statistical Models. This is discussed below.

7.2.2.1 Compressive strength. The contour diagrams in Figure 7-3 show the variations of 91-day compressive strength with EX, IMCP, and LWS replacement for mixtures without any SRA. The presence of IMCP or LWS replacement was shown to significantly affect the compressive strength of mixtures containing EX. For example, in the absence of IMCP, the EX1 mixture containing 15% CSA-based EX exhibited 40% lower compressive strength at 91 days compared to the similar mixture with 6 days of IMCP. However, this value was about 22% for the control mixture made with 100% OPC. As presented in Table 7-5, the greatest 91-day compressive strength of 74 MPa was observed for the moist-cured EX1-L mixture containing 15% CSA-based EX and 20% LWS. This reflects that the effect of wet curing supplied by IMCP is more crucial for

mixtures containing EX. This is likely due to the higher water demand of mixtures containing EX, and consequently the absence of sufficient wet curing leads to a reduction in the hydration products and an increase in the volume of unhydrated cementitious materials.

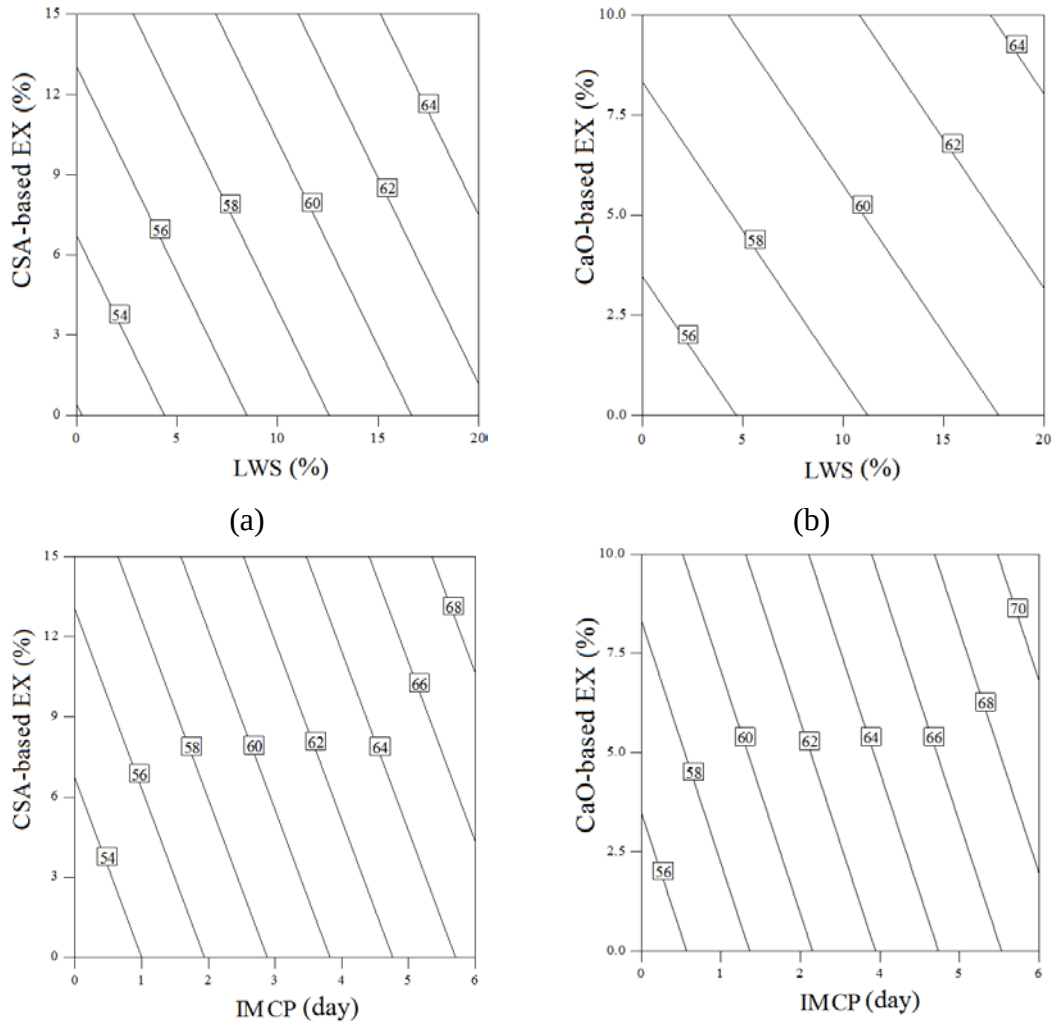

Figure 7-3 Variations in 91-day compressive strength for (a) CSA-based EX vs. LWS, (b) CaO-based EX vs. LWS, (c) CSA-based EX vs. IMCP, and (d) CaO-based EX vs. IMCP.

Regardless of EX type, the moist-cured mixtures were shown to have marginally higher 91-day compressive strength (less than 10%) than similar mixtures containing LWS replacement under non moist curing. For example, in the absence of IMCP, mixture

containing 15% CSA-based EX and 20% LWS replacement exhibited 16% higher 91-day compressive strength than that of similar mixture without any LWS. However, this value for mixture without any LWS and subjected to 6 of IMCP was about 21%. Therefore, the internal curing water provided by LWS is significantly beneficial at elevating the compressive strength for mixture containing EX when no IMCP is applied. This is attributed to the more hydration products surrounding the LWS particles due to internal curing as well as more uniform and dense interfacial transition zone (ITZ) around the LWS. Figure 7-4 shows the SEM images at 91 days of ITZ surrounding LWS and sand particles for mixture made with 15% CSA-based EX without any IMCP. The interface boundary between LWS and paste matrix is not distinct, reflecting better interfacial bond to aggregate which can result in higher compressive strength. On the contrary, the boundary surrounding sand particle is sharp and contains incomplete hydration of cementitious grains. This is partly due to the lower wall effect (i.e., better arrangement of cementitious grains around aggregate) and mechanical interlocking that promotes the quality of ITZ between lightweight aggregate and paste matrix (Zhang and Gjørv, 1990; Bentz and Stutzman, 2008). In addition, the paste matrix surrounding LWS surface is more homogeneous and lower porous with less unhydrated cementitious materials compared to that of mixture made without any LWS. The results obtained from SEM observations are consistent with previous studies carried out on mixtures containing 100% OPC without any EX. (Elsharief et al., 2005; Bentz and Stutzman, 2008; Bentz, 2009).

In order to characterize the quality of ITZ and paste matrix surrounding the aggregate particles, the gray level histograms of SEM images shown in Figure 7-4 are demonstrated in Figure 7-5. The microstructure of the paste matrix in vicinity of aggregate particles was characterized using horizontal strips (e.g., strip (a) in Figure 7-4) located in paste matrix adjacent to aggregate surface, as well as strip around the aggregate particles (i.e., strip (b) in Figure 7-4). The variations in the gray level histogram from the lowest to highest intensity correspond to porosity, C-S-H and CH hydration products, as well as unhydrated cementitious materials, respectively (Scrivener, 2004). The histograms of strips for sand particle exhibited higher scattering, thus reflecting higher inhomogeneity in paste matrix and ITZ surrounding the aggregate

particle. On the other hand, in the case of LWS, the majority of gray level intensity lied within the narrow range varying from 50 to 125, ensuring higher homogeneity and formation of hydration products in vicinity of LWS particle.

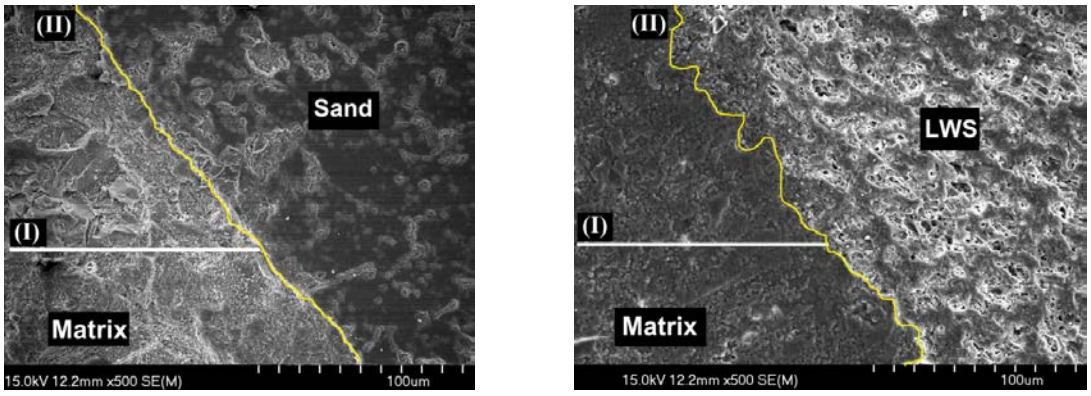

(a) (b)

Figure 7-4 SEM images at 91 days for mortars made with 15% CSA-based EX that had no moist curing (i.e., MC = 0): (a) ITZ surrounding sand and (b) ITZ surrounding LWS. All SEM images were acquired in the secondary electron mode, while operating at an acceleration voltage of 15 kV. The magnification of each image is 500x.

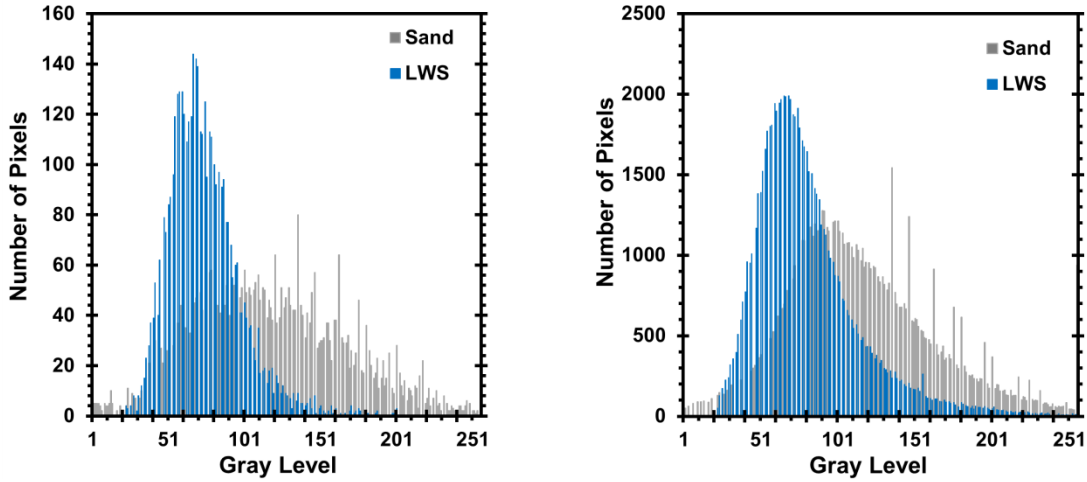

(a) (b)

Figure 7-5 Gray level histograms of SEM images shown in Figure 7-4 for (a) average of horizontal strips (i.e., strips (I)) located in matrix adjacent to aggregate surface and (b) strips surrounding aggregate (i.e., strip (II)).

Figure 7-6(a) shows the evolution of compressive strength as a function of time for the plain OPC and OPC-CSA systems under different curing conditions. As Expected,

mortars subjected to 6 days of moist curing developed higher strength at early and later ages as well as faster rate of strength gain compared to the corresponding mixtures that had no moist curing. The enhanced hydration reaction and improved solid-to-solid connectivity due to the moist curing are responsible for this effect. The effect of moist curing on strength gain is more evident in the OPC-CSA systems. This is attributed to the higher amount of water required to complete hydration in OPC-CSA systems compared to the plain OPC. For example, the moist cured OPC-CSA system exhibited 22% and 52% higher 7- and 91-day compressive strengths, respectively, than that of the similar mixture without any moist curing. However, for the plain OPC system, the extents of strength reduction due to absence of moist curing were 20% and 32% at 7 and 91 days. The lack of moist curing on strength reduction for the OPC-CSA systems further magnifies at later ages. It is important to note that in the presence of moist curing, the OPC-CSA system containing 15% CSA-based EX exhibited equivalent strength at both early and later ages to that of the plain OPC mortar.

The addition of SRA in OPC-CSA mixture resulted in a lower strength at early-age compared to the OPC-CSA system alone, while this strength reduction at early-age was not carried over to the later ages. For example, the OPC-CSA-SRA mixture exhibited 6% lower 7-day strength compared to the OPC-CSA mixture without any SRA; however, the former system had 20% and 27% higher strength at 28 and 91 days, respectively. This drop in strength at early-age in the presence of SRA can be attributed to the slower dissolution of alkalis in pore fluid, and hence slower rate of strength development compared to the similar mixture without any SRA (Bentz 2006b; Rajabipour et al. 2008; Shh et al. 1992; Weiss et al. 2008). Higher strengths observed at 28 and 91 days in OPC-CSA system containing SRA can be due to the: (i) larger amount of formation of space-filling ettringite in this system; and (ii) enhanced hydration kinetics, as evidenced by TGA data that shows larger amount of non-evaporable water in OPC-CSA-SRA system as compared to the similar system devoid of any SRA. Figure 7-6(b) shows the evolution of UPV for the evaluated systems under different moist curing conditions. The results of UPV are generally related to the stiffness, so system having higher UPV values is expected to have higher stiffness (Bogas et al. 2013; Chandrappa and Biligiri n.d.).

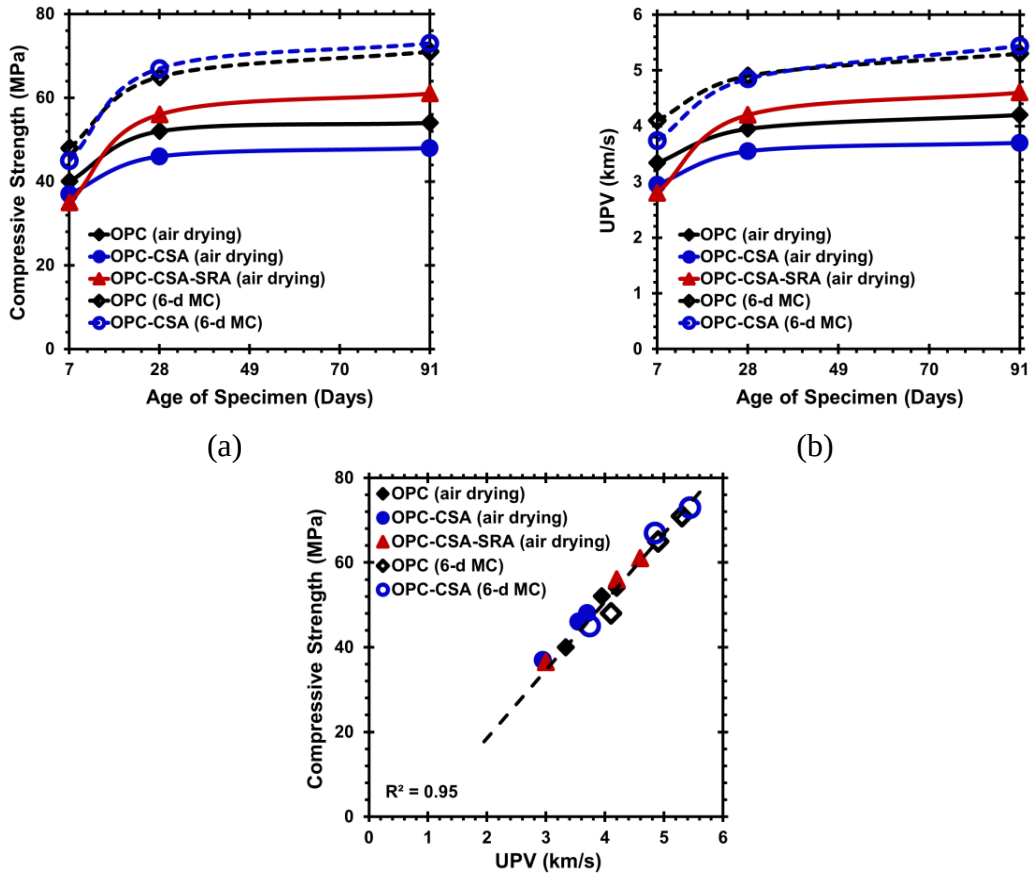

Figure 7-6 Hardened properties as a function of specimen age for the OPC and OPC-CSA systems under different curing conditions: (a) compressive strength development, (b) UPV development, and (c) correlation between strength and UPV evolution of the investigated systems.

The UPV trends observed for the evaluated systems are similar to those obtained for compressive strength results. As expected, all moist cured mixtures developed larger UPV values than those without moist curing. Similar to the compressive strength results, the fastest rate in UPV development was observed for the OPC-CSA system containing SRA. Given the linear correlation observed between strength and UPV results in Figure 7-6 (c), a lower strength can translate to a reduction in stiffness, thus potentially suggesting a lower resistance to deformation. This has an important implication in shrinkage and expansion characteristics of cementitious materials, wherein system with lower stiffness is expected to experience a higher deformation (i.e., shrinkage or expansion). For the OPC-CSA-SRA mixture, the reduction in stiffness at early-age

induced by SRA would contribute towards facilitating the expansion potential provided by CSA-based EX. The effect of stiffness on expansion characteristics of CSA cement in combination with supplementary cementitious materials has been highlighted by several researchers (Chaunsali and Mondal 2015a; b).

7.2.3. Autogenous Shrinkage. The contour diagrams of 28-day autogenous shrinkage in Figure 7-7 illustrate the trade-off between EX, LWS, and SRA. The magnitude of expansion induced by EX was shown to be affected by the EX type. For an equivalent content of EX, the use of CaO-based EX substantially generated higher magnitude of expansion than that of the CSA-based EX. For example, the variations in CSA-based EX from 0 to 15%, by mass, resulted in a shrinkage ranging from −240 to −40 μstrain after 28 days. On the other hand, these values varied from −240 (shrinkage) to +1250 (expansion) μstrain as the replacement rate of CaO-based EX increased from 0 to 10%. Among various proposed mechanisms of expansion, the crystal growth pressure theory is mostly accepted mechanism according to which crystals grow from the supersaturated solution (Ping and Beaudoin, 1992; Scherer, 2004; Flatt and Scherer, 2008). The crystallization stress depends on supersaturation level with respect to a crystal, the volume of crystals exerting pressure, microstructure, and the locations where the crystals are formed (Chaunsali and Mondal, 2016).

The transformation of CaO into $Ca(OH)_2$ causes an increase in molar solid volume (ratio of molar mass to mass density) by 90%, thus resulting in a significant expansion induced by the crystal growth pressure through the massive formation of CH hexagonal plates (Chatterji, 1995; Maltese et al., 2005). In the case of CSA-based EX, the formation of rich amount of prismatic ettringite needles exerts crystallization stress on the surrounding paste matrix, thus leading to expansion of the system (Chen et al., 2012; Bizzozero et al., 2014; Chaunsali and Mondal, 2015(b)). SEM images in Figure 7-8 show the formation of prismatic ettringite needles and CH hexagonal plates for mixtures made with 15% CSA-based EX and 10% CaO-based EX at 28 days of hydration, respectively. The synergistic effect of using EX with either SRA or LWS replacement resulted in lower autogenous shrinkage or higher magnitude of expansion for a longer duration. In other words, the incorporation of LWS or SRA can enable the reduction in EX content to maintain a fixed autogenous shrinkage, especially for CSA-based EX system. This was

reflected by larger slope of the contour diagram in Figure 7-7 for mixtures containing CSA-based EX. For instance, in order to secure an expansion of 50 μstrain, a minimum CSA-based EX content of 13.5%, by mass, is required in combination with 15% LWS replacement, by volume.

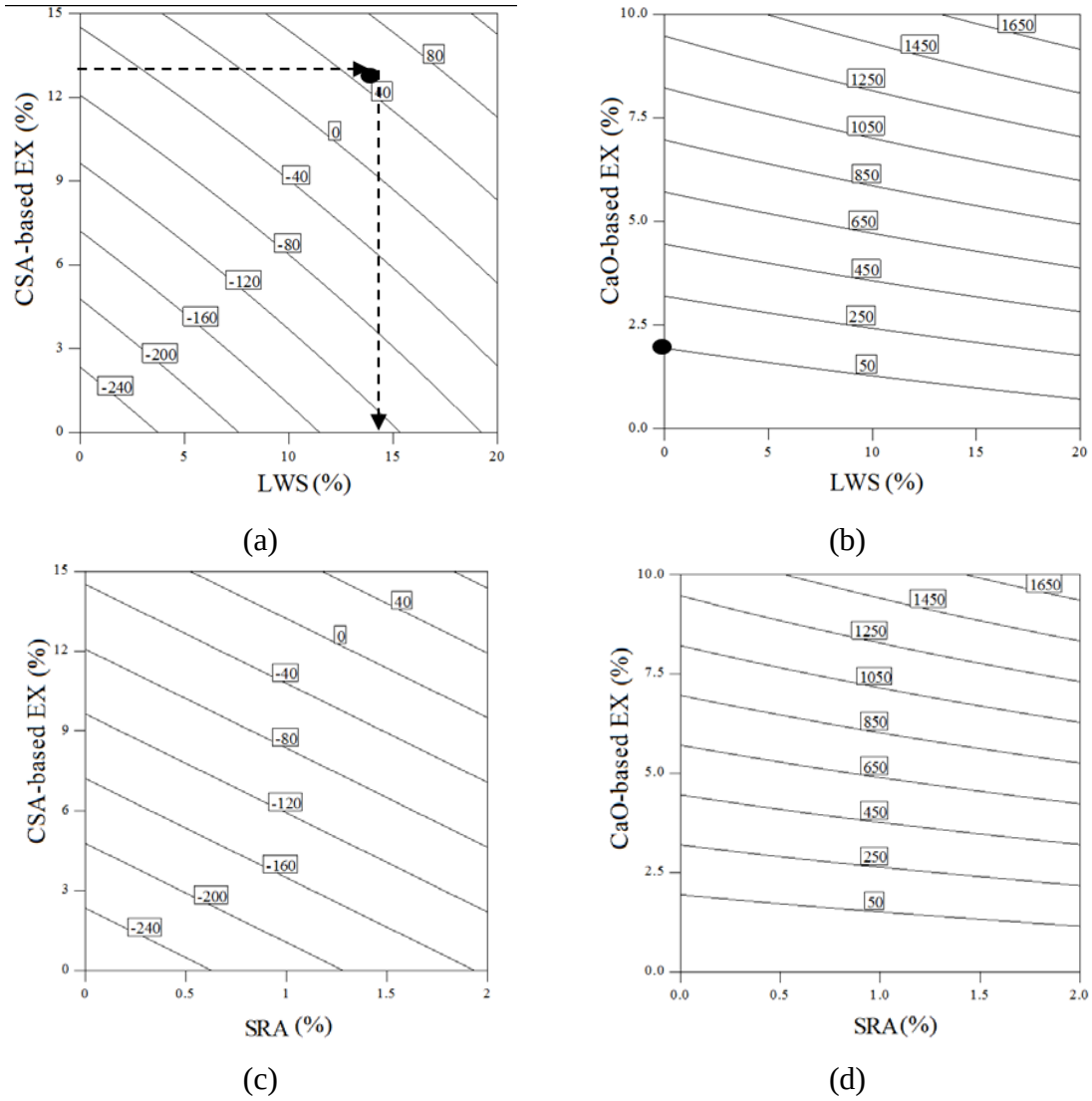

Figure 7-7 Variations in 28-day autogenous deformation for (a) CSA-based EX vs. LWS, (b) CaO-based EX vs. LWS, (c) CSA-based EX vs. SRA, and (d) CaO-based EX vs. SRA.

However, in the case of CaO-based EX, the use of 2% EX with no LWS can result in an expansion of 50 μstrain. This is attributed to the lower autogenous shrinkage and higher degree of saturation of paste matrix resulting from the use of SRA and LWS.

Figure 7-9 shows the effect of SRA and LWS replacement on internal RH of mortars made with 15% CSA-based EX. Mixture proportioned with 20% LWS replacement had 18% and 17% higher RH after 10 days under sealed and unsealed conditions, respectively, than that of mixture with only CSA-based EX.

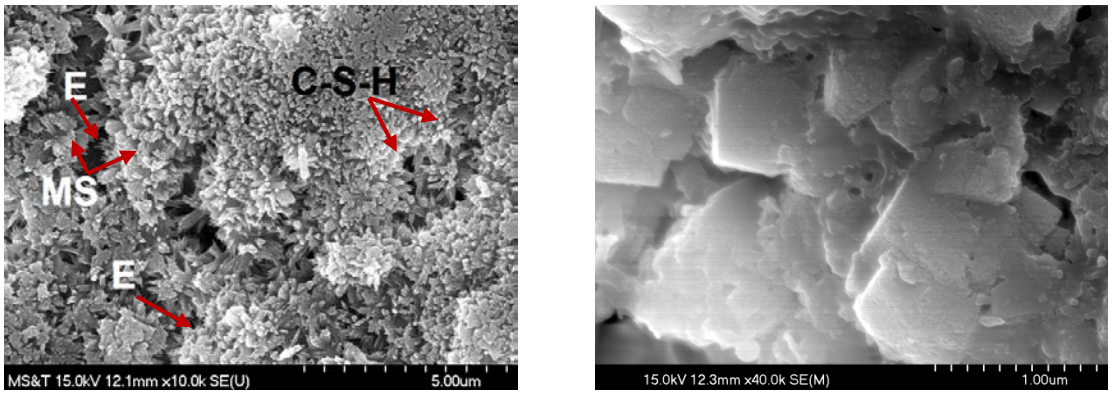

(a) (b)

Figure 7-8 SEM images at 28 days under sealed condition for (a) OPC-15%CSA system showing formation of prismatic ettringite and (b) OPC-10%CaO system showing formation of CH hexagonal plates. Here: E: ettringite, MS: monosulfoaluminate, C-S-H: calcium-silicate-hydrate gel. All SEM images were acquired in the secondary electron mode, while operating at an acceleration voltage of 15 kV. The magnification of each image is 10,000x.

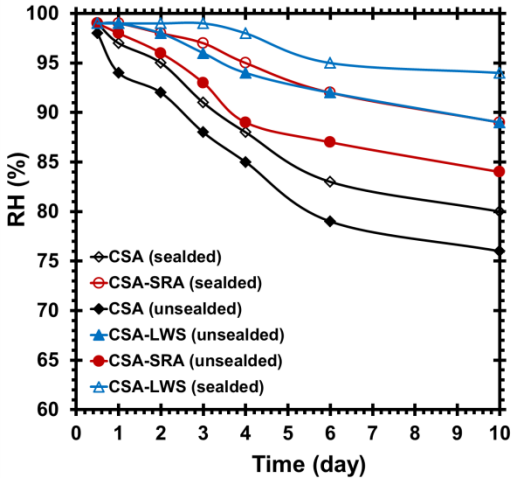

Figure 7-9 Effect of LWS and SRA on internal RH of mortars made with 15% CSA-based EX.

The addition of SRA also resulted in 12% and 10% higher RH values after 10 days under sealed and unsealed conditions, respectively. This is in agreement with previous research studies (Bentz et al., 2001; Weiss et al., 2008). The higher degree of saturation of paste matrix and lower surface tension of pore solution associated with the use of SRA can reduce the development of capillary stresses induced by self-desiccation, thus resulting in lower autogenous shrinkage (Rajabipour et al., 2008). To better examine the synergistic effect of using EX with either SRA or LWS on rate of hydration reaction, the heat flow profile and cumulative heat release of mortars made with different EX types are plotted in Figure 7-10.

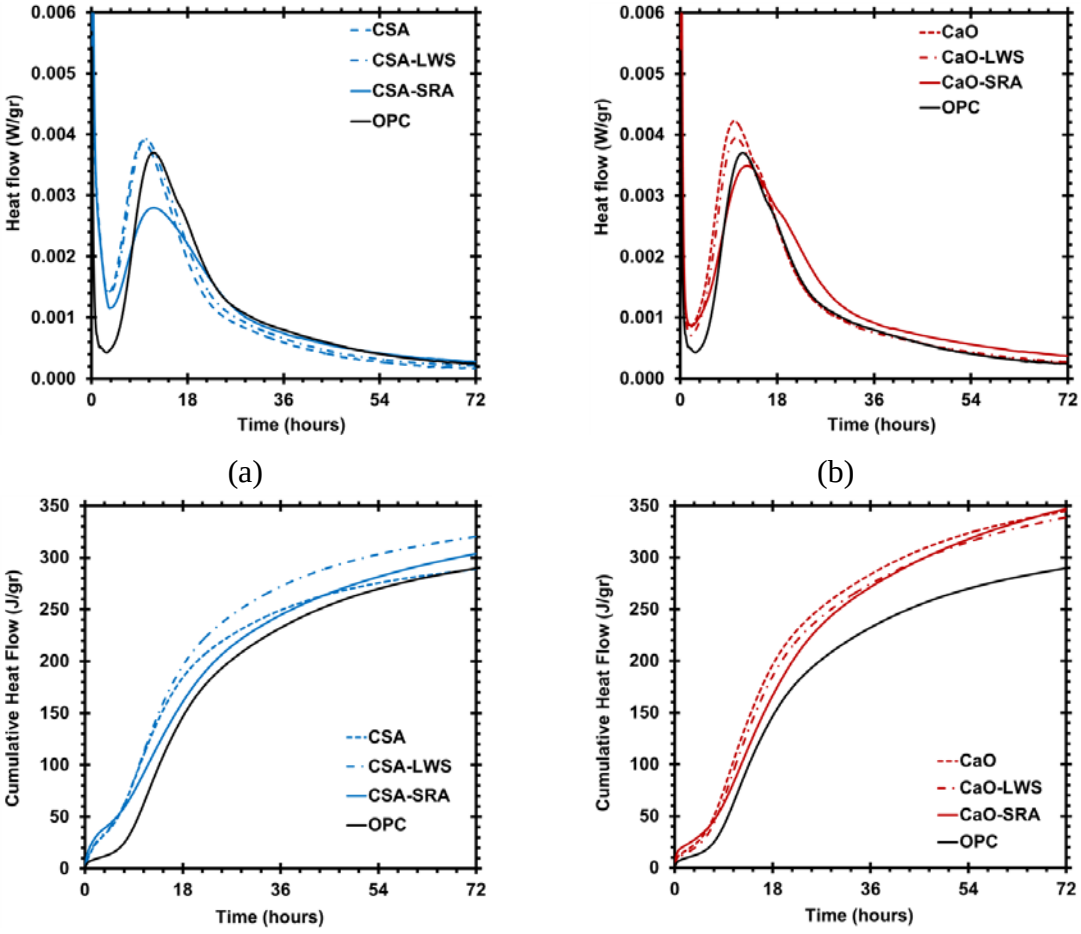

Figure 7-10 Effect of LWS and SRA on heat flow rate and cumulative heat release of OPC-15%CSA and OPC-10%CaO systems. Results were normalized by OPC fraction.

As expected, the particle replacement of cement with EX resulted an acceleration in hydration reaction, indicating higher magnitude of heat at peak and earlier appearance of time of main peak (i.e., shorter induction period), especially for CaO-based EX. For example, the amplitude of hydration peak, time of appearance of hydration peak, and slope of acceleration region for 10% CaO-based EX system are 15% higher, 17% earlier, and 13% steeper, respectively, than that of the plain OPC system. This is consistent with test results obtained from setting time, as presented in Table 7-5. It is interesting to note that the combination of EX with either LWS or SRA resulted in an improved hydration reaction, especially for CSA-based EX. The use 15% CSA-based EX in combination with either 2% SRA or 20% LWS led to 6% and 12% higher cumulative heat release after 72 h, respectively, compared to the mixture prepared with only CSA-based EX. This implies that the incorporation of SRA and LWS can facilitate the hydration of EX and elevate the rate of reaction, thus inducing higher expansion on paste matrix.

7.2.4. Drying Shrinkage. The contour diagrams in Figure 7-11demonstrate the trade-off between EX and IMCP on 3 and 180-day drying shrinkage for mixtures made without any LWS and SRA. The effectiveness of using EX to generate its expansion potential and compensate drying shrinkage (under unsealed condition) at early and later ages is highly affected by the IMCP, especially for CSA-based EX.

In the absence of IMCP, the use of CSA-based EX up to 15% resulted in similar drying shrinkage to that of the control mixture made without any EX. However, in the presence of 6 days of IMCP, the EX1 mixture resulted in an expansion of 300 μstrain (after 3 days) followed by shrinkage of −400 μstrain after 180 days of drying compared to −700 μstrain for the control mixture. Contrary to the CSA-based EX, the incorporation of 10% CaO-based EX developed an expansion of 100 μstrain after 180 days even in the absence of IMCP. For CaO-based EX, the magnitude and rate of expansion were significantly influenced by the IMCP. Mixture incorporating 10% CaO-based EX and 6 days of IMCP exhibited expansion of 1000 μstrain after 180 days compared to 100 μstrain for similar mixture under non-moist curing condition. This is attributed to relatively high water consumption of CSA-based EX to complete hydration and form ettringite.

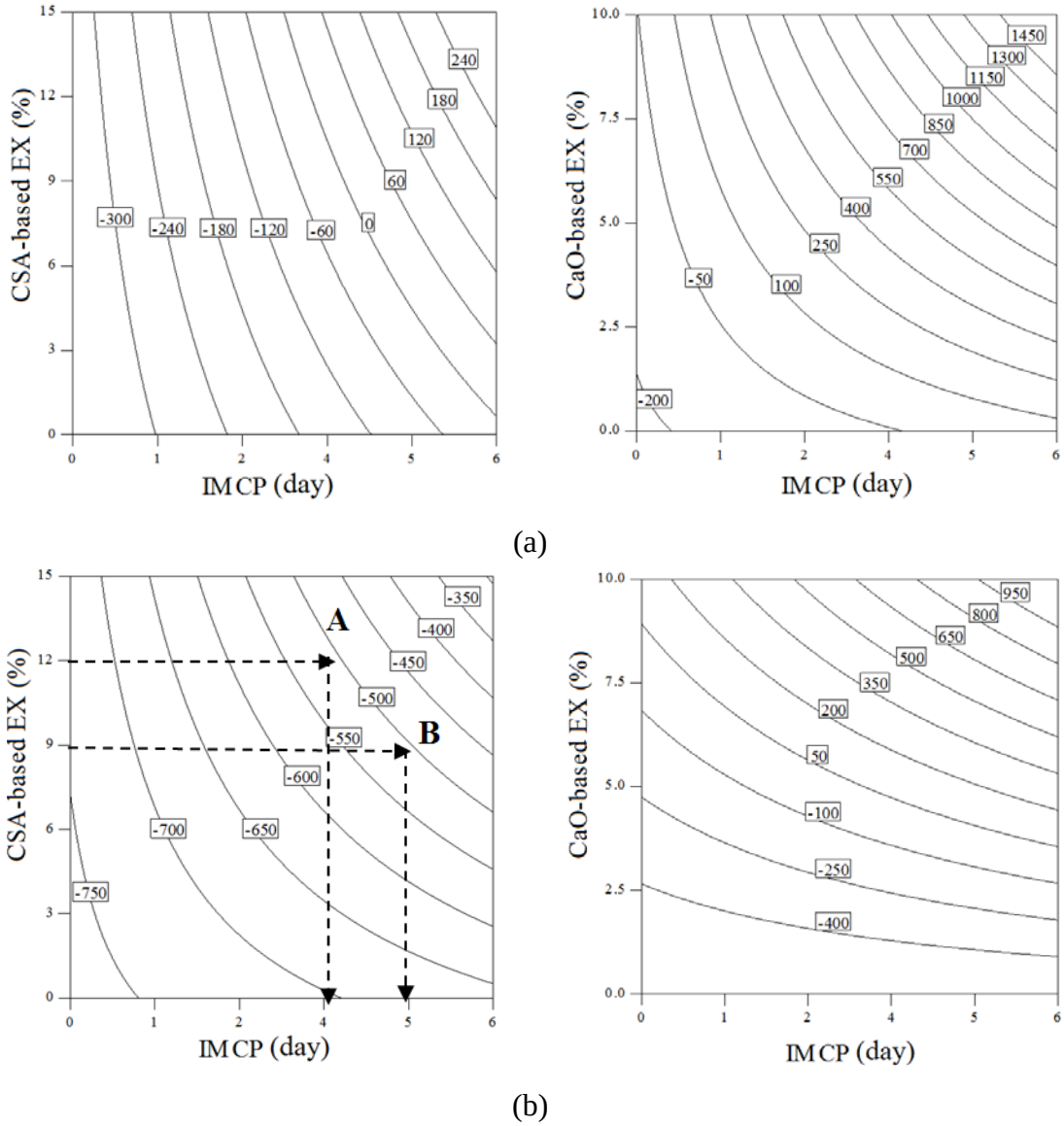

Figure 7-11 Contour diagrams of drying shrinkage for (a) 3 days and (b) 180 days.

As expressed in Eqs. (1) and (2), the theoretical water-to-solid ratio for the complete hydration of CSA- and CaO-based EXs are evaluated to be 0.82 and 0.33. This implies that w/b of 0.4 used in this study is theoretically insufficient for complete hydration of CSA-based EX. Therefore, the water supplied by exterior wet curing is the key factor in enhancing hydration and developing the expansion potential in CSA-based EX system. Similar results have been reported by Collepardi et al. (2005), who noted that the CSA-based EX needs a continuous wet curing between 5 and 7 days to develop the potential of expansion. For a given target drying shrinkage, the prolonging IMCP enables

the reduction in EX content, especially for the case of CSA-based EX. As illustrated in Figure 7-11(b), extending the IMCP from 4 to 5 days can reduce the CSA-based EX content from 12% to 9%, by mass, to maintain the 180-day drying shrinkage of 500 μstrain (points A and B).

The response surfaces in Figure 7-12 illustrate the effect of SRA and LWS on 180-day drying shrinkage of mixtures made with EX under non-moist curing condition. In the absence of IMCP, the combination of CSA-based EX with either LWS or SRA was highly effective in mitigating drying shrinkage compared to the CSA-based EX alone. For example, the combination of 15% CSA-based EX and 2% SRA reduced the 180-day drying shrinkage from 780 to 440 μstrain. However, no significant improvement in drying shrinkage was found for the combination of CaO-based EX with either SRA or LWS, as shown in Figure 7-12. It is important to point out that although the combination of CaO-based EX and SRA resulted in higher magnitude of expansion than that of similar mixture without any SRA, this improvement was not evaluated to be statistically significant, as indicated in Table 7-6. The synergistic effect between SRA and EX on early-age expansion is attributed to the fact that the presence of SRA increases the supersaturation level with respect to ettringite and portlandite crystals (Maltese et al., 2005; Rajabipour et al., 2008; Sant et el., 2011). Given the fact that supersaturation level of a phase is directly proportional to crystal growth pressure, the increase in supersaturation level with respect to ettringite/portlandite crystals results in higher crystallization pressure, thus inducing larger expansion (Bizzozero et al., 2014; Chaunsali and Mondal, 2015(b)).

In addition to higher degree of internal relative humidity and lower surface tension of pore fluid features, the synergistic effect between SRA and CSA-based EX on early-age expansion is attributed to the increase in supersaturation level with respect to ettringite and portlandite crystals in the presence of SRA (Rajabipour et al. 2008; Sant et al. 2011). It is also important to note that the presence of SRA alters the viscosity of pore fluid. The viscosity measurement of a concentration of 5% SRA (by mass) in distilled water solution exhibited a viscosity of 0.0092 Pa.s compared to 0.00089 Pa.s for the distilled water. The increase in viscosity of pore solution can reduce the moisture diffusion coefficient, thus maintaining a higher degree of saturation in paste matrix

(Bentz et al. 2008; Sant et al. 2010; Villani et al. 2014). Further details corroborating these hypotheses pertaining to effect of SRA on reaction kinetics and hydration products of OPC-CSA system are discussed in the next section.

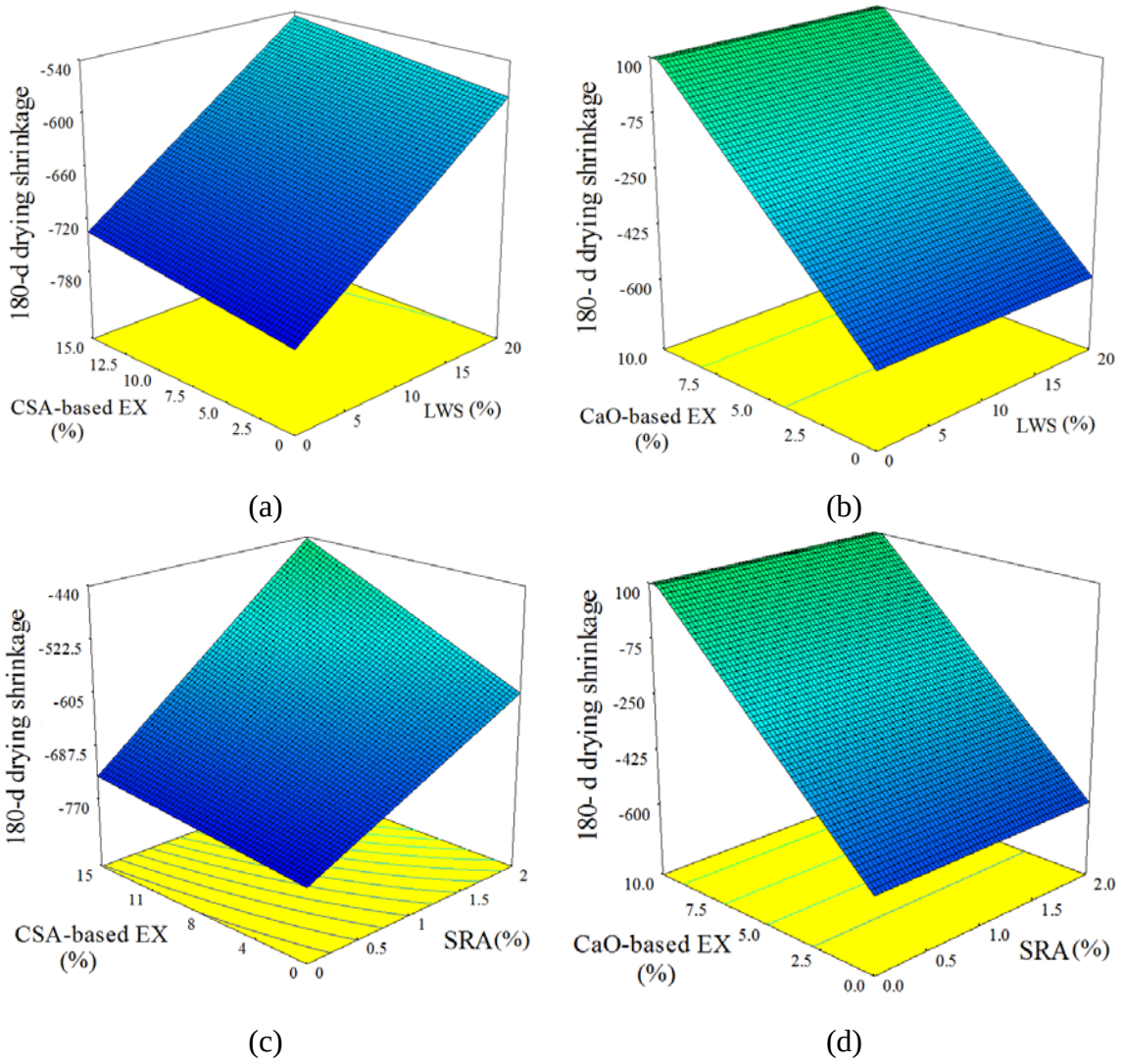

Figure 7-12 Surface responses of 180-day drying shrinkage without any IMCP for (a) CSA-based EX vs. LWS, (b) CaO-based EX vs. LWS, (c) CSA-based EX vs. SRA, and (d) CaO-based EX vs. SRA.

The enhanced hydration rate at later ages for OPC-CSA system containing SRA is due to the delay in drop of internal relative humidity, thus maintaining higher degree of saturation for a longer duration. The reduced water consumption and increased degree of saturation in paste matrix can promote the formation of ettringite in OPC-CSA blend.

This hypothesis is corroborated with XRD pattern data (Figure 7-13), which shows that in the absence of moist curing, the OPC-CSA system containing SRA exhibited larger intensity of ettringite peak as compared to the OPC-CSA system alone.

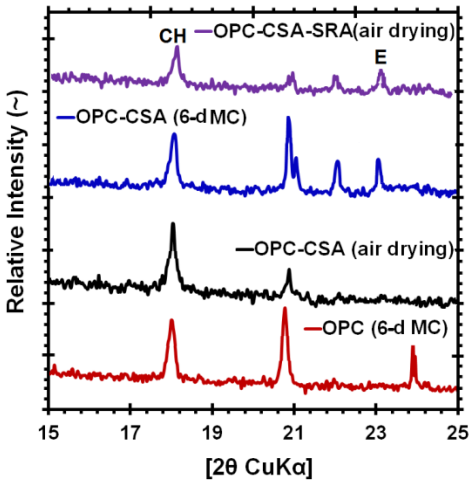

Figure 7-13 Representative XRD patterns at 28 days for the OPC and OPC-CSA systems under different curing conditions. Here, E: ettringite and CH: portlandite.

The intensity of ettringite peak at 28 days for moist cured OPC-CSA system significantly differs from that observed for the similar mixture when no moist curing was adopted. In the absence of moist curing, no significant intensity peak associated with ettringite was identified for the OPC-CSA system. This distinction in XRD pattern features the superior expansion behavior induced by ettringite formation for the moist cured OPC-CSA system compared to the corresponding mixture that had no moist curing. It is also important to point out that in the presence of moist curing, the OPC-CSA system had smaller intensity corresponding to portlandite peak than that of non-moist cured OPC-CSA mixture. The lower residual CH content (i.e., higher CH consumption) in CSA system can be due to the ettringite formation according to the reaction expressed in Eq. (2), which implies that in the process of forming ettringite, the portlandite is consumed and contributes towards a larger formation of ettringite (Collepardi et al. 1972; Kasselouri et al. 1995).

In order to evaluate the effect of wet curing on formation of hydration products, the TGA profiles at 28 days under unsealed condition for mixtures made with EX are depicted in Figure 7-14. All mixtures indicated distinguishable peaks at 130 °C and 450

°C, corresponding to decomposition of C-S-H/ettringite and the dehydroxylation of CH, respectively (Damidot et al., 2011).

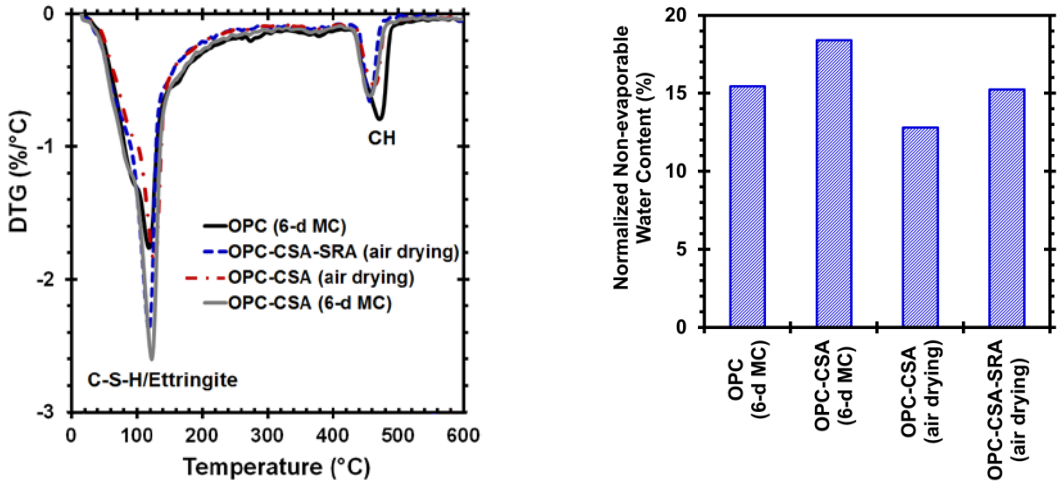

(a) (b)

Figure 7-14 (a) Representative DTG traces at 28 days for the OPC and OPC-CSA systems at different curing conditions and (b) normalized non-evaporable water content at 28 days determined from DTG traces (results are normalized by OPC replacement).

From Figure 7-14, it can be clearly seen that moist-cured mixtures exhibited larger weight loss at 600 °C compared to the similar mixtures without any IMCP, which is due to the higher degree of hydration when IMCP is applied. The incorporation of 15% CSA-based EX was shown to increase the weight loss in the range of the range of 20–200 °C compared to the plain OPC system, potentially suggesting higher amount of ettringite in the presence of CSA-based EX. The weight loss between 20–200 °C was evaluated to be 8.7%, 9.3%, 9.8%, and 12% for 100% OPC (6d IMCP), OPC-15%CSA (No IMCP), OPC-15%CSA-2%SRA (No IMCP), and OPC-15%CSA (6d IMCP), respectively. When subjected to 6 days of IMCP, mixture containing 15% CSA exhibited 30% higher mass loss in the range of 20–200 °C compared to the similar mixture without any IMCP. This reveals that the presence of wet curing promotes the hydration of CSA-OPC system, thus indicating higher formation of C-S-H/ettringite hydration phases. The normalized non-evaporable water content at 28 days for the evaluated systems under different curing conditions is depicted in Figure 7-14(b). The non-evaporable water content is generally considered to be one of the key indicators of hydration reaction progress in cement. The

highest non-evaporable water content was observed for OPC-CSA system subjected to 6 days of moist curing, whereas in the absence of moist curing, this system exhibited the lowest non-evaporable water content. In the absence of moist curing, the OPC-CSA system incorporating SRA exhibited 20% higher normalized water content compared to the similar system devoid of any SRA, confirming the effect of SRA addition on hydration progress of OPC-CSA system.

7.3. COMPARISON BETWEEN CSA- AND CaO-BASED EX SYSTEMS

In order to compare the performance of CSA- and CaO-based EX systems, a multi-objective optimization technique was carried out to determine the optimum combination of EX and IMCP required for a given target properties. This technique involves satisfying the defined properties without compromising any of the requirements (Montgomery, 2005). For the defined target properties, the desirability functions (d_i) are obtained and these functions are simultaneously optimized to determine the best combination. The overall desirability function (D) proposed by Derringer and Suich (1980) is expressed as follows:

$$D = (d_1^{r_1} \times d_2^{r_2} \times d_3^{r_3} \times \ldots \times d_n^{r_n})^{1/\sum r_i} = (\prod_{i=1}^{n} d_i^{r_i})^{1/\sum r_i} \quad 7\text{-}8$$

where n is the number of individual responses in the optimization, and r_i refers to the relative importance of each individual property. The r_i varies from 1 to 5, reflecting the least to most degree of importance, respectively. The d_i ranges between 0 (for a completely undesired response) and 1 (for a fully desired response). The D value close to 1 reflects that the optimal combination of variables is able to secure the targeted properties. Table 7-8 presents an example of target properties used in this investigation to design non-shrinkage mixture. The target values for both autogenous and drying shrinkage were zero, corresponding to complete elimination of shrinkage (i.e., non-shrinkage system). Given the importance of deformation rate, the numerical optimization aimed at minimizing the rate of drying deformation. This parameter for each mixture was calculated as the difference between 180-day drying deformation and deformation at the initiation of drying, normalized by the time required to achieve steady-state deformation. The additional material cost resulting from the incorporation of shrinkage mitigating

materials per unit volume of mixture ($/m^3) was also considered in the multi-objective optimization. The target was set to minimize material cost to secure a balance between performance improvement and material cost. The degree of importance values of 3, 3, and 5 were assigned to the additional material cost, compressive strength and deformation (autogenous and drying deformation and rate of drying deformation), respectively.

Table 7-8 Defined target properties for mix design optimization.

Response	Defined criteria	
	Target	Importance
91-day compressive strength (MPa)	> 50	3
28-day autogenous deformation (μstrain)	> 0	5
180-day drying deformation (μstrain)	> 0	5
Drying deformation rate (μstrain/day)	Minimize	5
Additional material cost ($/m^3)	Minimize	3

Note: Positive and negative values refer to expansion and shrinkage, respectively.

The contour diagrams of overall desirability for target properties are plotted in Figure 7-15. For performance-based requirements indicated in Table 7-8 and in the absence of SRA and LWS, mixtures containing CaO-based EX developed higher desirability function of 0.90 compared to 0.60 for CSA-based EX system. The overall desirability for mixtures containing CSA-based EX is significantly affected by duration of moist curing at which higher desirability values require an increase in the IMCP. The optimum combination for mixture containing CaO-based EX corresponds to 6% EX and 1.5 day of IMCP. However, in the case of CSA-based EX, the highest desirability value of 0.60 corresponds to 15% EX and 6 days of IMCP. Therefore, in the case of limited IMCP, the use of CaO-based EX can be more beneficial at developing low shrinkage concrete. Figure 7-16 shows the trade-off between CSA-based EX and IMCP for mixtures containing 1% SRA. The combination of 1% SRA and 15% CSA-based EX enables the increase in desirability function from 0.60 to 0.80 even with lower IMCP of 4.5 days. Therefore, in the case of limited IMCP, the effectiveness of using CSA-based EX can be significantly improved when SRA is incorporated. This is due to the

combination of lower surface tension of capillary pores, delay the drop in RH, and promoting degree of hydration for CSA-based EX resulting from SRA addition.

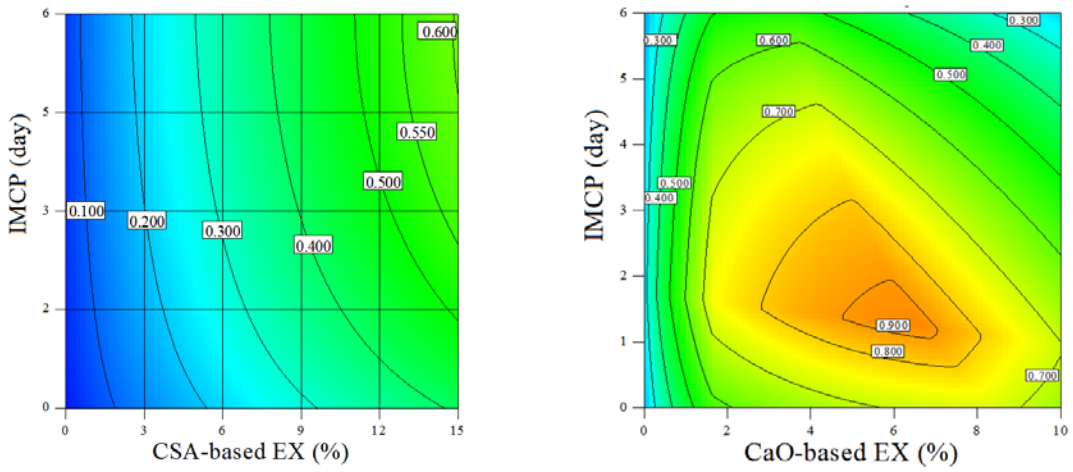

(a) (b)

Figure 7-15 Variations in overall desirability to achieve target properties for (a) OPC-CSA system and (b) OPC-CaO system.

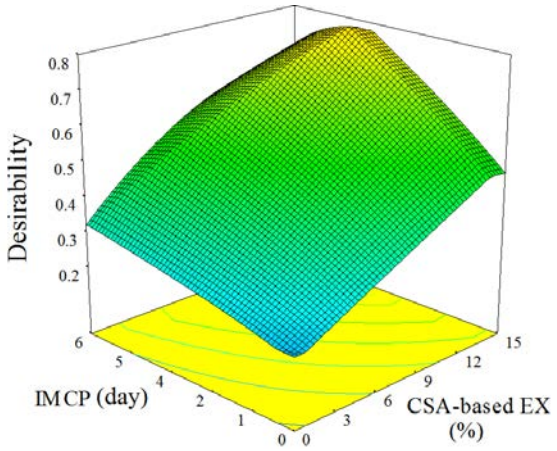

Figure 7-16 Variations in overall desirability for CSA-based EX system to achieve target properties (SRA = 1% and LWS = 0).

7.4. SUMMARY

This study reported test results carried out to evaluate the effect of wet curing and SRA on hydration, internal RH, reaction products, shrinkage, and compressive strength of mortar mixtures containing CSA- and CaO-based EX systems. The investigated wet curing included external wet curing supplied by initial moist curing and internal curing

water provided by LWS. Based on the results presented in this study the following conclusions can be drawn:

- The effect of wet curing supplied by IMCP or LWS on compressive strength is more crucial for mixtures containing EX systems compared to the plain OPC system. In the absence of IMCP, mortar containing 15% CSA-based EX exhibited 40% lower compressive strength at 91 days compared to the similar mixture with 6 days of IMCP. However, this value was about 22% for the control mixture made with 100% OPC.
- In the absence of IMCP, the internal curing provided by LWS is substantially beneficial at elevating the compressive strength of mixture containing EXs. The ITZ between paste matrix and LWS particle was shown to be more dense and homogeneous with lower porosity than that of similar mixture with only EX.
- The effectiveness of using EX to generate expansion and compensate drying shrinkage (under unsealed condition) is highly affected by the IMCP, especially for CSA-based EX due to the relatively large water consumption. In the absence of IMCP, similar drying shrinkage spread was found between control mixture made with 100% OPC and mixture containing 15% CSA-based EX.
- From thermogravimetric analysis, the moist-cured mixture containing 15% CSA-based EX exhibited 30% higher mass loss in the range of 20−200 °C compared to the similar mixture without any IMCP, thus suggesting higher formation of C-S-H/ettringite hydration phases when IMCP is applied.
- The synergistic effect of EX combined with either LWS or SRA resulted in higher early-age expansion and lower shrinkage at later age, especially for CSA-based EX system. In the absence of IMCP, the effectiveness of using CSA-based EX can be significantly improved when SRA is incorporated.
- The incorporation of SRA and LWS can delay the drop in internal RH and facilitate the hydration reaction of EX systems, thus promoting expansion potential induced by EX. The use 15% CSA-based EX in combination with either 2% SRA or 20% LWS led to 6% and 12% higher cumulative heat release after 72 h, respectively, compared to the mixture prepared with only CSA-based EX.

- In the case of inadequate moist curing, the presence of LWS or SRA was found to be effective in enhancing the performance of OPC-CSA system. For a given overall desirability value of 0.65 determined by multi-objective optimization, the incorporation of 1% SRA or 10% LWS was found to reduce the required moist curing duration of the OPC-CSA system from 6 days to 5 and 3 days, respectively.
- For a given moist curing duration and CSA-based EX content, the incorporation of 10% LWS or 1% SRA in OPC-CSA system was found to enhance the overall desirability function (in relation to shrinkage, material cost, and compressive strength) from 0.53 to 0.65 and 0.70, respectively. Therefore, the combined use of either LWS or SRA in OPC-CSA system can reduce the required period of moist curing and enhance the desirability value, thus indicating a greater overall performance.
- Based on the obtained results from statistical analysis, mixtures were ranked using performance ranking analysis. Two shrinkage mitigating strategies with the highest overall performance were selected, as presented in Table 7-9. The performance of selected shrinkage reducing strategies on shrinkage and early-age cracking of concrete mixtures will be discussed in the next sections.

Table 7-9 Selected shrinkage mitigating strategies from statistical analysis.

Shrinkage mitigating strategy	CaO-based EX (%)	LWS (%)	IMCP (day)	28-d Compressive strength (MPa)	7-d Total deformation (μstrain)	180-d Total deformation (μstrain)
1	0	25	3	65.5	(-) 53.5	(-) 125.1
2	7.5	0	3	60.5	(+) 885	(+) 431

8. OPTIMIZATION OF MIXTURE DESIGN PARAMETERS TO DEVELOP ECO AND CRACK-FREE HIGH-PERFORMANCE CONCRETE

In spite of a large body of existing literature demonstrating the benefits of using SCMs on mechanical properties and durability aspects, the underlying correlations of SCMs' properties and the resultant reactions with shrinkage cracking tendency of concrete have not been systematically investigated. A delay in the early-age hydration and rate of strength development of the concrete can lead to lower cracking potential due to the increase in the early-age creep, and consequently higher tensile stress relaxation. A more comprehensive understanding of the correlations between the characteristics of the binder composition, hydration kinetics, shrinkage, and restrained shrinkage cracking is required to design more environmentally friendly concrete with high resistance to shrinkage cracking. The results obtained from binder optimization, aggregated characteristics, and shrinkage mitigating materials were used to design Eco and crack-free HPC mixtures for different construction application. The experimental program presented in this section consists of two phases.

- The first phase was undertaken to elucidate the role of SCMs' compositions on shrinkage and restrained shrinkage cracking of flowable and Eco-concrete proportioned with a low binder content of 315 kg/m^3, containing 50% SCM replacement. A set of experimental observations, including the hydration kinetics (using isothermal induction calorimetry), non-evaporable water and residual CH contents (derived from thermogravimetric analysis) of binders, as well as autogenous and drying shrinkage, mechanical properties development, and capillary water absorption of concrete are evaluated to characterize the effect of SCMs' compositions on shrinkage cracking tendency of concrete. A focus is placed to link the hydration kinetics of binder systems to shrinkage cracking resistance and tensile creep behavior of Eco-concrete. To design Eco-concrete, particle packing density approach was employed to optimize aggregate proportion and achieve maximum packing density of aggregate skeleton.
- The second phase aimed at validating the performance of Eco and crack-free HPC mixtures targeted for different construction applications. A number of parameters affecting concrete characteristics were investigated, including binder type and

content, fiber type, and use of shrinkage mitigating materials. Based on the test results, performance-based specifications required for the design of such concrete mixtures are summarized in Table 8-1.

Table 8-1 Performance-based specifications for Eco-HPC mixtures.

Eco-Pave-Crete (with different workability levels)	
Binder content	320 kg/m^3
Slump (without fibers)	50 ± 25 mm
Slump (with fibers)	100 ± 25 mm
Compressive strength at 56 days	≥ 35MPa
Drying shrinkage after 120 days (7-d moist curing)	≤ 300 μstrain
Restrained shrinkage cracking potential	Low (time-to-cracking > 28days according to ASTM C1581)
Durability (frost and abrasion resistance)	High (durability factor higher than 70% after 300 freeze-thaw cycles according to ASTM C666)
Eco-Bridge-Crete (with different workability levels)	
Binder content	350 kg/m^3
Slump (without fibers)	100 ± 25 mm
Slump (with fibers)	200 ± 25 mm
Compressive strength at 56 days	40 to 50 MPa
Drying shrinkage after 120 days (7-d moist curing)	≤ 300 μstrain
Restrained shrinkage cracking potential	Low (time-to-cracking > 28days according to ASTM C1581)
Durability (frost, corrosion, and abrasion resistance)	High (durability factor higher than 70% after 300 freeze-thaw cycles according to ASTM C666)

8.1. EXPERIMENTAL APPROACH

8.1.1. Materials and Mixture Proportions. The cementitious materials used in this study included Type I/II OPC conforming to ASTM C150 (Annual Book of ASTM Standards n.d.), CFA, FFA, SL, and SF. The chemical compositions of the cementitious materials are presented in Table 8-2. The OPC has an estimated Bogue phase composition (mass fraction) of 61.2% C_3S, 12.3% C_2S, 6.1% C_3A, and 9.2% C_4AF.

The PSDs of the cementitious materials are shown in Figure 8-1. The PSDs were determined using a Microtrac S3500 laser diffraction analyzer on a suspension of ultrasonificated powder particles diluted in isopropanol suspending liquid. The median

particle size diameters (d_{50}) were determined to be 15, 11, 12, 8.5, and 0.4 μm for the OPC, CFA, FFA, SL, and SF, respectively.

Table 8-2 Chemical compositions of cementitious materials (% by mass).

Component (%)	OPC	CFA	FFA	SL	SF
SiO_2	19.32	35.64	51.69	39.32	97.43
Al_2O_3	4.38	23.76	21.13	9.75	0.42
Fe_2O_3	3.15	4.95	15.69	0.81	0.53
CaO	62.53	27.72	7.11	39.58	–
MgO	2.63	4.95	1.15	10.16	–
SO_3	3.31	2.47	2.21	0.06	–
Na_2O eq.	–	–	–	0.32	–
LOI	1.46	0.51	1.02	–	1.72
$CaCO_3$	3.21	–	–	–	–

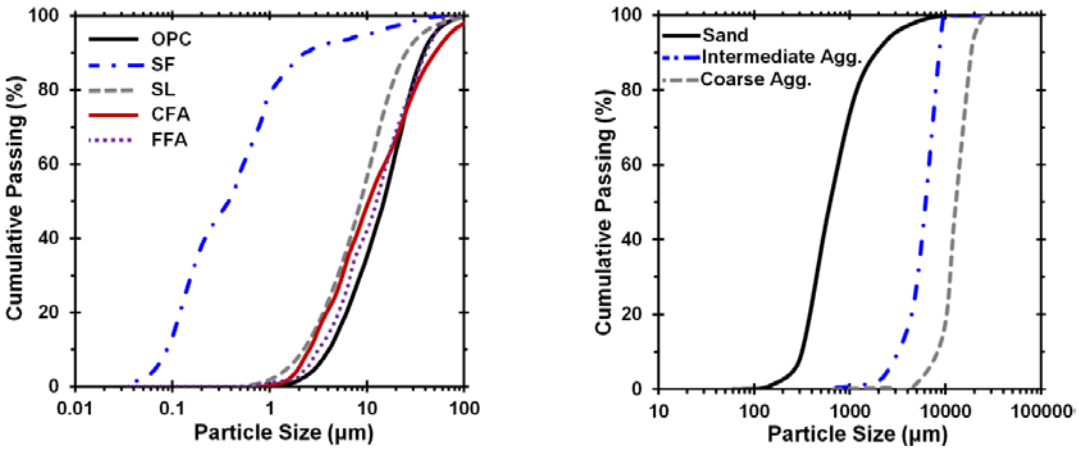

(a) (b)

Figure 8-1 PSDs of (a) cementitious materials and (b) fine and coarse aggregates.

In this study, a ternary aggregate blend of coarse, intermediate, and fine (i.e., sand) aggregates was incorporated to enhance the packing density of the aggregate skeleton. Continuously graded siliceous natural coarse, intermediate, and fine aggregates (see Figure 8-1(b)) with nominal maximum sizes of 19, 9, and 5 mm were used. All aggregates are river based with relatively rounded shape and smooth surface texture. The coarse, intermediate, and fine aggregates have densities of 2450, 2580, 2500 kg/m^3, and water absorption values of 2.0%, 0.8%, 0.6%, respectively.

A polycarboxylate-ether (PCE) with a solid mass content of 23% and a density of 1050 kg/m^3 was used to enhance fluidity. A synthetic-based air-entraining agent (AEA) was incorporated to adjust the fresh air volume. The PCE and AEA dosage rates for the investigated mixtures were adjusted to secure an initial slump flow of 500 ± 20 mm and air volume of 6% ± 1%.

Two types of fibers, including synthetic fibers and steel fibers recycled from waste tires were used, as shown in Figure 8-2. The synthetic fiber (structural fiber) is multi-filament with a length and diameter of 50 mm and 0.67 mm, respectively. It has a specific gravity of 0.92 and tensile strength of 625 MPa. Recycled steel fibers are generally recovered by a shredding process of tires, followed by an electromagnetic procedure aiming at separating steel fibers from the rubber. The fibers obtained are typically characterized by an irregular shape (wavy shape) and variable lengths and thicknesses, as shown in Figure 8-2. The geometry of recovered steel fibers was characterized using statistical distribution of around 100 steel fibers that were randomly selected. The statistical distributions of variation in lengths and thicknesses of recycled steel fibers are presented in Figure 8-3. The fiber thickness and length varied between 0.2–1.6 mm and 5–55 mm, respectively. Based on the results, the majority of steel fibers had lengths varying between 10–30 mm and thicknesses of 0.2–0.4 mm. It should be noted that limited studies have examined the performance of recycled steel fibers in the laboratory scale, and more research is required to evaluate the performance of such fibers for the use in pavement and structural applications in comparison with synthetic fibers or steel fibers (industrial steel fibers).

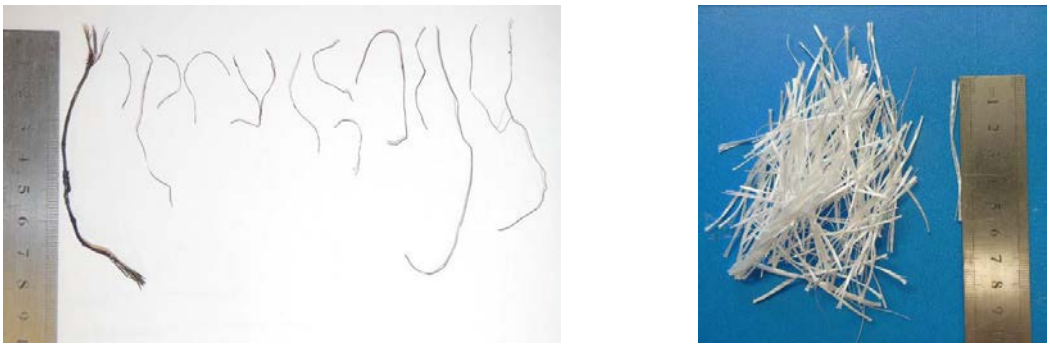

(a) (b)

Figure 8-2 Fiber types used in this study: (a) recycled steel fibers and (b) synthetic fibers.

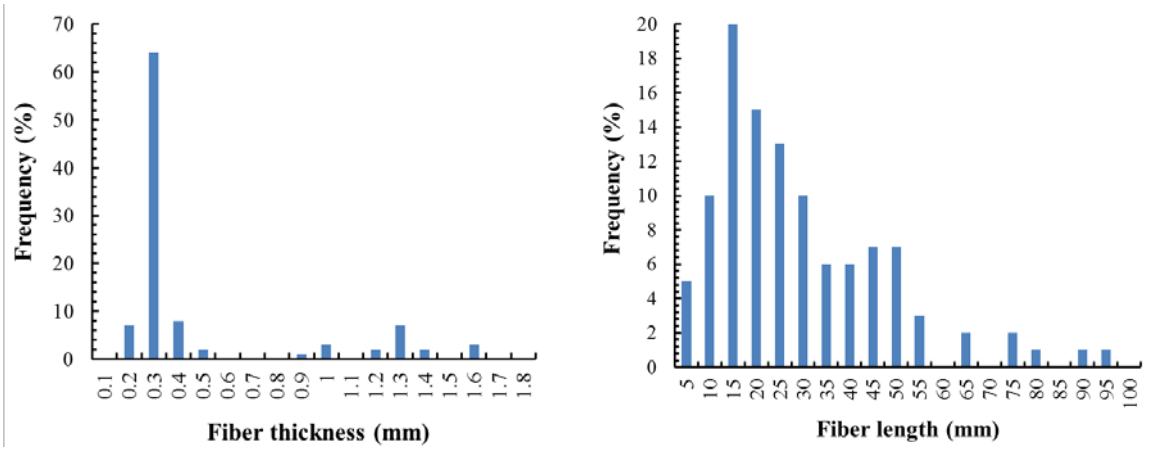

(a) (b)

Figure 8-3 Variation in geometries of recycled steel fibers: (a) fiber thickness and (b) fiber length.

8.1.2. Mixture Proportions. This is discussed below.

8.1.2.1 Phase I. In total, six concrete mixtures were designed with various binary and ternary binders including: (i) the plain OPC (subsequently designated as OPC); (ii) three binary systems with 50% substitution (by mass) of OPC by CFA, FFA, or SL (subsequently designated a CFA50, FFA50, and SL50); and (iii) two ternary systems with 50% OPC replacement with the combinations of CFA with either SF or SL (subsequently designated as CFA45SF5 and CFA30SL20). The contents of SCMs and chemical admixtures are summarized in Table 8-3.

Table 8-3 Mixture proportions of the investigated Eco-concrete mixtures.

Mixture ID	Cementitious materials (kg/m^3)				Chemical admixtures (l/m^3)	
	OPC	FA	SL	SF	PCE	AEA
OPC	315.0	–	–	–	1.25	0.040
CFA50	157.5	157.5 (C)	–	–	0.75	0.045
FFA50	157.5	157.5 (F)	–	–	0.80	0.045
SL50	157.5	–	157.5	–	0.90	0.040
CFA45SF5	157.5	141.7 (F)	–	15.7	0.70	0.05
CFA30SL20	157.5	94.5 (C)	63.0	–	0.80	0.045

The binder content of the Eco-concrete was limited to 315 kg/m^3. The mixtures were proportioned with a fixed water-to-binder ratio (w/b) of 0.40 and a relative volume

fraction of total aggregate of 0.70. The fraction of each phase (i.e., fine, intermediate, and coarse aggregates) was optimized to achieve the maximum packing density, that is discussed in detail later.

8.1.2.2 Phase II. Table 8-4 summarizes the investigated mixture design parameters to optimize the performance of Eco and crack-free HPC. The mixture proportions of the investigated Eco- and crack-free mixtures are presented in Table 8-5. The binder contents varied between 320 and 350 kg/m^3 for pavement and transportation infrastructure applications, respectively. Two reference mixtures were considered including: (i) the plain OPC mixture with binder content of 350 kg/m^3 containing 100% OPC; and (ii) MoDOT reference mixture proportioned with binder content of 375 kg/m^3 with 25% replacement of OPC with Class C FA. The investigated mixture design parameters included four different binder compositions, two types of fibers, and two various shrinkage mitigating materials. Depending on the targeted application, the HRWR dosage was adjusted to secure the slump consistencies varying between 50 mm and 200 mm. The target slump consistencies for Eco-Pave-Crete (binder content of 320 kg/m^3) and Eco-Bridge-Cretes (binder content of 350 kg/m^3) were 50 and 200 mm, respectively. The AEA concentration was also adjusted to ensure the fresh air volume of 6% ± 1% for all mixtures. The w/cm was fixed at 0.4 for all mixtures.

8.1.3. Experimental Procedures. Packing density measurement: In this study, the solid concentrations of the investigated binders were determined using the wet density approach (Wong and Kwan 2008b). The test consists of measuring the wet density of the pastes prepared with various w/b and determining the wet density of the sample. The maximum solid concentration occurs when the binder have achieved its maximum wet density.

For the aggregate phase, the packing density of ternary aggregate blends at different sand-to-total aggregate ratios (S/A) was measured using a gyratory intensive compaction tester (ICT). To compact a sample, the ICT applies the combination of axial pressure and shear stress on sample due to the gyratory inclination. The couple effect of compaction-shear forces enables reorientation of particles, which can lead to more efficient arrangement of solid particles.

Table 8-4 Investigated mixture design parameters.

Codification	Description	Binder content			Binder type					Fiber type and content			Shrinkage mitigating strategy	
		320 (kg/m^3)	350 (kg/m^3)	375 (kg/m^3)	100% OPC	75% OPC +25% FA	60% OPC + 40% FA	45% OPC + 20% SL + 35% FA	35% OPC + 60% SL + 5% SF	TUF strand fiber (0.35%)	STRUX® 90/40 synthetic fiber (0.35%)	Recycled steel fiber from tire (0.35%)	25% LWS	7.5% CaO-based EX
350-OPC	Reference mixture		x		x									
375-FA25	MoDOT reference mixture			x		x								
320-20SL-35FA	Effect of binder type	x						x						
350-20SL-35FA			x					x						
320-40FA		x					x							
350-60SL-5SF			x						x					
350-20SL-35FA-25LWS	Effect of LWS		x					x					x	
320-40FA-25LWS		x					x						x	
350-60SL-5SF-25LWS			x						x				x	
350-20SL-35FA-0.35FT	Effect of fiber type		x					x		x				
350-20SL-35FA-0.35FG			x					x			x			
350-20SL-35FA-0.35FRW			x					x				x		
350-20SL-35FA-7.5EX	Effect of EX		x					x						x
350-20SL-35FA-7.5EX-0.35FT	Combined effect of fiber and EX		x					x		x				x
350-20SL-35FA-7.5EX-0.35FRW			x					x				x		x

OPC: Ordinary Portland cement, SL: Blast furnace slag, CFA: Class C fly ash, and SF: silica fume, EX: expansive agent, LWS: lightweight sand

Codification: 350-20SL-35FA-7.5EX-0.35FRW: Binder content of 350 kg/m^3 containing 20% SL, 35% FA and 7.5% CaO-based EX and 35% recycled steel fibers

Table 8-5 Mixture proportions of the investigated Eco and crack-free HPC mixtures.

Material	350-OPC	320-20SL-35FA	320-40FA	350-60SL-5SF	320-40FA-25LWS	350-20SL-35FA-25LWS	350-60SL-5SF-25LWS	350-20SL-35FA-0.35FT	350-20SL-35FA-0.35FG	350-20SL-35FA-0.35FRW	350-20SL-35FA-7.5EX	350-20SL-35FA-7.5EX-0.35FT	350-20SL-35FA-7.5EX-0.35FRW
Cement (kg/m^3)	350	144	192	158	192	158	158	158	158	158	145	158	158
Fly ash (kg/m^3)	—	97	111	—	111	106	—	106	106	106	98	106	106
Slag (kg/m^3)	—	60	—	192	—	64	192	64	64	64	60	64	64
Silica fume (kg/m^3)	—	—	—	13	—	—	13	—	—	—	—	—	—
Water (kg/m^3)	140	128	128	140	128	140	140	140	140	140	140	140	140
Sand (kg/m^3)	744	761	761	744	570	560	560	744	744	744	560	744	744
Agg. 3/8" (kg/m^3)	465	475	475	465	476	465	465	555	555	650	465	555	650
Agg. 1" (kg/m^3)	650	666	666	650	666	650	650	565	565	480	650	565	480
LWS (kg/m^3)	—	—	—	—	190	186	186	—	—	—	—	—	—
CaO-EX (kg/m^3)	—	—	—	—	—	—	—	—	—	—	23	23	23
Fiber, by volume	—	—	—	—	—	—	—	0.35	0.35	0.35	—	0.35	0.35
	—	—	—	—	—	—	—				—		
HRWR (l/kg^3)	1.12	0.45	0.9	1.05	1.1	1.05	1.25	1.05	1.2	1.2	0.9	1.1	1.4
AEA (ml/kg^3)	28	26	16	17	17	14	17	20	20	14	15	15	15

In this study, the axial overhead pressure applied to compact the aggregate skeleton was set at 20 kPa. The gyratory angle and number of gyrations were fixed at 40 mrad and 160 cycles, respectively. These parameters were obtained after preliminary evaluations to prevent any grinding and/or crushing of aggregates during testing.

In addition to packing density measurements, the effect of binder composition on the compaction-gyration curve was evaluated under dry condition (i.e., dry mixture of all solids including cementitious materials and aggregates) and wet condition (i.e., concrete made with w/b of 0.40 and 0% PCE). A typical compaction-gyration curve can be identified by two distinct parts (see an example in Figure 8-9). The first part is characterized with relatively steep slope wherein air voids among particle are removed due to the arrangement of particles under the initial (i.e., short term) compaction. However, the second part represents a smaller slope due to the rearrangement of particles. The area under the compaction-gyration curve from one to eight gyrations (i.e., first part) is defined as a workability energy index (WEI), which represents the workability/compactibility of mixture. The second part, corresponding to the area between 8 and 160 gyrations, is expressed as a compaction densification index (CDI), which describes the resistance of mixture to segregation upon further compaction effort. The ideal mixture, therefore, is characterized with relatively high WEI and low CDI values (DelRio-Prat et al. 2011; Kappi and Nordenswan 2007; Kevern et al. 2009; Mikanovic et al. 2010). The higher WEI represents the mixture with a higher workability and a lower energy needed to compact sample, and the lower CDI corresponds to the mixture with a higher resistance to segregation and plastic settlement.

Fresh properties: The flowability of Eco-concrete mixtures was characterized by determining the slump flow (ASTM C1611), J-ring (ASTM C1621), and V-funnel flow time. The visual stability index (VSI) and column segregation test were used to examine the stability characteristics of the concrete. The rheological properties of the concrete were determined using the ICAR rheometer with four-blade vane measuring 63.5 mm in radius and 127 mm in height. The testing procedure consisted of pre-shearing the fresh sample at the maximum rotational velocity of 0.6 revolution-per-second (rps) for 30 sec, followed by a step-wise (7 steps of 5 seconds each) decrease of the rotational velocity from 0.6 to 0.03 rps. Attention was paid to identify and eliminate artifacts, such as

thixotropy, plug flow, and segregation (Wallevik et al. 2015). The Reiner–Riwlin transformation (Reiner 1949) was applied on torque-rotational velocity profiles to calculate the dynamic yield stress and plastic viscosity of concrete.

Hydration kinetics: The extents of heat release occurring during hydration of binders were determined using an isothermal conduction calorimetry (Calmetrix I-CAL 8000) operating at a constant temperature of 20 ± 0.1 °C for 7 days. The thermal power and measured energy were used to evaluate the influence of SCM type on hydration kinetics of the binder system.

Thermogravimetric analysis: A Netzsch Simultaneous instrument (Model 429) was used to measure various phases present in binders. The mass loss (TG) and derivative mass loss (DTG) profiles at 28 days were used to quantify the effect of SCMs on non-evaporable water and CH contents present in the system. Powder samples were heated from 20 to 1000 °C in a nitrogen gas flow (to prevent carbonation) at a heating rate of 10 °C/min. The non-evaporable water content was determined as the difference between the mass values at 105 °C and 950 °C, and corrected for the loss on ignition of the cement powder (based on its mass fraction in the paste) and the calcium carbonate content (650–800 °C).

Restrained shrinkage: Instrumented ring test was employed to evaluate the restrained shrinkage cracking tendency and tensile creep behavior of the investigated mixtures in accordance with ASTM C1581(*Annual Book of ASTM Standards* n.d.). The inner rigid steel ring has an internal diameter of 300 mm, a thickness of 12.5 mm, and a height of 150 mm. The concrete ring has height and thickness of 150 and 37.5 mm, respectively. It is important to note that the sample used for the ring test was extracted by sieving fresh concrete to limit the nominal maximum of aggregate to 12.5 mm in compliance with ASTM C1581(*Annual Book of ASTM Standards* n.d.). The test procedure consists of casting concrete in the annular spacing with two concentric rings, and the inner steel ring is instrumented with three electrical strain gauges. The gauges are used to monitor stress development in the steel ring which is induced by restrained shrinkage of concrete. The strain is monitored immediately after casting with subsequent readings taken every 20 min until the concrete shell element begins to crack. Two ring specimens were cast for each mixture. The concrete rings were moist cured for 24 hours

using wet burlap and covered with plastic sheet. The specimens were demolded and moist cured for additional two days before exposure to air drying at 23 ± 1 °C and 50% ± 3% RH. The top surface of the ring specimens was then sealed with adhesive aluminum tape, thus restricting drying to the outer circumferential surface of the concrete ring.

The induced tensile stress in the concrete due to the restrained shrinkage and the tensile creep behavior of concrete can be evaluated by knowing the dimensions of the specimen, moduli of elasticity of the steel ring and concrete, the steel ring strain and free total deformation of the concrete (See et al. 2003, 2004). The shrinkage-induced tensile stress in the concrete after initiation of drying, $\sigma_t(t)$, at time t can be quantified as follows (See et al. 2003, 2004):

$$\sigma_t(t) = G\varepsilon_{st}(t) = G\left[\varepsilon_{sh}(t) - \varepsilon_e(t) - \varepsilon_{cp}(t)\right] \quad 8\text{-}1$$

where $\varepsilon_{st}(t)$ represents the strain in the steel ring at time t after initiation of drying, and $\varepsilon_{sh}(t)$, $\varepsilon_e(t)$ and $\varepsilon_{cp}(t)$ refer to the free total deformation strain, elastic strain, and tensile creep strain, respectively, at time t. G is a constant for the ring setup and is calculated as follows:

$$G = \frac{E_{st} r_{ic} h_{st}}{r_{is} h_c} \quad 8\text{-}2$$

where E_{st} is the modulus of elasticity of the inner steel (200 GPa), h_{st} and h_c are the thicknesses of the steel and concrete rings, respectively. The parameters r_{is} and r_{ic} refer to the inner radii of the steel and concrete, respectively. Knowing the steel ring strain and free total deformation of the concrete, the tensile creep coefficient, $C_r(t)$, of the concrete can be expressed as (See et al. 2003, 2004):

$$C_r(t) = \frac{E_c(t) r_{is} h_c}{E_{st} r_{ic} h_{st}} \left[\frac{\varepsilon_{sh}(t)}{\varepsilon_{st}(t)} - 1\right] - 1 \quad 8\text{-}3$$

where $E_c(t)$ is the modulus of elasticity of the concrete at time t.

Time-dependent volume changes: Prismatic specimens measuring 75 × 75 × 285 mm^3 were used to evaluate the free total deformation according to ASTM C157 (*Annual Book of ASTM Standards* n.d.) using a digital type extensometer. After demolding at 24 hours, specimens underwent similar curing condition to those of the concrete ring specimens to evaluate the tensile creep behavior of Eco-concrete provisioned with

different SCMs. In order to maintain the same volume-to-surface area ratio as that of the concrete ring specimen, 64 mm lengths from the ends of the prismatic specimens were sealed (See et al. 2003). The total deformation of specimens was measured until 200 days, when all length change measurements reached the steady-state condition. Similar to specimens taken for total shrinkage measurement, prismatic specimens were cast and wrapped (i.e., sealed) after demolding (at 24 hours) using a double layer of adhesive aluminum tape to examine autogenous deformation of concrete. The mass measurements of sealed concrete specimens used for autogenous shrinkage confirmed that no mass loss occurred during testing.

Mechanical properties: Cylindrical specimens measuring 100 × 200 mm^2 were cast to determine compressive strength (ASTM C39), modulus of elasticity (ASTM C469), and splitting tensile strength (ASTM C496) at 3, 7, 28, 56, and 91 days. Following demolding at 24 hours, all specimens were stored in lime-saturated solution at 21 ± 2 °C until testing age. Additional cylindrical specimens were taken and subjected to similar curing condition to their corresponding ring specimens. These specimens were tested for modulus of elasticity to determine the tensile creep behavior of concrete. The results of mechanical properties reported herein represent the average of three replicates. Prismatic specimens measuring 75 × 75 × 400 mm were cast to determine the flexural strength and toughness of fiber-reinforced concrete according to ASTM C1609 (Figure 8-4). The toughness of the FRC was calculated from the load-deflection curve under displacement control.

Figure 8-4 Test setup for flexural toughness measurement of FRC beams.

The abrasion resistance of concrete mixtures was evaluated in accordance with ASTM C944, as shown in Figure 8-5. The specimens were moist cured for 56 days before testing. The abrasion test consists of three abrasion cycles at which each cycle lasts two minutes. A double load of 197 N was applied at a rate of 300 rpm using a drill press. After each cycle, mass loss was calculated by subtracting the initial from final mass.

Figure 8-5 Abrasion resistance test setup.

Durability characteristics: Prisms measuring 75 × 75 × 400 mm were prepared to evaluate freeze-thaw resistance of concrete mixtures according to the ASTM C666, procedure A (Freezing and thawing in water). Given pozzolanic reactivity of SCMs, concrete made with a high replacement rate of SCMs requires higher curing time compared to concrete made with 100% OPC. In general, the use of longer period of moist curing for concrete containing high volume of SCMs can result in a denser microstructure and lower capillary porosity compared to the similar mixture subjected to lower moist curing period. Therefore, the specimens were moist cured for 56 days before freeze-thaw testing. Specimens were subjected to 300 freeze-thaw cycles, and after every 36 cycles, the mass loss and transverse frequency of concrete specimens were monitored. The ultrasonic pulse velocity test was used to determine the dynamic modulus of elasticity of the specimens. Figure 8-6 shows the freeze-thaw chamber and ultrasonic pulse velocity instrument.

The de-icing salt scaling was determined in accordance with ASTM C672. Slabs had a minimum surface area of 0.045 m^2 and 75 mm in depth. A dike was placed on the finished surface of the specimen. This dike was used for ponding the surface of the

specimen with a solution of calcium chloride with a concentration of 4.0%. The specimens were subjected to 50 cycles of freezing and thawing. The top surface of the slab was washed, and the damage was qualitatively assessed after every five cycles. In this procedure, the surfaces of samples were rated based on a scale of 0 to 5, corresponding to no scaling to severe scaling, respectively. The mass of scaling residue of the tested mixtures was also measured.

Figure 8-6 Freeze-thaw chamber (left) and ultrasonic velocity instrument (right).

The electrical resistivity measurement was used to classify the concrete according to the corrosion rate. The measurement of electrical resistivity was determined using two different methods; direct two-electrode method (ASTM C1760) and the four-point Wenner probe method (AASHTO TP 95-11), corresponding to bulk electrical conductivity and surface resistivity, respectively (Figure 8-7). The electrical resistivity was measured using cylindrical samples measuring 100 mm in diameter and 200 mm in height and cured in saturated lime water until the age of testing. The electrical resistivity is calculated as follows:

$$\rho = R \times k \tag{8-4}$$

where ρ is the resistivity, and R and k refer to measured resistance and geometry correction factor, respectively. The geometry correction factor for surface resistivity and bulk electrical conductivity can be calculated as:

$$k\,(surface\ resistivity) = \frac{2\pi a}{1.1 - \frac{0.73}{d/a} + \frac{7.82}{(d/a)^2}} \tag{8-5}$$

$$k\,(bulk\ electrical\ conductivity) = \frac{A}{L} \qquad 8\text{-}6$$

where d, A, a, and L refer to diameter, cross section area, probe spacing, and length of the specimen, respectively.

Figure 8-7 Bulk electrical conductivity (left) and surface resistivity (right).

Capillary water absorption: In order to evaluate water transport properties, capillary water absorption was evaluated in accordance with ASTM C1585 (*Annual Book of ASTM Standards* n.d.). This test was conducted on disc samples measuring 100 mm in diameter and 50 mm in height. After 28 days of moist curing, the specimens were placed in the environmental chamber at 50 ± 1 °C and 80% ± 3% RH for three days. Subsequently, specimens were placed inside a sealable container and stored at 23 ± 2 °C for at least 15 days until their mass reached equilibrium. The bottom surface of the samples placed in contact with water to a depth between 1-3 mm.

The mass change due to capillary draw was recorded. The amount of absorbed water is normalized by the cross-section area of the sample exposed to the water, which is calculated as follows:

$$I = \frac{m_t}{a \times d} \qquad 8\text{-}7$$

where I is the capillary absorption (mm^3/mm^2), m_t is the sample mass at time t (g), a is the exposed surface area of the sample (mm^2), and d is the density of water (g/mm^3).

8.2. RESULTS AND DISCUSSION

8.2.1. Phase I: Elucidating the Role of Supplementary Cementitious Materials on Shrinkage and Restrained Shrinkage Cracking of Flowable Eco-Concrete.

8.2.1.1 Particle packing of granular skeleton. The packing density diagram in Figure 8-8 shows the variations in packing density of aggregate skeleton for different aggregate proportions. The packing density of blended aggregate was shown to vary from 0.60 to 0.81. The highest packing density was achieved when incorporating ternary aggregate blend of sand, intermediate, and coarse aggregates. There exists a threshold value of S/A beyond which the packing density drops with further addition of sand content (i.e., higher S/A). This is due to the loosening and wall effects when excessive sand is present in the solid skeleton. The highest packing density for binary blend of sand and coarse aggregate was determined to be 0.79. However, when intermediate aggregate was incorporated in addition to sand and coarse aggregate, the packing density of the aggregate combination improved from 0.79 to 0.81. Based on these results, the optimal aggregate blend corresponds to 42% sand, 20% intermediate aggregate, and 38% coarse aggregate (by volume), that achieved a packing density of 0.81. This aggregate combination was selected to proportion Eco-concrete mixtures investigated in this study.

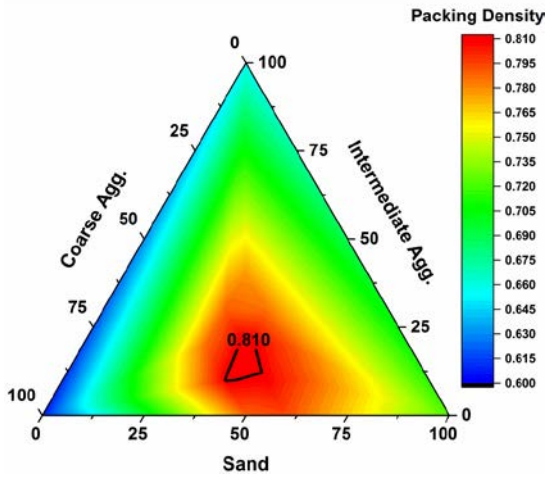

Figure 8-8 Variations in packing density of aggregate skeleton determined by the gyratory ICT.

In order to evaluate the effect of binder composition on packing density of all solids, including cementitious materials and optimized aggregate blend, compaction behavior of mixtures was investigated using the gyratory ICT. A representative example of the compaction-gyration curve for two different mixtures under both dry and wet conditions is shown in Figure 8-9.

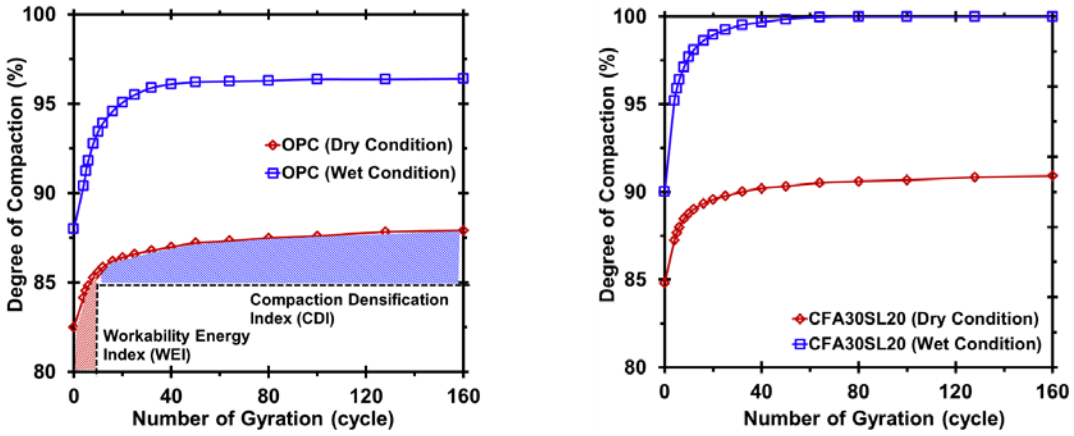

(a) (b)

Figure 8-9 Compaction-gyration curves under dry and wet conditions for the: (a) plain OPC mixture and (b) CFA30SL20 mixture. Dry condition refers to dry mixture composed of all aggregates and cementitious materials, while wet condition represents concrete made with 0.40 w/b and 0% PCE.

As Expected, the incorporation of cementitious materials in combination with aggregate enhances the packing density of the solid skeleton, especially under wet condition. The enhanced packing density is more evident when SCM is incorporated as a partial OPC replacement. For example, the CFA30SL20 mixture exhibited 3.5% and 4.5% higher packing densities under dry and wet conditions, respectively, compared to the plain OPC mixture. This is attributed to the synergistic effect between OPC and SCM to enhance the packing density of the solid skeleton. This effect is highlighted in Figure 8-10(a), which shows the correlation between solid concentration of binders and packing density of all granular materials. A good linear fit shown in Figure 8-10(a) confirms the effect of binder type on packing density of all solids. All blended binders developed higher solid concentration values than that of the plain OPC (see Table 8-6). The enhanced solid concentration due to the SCM replacement becomes more dominant for

the ternary blend of CFA with SF. The CFA45SF5 binder with the highest solid concentration was noted to develop the largest packing density of solids. This is attributable to both filling (since they have finer SSA) and shape features (e.g., spherical shape and smooth surface texture) of SCMs which can effectively fill the voids among cement grains and produce more efficient arrangement of solid particles. The effect of SCM replacement on WEI and CDI (extracted from compaction-gyration curve) of solid skeleton under dry and wet conditions is depicted in Figure 8-10(b) and (c).

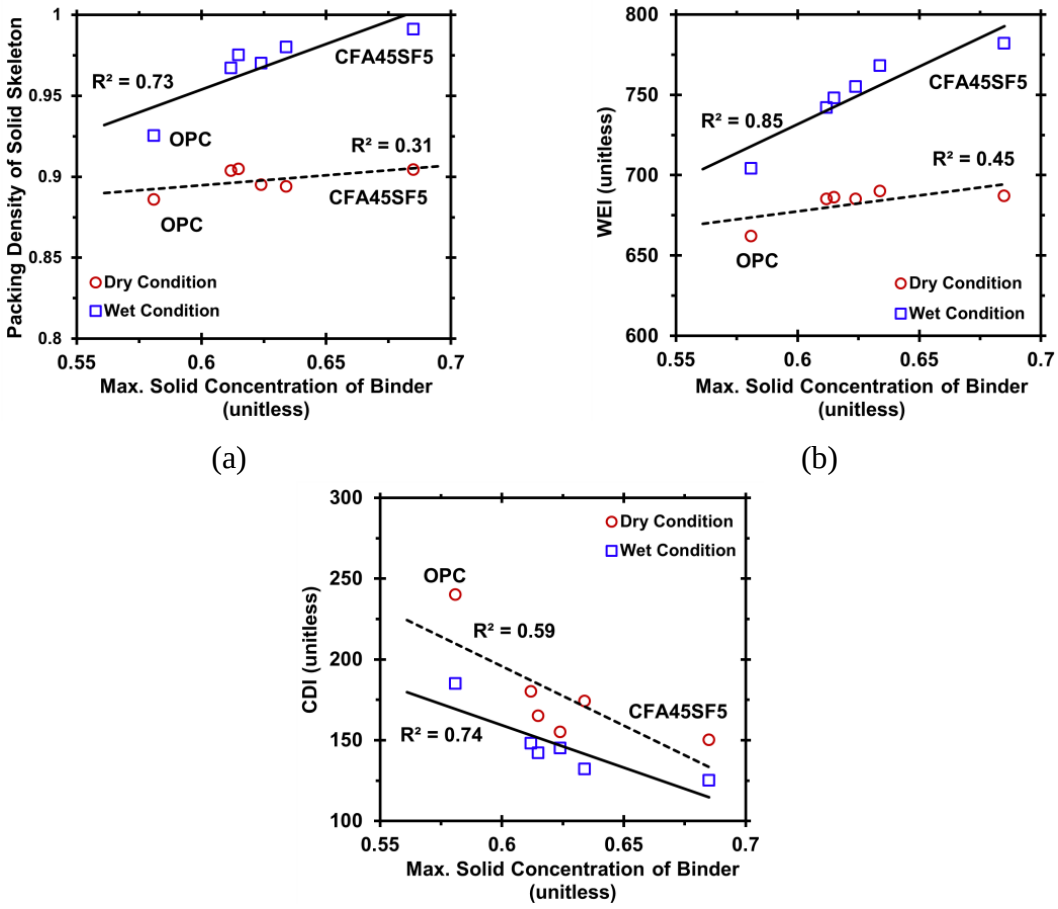

Figure 8-10 Effect of solid concentration of binder on (a) packing density of solid skeleton, (b) WEI, and (c) CDI determined from gyratory ICT. Dry condition refers to dry mixture composed of all aggregates and cementitious materials, while wet condition represents concrete made with 0.40 w/b and 0% PCE.

All mixtures containing SCMs developed higher WEI and lower CDI values in comparison with the plain OPC system. This is an important implication of SCMs, as it

suggests that mixture incorporating SCM: (i) has more workability and needs a little energy to be consolidated; and (ii) has higher resistance to segregation. It is important note that the enhancement of packing density of granular skeleton can increase the lattice effect (Esmaeilkhanian et al. 2017a), which can improve the resistance of suspension to segregation, when maintained at rest or subjected to additional consolidation energy.

Having determined the volumetric proportions of aggregates (i.e., sand, intermediate, coarse aggregates), the amounts of PCE and AEA concentrations for the Eco-concrete mixtures were adjusted to achieve the target flow spread (500 ± 20 mm) and air volume (6% ± 1%) for the investigated concrete mixtures in Phase I. Table 8-6 summarizes the fresh characteristics of the investigated mixtures. Regardless of the binder type, all mixtures exhibited satisfactory passing ability and stability characteristics with no evidence of bleeding and aggregate segregation.

Compared to the plain OPC concrete, Eco-concrete mixtures containing SCMs were found to have higher resistance to aggregate segregation as identified by the column segregation test. This is attributed to the higher solid concentration (i.e., less inter-particle spacing) of binder prepared with SCMs which can enhance the packing density of solid skeleton. This observation is consistent with the CDI data shown in Figure 8-10(c).

In spite of having the same initial yield stress, the plastic viscosity of Eco-concrete was found to vary with the binder composition. The highest plastic viscosity was observed for concrete containing 50% SL. This is attributed to the higher SSA and more importantly, angular geometry of SL particles in the binder. The angular geometry of the particles enhances the inter-particle friction among the particles. To further elaborate on the importance of particle geometry, the rheological properties in the CFA45SF5 mixture can be highlighted. In spite of having the highest SSA, this concrete had the lowest plastic viscosity due to the ball-bearing feature associated with spherical shape and smooth surface texture of both SF and FA particles.

Table 8-6 Fresh characteristics of the evaluated Eco-concrete mixtures.

Properties	Mixture ID					
	OPC	CFA50	FFA50	SL50	CFA45SF5	CFA30SL20
Solid concentration of binder	0.581	0.621	0.610	0.622	0.685	0.632
Yield stress (Pa)	113	107	109	118	104	110
Plastic viscosity (Pa.s)	36	26	27	48	22	31
Slump flow (mm)	510	515	500	510	520	510
Fresh air volume (%)	5.5	6.0	5.5	6.5	5.5	6.0
VSI	0	0	0	0	0	0
J-ring spread (mm)	450	485	475	465	495	480
V-funnel flow time (sec)	8.4	6.9	7.3	9.8	6.4	7.8
Column segregation (%)	7.1	3.5	3.2	1.2	2.6	2.1

8.2.1.2 Mechanical properties evolution. Figure 8-11 shows the development of mechanical properties for the investigated mixtures. The 3- and 91-day compressive strength results were 13–26 and 50–59 MPa, respectively. As expected, all Eco-concrete mixtures containing SCMs exhibited lower early-age compressive strength than the plain OPC mixture due to the dilution effect of cement replacement (i.e., higher initial effective water content).

All mixtures provisioned with SCMs developed greater rate of strength gain as identified with larger slope of strength-time relationship, ultimately developing 91-day strengths that are equivalent or even higher than mixture made without any SCM. The higher rate of strength development of concrete provisioned with SCM is primarily attributed to the later-age pozzolanic reaction between the SCM and CH. This leads to the formation of space-filling pozzolanic C-S-H gel, which counteracts the dilution effect of cement replacement. Although the reduction in early-age strength is more noticeable for the mixture containing 50% FFA due to its relatively high pozzolanic feature, this mixture developed superior strength gain over other SCMs in use. The highest strength at early- and later-age was observed for the ternary binder containing 45% CFA and 5% SF. This mixture had 3-day strength equivalent to the plain OPC mixture, and manifested 12% larger strength at 91 days**.**

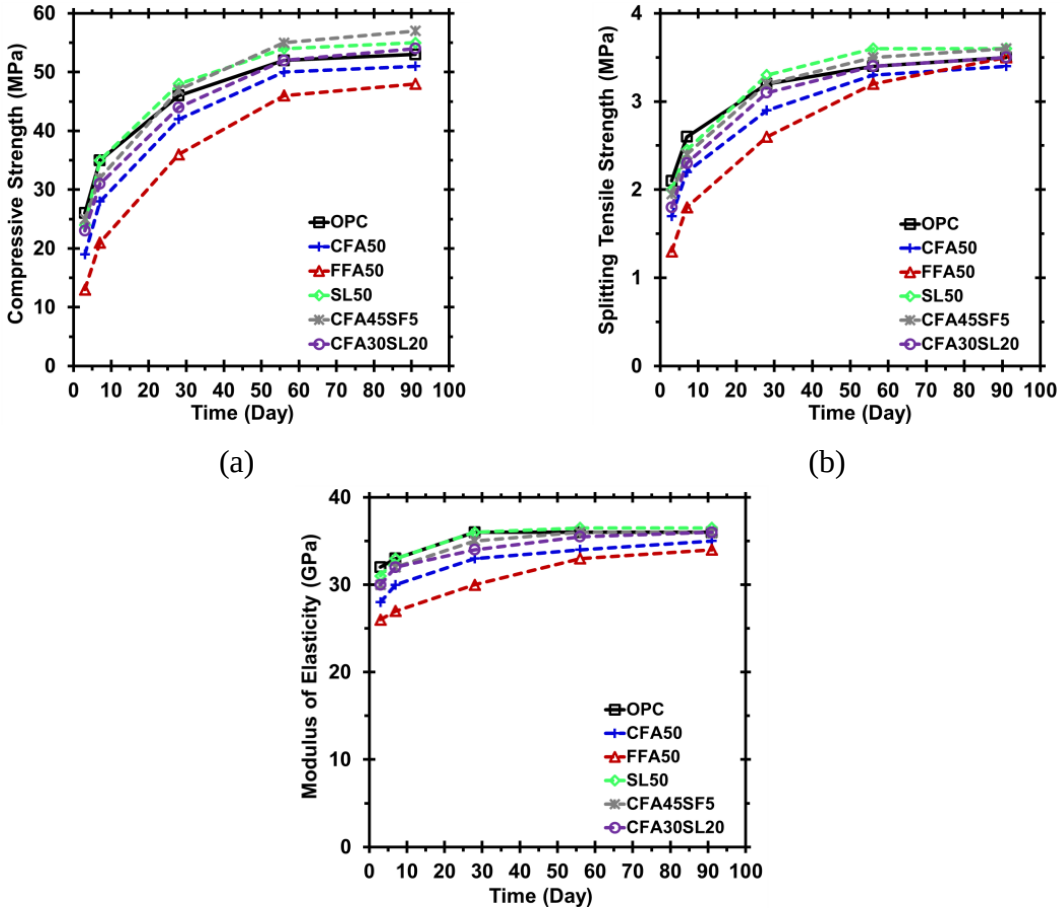

Figure 8-11 Hardened properties as a function of specimen age for the OPC and OPC-CSA systems under different curing conditions: (a) compressive strength development, (b) UPV development, and (c) correlation between strength and UPV evolution of the investigated systems.

When binary blends of FFA, CFA, or SL are compared, mixture incorporating SL developed consistently higher compressive strength. This is attributed to both chemical and physical features of SL. The TGA results in Figure 8-12 indicates that SL has higher pozzolanic activity than FA, as evidenced by the smaller amount of residual CH content and larger non-evaporable water content. In addition to the chemical effect, the rapid strength gain in SL compared to the FA can be due to the higher SSA of SL. This feature decreases the inter-particle spacing and ensures faster dissolution and larger extent of reaction, thus enabling relatively larger formation of pozzolanic C-S-H gel.

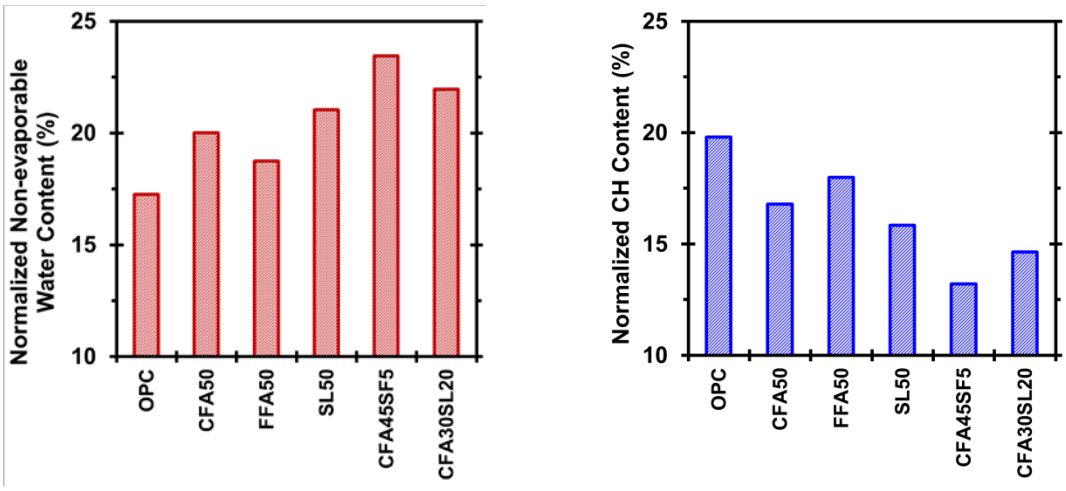

(a) (b)

Figure 8-12 Effect of binder composition on: (a) normalized non-evaporable water content and (b) normalized CH content at 28 days calculated from DTG profiles. Results were normalized by OPC fraction in each mixture to account for dilution effect.

For the same SCM replacement level, the ternary binder prepared with 30% CFA and 20% SL developed 21% and 10% greater 3- and 91-day compressive strengths as compared to the binary mixture containing CFA. Further, such ternary mixture exhibited similar later-age strength to the control OPC mixture. This suggests that the synergistic effect between CFA and SL results in improved properties at early age, while securing later-age properties equivalent to the plain OPC mixture. This synergistic effect can be evidenced with the TGA data shown in Figure 8-12, which indicates higher non-evaporable water content and smaller amount of residual portlandite for the ternary binder of SL and CFA compared to the binary blends of CFA or SL. As a result, it is expected that larger amount of pozzolanic C-S-H gel forms which can improve the solid-to-solid connectivity, thus enhancing strength. As shown in Figure 8-11 the trends observed for splitting tensile strength and modulus of elasticity of Eco-concrete made with various binder types are similar to those obtained for compressive strength results.

8.2.1.3 Shrinkage. The autogenous deformation from the time of demolding and total deformation from the time of drying initiation for the investigated mixtures are shown in Figure 8-13. As expected, the rate and magnitude of deformation are significantly influenced by the binder composition in use. From Figure 8-13(a), it can be noticed that the OPC mixture exhibited faster autogenous deformation followed by a

plateau in shrinkage after 25 days. However, all mixtures containing SCM reached the steady-state shrinkage after 60 days compared to 25 days for the plain OPC mixture. This implies that the incorporation of SCMs slows down the progressive rate of shrinkage, thus extending the time corresponding to the steady-state shrinkage. The slower rate of autogenous deformation observed for mixtures incorporating SCMs is due to the delay in early-age hydration kinetics and the dilution effect of cement replacement, which can provide initially higher free water and reduce the degree of self-desiccation at early-age (Bouasker et al. 2014; Termkhajornkit et al. 2005).

In spite of having slower deformation rate, all Eco-concrete mixtures containing SCMs underwent ultimately larger extent of autogenous deformation as compared to the plain OPC mixture. This can be attributed to: (i) pozzolanic reaction of SCMs and formation of space-filling pozzolanic C-S-H gel which result in the refinement of pore structure (i.e., smaller pore size); and (ii) larger extent of hydration kinetics due to the pozzolanic reaction which can lead to higher consumption of free water (and transformation to chemically bound water) at later age as the hydration progresses.

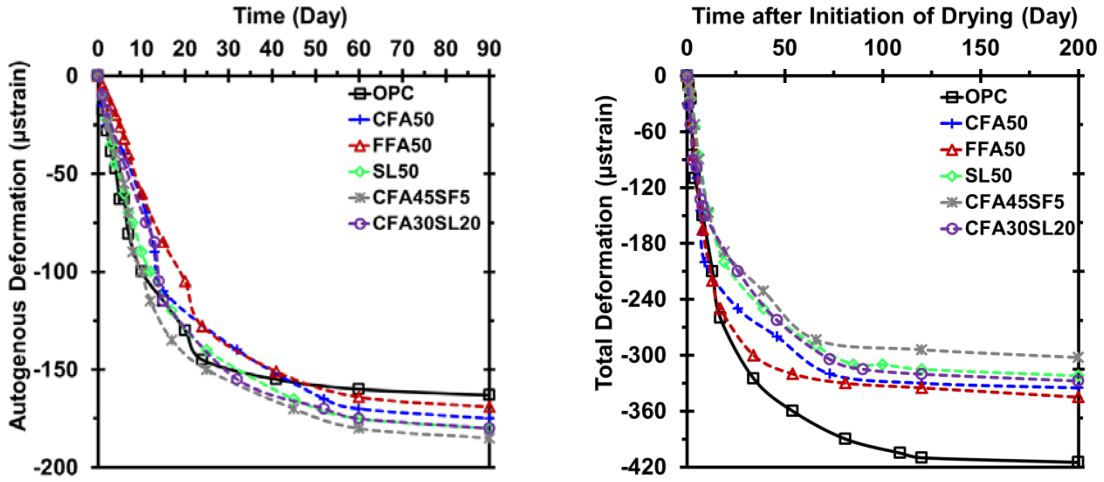

(a) (b)

Figure 8-13 Deformation profiles of investigated Eco-concrete mixtures: (a) autogenous deformation from the time of demolding and (b) total deformation from the time after initiation of drying (after 3 days of moist curing).

These hypotheses are corroborated by the capillary water absorption and isothermal calorimetry results indicated in Figure 8-14. The capillary water absorption

profiles confirm that the incorporation of SCMs (especially SF) leads to lower capillary absorption due to the lower porosity and denser microstructure. As capillary pore pressure increases with decreasing pore size, the degree of self-desiccation is expected to increase, thus resulting in higher autogenous deformation at later ages (Wittmann 1976). Further, the cumulative heat release profiles normalized per gram of cement (i.e., clinker fraction) in Figure 8-14(b) show that all SCM containing mixtures developed greater cumulative heat release at 168 h compared to the corresponding mixture without any SCMs. The enhanced kinetics of SCMs' reaction is due to a combination of the physical (i.e., filler effect) and chemical (pozzolanic reaction) effects. In the context of the physical effect, the SCMs are able to act as fillers which tend to enhance cumulative heat release. The enhanced hydration kinetics induced by SCMs leads to a higher non-evaporable water content, as evidenced by the TGA data in Figure 8-12(a). These results are in agreement with previous studies (Bouasker et al. 2014; Lee et al. 2006; Lim and Wee 2000; Termkhajornkit et al. 2005), which noted that the incorporation of SCM such as SL or FA increases the later-age autogenous shrinkage.

As indicated in Figure 8-13(b), the OPC mixture experienced consistently higher total deformation than those observed for mixtures containing SCMs. As evidenced by capillary absorption profiles in Figure 8-14(a), the OPC mixture exhibited the highest capillary water absorption, implying higher porosity. The synergistic effect of using CFA in conjunction with SF resulted in the lowest total deformation. In contrast to the total deformation, this mixture experienced the highest autogenous deformation at 90 days. This distinction in performance is attributed to the superior pozzolanic reaction and lower capillary porosity observed for this binder, as demonstrated in Figure 8-14. Although the finer porosity and larger consumption of free water due to the pozzolanic reaction can reduce the water evaporation due to the drying, such features can promote the capillary pressure, thus leading to a larger autogenous deformation. Therefore, the hydration kinetics induced by SCMs has an important effect on autogenous and drying shrinkage.

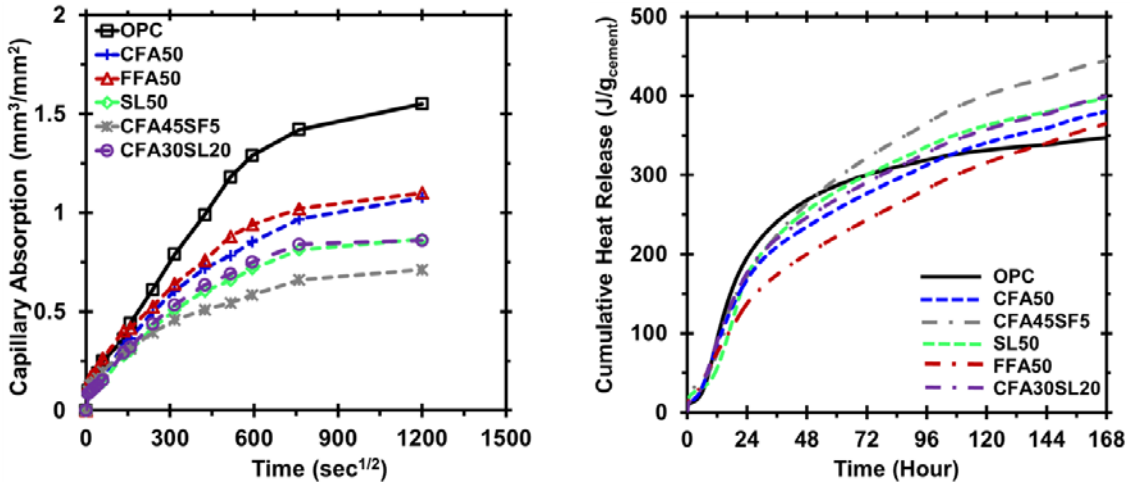

(a) (b)

Figure 8-14 Effect of binder composition on: (a) capillary water absorption and (b) cumulative heat release of investigated Eco-concrete mixtures.

8.2.1.4 Shrinkage-induced cracking. Restrained shrinkage and tensile creep (deduced from Eq. (4)) profiles of the investigated mixtures are plotted in Figure 8-15. Due to its higher total deformation, larger early-age mechanical properties, and lower tensile creep coefficient, the OPC mixture exhibited the lowest resistance to shrinkage cracking. The SCM containing mixtures exhibited 5% to 60% longer elapsed time to cracking and developed 2.4 to 4.4 times larger tensile creep coefficient at the time of crack initiation. This can be attributed to the: (i) delay in early-age hydration reaction; (ii) lower total deformation; and (iii) slower rate of elastic properties development (i.e., stiffness) at early-age.

The combination of the aforementioned effects is reflected by developing larger tensile creep behavior for mixtures containing SCMs, as shown in Figure 8-15(c). The enhanced tensile creep coefficient leads to higher capacity of stress relaxation in mixture. The reduced elastic properties and enhanced tensile stress relaxation in SCM mixtures resulted in lower rate of shrinkage-induced tensile stress evolution, as indicated by the smaller slope of induced tensile stress-time profiles in Figure 8-15(b). Despite higher autogenous deformation at the time of steady-state (i.e., after 60 days), all mixture provisioned with SCMs had lower autogenous deformation for the initial 30 days as compared to the OPC mixture. This implies that mixtures containing SCMs had

simultaneously lower autogenous and total deformations during the time before crack initiation than plain OPC mixture.

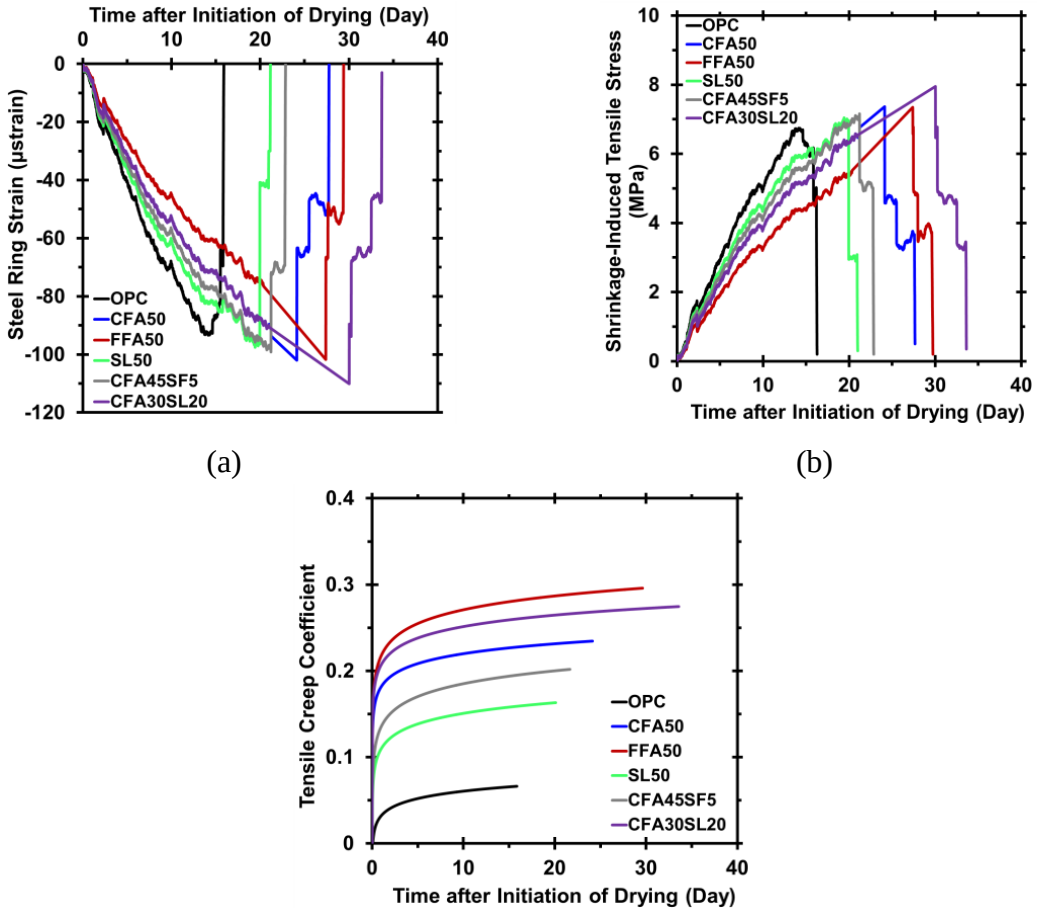

Figure 8-15 Restrained shrinkage cracking tendency of investigated Eco-concrete mixtures from the time after initiation of drying: (a) steel ring strain profiles, (b) induced tensile stress profiles, and (c) tensile creep coefficient profiles as a function of time.

The longest time to shrinkage cracking was noticed for the binary system of 50% FFA and ternary system of 30% CFA combined with 20% SL. The FFA50 and CFA30SL20 mixtures underwent 4.4 and 4 times, respectively, higher tensile creep coefficient at the time of crack initiation than that of the plain OPC mixture. Considering the fly ash type, the FFA50 mixture developed longer time to crack initiation and larger extent of tensile creep coefficient than the CFA50 mixture. This can be due to the slower hydration kinetics and elastic properties evolution, and hence larger tensile stress

relaxation in the former mixture. The synergistic effect provided by the ternary combination of 30% CFA and 20% SL developed considerably higher shrinkage cracking resistance compared to the binary 50% CFA or (more especially) 50% SL mixtures. This ternary mixture had 17% and 70% larger extents of tensile creep coefficient at the time of crack initiation compared to the CFA50 and SL50 mixtures, respectively.

Upon comparison between the CFA50 and CFA45SF5 mixtures, the addition of SF was found to reduce the resistance of mixture to shrinkage cracking and decrease the tensile creep behavior. This is due to the enhanced hydration kinetics and faster development of mechanical properties which can reduce the capacity of tensile stress relaxation.

It is important to note that the shrinkage-induced cracking in system containing SF is influenced by two simultaneous competing effects. First, the addition of SF tends to significantly reduce the total deformation, the CFA45SF5 mixture exhibited the lowest total deformation. This effect can be offset by the second action, which is noticeable enhancement in hydration kinetics and elastic properties evolution, thus reducing the capacity of tensile stress relaxation. The lower shrinkage cracking resistance observed in the CFA45SF5 mixture suggests that the second effect becomes more predominant.

The aforementioned discussion highlights that the hydration kinetics of the binder system is an important factor in controlling the shrinkage-induced cracking of concrete. In order to better understand the correlation between the composition-reaction-properties of mixtures containing various SCMs, a focus was placed to correlate the hydration kinetics to shrinkage cracking potential. Several studies have shown the existence of linear correlation between strength evolution and hydration heat release for mixtures containing various binder systems (Bentz et al. 2012a; Kumar et al. 2013b; a; Lothenbach et al. 2008b; Mehdipour et al. 2017b).

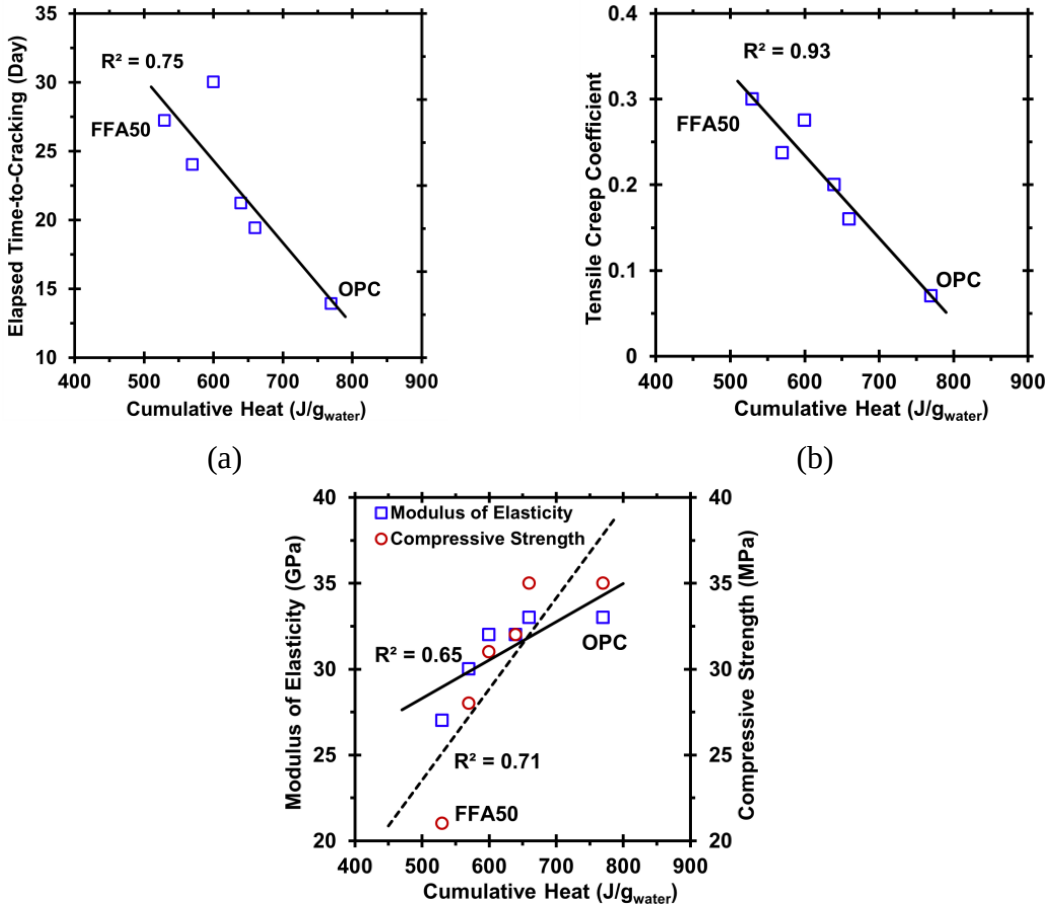

Figure 8-16 Correlation between 7-day cumulative heat release and various hardened concrete responses: (a) elapsed time to shrinkage cracking, (b) tensile creep coefficient at the time of crack initiation, and (c) modulus of elasticity at 7 days. In (c), the secondary Y-axis represents the 7-day compressive strengths for the investigated mixtures. Note that cumulative heat release results of binders were normalized by initial water content.

To further examine the implication of composition-reaction-property correlations, the results of elapsed time to shrinkage cracking and tensile creep coefficient at the time of crack initiation are plotted against cumulative heat release through hydration reaction in Figure 8-16. The cumulative heat release at 7 days was normalized by the water content of each mixture, since water content serves as a measure of the initial porosity that needs to be filled by hydration products for the microstructural evolution.

As can be seen, similar to those observed for strength and elastic properties, a good linear correlation can be established between cumulative heat release, time to shrinkage cracking, and tensile creep coefficient for the investigated mixtures. This linear

correlation reflects that mixtures with higher early-age reactivity are expected to have lower tensile creep behavior, and hence less resistance to shrinkage-induced cracking. This is due to the larger development rate of elastic properties in system with higher extent of heat release, which can increase the rate of shrinkage-induced tensile stress, thus increasing the risk of shrinkage cracking.

Therefore, the development of such composition-reaction-property correlations can be applied to estimate the restrained shrinkage cracking potential of cementing systems containing SCMs by using the experimentally measured hydration reaction that dictates the properties evolution.

8.2.2. Phase II: Performance Evaluation of Eco and Crack-Free HPC. The results of HRWR demand and slump consistency of the investigated HPC mixtures are shown in Figure 8-17. For a given slump consistency, HPC mixtures prepared with binary and ternary of SCMs required lower HRWRA demand to achieve required slump consistency compared to the control mixture made with 100% cement. This can be due to the lower water demand and higher packing density of SCMs binders.

All mixtures exhibited no surface bleeding which is usually measured by collecting the excess surface solution as a function of time after placement (ASTM C232). As expected, mixtures containing fibers exhibited higher HRWR demand compared to similar mixtures made without any fibers.

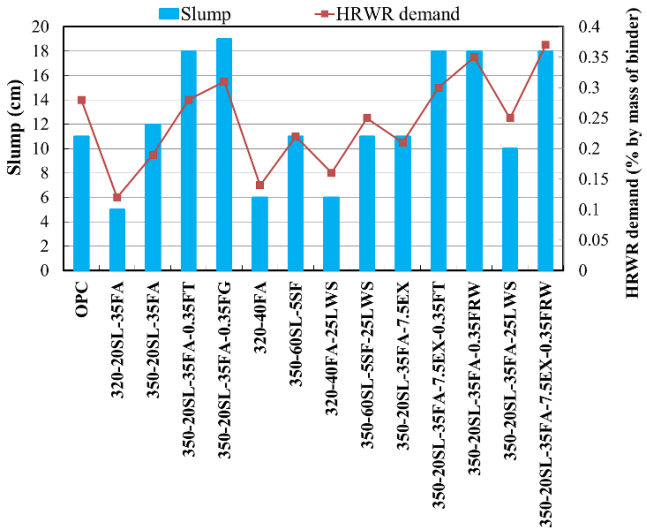

Figure 8-17 Slump consistency and HRWR demand of HPC mixtures.

8.2.2.1 Mechanical properties. The results of mechanical properties development of the investigated concrete mixtures are compared in Figure 8-18.

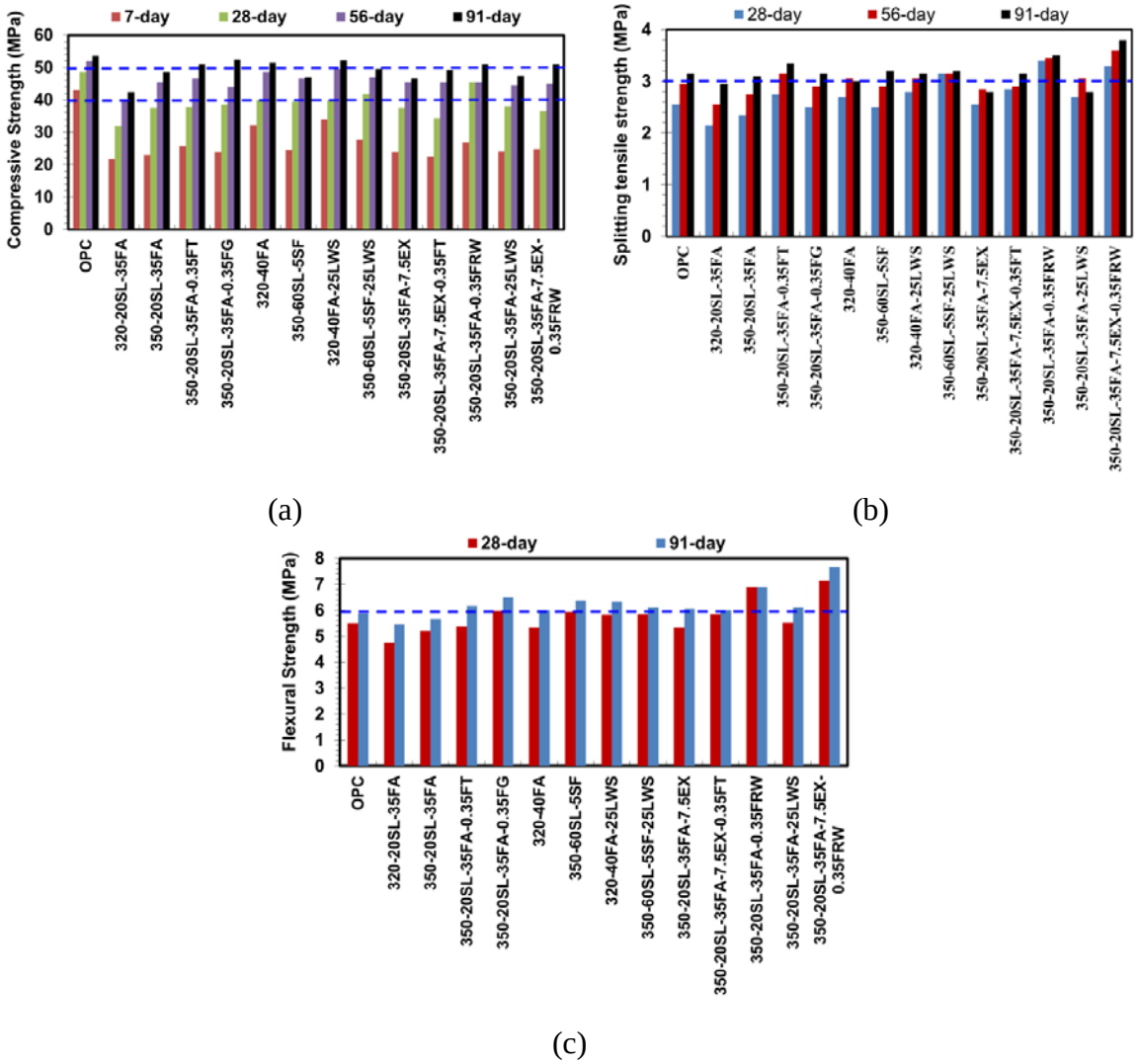

Figure 8-18 Mechanical properties of the investigated HPC mixtures: (a) compressive strength, (b) Slitting tensile strength, and (c) flexural strength.

As expected, the mixture made with 100% cement developed higher early-age compressive strength. On the other hand, the majority of the investigated mixtures resulted in approximately similar compressive strength value of 50 MPa as that of the control mixture made with 100% OPC. The incorporation of fibers in concrete containing high volume of SCMs was shown to have 0 to 35% higher splitting tensile and flexural strengths than the control mixture made with 100% cement. The highest splitting tensile

and flexural strength was obtained for the mixture made with 0.35% recycled steel fibers containing 20% SL and 35% FA. This mixture also exhibited similar compressive strength to the control mixture. For a given binder type and content, mixtures incorporating steel fibers recycled from scrap tires resulted in higher mechanical properties compared to the synthetic fibers for a given fiber content. All mixtures met the compressive strength requirements.

8.2.2.2 Shrinkage. The drying shrinkage of the reference and Eco-HPC mixtures is presented in Figure 8-19. Mixture made with 100% cement exhibited the highest autogenous and drying shrinkages of 180 and 550 µstrain after 120 and 300 days of drying, respectively, compared to other Eco-HPCs made with SCMs and fibers. The incorporation of 7.5% CaO-based EX resulted in significant early-age expansion in autogenous and drying shrinkage. The 350-SL20FA35 mixture containing 7.5% CaO-based EX exhibited 180 µstrain expansion after three days of moist curing followed by 250 µstrain shrinkage after 300 days of drying.

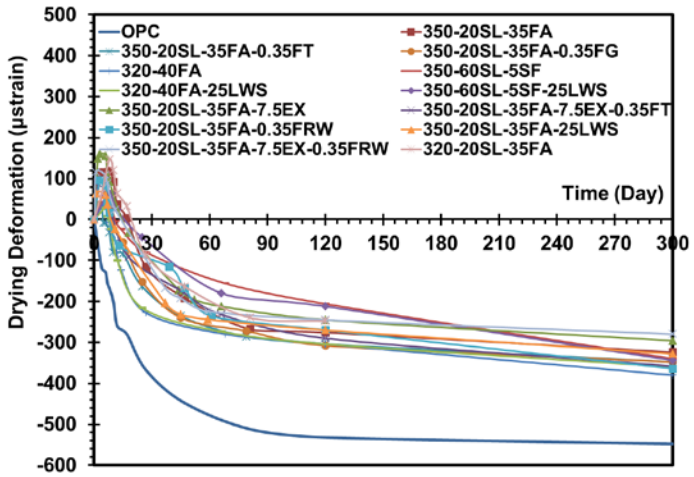

Figure 8-19 Drying shrinkage profiles of Eco-HPC mixtures.

8.2.2.3 Frost durability. The results of deicing salt scaling rating and cumulative mass of scaling residue of the investigated mixtures are presented in Table 8-7 and Figure 8-20, respectively. For a given w/cm, the partial substitution of cement by SCMs was shown to increase the mass of scaling residue compared to the reference mixture made

with 100% OPC. Relatively high scaling values were obtained for binder compositions made with high volume SCM replacements of more than 50%.

Table 8-7 Deicing salt scaling rating of HPC mixtures.

Mixture	Number of freeze-thaw cycles						
	7	14	21	28	35	42	50
OPC	0	0	0	0	1	2	3
320-20SL-35FA	0	1	1	2	3	3	4
350-20SL-35FA	0	0	1	1	2	3	3
320-40FA	0	1	1	2	2	3	4
350-60SL-5SF	0	1	1	2	3	3	4
320-40FA-25LWS	0	1	1	2	2	3	3
350-60SL-5SF-25LWS	0	1	1	2	2	3	3
350-20SL-35FA-7.5EX	0	1	1	1	2	3	3
350-20SL-35FA-7.5EX-0.35FT	0	0	1	2	3	3	3
350-20SL-35FA-0.35FRW	0	1	1	2	3	3	4
350-20SL-35FA-25LWS	0	1	1	2	3	4	3
350-20SL-35FA-7.5EX-0.35FRW	0	0	1	1	2	2	3

As presented in Table 8-7, all Eco-HPC mixtures exhibited the mass scaling rating lower than 4 after 50 freeze-thaw cycles. In the case of using high volume SCMs, the reduction of w/cm and stability of air void system would be beneficial in enhancing the resistance to de-icing salt scaling.

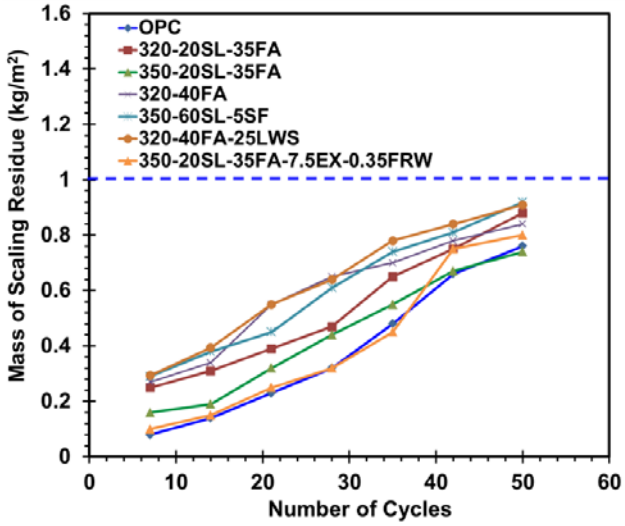

Figure 8-20 Mass of scaling residue of HPC mixtures subjected to freeze-thaw cycles.

8.2.3. Key Engineering Properties and Durability of Selected Mixtures. This phase was conducted to further evaluate key engineering properties and durability aspects of the optimal Eco-HPC mixtures. Based on the obtained results, four optimal concrete mixtures (with and without fibers) were selected for targeted applications, as listed in Table 8-8.

Table 8-8 Selected concrete mixtures.

Concrete type	Mixture	Binder content		Binder type				Fiber type and content		Shrinkage mitigating materials	
		320 (kg/m^3)	350 (kg/m^3)	100% OPC	60% OPC + 40% Class C FA	45% OPC + 20% SL + 35% Class C FA	35% OPC + 60% SL + 5% SF	TUF strand fiber (0.35%)	Recycled steel fiber from tire (0.25%)	25% LWS	7.5% Type G EX
Eco-Pave-Crete	320-40FA-25LWS	x			x					x	
	320-20SL-35FA-7.5EX-0.35FT	x				x		x			x
Eco-Bridge-Crete	350-60SL-5SF-25LWS		x				x			x	
	350-20SL-35FA-7.5EX-0.35FRW		x			x			x		x

8.2.3.1 Mechanical properties. The development of mechanical properties of the selected Eco-HPCs is presented in Figure 8-21. The mixture made with 0.35% recycled fibers and containing 20% slag and 35% fly ash replacements developed approximately similar compressive strength as that of the control mixture made with 100% cement. The incorporation of fibers in concrete made with high volume of SCMs is shown to have 30% higher splitting tensile strength than that of the control mixture made with 100% cement. The mixture made with 0.35% recycled steel fibers developed the greater area under load-deflection curve compared to other mixtures proportioned with synthetic fiber. The reference mixture developed the lowest ductility behavior and residual strength among all mixtures. The 56-day flexural toughness (area under the load-deflection curve) results of mixtures made with fibers are compared in Figure 8-21 (e). It is interesting to

note that for a given fiber content, the use of steel fibers recovered from waste tires had two times higher flexural toughness compared to the similar mixture made with synthetic fibers. In addition, the incorporation of expansive agent in combination with fibers (especially steel fibers) would enhance the reinforcing mechanism provided by fibers. This may be due to the induced compressive stress provided by expansive cements which can lead to forming of internal pre-stressed condition in concrete. Internal pre-stressed concrete may result in higher residual strength and flexural toughness. Bentz and Jensen (2004) also reported that as long as proper restraint is provided, the expansion of self-stressing materials can pre-stress concrete and improve its tensile capacity.

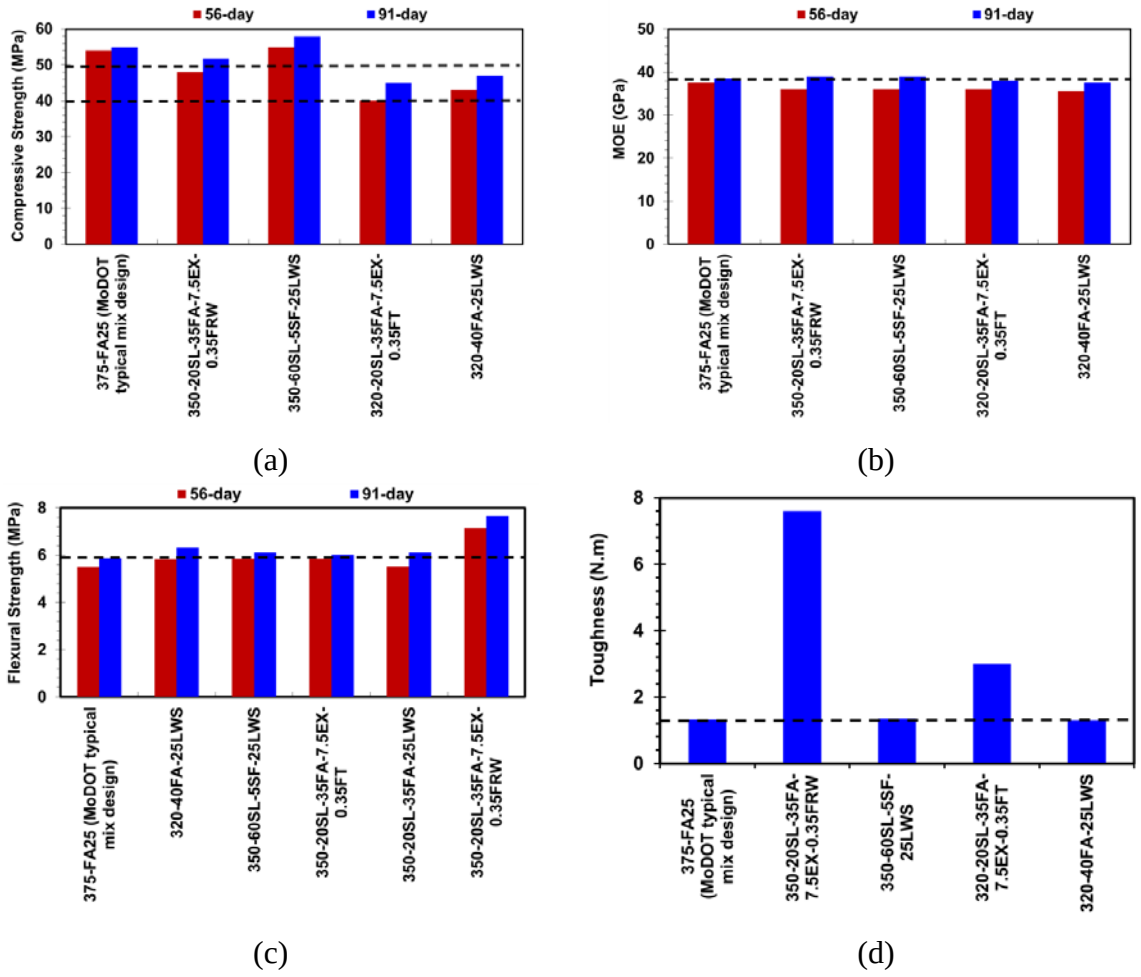

Figure 8-21 Mechanical properties of selected HPC mixtures: (a) compressive strength, (b) modulus of elasticity, (c) flexural strength, and (d) toughness of mixtures at 56 days.

8.2.3.1 Shrinkage and restrained shrinkage cracking. The results of drying and restrained shrinkage of the selected mixtures are shown in Figure 8-22. Restrained shrinkage and cracking potential of mixtures were evaluated using ASTM C1581 ring test. Mixture made with 100% cement exhibited the highest drying shrinkages of 550 µstrain after 250 days of drying. The optimized Eco-HPC mixtures had lower drying shrinkage of 300 µstrain after 250 days of drying. The incorporation of 7.5% Type G expansive agent resulted in a significant early-age expansion of 100 µstrain. It is interesting to point out that no restrained shrinkage cracking was observed for the optimized concrete mixtures after 55 days of testing. However, the control mixture made with 100% cement exhibited elapsed time to cracking after 22 days. For mixtures containing EX, the tensile stress induced by restrained shrinkage was compensated by expansion induced by using EX, thus reflecting no cracking after 55 days.

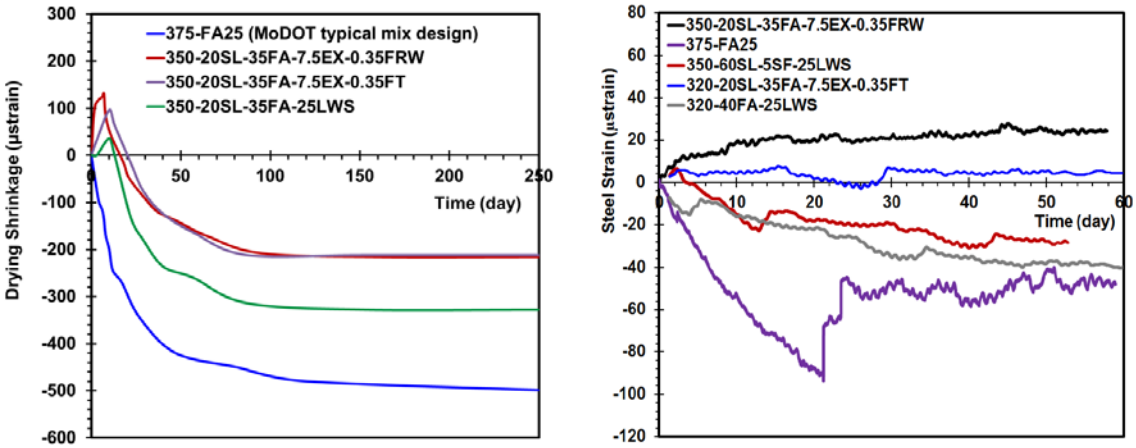

(a) (b)

Figure 8-22 Shrinkage of HPC mixtures: (a) drying shrinkage and (b) restrained shrinkage.

Average stress rate and cracking potential classification of investigated mixtures are summarized in Table 8-9.

Table 8-9 Cracking potential classification of HPC mixtures.

Mixture ID	Time to cracking (day)	Average strain rate factor (μstrain/day$^{1/2}$)	Average stress rate (MPa/day)	Potential of cracking (ASTM C 1581)
375-FA25	24	-23.6	-26.4 (tension)	Moderate
350-20SL-35FA-7.5EX-0.35FRW	—	2.4	1.7 (compression)	Low
350-60SL-5SF-25LWS	—	-4.9	-3.5 (tension)	Low
320-20SL-35FA-7.5EX-0.35FT	—	1.3	1 (compression)	Low
320-40FA-25LWS	—	-9.7	-6.9 (tension)	Low

In accordance with ASTM C1581, the stress rate development induced by restrained shrinkage at the age of cracking can be calculated as follows:

$$q = \frac{G\left|\alpha_{avg}\right|}{2\sqrt{t_r}} \qquad 8\text{-}8$$

where q is the stress rate in each test specimen, MPa/day, G is a constant based on the ring dimension 72.2 GPa, and t_r is the elapsed time to cracking or elapsed time when the test is terminated for each test specimen. $|\alpha_{avg}|$ is the absolute value of the average strain rate factor for each test specimen, (μstrain/day$^{1/2}$) which is determined as a slope of a fitted line between steel strain and square root of elapsed time. Mixtures made with EX had positive strain rate factor due to the expansion of such mixtures. In accordance with ASTM C1581, the reference mixture made with 100% cement was considered to exhibit moderate shrinkage cracking potential. On the other hand, mixtures proportioned with shrinkage reducing materials have low cracking potential with compressive stress rate ranging between -6.9 to 1.7 MPa/day.

8.2.3.2 Durability. The performance of the selected Eco-HPCs for different durability aspects is presented in Figure 8-23. All selected Eco-HPC mixtures developed approximately similar performance as that of the control mixture made with 100% OPC. All Eco-HPCs developed frost durability factor values higher than 80% after 300 freeze-thaw cycles, except for ternary blends of 60% SL and 5% SF with durability factor of 70%.

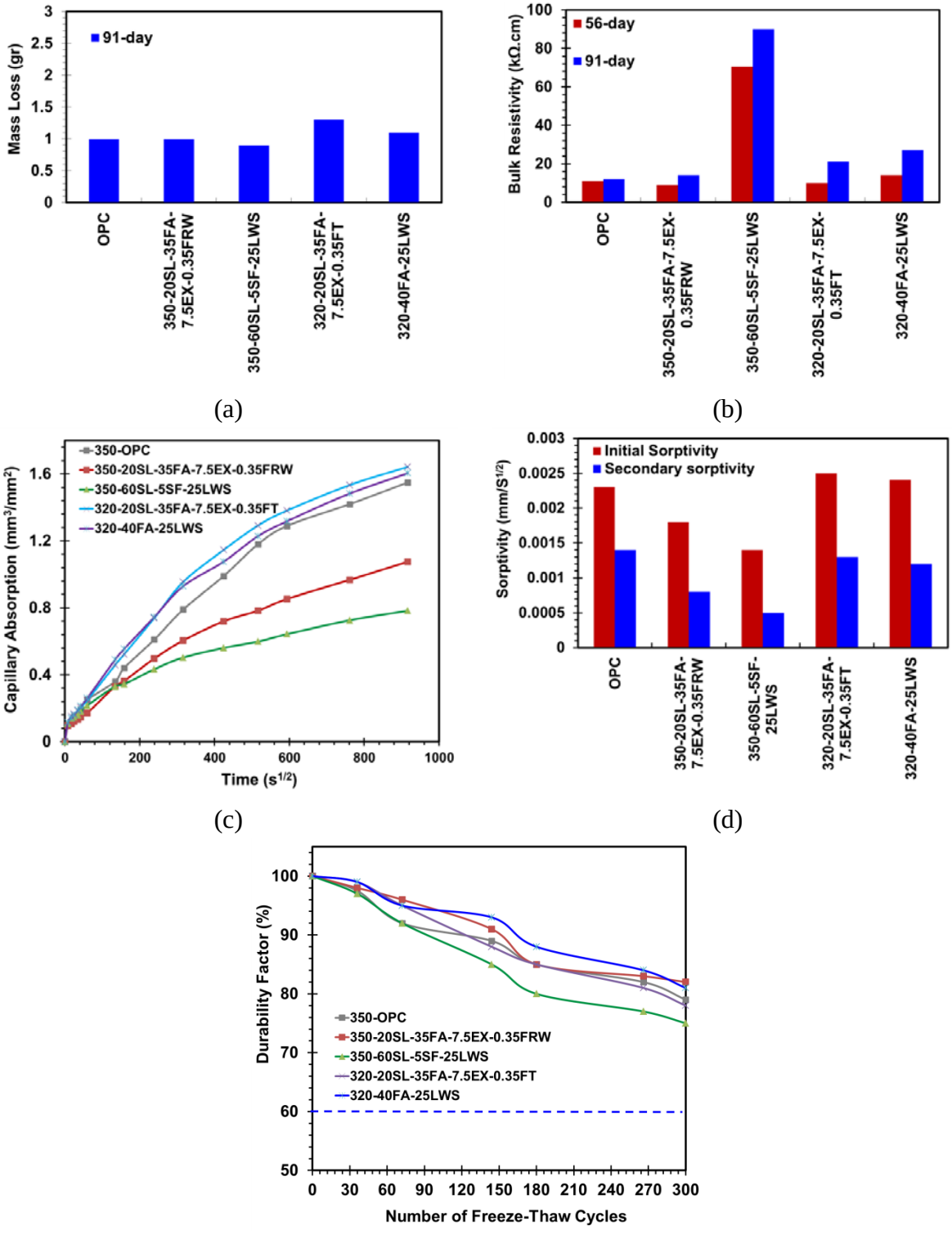

Figure 8-23 Durability performance of selected HPC mixtures: (a) abrasion resistance, (b) electrical resistivity, (c) capillary absorption, (d) sorptivity index, and (e) frost durability factor.

8.3. SUMMARY

A comprehensive investigation was carried out to elucidate the influence of composition and resultant reaction of blended binders proportioned with high volume of SCMs on shrinkage and restrained shrinkage cracking of flowable Eco-concrete. Furthermore, the effect of different shrinkage mitigating materials was evaluated and the results were analyzed to design Eco- and crack-free HPC for different targeted applications (Eco-Pave-Crete and Eco-Bridge-Crete). Based on the obtained results, the following conclusions can be warranted:

- The incorporation of SCMs slows down the progressive rate of autogenous shrinkage, thus extending the time corresponding to the steady-state shrinkage.
- In spite of having slower deformation rate, the Eco-concrete mixtures containing SCMs exhibited higher autogenous shrinkage at later age compared to the plain OPC mixture. This is attributed to the: (i) pozzolanic reaction of SCMs which results in the refinement of pore structure; and (ii) larger transformation of free water to chemically bound water, as evidenced by the TGA data.
- Eco-concrete provisioned with SCMs exhibited up to 60% longer elapsed time to cracking and developed 2.4 to 4.4 times larger tensile creep coefficient at the time of crack initiation compared to the control mixture without any SCM. Such spread in shrinkage cracking resistance for mixtures containing SCMs can be due to the resultant reaction and pozzolanic activity induced by SCMs, that dominates the rate of elastic properties development and shrinkage at early- and later-age.
- The synergistic effect provided by the ternary combination of CFA and SL developed considerably higher tensile creep behavior and greater shrinkage cracking resistance compared to the binary blends of CFA or SL. Opposite trend was observed when SF incorporated in conjunction with CFA, reflecting lower tensile creep coefficient and increased shrinkage cracking potential compared to the binary blend of CFA.
- Hydration kinetics of binder systems can be correlated with shrinkage cracking resistance and tensile creep behavior of the Eco-concrete. Binders with greater early-age hydration reaction tend to exhibit lower tensile creep behavior and larger rate of shrinkage-induced tensile stress, thus increasing the risk of

shrinkage cracking potential. Such composition-reaction property correlations can provide insights into proportioning sustainable binders with the aim of high resistance to shrinkage cracking.

- The synergetic effect of the combination of shrinkage reducing materials, including LWS and EX coupled with fibers (synthetic fibers or recycled steel fibers) is quite effective to design low cracking potential concrete.
- The internal curing provided by the LWS can reduce the shrinkage and risk of early-age shrinkage cracking, especially for mixtures subjected to air drying without using any initial moist-curing.
- Given higher packing density and lower water demand of the optimized SCMs, the Eco-Crete mixtures prepared with binary and ternary of binders necessitated 10% to 40% lower HRWR demand to achieve the required fluidity compared to the control mixture made with 100% cement.
- The incorporation of fibers (synthetic fibers and recycled steel fibers) in concrete containing a high volume of SCMs was shown to have up to 35% higher splitting tensile and flexural strengths than the MoDOT reference mixture. The highest splitting tensile and flexural strengths were obtained for the mixture made with 35% recycled steel fibers containing 20% SL and 35% FA.
- For a given fiber content, the use of steel fibers recovered from waste tires had two-fold higher flexural toughness compared to the similar mixture made with synthetic fibers.
- The optimized Eco-HPC mixtures had lower drying shrinkage of 300 μstrain after 250 days of drying compared to 450 μstrain for the MoDOT reference mixture. The incorporation of 7.5% Type G EX resulted in a significant early-age expansion of 100 μstrain followed by shrinkage of 200 μstrain after 250 days of drying.
- The MoDOT reference mixture exhibited elapsed time to cracking of 24 days under restrained shrinkage condition. In case of mixtures made with shrinkage reducing materials no cracking was observed until 55 days of testing.

- Regardless of the binder type, concrete mixtures made with 7.5% CaO-based EX exhibited an expansion of 20 μstrain compared to the 60 μstrain of shrinkage for the reference mixture under restrained shrinkage.

9. VALIDATION OF ECO-HPC PERFORMANCE IN LARGE-SCALE ELEMENTS

The aim of this section is to validate the performance of optimized Eco-HPCs in large-scale elements. Focus was placed to evaluate the shrinkage of slab sections and flexural performance of reinforced concrete beams made with optimized Eco-Bridge-Crete. As such, large-scale specimens, including reinforced slab and beam elements were cast, which is described in detail below.

9.1. SHRINKAGE OF CONCRETE SLAB SECTION

The aim of this subtask was to evaluate the shrinkage deformation of concrete slabs made with selected concrete mixtures. As shown in Figure 9-1, three slabs measuring 1.8 × 1.8 m and 150 mm in depth were constructed to evaluate shrinkage deformation of different concrete mixtures.

The investigated mixture parameters include the incorporation of fiber, lightweight sand, expansive agent, and high volume SCMs and the results were compared with that of the MoDOT reference mixture. The mix design parameters of selected concrete mixtures for slab sections are presented in Table 9-1.

Figure 9-1 Slab section used for shrinkage deformation evaluation.

Table 9-1 Selected concrete mixtures for slab sections.

Concrete type	Codification	Reinforcement	w/cm	Binder content		Binder type		Fiber type and content		Shrinkage mitigating materials	
			0.40	350 kg/m^3 (590 lb/yd^3)	375 kg/m^3 (630 lb/yd^3)	75% OPC + 25% Class C FA	45% OPC + 20% SL + 35% Class C FA	TUF strand fibers (0.35%)	Steel fibers from tire (0.35%)	25% LWS	7.5% Type G EX
MoDOT reference mixture	FA25	x	x		x	x					
Optimized Eco-Bridge-Crete	SL20FA35-25LWS	x		x			x			x	
	SL20FA35-7.5EX-0.35FRW	x		x			x		x		x

9.1.1. Instrumentation Plan. The investigated slabs were fully instrumented by utilizing strain gauges, relative humidity sensors, and thermocouples to monitor the deformation caused by concrete shrinkage, humidity and temperature variations over time. A detailed description of the instrumentation used in this investigation is provided below.

Embedded strain gauges: In this study, the embedment type of strain gauges (KM-120-120-H2-11, manufactured by KYOWA) was used to monitor the shrinkage deformation of concrete, as shown in Figure 9-2. The sensor has the outer body of 120 mm sensing grid with an effective gauge length of 75 mm. The gauge is waterproof and is designed to be placed in fresh concrete to directly measure the shrinkage deformation associated with concrete. The sensor consists of a 75 mm 120 ohm (Ω) foil strain gage (nickelchromium alloy on polymide backing). The surface of the gauge is designed to have a honeycomb pattern that enables adequate bond to concrete.

Thermocouple: The thermocouple wire (UX-08542-24, manufactured by Coleparmer) used in the instrumentation was a Type T 20 gage wire. These thermocouples consist of copper and constantan wires, and are functional between -250

to 250° C. The ends of the solid thermocouple wires were twisted and then soldered to ensure an adequate electrical connection.

Figure 9-2 Embedded strain gauge for monitoring shrinkage deformation.

Relative humidity sensor: The small (6 × 20 mm) capacitive relative humidity sensor (HIH-4030, manufactured by Sparkfun) was used to measure the relative humidity inside concrete. The accuracy of the sensors is reported by the manufacturer to be ±2% RH between 10% and 90% RH, and range up to ±4% at 100% RH. In order to embed the RH sensor in concrete, the RH sensor was placed inside the 1/2” PVC tube and the end of the tube was covered by Gore-Tex to allow moisture transmission, while preventing the penetration of liquid water and solid particles that may lead to an error in measurement. The encapsulated RH sensor before embedding in concrete is shown in Figure 9-3.

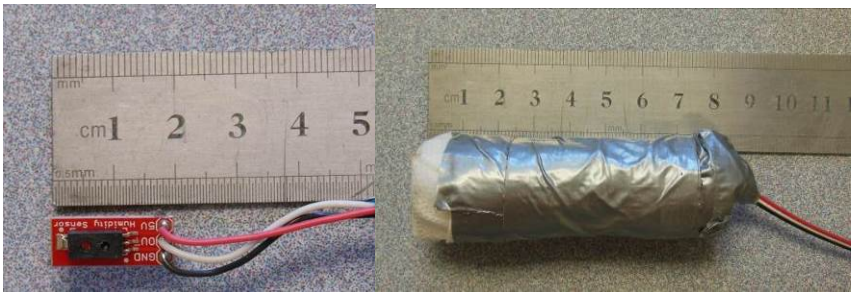

Figure 9-3 Encapsulated relative humidity sensor before embedment in concrete.

Figure 9-4 shows the instrumentation layout, including embedded concrete strain gauge, relative humidity sensor, and thermocouple for monitoring the shrinkage deformation of concrete used for slab sections. As indicated in Figure 9-5, each slab was instrumented at three different locations to monitor the concrete shrinkage behavior at the center, edge, and corner of the slab, corresponding to points A, B, and C, respectively. Station A located at the center of slab has three embedded strain gauges in the

longitudinal direction, three thermocouples, and three relative humidity sensors placed along the height of the slab. Stations B and C located at the edge and corner of the slab have similar instrumentation layout, including four embedded strain gauges (two in the longitudinal as well as two in the transverse direction), two thermocouples, and two relative humidity sensors, as presented in Figure 9-4. Sensors were placed at different thicknesses of slab to monitor strain, temperature and relative humidity along the height of slabs as shown in as presented in Figure 9-4.

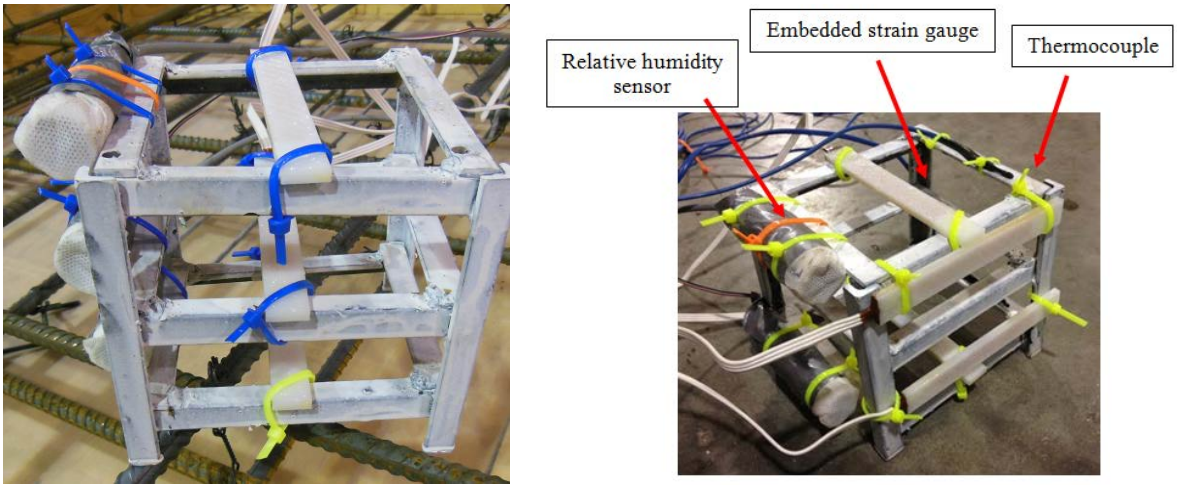

(a) (b)

Figure 9-4 Instrumentation layouts for (a) Layout A: 3 embedded strain gauges in longitudinal direction, 3 thermocouples and 3 relative humidity sensors and (b) Layout B: 4 embedded strain gauges (two longitudinal and two transverse directions), 2 thermocouples and 2 relative humidity sensors

Both the strain and the temperature data was recorded using Campbell Scientific data acquisition hardware and software. Lead wires from the strain gages were routed through AM16-32 multiplexer, using a separate completion module for each gage on the multiplexer. The data logger used was a Campbell Scientific CR1000. The thermocouple wires were routed through an AM25T multiplexer, which has an internal RTD (resistance temperature detector) to measure the cold junction temperature required to compute the temperature at the soldered end of the thermocouple. The multiplexer was controlled by the CR1000 data logger. In addition to the strain and temperature instrumentation, relative humidity sensors were collected.

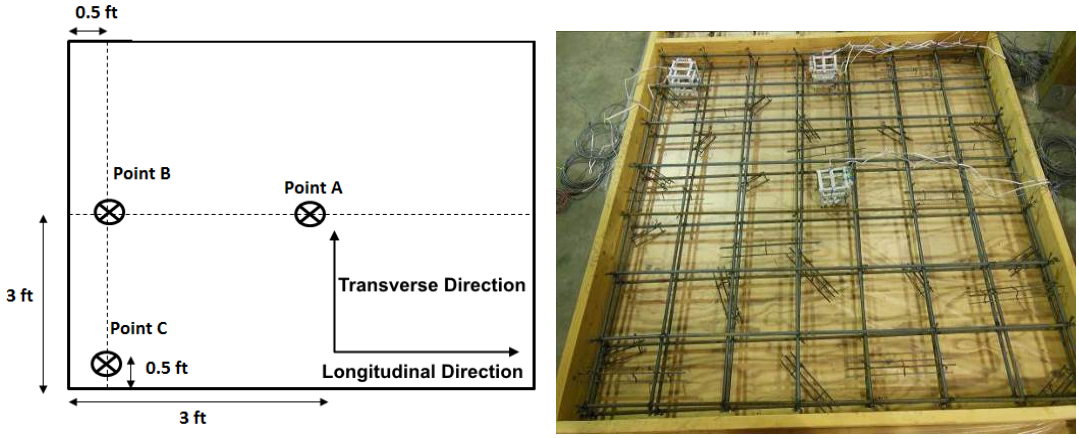

Figure 9-5 Instrumentation location plan for each slab.

The summary of instrumentation plan and designation of sensors utilized for each slab are listed in Table 9-2 and Table 9-3, respectively.

Table 9-2 Summary of instrumentation plan used for each slab.

Point	# Embedded strain gauge	# Relative humidity sensor	# Thermocouple
A	3 (longitudinal direction)	3	3
B	4 (two longitudinal and two transverse directions)	2	2
C	4 (two longitudinal and two transverse directions)	2	2
Sum	11	7	7

All slabs were reinforced with two reinforcement mats of longitudinal #4 bars spaced at 250 mm which were placed at the top and bottom parts of slabs, as shown in Figure 9-5. The top and bottom rebar mats were located 25 mm and 50 mm from the top and bottom of the concrete, respectively. All concrete mixtures were made in local concrete batching plant to confirm the ability of proposed concrete mixtures to apply under actual field conditions. The HRWR dosage was adjusted to secure the slump consistencies varying between 150 mm and 200 mm. The AEA concentration was also adjusted to ensure the fresh air volume of 5% ± 2% for all mixtures. The w/cm was fixed at 0.4 for all mixtures. In total three concrete slabs were constructed including two optimized Eco- and crack-free HPC and a control concrete slab using MoDOT reference mixture targeted for bridge deck, as given in Table 9-1.

Table 9-3 Codifications of sensors used for slab instrumentation.

Slab #1 made with 25% FA (FA25)			
Strain sensors	Humidity sensors	Temperature sensors	Codifications
1-M-SL-1	1-M-H-1	1-M-T-1	• 1 refers to slab made with FA25 mixture (MoDOT reference mixture). • M, S, and C refer to center, side and corner points of slab. • S, H, and T refer to strain, humidity and temperature sensors. • SL and ST refer to strain gauges in longitudinal and transvers directions. • 1, 2, and 3 represents bottom, middle, and top parts along height of concrete slab. • Similar designations are used for other slabs, except that slabs made with SL20FA35-25LWS and SL20FA35-7.5EX-0.35FRW mixtures are designated as 2 and 3, respectively.
1-M-SL-2	1-M-H-2	1-M-T-2	
1-M-SL-3	1-M-H-3	1-M-T-3	
1-S-SL-1	1-S-H-1	1-S-T-1	
1-S-ST-1	1-S-H-3	1-S-T-3	
1-S-SL-3	1-C-H-1	1-C-T-1	
1-S-ST-3	1-C-H-3	1-C-T-3	
1-C-SL-1			
1-C-ST-1			
1-C-SL-3			
1-C-ST-3			

After casting, the top surface of the beams was covered with wet burlap and plastic sheeting, and a wet surface was maintained for seven days to retain moisture for a proper initial moist curing.

Affter seven days, the burlaps and plastic sheets were removed, and the slabs were demolded and exposed to air drying in the lab environment. Shrinkage of the investigated concrete mixtures is not affected by humidity and temperature variations caused by seasonal changes. Therefore, the shrinkage results of the investigated concrete mixtures can be isolated from warping and curling deformations caused by seasonal variations.

The slab construction procedures, including concrete arrival using mixing truck, placement, consolidating, finishing, and curing, are presented in Figure 9-6.

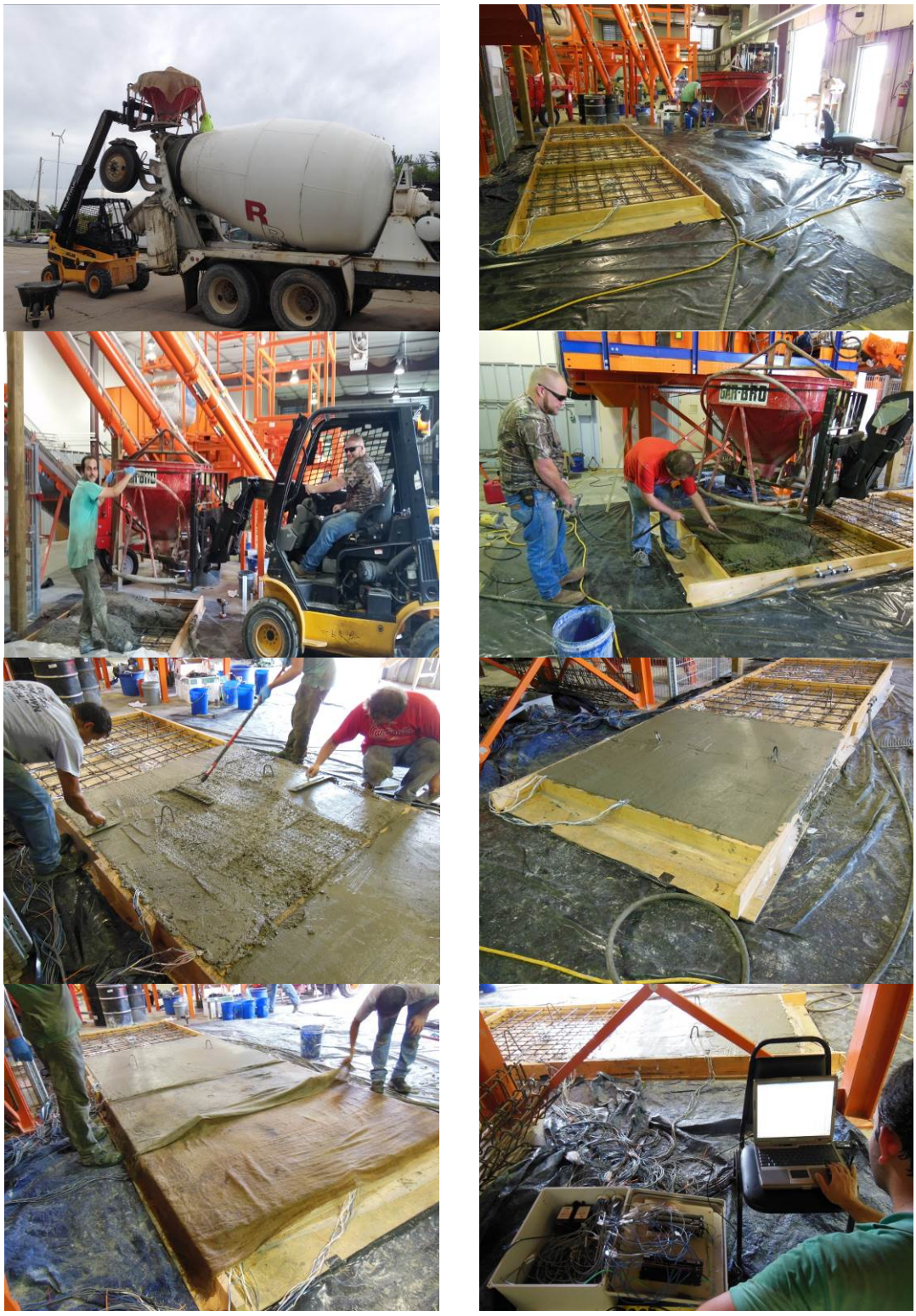

Figure 9-6 Concrete slab construction procedures.

9.1.2. Shrinkage and Relative Humidity Measurement. Figure 9-7 present the results of shrinkage deformation along the height at different stations of the investigated slabs. In this figure, negative and positive signs correspond to shrinkage and expansion, respectively. As mentioned earlier, all slabs were subjected to wet curing using wet burlap and plastic sheet for seven days before exposure to air drying condition. The results of shrinkage deformation were shown to be a function of concrete mix design, location, and depth of slab. Expectedly, slab made with 25% FA replacement exhibited higher magnitude and rate of shrinkage deformation compared to the optimized Eco-Bridge-Crete. This difference became more dominant for the top surface of concrete slab. For instance, cluster A (i.e., station A in Figure 9-5) of the control slab had an expansion of 100 μstrain after 7 days of wet curing followed by 100 μstrain shrinkage after 30 of drying (see sensor 1-M-SL-3 in Figure 9-7). However, no shrinkage deformation was observed for other slabs prepared with optimized Eco-Bridge-Crete, as shown in Figure 9-7. Regardless of the concrete composition, the top part of slab underwent larger shrinkage deformation compared to the mid-height and bottom part of slab thickness. This is attributed to faster evaporation rate of top surface of concrete, as indicated in Figure 9-8. Given the expansion induced stresses, the SL20FA35-7.5EX-0.35FRW mixture containing 7.5% CaO-based EX exhibited significant expansion. The magnitude of expansion was shown to vary along the height of slab. Strain gauges located at the top part of concrete slab experienced larger extent of expansion compared to the middle and bottom parts of slab. For example, top surface of concrete exhibited 600-800 μstrain expansion compared to 350-400 μstrain expansion recorded for sensors located at the middle and bottom parts of slab. This is on account of higher exposure of top surface to the moist curing provided by wet burlap during the first seven days. As explained earlier, the effectiveness of EX to generate expansion is significantly affected by the initial moist curing. The penetration of water into concrete slab at early-age can provide more water to facilitate the hydration of CaO-based EX, thus indicating larger magnitude of expansion. The incorporation of 25% LWS was shown to be fully effective at reducing shrinkage rate and magnitude. No shrinkage was obtained for slab made with 20% SL and 35% FA containing 25% LWS. This confirms that the combined use of SCM replacement and LWS can be fully beneficial at reducing shrinkage rate and magnitude. As presented in

Figure 9-8, slab containing 25% LWS exhibited higher relative humidity after 30 days of drying. This enhanced relative humidity of paste matrix is attributed to the internal curing provided by LWS which can maintain larger relative humidity within the paste matrix for a longer duration.

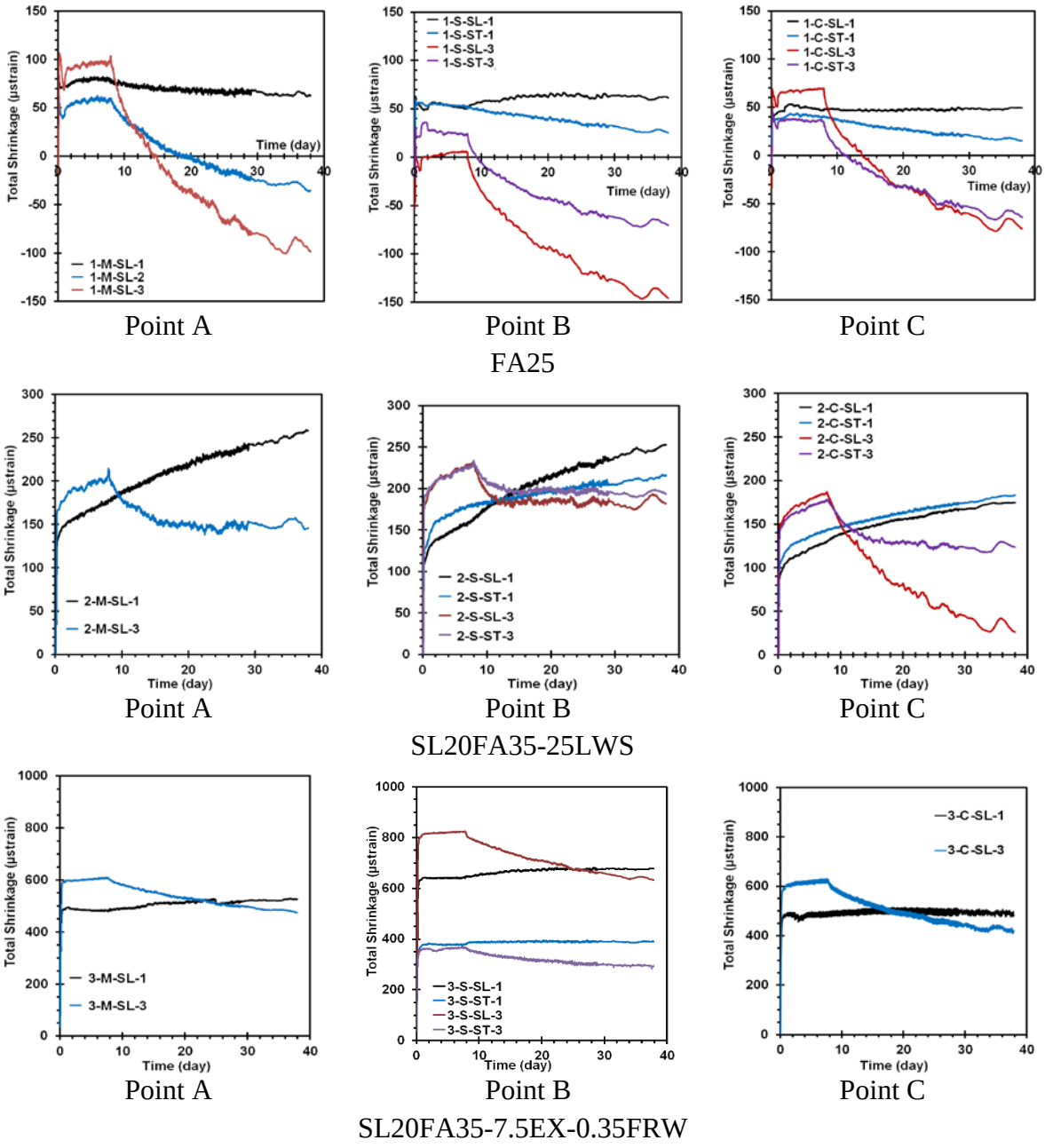

Figure 9-7 Shrinkage deformation over height of slabs at different stations. All slabs were moist cured for seven days before exposure to air drying.

It can be noticed from Figure 9-7 that shrinkage deformations recorded for side and corner (stations B and C in Figure 9-5) points of slab were larger than that of the sensors located at the center (station A) of slab. This is due to faster rate of evaporation of concrete surface, as confirmed in Figure 9-8. This was consistent with results of humidity sensors placed at the side and corner parts of slab, where exhibited larger drop in relative humidity compared to that of the middle sensor, irrespective of concrete composition. Interestingly, this effect was less dominant for slab made with 25% LWS. The lowest relative humidity values observed for the FA25, SL20FA35-25LWS, and SL20FA35-7.5EX-0.35FRW mixtures were 82%, 96%, and 90%, respectively, which were recorded by RH sensors located at the top-corner part of slab. The shrinkage deformation values corresponding to such RH sensors were 80 µstrain (shrinkage), 40 µstrain (expansion), and 400 µstrain (expansion) for the FA25, SL20FA35-25LWS, and SL20FA35-7.5EX-0.35FRW mixtures, respectively, after 30 days of drying. Such shrinkage values corresponded to the largest deformation registered by sensors (the most critical point) after 30 day of drying. Trends of shrinkage deformation recorded by the transverse strain sensors are similar to those of the longitudinal sensors. This phase is currently underway to achieve the stabilized shrinkage deformation.

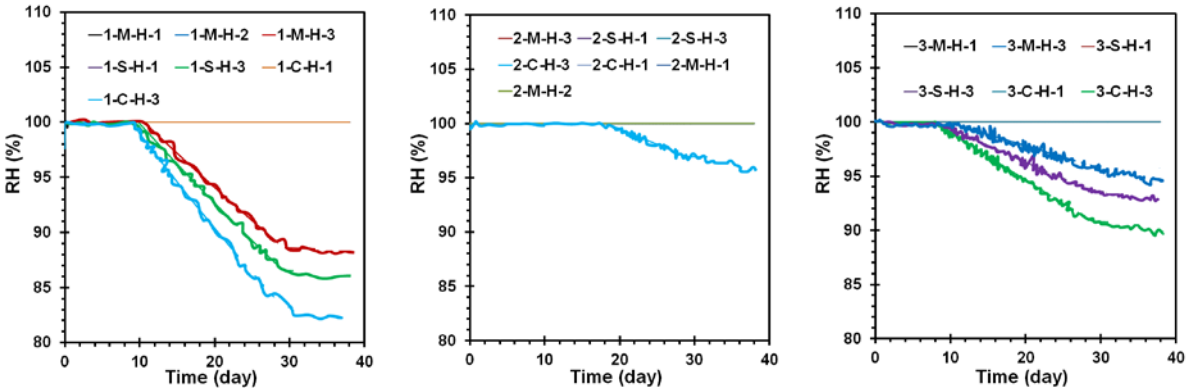

FA25 SL20FA35-25LWS SL20FA35-7.5EX-0.35FRW

Figure 9-8 Relative humidity variations along height of slabs at different stations. All slabs were moist cured for seven days before exposure to air drying.

9.1.3. Temperature Measurement. Figure 9-9 shows the temperature variations at different locations along the height of the investigated slabs. It is interesting to note that the slab FA25 made with higher binder content and lower OPC replacement (i.e.,

only 25% FA substitution) developed higher temperature rise (due to the hydration evolution of binder after concrete placement) compared to other slabs made relatively high volume SCMs.

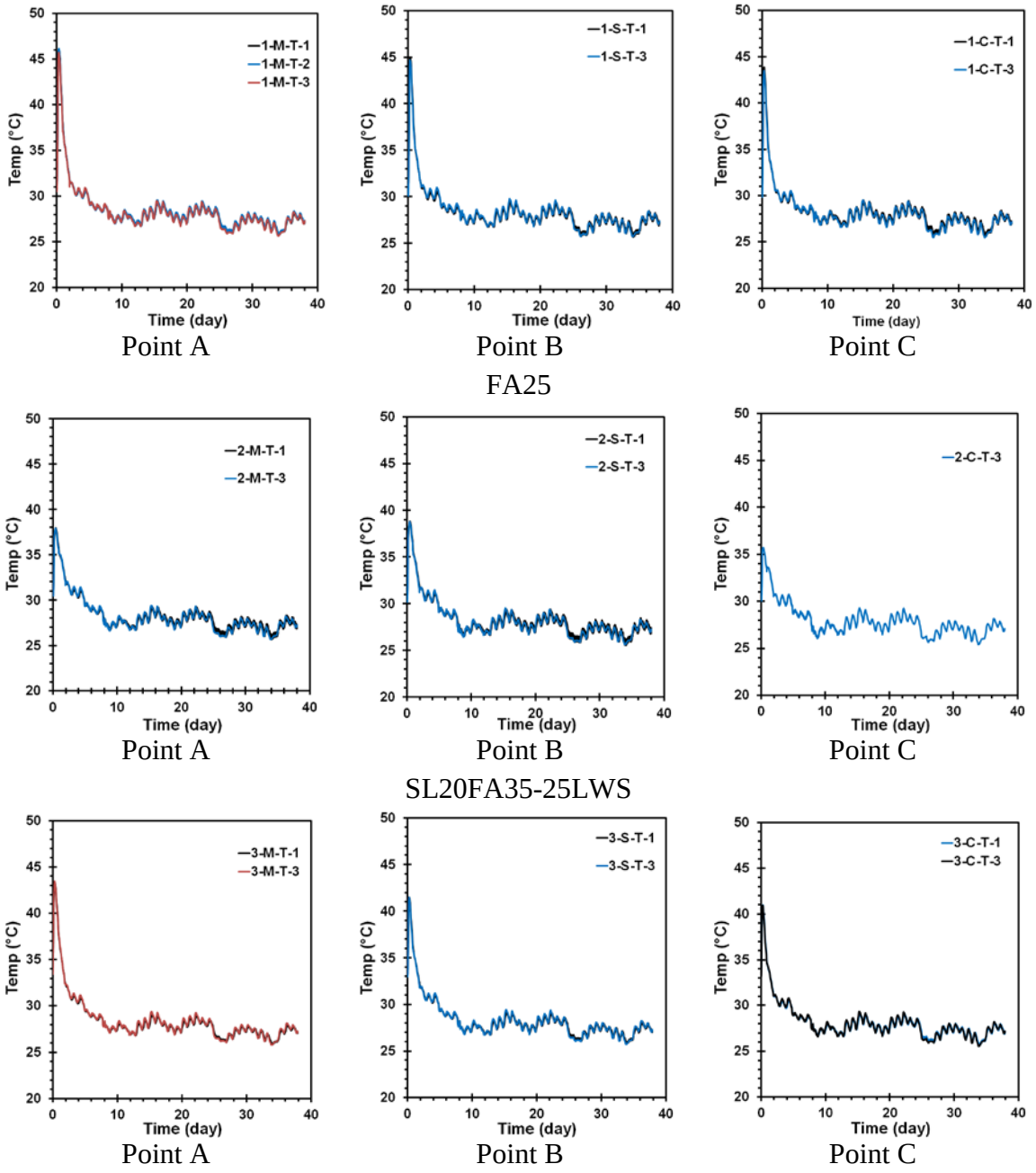

Figure 9-9 Temperature variations along height of slabs at different stations. All slabs were moist cured for seven days before exposure to air drying.

The maximum temperature recorded for slabs made with FA25, SL20FA35-25LWS, and SL20FA35-7.5EX-0.35FRW mixtures were 46°C, 38°C, and 42°C, respectively. The lowest temperature rise registered by embedded thermocouples was obtained for slab prepared with 25% LWS. This mixture also exhibited lower rate of heat transfer compared to the faster heat reduction observed for other mixtures. As shown in Figure 9-9, the embedded thermocouples located at three depths within the deck depth captured similar temperature variation throughout the section. This is due to placement of slabs in lab environment which had consistent daily temperature. Regardless of the concrete mix design, all slabs had similar temperature of 25°C after 30 days of drying which was consistent with ambient temperature registered for lab condition.

9.2. STRUCTURAL PERFORMANCE OF REINFORCED CONCRETE BEAMS

The aim of this phase was to evaluate the flexural strength of reinforced concrete beams made with selected Eco-Bridge-Crete mixtures. The results were compared with those obtained from MoDOT reference mixture. The detail of the selected concrete mixtures used for reinforced concrete beams is given in Table 9-4.

Table 9-4 Selected concrete mixtures for reinforced concrete beams.

Concrete type	w/cm	Binder content		Binder type			Fiber type and content		Shrinkage reducing/compensating materials	
	0.40	350 kg/m^3	375 kg/m^3	75% OPC + 25% Class C FA	45% OPC + 20% SL + 35% Class C FA	35% OPC + 60% SL + 5% SF	TUF strand fibers (0.35%)	Steel fibers from tire (0.35%)	25% LWS	7.5% Type G EX
MoDOT reference mixture	x		x	x						
Eco-Bridge-Crete	x	x			x				x	
	x	x			x					
	x	x			x		x			x
	x	x			x			x		x
	x	x				x			x	
	x	x				x		x		x

9.2.1. Reinforcement Layout and Instrumentation. The beam dimensions, reinforcement layout, and position of strain gauges are depicted in Figure 9-10. All beams were designed to be underreinforced (longitudinal reinforcement ratio = 0.72%), and had identical reinforcement layout, as shown in Figure 9-10. The beams were reinforced with three longitudinal #4 bars for tension, two longitudinal #3 bars for compression, and steel stirrups of #3. The side and vertical clear covers were kept constant at 25 mm for all the beams. Each beam measured 2.40 m in length with a cross section of 200 × 300 mm. All of the beams had #3 stirrups spaced at 10 cm within the bearing area to prevent premature failure, as well as #3 stirrups spaced at 12.5 cm within the middle region. The longitudinal and shear steel reinforcements consisted of ASTM A615, Grade 60 material.

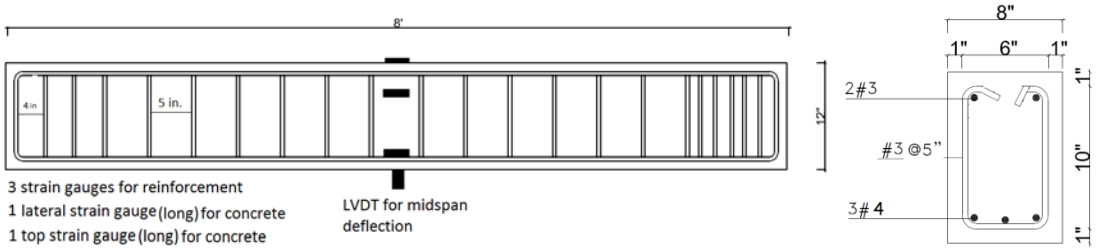

Figure 9-10 Reinforcement layout and locations of strain gauges for test beams.

Figure 9-11 shows the fabrication and instrumentation of reinforcing cages. After assembling of reinforcement cages, the beam specimens were instrumented with different types of measurement devices in order to monitor global and local deformations and strains. The load is directly measured from the load cell of the actuators. All devices are connected to a data acquisition system capable of reading up to 120 channels. Two types of electrical resistance gauges were used to monitor local strains in the longitudinal reinforcing bars and concrete of the test beams. The strain gauges consisted of constantan foil with 120 ohm resistance and had a linear pattern (uniaxial) with various gauge lengths of 6 and 70 mm. All beams were instrumented using three small strain gauges installed at longitudinal reinforcing bars located at the bottom at midspan (see Figure 9-11) as well as two long strain gauges placed on top and lateral side of concrete surface

at the mid-span. In addition to strain gauges, a linear variable displacement transducer (LVDT) was used to monitor vertical deflection of the test beam under flexural testing.

Figure 9-11 Fabrication and instrumentation of reinforcing cages.

A loading system with hydraulic jacks and a load cell of 500 kN (maximum capacity) closed-loop MTS actuator was used to test beams under four-point bending, as demonstrated in Figure 9-12 . A displacement controlled mode at a rate of 1.2 mm/min was selected for applying the load. The actuator was supported by a steel frame and the load was transferred from the actuator to the tested beam through a steel spreader I-beam applied on the full width of the beam. A roller support was obtained by placement a steel cylinder between two steel flat plates. A pin support was obtained by using specially adapted steel I-beam. The upper plate of the I-beam had a spherical groove and the plate was supported on the web plate which had a spherical end to house the plate and allow rotation. At each end of the tested beam, the roller and pin support were rested on steel I-beam, which was secured on the rigid floor of the lab. The combination of the two point loads and the two supports resulted in the desired four-point loading system. During loading, the crack pattern on the sides of the beams was marked and recorded. The applied load, deflection, and strain readings were electronically recorded during the test using data acquisition system monitored by a computer.

Figure 9-12 Beam flexural test setup.

The beam was supported at two points 150 mm from the both ends and was loaded in the middle using two point loads separated by 460 mm, as shown in Figure 9-13. The applied load was measured by the internal load cell on the actuator and the beams were instrumented with LVDT and strain gauges for steel reinforcement and concrete, as shown in Figure 9-14. The loading was stopped when the first crack appeared. The first crack appearance was manually monitored and the width of the major crack was measured using a hand-held microscope. The visual observation of crack development was followed up throughout the loading operation. The crack network distribution on the lateral surface of the beams was marked.

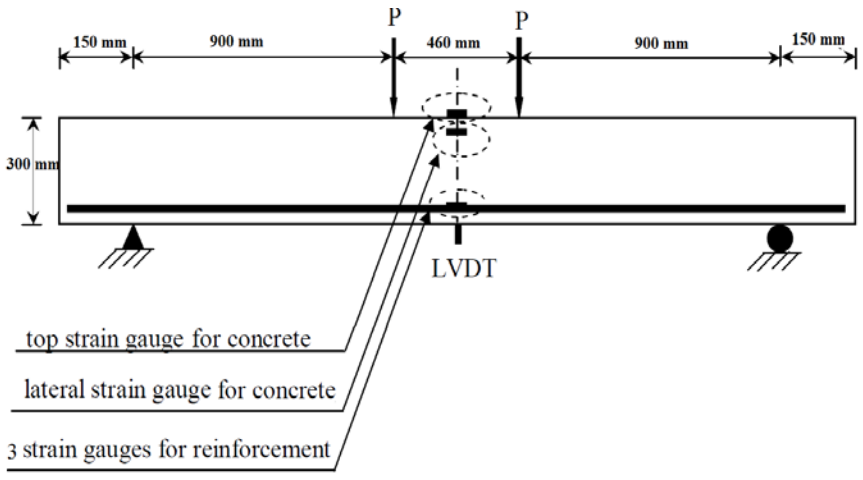

Figure 9-13 Loading and strain-control systems.

Figure 9-14 Installation of LVDT (left) and strain gauges on surface of concrete beam (right).

All concrete mixtures were made in local concrete batching plant to confirm the ability of proposed concrete mixtures to apply under actual field conditions. The beam construction procedure is shown in Figure 9-15. Due to the incorporating high-volume SCMs in proportioning of Eco-HPC mixtures, the beams were cured between 40-55 days using wet burlap and plastic sheet before testing.

Concrete cylinders measuring 100 × 200 mm were prepared to evaluate the compressive strength of concrete mixtures used for beams. All samples were subjected to similar environmental condition to those of the concrete beams to simulate match curing condition. The compressive strength results of concrete mixtures are present in

Table 9-5. Regardless of binder composition and fiber inclusion, all mixtures achieved target range of 40 to 50 MPa (5800-7300 psi) at the age of testing.

Table 9-5 Compressive strength results of concrete mixtures used for beams.

Mixture no.	Codification	Testing age (day)	Compressive strength (MPa)
B1	SL20FA35	55	47
B2	SL20FA35-7.5EX-0.35FT	50	53
B3	SL60SF5-25LWS	45	55
B4	SL60SF5-7.5EX-0.35FRW	45	50
B5	FA25 (MoDOT reference mixture)	40	50
B6	SL20FA35-25LWS	40	47
B7	SL20FA35-7.5EX-0.35FRW	40	45

Figure 9-15 Concrete beam construction procedures.

9.2.2. Test Results. This is discussed below.

9.2.2.1 Load-deflection response. The load-deflection responses of the investigated reinforced concrete beams are shown in Figure 9-16. The load-deflection relationship is tri-linear for all beams. The initial part up to flexural cracking was similar for all beams, which represents the behavior of the uncracked beam that depends on the gross moment of inertia of the concrete cross-section. The second part, corresponding to post-cracking up to steel yielding, represents the cracked beam with reduced moment of inertia. The third part, corresponding to steel yielding up to failure, shows degradation in

the stiffness of the beams due to yielding of the reinforcing steel. Regardless of the binder composition, all concrete beams made with relatively high volume SCMs exhibited approximately comparable ultimate load to that of the FA25 (MoDOT reference mixture), as shown in Figure 9-16. It is noticed that the incorporation of either 0.35% structural synthetic fibers or 0.35% recycled steel fibers led to higher ductility compared to the concrete beams made without any fibers. In other words, the use of fibers substantially improved the post-cracking behavior and enhanced energy absorption. This is attributed to the fact that the addition of fibers acts as an additional reinforcement for concrete to the rebar, where the fibers delayed yielding of steel bars compared to case of concrete made without any fibers. The maximum load carrying capacity was attained for beams containing fibers, especially for the case of 0.35% recycled steel fibers combined with 7.5% CaO-based expansive agent (EX). This can be attributed to the wavy form of recycled steel fibers which can provide better bond to the paste matrix as well as higher tensile strength compared to the synthetic fibers. This made steel fibers effective in contributing to the tensile strength of the concrete beam. This tensile strength is added to that contributed by the reinforcing bars to obtain the ultimate capacity of the beam.

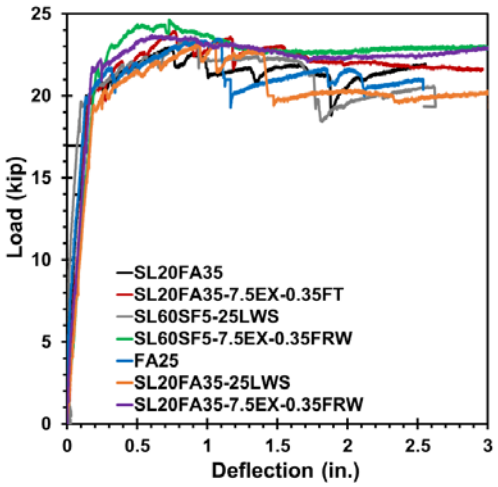

Figure 9-16 Load-deflection responses of tested beams.

The results of ultimate load (i.e., maximum load) of the tested beams are presented in Figure 9-17. In all beams, the longitudinal tensile steel bars initially yielded followed by the concrete crushing, which is a ductile failure mode, called tension failure.

It is interesting to note that all beams made with optimized concrete mixtures containing more than 50% SCM replacements exhibited comparable ultimate load as that of the control beam made with MoDOT reference mixture (F25). All beams made with fibers exhibited slightly higher ultimate flexural strength compared to the similar beams without any fibers. However, given the relatively low volume fraction, the contribution of fibers to enhance ultimate load is not quite significant.

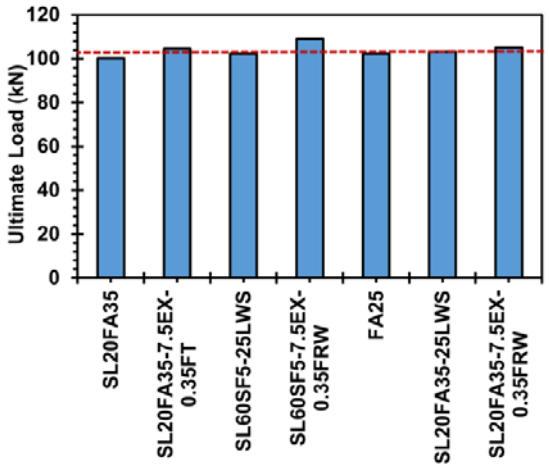

Figure 9-17 Ultimate load of tested beams.

9.2.2.2 Cracking behavior and strains. Figure 9-18 shows the crack patterns at failure of tested beams. Similar characteristics of the crack and failure patterns were observed for all beams. Crack formation was initiated in the flexural span between the two concentrated loads where the flexural stress is highest and shear stress is zero. The cracks were generally perpendicular to the direction of the maximum principal tensile stress induced by pure bending. As load increased, additional flexural cracks opened within the shear span. However, because of the dominance of the shear stresses, the cracks became progressively more inclined and propagated towards the load point. As the load reached the yielding capacity of the beams, the crack opening rate increased, and the beams failed due to crushing of the concrete in the constant moment zone. It is important to note that for fibrous beams, tightly spaced cracks formed perpendicular to flexural tensile stresses on the lower face of the beam.

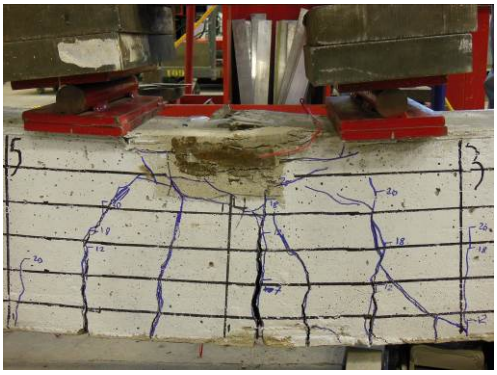

SL20FA35

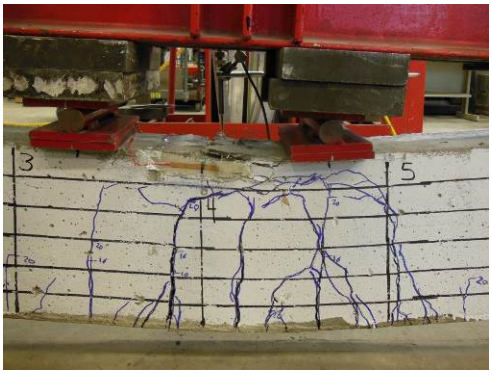

SL20FA35-7.5EX-0.35FT

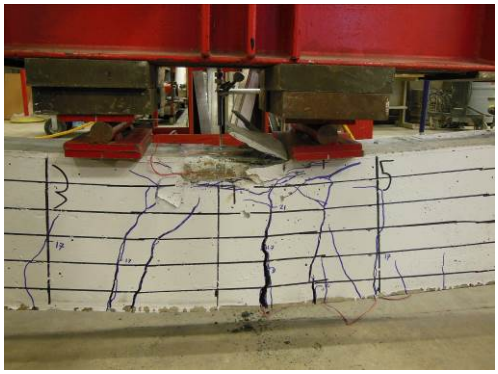

SL60SF5-25LWS

SL60SF5-7.5EX-0.35FRW

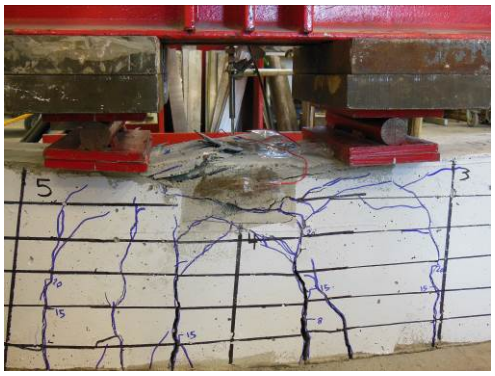

SL20FA35-25LWS

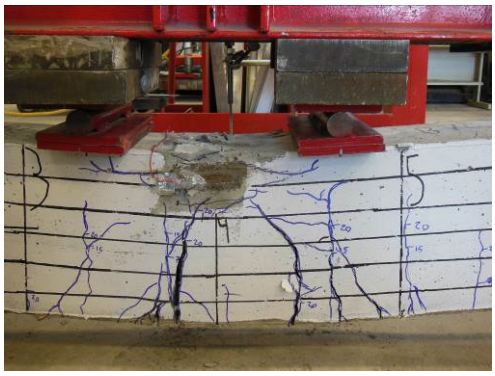

SL20FA35-7.5EX-0.35FRW

FA25

Figure 9-18 Crack patterns of tested beams at failure.

These results indicated that the use of recycled steel fibers can redistribute stresses and undergo multiple cracking before fiber pullout failure. However, non-fibrous beams underwent wider cracks and more crushing in their compression zones. The deflection-crack width propagation (major crack) of the tested beams is depicted in Figure 9-19. The crack width development of tested beam was found to vary with fiber addition and lightweight sand. For a given beam deflection, the use of recycled steel fibers significantly reduced the crack width in relation to that of the non-fibrous beams. Furthermore, the inclusion of lightweight sand was shown to improve the post-cracking response and decrease the crack width (given higher distribution of cracks). Such beams indicated smaller crack width and more distributed crack pattern in comparison with the control beam containing 25% FA replacement.

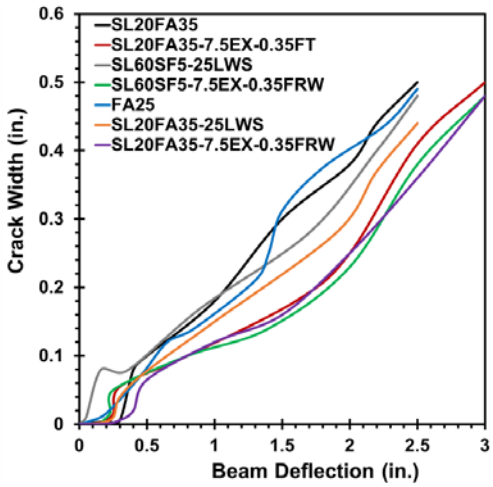

Figure 9-19 Deflection-crack width relationship of tested beams.

The load-strain traces of steel reinforcement and concrete of the tested beams are shown in Figure 9-20. As expected, the top surface of concrete developed more strain values compared to the lateral side of concrete surface, regardless of concrete composition. The strains were proportional to the mid-span deflections and consistent with crack widths indicated in Figure 9-18 and Figure 9-19. It can be noticed from Figure 9-20 that the use of fibers, especially recycled steel fibers, can delay yielding point of rebars and enhance the capacity of concrete before subjected to crushing in the

compression zones. This is attributed to the inclusion of fibers which restrict the opining of cracks under loading.

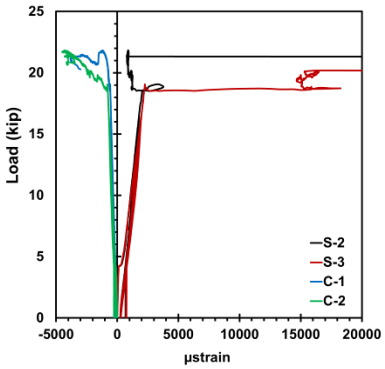

SL20FA35

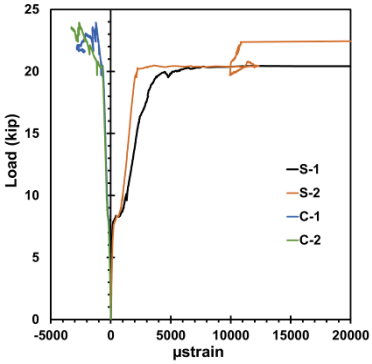

SL20FA35-7.5EX-0.35FT

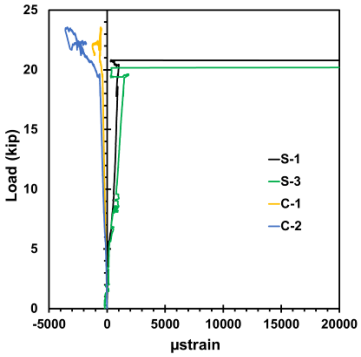

SL60SF5-25LWS

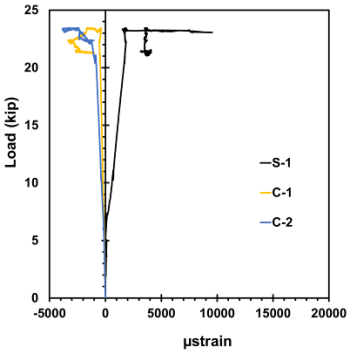

SL60SF5-7.5EX-0.35FRW

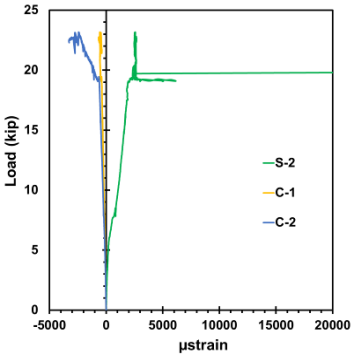

SL20FA35-25LWS

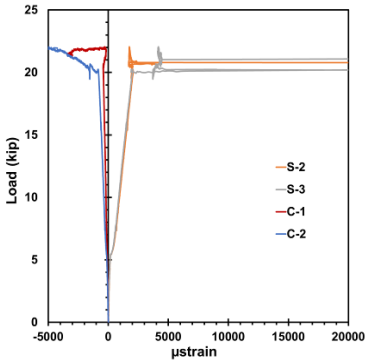

SL20FA35-7.5EX-0.35FRW

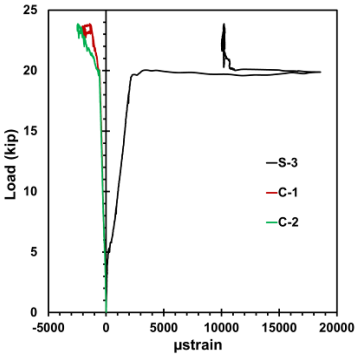

FA25

Figure 9-20 Load-strains of steel reinforcement and concrete response of tested beams.

9.2.2.3 Toughness. Figure 9-21 compares the flexural toughness of RC beams up to the failure or 75 mm midspan deflection of the tested beams. The toughness was obtained by calculation of the surface area under the curve of load-deflection of the beam. The inclusion of either structural synthetic fibers or recycled steel fibers was

shown to substantially enhance the toughness of beam. For example, beams made with SL20FA35-7.5EX-0.35FT, SL60SF5-7.5EX-0.35FRW, and SL20FA35-7.5EX-0.35FRW concrete mixtures developed 120%, 135%, and 130% higher flexural toughness, respectively, compared to the control beam prepared with MoDOT reference mixture. The highest load carrying capacity was obtained for concrete beam made with 60% slag and 5% SF replacements and having 0.35% recycled steel fibers. In the absence of fibers, all concrete beams made with 350 kg/m^3 more than 50% OPC replacement exhibited comparable flexural toughness to that of the control beam prepared with 375 kg/m^3 containing 25% FA replacement. Therefore, in spite of incorporating high volume SCM replacements (more than 50% OPC replacement), the use of fibers was shown to be have good bond with matrix, thus attaining load carrying capacity. This tensile strength is added to that contributed by the reinforcing bars to obtain the ultimate capacity of the beam.

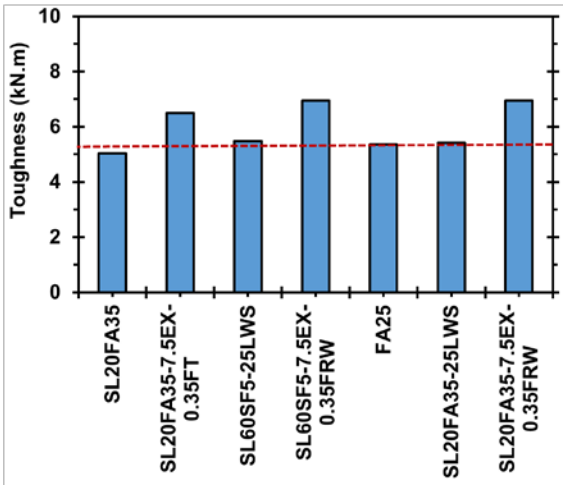

Figure 9-21 Toughness of tested beams.

9.3. SUMMARY

Three slabs and eight reinforced concrete beams were cast to validate the performance of Eco and crack-free HPC mixtures in terms of the shrinkage and flexural strength under large-scale elements. The results were compared with that of the MoDOT reference mixture. Based on the obtained results the following conclusions can be drawn:

- The control slab made with 25% FA replacement exhibited higher magnitude and rate of shrinkage deformation compared to the optimized Eco-Bridge-Crete mixtures. This difference became more dominant for the top surface of concrete slab.
- Given the expansion induced stresses, the SL20FA35-7.5EX-0.35FRW mixture containing 7.5% CaO-based EX exhibited significant expansion. The magnitude of expansion was shown to vary along the height of slab.
- The incorporation of 25% LWS was shown to be fully effective at reducing shrinkage rate and magnitude. This slab exhibited higher relative humidity after 30 days of drying compared to the other slabs made without any LWS.
- Shrinkage deformation recorded for side and corner points of slab were larger than that of the sensors located at the center of slab. This was consistent with results of humidity sensors placed at the side and corner parts of slab, where exhibited larger drop in relative humidity compared to that of the middle sensor.
- All reinforced beams made with optimized concrete mixtures containing more than 50% SCM replacements exhibited equivalent or even higher ultimate flexural load than of the control beam made with MoDOT reference mixture (FA25).
- The use of recycled steel fibers can redistribute stresses and undergo multiple cracking before fiber pullout failure. However, non-fibrous beams underwent wider cracks and more crushing in their compression zones.
- The inclusion of either structural synthetic fibers or recycled steel fibers was shown to substantially enhance the toughness of beam. The SL20FA35-7.5EX-0.35FT, SL60SF5-7.5EX-0.35FRW, and SL20FA35-7.5EX-0.35FRW concrete beams developed 120%, 135%, and 130% higher flexural toughness, respectively, compared to the control beam prepared with MoDOT reference mixture.

10. SUMMARY AND CONCLUSIONS

The research presented in this dissertation was developed in several directions to design and formulate a ntew class of environmentally friendly, cost-effective, and crack-free high-performance concrete (HPC) for the use in pavement (Eco-Pave-Crete) and bridge infrastructure (Eco-Bridge-Crete) applications. The binder content of these novel materials were limited to 320 kg/m^3 and 350 kg/m^3, respectively, in order to reduce paste content, cost, CO_2 emissions, and shrinkage cracking. Both Eco-HPC types were optimized to develop high resistance to restrained shrinkage cracking as well as to secure high durability. A number of parameters contributing towards the formulation of such advanced concrete mixtures were investigated, including binder type and content, aggregate proportions, fiber type, and shrinkage mitigating materials. Based on the test results from this research, the following conclusions can be drawn:

10.1. OPTIMIZATION OF BINDER COMPOSITION

The particle-size distribution (PSD) and specific surface area (SSA) of binders significantly affect the fresh and hardened characteristics of cement-based materials. An experimental investigation was undertaken to evaluate the influence of PSD and calculated SSA of various binary and ternary binder systems on flow characteristics, packing density, and compressive strength development of cement paste. The influence of dispersion state of the binder on packing density was evaluated using the wet packing density approach to determine the optimum water demand (OWD) needed to achieve maximum wet density. The modified Andreasen and Andersen (A&A), Rosin–Rammler (RR), and power law grading models were employed to optimize the PSD of binder system to achieve maximum packing density, while maintaining relatively low water demand.

- The packing density of colloidal particles is significantly related to the degree of dispersion of particles. In order to elicit the full benefit of the higher SSA for particle packing improvement, it is crucial to incorporate dispersing admixtures at the optimum dosage rate. The effectiveness of incorporating high volume of SCM to enhance packing density is shown to increase with the increase of HRWR

dosage resulting from greater degree of dispersion of the binder. The incorporation of sufficient dosage of HRWR led to lower OWD needed to achieve maximum density and higher packing density. The coupled effect of these changes results in higher compressive strength. Compared to the packing density of 0.58 for binder with 100% cement, the use of SCMs in a well-dispersed system is shown to secure packing density of 0.60 to 0.73. The ternary binders containing 40% or 50% slag and 5% or 10% silica fume, by volume of total binder, can ensure lower water demand, greater packing density, lower CO_2 emission, and higher compressive strength. Such binder systems can be adopted for use in sustainable cement-based materials.

- The SSA of binder system was found to have considerable influence on flow characteristics and packing density of binders. Blended cements with higher SSA values developed greater RWD, thus reflecting higher robustness compared to the control mixture with 100% OPC. The modified A&A model can be used to optimize the PSD of binder system to achieve maximum packing density, while maintaining relatively low water demand. Binder systems with the A&A distribution modulus (q) between 0.21 and 0.235 were shown to have 20% to 40% lower MWD to initiate flow, 8% to 35% lower OWD to reach maximum wet density, and 15% to 25% higher packing density compared to the binder with 100% OPC. Good correlations were established between the A&A distribution modulus, SSA, Rosin–Rammler (R–R) spread factor, and power law distribution exponent grading models.
- Regardless of the binder content, all mixtures made with binary and ternary blends of SCMs (targeted for Eco-Pave-Crete and Eco-bridge-Crete) resulted in lower drying shrinkage compared to that of the control mixture made with 100% OPC. As expected, the increase in the binder content resulted in higher drying shrinkage, regardless of the binder compositions. The control OPC mixtures with binder contents of 320 kg/m^3 and 350 kg/m^3 and w/c of 0.40 exhibited the highest drying shrinkage of 840 and 940 μstrain, respectively, after 150 days of drying among the investigated binder compositions.

- Hydration kinetics is found to correlate well with rheological properties and compressive strength development of OPC and PLC systems containing high volume of SCM replacements that are provisioned with PCE. Such correlations provide a reliable basis for apriori estimation of key engineering properties, both in the fresh and hardened state, and thus enable the optimization of binder formulation to provide more sustainable solution for concrete construction applications.

10.2. OPTIMIZATION OF AGGREGATE SKELETON

In total, 17 different aggregate samples with different shapes, textures, and PSDs from various aggregate quarries were evaluated to study the effect of aggregate characteristics on packing density of aggregate skeleton.

- The packing densities of aggregates are shown to vary with size, shape, surface texture, and angularity of aggregate. The packing densities of the investigated fine, intermediate, and coarse aggregates varied between 0.58-0.73, 0.6-0.73, and 0.57-0.61, respectively.
- The proportion of blended aggregate has substantial influence on the packing density of concrete. Based on the obtained results, the packing density of various aggregate proportions varied from 0.65 to 0.815 and 0.65 to 0.80 for rounded and crushed aggregates, respectively. The difference between the packing density of poorly-graded aggregate and well-graded aggregate was about 0.15, which significantly affects the required paste volume to fill the voids between solid particles. This can have considerable effect of material cost, CO_2 emission, and shrinkage.
- The selected aggregate blend for the investigated concrete mixtures had a packing density of 0.81. The PSD of such aggregate was close to the modified Andreasen and Andersen model with a q value of 0.275.
- Multiple criteria such as theoretical packing and grading models should be applied to select the optimum aggregate combination. A proposed statistical mixture design method was shown to be an effective in optimizing the

proportioning of the blended aggregate to achieve the maximum possible packing density as well as to predict the packing density of the blended aggregates.

10.3. COMPARISON OF SHRINKAGE MITIGATING STRATEGIES

An experimental investigation was undertaken to evaluate the effect of initial moist curing period (IMCP), internal curing of lightweight sand (LWS), and shrinkage reducing admixture (SRA) on performance of calcium sulfoaluminate-based (CSA-based) and calcium oxide-based (CaO-based) EXs. The hydration reaction, autogenous and drying shrinkage, internal relative humidity (RH), thermogravimetry, and scanning electron microscopy (SEM) were studied to examine the expansion potential of EXs. Statistical factorial design was conducted to assess the level of significance of the investigated materials and their interaction on autogenous and drying shrinkage as well as compressive strength of mixtures.

- The magnitude, rate, and duration of expansion provided by the EX was significantly influenced by the initial moist curing duration. Prolonged wet curing extends the duration of expansion caused by a given dosage of EX.
- The presence of moist curing is shown to be more crucial for mixture containing CSA-based EX system given relatively higher water consumption compared to the CaO-based EX system. In the absence of IMCP, similar drying shrinkage spread was found between control mixture made with 100% cement and mixture containing 15% CSA-based EX, by mass. The incorporation of SRA and LWS was shown to delay the drop in internal RH and facilitate the hydration reaction, thus promoting expansion potential of EX systems.
- The internal curing provided by LWS is substantially beneficial at elevating the compressive strength of mixture containing EXs when no IMCP is applied. The microstructural observation verified higher density and homogeneity of ITZ compared to similar mixture with only EX system.
- In the case of inadequate moist curing, the presence of LWS or SRA was found to be effective in enhancing the performance of OPC-CSA system. For a given overall desirability value of 0.65 determined by multi-objective optimization, the incorporation of 1% SRA or 10% LWS was found to reduce the required moist

curing duration of the OPC-CSA system from 6 days to 5 and 3 days, respectively.

- For a given moist curing duration and CSA-based EX content, the incorporation of 10% LWS or 1% SRA in OPC-CSA system was found to enhance the overall desirability function (in relation to shrinkage, material cost, and compressive strength) from 0.53 to 0.65 and 0.70, respectively. Therefore, the combined use of either LWS or SRA in OPC-CSA system can reduce the required period of moist curing and enhance the desirability value, thus indicating a greater overall performance.
- The synergistic effect between EX with LWS resulted in lower autogenous shrinkage or higher expansion magnitudes for a longer duration. This is attributed to the coupled effect of lower self-desiccation and larger expansion resulting from the use of LWS along with EX systems.

10.4. DEVELOPMENT OF ECO AND CRACK-FREE HPC

Based on the obtained results from previous phases, the effect of different binder compositions, aggregate characteristics, and shrinkage mitigating materials were evaluated and the results were analyzed to design Eco- and crack-free HPC for different targeted applications (Eco-Pave-Crete and Eco-Bridge-Crete). The influence of composition and resultant reaction of blended binders proportioned with high volume of SCMs on shrinkage and restrained shrinkage cracking of Eco-concrete was investigated.

- Mixtures provisioned with SCMs exhibited up to 60% longer time-to-cracking and developed 2.4 to 4.4 times larger tensile creep coefficient at the time of crack initiation compared to the control mixture without any SCM. Such spread can be attributed to: (i) resultant reaction and pozzolanic activity; and (ii) improved capillary porosity induced by SCMs, which can control the rate of elastic properties evolution and shrinkage at early- and later-age.
- The synergistic effect provided by the ternary combination of CFA and SL developed considerably higher tensile creep behavior and greater shrinkage cracking resistance compared to the binary blends of CFA or SL. Opposite trend was observed when SF incorporated in conjunction with CFA, reflecting lower

tensile creep coefficient and increased shrinkage cracking potential compared to the binary blend of CFA.

- Hydration kinetics of binder systems can be correlated with shrinkage cracking resistance and tensile creep behavior of the Eco-concrete. Binders with greater early-age hydration reaction tend to exhibit lower tensile creep behavior and larger rate of shrinkage-induced tensile stress, thus increasing the risk of shrinkage cracking potential. Such composition-reaction property correlations can provide insights into proportioning sustainable binders with the aim of high resistance to shrinkage cracking.
- The synergetic effect of the combination of shrinkage reducing materials, including LWS and EX coupled with fibers (synthetic fibers or recycled steel fibers) is quite effective to design low cracking potential concrete. The internal curing provided by the LWS can reduce the shrinkage and risk of early-age shrinkage cracking, especially for mixtures subjected to air drying without using any initial moist-curing.
- The incorporation of fibers (synthetic fibers and recycled steel fibers) in concrete containing a high volume of SCMs was shown to have 0 to 35% higher splitting tensile and flexural strengths than the control mixture made with 100% cement. The highest splitting tensile and flexural strengths were obtained for the mixture made with 35% recycled steel fibers containing 20% SL and 35% FA. This mixture also exhibited similar compressive strength to that of the control mixture.
- For a given fiber content, the use of steel fibers recovered from waste tires had two times higher flexural toughness compared to the similar mixture made with synthetic fibers. The reference mixture (100% OPC) made without any fibers developed the lowest ductility behavior and residual strength among all mixtures.
- The optimized Eco-HPC mixtures had lower drying shrinkage of 300 μstrain after 250 days of drying compared to 550 μstrain for the control mixture with 100% OPC. The incorporation of 7.5% CaO-based EX resulted in a significant early-age expansion of 100 μstrain followed by shrinkage of 200 μstrain after 250 days of drying.

- Eco-HPC mixtures made with proper combination of SCMs coupled with shrinkage mitigating materials can lead to crack-free properties with high resistance to shrinkage cracking. Based on the obtained results from this study, the use of 25% LWS or 7.5% CaO-based EX is quite effective in developing Eco-HPC with low risk of cracking.

10.5. PERFORMANCE VALIDATION OF ECO AND CRACK-FREE HPC

Large-scale concrete slabs were constructed to evaluate shrinkage of different optimized concrete mixtures and compare their performance with respect to the MoDOT reference mixture targeted for bridges. In addition, reinforced concrete beams were cast to evaluate the flexural strength of reinforced concrete beams made with optimized Eco-Bridge-Crete mixtures. The investigated mixture parameters include the incorporation of fibers, lightweight sand, expansive agent, and high volume of SCMs.

- The MoDOT control slab made with 25% FA replacement exhibited higher magnitude and rate of shrinkage compared to the optimized Eco-Bridge-Crete mixtures. This difference became more dominant for the top surface of concrete slab.
- The incorporation of 25% LWS was shown to be fully effective at reducing shrinkage rate and magnitude. The lowest relative humidity values observed for the FA25, SL20FA35-25LWS, and SL20FA35-7.5EX-0.35FRW mixtures were 82%, 96%, and 90%, respectively. This confirms that the combined use of SCM replacement and LWS can be fully beneficial at reducing shrinkage rate and magnitude.
- The shrinkage deformation values corresponding to such RH sensors were 80 μstrain shrinkage, 40 μstrain expansion, and 400 μstrain expansion for the FA25, SL20FA35-25LWS, and SL20FA35-7.5EX-0.35FRW mixtures, respectively, after 30 days of drying.
- All beams made with optimized concrete mixtures containing more than 50% SCM replacements exhibited equivalent or even higher ultimate flexural load than of the control beam made with MoDOT reference mixture containing 25% Class C FA.

- The inclusion of either structural synthetic fibers or recycled steel fibers was shown to substantially enhance the toughness of beam. The SL20FA35-7.5EX-0.35FT, SL60SF5-7.5EX-0.35FRW, and SL20FA35-7.5EX-0.35FRW concrete beams developed 120%, 135%, and 130% higher flexural toughness, respectively, compared to the control beam prepared with MoDOT reference mixture. The highest load carrying capacity was obtained for concrete beam made with 60% slag and 5% SF replacements having 0.35% recycled steel fibers.

10.6. FUTURE RESEARCH

Based on the scope and derived conclusions and findings from the present research work, the following aspects are recommended for the potential future investigations:

- In this study, the performance of the developed Eco-Pave-Crete and Eco-Bridge-Crete were evaluated through laboratory scale investigation and validated in large scale elements. However, for further validation, the performance (i.e., deformation and structural behavior) of such concretes should be verified under actual field conditions, such as pavement or bridge deck applications. The Missouri S&T research team is currently consulting with Missouri Department of Transportation (MoDOT) to finalize element type and location for the implementation of Eco and crack-free HPC mixture under field condition.
- The life cycle assessment and degree of sustainability of the Eco and crack-free HPC mixtures in comparison with reference concrete mixtures could be the scope of future research. The Missouri S&T research team is currently collaborating with New York University research team to evaluate the degree of sustainability and cost effectiveness of the Eco and crack-free HPC mixtures. The research is in progress with follow-up publications.
- In this research work, the effect of the dispersing admixture on mitigation of agglomeration of particles was only measured indirectly by measuring the packing density of particle structures. Implementing the effects of dispersants and morphological parameters of particles in the theoretical packing density models would be a valuable contribution.

- Test results presented and discussed in this investigation confirm the effectiveness of utilizing packing density approach for developing Eco-concrete materials. Further research is required to study the effectiveness of theoretical packing models and determining the proper packing parameters for HPC mixtures with low binder content to achieve optimal particle packing while maintaining adequate stability and flow characteristics.
- In this study, the performance of calcium sulfoaluminate-based and calcium oxide-based expansive agents as a partial replacement of ordinary Portland cement was evaluated. The expansion, hydration, and microstructural development of such expansive agents in the presence of calcium carbonate resulting from the use of Portland limestone cement would be of interest to improve both sustainability and performance of such materials.
- In this research, the synergy between fibers expansive cement was shown to enhance the mechanical properties and restrained shrinkage cracking. The underlying mechanism of such improvement can be partly due to the chemically pre-stressing condition provided by expansive cements. The further work would focus on understanding the mechanism of internal compressive pre-stressing effect under different degree of restraints.

APPENDIX A

APPLICATION OF MICROWAVE NON-DESTRUCTIVE TECHNIQUE TO EVALUATE STEEL FIBER DISTRIBUTION IN CEMENT-BASED MORTARS

INTRODUCTION

Fibers are commonly introduced in cement-based materials to reduce tendency for cracking, improve post-cracking response, and enhance energy absorption (Rossi 1992; Grünewald and Walraven 2001; Khayat and Roussel 2000; Khayat et al. 2014). However, the interaction between fibers and concrete constitutive materials can reduce workability and increase the amount of energy needed for placement, consolidation, and finishing of fiber-reinforced cement-based materials. The effectiveness of incorporating fibers to enhance mechanical characteristics of cement-based materials is strongly influenced by the level of fiber distribution (Soroushian and Lee 1990; Gettu et al. 2005; Ferrara and Meda 2006; Özyurt et al. 2007; Ferrara et al. 2008; Martinie et al. 2010; Kang et al. 2011; Akcay and Tasdemir 2012; Di Prisco et al. 2013; Mehdipour et al. 2013; Emdadi et al. 2015). Most of the existing performance models assume that fibers have a uniform spatial distribution throughout the sample. Contrary to this assumption, a non-uniform fiber distribution can lead to mechanical anisotropy, thus resulting in undesirable and unpredictable variability in mechanical properties. Kang et al. (2011) pointed out that the measured flexural strength of fiber-reinforced concrete is significantly lower compared to the predicted flexural strength, when fibers are non-uniformly distributed. Mehdipour et al. (2013) identified critical limits for fiber content, which can affect workability and mechanical properties of fiber-reinforced cement-based mortar (FRCM). In the case of relatively low fiber content, the workability of FRCM may not be adversely affected, given the lower level of potential interaction and relatively larger spacing among the fibers. The interaction among fibers increases as the fiber content increases, which leads to a reduction in workability. On the other hand, beyond a critical threshold, the contact between fibers can substantially increase, resulting in the potential for formation of fiber clumping (or fiber balling). Fiber clumping leads to non-uniform fiber distribution within the mixture, resulting in significant reduction in workability and mechanical properties. The tendency for fiber clumping in the fresh state of a mixture was found to be affected by several parameters, such as maximum size and overall gradation of the coarse aggregates, fiber content and aspect ratio (length to diameter ratio), mixing method, and casting procedure (Gettu et al. 2005; Ferrara and Meda 2006; Özyurt et al. 2007; Ferrara et al. 2008; Martinie et al. 2010; Mehdipour et al. 2013; Emdadi et al. 2015).

Various destructive and nondestructive testing (NDT) methods have been developed to evaluate the level of uniformity of fiber distribution in hardened FRCM. The most common approach for evaluating fiber distribution involves drilling a core, crushing it, and then counting the number of present fibers. This technique is destructive, time consuming, and is a localized test so that the results cannot be generalized to the entire structure (Gettu et al. 2005; Kang et al. 2011). Alternatively, a number of NDT techniques have been utilized to assess level of uniformity in fiber distribution in FRCM, including X-ray tomography (Redon et al. 1999; Suuronen et al. 2013; Bordelon and Roesler 2014; Ponikiewski and Katzer 2015), image processing technique (Kang et al. 2011; Ferrara et al. 2011; Akcay and Tasdemir et al. 2012), electrical resistivity (Lataste et al. 2008; Barnett et al. 2010), alternating-current impedance spectroscopy (AC-IS) [Özyurt et al. 2006a; Özyurt et al. 2006b], infrared thermography (Keo et al. 2014), and magnetic method (Orbe et al. 2012; Ferrara et al. 2012; Orbe et al. 2014).

Extensive works in using near-field microwave reflectometry has shown it to be an effective NDT tool for evaluating and characterizing material constituents of cement-based materials. In this method, a microwave signal interacts with material media at the molecular (i.e., chemical properties, water-to-cement ratio (*w/c*), curing state and condition, etc.) and physical (sand-to-cement ratio (*s/c*), coarse aggregate-to-cement ratio (*ca/c*), aggregate grade, etc.) levels (Sihvola 1999). As microwave signals reflect from dielectric materials, their signal properties (magnitude and phase) change as function of parameters, including material constituents dielectric properties, their individual volume contents, and their level of homogeneity (Zoughi 2000). In these works, the magnitude of reflection coefficient, $|\Gamma|$, of microwave signals conducted at different operating frequencies has been shown to correlate well with the properties mentioned above.

Thermography is a well-established NDT method which is used extensively for structural health monitoring with numerous benefits, including noncontact inspection, fast, readily available high-sensitivity cameras, and easy-to-interpret results (Maldague and Marinetti 1996; Meola and Giovanni 2004; Valluzzi et al. 2009). However, thermography often requires the application of high thermal energy over a short period of time, which results in a sudden temperature rise (e.g., greater than ~15 °K) [Meola and Giovanni 2004]. Such temperature increases may risk damaging the material under test.

Hence, in order to overcome this risk and improve the method as an efficient NDT tool, microwave NDT has been integrated with thermography, herein referred to as active microwave thermography (AMT) [Foudazi et al. 2014a, b; Foudazi et al. 2015a, b]. AMT utilizes the combination of microwave energy to generate controlled and localized heating and commercially-available infrared (thermal) cameras to capture surface thermal images of a structure under test in real-time. AMT has shown potential as an NDT solution for various applications in the transportation and aerospace industries, including detection of delamination and debonding in structures rehabilitated with carbon fiber reinforced composites (Foudazi et al. 2014a, b), as well as corrosion detection in steel-based materials (Foudazi et al. 2015a).

The subject of this study is to nondestructively evaluate the steel fiber distribution in FRCM using two different approaches: (i) near-field microwave reflectometry and (ii) active microwave thermography (AMT). The statistical properties of microwave reflection properties ($|\Gamma|$) at different operating frequencies (3 and 10 GHz) were used to evaluate fiber content and distribution for FRCM samples made with various steel fiber contents ranging from 0 to 3%. In order to assess the sensitivity of different frequencies to the fiber content and distribution, AMT measurements were conducted at 2, 2.4, and 3 GHz. Full-wave coupled electromagnetic-thermal numerical modeling was also conducted to evaluate the effect of dielectric properties, fiber depth, and clumping of fibers on the surface thermal profile. Furthermore, the effect of fiber addition on flow consistency, packing density, fiber homogeneity along the freshly cast prism, and hardened properties of FRCMs were assessed, and the results were correlated with those obtained from microwave measurements and image analysis on the hardened samples.

EXPERIMENTAL APPROACH

Materials and Mixture Proportions. A Type I/II OPC and a well-graded siliceous sand with maximum aggregate size of 4 mm were used for all mixtures.

Hooked-end steel fibers with lengths of 30 mm and diameters of 0.55 mm, specific gravity of 7.87, and tensile strength of 1500 MPa were employed. In total, four mortar mixtures were prepared, including a control mixture made without any fibers and three mixtures with fiber contents of 1%, 2%, and 3%. All of the investigated mixtures

were proportioned with a fixed *w/c* of 0.45 and *s/c* of 2.5. No chemical admixture was added. This was intentionally done to reduce the flow consistency of the mixtures as a function of increasing the fiber content. The reduction in flow consistency increases the risk of non-uniform distribution of fibers throughout the sample. This can consequently enhance the potential for detecting fiber clumping using the proposed microwave NDT technique.

The mixing sequence consisted of homogenizing the sand for 30 seconds before introducing half of the mixing water. Cement was then added and mixed for 30 seconds followed by the remaining water. The fibers were gradually introduced, and the mixture was mixed for 3 minutes and kept at rest for 2 minutes before remixing for 3 minutes. Visual observation during mixing indicated that mortar made with 3% fiber content exhibited instability signs of fiber clumping and bleeding.

Test Methods.

Fresh and hardened properties. The effect of fiber addition on packing density (ϕ) of the dry mixture containing sand and steel fibers was determined in accordance with ASTM C29. Subsequently, the results of the packing density were used to determine the void fraction (1-ϕ) of the investigated FRCMs.The flow consistency of mortars was determined using the flow table test in accordance with ASTM C1437. The flow (*F*, %) is calculated as the percentage of the difference between the spread diameter of the mortar after 25 drops and the original base diameter divided by the latter value.

For the investigated FRCMs, the homogeneity of fiber content along a cast prism was quantitatively evaluated in the fresh state. This method involves measuring the variation of fiber concentration along a cast prism measuring 75 × 75 × 285 mm^3. The sequence of casting and measurement procedure is schematically illustrated in Figure A-1. It involves the casting of the FRCM in the prismatic sample parallel to the longitudinal direction. This is followed by inserting the thin metal plates into the plastic mixture, shortly after casting, to divide the prism into four zones. Each zone measured approximately 70 mm in length. The content of FRCM corresponding to each section was weighed, then washed out on a 75 μm sieve to determine the fiber content retained on the sieve. The variation in fiber content throughout the mixture was quantified by determining the inhomogeneity index (*IHI*, %). The *IHI* was taken as the coefficient of

variation (COV) of the fiber contents corresponding to four zones along the cast prism, which is expressed as follows:

$$IHI(\%) = \frac{\sqrt{\frac{1}{4}\sum_{i=1}^{4}(M_{Fi} - M_{Fave})^2}}{M_{Fave}} \times 100 \quad \text{A-1}$$

where M_{Fi} refers to the fiber content in each zone, and M_{Fave} represents the average fiber content corresponding to all four zones along the cast prism. The calculation of COV enables determination of the level of fiber homogeneity along the cast prism for a given FRCM. A higher COV value reflects lower level of fiber homogeneity throughout the mixture.

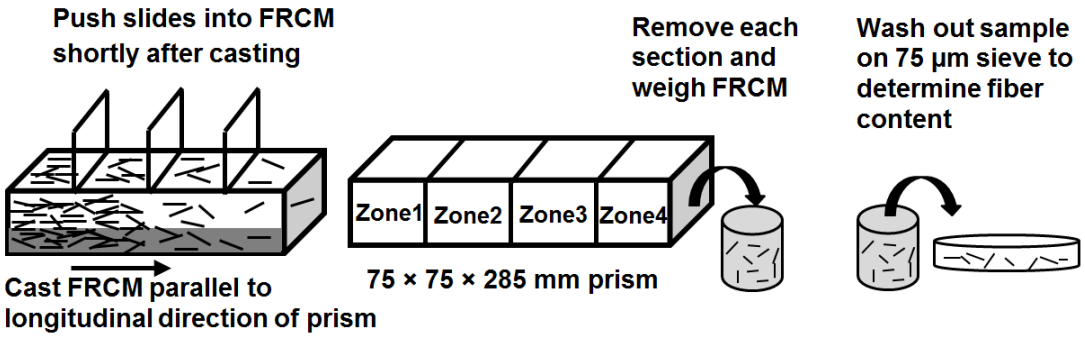

Figure A-1 Schematic illustration of fiber homogeneity evaluation along cast prism in fresh state

Cylindrical samples measuring 100 mm in diameter and 200 mm in length were cast to determine the compressive (ASTM C39) and splitting tensile (ASTM C496) strengths. Prismatic samples measuring 75 × 75 × 400 mm^3 were tested to determine the peak flexural strength and toughness of FRCM in accordance with ASTM C1609. All samples were cast in two layers, and consolidated on a vibrating table for 30 seconds. After demolding at 24 hours, all samples were subjected to standard moist-curing (23 ± 1 °C and 100% RH) until the age of testing at 28 days. The results of mechanical properties reported here represent the mean values of three samples.

MICROWAVE REFLECTION MEASUREMENT

The microwave reflection measurements were conducted on FRCM samples measuring 200 × 200 × 200 mm^3. The dimensions of the samples were selected to be sufficiently large to ensure that the microwave signal penetration depth at the evaluated operating frequencies is less than the thickness of the sample (Bois et al. 1997), so that backside of the sample did not contribute to the measured reflection coefficient. After demolding at 24 hours, all samples were moist cured for 48 hours using a wet burlap. The samples were then dried in an oven at a temperature of 110 ± 5 °C for three days. This was done to remove some of the free water particularly near the surface sides of the sample. Following oven drying, all samples were stored in a temperature and humidity controlled room at 23 ± 2 °C and 30% ± 5% RH until the age of microwave measurement at 14 days. The microwave measurements were conducted using an open-ended rectangular waveguide (OERW) probe along with an HP8510C vector network analyzer (VNA), as shown in Figure A-2. An OERW is a linearly polarized probe suitable for the type of measurements required in this investigation (Zoughi 2000). The VNA transmits the microwave signal through the OERW and measures the reflected signal received by the OERW to determine |Γ| (i.e., the complex ratio of these two signals).

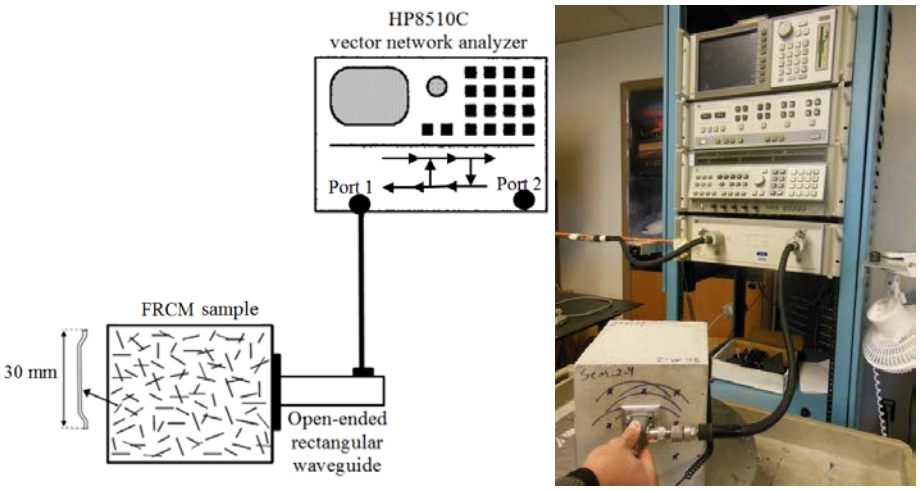

Figure A-2 Microwave measurement test setup.

The microwave measurements were conducted across the four sides of the samples (excluding top and bottom surfaces) at S-band (2.6-3.95 GHz) and X-band (8.2-

12.4 GHz) frequency ranges. The analysis of the microwave measured results reported in this study was performed for two frequencies of 3 GHz (S-band) and 10 GHz (X-band), representing each frequency band. Signal wavelengths in air at 3 and 10 GHz correspond to 100 and 30 mm, respectively. These values are affected by the dielectric properties of the mortar at these frequencies (Bois et al. 1998). Generally, dielectric materials are defined by their complex relative (to free-space) dielectric constant (ε_r) as follows:

$$\varepsilon_r = \varepsilon_r' - \mathrm{j}\varepsilon_r'' \tag{A-2}$$

where ε_r' (real part) and ε_r'' (imaginary part)refer to the permittivity and loss factor, respectively. Permittivity represents the ability of a material to store microwave energy, and loss factor refers to the ability of the material to absorb microwave energy. Using the measured complex reflection coefficient of the reference sample, its complex dielectric constant was calculated to be ε_r = 4.8 – j0.2 (Ghasr et al. 2009). These values correspond to wavelength values of ~45 and ~13 mm at 3 and 10 GHz, respectively, in the mortar medium (Ulaby et al. 1986). The wavelengths of ~13 and ~45 mm are equal to half and three halves, respectively, of the fiber length of 30 mm used in this investigation.

It is noted that that microwave reflection properties are obtained from the volume of the test sample. The depth of penetration of power (δ_P) is a function of dielectric properties and distance from the surface of the sample, which can be expressed as follows (Ulaby et al. 1986):

$$\delta_P(m) = \frac{1}{\kappa_a} \tag{A-3}$$

where κ_a is the power absorption coefficient, which is calculated as follows:

$$\kappa_a = 2 \times \alpha = 2\left(\frac{2\pi f}{c}\left|\mathrm{Im}\left\{\sqrt{\varepsilon_r}\right\}\right|\right) \tag{A-4}$$

where α refers to absorption constant of medium (Np/m), f is the operating frequency (Hz), c is the speed of light (3×10^8 m/s). $\mathrm{Im}\left\{\sqrt{\varepsilon_r}\right\}$ represents the imaginary part of square root of dielectric constant. As deduced from Eqs. (3) and (4), higher operating frequency can lead to lower depth of penetration of power in the dielectric materials. Considering the dielectric constant calculated for reference sample and using Eqs. (3) and (4), the

penetration depth of power at operating frequencies of 3 and 10 GHz in mortar medium is estimated to be ~160 and ~45 mm, respectively. Therefore, this confirms that the microwave signals are remained in the mortar medium and all microwave measurement results reported in this investigation are isolated from air interference (i.e., the back surface of the sample).

In order to determine the mean and COV of $|\Gamma|$, each surface was divided into five and nine equivalent zones with respect to the probe dimensions used for operating frequencies at 3 and 10 GHz, respectively. In total, 20 [4 (surfaces) × 5 (points)] and 36 [4 (surfaces) × 9 (points)] measurements were conducted on each sample at 3 and 10 GHz, respectively. At 3 GHz, the size of the probe in use is 72.1 × 34 mm^2, which is three times larger than the size of 10 GHz probe with dimensions of 22.28 × 10.1 mm^2. The large probe size used for 3 GHz (S-band) limits the number of measurements conducted on each surface to five points compared to nine points on each surface of test sample when using smaller probe at 10 GHz (X-band). The number of measurements and spacing between data points were adjusted to ensure that the measured $|\Gamma|$ results are statistically independent, so no overlapping areas were examined on any of the samples. The measured results at 10 GHz were then passed through the three-dimensional synthetic aperture radar (SAR) algorithm to produce a three-dimensional microwave image of the entire FRCM sample, as outlined in (Case et al. 2011).

IMAGE ANALYSIS

In order to verify the microwave NDT results, image analysis was carried out on the same samples that were used for microwave measurements. Each surface of the FRCM samples was vertically cut, as illustrated in Figure A-3(a). For each sample, four different surfaces were cut at various distances from the sides corresponding to 10, 20, 30, and 40 mm, as illustrated in Figure A-3(a).

In order to compare the results with microwave measurements, image analysis was conducted on different thicknesses to assess the variation of fiber distribution with sample depth. In order to enhance the contrast between the fibers and the matrix, the cut surfaces were polished and cleaned using acetone. A high-resolution digital camera was then used to capture a RGB (red, green, blue) picture from each cut plane (Figure A-

4(a)). The RGB image was converted to a grayscale image, and then was transformed to a binary image based on a set threshold object detection method (Figure A-4(b)). The obtained image was processed using FIJI image processing and analysis software (Rasband 1997–2012) to determine the number of fibers appeared on each surface.

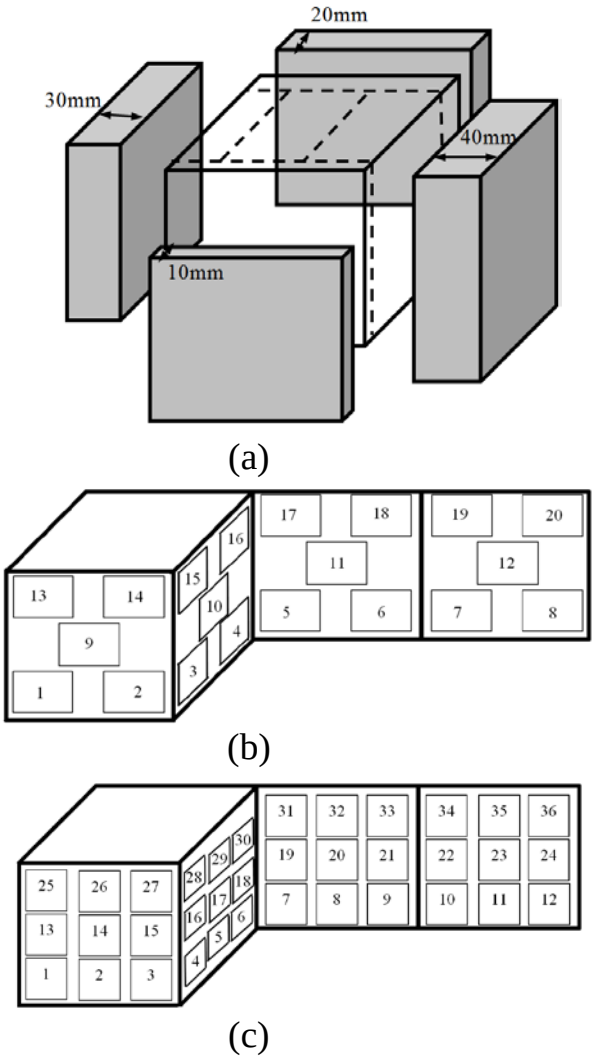

Figure A-3 Schematic illustration of cut surfaces and zones used for image analysis of FRCM samples: (a) cut surfaces at different depths of FRCM samples, (b) 20 measurement zones (80 × 50 mm^2) adapted for operating frequency at 3 GHz, and (c) 36 measurement zones (30 × 30 mm^2) adapted for operating frequency at 10 GHz.

In order to quantitatively evaluate the level of fiber distribution, for each cut surface the fiber density (F_{Ni}) and COV of fiber density (COV_F) were calculated. As shown in Figure A-3(b) and (c), in order to compare the results with microwave

measurements, the surface of each cut surface was divided into either five zones (80 × 50 mm^2) or nine zones (30 × 30 mm^2) that were identical to microwave measurements carried out at 3 and 10 GHz, respectively. For each surface, the F_{Ni}, corresponding to the number of fibers located in each zone (five or nine zones per cut surface), and the COV_F corresponding to all zones of the investigated sample (20 or 36 zones per sample), were determined, as follows:

$$F_{Ni} = \frac{N_i}{A_i} \tag{A-5}$$

$$COV_F\,(\%) = \frac{\sqrt{\frac{1}{n}\sum_{i=1}^{n}(F_{Ni} - F_{N\,ave})^2}}{F_{N\,ave}} \times 100 \tag{A-6}$$

where F_{Ni} refers to the number of fiber located in each zone and A_i is the area of the investigated zone (30 × 30 mm^2 or 80 × 50 mm^2). F_{Nave} represents the average fiber density corresponding to all zones for a FRCM sample. *n* is the number of zones for each investigated FRCM sample, which was taken as 20 and 36 corresponding to operating frequencies at 3 and 10 GHz, respectively.

Therefore, larger COV_F value represents higher non-uniformity of fiber distribution (i.e., lower level of fiber distribution).

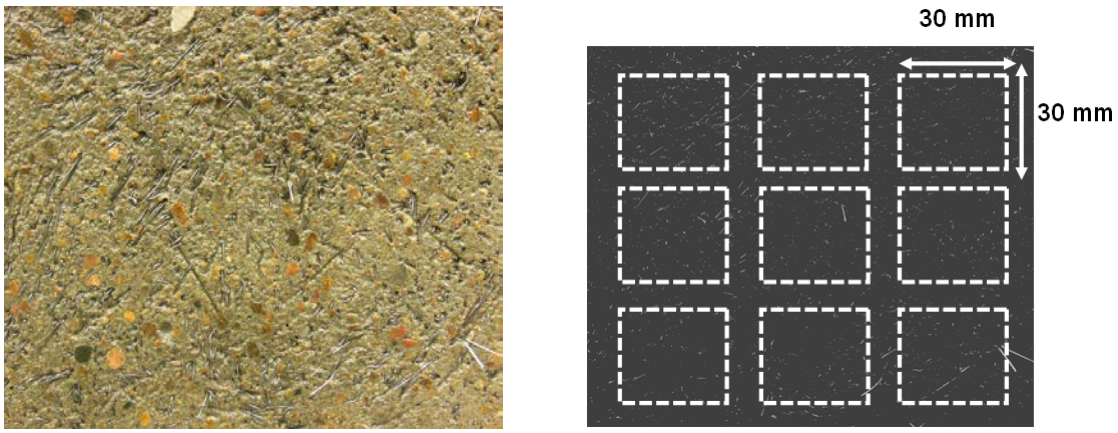

(a) (b)

Figure A-4 Image processing procedure to evaluate fiber density along various surfaces of FRCM samples: (a) RGB image of FRCM surface and (b) threshold function in binary image of FRCM surface.

ACTIVE MICROWAVE THERMOGRAPHY—PRINCIPLES

As mentioned above, AMT is based on the integration of microwave and thermographic NDT techniques. As AMT utilizes a microwave heat excitation, two different heating mechanisms can be generated depending on the material properties of the structure under test. The first heating mechanism is based on dielectric heating which takes place due to the interaction between dielectric materials (i.e., non-conducting materials) and incident electromagnetic energy. The amount of (dielectric) heat generated for a given material is related to the loss factor, operating frequency, and incident power. Assuming a plane-wave excitation (i.e., a uniform electric field with a constant phase front/no phase variation) with an (initial) magnitude of E_0 irradiated toward the dielectric material, the magnitude of this incident signal, $E(z)$, a distance of z from the surface of the dielectric is expressed as:

$$E(z) = E_0 e^{-\alpha z} \tag{A-7}$$

where α represents the attenuation constant (Np/m) which is calculated as follows:

$$\alpha = \frac{\omega}{c}\sqrt{\frac{\mu_r \varepsilon_r'}{2}\left[\sqrt{1+\left(\frac{\varepsilon_r''}{\varepsilon_r'}\right)^2}-1\right]} \tag{A-8}$$

where $\omega = 2\pi f$ (rad/m), f is the operating frequency (Hz), c is the speed of light (3×10^8 m/s), and μ_r is the relative magnetic permeability (μ_r = 1 for dielectric/non-magnetic materials). As shown in Eq. (3), higher operating frequency or loss factor can lead to increased attenuation of the incident wave in the dielectric material. Knowing the magnitude of the incident electric field ($|E|$) inside the dielectric material (at any point) allows for the dissipation of electromagnetic energy, Q (W/m^3) in the material to be determined as follows:

$$Q = \omega\, \varepsilon_0\, \varepsilon_r''\, |E|^2 \tag{A-9}$$

where ε_0 is the dielectric constant of free-space (8.854×10^{-12} F/m). The energy dissipated inside the dielectric material is subsequently related to a change (with respect to time and space) in temperature (i.e., heat generation) based on the heat transfer equation, expressed as:

$$\rho C \frac{\partial T}{\partial t} = k \frac{\partial^2 T}{\partial^2 z} + Q \tag{A-10}$$

where ρ is the density (kg/m^3), C is the specific heat (J/g.K), k is thermal conductivity (W/m.K), T is temperature (K) and t is time (sec). The second heating mechanism in AMT occurs when conductive materials are present. As outlined in (Meola and Giovanni 2004; Foudazi et al. 2014a), when a conductor is irradiated with electromagnetic energy, surface currents (J) are induced on the conductor. Such surface currents serve as a secondary source of radiated electromagnetic energy which can generate an additional (secondary) source of heat. When a conductor is embedded within a lossy dielectric material (i.e., $\varepsilon_r'' \neq 0$), these surface currents will cause an increase in the concentration of electromagnetic energy (as compared to areas without a conductor). Hence, through Eq. (5), the presence of embedded conductors inside lossy dielectric materials will cause an increase in heat and subsequent temperature.

In this study, since steel fibers (an electrically conductive material) are distributed inside the mortar (a lossy dielectric material), the potential for both heating mechanisms exists. More specifically, when an FRCM is illuminated with electromagnetic energy, the material will experience (volumetric) dielectric heating as the electromagnetic energy propagates into the material. Furthermore, at the location of steel fibers, the induced surface current leads to an additional increase in temperature. The variation in surface temperature can be utilized to distinguish areas with fibers from those without fibers. Further, the variation in surface temperature is dependent on the fiber characteristics (length and volume), depth of fibers (from the surface), etc. For a given fiber distribution, fibers located further from the surface could experience less induced surface current due to the increased attenuation of the incident electromagnetic energy. Thus, those fibers could contribute less to the temperature variation on the surface.

AMT Measurements. The AMT measurements were conducted on FRCM samples with dimensions of 200 × 200 × 200 mm. After demolding at 24 hours, samples were stored in a temperature and humidity controlled room at 23 ± 2 °C and 35% ± 5% RH until the age of AMT measurement at 28 days.

The AMT measurement test setup is schematically illustrated in Figure A-5. A signal generator was utilized to produce a microwave signal at the desired frequency. The power level was amplified using a 50 W power amplifier. The microwave energy was radiated toward the FRCM sample using a horn antenna. The horn antenna is capable of

handling high power microwave signals as well as concentrating the microwave energy toward the surface of the sample and providing a relatively uniform microwave excitation (similar to a plane wave). In order to measure the surface thermal profile, a DRS Tamarisk 320 thermal camera was utilized. Each measurement included 30 sec of microwave illumination followed by an additional 90 sec of thermal measurements (i.e., measurements continued during the cooling period).

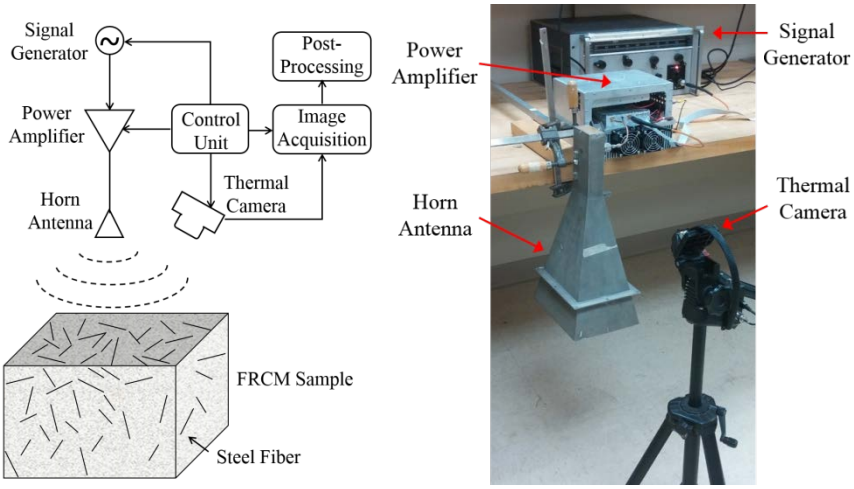

Figure A-5 AMT measurement test setup.

The AMT measurements were conducted on the four sides of the samples, excluding the top and bottom surfaces (since these surfaces have some roughness which may affect the AMT results). Considering a frequency of 2.4 GHz (midpoint of the frequencies utilized here) and a mortar with permittivity of 4.8, the wavelength in air and mortar is 125 mm and 57 mm, respectively. Thus at this frequency, the length of steel fiber (30 mm) is near the resonant length (i.e., half of the wavelength of the signal in mortar, 28 mm), and the maximum current distribution on the fiber surface will be induced. For areas containing steel fibers, the induced surface current on the steel fibers contribute to a larger temperature difference (as explained above). As such, it is expected that the temperature will increase with increasing volume content of steel fibers.

An illustration of the thermal image acquisition process is shown in Figure A-6. The temperature profile was acquired at a rate of 1/30 sec, resulting in a frames-per-second rate of 1/30. All acquired frames, $T(t)$, were subtracted from the first frame (i.e.,

ambient condition, *T(0)*) in order to highlight the temperature changes taking place during testing. As shown in Figure A-6, initially a temperature difference of zero is measured (as for the first measured frame, no microwave heating has taken place) for all measurement points (example measurement points shown as *u*, *v*, and *w* in Figure A-6). Then, after the microwave illumination begins, the temperature difference increases. In the zone surrounding point *u*, the concentration of fibers is higher than those near points *v* and *w*. As a result, the temperature difference in zone *u* will be larger, as illustrated in Figure A-6. Also, the zone near point *v* will experience a greater temperature difference than areas with no fibers (i.e., around point *w*). Additionally, the temperature difference decreases after the microwave excitation is removed (during the cooling period) for all points.

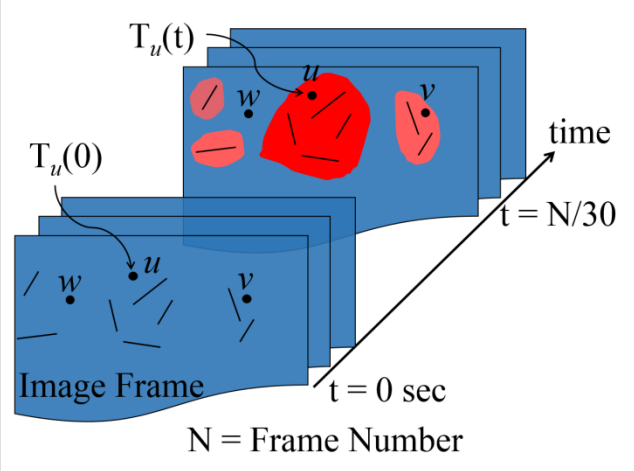

Figure A-6 Illustration of image acquisition.

In order to quantitatively evaluate the fiber distribution along the surface of an FRCM sample, the middle portion of each surface can be divided into few equivalent zones, and the results of each zone can be used to evaluate fiber distribution. The mean temperature at time *t* for the corresponding surface (*s*) and zone (*z*), $\mu_{Zone}(s,z,t)$, can be calculated as follows:

$$\mu_{Zone}(s,z,t) = \frac{1}{N_P}\sum_{p=1}^{N_P}\Delta T_p(t) \qquad \text{A-11}$$

where $\Delta T_p(t)$ is the temperature difference at pixel *p* and time *t*, and N_P refers to total number of pixels for a corresponding zone. Then, the overall mean of the temperature difference of each sample ($\mu_{total}(t)$) can be expressed as follows:

$$\mu_{total}(t) = \frac{1}{N_S N_Z} \sum_{s=1}^{N_S} \sum_{z=1}^{N_Z} \mu_{Zone}(s,z,t) \qquad \text{A-12}$$

where N_Z and N_S refer to the number of zones and surfaces, respectively, of each tested sample. Since the presence of fiber affects the surface temperature (through induced surface current mechanism), a comparison of mean values ($\mu_{Zone}(s,z,t)$) of each zone across the surface may provide an indication of the fiber distribution of test sample. Thus, it is expected that the concentration of fibers can be quantitatively evaluated by analyzing the mean of the temperature difference at each zone.

FRESH AND MECHANICAL PROPERTIES

The effect of fiber addition on flow consistency and void content on the investigated FRCMs is shown in Figure A-7. The incorporation of steel fibers led to lower flow consistency and higher void content for all samples. The increase in fiber content from 0% to 3% resulted in 82% lower flow and 30% higher void content compared to the reference mixture. A significant drop in flow consistency was observed for FRCM containing 3% steel fiber. This can be attributed to the relatively high interaction among the fibers and potential formation of fiber clumping.

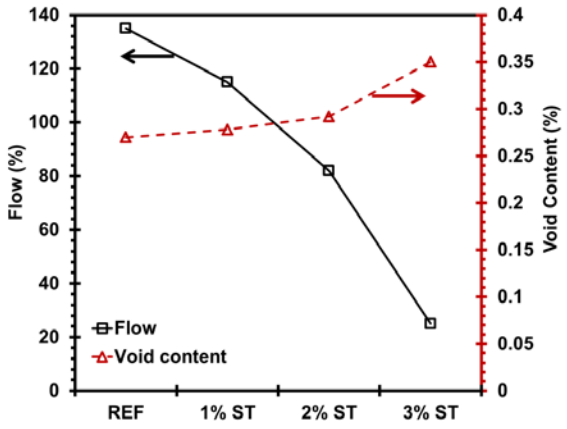

Figure A-7 Effect of fiber addition on flow consistency and void content of FRCM.

Figure A-8 shows the flow consistency of FRCMs after 25 drops in the flow table test. For mixture made with 3% fiber content, fibers tended to entangle together and formed clumps at the center of the flow spread, as shown in Figure A-8(d). A layer of water also appeared on the outer edge of this mixture at the end of stump test, indicating low level of stability.

(a) (b) (c) (d)

Figure A-8 Flow consistency of FRCM made with various fiber contents for (a) REF, (b) 1% ST, (c) 2% ST, and (d) 3% ST.

Figure A-9 illustrates the normalized mechanical properties of the investigated FRCMs using star-plot approach. The investigated mechanical properties included compressive, splitting tensile, and flexural strengths as well as toughness. In the star-plot approach used in this study, each branch represented a given mechanical property. To better explain the experimental data, all results were normalized by diving each to their corresponding maximum value for given mechanical property, and the overall mechanical performance (unitless) for each mortar mixture was calculated as the area of its corresponding close-loop-area in the tetragonal plots (Figure A-9). Therefore, the smallest and largest close-loop-areas represent the lowest and highest performing mixtures, respectively. The addition of steel fibers increased the overall mechanical performance up to a certain threshold value, beyond which the overall performance reduced with further fiber addition. The increase in fiber content from 0% to 1% and 2% resulted in 250% and 445% improvement in the overall performance, respectively. On the other hand, for the mixture made with 3% steel fiber, this trend was reversed. This mixture exhibited 25% lower mechanical performance compared to mixture containing 2% fiber content. This is attributed to the potential formation of fiber clumping and non-uniform fiber distribution in this mixture as well as lack of proper consolidation. Fiber

clumping can reduce the reinforcing mechanism provided by fibers to transfer stress, thus resulting in a significant drop in mechanical properties (Mehdipour 2013; Emdadi et al. 2015). It is important to note that the entrapment of air bubbles between fiber clumps can also reduce the bond strength and weaken the interfacial transition zone between fibers and matrix (Khayat et al. 2014; Emdadi et al. 2015).

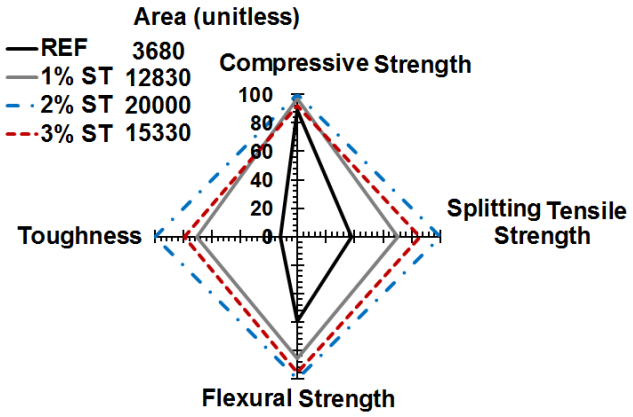

Figure A-9 Overall mechanical performance of FRCM (All results were normalized by diving each to their corresponding maximum value for given mechanical property. Overall mechanical performance (unitless) for each mortar mixture was calculated as the area of its corresponding close-loop-area in the tetragonal plots.).

MICROWAVE REFLECTION RESULTS

Figure A-10 depicts the variation in |Γ| and fiber density determined from microwave measurement and image analysis, respectively, across different zones. It is noted that the zone numbers of each sample were arranged in order of bottom, middle, and top parts of sample. For operating frequency of 3 GHz, zones 1–8, 9–12, and 13–20 correspond to bottom, middle, and top parts, respectively, of the investigated sample, as shown in Figure A-3(b). In the case of 10 GHz, zones 1–12, 13–24, and 25–36 represent bottom, middle, and top parts, respectively, as shown in Figure A-3(c). Therefore, the order of zone numbers was arranged to evaluate the variation of test results along the height of FRCM samples, as indicated in Figure A-10. Given the relatively homogeneous nature of sample made without any fibers, the majority of |Γ| measurements lie within the narrow range, especially at operating frequency of 3 GHz. Compared to 3 GHz, the measured |Γ| values for the reference sample were shown to have higher variation at 10

GHz. It is important to point out that measurement conducted at higher frequencies (smaller wavelength) is more sensitive to the level of inhomogeneity of sample caused by air (i.e., larger sample porosity) and sand particles.

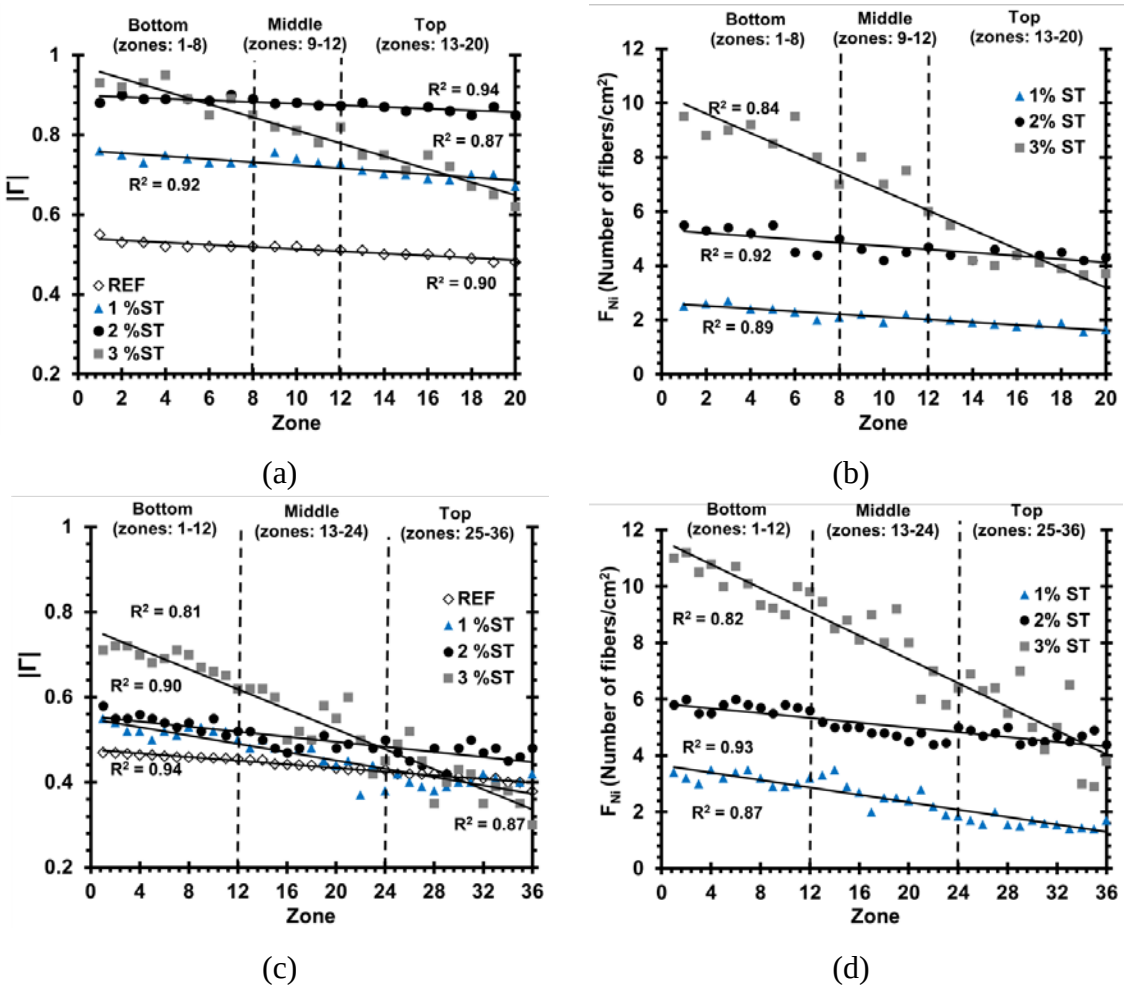

Figure A-10 Effect of fiber addition on microwave reflection properties and fiber density for FRCM samples made with different fiber contents: (a) |Γ| at 3 GHz determined from microwave NDT (20 zones), (b) fiber density determined from image analysis (20 zones), (c) |Γ| at 10 GHz determined from microwave NDT (36 zones), and (d) fiber density determined from image analysis (36 zones).

The addition of fibers resulted in significantly higher variation in |Γ| compared to the reference sample, especially at 10 GHz. The incorporation of fibers causes point-to-point measurement variations due to the scattering of the microwave signals by the fibers. This scattering is expected to be more significant at higher microwave frequencies, where

the exciting wavelength is comparable with (or smaller than) the dimension of the fibers. The highest variation in |Γ| and fiber density was obtained for the sample with 3% steel fiber. These values varied between 0.30–0.72 for |Γ| (at 10 GHz) and 3–11 for fiber density, ensuring the fact that fibers are non-uniformly distributed in this sample. It is interesting to note that for the sample made with 3% fibers, the highest and lowest values of |Γ| and fiber density were obtained for bottom (zones 1-12) and top (zones 25-36) parts of the sample, respectively, especially at higher operating frequency. Unlike the samples made with 1% and 2% fiber content, the results of fiber density and microwave reflection properties were shown to be varied with the height of sample with 3% fiber. This reflects the fact that majority of fibers was located at the bottom of sample, thus indicating relatively higher fiber density and reflection properties values. However, samples made with 1% and 2% steel fibers exhibited approximately uniform reflection coefficient and fiber density across the zones, thus indicating relatively homogenous nature and uniform fiber distribution. It should be noted that for the investigated FRCM samples, similar trends were found between the results of |Γ| from microwave measurement and fiber density determined from image analysis on hardened samples, corroborating the sensitivity of the microwave reflection properties to fiber distribution.

Figure A-11(a) shows the variation in mean of |Γ| as a function of fiber content at different operating frequencies. Unlike for 10 GHz, the mean of |Γ| at 3 GHz was shown to be significantly affected by the fiber addition. Regardless of fiber content, all samples made with fibers resulted in higher |Γ| values compared to the reference sample. An increase in the fiber content from 0 to 1% and 2% resulted in 62% and 93% higher |Γ| values, respectively. However, no significant change in |Γ| was observed with fiber addition at 10 GHz. This suggests that microwave measurement conducted at 3 GHz can be an indication of fiber content. As the fiber content increases the |Γ| measured at 3 GHz increases, except for sample with potential formation of fiber clumping and non-uniform fiber distribution.

At 3 GHz, sample containing 3% steel fiber exhibited 12% lower |Γ| compared to the sample made with 2% steel fiber. As shown in Figure A-10, some zones for sample with 3% fiber content exhibited lower values of reflection properties and fiber density compared to the sample containing 2% steel fibers. This is primarily due to the fact that

as a result of fiber clumping some regions contained less number of fibers and hence increasing the inhomogeneity level in this sample.

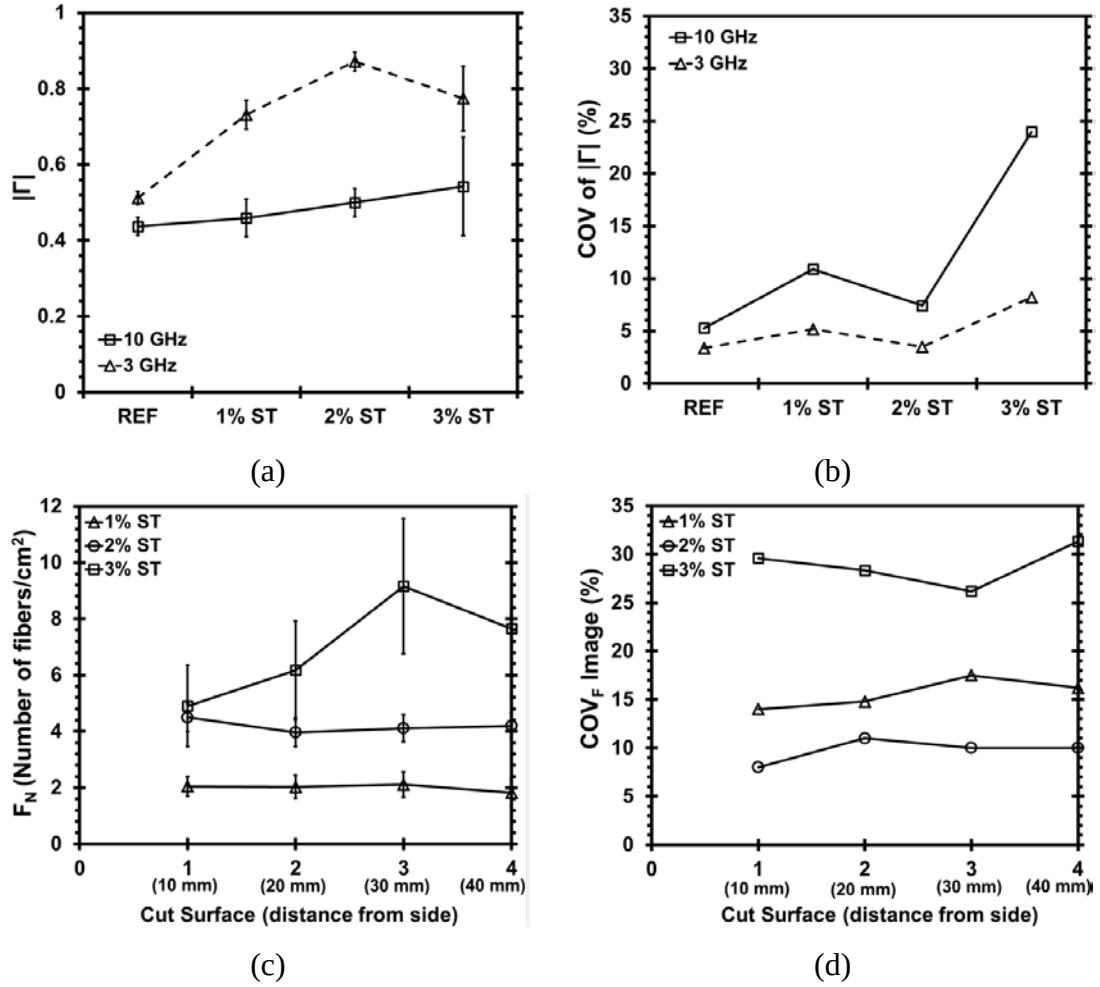

Figure A-11 Variations in |Γ| and fiber density for FRCM samples made with different fiber contents: (a) mean of |Γ| determined from microwave NDT, (b) COV of |Γ| determined from microwave NDT, (c) mean of fiber density obtained from image analysis, and (d) COV of fiber density obtained from image analysis.

The highest variation in reflection properties was observed for sample with 3% fiber content. As shown in Figure A-11(b), the COV of |Γ| for sample made with 3% fiber content was approximately two and three times higher than that of the sample containing 2% fiber volume at operating frequencies of 3 and 10 GHz, respectively. As mentioned earlier, the microwave measurements at higher operating frequency is more sensitive to the level of inhomogeneity of medium, thus leading to larger variation in |Γ|. The fiber

clumping formation and lower level of fiber homogeneity for sample with 3% fiber resulted in higher scattered signal by the fibers. Among the FRCM samples, the lowest variation in |Γ| was obtained for sample made with 2% fiber content. The COV of |Γ| for sample with 2% fiber was close to that of the sample without any fibers. For 10 GHz, this sample had COV value of 7.4% compared to 5.3% for the reference sample. The similar COV |Γ| values obtained for samples made with 0% and 2% fibers is on account of the relatively high level of homogeneity (i.e., relatively uniform fiber distribution) of medium, which in turn leads to lower point-to-point variation in reflection properties determined by microwave NDT. This was also supported by image analysis on hardened samples. Sample with 2% steel fibers exhibited uniform fiber distribution (i.e., lowest COV of fiber density) throughout the sample. Therefore, the comparison of COV |Γ| values (especially at higher frequencies) determined between fibrous and non-fibrous samples enables the determination of the level of fiber distribution, wherein sample with relatively uniform fiber distribution is expected to have comparable variation in |Γ| values to that of sample made without any fibers.

Figure A-11(c) shows the variation in fiber density obtained from image analysis as a function of cut surfaces. As expected, the increase in fiber content resulted in higher fiber density (number of fibers per cm^2). Fibers in samples made with 1% and 2% were more uniformly distributed compared to the sample with 3% steel fiber. The fiber density for sample containing 3% steel fiber was shown to vary from 4.9 to 9.2. As shown in Figure A-11(d), this sample exhibited the largest COV values of fiber density for each cut surface. Figure A-11 depicts similar trends between results determined from image analysis and those obtained from microwave NDT. The lowest and highest COV values corresponded to samples made with 2% and 3% fiber contents, respectively. It is important to note that although the analysis of the microwave measured results reported in this study was performed for two frequencies of 3 GHz (S-band) and 10 GHz (X-band), representing each frequency band, all trends obtained for 3 and 10 GHz were consistent with entire frequency ranges at S-band (2.6-3.95 GHz) and X-band (8.2-12.4 GHz), respectively. Therefore, the microwave results conducted at 3 and 10 GHz represent the entire frequency ranges at S-band (2.6-3.95 GHz) and X-band (8.2-12.4 GHz), respectively. The analysis of variance (ANOVA) test was conducted to determine

whether the variations in the mean of |Γ| with the fiber addition and sample side obtained from microwave NDT are statistically significant. In the ANOVA test, the null hypothesis (H_0) represents that there is no statistically significant difference in the mean |Γ| of sample for a given parameter (e.g., fiber content and sample side). However, alternative hypothesis (H_a) denotes that the assumption of H_0 is not correct, and the contribution of a given parameter to the mean of |Γ| is statistically significant for a given significance level.

The significance level is a probability threshold. For the calculated probability (P-value) less than the significance level, the null hypothesis is rejected, which means that the variation in mean of |Γ| of samples is statistically significant. The significance level is commonly taken as 0.05 or 0.10 (Montgomery 2005). In this study, the significance level was considered to be 0.05. In other words, a P-value less than 0.05 reflects the fact that there is less than a 0.05 probability that the observed behavior is due to the noise and experimental error, ensuring that the effect of fiber content and/or sample side on reflection properties is statistically significant.

Table A-1 presents the results of the ANOVA test for the investigated parameters (fiber content and sample side) at different operating frequencies. In contrast to the results at 10 GHz, the fiber content was shown to have significant influence on mean of |Γ| at 3 GHz.

Table A-1 ANOVA results at different operating frequencies.

Response	Frequency	Parameter		DOF	P-value	Remark
|Γ|	3 GHz	Fiber content		3	0.0005	S
		Sample side	REF	3	0.551	NS
			1% ST	3	0.082	NS
			2% ST	3	0.198	NS
			3% ST	3	0.041	S
	10 GHz	Fiber content		3	0.878	NS
		Sample side	REF	3	0.162	NS
			1% ST	3	0.185	NS
			2% ST	3	0.512	NS
			3% ST	3	0.002	S

Notes: DOF: degree of freedom which is equal to N – 1 (N refers to the number of variables), NS: not significant, and S: significant

As mentioned earlier, the mean of |Γ| at 3 GHz consistently increased with fiber addition, expect for the case of fiber clumping. However, the results of mean |Γ| at 10 GHz were shown not to vary with fiber addition. The significance of sample side was found to be the function of fiber content. For samples made with 1% and 2% fiber contents, sample side was shown to have no significant effect on the mean of |Γ|, indicating the uniformity of fiber distribution at different sample sides. This reflects that in the case of relatively uniform fiber distribution, the measurements have good repeatability, regardless of the sample side. On the other hand, sample side for FRCM sample with 3% steel fiber had significant influence on the measurements, especially at 10 GHz (lower P-value). This implies that the reflection properties for different sample sides are not consistent when fibers are non-uniformly distributed throughout the sample.

In order to qualitatively demonstrate the fiber inhomogeneity throughout the sample, the volumetric (3-D) SAR images for the samples made with 2% and 3% fiber contents were obtained. This was done using scanning an X-band (8.2-12.4 GHz) rectangular waveguide probe over the sample using an automated scanning table. The measured reflection properties (magnitude and phase of Γ) of the samples were collected and subsequently passed through the SAR imaging algorithm outlined in (Case et al. 2011).

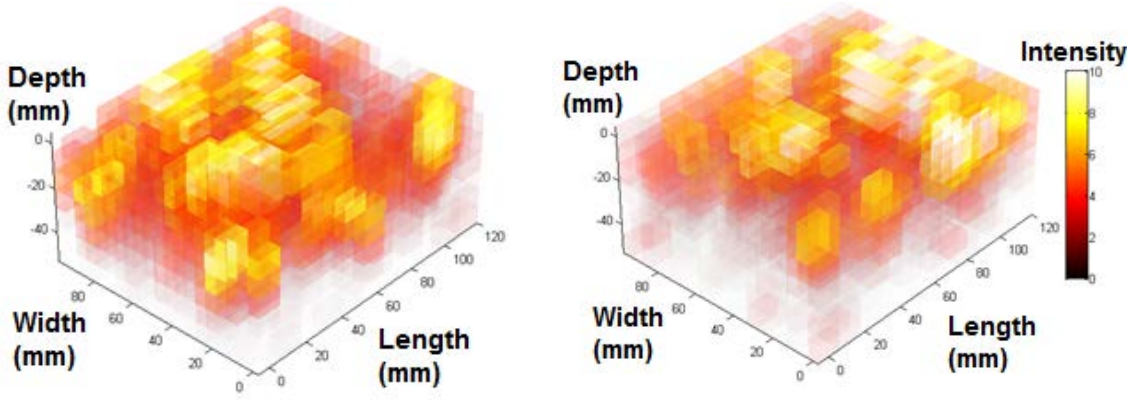

(a) (b)

Figure A-12 SAR microwave image at X-band for samples made with different fiber contents: (a) 2%, (b) 3%.

A liftoff (distance between the open-ended waveguide probe and the sample surface) of 1 mm was applied to allow the probe to freely scan over the sample. Figure A-12 shows the 3-D microwave images for samples with 2% and 3% steel fibers. Compared to the sample with 2% fiber content, the microwave image for the sample with 3% fiber exhibits more non-uniform image intensity. The high intensity spots (white regions) observed for sample with 3% fiber content can represent relatively high concentration of fibers. Given the relatively high image intensity regions, most of the fibers in sample with 3% fiber content appears to be far from the edge (x = 0) of sample. On the other hand, the sample made with 2% fiber content exhibited relatively uniform image intensity of microwave reflection properties throughout the sample, indicating the fact that this sample has higher level of uniformity and homogeneity.

CORRELATION BETWEEN REFLECTION PROPERTIES, FIBER DENSITY, AND FIBER INHOMOGENEITY INDEX

The correlation between |Γ| determined from microwave measurement and fiber density obtained from image analysis for hardened samples made with various fiber contents is shown in Figure A-12. In general, the measured |Γ| at 3 GHz increases with increasing fiber density, except for the case of 3% fiber content. The results in Figure A-12 can be distinguished in two different zones in terms of the level of fiber distribution. Those made with 1% and 2% steel fibers exhibited approximately consistent results in terms of fiber density and reflection properties, given relatively uniform distribution of fibers. For such samples exponential trend can be established between |Γ| at 3 GHz and fiber density. However, sample containing 3% fiber had significant scattering caused by fibers, given non-uniform fiber distribution. For this sample, no clear trend can be observed between |Γ| and fiber density. Sample with 3% fiber content developed relatively high scattering of refection properties and fiber density, especially at higher operating frequency of 10 GHz.

Figure A-14 shows the correlation between overall mechanical performance and fiber inhomogeneity index (*IHI*) measured from freshly cast prism. As mentioned earlier, higher *IHI* values correspond to higher variation in fiber content along the cast prism, thus indicating lower fiber homogeneity inside the sample. In addition to the fiber

content, the homogeneity of fibers was shown to significantly affect the overall mechanical performance of the investigated FRCMs. Higher *IHI* value of 15% for FRCM made with 3% fiber content resulted in 25% lower overall mechanical performance compared to the mixture containing 2% fiber with *IHI* value of 1.5%. This is attributed to the lower level of fiber homogeneity and higher potential of fiber clumping in this mixture, which can lead to localized weakness points inside the sample and reduce the reinforcing efficiency of fiber.

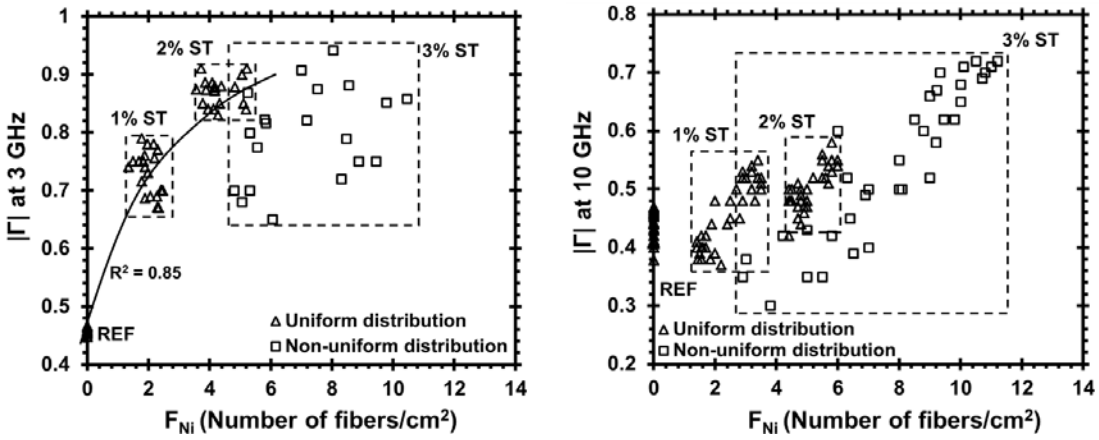

(a) (b)

Figure A-13 Correlation between |Γ| and fiber density for samples made with different fiber contents: (a) 3 GHz and (b) 10 GHz.

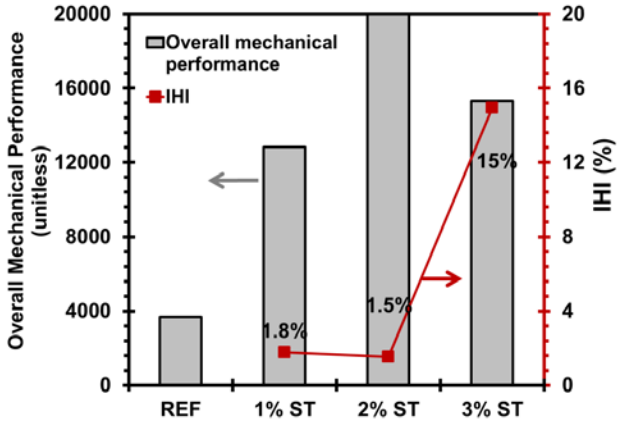

Figure A-14 Correlation between overall mechanical performance and fiber inhomogeneity index (IHI) measured from freshly cast prism.

The correlation between COV of |Γ| and fiber density with IHI for FRCMs made with different fiber contents is shown in Figure A-15. A linear correlation between IHI and COVF (image) indicates that sample with higher IHI value (higher level of fiber inhomogeneity) is expected to have higher variation in fibers located at different zones across the sample. Regardless of operating frequency, sample with higher IHI and COVF values was found to have higher COV in |Γ| values. It is important to note that this correlation was more pronounced for |Γ| measured at the higher operating frequency of 10 GHz, which is reflected by steeper linear fit line in Figure A-15(b). This is attributed to the higher sensitivity of such operating frequency to level of inhomogeneity of medium caused by fibers. The highest IHI, COVF (image), and COV |Γ| values was observed for the FRCM sample made with 3% fiber content, given non-uniform fiber distribution and fiber clumping. Such good correlations confirm that microwave NDT can be successfully employed to detect the level of steel fiber distribution inside the cement-based materials.

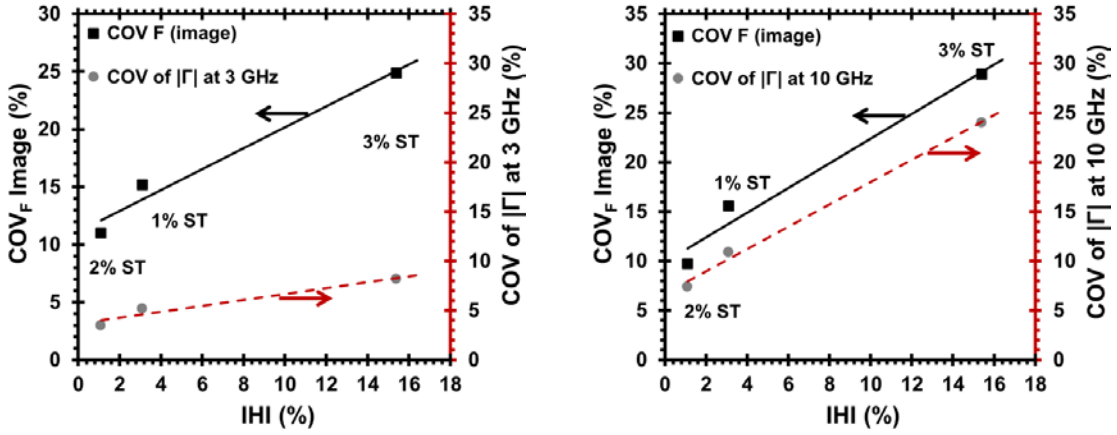

(a) (b)

Figure A-15 Correlation between COV of fiber density obtained from image analysis and fiber inhomogeneity index (IHI) measured from freshly cast prisms with COV of |Γ| determined from microwave NDT for (a) 3 GHz and (b) 10 GHz.

AMT RESULTS

Numerical Simulation of AMT. For numerical modeling, a full-wave coupled electromagnetic-thermal simulation was conducted to evaluate the effect of dielectric properties and fiber depth and clumping on the surface temperature of FRCM samples using CST MultiPhysics Studio^{TM}. The simulation was carried out in two parts. First,

assuming a 50 W plane wave excitation, the electric and magnetic fields inside the FRCM and subsequently the induced surface current on the steel fibers were determined. The solution is based on the finite difference time domain technique. Subsequently, for the thermal simulation, the computed electric and magnetic fields and induced surface current are utilized to determine the transient heat diffusion. The transient thermal response (i.e., heat generation, diffusion, etc.) of the structure is based on Eq. (4).

The transient thermal simulation includes two parts, in which the FRCM is first illuminated by incident electromagnetic power (i.e., heating period) for a given heating time, t_h, and subsequently the heat source is removed (i.e., cooling period) and the thermal profile is recorded for a given cooling time, t_c (i.e., total time of $t = t_h + t_c$). For numerical modeling, the operating frequency was chosen to be 2.4 GHz with 50 W of incident electromagnetic energy (plane wave illumination). As in (Bois et al. 2000) at low frequencies, such as 2.4 GHz, the mortar sample can be considered a homogeneous material. Therefore, each mortar sample was modeled as a homogeneous solid material measuring 140 × 140 × 70 mm. The steel fiber was modeled with a length of 30 mm and diameter of 0.55 mm. The dielectric and thermal properties of the material constituents of FRCM sample were considered as follows: mortar was assumed to have a dielectric properties of $\varepsilon_r = 4.8 - j0.05$, thermal conductivity of $k = 1.2$ W/m.K, specific heat of $C = 0.9$ J/g.K, and density of $\rho = 2200$ kg/m^3; air has dielectric properties of $\varepsilon_r = 1$, $k = 0.026$ W/m.K, $C = 1.005$ J/g.K, and $\rho = 1.204$ kg/m^3; steel fiber was considered to have electric conductivity of $\sigma = 7.69 \times 10^6$ (S/m), $k = 59.5$ W/m.K, $C = 0.48$ J/g.K, and $\rho = 7870$ kg/m^3.

Effect of embedded single fiber on surface temperature. The first phase of numerical simulation was undertaken to evaluate the effect of mortar loss factor and the depth (from the surface) of a single steel fiber on the surface temperature profile. The fiber depth and loss factor of mortar contributes to change in temperature due to induced surface current and dielectric heating, respectively. The surface temperature difference of a sample as well as induced surface current on steel fiber at $t_h = 30$ sec is shown in Figure A-16(a). Assuming fixed mortar dielectric properties, the surface temperature reduces as the fiber depth increases. As expected, the surface current induced by the incident electromagnetic signal decreases since the amount of energy that reaches the fiber

decreases with distance from the surface. For this material, after 8 mm, the fiber depth does not affect the temperature. Thus, fibers placed deeper than ~10 mm are not likely to contribute to the surface temperature (nor AMT inspection results). Related to this, the induced surface current on the steel fibers is also a function of the fiber orientation with respect to the polarization of incident electric field. The effect of incident polarization on the fiber can be quantified using through the polarization loss factor (Balanis 1997). In general, the greatest induced surface current occurs when the fiber is parallel to the incident electric field, and approaches zero for a perpendicular orientation of the fiber. This dependency on fiber orientation causes a subsequent dependency of surface temperature (and overall AMT sensitivity) to the fiber alignment.

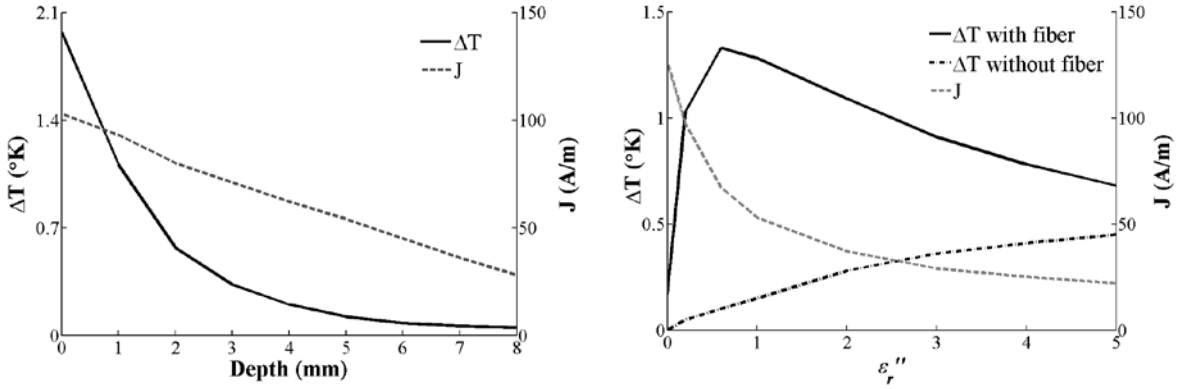

(a) (b)

Figure A-16 Simulated surface temperature and induced surface current on fiber for sample with a single fiber: (a) Variation in fiber depth (b) Variation in sample loss factor.

The temperature difference on a sample without and with a single fiber (located 1 mm from the top surface) along with induced surface current on fiber is shown in Figure A-17(b) as a function of loss factor. For the mortar without fiber, the surface temperature increases with increasing loss factor (resulting from dielectric heating). However, in the case of mortar with a single steel fiber, as the loss factor increases, the temperature difference initially also increases as a result of both dielectric heating and induced surface current on the fiber (up to a loss factor of ~0.6). After this point, the contribution of the induced surface current (on the fiber) is less dominant, and therefore the temperature difference begins to decrease. This is a result of the increased attenuation of the electric

field impinging on the fiber (and subsequently a reduction in induced surface current). Therefore, the temperature difference between samples made with and without fibers is highly dependent on the material properties (dielectric properties) of mortar.

Effect of fiber distribution on surface temperature. The second simulation phase was carried out to evaluate the effect of fiber distribution on surface temperature for sample containing 0.5% steel fibers. Two different fiber distributions were considered; namely, a random distribution and a clumped distribution, as shown in Figure A-17. For both distributions, the fibers were distributed within the first 50 cm (i.e., a 50-cm depth from the surface) of the sample. The location and orientation of the i^{th} fiber was determined by generating a random Cartesian starting position (x_i, y_i, z_i) within the geometrical boundaries of the sample, and the direction of the fiber was randomly assigned using angles θ_i and ϕ_i of the spherical coordinate system. For both distributions, the depth and orientation (θ_i and ϕ_i) are identical.

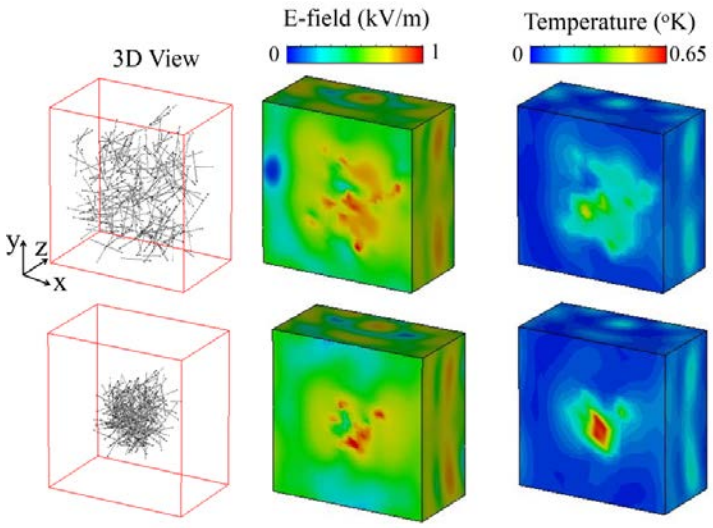

Figure A-17 Numerical modeling results of E-field and temperature variation for random (top row) and clumped (bottom row) fiber distributions.

The difference between the distributions is in the lateral placement (i.e., x and y directions as shown in Figure A-17), meaning that the randomly distributed fibers cover a greater (lateral) surface area than the clumped distribution. The magnitude of electric field (E-field) and temperature difference for both distributions are shown in Figure A-

17. From these results, it can be seen that the E-field distribution is affected by the fiber distribution. In the case of clumped distribution, the E-field and temperature values were substantially higher at the center of the sample and rapidly decreased with distance from the center. Therefore, in the clumped model, the high intensity temperature in the center of the sample is attributed to the higher concentration of fibers placed in this zone. However, for the random distribution, the distribution and magnitude of the E-field are more uniform across the surface.

In order to quantitatively evaluate the distribution of surface temperature, the surface of these two models was divided into 25 equal zones with dimensions of 25 × 25 mm. The greatest mean value of 0.4 was obtained in the center of the clumped fiber sample, and this value sharply decreases with distance from the center of sample. Further, the mean value of the temperature for sample with random distribution and clumped fiber are 0.20 and 0.14, respectively. However, the random distribution sample has a standard deviation for temperature difference of 0.06 compared to 0.12 for the clumped distribution sample, thus supporting the conclusion of a more uniform distribution of temperature difference for the random distribution sample. It should be pointed out that open boundary conditions were employed for simulations which consider an infinite FRCM sample in the lateral direction (i.e., x and y directions as shown in Figure A-17). As a result of the open boundary condition applied along the x- and y-axes, heat diffusion is the only mechanism of heat transfer in these directions. Additionally, the top and bottom of the SFRC sample (along the z-axis in Figure A-17) is considered to be surrounded by an infinite half-space of air. Thus, both heat diffusion and heat convection take place in this direction. In order to address the boundary conditions at the two interfaces between FRCM and air, the heat transfer coefficient of h_C = 10 W/m^{2}K is considered (Lee et al. 2009).

AMT Measurement Results. Surface temperature differences (ΔT) determined on one side of the investigated samples (1%, 2%, and 3% fiber contents) after 30 sec of microwave illumination at a frequency of 2.4 GHz are shown in Figure A-18. For each sample, ten zones with dimensions of 25 × 25 mm were considered to quantitatively analyze the distribution of fibers. For a given sample side (i.e., side 1), samples made with 1% and 2% steel fibers exhibited a higher temperature difference across the surface

compared to the sample containing 3% steel fibers. The high intensity spot in the temperature profile of the sample containing 3% fiber content can reflect the relatively high concentration of fibers (fiber clumping) in that zone. In addition, the relatively high quantity of blue zones observed for this sample represents zones without steel fibers.

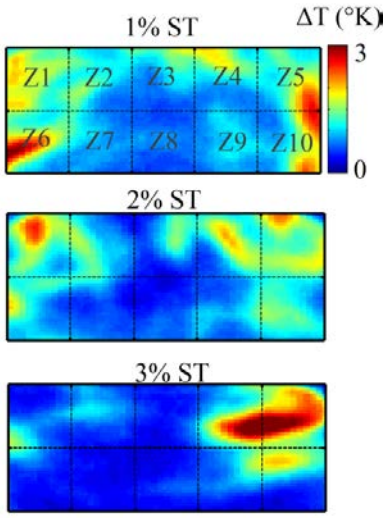

Figure A-18 Surface temperature variation of samples made with different fiber contents.

The histogram of the mean of the temperature difference ($\mu_{total}(t)$) for all surfaces of samples made with 2% and 3% fibers is shown in Figure A-19. The sample made with 3% fiber content resulted in the higher variation (density) in surface temperature, ranging from 0.1 to 2.5 °K. In addition, the majority of measured surface temperature in this sample lies within a narrow range between 0.2 to 0.4 °K, resulting in a narrow and steep histogram for this sample. Compared to the sample with 3% steel fiber, sample containing 2% fiber exhibited a more uniform distribution of measured surface temperature (indicative of a more uniform distribution of steel fibers), as shown in Figure A-19.

The mean of temperature difference for 120 sec (30 sec heating time plus 90 sec cooling time) for all three samples at operating frequency of 2.4 GHz is shown in Figure A-20. It is expected that samples with higher fiber content will undergo a greater increase in surface temperature, as is observed for samples made with 1% and 2% fiber contents. However, this tendency is reversed with further fiber addition (from 2% to 3%). This

behavior was observed for both the heating and cooling stages. Further, the decrease in surface temperature for the sample with 3% fiber content may be an indication of zones without fibers, in which the surface temperature is only affected by dielectric heating.

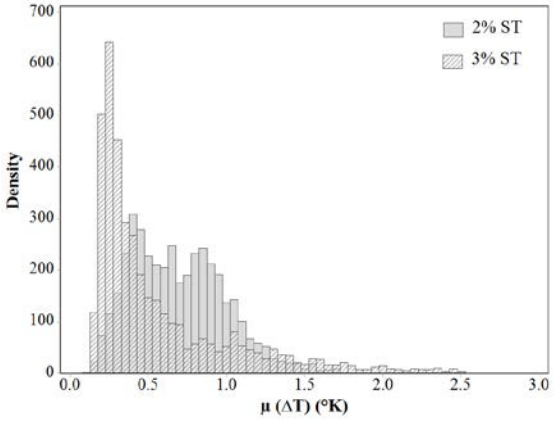

Figure A-19 Histograms of surface temperature for samples made with different fiber contents.

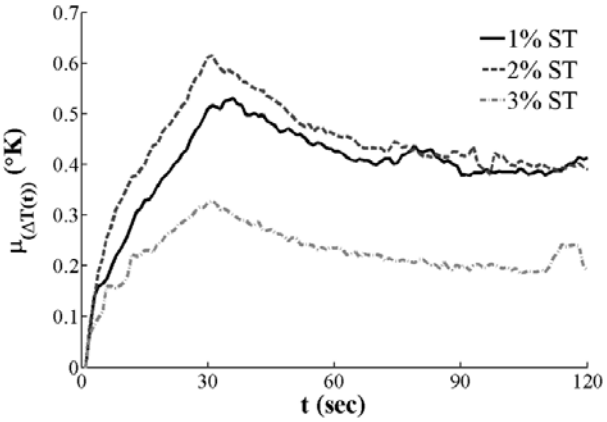

Figure A-20 Transient surface temperature of samples made with different fiber contents at operating frequency of 2.4 GHz.

The variation in the mean value of the surface temperature as a function of fiber content at various operating frequencies is shown in Figure A-21. Regardless of operating frequency, an increase in fiber content from 1% to 2% resulted in higher mean value of the surface temperature. On the other hand, for the sample made with 3% fiber content, significant decrease in the mean (from the 2% sample) occurred. This decrease is attributed to the non-uniform fiber distribution in the sample with 3% fiber content.

These results are in agreement with those obtained from the simulated AMT results, in which for the sample with uniform fiber distribution, the temperature variation across the entire surface is more uniform than the temperature variation of the sample with non-uniform fiber distribution. As shown in Figure A-21, it appears that the temperature difference between the sample with 3% fiber content and the samples with 1% and 2% fiber content is more substantial at 2.4 GHz. However, this difference is quite small (~<0.1 °K) and is attributed to measurement error.

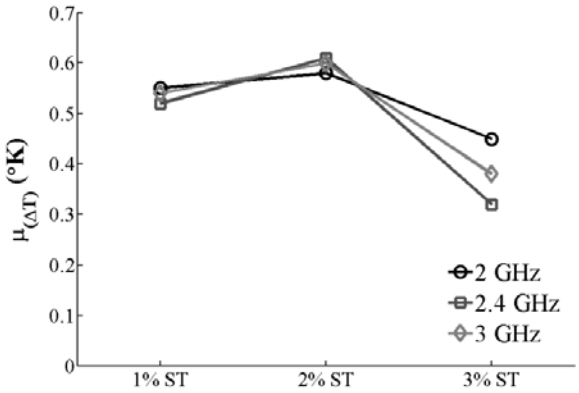

Figure A-21 Variation in mean value of surface temperature at different operating frequencies after 30 sec heating.

The significance of variation (due to fiber content and sample side) in the mean value of surface temperature for different samples was statistically evaluated using the ANOVA test. The null hypothesis indicates that a variable has no significant influence on surface temperature, whereas the alternative hypothesis represents that the contribution of a given parameter to the surface temperature is statistically significant for a given level of significance. The level of significance is a probability threshold below which the null hypothesis is rejected. Commonly used values for the level of significance are 0.05 and 0.10 (Montgomery 2005). In this investigation, the probability (P-value) of 0.05 was considered as the level of significance. The results of the ANOVA test for the investigated parameters (fiber content and sample side) at frequency of 2.4 GHz are presented in Table A-2. The results indicate that the fiber volume has a significant influence on the variation of the mean of surface temperature. It is interesting to note that

the significance of measurements conducted on different sides of each sample is as a function of fiber content. In the case of samples made with 3% steel fibers, the investigated sample sides (surfaces) had a significant effect on the variation of the mean value of surface temperature (P-value << 0.05). However, for samples made with 1% and 2% steel fibers, the investigated sample side resulted in no significant influence on the mean value of surface temperature (P-value > 0.05). This reflects that in the case of relatively uniform fiber distribution, the measurements have good repeatability, regardless of the sample side.

Table A-2 ANOVA results at 2.4 GHz

Response	Parameter		DOF	P-value	Remark
Surface temperature	Fiber		2	0.0001	S
	Sample side	1% ST	3	0.053	NS
		2% ST	3	0.091	NS
		3% ST	3	0.0001	S

Notes: DOF: degree of freedom which is equal to N – 1 (N refers to the number of variables.) NS: not significant, S: significant

Figure A-22 shows the variation in the mean of temperature difference across the surface (i.e., as a function of zones) for the three samples. Each sample is divided into 40 zones resulting from $N_Z = 10$ and $N_S = 4$.

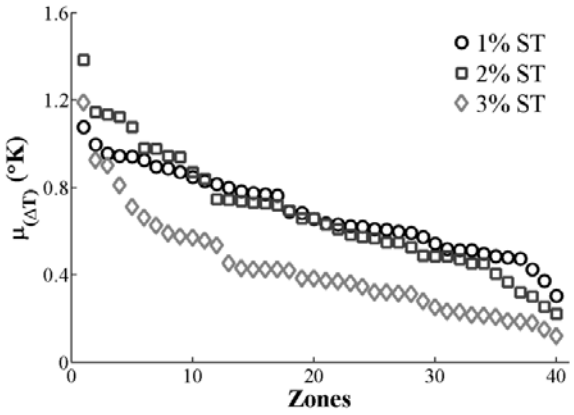

Figure A-22 Variation in mean value of surface temperature for 40 zones across each sample after 30 sec heating.

The highest variation in the mean of surface temperature was found for the sample made with 3% fiber content, indicating non-uniform fiber distribution across different zones. Even with higher fiber content, the majority of zones of the sample containing 3% fibers exhibited lower temperature difference compared to the other two samples. This may indicate that for the sample with 3% fiber content, most of the fibers are located away from the surface of sample, thus leading to a lower temperature difference. This can be attributed to the potential of clumping of fibers in this sample. Samples made with 1% and 2% fiber contents exhibited a similar mean of temperature difference. This may be due to the similar fiber distribution of these samples.

Figure A-23 shows the correlation between the mean of surface temperature and the fiber density for both numerical modeling and measurement. Due to the extensive computation time and mesh cell density, numerical modeling could not be conducted on a sample similar to those measured. Rather, a fiber density of 0.5% was considered to keep the computational domain manageable. In order to validate the numerical modeling, the results of simulation (sample modeled with 0.5% steel fibers) and measurement (sample with 2% steel fibers) were compared as a function of fiber density. In all cases (simulation and measurement), there are no fibers present on the surface of the samples.

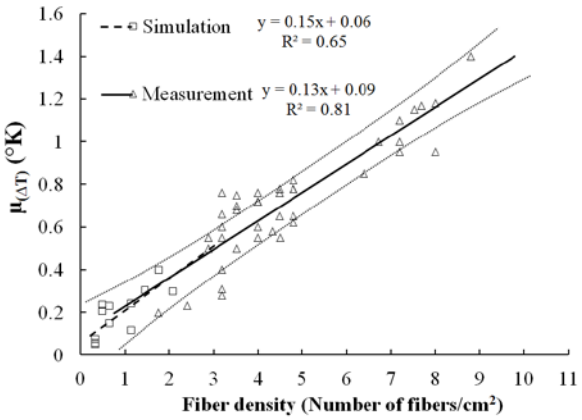

Figure A-23 Correlation of fiber density with mean of surface temperature for both simulations and measurements.

Therefore, the fiber density (simulation and measurement), expressed as the number of fibers located within a sample zone, was determined at a depth of 10 mm (for

the 2% sample, 10 mm of sample material was cut/removed from all four sides of the sample). The 25 zones were considered for the simulated sample, and 40 zones were considered for the (measured) 2% fiber sample. All zones had dimensions of 25 × 25 mm (similar to the zones discussed in Section 4.2 and 5.2). Subsequently, the fiber density was related to the mean surface temperature of each zone, as is shown in Figure A-23. As seen, a linear trend for simulation and measurement was observed between the mean of surface temperature and fiber density. An extension of the fitted trend line of the measured data agrees well with the trend line obtained for numerical modeling, thus ensuring that the results of numerical modeling match well with measurements.

Correlation between mean of surface temperature difference (corresponding to 40 zones) and normalized toughness of hardened samples with fiber homogeneity determined from cast prism in fresh state (*IHI*) is shown in Figure A-24. As discussed above, higher *IHI* (see Eq. (8)) reflects higher variation (i.e., lower homogeneity) in fiber content throughout the cast prism.

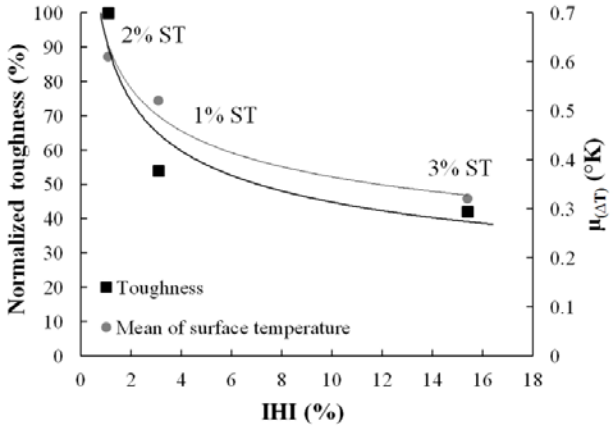

Figure A-24 Correlation between surface temperature and normalized toughness of hardened samples with fiber homogeneity determined from freshly cast prism.

The effectiveness of incorporating fibers to enhance flexural toughness is shown to be significantly affected by the level of fiber homogeneity along the cast prism. A higher *IHI* value of 15% for mixture made with 3% fiber content resulted in 55% lower flexural toughness compared to the mixture containing 2% fiber. A lower fiber homogeneity and fiber clumping observed in this mixture led to lowering the reinforcing

efficiency of fibers to enhance mechanical properties. Similar trend was observed for mean of surface temperature difference of FRCMs, as indicated in Figure A-24. Samples with lower *IHI* values (i.e. higher level of fiber homogeneity) were found to have a higher mean temperature difference. This is due to the increased (more uniform) level of fiber distribution for samples made with 1% and 2% steel fibers. On the other hand, the reduced level of fiber homogeneity in the sample with 3% steel fiber contributed to a lower mean of temperature difference.

SUMMARY

Near-field microwave reflectometry and active microwave thermography were utilized to nondestructively evaluate the fiber content and distribution of fiber-reinforced cement-based mortar (FRCM). Based on the obtained results, the following conclusions can be drawn:

- The results of microwave reflection properties were found to correlate well with those determined from image analysis on hardened samples and fiber inhomogeneity evaluated freshly cast prism samples. A FRCM with higher COV of |Γ| exhibited larger fiber inhomogeneity determined from freshly cast prism sample and image analysis on hardened samples.
- Mean of |Γ| at 3 GHz and COV of |Γ| at 10 GHz were found to be an indication of fiber content and fiber distribution, respectively. Regardless of the fiber content, the microwave measurement at higher frequency of 10 GHz is more sensitive to detecting the inhomogeneity and scattering caused by fibers, thus resulting in higher point-to-point measurement variations compared to 3 GHz.
- The level of fiber homogeneity was shown to significantly affect the overall mechanical performance of FRCM. Higher *IHI* value of 15% for FRCM made with 3% fiber content resulted in 25% lower overall mechanical performance compared to the mixture containing 2% fiber with *IHI* value of 1.5%.
- For operating frequency at 3 GHz, all FRCM samples was shown to have higher |Γ| values compared to the reference sample made without any fibers. The mean of |Γ| increased with fiber addition, except for sample with potential formation of

fiber clumping and non-uniform fiber distribution, where the mean of |Γ| was 12% lower than sample with 2% fiber content.

- The highest COVs of |Γ| and fiber density were obtained for sample containing 3% fiber. |Γ| at 10 GHz and fiber density varied between 0.3–0.72 and 3–11, respectively, ensuring the fact that fibers are non-uniformly distributed throughout the sample.
- Unlike the samples made with 1% and 2% fiber contents, the results of fiber density and |Γ| were found to significantly vary along the height of sample containing 3% fiber.
- The AMT simulation results indicated that fiber depth and dielectric properties of mortar have significant influence on temperature difference at the surface of sample, due to variation in heating associated with induced surface current and dielectric heating. The sample with random fiber distribution had lower standard deviation for temperature difference compared to the clumped distribution sample. This is attributed to the more uniform distribution of temperature difference for this sample.
- Based on the AMT measurement results, FRCMs containing 1% and 2% steel fibers are shown to have higher surface temperature difference compared to the sample made with 3% fiber content. This is due to the non-uniform distribution and possible fiber clumping.
- The high and low intensity spots in the temperature profile of the sample containing 3% steel fiber can be an indication of relatively high and low concentrations of fibers, respectively, in corresponding zones.
- The relationship between mean temperature difference of hardened samples and level of fiber homogeneity determined from freshly cast prism shows that FRCMs with higher level of fiber homogeneity (i.e. lower IHI) along the cast prism resulted in higher mean temperature difference determined for four sides of the test samples.

APPENDIX B

MONITORING AUTOGENOUS CRACK HEALING IN CEMENTITIOUS MATERIALS USING NEAR-FIELD MICROWAVE REFLECTOMETRY

INTRODUCTION

Concrete structures are inherently susceptible to microcracking. Over time, microcracking can lead to formation of larger cracks under structural and/or environmental factors. Cracking can adversely impact durability and structural integrity of a concrete structure, thus limiting service lifespan. However, given the autogenous healing capability of cementitious materials under certain conditions, cracks can be healed due to additional interaction between cementitious materials, water, and the surrounding environment (Qian et al. 2009; Sakai et al. 2003). Autogenous crack healing in concrete is related to the physical and/or chemical composition of the cementitious matrix (Tang et al. 2015; Van Tittelboom and De Belie 2013; Wu et al. 2012). Autogenous crack healing process is primarily caused by: (i) the formation of calcium carbonate ($CaCO_3$) or calcium hydroxide ($Ca(OH)_2$); (ii) the sedimentation of particles and loose cement grains in the presence of water (Van Tittelboom and De Belie 2013); (iii) the continuing hydration of unhydrated cementitious materials and pozzolanic reaction associated with supplementary cementitious materials (SCMs) (Ferrara et al. 2016; Huang 2014; Jaroenratanapirom and Sahamitmongkol 2011; Snoeck and De Belie 2015; Van Tittelboom 2012; Wu et al. 2012); and (iv) further swelling of the cement matrix (Sakai et al. 2003). Although ongoing hydration of unhydrated cementitious materials and pozzolanic reaction due to the use of SCMs are thought to be the main contributing factors to crack healing at early-age, autogenous crack healing at later ages is mostly associated with the precipitation of calcium carbonate (Edvardsen 1999; Homma et al. 2009; Snoeck and De Belie 2012; Yang et al. 2009a). It is important to note that the presence of water is a primary component for the occurrence of autogenous crack healing. Hence, exposure condition plays an important role in this process. Sisomphon et al. (Sisomphon et al. 2013) reported that optimal recovery of mechanical properties caused by autogenous healing in cracked concrete can occur under cyclic wet-dry exposure, while no recovery was observed for samples exposed to sole air drying. Autogenous crack healing is reported to mainly occur in relatively narrow cracks even in the presence of water (Aldea et al. 2000; Clear 1985; Edvardsen 1999; Ferrara et al. 2016; Jacobsen et al. 1995). Cracks with maximum widths of 200-300 μm are found to become closed due to the autogenous healing (Aldea et al. 2000; Clear 1985;

Ebrahimkhanlou et al. 2016; Edvardsen 1999; Jacobsen et al. 1995; Reinhardt and Jooss 2003).

A number of destructive and nondestructive testing (NDT) techniques have been employed to evaluate and monitor autogenous self-healing capability in concrete. Tests involving resonant frequency (Kan et al. 2010; Yang et al. 2009a), acoustic emission (Van Tittelboom et al. 2012), electrical resistivity (Yildirim et al. 2015), X-ray computed tomography (Snoeck et al. 2016), ultrasonic pulse velocity (UPV) (Jacobsen et al. 1995, 1996; Şahmaran et al. 2008; Watanabe et al. 2011; Zhong and Yao 2008), and more recently diffuse ultrasound (In et al. 2013) and coda wave interferometry (Liu et al. 2016) have been employed as nondestructive means to evaluate the degree of self-healing process in cementitious materials. Autogenous crack healing is inherently a slow process, in which small changes in material characteristics occur gradually. NDT methods used for this purpose must be sufficiently sensitive to small changes in materials properties. For instance, in the UPV test, measurement variation due to sensor coupling condition can be larger than that caused by self-healing (Aldea et al. 2000). Therefore, it is important to develop a practical and robust NDT methodology for monitoring variations in materials and water transport properties pertinent to autogenous crack healing process. Microwave nondestructive testing and evaluation (NDT&E) techniques have shown great promise for evaluating and characterizing a diverse array of cement-based materials. The effective dielectric constant of a cement-based material is directly affected by its constituent dielectric constants and their volumetric content (i.e., paste, water-to-cement ratio, aggregate content, etc.) as well as any ongoing chemical reaction (i.e., cement hydration, variation in chemistry of pore solution, etc.). As a microwave signal reflects from a dielectric material, its signal properties (magnitude and phase) change as a function of parameters, including dielectric properties, volume contents, and level of homogeneity of material constituents (Zoughi 2012). In the microwave NDT regime, the magnitude of the reflection coefficient, $|\Gamma|$, measured by an open-ended rectangular waveguide and conducted at different operating frequencies, has shown to correlate well with the aforementioned parameters. Some of the previous studies undertaken using microwave NDT technique include: (1) determination of water-to-cement ratio (w/c) (Bois et al. 1998, 2000; Mubarak et al. 2001) and compressive strength of cement paste

and mortar (Zoughi et al. 1995); (2) evaluation of sand-to-cement ratio in mortar; (3) detection of aggregate segregation (Bois et al. 1999); (4) monitoring of cure-state and material properties of concrete (Bois et al. 1998); (5) evaluation of chloride ingress and cyclical exposures in mortar (Peer et al. 2003); (6) evaluation of crack formation for mortar samples subjected to cyclic compressive loading (Peer et al. 2003); (7) detection of carbonation and alkali-silica reactions (Donnell et al. 2013; Hashemi et al. 2014, 2015); and (8) evaluation of steel fiber distribution in mortar (Foudazi et al. n.d.; Mehdipour et al. 2017a).

Sensitivity of microwave signals to variations caused by water transport properties (i.e., presence of free water and transformation into bound water, capillary draw during wetting cycle, etc.) and formation of cracks due to loading, makes microwave NDT technique an attractive approach for monitoring crack healing performance in cementitious materials. Therefore, the aim of this study is to demonstrate the feasibility of using near-field microwave reflectometry to nondestructively monitor autogenous crack healing in mortar samples. Two sets of mortar samples with different binder compositions were prepared and subjected to compressive loading to generate internal and external (surface-breaking) cracks with varying widths. In order to initiate autogenous crack healing, both cracked and uncracked (i.e., reference sample) mortar samples were exposed to several wet/dry cycles. The statistical properties (i.e., mean and coefficient of variation (COV)) of the magnitude of reflection coefficient ($|\Gamma|$), measured using open-ended rectangular waveguide probes, at operating frequencies of 3 and 10 GHz were determined to assess the degree of variations in microwave reflection properties. An independent set of experimental assessments, including ultrasonic transmission time, capillary water absorption, crack healing quantification, as well as X-ray diffraction (XRD) and scanning electron microscopy (SEM) were carried out to corroborate the results derived from microwave measurements.

EXPERIMENTAL APPROACH

Materials and Sample Preparation. In this study, Type I/II ordinary Portland cement (OPC) conforming to ASTM C150 (*Annual Book of ASTM Standards* n.d.) was used. In order to examine the effect of SCMs on autogenous crack healing, Class C fly

ash (FA) and blast-furnace slag (SL) were incorporated as a partial replacement for OPC. In addition to the cementitious materials, a continuously graded natural sand with a maximum size of 5 mm, density of 2500 kg/m^3, and water absorption capacity of 0.6% was incorporated.

In order to assess the effect of SCMs on autogenous crack healing performance, two sets of mortar samples were prepared including: (i) plain OPC mortar (referred to as OPC); and (ii) mortar in which 55% of OPC was replaced by 20% SL and 35% FA, by mass (referred to as OPC-SCM). The synergistic interactions between FA in conjunction with SL have previously demonstrated improved early and later ages properties due to the pozzolanic reaction (Jiang et al. 2015; Li and Zhao 2003; Na et al. 2012; Toutanji et al. 2004). For both mortar mixtures, the water-to-binder ratio (w/b) and sand-to-binder ratio were kept constant at 0.40 and 2.5, respectively.

Crack initiation and exposure condition. After demolding the mortar samples at 24 hours, they were moist cured for three days using wet burlap. After 3 days, one sample from each set of mixtures was subjected to a compression load corresponding to 90% of its 3-day compressive strength, as identified by 100 × 200 mm^2 cylindrical samples. This was performed to generate internal and external cracks with different widths, lengths and distributions throughout the sample. After crack formation, the widths of surface cracks were measured at 40 points along their lengths using an optical microscope. For all samples, the measured crack widths varied from 10–500 μm. It is important to note that the cracks in this study were non-uniform cracks (i.e., in terms of surface crack distribution and dimensions), representing more realistic cracks seen in practice. Unloaded samples (i.e., sound samples) were used as a reference for each set.

Following crack formation, all mortar samples were subjected to wet-dry cycles to initiate autogenous crack healing process. Each cycle took 7 days consisting of soaking the samples in a curing tank filled with tap water (22 ± 2 °C) for 4 days followed by 3 days of air drying at 22 ± 2 °C and 50% ± 3% RH. During each cycle of wetting and drying, the water in the curing tank was replaced by fresh tap water to prevent it from becoming saturated with leached calcium from prior cycles.

AUTOGENOUS CRACK HEALING EVALUATION METHODS

In addition to the microwave reflection measurements, the variations in capillary water absorption and surface crack widths of the samples over the exposure cycles were examined to corroborate the results derived by microwave measurements. A detailed description of the testing procedures applied in this study is provided below.

Microwave Measurement Approach. The microwave measurements were conducted using an open-ended rectangular waveguide (OERW) probe along with an HP8510C vector network analyzer (VNA), as shown in Figure B-1(a). An OERW is a linearly polarized probe suitable for the type of measurements required in this investigation (Qaddoumi and Zoughi 1997; Zoughi 2012). The (calibrated) VNA transmits the microwave signal through the OERW onto the sample and measures the reflected signal received by the OERW to determine |Γ| (i.e., the complex ratio of these two signals). Past microwave reflectometry investigations have shown that this parameter is sensitive to materials variations in cement-based materials (Bois et al. 1999, 1998, 2000; Hashemi et al. 2015; Peer et al. 2003; Zoughi et al. 1995).

The microwave measurements were conducted across the four sides of the samples (excluding top and bottom surfaces) at S-band (2.6-3.95 GHz) and X-band (8.2-12.4 GHz) frequency ranges. The analysis of the microwave measurement results reported in this study was performed for two frequencies of 3 and 10 GHz, representing each frequency band. Signal wavelengths in air at 3 and 10 GHz correspond to 100 and 30 mm, respectively. These values are affected by the dielectric properties of the mortar samples at these frequencies (Bois et al. 1998). Dielectric materials are represented by their complex relative (to free-space) dielectric constant (ε_r) as follows:

$$\varepsilon_r = \varepsilon_r' - \mathrm{j}\varepsilon_r'' \qquad \text{B-1}$$

where ε_r' (real part) and ε_r'' (imaginary part) refer to the permittivity and loss factor, respectively. The permittivity represents the ability of a material to store microwave energy, and the loss factor refers to the ability of the material to absorb microwave energy. The complex dielectric constant values at 3 days for the reference OPC mortar sample at S-band and X-band were calculated to be ε_r = 6.2 – j0.9 and ε_r = 5.2 – j0.4 , respectively, using the measured complex reflection coefficient of sample (Ghasr et al.

2009). Consequently, the wavelengths in the mortar sample are calculated to be ~40 and ~13 mm at 3 and 10 GHz, respectively (Ulaby et al. 1986).

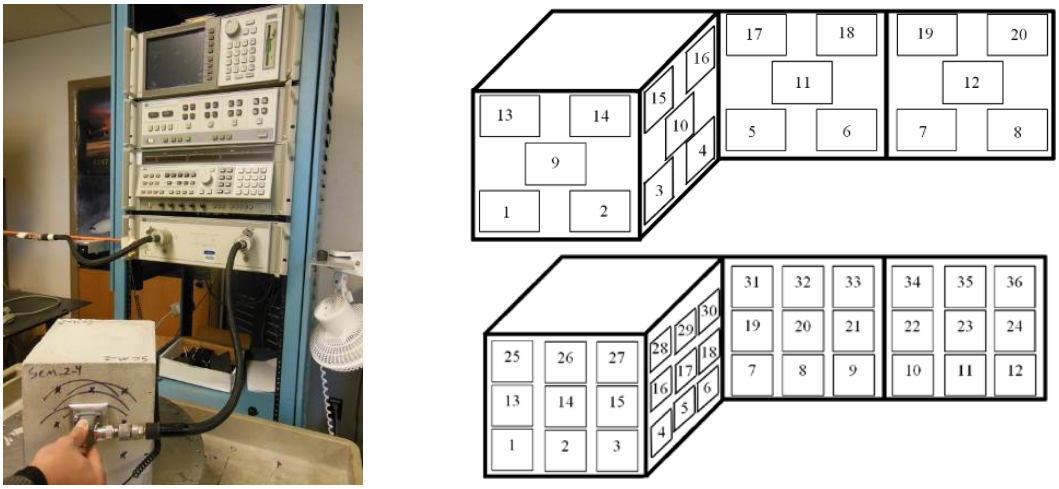

(a) (b)

Figure B-1 (a) Microwave measurement setup, and (b) Schematic illustration of zones: 20 measurement zones (80 × 50 mm^2) for measurements at 3 GHz; and (ii) 36 zones (30 × 30 mm^2) for measurements at 10 GHz.

The microwave reflection measurements were conducted on mortar samples measuring 200 × 200 × 200 mm^3. The dimensions of the samples were selected to be sufficiently large to ensure that the microwave signal penetration depth at the evaluated operating frequencies is less than the thickness of the sample (Bois et al. 1998), so that the backside of the sample did not contribute to the measured reflection coefficient. It is noted that that microwave reflection properties are volumetric measurements. The depth of penetration of power (δ_P) is a function of dielectric properties and distance from the surface of the sample, which can be quantified as follows (Ulaby et al. 1986):

$$\delta_P(m) = \frac{1}{\kappa_a} \tag{B-2}$$

where κ_a is the power absorption coefficient, which is calculated as follows:

$$\kappa_a = 2 \times \alpha = 2\left(\frac{2\pi f}{c}\left|\mathrm{Im}\left\{\sqrt{\varepsilon_r}\right\}\right|\right) \tag{B-3}$$

where α refers to absorption constant of medium (Np/m), f is the operating frequency (Hz), and c is the speed of light (3×10^8 m/s). $\mathrm{Im}\left\{\sqrt{\varepsilon_r}\right\}$ represents the imaginary part of

square root of dielectric constant. As deduced from Eqs. (2) and (3), the depth of penetration decreases as a function of increasing operating frequency. Considering the dielectric constant calculated for the reference sample and using Eqs. (2) and (3), the penetration depths of power at operating frequencies of 3 and 10 GHz in a mortar medium can be estimated to be ~95 and ~33 mm, respectively. Therefore, this confirms that the microwave signals were contained within the mortar samples, and so the sample back surfaces did not contribute to the $|\Gamma|$ measurements, while interior cracks within the sample were exposed to these signals.

After sample demolding at 24 hours, all samples were wet cured for 72 hours using a wet burlap and covered with plastic sheet. Following wet curing (i.e., 3 days of sample age) and prior to crack initiation, the first microwave measurement (hereon referred to as measurement set A) was conducted on mortar samples. One mortar sample from each set was immediately subjected to compressive loading to initiate cracks, then the second microwave measurement (hereon referred to as measurement set B) was conducted on both cracked and uncracked samples. Subsequently, all mortar samples were exposed to 10 wet-dry cycles (hereon referred to as measurement sets C1-C10) and microwave reflection properties of samples were consecutively measured before the initiation of subsequent soaking (i.e., at the end of each drying period). Table B-1 summarizes the timeline of sample preparation and microwave measurement sets conducted on test samples.

Table B-1 Timeline of sample preparation and microwave measurement protocol.

Sample age (days)	Measurement set	Summary of processing
0	–	Preparing mortar mixtures and casting samples
3	–	3 days of wet curing for mortar samples
3	A	First microwave measurement
3	B	Crack initiation and second microwave measurement
10, 17, 24, 31, 38, 45, 52, 59, 66, and 73	C1–C10	10 wet-dry cycles consisting of 4 days of water soaking followed by 3 days exposure to air drying; taking microwave measurement at the end of each drying cycle prior to initiation of subsequent soaking

In order to quantitatively assess the variations in microwave reflection properties caused by crack initiation and crack healing evolution, the mean and COV of $|\Gamma|$ for each

sample after every measurement were calculated. As such, each surface of mortar sample was divided into five and nine equivalent zones with respect to the probe dimensions used at 3 and 10 GHz, respectively. As illustrated in Figure B-1(b), 20 [4 (surfaces) × 5 (points)] and 36 [4 (surfaces) × 9 (points)] measurements were conducted on each sample at 3 and 10 GHz, respectively. At 3 GHz, the size of the waveguide probe is 72.1 × 34 mm^2, which is about three times larger than the size of the probe used at 10 GHz with dimensions of 22.28 × 10.1 mm^2. The number of measurements and spacing between data points were adjusted to ensure that the results of microwave reflection properties are statistically independent, so no overlapping areas were examined on any of the samples. For each microwave measurement set, the overall mean and COV of $|\Gamma|$, corresponding to all zones for each sample (20 or 36 zones per sample), were quantified as follows:

$$\text{Mean of } |\Gamma| = \frac{\sum_{i=1}^{n} |\Gamma|_i}{n} \tag{B-4}$$

$$\text{COV of } |\Gamma|(\%) = \frac{\sqrt{\frac{1}{n}\sum_{i=1}^{n}(|\Gamma|_i - |\Gamma|_{mean})^2}}{|\Gamma|_{mean}} \times 100 \tag{B-5}$$

where $|\Gamma|_i$ refers to the magnitude of reflection coefficient measured in each zone and n is the number of zones for each sample, which was taken as 20 and 36 corresponding to the measurements frequencies at 3 and 10 GHz, respectively. Therefore, a larger COV value represents higher non-uniformity and inhomogeneity of sample due to the crack formation.

Ultrasonic Transmission Measurement Approach. The effect of crack formation and autogenous crack healing on ultrasonic wave propagation through the mortar samples were measured. Ultrasonic waves travel faster in solids such as hardened cement-based materials (4000–5000 m/s) than in water (1480 m/s) or air (350 m/s) (Krautkrämer and Krautkrämer 2013; Popovics et al. 1990). Therefore, it is expected that the ultrasonic transmission time will be higher in a cracked sample than uncracked sample (i.e., ultrasonic waves must travel around the cracks), resulting in a decrease in the associated pulse velocity. However, the ultrasonic transmission time is expected to decrease as the sample heals and densifies over wet/dry cycles. In this study, the

ultrasonic test was conducted on the same samples that were used for the microwave measurements. In this test, transducers (transmitter and receiver) operating at 54 kHz conforming to ASTM C597 (*Annual Book of ASTM Standards* n.d.) were placed perpendicular to the samples surfaces at nine different zones for every two sides of sample surfaces (the same zones at which the microwave measurements were conducted at 10 GHz (see Figure B-1(b)). Therefore, for every measurement set, 18 ultrasonic measurements (i.e., 9 readings for every two parallel sides) were conducted. The wave transmission (travel) time (subsequently referred to as ultrasonic transmission time) through the 200 mm long cubic samples, was measured. Similar to the microwave approach, the mean and COV of ultrasonic transmission time of each sample were calculated for every measurement set. The ultrasonic transmission time was determined immediately before and after cracking to evaluate the impact of crack formation in terms of increase in mean and COV values of ultrasonic transmission time. Subsequently, the ultrasonic measurements were conducted at different wet/dry cycles (see Table 1) to monitor the crack healing process and correlate the results to those determined from microwave reflectometry technique.

Capillary Water Absorption Approach. In order to evaluate the water transport properties, the capillary water absorption of the investigated mortar samples was measured in accordance with ASTM C1585 (*Annual Book of ASTM Standards* n.d.). The samples were oven-dried at 80 °C for 3 days. Similar to those samples prepared for the microwave measurement. The bottom surface of the samples was then placed in contact with water to a depth between 1-3 mm. The temporal changes in mass of the samples due to capillary draw were recorded. The amount of absorbed water is normalized by the cross-section area of the sample exposed to the water, which is calculated as follows:

$$I = \frac{m_t}{a \times d} \tag{B-6}$$

where I is the capillary absorption (mm^3/mm^2), m_t is the sample mass (g) at time t, a is the exposed area (mm^2) of the sample, and d is the density of water.

Crack Healing Quantification and Characterization of Healing Products. An optical microscope (CrackScope CS-1000) was used to monitor the variations in crack

width of cracked samples during the crack healing process. The crack healing efficiency of cracked samples over wet-dry cycles is quantified as follows:

$$\text{Crack healing efficiency}\,(\%) = \frac{cw_i - cw_t}{cw_i} \times 100 \qquad \text{B-7}$$

where cw_i and cw_t refer to initial crack width (i.e., before cyclic exposure) and crack width at time t, respectively. Thus, in the case of complete crack closure at a specific location, the crack healing efficiency is calculated to be 100%. Each time, crack width measurements were carried out at the exact same locations. Per each measuring period and at 40 points along different crack lengths, crack widths were measured.

X-ray diffraction (XRD) analysis was conducted using a Philips X'pert diffractometer in a θ–θ configuration using CuKa (k = 1.54 Å) radiation. The powdered samples were taken from cracked mortar samples to analyze the healing products formed onto the surface of cracks. Scanning electron microscopy (SEM) coupled with energy-dispersive spectrometry (EDS) detector (Hitachi S4700-SEM) was used to characterize the microstructure and chemical composition of crack healing products. Samples with dimensions of 15 × 15 mm^2 were extracted from the interior part of cracks and were prepared for SEM-EDS imaging.

TEST RESULTS

Effect of Hydration Process and Moisture Ingress. Aside from crack formation and autogenous crack healing, the other potential causes for the variations in microwave reflection properties and ultrasonic transmission time are related to combined effect of hydration progress and moisture ingress for samples subjected to wet/dry cycles. After wetting cycle, sample is expected to result in an increase in the microwave refection coefficient, while leading to a decrease in the ultrasonic transmission time. on the other hand, drying cycle can cause a reverse effect on these measurements. The results of microwave reflection and ultrasonic transmission time in Figure B-2 reveal the effect of wet/dry cycles on continuing hydration and/or moisture ingress changes for uncracked samples. The results indicate that samples exhibited an increase in the mean of |Γ| and a decrease in the mean of ultrasonic transmission time during wet/dry exposures. For

instance, after 10 wet/dry cycles, the OPC-SCM sample exhibited 8% increase in |Γ| at 10 GHz and 12% reduction in ultrasonic transmission time.

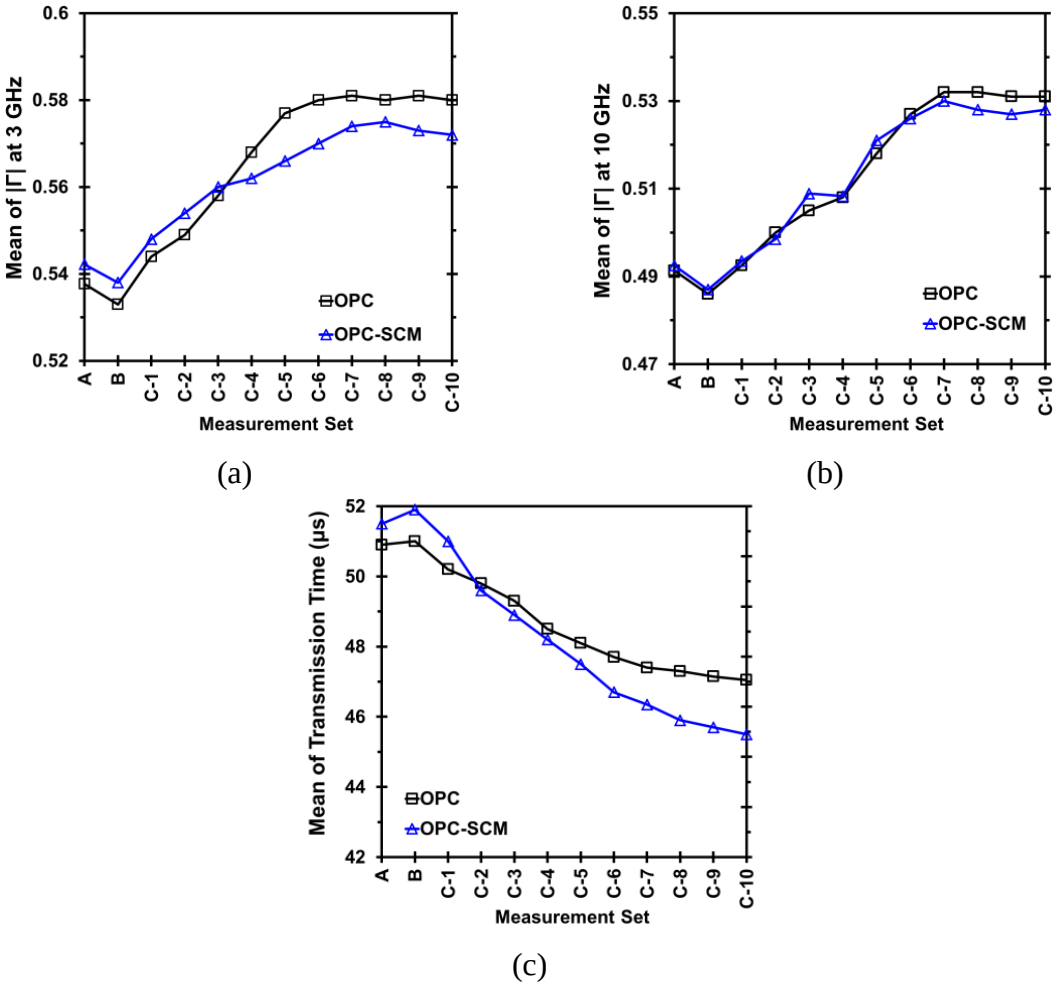

Figure B-2 Combined effect of hydration progress and moisture ingress on various responses for uncracked samples at different measurement sets: (a) mean of |Γ| at 3 GHz, (b) mean of |Γ| at 10 GHz, and (c) mean of ultrasonic transmission time.

The decrease in the transmission time, during cyclical exposure, can be attributed to the: (i) microstructural evolution and enhanced solid-to-solid connectivity as the hydration progresses (Boumiz et al. 1996); and (ii) water movement due to the capillary draw which can partially fill the pores, thus decreasing the wave transmission time travelling through the sample. These effects contribute to the changes in microwave reflection properties of mortar samples subjected to the same cyclical exposures. Given the relatively low dielectric properties of the other constituents of mortar, the dielectric

properties of (free) water dominates the overall dielectric properties of the mortar sample (Bois et al. 1998; Hashemi et al. 2015). Therefore, any changes in the microwave reflection properties of the sample are expected to be primarily related to the presence of free water (i.e., water existing in pores) in the sample. During the wetting cycle, two competing effects are present. First, the transformation of free water to (chemically) bound water with progressing hydration reactions reduces the microwave reflection coefficient, since free water has higher dielectric constant (i.e., permittivity and loss factor) compared to the bound water (Donnell et al. 2013; Hashemi et al. 2015). However, this action is counteracted by the second effect, which is a significant increase in the reflection coefficient due to the ingress of moisture and capillary draw action when sample is soaked. Given the fact that the dielectric properties of free water is considerably larger than that of bound water (Ulaby et al. 1986), the increase in the amount of free water in the sample increases the microwave reflection properties.

Given higher porosity of samples at early age, particularly for the OPC-SCM sample, the permittivity increases with penetration of free water in sample during wetting cycles. However, the porosity of samples is expected to decrease with increasing the number of wetting and drying cycles due to the hydration progress and pozzolanic reaction, as indicated by the reduction in ultrasonic transmission time in Figure B-2(c). As such, the difference between water absorption during wetting cycle and evaporation over drying cycle become less, and moisture transport properties tend to stabilize. This tendency contributes to no further changes in microwave measurements with subsequent cyclic exposures, and consequently microwave reflection properties remain constant.

Upon comparing the microwave measurement results at 3 and 10 GHz, the mean of $|\Gamma|$ at 3 GHz was found to be more affected by the moisture content changes in the samples. This is consistent with results reported by Hashemi et al. (Hashemi et al. 2015), who noted that microwave measurement at lower frequencies (e.g., S-band) is more affected by the free water present in the pores compared to the higher frequencies (e.g., X-band). From Figure B-2(a), it can be seen that the OPC-SCM sample had, on average, lower mean value of reflection properties as compared to that of the plain OPC sample. This is primarily due to the pozzolanic reaction in sample containing SCMs when exposed to wetting cycles, which can refine the pore structure and reduce the pore-to-

pore connectivity, thus resulting in greater densification of microstructure and lower water absorption. This is corroborated in Figure B-2(c) which indicates that the OPC-SCM sample had lower ultrasonic transmission time at later age compared to the plain OPC sample. These results are in agreement with capillary absorption profiles, which are discussed in detail later.

Therefore, to isolate the effect of autogenous crack healing from further hydration and/or moisture transport properties in the samples (regardless of crack formation), the *normalized* COV values were used in this study. This was calculated by dividing the COV value obtained for the cracked sample by its corresponding uncracked value for a given cycle. This approach has been applied in the previous studies (Kan et al. 2010; Van Tittelboom et al. 2010; Yang et al. 2009b). Therefore, a reduction in the overall normalized COV for a given cracked sample can be an indication of crack healing evolution, featuring an increase in sample homogeneity (recovery), and consequently a reduction in point-to-point measurement variations.

Effect of Crack Formation. Figure B-3 shows representative histograms of microwave $|\Gamma|$ for the OPC-SCM sample at different operating frequencies for two different measurement sets: before cracking (set A) and after cracking (set B). Given the relatively homogeneous nature of the mortar sample prior to crack generation, the majority of $|\Gamma|$ measurements fell within a narrow range (i.e., uniform reflection coefficient), especially at operating frequency of 3 GHz (Figure B-3(a)). Compared to 3 GHz, the microwave measurements were found to have larger variations in $|\Gamma|$ at operating frequency of 10 GHz. It is important to point out that microwave measurements conducted at higher frequency (smaller wavelength) is more sensitive to the level of sample inhomogeneity caused by variations in, e.g., air voids and sand particles. The formation of cracks due to the loading induced considerable variations in microwave reflection properties, as indicated in Figure B-3(b) and (d). This variation is attributed to the formation of internal and external cracks and increased porosity (i.e., increased air void) as well as moisture movement within pores as a consequence of compressive loading, that can lead to property variations within the sample and then point-to-point measurement variations in the microwave signal.

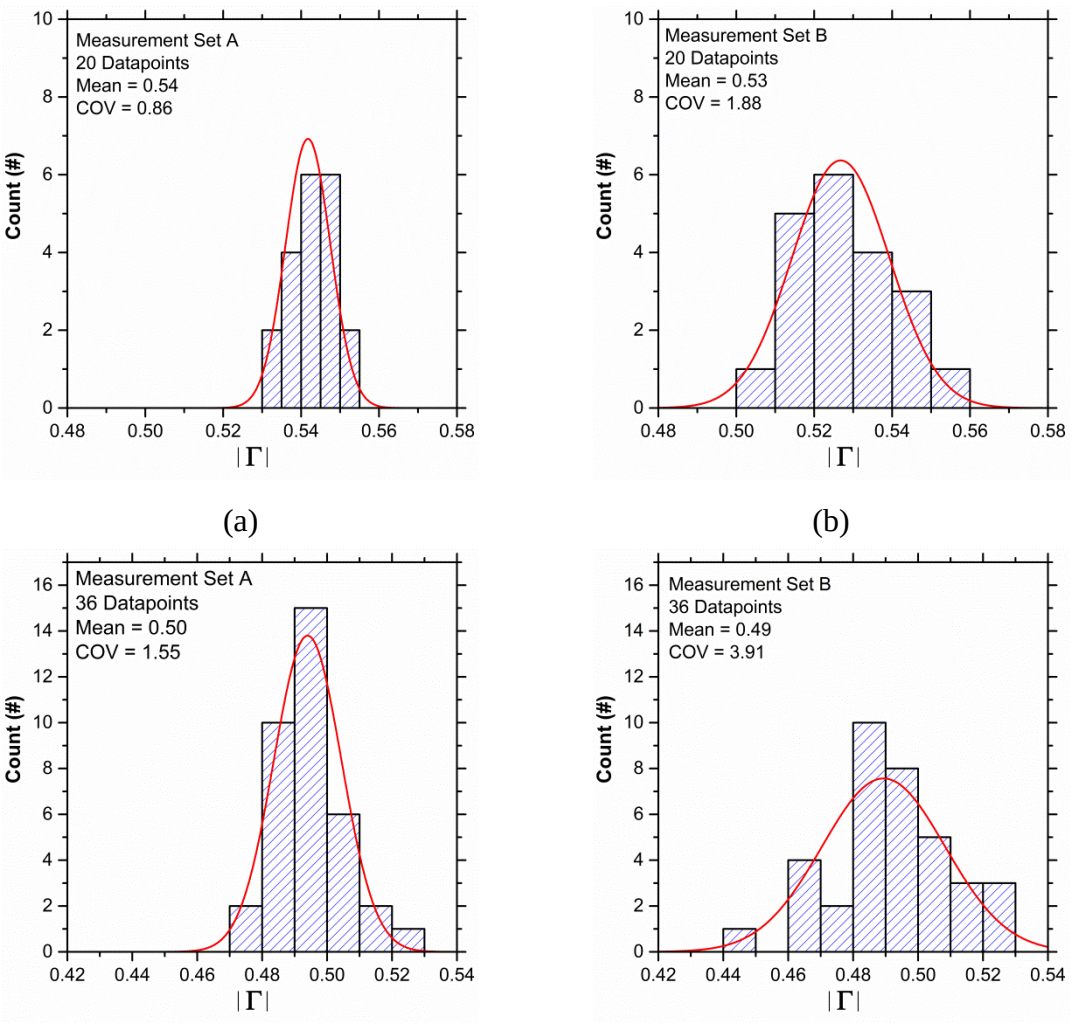

Figure B-3 Representative histograms of microwave |Γ| for the OPC-SCM sample at: (a) 3 GHz before cracking, (b) 3 GHz after cracking, (c) 10 GHz before cracking, and (d) 10 GHz after cracking.

The variations in |Γ| induced by crack formation were found to be more evident at operating frequency of 10 GHz. For instance, microwave measurements conducted at 10 GHz exhibited 80% and 107% larger COV values of |Γ| for before and after cracking, respectively, compared to those obtained at 3 GHz. As noted above, this signal variation is expected to be more significant at higher microwave frequencies, where the operating signal wavelength is relatively small. It is important to note that the microwave measurement sets A and B were conducted at the same day to reduce/eliminate the effect of water evaporation. This was supported by the mass measurement which showed no

mass changes in samples before and after compressive loading. Based on the visual observations from sample surfaces, the crack widths were not identical along their lengths, and they became narrower upon crack propagation from top to bottom part of sample. It is interesting to note that microwave measurements conducted in the middle (13–24) and top (25–36) parts of the cracked sample had higher variations in reflection properties compared to the bottom part of the same sample. This can be the result of larger crack widths formed at the top, which can result in higher variation in the measured |Γ| values. The variations in microwave reflection properties, therefore, confirm the sensitivity of microwave reflectometry approach to the crack formation induced by compressive loading.

The histograms in Figure B-4 show the variations in ultrasonic transmission times before and after cracking for the OPC-SCM sample. The variations in ultrasonic transmission time can be used to quantify the level of damage induced by compressive loading.

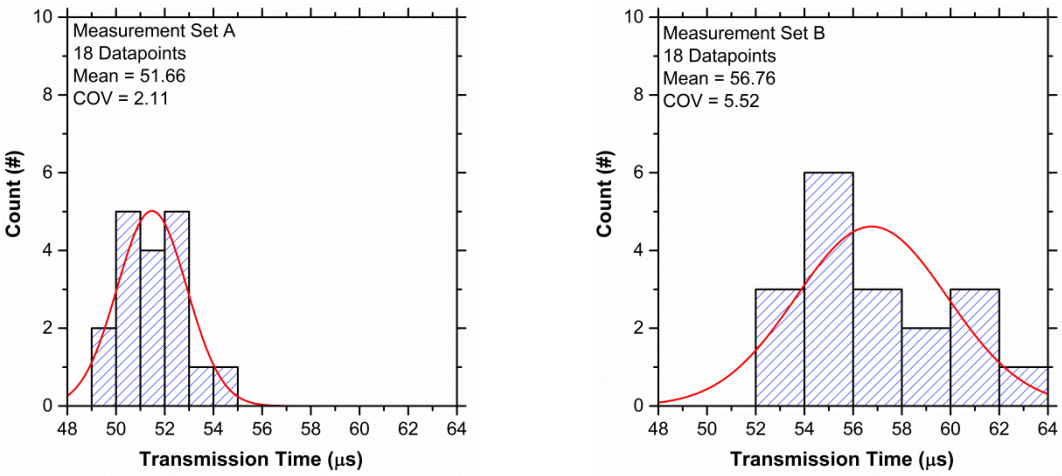

(a) (b)

Figure B-4 Representative histograms of ultrasonic transmission time variations due to the crack formation for the OPC-SCM sample: (a) before cracking and (b) after cracking.

The crack formation resulted in a significant increase in the mean and COV values of ultrasonic transmission time of around 10% and 160%, respectively. Although crack formation induces small changes in overall mean value of ultrasonic transmission

time (10%), the variations in transmission times obtained for 18 different zones across the mortar sample produced 1.5 times higher COV values compared to the uncracked sample. This implies that the changes in material properties induced by crack formation are not consistent and cracks are non-uniformly distributed within the sample medium. These results are in agreement with those determined from microwave measurements which indicated larger variations in overall COV of |Γ| due to the crack generation compared to the changes in overall mean value of |Γ|, especially at microwave frequency of 10 GHz.

Effect of Crack Healing Evolution. Figure B-5 shows the variations in normalized COV values of |Γ| at different measurement sets and operating frequencies. As expected, cracked samples exhibited consistently higher point-to-point measurement variation due to the scattering of microwave signals caused by cracks. This is more evident after the first wet/dry exposure (measurement set C-1) due to the changes in the moisture content of cracked samples, as explained earlier. This effect was more pronounced at higher operating frequency of 10 GHz compared to 3 GHz.

As mentioned earlier, microwave measurements at higher operating frequency are more sensitive to the level of inhomogeneity of the medium, especially for changes occurring near the sample surface. Upon further exposure to wet/dry cycles, the variations in microwave measurements for the cracked samples were found to decrease, resulting in lower COV values of |Γ|. This feature is more evident for the cracked OPC-SCM sample due to the pozzolanic activity, thus contributing to a higher crack healing efficiency compared to the plain OPC sample. Although the cracked OPC-SCM sample had initially larger variation in reflection properties measured at the first wet/dry cycle, this sample underwent less variations in COV of |Γ| upon further wet/dry exposures compared to the cracked OPC sample. For instance, at operating frequency of 10 GHz, the OPC-SCM sample after 10 wet/dry exposures exhibited 52% lower normalized COV value compared to the COV value determined at first cycle. However, the OPC sample only experienced 17% reduction in normalized COV value after undergoing 10 cycles. This is due to the (i) pozzolanic reaction; and (ii) formation of calcium carbonate, thus leading to the formation of space-filling materials to fill the cracks and reduce the level of inhomogeneity of cracked sample. This is corroborated in the next section by characterizing the healing products formed to fill the cracks.

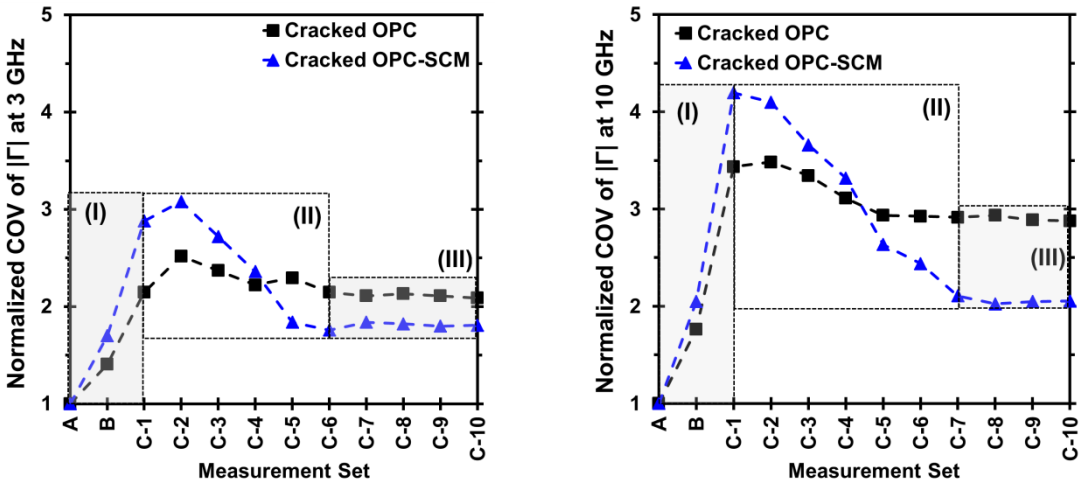

(a) (b)

Figure B-5 Variations in normalized COV of |Γ| for cracked samples at different measurement sets for: (a) 3 GHz and (b) 10 GHz.

It is important to note that the COV values of |Γ| for cracked samples stabilized after a certain number of cyclic exposures, as shown in Figure B-5. Although this phenomenon was observed for both the plain OPC and OPC-SCM samples, the latter sample necessitated larger number of wet/dry cycles to reach a constant COV value. This can be due to the higher demand of OPC-SCM sample to water provided by wetting cycle to complete its hydration and promote crack healing process compared to the plain OPC sample. The constant COV values of |Γ| for cracked samples can be an indication of the end of crack healing process, after which cracked sample is not able to continue healing cracks, and hence microwave measurements remain unchanged upon further wet/dry cycles. As can be noticed from Figure B-5, the COV values for the cracked samples did not reach the state of uncracked sample. The difference in COV values between before cracking and after cracking with undergoing 10 cycles implies that cracks were not fully healed. This is supported by the results of crack healing efficiency which highlights that some cracks were partially healed or even unhealed after undergoing 10 wet/dry cycles, particularly for crack widths wider than 300 µm.

Based on the aforementioned discussion, the COV trends obtained for |Γ| can be divided into three parts, as indicated in Figure B-5. Part (I) corresponds to a significant point-to-point microwave reflection coefficient variations resulting from crack formation

and moisture ingress after the first cycle. Part (II) indicates the onset of crack healing evolution as identified by the reduction in COV values. Finally, part (III) represents the end of potential for crack healing process as indicated by relatively constant COV values during additional cyclic exposures. Therefore, based on these results, the comparison of COV values of |Γ| can be used as an indication for monitoring crack healing capability of cementitious materials. Sample with a greater autogenous healing capacity tends to have a larger reduction in overall COV values throughout the measurement sets. Therefore, the reduction in COV values of |Γ| implies that the homogeneity (recovery) associated with cracked sample increases, thus resulting lower point-to-point microwave reflection properties variations.

Figure B-6 depicts the correlation between COV of |Γ| and COV of ultrasonic transmission time for the cracked samples for all the measurements sets (Table 1). The resulting linear correlation between microwave reflectometry and ultrasonic test indicates that sample with larger point-to-point microwave reflection coefficient variation is expected to have higher variations in ultrasonic transmission time.

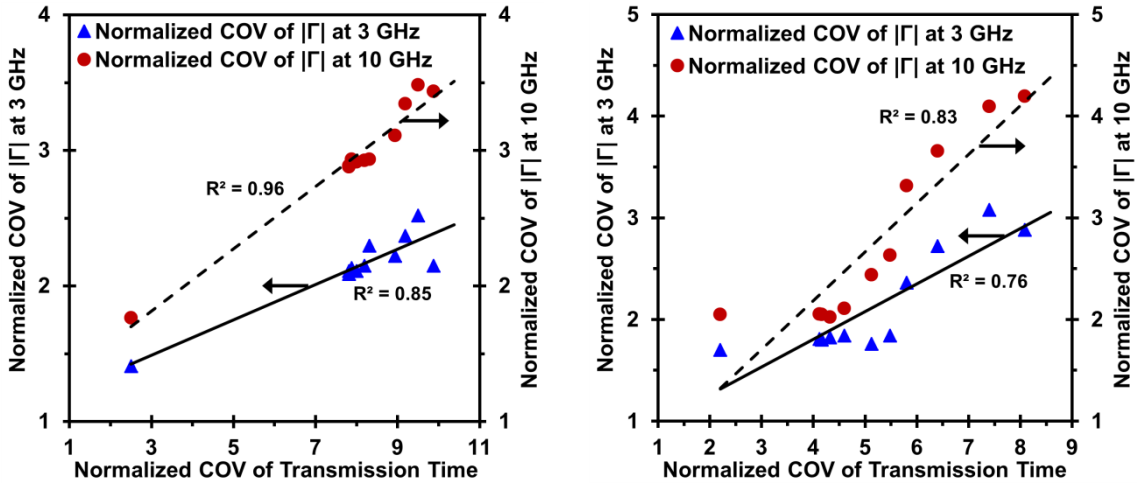

Figure B-6 Correlation between COV of |Γ| determined from microwave measurement and transmission time measured from ultrasonic test for: (a) cracked OPC sample and (b) cracked OPC-SCM sample.

Regardless of the binder composition, this correlation was more pronounced for microwave measurements conducted at operating frequency of 10 GHz, which is

identified by the steeper linear trend-line in Figure B-6. Furthermore, independent of the microwave frequency used, the OPC-SCM sample exhibited larger spread in COV values compared to the plain OPC sample. This is due to the higher autogenous healing capability of sample made with SCM replacements compared to the pure OPC sample, thus indicating a larger spread in the test responses during wet/dry cycles.

DISCUSSION

When a mortar sample is soaked, water penetrates into the pores through a capillary draw mechanism. The formation of cracks aids in the absorption process by increasing the amount of water drawn inside the cracks. Upon initiation of drying cycle, a portion of the water, mostly from the near surface regions (i.e., within cracks and pores) is evaporated. However, the remaining portion of water can be drawn towards the core of sample (i.e., water movement due to capillary draw) that can promote the hydration of unhydrated cementitious materials and form self-healing products. As the cracks heal and fill with healing products, the rate of water absorption (by capillary draw) decreases. To further elaborate on the water transport characteristics of samples, the capillary water absorption of the mortar samples were evaluated. Figure B-7(a) shows the profiles of capillary water absorption for both cracked and uncracked samples. As expected, cracked samples experienced larger extent and faster rate (i.e., larger slope) of capillary water absorption over the testing period. The cracks were gradually filled by the healing products once the sample was soaked in water. Figure B-7(b) shows the evolution of crack healing process for the cracked OPC-SCM sample using optical microscopy. It can be seen that surface cracks with different widths are filled with white healing products, thus leading to a decrease in water absorption rate over time. The crack healing products observed on the surface of cracked sample appears to be due to the precipitation of calcium carbonate crystals, which will be corroborated later. To account for cement replacement (i.e., cement dilution), both uncracked and cracked OPC-SCM samples exhibited higher water absorption at early-age compared to the corresponding OPC samples. However, this trend is reversed at later ages due to the pozzolanic reaction and higher formation of hydration products that can reduce porosity. These trends observed for water absorption support the results of microwave measurements conducted at the

lower frequency of 3 GHz. The OPC-SCM sample had initially higher reflection properties than that of the plain OPC sample. However, the former sample tended to have lower reflection properties at later ages compared to the latter sample, suggesting lower presence of free water in OPC-SCM sample at later ages.

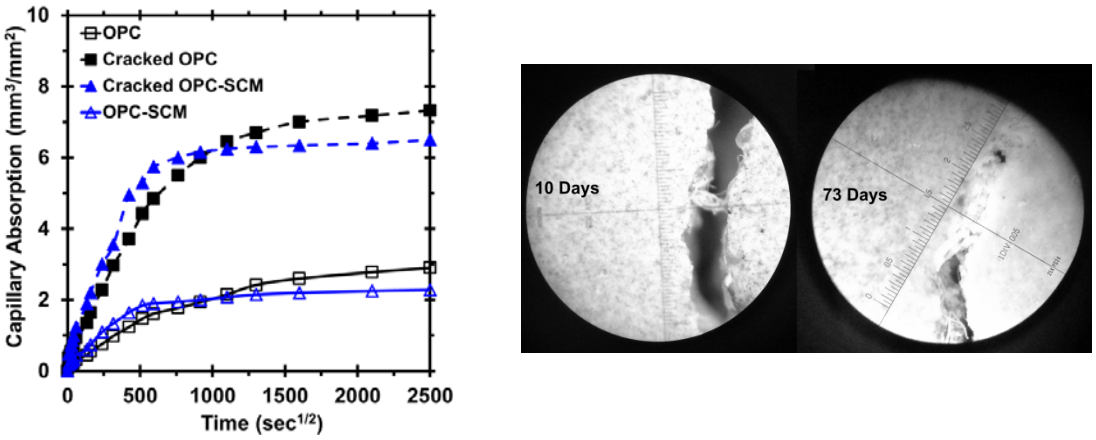

(a) (b)

Figure B-7 (a) Capillary water absorption profiles for both cracked and uncracked samples as a function of time. (b) Showing autogenous crack healing evolution for OPC-SCM sample after one and 10 wet-dry cycles.

In order to monitor the crack healing efficiency, the surface crack widths of samples were quantified using optical microscope after each wet-dry exposure. From Figure B-8, it can be seen that cracked mortar sample containing SCMs exhibited larger crack healing capability at different exposure cycles than that of the cracked OPC sample. After 10 wet-dry cycles, the cracked OPC-SCM sample was able to completely heal crack widths up to 220 μm compared to 90 μm for the OPC sample. As expected, the capability of autogenous healing to fill a crack reduces with increasing crack width. The cracked OPC-SCM sample underwent partial crack healing for crack width between 250 and 400 μm and no healing for crack width more than 400 μm. As mentioned earlier, the lower variations (i.e., smaller COVs) of microwave reflection properties over exposures is an indication of crack healing process for cracked samples. This feature was more pronounced for OPC-SCM sample due to its higher crack healing potential. However, the mean and COV values of cracked sample did not reach similar values to that of the corresponding uncracked sample, since cracked sample was not able to completely heal

cracks. Therefore, the reduced trend in COV and the consistent trend of mean values of microwave reflection properties over cyclic exposure can be an indication of crack healing evolution and reduced changes in water transport properties in cracked sample, as corroborated in Figures B-7 and B-8.

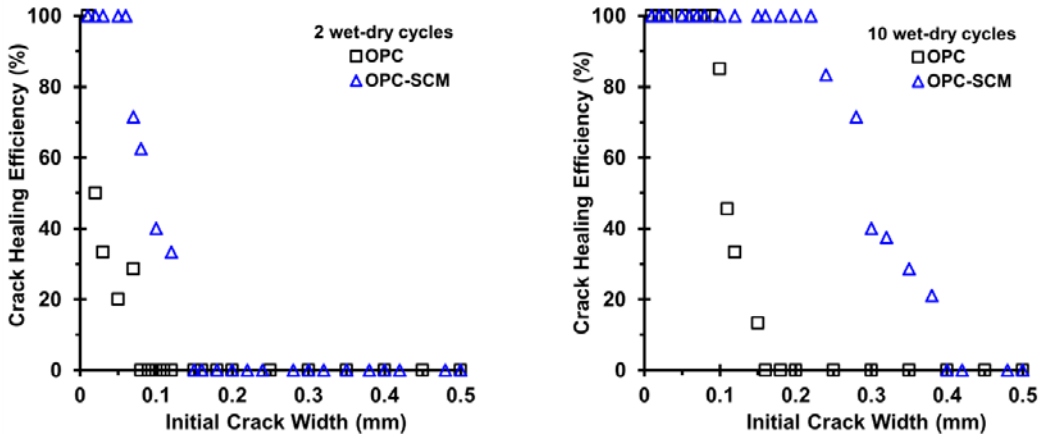

(a) (b)

Figure B-8 Representative crack healing efficiency results of cracked samples after: (a) 2 wet-dry cycles and (b) 10 wet-dry cycles.

Two main mechanisms are generally responsible for the autogenous crack healing: (i) secondary hydration of the unhydrated cement and pozzolanic reaction associated with incorporating SCMs; and (ii) precipitation of calcium carbonate crystals, wherein the CO_2 from atmosphere dissolves in water and generates CO_3^{2-}, which can react with free dissolved Ca^{2+} from mortar medium to form $CaCO_3$. The formation of calcite on crack and internal side of cracks can change the dielectric properties of materials, thus altering microwave reflection properties. Several studies have demonstrated that the permittivity of calcite varies between 7 and 9 (Friedman 1998; Lebron et al. 2004), which is significantly higher than the permittivity of cement-based materials. This implies that in addition to water transport properties of sample, the precipitation of calcite can elevate the measured microwave reflection properties. To verify this, XRD analysis and SEM-EDS imaging were applied to examine the composition of healing products formed onto the surface and internal part of cracks after 10 wet-dry cycles. As shown in Figure B-9(a), the cracked OPC-SCM sample had larger

intensity of calcite and portlandite peaks compared to the uncracked sample. The SEM observation for cracked OPC-SCM sample in Figure B-9(b) confirms the formation of stone-like calcite crystals, which are intermixed with hydration products (i.e, C-S-H and $Ca(OH)_2$).

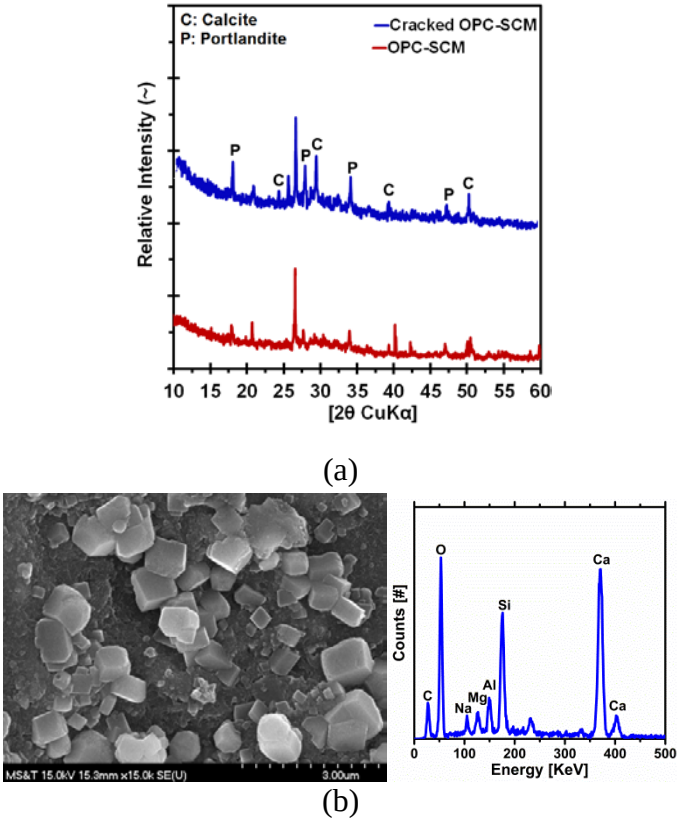

Figure B-9 Characterization of healing product composition: (a) representative XRD patterns for surface layer of OPC-SCM samples after 10 wet-dry cycles (for cracked sample, XRD analysis was performed on healing products formed on cracked surface) and (b) SEM image coupled with EDS pattern from internal part of healed crack for OPC-SCM sample after 10 wet-dry cycles.

The SEM-EDS examination revealed that Ca, Si, O, Al, and C are the main elements present in healing products, hence suggesting that the healing products are mainly composed of calcium carbonate intermixed with C-S-H/$Ca(OH)_2$. These observations are consistent with previous studies, where note that autogenous self-healing is attributed to the formation of C-S-H, the dissolution and re-deposition of $Ca(OH)_2$, and calcium carbonate (Maes et al. 2016; Sahmaran et al. 2013; Snoeck et al. 2016).

SUMMARY

This study was undertaken to evaluate the feasibility of using near-field microwave reflectometry to nondestructively monitor the autogenous crack healing process of mortar samples. The results of interaction of microwave signals with cracked mortar samples containing ternary binder of 20% slag and 35% fly ash and that without any SCMs (i.e., plain OPC mortar sample) were compared. The results of microwave reflectometry were also compared/correlated with ultrasonic transmission time for the cracked samples throughout crack healing process. Based on the obtained results, the following conclusions can be drawn:

- Cracked samples underwent higher point-to-point microwave measurement variations due to the scattering of microwave signals caused by cracking, especially at higher operating frequency. Microwave measurements conducted at 10 GHz exhibited 80% and 107% larger COV values of $|\Gamma|$ for before and after cracking, respectively, compared to those obtained at 3 GHz. This is attributed to the larger sensitivity of high operating frequency to level of inhomogeneity of the mortar sample medium caused by cracks.
- When subjected to wet/dry cycles, the point-to-point microwave reflection variations for the cracked samples decreased, thus resulting in lower COV values, especially at operating frequency of 10 GHz. This behavior is more evident for cracked OPC-SCM sample due to its pozzolanic reaction. The OPC-SCM sample after 10 wet/dry cycles exhibited 52% lower COV value compared to the first cycle. However, the OPC sample only had 17% reduction in COV value after undergoing the same number of cycles.
- For the cracked samples, the COV trends obtained for $|\Gamma|$ can be divided into three parts as a function of wet/dry cycles: part (I) corresponding to a significant variation in microwave reflection properties resulting from crack formation and moisture ingress after the first wetting cycle; part (II) indicating the start of crack healing process as identified by the reduction in the COV trends; and part (III) representing the end of potential for crack healing process as identified by the relatively constant COV values during additional wet/dry cycles.

- The variations in microwave reflection properties for cracked mortar samples are linked to the changes in water transport properties induced by cracking and subsequent autogenous crack healing process. The XRD analysis coupled with SEM-EDS examination revealed the formation of $CaCO_3$ intermixed with C-S-H/$Ca(OH)_2$ in the cracked OPC-SCM sample.
- A linear correlation was obtained between COV trends of reflection coefficient determined from microwave measurement and transmission time obtained from ultrasonic test. Samples with larger point-to-point microwave measurement variations showed larger variations in ultrasonic transmission times.
- The results of the microwave measurements presented in this study demonstrate the clear potential of this one-sided microwave nondestructive diagnosis technique for monitoring autogenous crack healing evolution. The reported results are promising and can be extended upon further investigations involving a more expanded set of important parameters, such as constitutive materials, exposure condition, and other types of self-healing approaches.

APPENDIX C

RESUME

Iman Mehdipour

Email: iman.mehdipour@mst.edu

Education

2013- 2017 Ph.D. Candidate, Civil Engineering
Missouri university of Science and Technology, MO, USA
Advisor: Dr. Kamal H. Khayat
GPA: 4.0/4.0

2009-2012 Graduate Student (M.Sc.), Civil and Geotechnical Engineering
Department of Civil Engineering, International University of Qazvin, Qazvin, Iran
Advisors: Dr. M. Ghazavi & Dr. R. Ziaie
GPA: 17.99/20 (Ranked 1st among 15 M.Sc. students)

2004-2009 Undergraduate Student (B.Sc.), Civil Engineering
Department of Civil Engineering, Islamic Azad University of Qazvin, Qazvin, Iran
GPA: 18.26/20 (Ranked 1st among 85 B.Sc. students)

Academic and Professional Experience

2013-2017	Graduate Research Assistant, Center for Infrastructure Engineering Studies (CIES), Missouri S&T, Rolla, MO, USA
2015-2017	Researcher, Applied Microwave Nondestructive Testing Laboratory (*amntl*), Missouri S&T, Rolla, MO, USA
2012-2013	Lecturer, Islamic Azad University, Buinzahra Branch, Buinzahra, Iran
2007-2013	Research Assistant, Construction Materials Institute (CMI), University of Tehran, Tehran, Iran
2010-2012	Research Specialist, Construction of Concrete Research Center (CCRC), Islamic Azad University, Qazvin Branch, Qazvin, Iran
2009-present	Teaching Assistant, Missouri S&T Rolla, MO, USA and , Azad University, Qazvin, Iran

Awards and Honors

2017 ASNT Student Travel Grant for 26th ASNT Research Symposium
2016 ACI Charles Pankow Fellowship, American Concrete Institute

2016 ASNT Student Travel Grant for 25th ASNT Research Symposium
2015 Honorary DJ Belarbi Graduate Scholarship Award, American Concrete Institute Missouri Chapter
2015 ASNT Student Travel Grant for 24th ASNT Research Symposium
2012 1st rank, M.Sc graduation, Civil and Geotechnical Engineering, International University of Qazvin
2009 1st rank, B.Sc graduation, Civil Engineering, Islamic Azad University
2009 1st Place Student concrete competition, Iranian Concrete Institute
2009 3rd Place Student concrete competition, Iranian Concrete Institute
2006 1st Place Student concrete competition, Iranian Concrete Institute
2006 Best research award, Civil Engineering, Islamic Azad University
2006 Awarded of "Exceptional Talent Student", Civil Engineering, Islamic Azad University

Membership in Scientific and Professional Societies

Associate member ACI Committee 237, Self-Consolidating Concrete
Student member American Society for Engineering Education (ASEE)
Student member American Society for Nondestructive Testing (ASNT)
Student member American Society of Civil Engineers (ASCE)

Academic Service and Activities

Reviewer

ACI Materials Journal, American Concrete Institute
Cement and Concrete Composite, Elsevier publication
Journal of Materials in Civil Engineering, American Society of Civil Engineering
Journal of Transportation Engineering, American Society of Civil Engineering
Journal of Construction and Building Materials, Elsevier publication
Journal of Materials & Design, Elsevier publication
Journal of Building Engineering, Elsevier publication
Geotextiles and Geomembranes, Elsevier publication
The Open Civil Engineering Journal, Bentham Open

Mentoring Activities

2010-2013 Mentoring ~20 Undergraduate Civil Researchers with Emphasis on Cement-Based Materials, Azad University, Iran

Session Chair

2016 25th American Society for Nondestructive Testing Research Symposium (NDT in Cement-Based Materials)
2017 26th American Society for Nondestructive Testing Research Symposium (Materials Characterization)

Co-Organizer

2015 Popsicle Stick Bridge Competition, Youth Transportation Conference, Missouri S&T, Rolla, MO, USA

2016-present Organizing Committee (OC) member for American Society for Nondestructive Testing (ASNT) Research Symposium

Publications

Contributions to Book

M. Shekarchi, N.A. Libre, F. Sabet, I. Mehdipour, “Guidelines for Hot Weather Concreting”, Pendare Pars publication, Tehran, 2012 (in Persian), 134 pp, ISBN: 978-600-6529-20-2.

M. Jesmani, I. Mehdipour, M. Arabshahi, “Problem Solving in Soil Mechanics”, Pouran Pazhuhesh publications, Tehran, 2011 (in Persian), 335 pp, ISBN: 4-165-184-964-978.

Peer-reviewed Journal Articles

[1] I. Mehdipour, A. Kumar, K.H. Khayat, “Rheology, Hydration, and Strength Evolution of Interground Limestone Cement Containing PCE Dispersant and High Volume Supplementary Cementitious Materials”, Materials & Design, 127 (2017) 54–66.

[2] I. Mehdipour, K.H. Khayat, "Effect of Particle-Size Distribution and Specific Surface Area of Different Binder Systems on Packing Density and Flow Characteristics of Cement Paste”, Cement and Concrete Composites, 78 (2017) 120–131.

[3] I. Mehdipour, M. Horst, R. Zoughi, K.H. Khayat, “Use of Near-Field Microwave Reflectometry to Evaluate Steel Fiber Distribution in Cement-Based Mortars”, Journal of Materials in Civil Engineering, 1–12.

[4] I. Mehdipour, N.A. Libre, “Linking Fiber Factor to Material Performance of Fiber-Reinforced Self-Consolidating Cement-Based Materials”, ACI Materials Journal, 114 (1) (2017) 77–912.

[5] Mehdipour, M. Ghazavi, R.Z. Moayed, ”Stability Analysis of Geocell-Reinforced Slopes Using Limit Equilibrium Horizontal Slice Method” International Journal of Geomechanics (accepted for publication).

[6] I. Mehdipour, K.H. Khayat, "Effect of SCM Content and Binder Dispersion on Packing Density and Compressive Strength of Sustainable Cement Paste”, ACI Materials Journal, 113 (3) (2016) 361–372.

[7] A. Foudazi, I. Mehdipour, K.M. Donnell, K.H. Khayat, “Evaluation of Steel Fiber Distribution in Cement-Based Mortars Using Active Microwave Thermography”, Materials and Structures, 49 (12) (2016) 5051–5065.

[8] A. Emdadi, I. Mehdipour, N.A. Libre, M. Shekarchi, "Optimized Workability and Mechanical Properties of FRCM by Using Fiber Factor Approach: Theoretical and Experimental Study", Materials and Structures, 48 (4) (2015) 1149–1161.

[9] I. Mehdipour, M. Vahdani, K. Amini, M. Shekarchi "Linking Stability Characteristics to Material Performance of Self-Consolidating Concrete-Equivalent-Mortar Incorporating Fly ash and Metakaolin" Construction and Building Materials, 105 (2016) 206–217.

[10] K. Amini, I. Mehdipour, S-D. Hwang, M. Shekarchi "Effect of binder composition on time-dependent stability and robustness characteristics of self-consolidating mortar subjected to prolonged agitation" Construction and Building Materials 112 (2016) 654–665.

[11] M. Jesmani, A. Kasrania, M. Kamalzare, I. Mehdipour, "Undrained Vertical Bearing Capacity of Pile Located Near Soft Clay Slope", Journal of Engineering Research, 3 (3) (2015) 21–38.

[12] I. Mehdipour, N.A. Libre, M. Shekarchi, M. Khanjani, "Effect of Workability Characteristics on the Hardened Performance of FRSCCMs", Construction and Building Materials, 40 (2013) 611–621.

[13] I. Mehdipour, M. Vahdani, N.A. Libre, M. Shekarchi, "Relationship between Workability and Mechanical Properties of Fibre-Reinforced Self-Consolidating Mortar", Magazine of Concrete Research, 65(17) (2013) 1011–1022.

[14] I. Mehdipour, M.S. Razzaghi, K. Amini, M. Shekarchi, "Effect of Mineral Admixtures on Fluidity and Stability of Self-Consolidating Mortar Subjected to Prolonged Mixing Time", Construction and Building Materials, 40 (2013) 1029–1037.

[15] I. Mehdipour, M. Ghazavi, R.Z. Moayed, "Numerical Study on Stability Analysis of Geocell Reinforced Slopes by Considering the Bending Effect", Geotextiles and Geomembranes, 37 (2013) 23–34 (Recognized as top 10 most downloaded paper).

[16] R.Z. Moayed, I. Mehdipour, A. Judi, "Undrained Lateral Behavior of Short Pile Under Combination of Axial, Lateral and Moment Loading in Clayey Soils", Kuwait Journal of Science and Engineering, 39 (1B) (2012) 59–78.

[17] M. Jesmani, I. Mehdipour, A. Ajami, "Comparison between 2-D and 3-D Behaviour of Sheet Piles by Finite Element Method", Journal of science and engineering, 38(2B) (2011) 1–16.

[18] I. Mehdipour, N.A. Libre, M. Shekarchi, "Development of Fiber Reinforced SCM for Sustainable Construction", Journal of Structural Engineering and Geo-techniques, 1(1) (2011) 19–26.

Under Review

[19] I. Mehdipour, K.H. Khayat, “Enhancing the Performance of Calcium Sulfoaluminate Blended Cements with Shrinkage Reducing Admixture or Lightweight Sand” (Revision submitted to Cement and Concrete Composites).

[20] I. Mehdipour, K.H. Khayat, “Synergistic Effect of Moist Curing and Shrinkage Reducing Admixture on Expansion and Strength Evolution of Calcium Sulfoaluminate Blended Cement” (Under review in Materials and Structures).

[21] I. Mehdipour, R. Zoughi, K.H. Khayat, “Feasibility of using Near-Field Microwave Reflectometry for Monitoring Autogenous Crack Healing in Cementitious Materials” (Under review in Cement and Concrete Composites).

[22] I. Mehdipour, K.H. Khayat, “Elucidating the Role of Supplementary Cementitious Materials on Shrinkage and Restrained Shrinkage Cracking of Flowable Eco-Concrete” (Under review in Journal of Materials in Civil Engineering).

[23] I. Mehdipour, K.H. Khayat, “A Review on Understanding the Role of Particle Packing Characteristics in Cementitious Suspensions: Rheo-Physical Properties” (Under review in Construction and Building Materials).

[24] I. Mehdipour, K.H. Khayat, “Physico-mechanical Characteristics of Cement Paste over Transition from Concentrated to Flow State: The Role of Supplementary Cementitious Materials” (To be submitted to Cement and Concrete Composite).

Refereed Conference Proceedings

[1] I. Mehdipour, N.A. Libre, “Correlating Active Learning Questions to Student Performance through Their Responses to Querying Questions in Class” ASEE Annual Conference & Exposition, Columbus, Ohio, June 25-28, 2017 (abstract accepted).

[2] I. Mehdipour, N.A. Libre, K.H. Khayat, “Development of Eco-Friendly Superworkable Concrete Using Particle Packing Mix Design Methodology” Presented at American Concrete Institute (ACI) convention, Open Topic Session, Milwaukee, WI, April 17-21, 2016.

[3] I. Mehdipour, R. Zoughi, K. Khayat, “Monitoring of Self-Healing Capability in Cement-Based Mortar Using Near-Field Microwave Reflectometry—Preliminary Results,” Presented at the 25th American Society for Nondestructive Testing (ASNT) Spring Research Symposium, New Orleans, LA, April 11-14, 2016.

[4] I. Mehdipour, K.H. Khayat, “Shrinkage Mitigating Strategies for Low Shrinkage Self-Consolidating Concrete”, 6th North American Conference on Design and Use of Self-Consolidating Concrete, Washington, DC, May 15-18, 2016.

[5] K.H. Khayat, I. Mehdipour, “Optimization of Binder Compositions to Design Ecological Concrete: Wet Packing Density Approach”, ECO-CRETE, International Symposium on Sustainability, Iceland, August 13-15, 2014.

[6] I. Mehdipour, M. Horst, B. Conley, R. Zoughi, K.H. Khayat, “Determination of Steel Fiber Distribution in Cement-Based Materials Using Near-Field Microwave Method”, Presented at the 24th ASNT Research Symposium, California, USA, March 2015, pp. 164-165.

[7] A. Foudazi, I. Mehdipour, K.M. Donnell, K.H. Khayat, “Detection of Steel Fibers in Cement-Based Materials by Active Microwave Thermography”,14th International Symposium on Nondestructive Characterization of Materials, Marina del Rey California, June 22-26, 2015, pp. 22-26.

[8] S. Fakhretaha, R. B. Ardalan, N.A. Libre, I. Mehdipour, M. Shekarchi, “The Effect of Inert and Pozzolanic Powders on Properties of Self-Consolidating Mortar”, Proceedings of the Fifth North American Conference on the Design and Use of Self-Consolidating Concrete, Chicago, Illinois, USA, May 12–15, 2013.

[9] N. Nouri, M.H. Karimnezhad, I. Mehdipoure, M.R. Sohrabi, S.M. Noroozzadeh, “Influence of Chemical Admixtures on Fluidity And Stability of Self-Consolidating Mortar Subjected To Prolonged Agitating”, The fifth North American conference on the design and use of self-consolidating concrete, Chicago, USA, 2013.

[10] I. Mehdipoure, N. Nouri, M. H. Karimnezhad, H.R. Salehi, M. Shahrabadi, “Effect of Prolonged Mixing Time on Fresh and Hardened Properties of Self-Consolidating Mortar”, 7th international conference on self-compacting concrete and/or the 1st conference on rheology and processing of construction materials, Paris, 2013.

[11] I. Mehdipour, M.S. Razzaghi, K. Amini, “Correlation of Stability and Durability Performance of Self- Consolidating Mortar Containing Supplementary Cementitious Materials”. International Congress on Durability of Concrete, ICDC, Norway, 2012.

[12] I. Mehdipour, Sh. Karimzadeh, M.H. Karimnezhad, M. Khanjani, ”Effect of Glass Fiber on Mechanical Properties and De-Icing Salt Scaling Resistance of Decorative Self-Consolidating Cementitious Materials”, 8th RILEM international symposium on fibre reinforced concrete: challenges and opportunities, Portugal, 2012.

[13] I. Mehdipour, K. Amini, M. Khanjani, “Coupled Effects of Glass Fiber and Time on Fluidity and Stability of Self-Compacting Composites”, 8th RILEM international symposium on fibre reinforced concrete: challenges and opportunities, Portugal, 2012.

[14] R.Z. Moayed, M. Ghazavi, I. Mehdipour, ”Equivalent Composite Model of Geocell Reinforcement in Slope Stability Analysis”, 5th Asia-Pacific Conference on Unsaturated Soils, Pattaya, Thailand, 2011.

[15] I. Mehdipour, N.A. Libre, M. Vahdani, M. Shekarchi, "Effects of Polypropylene Fibers on the Stability of Self-Consolidating Engineered Cementitious Composites", In: 6th International RILEM Symposium on Self Consolidating Concrete, 2010, Montreal, Canada, pp. 1303-1312.

[16] A.A. Taheri, N.A. Libre, I. Mehdipour, M.H. Rokhforooz, ”Effect of Volume Fraction of Glass Fiber on Rheology and Shrinkage of Self-Consolidating Cement Paste", In: 6th International RILEM Symposium on Self Consolidating Concrete, 2010, Montreal, Canada, pp. 1313-1321.

[17] M. Vahdani, I. Mehdipour, S. Yusefi, “Effect of Viscosity Modifying Admixtures on the Rheological Properties and Stability of Self-Consolidating Cementitious Materials”, The 35th Conference on our world in concrete & structures Singapore, 2010.

[18] I. mehdipour, M. Vahdani; N. Nouri, “Effect of Nano-Silica Gel on Fresh and Hardened Properties of Self-Consolidating Cementetious Material”, 3rd International Congress on Nanoscience and Nanotechnology, Shiraz, Iran, 2010.

[19] I. mehdipour, M. Ghazavi, S. Abdolalizadeh, “Interaction of Drainage Blanket and Cut-Off Wall on Downstream Slope Cover in Homogeneous Earth Dams”, ICOLD, Kyoto, 2012.

[20] R.Z. Moayed, I. Mehdipour, A. Judi, "Numerical Modeling of The Combined Axial, Lateral And Moment Loading of Piles in Clayey Soils", International Conference Geotechnical Challenges in Megacities, Moscow, 2010.

[21] M. Ghazavi, R.Z. Moayed, I. Mehdipour, ”Numerical Modeling for Stability Analysis of Geocell Reinforced Slopes”, International Symposium on Deformation Characteristics of Geomaterials, Seoul, Korea, 2010.

[22] N.A. Libre, I. Mehdipour, A. Alinejad, N. Nouri, "Effect of Glass Fiber on Shrinkage and Mechanical Properties of Highly Flowable Cement Paste", 1st International Conference on Concrete Technology, Tabriz, Iran, 2009.

[23] I. Mehdipour, A. Sangtarashha, A. Shafieefar, N.A. Libre, M. Shekarchi, "Shrinkage of Highly Flowable Cement Paste Reinforced with Glass Fiber", Advanced concrete materials (ACM) international conference, Stellenbosch, South Africa, 2009.

[24] N.A. Libre, M. Shekarchi, I. Mehdipour, M. Dibaee, S. Moghaddam, "Rheological Properties of Polypropylene Fiber Reinforced Highly Flowable Mortar", Proceedings of 8th International Symposium on Utilization of High-Strength and High-Performance Concrete, Tokyo, Japan, 2008.

[25] N.A. Libre, I. Mehdipour, A. Sangtarashha, A. Shafieefar, M. Shekarchi, "Shrinkage of Highly Flowable Mortar Reinforced with Polypropylene Fiber", The 3rd Asian Concrete Federation International Conference, ACF/VCA, HoChi Minh city, Vietnam, 2008.

[26] N.A. Libre, I. Mehdipour, A. Alinejad, N. Nouri, "Rheological Properties of Glass Fiber Reinforced Highly Flowable Cement Paste" The 3rd Asian Concrete Federation International Conference, ACF/VCA 11-13 November, HoChi Minh city, Vietnam, 2008.

[27] N.A. Libre, A. Emdadi, I. Mehdipour, M. Vahdani, "SCC Mixtures with Different Aggregate Gradation and Limestone Powder", 5th international RILEM symposium on self-compacting concrete, Ghent, Belgium, 2007, pp. 155-162.

[28] A. Emdadi, N.A. Libre, I. Mehdipour, M. Vahdani, "Investigation on the Parameters That Influence Viscosity of Cement Paste", Advances in Cement Based Materials and Application to Civil Infrastructure, 12-14 December 2007, Lahor, Pakistan.

Technical Reports

[1] K.H. Khayat, I. Mehdipour, Economical and Crack-Free High Performance Concrete for Pavement and Transportation Infrastructure Constructions, Missouri Department of Transportation (MoDOT) and RE-CAST (REsearch on Concrete Applications for Sustainable Transportation) Tier-1 University Transportation Center (UTC), (No. TR2015-03), 2017.

[2] K.H. Khayat, I. Mehdipour, Design and Performance of Crack-Free Environmentally Friendly Concrete "Crack-Free Eco-Crete", National University Transportation Center, (No. NUTC R322), 2014.

[3] M. Shekarchi, N.A. Libre, I. Mehdipour, "Lightweight dry mix mortar", LECA Company 2012.

[4] M. Shekarchi, N.A. Libre, I. Mehdipour, "Lightweight concrete on steel deck", LECA Company, 2012.

[5] M. Shekarchi, N.A. Libre, F. Sabet, I. Mehdipour, "Guidelines for concreting in hot weather" MAPNA Company, Iran, 2012.

BIBLIOGRAPHY

Aim, R. B., and Le Goff, P. (1968). “Effet de paroi dans les empilements désordonnés de sphères et application à la porosité de mélanges binaires.” *Powder Technology*, 1(5), 281–290.

Aïssoun, B. M., Hwang, S.-D., and Khayat, K. H. (2016). “Influence of aggregate characteristics on workability of superworkable concrete.” *Materials and Structures*, 49(1–2), 597–609.

Aktan, H. M., Fu, G., Dekelbab, W., and Attanayaka, U. (2003). *Investigate causes & develop methods to minimize early-age deck cracking on Michigan bridge decks*.

Aldea, C.-M., Song, W.-J., Popovics, J. S., and Shah, S. P. (2000). “Extent of healing of cracked normal strength concrete.” *Journal of materials in civil engineering*, 12(1), 92–96.

Alexander, M., and Mindess, S. (2010). *Aggregates in concrete*. CRC Press.

Al-Rousan, T., Masad, E., Tutumluer, E., and Pan, T. (2007). “Evaluation of image analysis techniques for quantifying aggregate shape characteristics.” *Construction and Building Materials*, 21(5), 978–990.

Alshibli, K. A., Druckrey, A. M., Al-Raoush, R. I., Weiskittel, T., and Lavrik, N. V. (2014). “Quantifying morphology of sands using 3D imaging.” *Journal of Materials in Civil Engineering*, 27(10), 04014275.

Annual Book of ASTM Standards. (n.d.). American Society for Testing and Materials, West Conshohocken, PA.

Antoni, M., Rossen, J., Martirena, F., and Scrivener, K. (2012). “Cement substitution by a combination of metakaolin and limestone.” *Cement and Concrete Research*, 42(12), 1579–1589.

Arora, A., Sant, G., and Neithalath, N. (2016). “Ternary blends containing slag and interground/blended limestone: Hydration, strength, and pore structure.” *Construction and Building Materials*, 102, 113–124.

Artioli, G., Valentini, L., Voltolini, M., Dalconi, M. C., Ferrari, G., and Russo, V. (2014). “Direct imaging of nucleation mechanisms by synchrotron diffraction micro-tomography: superplasticizer-induced change of C–S–H nucleation in cement.” *Crystal Growth & Design*, 15(1), 20–23.

Asaga, K., and Roy, D. M. (1980). “Rheological properties of cement mixes: IV. Effects of superplasticizers on viscosity and yield stress.” *Cement and Concrete Research*, 10(2), 287–295.

ASCE. (2013). “Failure to Act, The Impact of Current Infrastructure Investment on America’s Economic Future.” American Society of Civil Engineers (ASCE).

Assaad, J., Khayat, K. H., and Mesbah, H. (2003). “Assessment of thixotropy of flowable and self-consolidating concrete.” *ACI Materials Journal*, 100(2), 99–107.

Bentz, D. P. (1997). “Three-Dimensional Computer Simulation of Portland Cement Hydration and Microstructure Development.” *Journal of the American Ceramic Society*, 80(1), 3–21.

Bentz, D. P. (2006a). “Influence of water-to-cement ratio on hydration kinetics: simple models based on spatial considerations.” *Cement and Concrete Research*, 36(2), 238–244.

Bentz, D. P. (2006b). “Influence of shrinkage-reducing admixtures on early-age properties of cement pastes.” *Journal of Advanced Concrete Technology*, 4(3), 423–429.

Bentz, D. P., Barrett, T., De la Varga, I., and Weiss, W. J. (2012a). “Relating compressive strength to heat release in mortars.” *Advances in Civil Engineering Materials*, 1(1), 1–14.

Bentz, D. P., Ferraris, C. F., Galler, M. A., Hansen, A. S., and Guynn, J. M. (2012b). “Influence of particle size distributions on yield stress and viscosity of cement–fly ash pastes.” *Cement and Concrete Research*, 42(2), 404–409.

Bentz, D. P., and Garboczi, E. J. (1991). “Percolation of phases in a three-dimensional cement paste microstructural model.” *Cement and Concrete Research*, 21(2–3), 325–344.

Bentz, D. P., and Jensen, O. M. (2004). “Mitigation strategies for autogenous shrinkage cracking.” *Cement and Concrete Composites*, 26(6), 677–685.

Bentz, D. P., Snyder, K. A., Cass, L. C., and Peltz, M. A. (2008). “Doubling the service life of concrete structures. I: Reducing ion mobility using nanoscale viscosity modifiers.” *Cement and Concrete Composites*, 30(8), 674–678.

Bessa, I. S., Branco, V. T. C., and Soares, J. B. (2012). “Evaluation of different digital image processing software for aggregates and hot mix asphalt characterizations.” *Construction and building materials*, 37, 370–378.

Bethmont, S. (2005). “Self-compacting concretes segregation mechanisms-Experimental study of granular interactions.” Ecole des Ponts ParisTech.

Bingham, E. C. (1922). *Fluidity and plasticity*. McGraw-Hill Book Compny, Incorporated.

Bishnoi, S., and Scrivener, K. L. (2009). “μic: A new platform for modelling the hydration of cements.” *Cement and Concrete Research*, 39(4), 266–274.

Bogas, J. A., Gomes, M. G., and Gomes, A. (2013). “Compressive strength evaluation of structural lightweight concrete by non-destructive ultrasonic pulse velocity method.” *Ultrasonics*, 53(5), 962–972.

Bogue, R. H. (1947). *The chemistry of Portland cement*. Reinhold publishing corporation.

Bois, K., Benally, A. D., Nowak, P. S., and Zoughi, R. (1999). “Application of near-field microwave sensing techniques for aggregate segregation detection in concrete members.” *Proceedings of the Twenty-sixth Annual Review of Progress in Quantitative Nondestructive Evaluation*, 19, 1717–1722.

Bois, K. J., Benally, A. D., Nowak, P. S., and Zoughi, R. (1998). “Cure-state monitoring and water-to-cement ratio determination of fresh Portland cement-based materials using near-field microwave techniques.” *IEEE transactions on Instrumentation and Measurement*, 47(3), 628–637.

Bois, K. J., Benally, A. D., and Zoughi, R. (2000). “Microwave near-field reflection property analysis of concrete for material content determination.” *IEEE transactions on instrumentation and measurement*, 49(1), 49–55.

Bouasker, M., Khalifa, N. E. H., Mounanga, P., and Kahla, N. B. (2014). “Early-age deformation and autogenous cracking risk of slag–limestone filler-cement blended binders.” *Construction and Building Materials*, 55, 158–167.

Boumiz, A., Vernet, C., and Tenoudji, F. C. (1996). “Mechanical properties of cement pastes and mortars at early ages: evolution with time and degree of hydration.” *Advanced cement based materials*, 3(3), 94–106.

Bouzoubaa, N., and Lachemi, M. (2001). “Self-compacting concrete incorporating high volumes of class F fly ash: Preliminary results.” *Cement and Concrete Research*, 31(3), 413–420.

Brouwers, H. J. H., and Radix, H. J. (2005). “Self-compacting concrete: theoretical and experimental study.” *Cement and Concrete Research*, 35(11), 2116–2136.

Cepuritis, R., Garboczi, E. J., and Jacobsen, S. (2017). “Three dimensional shape analysis of concrete aggregate fines produced by VSI crushing.” *Powder Technology*, 308, 410–421.

Chan, K. W., and Kwan, A. K. H. (2014). “Evaluation of particle packing models by comparing with published test results.” *particuology*, 16, 108–115.

Chandrappa, A. K., and Biligiri, K. P. (n.d.). “Influence of mix parameters on pore properties and modulus of pervious concrete: an application of ultrasonic pulse velocity.” *Materials and Structures*, 1–17.

Charlton, S. R., Macklin, C. L., and Parkhurst, D. L. (1997). “PHREEQCI—a graphical user interface for the geochemical computer program PHREEQC.” *US Geological Survey Water-Resources Investigations Report*, 9.

Chaunsali, P., and Mondal, P. (2015a). “Influence of mineral admixtures on early-age behavior of calcium sulfoaluminate cement.” *ACI Mater. J*, 112(1), 59–68.

Chaunsali, P., and Mondal, P. (2015b). “Influence of calcium sulfoaluminate (CSA) cement content on expansion and hydration behavior of various ordinary portland cement-CSA blends.” *Journal of the American Ceramic Society*, 98(8), 2617–2624.

Cheung, J., Jeknavorian, A., Roberts, L., and Silva, D. (2011). “Impact of admixtures on the hydration kinetics of Portland cement.” *Cement and Concrete Research*, 41(12), 1289–1309.

Chong, J. S., Christiansen, E. B., and Baer, A. D. (1971). “Rheology of concentrated suspensions.” *Journal of applied polymer science*, 15(8), 2007–2021.

Clear, C. A. (1985). *The effects of autogenous healing upon the leakage of water through cracks in concrete*.

Collepardi, M. (1998). “Admixtures used to enhance placing characteristics of concrete.” *Cement and concrete composites*, 20(2–3), 103–112.

Collepardi, M., Turriziani, R., and Marcialis, A. (1972). “The paste hydration of 4CaO· 3Al 2 O 3· SO 3 in presence of calcium sulphate, tricalcium silicate and dicalcium silicate.” *Cement and Concrete Research*, 2(2), 213–223.

Cox, M. R., and Budhu, M. (2008). “A practical approach to grain shape quantification.” *Engineering Geology*, 96(1), 1–16.

Damidot, D., Lothenbach, B., Herfort, D., and Glasser, F. P. (2011). “Thermodynamics and cement science.” *Cement and Concrete Research*, 41(7), 679–695.

Damtoft, J. S., Lukasik, J., Herfort, D., Sorrentino, D., and Gartner, E. M. (2008). “Sustainable development and climate change initiatives.” *Cement and concrete research*, 38(2), 115–127.

Day, K. W. (1999). *Concrete mix design, quality control and specification E&FN Spon*. London.

De Larrard, F. (1999). *Concrete mixture proportioning: a scientific approach*. CRC Press.

De Larrard, F., and Sedran, T. (2002). “Mixture-proportioning of high-performance concrete.” *Cement and concrete research*, 32(11), 1699–1704.

De Weerdt, K., Haha, M. B., Le Saout, G., Kjellsen, K. O., Justnes, H., and Lothenbach, B. (2011). “Hydration mechanisms of ternary Portland cements containing limestone powder and fly ash.” *Cement and Concrete Research*, 41(3), 279–291.

DelRio-Prat, M., Vega-Zamanillo, A., Castro-Fresno, D., and Calzada-Pérez, M. Á. (2011). “Energy consumption during compaction with a Gyratory Intensive Compactor Tester. Estimation models.” *Construction and Building Materials*, 25(2), 979–986.

Dewar, J. (2002). *Computer modelling of concrete mixtures*. CRC Press.

Diamond, S., Sahu, S., and Thaulow, N. (2004). “Reaction products of densified silica fume agglomerates in concrete.” *Cement and concrete research*, 34(9), 1625–1632.

Donnell, K. M., Zoughi, R., and Kurtis, K. E. (2013). “Demonstration of microwave method for detection of alkali–silica reaction (ASR) gel in cement-based materials.” *Cement and Concrete Research*, 44, 1–7.

Ebrahimkhanlou, A., Farhidzadeh, A., and Salamone, S. (2016). “Multifractal analysis of crack patterns in reinforced concrete shear walls.” *Structural Health Monitoring*, 15(1), 81–92.

Edvardsen, C. (1999). “Water permeability and autogenous healing of cracks in concrete.” *ACI Materials Journal-American Concrete Institute*, 96(4), 448–454.

Elizalde, M. P., and Aparicio, J. L. (1995). “Current theories in the calculation of activity coefficients—II. Specific interaction theories applied to some equilibria studies in solution chemistry.” *Talanta*, 42(3), 395–400.

Emdadi, A., Mehdipour, I., Libre, N. A., and Shekarchi, M. (2015). “Optimized workability and mechanical properties of FRCM by using fiber factor approach: theoretical and experimental study.” *Materials and Structures*, 48(4), 1149–1161.

Erdem, T. K., Khayat, K. H., and Yahia, A. (2009). “Correlating rheology of self-consolidating concrete to corresponding concrete-equivalent mortar.” *ACI Materials Journal*, 106(2), 154.

Esmaeilkhanian, B., Diederich, P., Khayat, K. H., Yahia, A., and Wallevik, Ó. (2017a). “Influence of particle lattice effect on stability of suspensions: application to self-consolidating concrete.” *Materials and Structures*, 50(1), 39.

Esmaeilkhanian, B., Khayat, K. H., and Wallevik, O. H. (2017b). “Mix design approach for low-powder self-consolidating concrete: Eco-SCC—content optimization and performance.” *Materials and Structures*, 50(2), 124.

Esmaeilkhanian, B., Khayat, K. H., Yahia, A., and Feys, D. (2014). “Effects of mix design parameters and rheological properties on dynamic stability of self-consolidating concrete.” *Cement and Concrete Composites*, 54, 21–28.

Fennis, S., Walraven, J. C., and Den Uijl, J. A. (2013a). “Compaction-interaction packing model: regarding the effect of fillers in concrete mixture design.” *Materials and structures*, 46(3), 463–478.

Fennis, S., Walraven, J. C., and Den Uijl, J. A. (2013b). “Defined-performance design of ecological concrete.” *Materials and structures*, 46(4), 639–650.

Ferrara, L., Krelani, V., and Moretti, F. (2016). “Autogenous healing on the recovery of mechanical performance of High Performance Fibre Reinforced Cementitious Composites (HPFRCCs): Part 2–Correlation between healing of mechanical performance and crack sealing.” *Cement and Concrete Composites*, 73, 299–315.

Ferrari, L., Kaufmann, J., Winnefeld, F., and Plank, J. (2011). “Multi-method approach to study influence of superplasticizers on cement suspensions.” *Cement and Concrete Research*, 41(10), 1058–1066.

Flatt, R. J., and Houst, Y. F. (2001). “A simplified view on chemical effects perturbing the action of superplasticizers.” *Cement and concrete research*, 31(8), 1169–1176.

Fonseca, J., O’Sullivan, C., Coop, M. R., and Lee, P. D. (2012). “Non-invasive characterization of particle morphology of natural sands.” *Soils and Foundations*, 52(4), 712–722.

Foudazi, A., Mehdipour, I., Donnell, K. M., and Khayat, K. H. (n.d.). “Evaluation of steel fiber distribution in cement-based mortars using active microwave thermography.” *Materials and Structures*, 1–15.

Friedman, S. P. (1998). “A saturation degree-dependent composite spheres model for describing the effective dielectric constant of unsaturated porous media.” *Water Resources Research*, 34(11), 2949–2961.

Fung, W. W. S., and Kwan, A. K. H. (2014). “Effect of particle interlock on flow of aggregate through opening.” *Powder Technology*, 253, 198–206.

Funk, J. E., and Dinger, D. (2013). *Predictive process control of crowded particulate suspensions: applied to ceramic manufacturing*. Springer Science & Business Media.

Garboczi, E. J., and Bullard, J. W. (2013). “Contact function, uniform-thickness shell volume, and convexity measure for 3D star-shaped random particles.” *Powder technology*, 237, 191–201.

Garbout, A., Munkholm, L. J., and Hansen, S. B. (2013). “Temporal dynamics for soil aggregates determined using X-ray CT scanning.” *Geoderma*, 204, 15–22.

Geiker, M. R., Brandl, M., Thrane, L. N., and Nielsen, L. F. (2002). “On the effect of coarse aggregate fraction and shape on the rheological properties of self-compacting concrete.” *Cement, concrete and aggregates*, 24(1), 3–6.

Genovese, D. B. (2012). “Shear rheology of hard-sphere, dispersed, and aggregated suspensions, and filler-matrix composites.” *Advances in colloid and interface science*, 171, 1–16.

Ghasr, M. T., Simms, D., and Zoughi, R. (2009). “Multimodal solution for a waveguide radiating into multilayered structures—Dielectric property and thickness evaluation.” *IEEE Transactions on Instrumentation and Measurement*, 58(5), 1505–1513.

Goltermann, P., Johansen, V., and Palbøl, L. (1997). “Packing of aggregates: an alternative tool to determine the optimal aggregate mix.” *ACI Materials Journal*, 94(5), 435–443.

Hafid, H., Ovarlez, G., Toussaint, F., Jezequel, P. H., and Roussel, N. (2016). “Effect of particle morphological parameters on sand grains packing properties and rheology of model mortars.” *Cement and Concrete Research*, 80, 44–51.

Hashemi, A., Donnell, K. M., Zoughi, R., Knapp, M. C. L., and Kurtis, K. E. (2014). “Microwave detection of carbonation in mortar using dielectric property characterization.” *Instrumentation and Measurement Technology Conference (I2MTC) Proceedings, 2014 IEEE International*, IEEE, 216–220.

Hashemi, A., Horst, M., Kurtis, K. E., Donnell, K. M., and Zoughi, R. (2015). “Comparison of alkali–silica reaction gel behavior in mortar at microwave frequencies.” *IEEE Transactions on Instrumentation and Measurement*, 64(7), 1907–1915.

Hendriks, C. A., Worrell, E., De Jager, D., Blok, K., and Riemer, P. (1998). “Emission reduction of greenhouse gases from the cement industry.” *Proceedings of the fourth international conference on greenhouse gas control technologies*, 939–944.

Hodne, H., and Saasen, A. (2000). “The effect of the cement zeta potential and slurry conductivity on the consistency of oil-well cement slurries.” *Cement and Concrete Research*, 30(11), 1767–1772.

Holt, E. E. (2001). *Early age autogenous shrinkage of concrete*. Technical Research Centre of Finland.

Homma, D., Mihashi, H., and Nishiwaki, T. (2009). “Self-healing capability of fibre reinforced cementitious composites.” *Journal of Advanced Concrete Technology*, 7(2), 217–228.

Hooton, R. D., and Bickley, J. A. (2014). “Design for durability: the key to improving concrete sustainability.” *Construction and Building Materials*, 67, 422–430.

Huang, H. (2014). “Thermodynamics of autogenous self-healing in cementitious materials.”

Hunger, M. (2010). “An integral design concept for ecological self-compacting concrete.”

Hüsken, G., and Brouwers, H. J. H. (2008). “A new mix design concept for earth-moist concrete: A theoretical and experimental study.” *Cement and Concrete Research*, 38(10), 1246–1259.

Hüsken, G., and Brouwers, H. J. H. (2012). “On the early-age behavior of zero-slump concrete.” *Cement and Concrete Research*, 42(3), 501–510.

Hüsken, G. G. (2010). “A multifunctional design approach for sustainable concrete: with application to concrete mass products.” Technische Universiteit Eindhoven.

In, C.-W., Holland, R. B., Kim, J.-Y., Kurtis, K. E., Kahn, L. F., and Jacobs, L. J. (2013). “Monitoring and evaluation of self-healing in concrete using diffuse ultrasound.” *NDT & E International*, 57, 36–44.

Jacobsen, S., Marchand, J., and Boisvert, L. (1996). “Effect of cracking and healing on chloride transport in OPC concrete.” *Cement and Concrete Research*, 26(6), 869–881.

Jacobsen, S., Marchand, J., and Hornain, H. (1995). “SEM observations of the microstructure of frost deteriorated and self-healed concretes.” *Cement and Concrete Research*, 25(8), 1781–1790.

Jansen, D., Neubauer, J., Goetz-Neunhoeffer, F., Haerzschel, R., and Hergeth, W.-D. (2012). “Change in reaction kinetics of a portland cement caused by a superplasticizer—Calculation of heat flow curves from XRD data.” *Cement and Concrete Research*, 42(2), 327–332.

Jaroenratanapirom, D., and Sahamitmongkol, R. (2011). “Self-crack closing ability of mortar with different additives.” *Journal of Metals, Materials and Minerals*, 21(1), 9–17.

Jeffrey, D. J., and Acrivos, A. (1976). “The rheological properties of suspensions of rigid particles.” *AIChE Journal*, 22(3), 417–432.

Jensen, O. M., and Hansen, P. F. (2001). “Water-entrained cement-based materials: I. Principles and theoretical background.” *Cement and concrete research*, 31(4), 647–654.

Jiang, Z., Li, W., and Yuan, Z. (2015). “Influence of mineral additives and environmental conditions on the self-healing capabilities of cementitious materials.” *Cement and Concrete Composites*, 57, 116–127.

Jones, M. R., Zheng, L., and Newlands, M. D. (2002). “Comparison of particle packing models for proportioning concrete constitutents for minimum voids ratio.” *Materials and structures*, 35(5), 301–309.

Juenger, M. C., and Siddique, R. (2015). “Recent advances in understanding the role of supplementary cementitious materials in concrete.” *Cement and Concrete Research*, 78, 71–80.

Kan, L.-L., Shi, H.-S., Sakulich, A. R., and Li, V. C. (2010). “Self-healing characterization of engineered cementitious composite materials.” *ACI Materials Journal*, 107(6), 617.

Kappi, A., and Nordenswan, E. (2007). “Workability of no-slump concrete.” *Concrete international*, 29(03), 37–41.

Karpov, I. K., Chudnenko, K. V., Kulik, D. A., Avchenko, O. V., and Bychinskii, V. A. (2001). “Minimization of Gibbs free energy in geochemical systems by convex programming.” *Geochemistry International*, 39(11), 1108–1119.

Kasselouri, V., Tsakiridis, P., Malami, C., Georgali, B., and Alexandridou, C. (1995). “A study on the hydration products of a non-expansive sulfoaluminate cement.” *Cement and concrete research*, 25(8), 1726–1736.

Kevern, J. T., Schaefer, V. R., and Wang, K. (2009). “Evaluation of pervious concrete workability using gyratory compaction.” *Journal of Materials in Civil Engineering*, 21(12), 764–770.

Khayat, K. H. (1999). “Workability, testing, and performance of self-consolidating concrete.” *ACI materials journal*, 96, 346–353.

Khayat, K. H., and Assaad, J. J. (2006). “Effect of w/cm and high-range water-reducing admixture on formwork pressure and thixotropy of self-consolidating concrete.” *ACI materials journal*, 103(3), 186.

Khayat, K. H., Eng, P., and Mehdipour, I. (2014). “Design and Performance of Crack-Free Environmentally Friendly Concrete ‘Crack-Free Eco-Crete.’” *Report NUTC R322*.

Khayat, K. H., and Libre, P. N. A. (2014). *Roller Compacted Concrete: Field Evaluation and Mixture Optimization*.

Kim, H. T., and Frederick Jr, W. J. (1988). “Evaluation of Pitzer ion interaction parameters of aqueous mixed electrolyte solutions at 25. degree. C. 2. Ternary mixing parameters.” *Journal of Chemical and Engineering Data*, 33(3), 278–283.

Kirby, D. M., and Biernacki, J. J. (2012). “The effect of water-to-cement ratio on the hydration kinetics of tricalcium silicate cements: testing the two-step hydration hypothesis.” *Cement and Concrete Research*, 42(8), 1147–1156.

Kirk, R. S., and Mallett, W. J. (2013). “Highway bridge conditions: Issues for Congress.” *Rep. No. R43103*.

Knop, Y., and Peled, A. (2016). “Packing density modeling of blended cement with limestone having different particle sizes.” *Construction and Building Materials*, 102, 44–50.

Koenders, E. A. B. (1997). “Simulation of volume changes in hardening cement-based materials.” TU Delft, Delft University of Technology.

Komba, J., Anochie-Boateng, J., and van der Merwe Steyn, W. (2013). “Analytical and laser scanning techniques to determine shape properties of aggregates.” *Transportation Research Record: Journal of the Transportation Research Board*, (2335), 60–71.

Koukkari, P., and Pajarre, R. (2006). “Calculation of constrained equilibria by Gibbs energy minimization.” *Calphad*, 30(1), 18–26.

Koukkari, P., and Pajarre, R. (2011). “A Gibbs energy minimization method for constrained and partial equilibria.” *Pure and Applied Chemistry*, 83(6), 1243–1254.

Krautkrämer, J., and Krautkrämer, H. (2013). *Ultrasonic testing of materials*. Springer Science & Business Media.

Krieger, I. M., and Dougherty, T. J. (1959). “A mechanism for non-Newtonian flow in suspensions of rigid spheres.” *Transactions of the Society of Rheology*, 3(1), 137–152.

Kulik, D. A., Wagner, T., Dmytrieva, S. V., Kosakowski, G., Hingerl, F. F., Chudnenko, K. V., and Berner, U. R. (2013). “GEM-Selektor geochemical modeling package: revised algorithm and GEMS3K numerical kernel for coupled simulation codes.” *Computational Geosciences*, 17(1), 1–24.

Kumar, A., Oey, T., Falla, G. P., Henkensiefken, R., Neithalath, N., and Sant, G. (2013a). “A comparison of intergrinding and blending limestone on reaction and strength evolution in cementitious materials.” *Construction and Building Materials*, 43, 428–435.

Kumar, A., Oey, T., Kim, S., Thomas, D., Badran, S., Li, J., Fernandes, F., Neithalath, N., and Sant, G. (2013b). “Simple methods to estimate the influence of limestone fillers on reaction and property evolution in cementitious materials.” *Cement and Concrete Composites*, 42, 20–29.

Kwan, A. K. H., Chan, K. W., and Wong, V. (2013). “A 3-parameter particle packing model incorporating the wedging effect.” *Powder technology*, 237, 172–179.

Kwan, A. K. H., and Wong, H. H. C. (2008). “Packing density of cementitious materials: part 2—packing and flow of OPC+ PFA+ CSF.” *Materials and structures*, 41(4), 773–784.

Kwan, A. K. H., Wong, V., and Fung, W. W. S. (2015). “A 3-parameter packing density model for angular rock aggregate particles.” *Powder Technology*, 274, 154–162.

Kwan, A. K., Mora, C. F., and Chan, H. C. (1999). “Particle shape analysis of coarse aggregate using digital image processing.” *Cement and Concrete Research*, 29(9), 1403–1410.

Lebron, I., Robinson, D. A., Goldberg, S., and Lesch, S. M. (2004). “The dielectric permittivity of calcite and arid zone soils with carbonate minerals.” *Soil Science Society of America Journal*, 68(5), 1549–1559.

Lecomte, A., Mechling, J.-M., and Diliberto, C. (2009). “Compaction index of cement paste of normal consistency.” *Construction and Building Materials*, 23(10), 3279–3286.

Lee, K. M., Lee, H. K., Lee, S. H., and Kim, G. Y. (2006). “Autogenous shrinkage of concrete containing granulated blast-furnace slag.” *Cement and Concrete Research*, 36(7), 1279–1285.

Li, G., and Zhao, X. (2003). “Properties of concrete incorporating fly ash and ground granulated blast-furnace slag.” *Cement and Concrete Composites*, 25(3), 293–299.

Li, L. G., and Kwan, A. K. (2013). “Concrete mix design based on water film thickness and paste film thickness.” *Cement and Concrete Composites*, 39, 33–42.

Lim, S. N., and Wee, T. H. (2000). “Autogenous shrinkage of ground-granulated blast-furnace slag concrete.” *Materials Journal*, 97(5), 587–593.

Liu, D.-M. (2000). “Particle packing and rheological property of highly-concentrated ceramic suspensions: φm determination and viscosity prediction.” *Journal of materials science*, 35(21), 5503–5507.

Liu, S., Bundur, Z. B., Zhu, J., and Ferron, R. D. (2016). “Evaluation of self-healing of internal cracks in biomimetic mortar using coda wave interferometry.” *Cement and Concrete Research*, 83, 70–78.

Lothenbach, B. (2013). “Hydration of blended cements.” *Cement-Based Materials for Nuclear Waste Storage*, Springer, 33–41.

Lothenbach, B., Le Saout, G., Gallucci, E., and Scrivener, K. (2008a). “Influence of limestone on the hydration of Portland cements.” *Cement and Concrete Research*, 38(6), 848–860.

Lothenbach, B., Le Saout, G., Gallucci, E., and Scrivener, K. (2008b). “Influence of limestone on the hydration of Portland cements.” *Cement and Concrete Research*, 38(6), 848–860.

Lothenbach, B., Scrivener, K., and Hooton, R. D. (2011). “Supplementary cementitious materials.” *Cement and Concrete Research*, 41(12), 1244–1256.

Lothenbach, B., and Winnefeld, F. (2006). “Thermodynamic modelling of the hydration of Portland cement.” *Cement and Concrete Research*, 36(2), 209–226.

Maes, M., Snoeck, D., and De Belie, N. (2016). “Chloride penetration in cracked mortar and the influence of autogenous crack healing.” *Construction and Building Materials*, 115, 114–124.

Mahaut, F., Chateau, X., Coussot, P., and Ovarlez, G. (2008a). “Yield stress and elastic modulus of suspensions of noncolloidal particles in yield stress fluids.” *Journal of Rheology*, 52(1), 287–313.

Mahaut, F., Mokeddem, S., Chateau, X., Roussel, N., and Ovarlez, G. (2008b). “Effect of coarse particle volume fraction on the yield stress and thixotropy of cementitious materials.” *Cement and concrete research*, 38(11), 1276–1285.

Martinie, L., Rossi, P., and Roussel, N. (2010). “Rheology of fiber reinforced cementitious materials: classification and prediction.” *Cement and Concrete Research*, 40(2), 226–234.

Masoero, E., Thomas, J. J., and Jennings, H. M. (2014). “A Reaction Zone Hypothesis for the Effects of Particle Size and Water-to-Cement Ratio on the Early Hydration Kinetics of C3S.” *Journal of the American Ceramic Society*, 97(3), 967–975.

Matschei, T., Lothenbach, B., and Glasser, F. P. (2007a). “The role of calcium carbonate in cement hydration.” *Cement and Concrete Research*, 37(4), 551–558.

Matschei, T., Lothenbach, B., and Glasser, F. P. (2007b). “The AFm phase in Portland cement.” *Cement and Concrete Research*, 37(2), 118–130.

Matschei, T., Lothenbach, B., and Glasser, F. P. (2007c). “Thermodynamic properties of Portland cement hydrates in the system CaO–Al 2 O 3–SiO 2–CaSO 4–CaCO 3–H 2 O.” *Cement and Concrete Research*, 37(10), 1379–1410.

Mehdipour, I., Horst, M., Zoughi, R., and Khayat, K. H. (2017a). “Use of Near-Field Microwave Reflectometry to Evaluate Steel Fiber Distribution in Cement-Based Mortars.” *Journal of Materials in Civil Engineering*, 04017029.

Mehdipour, I., and Khayat, K. H. (2016a). “Effect of supplementary cementitious material content and binder dispersion on packing Density and compressive strength of sustainable cement paste.” *ACI Materials Journal*, 113(3).

Mehdipour, I., and Khayat, K. H. (2016b). “Effect of Supplementary Cementitious Material Content and Binder Dispersion on Packing Density and Compressive Strength of Sustainable Cement Paste.” *ACI Materials Journal*, 113(3).

Mehdipour, I., and Khayat, K. H. (2017). “Effect of particle-size distribution and specific surface area of different binder systems on packing density and flow characteristics of cement paste.” *Cement and Concrete Composites*, 78, 120–131.

Mehdipour, I., Kumar, A., and Khayat, K. H. (2017b). “Rheology, hydration, and strength evolution of interground limestone cement containing PCE dispersant and high volume supplementary cementitious materials.” *Materials & Design*.

Mehdipour, I., and Libre, N. A. (2017). “Linking Fiber Factor to Material Performance of Fiber-Reinforced Self-Consolidating Cement-Based Materials.” *ACI Materials Journal*, 114(1).

Mehdipour, I., Razzaghi, M. S., Amini, K., and Shekarchi, M. (2013). “Effect of mineral admixtures on fluidity and stability of self-consolidating mortar subjected to prolonged mixing time.” *Construction and Building Materials*, 40, 1029–1037.

Mehdipour, I., Vahdani, M., Amini, K., and Shekarchi, M. (2016). “Linking stability characteristics to material performance of self-consolidating concrete-equivalent-mortar incorporating fly ash and metakaolin.” *Construction and Building Materials*, 105, 206–217.

Mehta, P. K. (1986). “Concrete. Structure, properties and materials.”

Meng, W., Lunkad, P., Kumar, A., and Khayat, K. (2016). “Influence of Silica Fume and PCE Dispersant on Hydration Mechanisms of Cement.” *The Journal of Physical Chemistry C*.

Mikanovic, N., Leclerc, A., Ponge, A., and Khayat, K. H. (2010). “Workability characteristics and performance criteria for design and control of super workable concrete.” *Design, Production and Placement of Self-Consolidating Concrete*, Montreal, Canada, 527–573.

Mitchell, D. R. G., Hinczak, I., and Day, R. A. (1998). “Interaction of silica fume with calcium hydroxide solutions and hydrated cement pastes.” *Cement and Concrete Research*, 28(11), 1571–1584.

Moini, M., Flores-Vivian, I., Amirjanov, A., and Sobolev, K. (2015). “The optimization of aggregate blends for sustainable low cement concrete.” *Construction and Building Materials*, 93, 627–634.

Monteiro, P. (2006). *Concrete: Microstructure, Properties, and Materials*. McGraw-Hill Publishing.

Mubarak, K., Bois, K. J., and Zoughi, R. (2001). “A simple, robust, and on-site microwave technique for determining water-to-cement ratio (w/c) of fresh Portland cement-based materials.” *IEEE Transactions on instrumentation and Measurement*, 50(5), 1255–1263.

Mueller, F. V. (2012). “Design criteria for low-binder self-compacting concrete. ECO-SCC.” PhD thesis. Reykjavik University, Iceland.

Mueller, F. V., Wallevik, O. H., and Khayat, K. H. (2014). “Linking solid particle packing of Eco-SCC to material performance.” *Cement and Concrete Composites*, 54, 117–125.

Na, S. H., Hama, Y., Taniguchi, M., Katsura, O., Sagawa, T., and Zakaria, M. (2012). “Experimental investigation on reaction rate and self-healing ability in fly ash blended cement mixtures.” *Journal of Advanced Concrete Technology*, 10(7), 240–253.

Nanthagopalan, P., and Santhanam, M. (2012). “An empirical approach for the optimisation of aggregate combinations for self-compacting concrete.” *Materials and structures*, 45(8), 1167–1179.

Nehdi, M., Pardhan, M., and Koshowski, S. (2004). “Durability of self-consolidating concrete incorporating high-volume replacement composite cements.” *Cement and Concrete Research*, 34(11), 2103–2112.

Neville, A. M., and Brooks, J. J. (1987). *Concrete technology*.

Oey, T., Kumar, A., Bullard, J. W., Neithalath, N., and Sant, G. (2013). “The filler effect: the influence of filler content and surface area on cementitious reaction rates.” *Journal of the American Ceramic Society*, 96(6), 1978–1990.

Okamura, H., and Ouchi, M. (2003). “Self-compacting concrete.” *Journal of advanced concrete technology*, 1(1), 5–15.

Parkhurst, D. L., Appelo, C. A. J., and others. (1999). “User’s guide to PHREEQC (Version 2): A computer program for speciation, batch-reaction, one-dimensional transport, and inverse geochemical calculations.”

Peer, S., Case, J. T., Gallaher, E., Kurtis, K. E., and Zoughi, R. (2003). “Microwave reflection and dielectric properties of mortar subjected to compression force and cyclically exposed to water and sodium chloride solution.” *IEEE Transactions on Instrumentation and Measurement*, 52(1), 111–118.

Pitzer, K. S. (1973). “Thermodynamics of electrolytes. I. Theoretical basis and general equations.” *The Journal of Physical Chemistry*, 77(2), 268–277.

Popovics, S., Rose, J. L., and Popovics, J. S. (1990). “The behaviour of ultrasonic pulses in concrete.” *Cement and Concrete Research*, 20(2), 259–270.

Powers, T. C. (1958). “Structure and physical properties of hardened Portland cement paste.” *Journal of the American Ceramic Society*, 41(1), 1–6.

Powers, T. C. (1969). “The properties of fresh concrete.”

Puerta-Falla, G., Balonis, M., Le Saout, G., Falzone, G., Zhang, C., Neithalath, N., and Sant, G. (2015a). “Elucidating the role of the aluminous source on limestone reactivity in cementitious materials.” *Journal of the American Ceramic Society*, 98(12), 4076–4089.

Puerta-Falla, G., Kumar, A., Gomez-Zamorano, L., Bauchy, M., Neithalath, N., and Sant, G. (2015b). “The influence of filler type and surface area on the hydration rates of calcium aluminate cement.” *Construction and Building Materials*, 96, 657–665.

Qaddoumi, N., and Zoughi, R. (1997). “Preliminary study of the influences of effective dielectric constant and nonuniform probe aperture field distribution on near field microwave images.” *Materials evaluation*, 55(10), 1169–1173.

Qian, S., Zhou, J., De Rooij, M. R., Schlangen, E., Ye, G., and Van Breugel, K. (2009). “Self-healing behavior of strain hardening cementitious composites incorporating local waste materials.” *Cement and Concrete Composites*, 31(9), 613–621.

Rajabipour, F., Sant, G., and Weiss, J. (2008). “Interactions between shrinkage reducing admixtures (SRA) and cement paste’s pore solution.” *Cement and Concrete Research*, 38(5), 606–615.

Ramge, P., Proske, T., and Kühne, H.-C. (2010). “Segregation of coarse aggregates in self-compacting concrete.” *Design, production and placement of self-consolidating concrete*, Springer, 113–125.

Reiner, M. (1949). *Deformation and flow: an elementary introduction to theoretical rheology*. HK Lewis.

Reinhardt, H.-W., and Jooss, M. (2003). “Permeability and self-healing of cracked concrete as a function of temperature and crack width.” *Cement and Concrete Research*, 33(7), 981–985.

Roquier, G. (2016). “The 4-parameter Compressible Packing Model (CPM) including a new theory about wall effect and loosening effect for spheres.” *Powder Technology*, 302, 247–253.

Roussel, N. (2006). “A theoretical frame to study stability of fresh concrete.” *Materials and structures*, 39(1), 81–91.

Roussel, N., Lemaître, A., Flatt, R. J., and Coussot, P. (2010). “Steady state flow of cement suspensions: a micromechanical state of the art.” *Cement and Concrete Research*, 40(1), 77–84.

Roussel, N., Ovarlez, G., Garrault, S., and Brumaud, C. (2012). “The origins of thixotropy of fresh cement pastes.” *Cement and Concrete Research*, 42(1), 148–157.

Şahmaran, M., Keskin, S. B., Ozerkan, G., and Yaman, I. O. (2008). “Self-healing of mechanically-loaded self consolidating concretes with high volumes of fly ash.” *Cement and Concrete Composites*, 30(10), 872–879.

Sahmaran, M., Yildirim, G., and Erdem, T. K. (2013). “Self-healing capability of cementitious composites incorporating different supplementary cementitious materials.” *Cement and Concrete Composites*, 35(1), 89–101.

Sakai, Y., Kitagawa, Y., Fukuta, T., and Iiba, M. (2003). “Experimental study on enhancement of self-restoration of concrete beams using SMA wire.” *Smart Structures and Materials*, International Society for Optics and Photonics, 178–186.

Sant, G., Eberhardt, A., Bentz, D., and Weiss, J. (2010). “Influence of shrinkage-reducing admixtures on moisture absorption in cementitious materials at early ages.” *Journal of Materials in Civil Engineering*, 22(3), 277–286.

Sant, G., Lothenbach, B., Juilland, P., Le Saout, G., Weiss, J., and Scrivener, K. (2011). “The origin of early age expansions induced in cementitious materials containing shrinkage reducing admixtures.” *Cement and concrete research*, 41(3), 218–229.

Santomaso, A., Lazzaro, P., and Canu, P. (2003). “Powder flowability and density ratios: the impact of granules packing.” *Chemical Engineering Science*, 58(13), 2857–2874.

Saric-Coric, M., Liotta, F., and Khayat, K. H. (2002). “Influence of thixotropy on stability characteristics of cement grout and concrete.” *ACI Materials Journal*, 99(3), 234–241.

Schneider, M., Romer, M., Tschudin, M., and Bolio, H. (2011). “Sustainable cement production—present and future.” *Cement and Concrete Research*, 41(7), 642–650.

See, H. T., Attiogbe, E. K., and Miltenberger, M. A. (2003). “Shrinkage cracking characteristics of concrete using ring specimens.” *ACI Materials Journal*, 100(3).

See, H. T., Attiogbe, E. K., and Miltenberger, M. A. (2004). “Potential for restrained shrinkage cracking of concrete and mortar.” *Cement, concrete and aggregates*, 26(2), 1–8.

Shen, W., Yang, Z., Cao, L., Cao, L., Liu, Y., Yang, H., Lu, Z., and Bai, J. (2016). “Characterization of manufactured sand: Particle shape, surface texture and behavior in concrete.” *Construction and Building Materials*, 114, 595–601.

Shh, S. P., Krguller, M. E., and Sarigaphuti, M. (1992). “Effects of shrinkage-reducing admixtures on restrained shrinkage cracking of concrete.” *Materials Journal*, 89(3), 289–295.

Shilstone, J. S., and others. (1990). “Concrete mixture optimization.” *Concrete International*, 12(6), 33–39.

Sisomphon, K., Copuroglu, O., and Koenders, E. A. B. (2013). “Effect of exposure conditions on self healing behavior of strain hardening cementitious composites incorporating various cementitious materials.” *Construction and Building Materials*, 42, 217–224.

Snoeck, D., and De Belie, N. (2012). “Mechanical and self-healing properties of cementitious composites reinforced with flax and cottonised flax, and compared with polyvinyl alcohol fibres.” *biosystems engineering*, 111(4), 325–335.

Snoeck, D., and De Belie, N. (2015). “From straw in bricks to modern use of microfibers in cementitious composites for improved autogenous healing–A review.” *Construction and Building Materials*, 95, 774–787.

Snoeck, D., Dewanckele, J., Cnudde, V., and De Belie, N. (2016). “X-ray computed microtomography to study autogenous healing of cementitious materials promoted by superabsorbent polymers.” *Cement and Concrete Composites*, 65, 83–93.

Stoian, J., Oey, T., Bullard, J. W., Huang, J., Kumar, A., Balonis, M., Terrill, J., Neithalath, N., and Sant, G. (2015). “New insights into the prehydration of cement and its mitigation.” *Cement and Concrete Research*, 70, 94–103.

Stovall, T., De Larrard, F., and Buil, M. (1986). “Linear packing density model of grain mixtures.” *Powder Technology*, 48(1), 1–12.

Suh, H. S., Kim, K. Y., Lee, J., and Yun, T. S. (2017). “Quantification of bulk form and angularity of particle with correlation of shear strength and packing density in sands.” *Engineering Geology*, 220, 256–265.

Sun, Y., Indraratna, B., and Nimbalkar Dr, S. (2014). “Three-dimensional characterisation of particle size and shape for ballast.”

Sun, Z., Ye, G., Shah, S. P., and others. (2005). “Microstructure and early-age properties of Portland cement paste–effects of connectivity of solid phases.” *ACI materials journal*, 102(2), 122–129.

Tang, W., Kardani, O., and Cui, H. (2015). “Robust evaluation of self-healing efficiency in cementitious materials–a review.” *Construction and Building Materials*, 81, 233–247.

Termkhajornkit, P., Nawa, T., Nakai, M., and Saito, T. (2005). “Effect of fly ash on autogenous shrinkage.” *Cement and Concrete Research*, 35(3), 473–482.

Thomas, J. J. (2007). “A new approach to modeling the nucleation and growth kinetics of tricalcium silicate hydration.” *Journal of the American Ceramic Society*, 90(10), 3282–3288.

Thomas, J. J., Biernacki, J. J., Bullard, J. W., Bishnoi, S., Dolado, J. S., Scherer, G. W., and Luttge, A. (2011). “Modeling and simulation of cement hydration kinetics and microstructure development.” *Cement and Concrete Research*, 41(12), 1257–1278.

Toufar, W., Klose, E., and Born, M. (1977). “Berechnung der packungsdichte von korngemischen.” *Aufbereitung-Technik*, 11, 603–608.

Toutanji, H., Delatte, N., Aggoun, S., Duval, R., and Danson, A. (2004). “Effect of supplementary cementitious materials on the compressive strength and durability of short-term cured concrete.” *Cement and Concrete Research*, 34(2), 311–319.

Toutou, Z., and Roussel, N. (2006). “Multi scale experimental study of concrete rheology: from water scale to gravel scale.” *Materials and Structures*, 39(2), 189–199.

Ulaby, F. T., Moore, R. K., and Fung, A. K. (1986). “Microwave remote sensing active and passive-volume III: from theory to applications.”

Valentini, L., Favero, M., Dalconi, M. C., Russo, V., Ferrari, G., and Artioli, G. (2016). “Kinetic model of calcium-silicate hydrate nucleation and growth in the presence of PCE superplasticizers.” *Crystal Growth & Design*, 16(2), 646–654.

Van Breugel, K. (1991). *Simulation of hydration and formation of structure in hardening cement-based materials*. TU Delft, Delft University of Technology.

Van Der Putten, J., Dils, J., Minne, P., Boel, V., and De Schutter, G. (2017). “Determination of packing profiles for the verification of the compressible packing model in case of UHPC pastes.” *Materials and Structures*, 50(2), 118.

Van Tittelboom, K. (2012). “Self-Healing Concrete through Incorporation of Encapsulated Bacteria-or Polymer-Based Healing Agents (’Zelfhelend beton door incorporatie van ingekapselde bacteri.” Ghent University.

Van Tittelboom, K., and De Belie, N. (2013). “Self-healing in cementitious materials—A review.” *Materials*, 6(6), 2182–2217.

Van Tittelboom, K., De Belie, N., De Muynck, W., and Verstraete, W. (2010). “Use of bacteria to repair cracks in concrete.” *Cement and Concrete Research*, 40(1), 157–166.

Van Tittelboom, K., De Belie, N., Lehmann, F., and Grosse, C. U. (2012). “Acoustic emission analysis for the quantification of autonomous crack healing in concrete.” *Construction and Building Materials*, 28(1), 333–341.

Vance, K., Aguayo, M., Oey, T., Sant, G., and Neithalath, N. (2013a). “Hydration and strength development in ternary Portland cement blends containing limestone and fly ash or metakaolin.” *Cement and Concrete Composites*, 39, 93–103.

Vance, K., Arora, A., Sant, G., and Neithalath, N. (2015). “Rheological evaluations of interground and blended cement–limestone suspensions.” *Construction and Building Materials*, 79, 65–72.

Vance, K., Kumar, A., Sant, G., and Neithalath, N. (2013b). “The rheological properties of ternary binders containing Portland cement, limestone, and metakaolin or fly ash.” *Cement and Concrete Research*, 52, 196–207.

Verwey, E. J. W., and Overbeek, J. T. G. (1955). “Theory of the stability of lyophobic colloids.” *Journal of Colloid Science*, 10(2), 224–225.

Villani, C., Spragg, R., Pour-Ghaz, M., and Jason Weiss, W. (2014). “The influence of pore solutions properties on drying in cementitious materials.” *Journal of the American Ceramic Society*, 97(2), 386–393.

Vincze, J., Valiskó, M., and Boda, D. (2010). “The nonmonotonic concentration dependence of the mean activity coefficient of electrolytes is a result of a balance between solvation and ion-ion correlations.” *The Journal of chemical physics*, 133(15), 154507.

Vuk, T., Tinta, V., Gabrovšek, R., and Kaučič, V. (2001). “The effects of limestone addition, clinker type and fineness on properties of Portland cement.” *Cement and Concrete Research*, 31(1), 135–139.

Wadell, H. (1933). “Sphericity and roundness of rock particles.” *The Journal of Geology*, 41(3), 310–331.

Wallevik, O. H., Feys, D., Wallevik, J. E., and Khayat, K. H. (2015). “Avoiding inaccurate interpretations of rheological measurements for cement-based materials.” *Cement and Concrete Research*, 78, 100–109.

Wallevik, O. H., Mueller, F. V., Hjartarson, B., and Kubens, S. (2009). “The green alternative of self compacting concrete.” *Eco-SCC, iBausil, Germany*.

Wang, L., Wang, X., Mohammad, L., and Abadie, C. (2005). “Unified method to quantify aggregate shape angularity and texture using Fourier analysis.” *Journal of Materials in Civil Engineering*, 17(5), 498–504.

Wang, X., Wang, K., Taylor, P., and Morcous, G. (2014). “Assessing particle packing based self-consolidating concrete mix design method.” *Construction and Building Materials*, 70, 439–452.

Watanabe, T., Fujiwara, Y., Hashimoto, C., and Ishimaru, K. (2011). “Evaluation of self healing effect in fly-ash concrete by ultrasonic test method.” *International Journal of Modern Physics B*, 25(31), 4307–4310.

Weiss, J., Lura, P., Rajabipour, F., and Sant, G. (2008). “Performance of shrinkage-reducing admixtures at different humidities and at early ages.” *ACI Materials Journal*, 105(5), 478–486.

Westerholm, M., Lagerblad, B., Silfwerbrand, J., and Forssberg, E. (2008). “Influence of fine aggregate characteristics on the rheological properties of mortars.” *Cement and Concrete Composites*, 30(4), 274–282.

Williams, D. A., Saak, A. W., and Jennings, H. M. (1999). “The influence of mixing on the rheology of fresh cement paste.” *Cement and Concrete Research*, 29(9), 1491–1496.

Wittmann, F. H. (1976). “On the action of capillary pressure in fresh concrete.” *Cement and Concrete Research*, 6(1), 49–56.

Wong, H. H. C., and Kwan, A. K. H. (2008a). “Rheology of cement paste: role of excess water to solid surface area ratio.” *Journal of materials in civil engineering*, 20(2), 189–197.

Wong, H. H., and Kwan, A. K. (2008b). “Packing density of cementitious materials: part 1—measurement using a wet packing method.” *Materials and structures*, 41(4), 689–701.

Wong, V., Wai Chan, K., and Kwok Hung Kwan, A. (2013). “Applying theories of particle packing and rheology to concrete for sustainable development.” *Organization, Technology & Management in Construction: An International Journal*, 5(2), 844–851.

Worrell, E., Price, L., Martin, N., Hendriks, C., and Meida, L. O. (2001). “Carbon dioxide emissions from the global cement industry 1.” *Annual Review of Energy and the Environment*, 26(1), 303–329.

Wu, C.-Y., Ruddy, O. M., Bentham, A. C., Hancock, B. C., Best, S. M., and Elliott, J. A. (2005). “Modelling the mechanical behaviour of pharmaceutical powders during compaction.” *Powder Technology*, 152(1), 107–117.

Wu, M., Johannesson, B., and Geiker, M. (2012). “A review: Self-healing in cementitious materials and engineered cementitious composite as a self-healing material.” *Construction and Building Materials*, 28(1), 571–583.

Yahia, A., and Khayat, K. H. (1998). “Simple field tests to characterize fluidity and washout resistance of structural cement grout.” *Cement, concrete and aggregates*, 20(1), 145–156.

Yammine, J., Chaouche, M., Guerinet, M., Moranville, M., and Roussel, N. (2008). “From ordinary rhelogy concrete to self compacting concrete: A transition between frictional and hydrodynamic interactions.” *Cement and Concrete Research*, 38(7), 890–896.

Yang, Y., Lepech, M. D., Yang, E.-H., and Li, V. C. (2009a). “Autogenous healing of engineered cementitious composites under wet–dry cycles.” *Cement and Concrete Research*, 39(5), 382–390.

Yang, Y., Lepech, M. D., Yang, E.-H., and Li, V. C. (2009b). “Autogenous healing of engineered cementitious composites under wet–dry cycles.” *Cement and Concrete Research*, 39(5), 382–390.

Yildirim, G., Aras, G. H., Banyhussan, Q. S., Şahmaran, M., and Lachemi, M. (2015). “Estimating the self-healing capability of cementitious composites through non-destructive electrical-based monitoring.” *Ndt & E International*, 76, 26–37.

Yu, A. B., Bridgwater, J., and Burbidge, A. (1997). “On the modelling of the packing of fine particles.” *Powder technology*, 92(3), 185–194.

Yu, A. B., Feng, C. L., Zou, R. P., and Yang, R. Y. (2003). “On the relationship between porosity and interparticle forces.” *Powder Technology*, 130(1), 70–76.

Yu, A. B., and Standish, N. (1993). “Characterisation of non-spherical particles from their packing behaviour.” *Powder technology*, 74(3), 205–213.

Yu, A. B., Zou, R. P., and Standish, N. (1996). “Modifying the linear packing model for predicting the porosity of nonspherical particle mixtures.” *Industrial & engineering chemistry research*, 35(10), 3730–3741.

Yu, A.-B., Standish, N., and McLean, A. (1993). “Porosity calculation of binary mixtures of nonspherical particles.” *Journal of the American Ceramic Society*, 76(11), 2813–2816.

Yu, Q. L., Spiesz, P., and Brouwers, H. J. H. (2013). “Development of cement-based lightweight composites–Part 1: mix design methodology and hardened properties.” *Cement and Concrete Composites*, 44, 17–29.

Yu, R., Spiesz, P., and Brouwers, H. J. H. (2014). “Mix design and properties assessment of ultra-high performance fibre reinforced concrete (UHPFRC).” *Cement and concrete research*, 56, 29–39.

Yu, R., Spiesz, P., and Brouwers, H. J. H. (2015). “Development of an eco-friendly Ultra-High Performance Concrete (UHPC) with efficient cement and mineral admixtures uses.” *Cement and Concrete Composites*, 55, 383–394.

Zhang, T., Yu, Q., Wei, J., and Zhang, P. (2011). “Effects of size fraction on composition and fundamental properties of Portland cement.” *Construction and Building Materials*, 25(7), 3038–3043.

Zhang, T., Yu, Q., Wei, J., and Zhang, P. (2012). “Efficient utilization of cementitious materials to produce sustainable blended cement.” *Cement and Concrete Composites*, 34(5), 692–699.

Zhang, Y., and Kong, X. (2015). “Correlations of the dispersing capability of NSF and PCE types of superplasticizer and their impacts on cement hydration with the adsorption in fresh cement pastes.” *Cement and Concrete Research*, 69, 1–9.

Zhang, Y.-R., Kong, X.-M., Lu, Z.-B., Lu, Z.-C., and Hou, S.-S. (2015). “Effects of the charge characteristics of polycarboxylate superplasticizers on the adsorption and the retardation in cement pastes.” *Cement and Concrete Research*, 67, 184–196.

Zhao, M., Zhang, X., and Zhang, Y. (2016). “Effect of free water on the flowability of cement paste with chemical or mineral admixtures.” *Construction and Building Materials*, 111, 571–579.

Zheng, J., and Hryciw, R. D. (2015). “Traditional soil particle sphericity, roundness and surface roughness by computational geometry.” *Géotechnique*, 65(6), 494–506.

Zheng, J., and Hryciw, R. D. (2016). “Roundness and sphericity of soil particles in assemblies by computational geometry.” *Journal of Computing in Civil Engineering*, 30(6), 04016021.

Zhong, W., and Yao, W. (2008). “Influence of damage degree on self-healing of concrete.” *Construction and building materials*, 22(6), 1137–1142.

Zingg, A., Winnefeld, F., Holzer, L., Pakusch, J., Becker, S., and Gauckler, L. (2008). “Adsorption of polyelectrolytes and its influence on the rheology, zeta potential, and microstructure of various cement and hydrate phases.” *Journal of Colloid and Interface Science*, 323(2), 301–312.

Zoughi, R. (2012). *Microwave non-destructive testing and evaluation principles*. Springer Science & Business Media.

Zoughi, R., Gray, S. D., and Nowak, P. S. (1995). “Microwave nondestructive estimation of cement paste compressive strength.” *Materials Journal*, 92(1), 64–70.

VITA

Iman Mehdipour was born in July, 1985 in Tehran, Iran. He received his B.S. and M.S. degrees in civil engineering, with emphasis in construction material from Azad University of Qazvin, Iran and International University of Qazvin, Iran, in August 2009 and 2012, respectively. He was one of the recipients of best outgoing students for his overall academic performance. His research was focused on the design of innovative structural materials, such as self-consolidating concrete and fiber-reinforced composites with adapted rheology. In March 2013, Iman was admitted into Ph.D. program in Civil Engineering at the Missouri University of Science and Technology under the supervision of Professor Kamal H. Khayat. His main research interests included the design of innovative advanced cement-based materials, such as crack-free concrete materials with adapted rheology, as well as nondestructive testing (NDT) techniques. He was given the opportunity to perform an interdisciplinary collaborative research project, in conjunction with the Missouri S&T electrical engineering department, to evaluate fiber distribution in concrete using microwave and thermography NDT techniques.

Iman worked as an engineer at the Construction Materials Institute (CMI) in Iran for six years. He served as a lecturer for undergraduates at Azad University in Iran for one year. As a research specialist in Civil Engineering and Construction Research Center (CCRC) at Azad University, Iman mentored nearly 20 undergraduate researchers, some of whom are currently studying in the U.S. He was a member of ACI committee 237, Self-Consolidating Concrete. He was assigned as a session chair for 25^{th} and 26^{th} American Society for Nondestructive Testing (ASNT) Research Symposiums. Over the span of his education, he authored and co-authored two books, 18 peer-reviewed journal articles, and 30 conference proceedings. His research efforts and professional services were recognized with several awards. He received the ACI Missouri Chapter Honorary Abdeldjelil “DJ” Belarbi Scholarship, travel grant award for 24^{th} ASNT Research Symposium, and outstanding young researcher award at Azad University. In July 2017, he received his Ph.D. degree in Civil Engineering from Missouri University of Science and Technology, Rolla, Missouri.